John Orcutt *Editor*

Earth System Monitoring

Selected Entries from the Encyclopedia of Sustainability Science and Technology

Springer

Earth System Monitoring

This volume collects selected topical entries from the *Encyclopedia of Sustainability Science and Technology* (ESST). ESST addresses the grand challenges for science and engineering today. It provides unprecedented, peer-reviewed coverage of sustainability science and technology with contributions from nearly 1,000 of the world's leading scientists and engineers, who write on more than 600 separate topics in 38 sections. ESST establishes a foundation for the research, engineering, and economics supporting the many sustainability and policy evaluations being performed in institutions worldwide.

John Orcutt
Editor

Earth System Monitoring

Selected Entries from the Encyclopedia of Sustainability Science and Technology

Springer

Editor
John Orcutt
Scripps Institution of Oceanography
University of California, San Diego
9500 Gilman Drive
La Jolla, CA 92093, USA

This book consists of selections from the Encyclopedia of Sustainability Science and Technology edited by Robert A. Meyers, originally published by Springer Science +Business Media New York in 2012. The contribution "Remote Sensing Applications to Ocean and Human Health" originally appeared as part of the Oceans and Human Health section, edited by Darrell Jay Grimes.

ISBN 978-1-4614-5683-4 ISBN 978-1-4614-5684-1 (eBook)
DOI 10.1007/978-1-4614-5684-1
Springer New York Heidelberg Dordrecht London

Library of Congress Control Number: 2012954277

Printed on acid-free paper

Springer is part of Springer Science+Business Media (www.springer.com)

Contents

Chapter 1
Earth System Monitoring, Introduction

John Orcutt

This section provides sensing and data collection methodologies, as well as an understanding of Earth's climate parameters and natural and man-made phenomena, to support a scientific assessment of the Earth system as a whole, and its response to natural and human-induced changes. The coverage ranges from climate change factors and extreme weather and fires to oil spill tracking and volcanic eruptions. This serves as a basis to enable improved prediction and response to climate change, weather, and natural hazards as well as dissemination of the data and conclusions. The data collection systems include satellite remote sensing, aerial surveys, and land- and ocean-based monitoring stations. Our objective in this treatise is to provide a significant portion of the scientific and engineering basis of Earth system monitoring and to provide this in 17 detailed articles or chapters written at a level for use by university students through practicing professionals. The reader is also directed to the closely related sections on Ecological Systems, Introduction and also Climate Change Modeling Methodology, Introduction as well as Climate Change Remediation, Introduction to. For ease of use by students, each article begins with a glossary of terms, while at an average length of 25 print pages each, sufficient detail is presented for use by professionals in government, universities, and industries. The chapters are individually summarized below.

Aircraft and Space Atmospheric Measurements Using Differential Absorption Lidar (DIAL) – A particular lidar technique called differential absorption lidar (DIAL) has proven to be an especially powerful method to measure atmospheric chemical species. It has been used both on the ground and in many aircraft to

This chapter, which has been modified slightly for the purposes of this volume, was originally published as part of the Encyclopedia of Sustainability Science and Technology edited by Robert A. Meyers. DOI:10.1007/978-1-4419-0851-3

J. Orcutt (✉)
Scripps Institution of Oceanography, University of California, San Diego,
9500 Gilman Drive, La Jolla, CA 92093, USA
e-mail: jorcutt@ucsd.edu

J. Orcutt (ed.), *Earth System Monitoring: Selected Entries from the Encyclopedia of Sustainability Science and Technology*, DOI 10.1007/978-1-4614-5684-1_1,

determine the concentration of gasses. DIAL systems can be deployed in fixed ground locations, in either piloted or unpiloted aircraft or in satellite platforms.

Coral Reef Ecosystems – Over the millennia, coral reef ecosystems have served as the basis of human survival and sustenance in many coastal areas in the tropics and subtropics. They are significant geologic formations that provide crucial protection from destructive forces of the sea. They also harbor the greatest diversity of animal phyla of any other habitat on the planet. Threats due to climate change are detailed.

Airborne and Space-borne Remote Sensing of Cryosphere – The cryosphere broadly constitutes all the components of the Earth system, which contain water in a frozen state. As such, glaciers, ice sheets, snow cover, lake and river ice, sea ice, and permafrost make up the terrestrial oceanic elements of the cryosphere. While ice particles in the upper atmosphere and icy precipitation near the surface are the representative members of the Cryosphere in atmospheric systems. Airborne and spaceborne remote sensing technologies are presented.

Heat Content and Temperature of the Ocean – Following years of research and development in autonomous float technology, major international cooperation under the Argo Project led to the seeding of the global ocean with more than 3,000 floats each with the capability of profiling temperature and other properties between depths of 2,000 m and the surface approximately every 10 days. Measurements are relayed by satellite while the floats are at the surface in between each cycle of ascent and descent. Coverage is almost global. Measuring variability in sea level using satellite altimetry in situ temperature observations are complementary in efforts to infer changes in heat content.

Hurricane and Monsoon Tracking with Driftsondes – During the international African Monsoon Multidisciplinary Analysis (AMMA) project, high flying balloons (called driftsondes) dropping meteorological sondes to take measurements over remote, but scientifically important locations, were deployed over West Africa and tropical Atlantic to study weak weather systems, called African easterly waves, that serve as seedlings for hurricanes.

Large-Scale Ocean Circulation: Deep Circulation and Meridional Overturning – Observations from long-term moorings and deep floats have illustrated a dynamic deep ocean environment, with energetic variability observed at a wide range of space and time scales, including narrow jets, eddies, and recirculating gyres.

Long-Term Ecological Research Network – The US Long Term Ecological Research (LTER) Network is the largest and longest-lived ecological network in the continental United States. Designed to provide long-term data from a broad range of key ecosystems, the LTER Network represents a unique national resource for addressing pressing environmental issues such as climate change, loss of biodiversity, and changes in patterns of land use.

Ocean Acidification – The oceans have absorbed about one third of the anthropogenic carbon emissions, which in part ameliorates global warming induced by human activity. However, this capacity to absorb CO_2 is challenged by the accelerated increase in human activities including the increasing burning of fossil fuels, cement production, agriculture, and deforestation. The accelerated rate of increase in the concentration of atmospheric CO_2 and the parallel rise in dissolved

CO_2 in seawater (and the associated chemical changes) can affect marine life. For example, increases in CO_2 can potentially disrupt the acid base balance in tissues, fluids, and cells of marine organisms.

Ocean Evaporation and Precipitation – Taken as a whole, the hydrological cycle is characterized by the evaporation of about half a million cubic kilometers of water per year, the bulk of which (86%) is from the ocean, with only 14% originating in the continents. The vast majority of the water that evaporates from the oceans (90%) is precipitated back into them, while the remaining 10% is transported to the continents, where it precipitates. About two thirds of this precipitation is recycled over the continents and only one third runs off directly into the oceans. This chapter covers the distribution of evaporation from the ocean and precipitation, oceanic heat reservoirs and evaporation, oceanic evaporation and monsoonal precipitation regimes, and the response of the relationship between evaporation and precipitation.

Ocean Observatories and Information: Building a Global Ocean Observing Network – Ocean observatories are collections of networks of sensors that are deployed to sample the ocean physics, chemistry, and biology. The goal of these networks is to overcome chronic under-sampling of the oceans by providing sustained measurements in space and time. The data collected by these networks are used to address a range of basic and applied research questions, hindered by a lack of data. This chapter covers the need for a global ocean observing network, design considerations, platforms, and information systems.

Oil Spill Remote Sensing – Remote sensing for oil spills is reviewed. The technical aspects of sensors are considered and the benefits and limitations of each sensor are assessed. Oil spill response often requires that remote sensing be used to detect, map and track the spill of interest. A wide variety of technologies are covered.

The Gravity Recovery and Climate Experiment (GRACE) Detection of Ice Mass Loss, Terrestrial Mass Changes, and Ocean Mass Gains – The gravity field of Earth, caused by the distribution of masses inside and on the surface of Earth, changes in time due to the redistribution of mass. Such mass fluxes can be due both to natural processes (such as the seasonal water cycle, ocean dynamics, or atmospheric variations), as well as due to human actions, such as the systematic withdrawal of groundwater for human consumption. The GRACE satellite pair has provided the first global measurements at horizontal resolutions from 300 km to global, and time scales from 10 days to interannual. These measurements have been used to assess the mass variability in the oceans, terrestrial water storage, and loss of ice mass in glaciers and ice sheets. Long-term trends, episodic variations such as result from large earthquakes, and seasonal changes have all been measured with unprecedented accuracy and detail.

Remote Sensing of Natural Disasters – Remote sensing involves the use of instruments to study phenomena from a distance. Natural disasters derive from hazards such as volcanoes, flooding, earthquake fires, and weather. Practically speaking, “remote sensing of natural disasters” principally refers to the use of airborne or spaceborne sensors to study natural disasters for detecting, modeling, predicting, analyzing, and mitigating effects on human populations and activities.

Satellite instruments can provide imagery of large areas of Earth's surface and overflights can often easily provide data for hard to access locations (either due to terrain, weather, or causes of the disaster itself). Airborne instruments can also provide much of the same utility from remote sensing with the potential advantages of greater loiter or dwell time and rapid response.

Remote Sensing of Ocean Color – The oceans cover over 70% of Earth's surface and the life inhabiting the oceans play an important role in shaping Earth's climate. Phytoplankton, the microscopic organisms in the surface ocean, are responsible for half of the photosynthesis on the planet. These organisms at the base of the food web take up light and carbon dioxide and fix carbon into biological structures releasing oxygen. Estimating the amount of microscopic phytoplankton and their associated primary productivity over the vast expanses of the ocean is extremely challenging from ships. However, as phytoplankton take up light for photosynthesis, they change the color of the surface ocean from blue to green. Such shifts in ocean color can be measured from sensors placed high above the sea on satellites or aircraft and are called "ocean color remote sensing." In open ocean waters, the ocean color is predominantly driven by the phytoplankton concentration and ocean color remote sensing has been used to estimate the amount of chlorophyll *a*, the primary light-absorbing pigment in all phytoplankton.

Earth System Environmental Literacy – This chapter details the standards of ecological, environmental, and science literacy needed by the public to support decisions involved with assessing climate change data and predictions and taking the required actions.

Contemporary Sea Level Variations, Observations and Causes – Sea-level change is a very sensitive index of climate change and variability. For example, as the ocean warms in response to global warming, seawaters expand, and thus sea level rises. When mountain glaciers melt in response to increasing air temperature, sea level rises because of freshwater mass input to the oceans. Similarly, ice mass loss from the ice sheets causes sea-level rise. Corresponding increases in freshwater transport into the oceans changes water salinity, hence seawater density as well as ocean circulation that in turn affects sea level and its spatial variability. Since the early 1990s, satellite altimetry has become the main tool for precisely and continuously measuring sea level with nearly global coverage and a few days revisit time. Compared to tide gauges which provide sea level relative to the ground, satellite altimetry measures "absolute" sea-level variations. The main factors causing current global mean sea-level rise are thermal expansion of seawaters, land ice loss, and freshwater mass exchange between oceans and land water reservoirs. These contributions vary in response to natural climate variability and to global climate change induced by anthropogenic greenhouse gas emissions.

Volcanoes, Observations and Impact – Volcanoes are critical geologic hazards that challenge our ability to make long-term forecasts of their eruptive behaviors. They also have direct and indirect impacts on human lives and society. As is the case with many geologic phenomena, the time scales over which volcanoes evolve greatly exceed that of a human lifetime. On the other hand, the time scale over which a volcano can move from inactivity to eruption can be rather short: months, weeks,

days, and even hours. Thus, the scientific study and monitoring of volcanoes is essential to mitigate risk as well as measure the influx of gasses and particulates into the atmosphere. There are thousands of volcanoes on Earth, and it is impractical to study and implement ground-based monitoring at them all. Fortunately, there are other effective means for volcano monitoring, including increasing capabilities for satellite-based technologies. The focus of this chapter is mainly on geophysical observations of volcanoes and calderas as they pertain to eruption forecasting and prediction.

To complete the coverage of this volume, we are pleased to have a contribution on Remote Sensing Applications to Ocean and Human Health.

Chapter 2
Airborne and Space-borne Remote Sensing of Cryosphere

Kenneth C. Jezek

Glossary

Cryosphere	Those components of the Earth system that contain water in its frozen form.
Radar	Radio detection and ranging systems.
Lidar	Light detection and ranging systems.
Radiometers	Radio frequency receivers designed to detect emitted radiation from a surface and in accordance with Planck's law.
Synthetic aperture radar	Radar system which increases along track resolution by using the motion of the platform to synthesize a large antenna.
Permafrost	Persistently frozen ground.
Ice sheet	Continental-scale, freshwater ice cover that deforms under its own weight.
Sea ice	Saline ice formed when ocean water freezes.
Glaciers	Long, channelized, slabs of freshwater ice thick enough to deform under their own weight.
Seasonal snow	The annual snow that blankets land cover in the winter and melts by summer.

This chapter was originally published as part of the Encyclopedia of Sustainability Science and Technology edited by Robert A. Meyers. DOI:10.1007/978-1-4419-0851-3

K.C. Jezek (✉)
Byrd Polar Research Center, School of Earth Sciences, The Ohio State University, 1090, Carmack Road, Columbus, OH, USA
e-mail: jezek.1@osu.edu

J. Orcutt (ed.), *Earth System Monitoring: Selected Entries from the Encyclopedia of Sustainability Science and Technology*, DOI 10.1007/978-1-4614-5684-1_2,

Definition of the Subject: The Cryosphere

The Cryosphere broadly constitutes all the components of the Earth system which contain water in a frozen state [1]. As such, glaciers, ice sheets, snow cover, lake and river ice, and permafrost make up the terrestrial elements of the Cryosphere. Sea ice in all of its forms, frozen sea bed and icebergs constitute the oceanic elements of the Cryosphere while ice particles in the upper atmosphere and icy precipitation near the surface are the representative members of the Cryosphere in atmospheric systems. This overarching definition of Earth's cryosphere immediately implies that substantial portions of Earth's land and ocean surfaces are directly subject in some fashion to cryospheric processes. Through globally interacting processes such as the inevitable transfer of heat from the warm equatorial oceans to the cold polar latitudes, it seems reasonable to argue that all regions of Earth are influenced by cryospheric processes and their integration into the modern climate of the planet. Observations of the cryosphere necessary to predict future variability in Earth's ice cover and its interaction with other Earth systems must be made on commensurate spatial and temporal scales. Consequently, airborne and space-borne remote sensing technologies with global reach play a key role in acquiring data necessary to understand the important physical processes and earth system interactions that govern the evolution of the Cryosphere (Fig. 2.1).

Introduction

The broad spatial and seasonally changing distribution of ice plays an important role in earth systems and human activities. At high latitudes, ice covered land and ocean surfaces are highly reflective thus redirecting incoming solar radiation back into space in the summer months. Indeed, reductions in the spatial area of snow and ice cover are believed to be an important feedback mechanism that enhances warming at high latitudes [2, 3]. Essentially, reduced snow and ice cover exposes darker land and ocean surfaces that retain rather than reflect solar energy. This results in increased warming and hence a further decrease in the area of snow and ice covered surfaces. Sea ice is an important habitat for birds such as penguins and mammals such as seals and polar bears which thrive in this icy environment [4]. But the underside of sea ice is also an important refuge for some of the smallest creatures including the shrimp-like krill which graze upon algae that grows just beneath and within the ice canopy [5, 6]. Terrestrial permafrost and frozen sediments beneath the oceans support an important reservoir of organic carbon and gas hydrates [7]. As permafrost melts, methane can be released contributing to the increasing concentration of greenhouse gases in the atmosphere. Glaciers and ice sheets are vast reservoirs of Earth's freshwater. As the ice sheets thin, water flows from the ice sheets into the oceans raising global sea level [8]. In terms of our daily activities, seasonal snow and glaciers are important sources of spring runoff

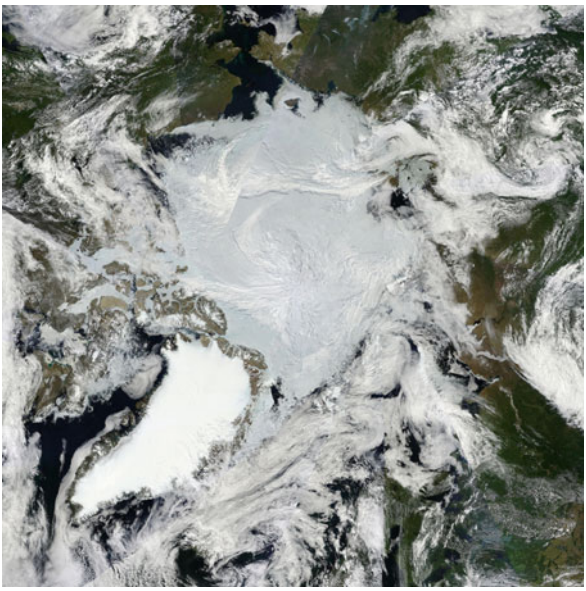

Fig. 2.1 NASA MODIS composite for July 7, 2010. Starting in the *lower left* quadrant and going clockwise, the Greenland sheet is almost cloud free as are the adjacent smaller ice caps on the Canadian Arctic Islands. Much of northern Canada and Alaska are cloud covered till the Bering Strait which is also almost sea ice free. Patches of sea ice cling to the Asian coast and there is a smattering of snow cover on the Putorana Mountains in western Siberia. The Gulf of Ob, Novaya Zemlya, the Franz Josef Land, and Spitsbergen Islands are barely visible through the cloud. The central Arctic basin is covered by sea ice. The image illustrates the scale of the cryosphere as well as some of the complications faced when trying to study it from space (Image prepared by NASA's MODIS Rapid Response team)

for irrigation and power generation, while ice jams on rivers constitute important obstacles to winter-time navigation and can cause low-land flooding [9]. Thawing permafrost causes the land near surface to become unstable which can result in catastrophic structural failures in buildings.

The global span of cryospheric processes and the strong daily to seasonal swing in the extent of snow and ice makes studying and monitoring the cryosphere an especially challenging scientific objective [10]. Moreover the variety of forms in which ice can be manifest in Earth systems means that no single observing system is capable of making adequate observations. Rather an ensemble of techniques is required to fully appreciate and eventually understand the complexities of the cryosphere and its interaction with other earth systems. Locally, observing tools may include direct, field measurements of snow pack thickness or physical temperature. Much different sets of tools are needed to characterize the cryosphere on a global and annual scale where the inhospitable climate and the physical remoteness of many sectors of the cryosphere represent obstacles to scientific investigation. Here, aircraft and spacecraft mounted instruments are required to infer geophysical properties from a remote distance (Fig. 2.2).

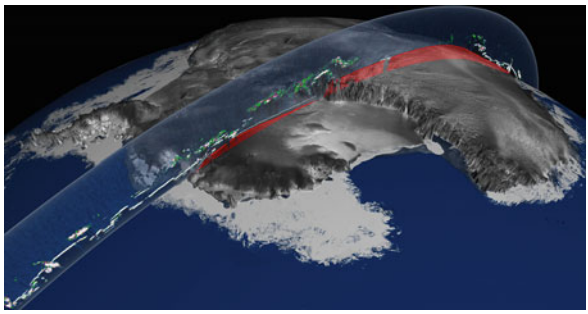

Fig. 2.2 Illustration of NASA's ICESat passing over the Antarctic. ICESat collected repeat elevation data over ice sheets and sea ice to study changing ice thicknesses. ICESat also sounded the atmosphere to study aerosols. NASA/Goddard Space Flight Center Scientific Visualization Studio, RADARSAT mosaic of Antarctica (Canadian Space Agency)

Compounded with these geographic challenges, observations of the icy surface often have to overcome cloud cover that frequently obscures the high latitudes, as well as continuing measurements during the long polar night. Consequently a range of instruments generally rely on distinguishing properties evident in the broad-spectral electrical characteristic of icy terrain. For example, even the cloudy atmosphere is largely transparent to microwave radiation. That fact combined with the very different microwave emission of open ocean and sea ice enables space-borne microwave observations of annual sea ice extent and concentration day and night and in all weather. Similarly the electrical contrast between rock and ice enables airborne radio frequency radar measurements of the thickness of polar ice sheets and glaciers. However some of the most recent advances in cryospheric science have been made by relying on one of the most basic properties of the icy cover, namely its mass. Space-borne measurements of the changing gravitational attraction of variably sized snow and ice bodies enables direct estimates of changing polar ice mass and the redistribution of melting ice into the liquid oceans. Indeed it can be argued that engineering and technological advances in airborne and remote sensing have had some of their greatest scientific impacts in the understanding the evolution of Earth's ice cover.

This article provides an overview of remote sensing of the cryosphere from both aircraft and spacecraft. A brief historical review of remote sensing of snow and ice is followed by a discussion of the physics of remote sensing of the cryosphere and how developments in remote sensing have led to a series of important scientific advances. These include the realization of the diminishing extent of Arctic sea ice and the thinning of glaciers, ice caps, and ice sheets worldwide. Both of these observations form critical, direct evidence of changing world climate. The article concludes with a discussion of developing international collaborations that are aimed at pooling technologically sophisticated and operationally expensive international assets so as to obtain an integrated system of continuing remote sensing observations necessary to predict future changes in Earth's ice and the consequent impacts on human activities.

Early History of Cryospheric Remote Sensing

The science and operational communities have always been quick to adopt new instruments and platforms for use in observing snow and ice in all of its forms. This section reviews early developments in cryospheric remote sensing – which were in part driven by science and in part by the basic desire to explore the most remote regions of Earth.

Airborne Photo-Reconnaissance

Aerial photography of ice covered terrain began during early twentieth century expeditions to the high atitudes and was used primarily to document the progress of the expedition. Survey quality aerial mapping was adopted using techniques primarily developed during World War I [11]. Mittelholzer and others [12] writing about the 1923 Junkers Expedition to Spitzbergen offer a very complete overview of the geographic and cartographic objectives for aerial photography in the North including a brief discussion of glacier formation as revealed by the aerial photographs. They also give an interesting technical discussion of the challenges faced when doing aerial photographic reconnaissance over highly reflective snow-covered terrain.

Wilkins documented ice cover in the Antarctic Peninsula during the first successful flight in Antarctica by using a hand-held, folding Kodak 3A camera [13, 14]. Richard E. Byrd devoted time and resources to aerial photography for quantitative surveying purposes during his first Antarctic Expedition of 1928–1930. In his book, "Little America," Byrd [15] writes that photographs from Ashley McKinley's laboratory provided "perhaps, the most important geographical information from the expedition." McKinley was third in command of the expedition and the aerial surveyor. McKinley operated his Fairchild K-3 mapping camera during Byrd's 1929 historic flight to the South Pole.

These early airborne photographic records were acquired with great skill and at considerable risk. The quality of the photographs is often exceptional and the photos themselves represent an oft under-utilized resource for directly gauging century-scale changes in Earth's ice cover.

Satellite Photography

A mere 32 years after Byrd's aerial photographic surveying in Antarctica, space-borne cameras began capturing unique pictures of Earth. CORONA, ARGON, and LANYARD were the first three operational imaging satellite reconnaissance systems and they acquired data during the early 1960s for both detailed reconnaissance purposes and for regional mapping [16–18]. Early reconnaissance satellite

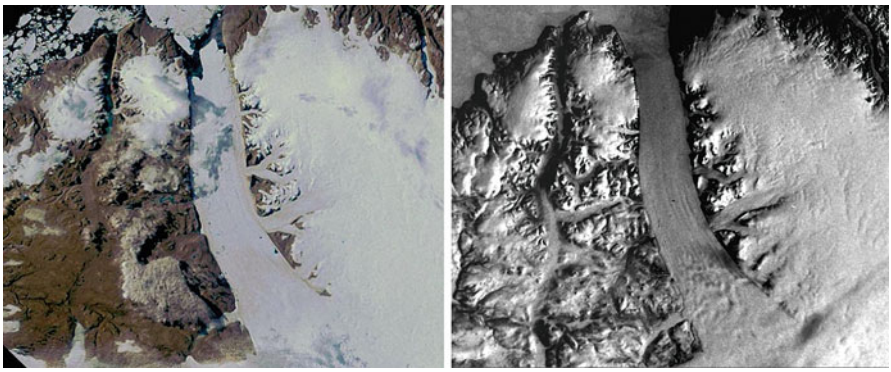

Fig. 2.3 European Space Agency MERIS image of Peterman Glacier, Greenland (*left*). The multispectral image was acquired in July, 2008 and before a large part of the floating ice tongue broke free. Argon panchromatic photograph acquired during the spring of 1962. The clarity of this early view from space is exceptional and provides a valuable gauge for assessing changes in glacier ice from the 1960s to the present

photographs provide a unique view of our world as it appeared at the beginning of the space age. Researchers in the environmental science community are the most recent beneficiaries of these data after they were declassified and made publicly available in 1995 through the efforts of Vice President Al Gore along with several government agencies working together with civilian scientists as part of the MEDEA program [19]. Polar researchers in particular inherited a wealth of detailed photography covering both of the great polar ice sheets. After processing with sophisticated digitizing instruments and subsequent analysis with modern photogrammetric and image processing techniques, investigators have shown that these data can be used to characterize local fluctuations in glacier termini [20, 21], investigate large-scale flow features on ice sheets [22, 23] and to measure long-term average velocity by feature retracking techniques [24] (Fig. 2.3).

Development of Depth Sounding Radar

Early suggestions that glaciers were penetrated by radio signals are attributed to observations made at Little America during Byrd's 2nd Antarctic Expedition [25]. This observation, along with reports that pulsed radar altimeters were yielding faulty readings over glaciers, led to the first radar experiments to measure ice thickness in 1955. In 1960, Waite and Schmidt [25] made measurements over Greenland from aircraft at 110, 220, 440, and 4,300 MHz. These results initiated a revolution in glaciology because the ice thickness and internal structure of glaciers and ice sheets could be rapidly sounded from aircraft [26].

Although the sophistication of ice sounding radar systems has increased tremendously, the basic principle of the technique remains the same and continues

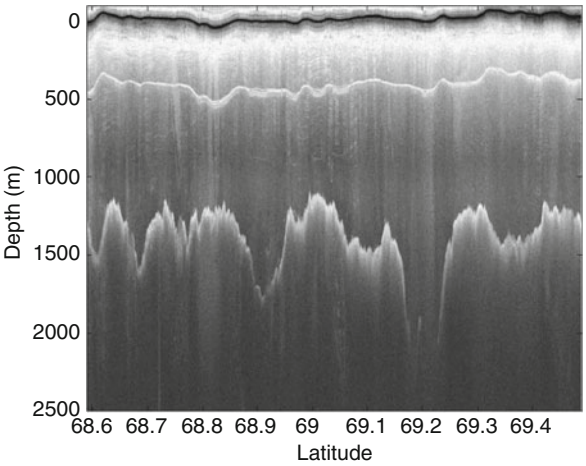

Fig. 2.4 North south airborne profile of ice thickness in west central Greenland. The *upper black line* is the radar reflection from the snow surface. The line at about 500 m depth is a multiple echo of the surface from the aircraft itself. The undulating line at an average depth of about 1,400 m is the reflection from the glacier bottom. The profile crosses the upstream segment of Jakobshavn Glacier at 69.2° N 48.1°W. There the 2,000 m thick ice has incised a deep channel into the bedrock. The data were acquired by the University of Kansas in 2008

to be a fundamental tool used by researchers (Fig. 2.4). Essentially, the one-way travel time of a radar pulse transmitted through the ice or snow is multiplied by the appropriate wave speed and the thickness so determined. More complex, two dimensional maps of the glacier bed topography can be assembled from multiple profiles that are combined using travel time migration techniques [27]. Several snow and ice sounding radars are part of the primary instrument suite presently carried aboard aircraft supporting NASA's IceBridge program [28].

Depth sounding radar remains one of the few techniques available to researchers interested in probing the volume of the terrestrial ice cover and the properties of the underlying bed. Airborne radars have been successfully used to study glacier, ice sheets, and to a more limited degree sea ice and permafrost. Seismic techniques yield important complementary information but can be carried out only in situ. Airborne gravity measurements provide important regional information but are generally less accurate than the radar technique for measurements on glaciers.

Scientific Advances from Airborne and Space-borne Remote Sensing

In most instances, airborne and space-borne platforms carry similar kinds of remote sensing instruments. Often times, space-borne instruments are first proto-typed as part of initial airborne campaigns. However, advantages of instrument installations

on multiple kinds of platforms go far beyond vetting the effectiveness of an instrument. For example, space-borne systems can provide global scale observations, with some imaging instruments yielding pole-to-pole observations on a daily basis. Manned and increasingly unmanned aircraft, with their ability to maneuver and loiter over an area, can provide much denser spatial and temporal coverage when profiling instruments, such as altimeters, are of interest. This section begins with a review of remote sensing physics and then summarizes key applications of remote sensing to several cold regions themes.

Basics of Remote Sensing of the Cryosphere

Airborne and space-borne sensors measure local changes in electromagnetic, gravitational, and magnetic force fields. Disturbances can arise from the passive, thermodynamically driven electromagnetic radiation emitted by the earth's distant surface, or the reflectance of incoming solar radiation from the Earth's surface, both of which change with the terrain type. Instruments and associated satellites of this type include the Electrically Scanning Microwave Radiometer (ESMR), Scanning Multichannel Microwave Radiometer (SMMR), Special Sensor Microwave Radiometer (SSMI), Advanced Very High Resolution Radiometer (AVHRR), Landsat, Moderate Resolution Imaging Spectrometer (MODIS), Medium Resolution Imaging Spectrometer (MERIS), Satellite Pour l'Observation de la Terre (SPOT). Disturbances can also arise from the active behavior of the sensor itself. Radars and lidars include the Airborne Topographic Mapper (ATM), Laser Vegetation Imaging Sensor (LVIS), synthetic aperture radar (SAR) and radar altimeters on the European Remote Sensing Satellite (ERS-1/2), RADARSAT 1/2, synthetic aperture radar and radar altimeter on Envisat, Phased Array L-band SAR, TerraSAR-X, GEOSAT, the Ice and Climate Experiment Satellite (ICESat) lidar, the Cryosat radar altimeter. These instruments illuminate the surface with electromagnetic signals, which upon reflection can be detected back at the sensor after an elapsed time. Local changes in the gravity field at airborne and space-borne elevations are indications of changes in the distribution of mass within the Earth. Such instruments include airborne gravimeters on NASA's IceBridge, NASA's Gravity Recovery and Climate Experiment (GRACE) satellite, and ESA's Gravity field and Ocean Circulation Explorer (GOCE) satellite.

The task of the remote sensing scientist is to take measurements of these basic force fields and infer from them geophysical properties about the Earth [29]. For the cryosphere, examples include using changes in the gravitational field to estimate changes in the mass of glaciers and ice sheets as is done with the GRACE satellite. Other examples include using radars and lidars to measure the time of flight of signals reflected off the ice surface and use that information to measure elevation and elevation changes on sea ice and ice sheets. Finally, scattered solar radiation can be used to acquire hyper-spectral images for surface characterization and for traditional mapping of surface features.

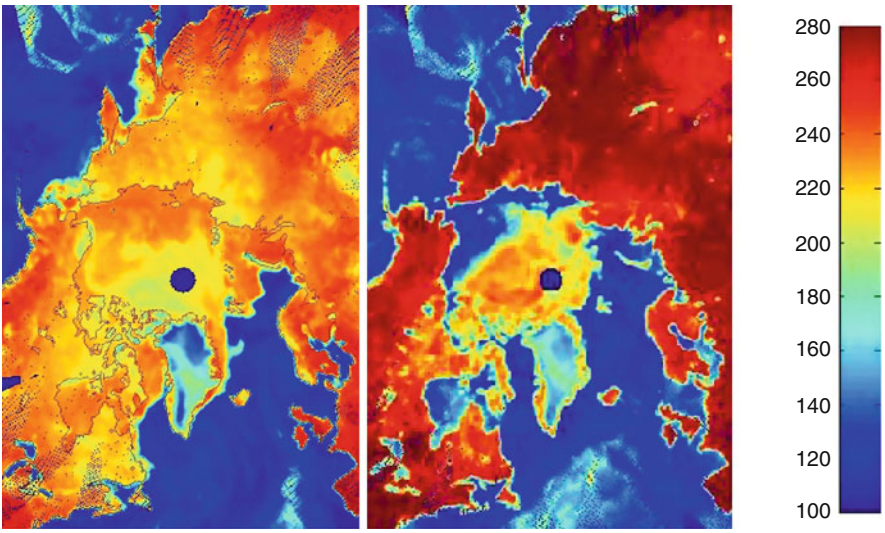

Fig. 2.5 19 GHz, horizontally polarized, special sensor microwave imager (SSM/I) brightness temperature data for the Arctic on February 15, 2004 (*left*) and August 25, 2004 (*right*). The brightness temperature scale (*far right*) is in degrees Kelvin. Differences between the emissivity of ocean, sea ice, land and ice sheets enable the relatively easy identification of the seasonal retreat in sea ice cover. Brightness temperature variations across the ice pack are caused by differences in ice type and age as well as in ice concentration

Accomplishing this task requires technical information about the behavior of the instrument, knowledge about the physical relationships between the measured field and the surface under study, and the development of algorithms that correctly invert the measured signal into some desired property [30, 31]. In some cases this task can be relatively easy. Because glacier ice is nearly homogeneous and because it is almost transparent at radar frequencies from about 1 to 500 MHz [32], the propagation time of a radar echo through the ice sheet and back can be converted to ice thickness by simply knowing the average ice dielectric constant, which in turn is readily convertible into a propagation velocity. In other cases, the task is more challenging because of heterogeneities in the material. The physical and electrical properties of sea ice change substantially as the ice ages [33]. This leads to changes in the thermally driven, microwave emission from the surface. The amount of energy received, measured in terms of a brightness temperature, is related to the product of the physical temperature and the emissivity of the surface. For open water, the microwave brightness temperature is cool because little energy escapes from the ocean surface. For sea ice, the brightness temperature is warm because more energy is transmitted across the electrically less reflective snow surface at these frequencies. Consequently, brightness temperature can be used to measure sea ice concentration and extent with high accuracy (several percent). Figure 2.5 shows that just on the basis of brightness temperature maps alone it is easy to distinguish the annual cycle of sea ice growth and decay across the arctic.

Sea Ice Extent, Concentration, Motion, and Thickness

Sea ice modulates polar climate by restricting the flow of heat from the relatively warm polar ocean into the relatively cold polar atmosphere. Because freezing ice preferentially rejects impurities from the crystalline lattice, the growth of sea ice modulates ocean circulation by releasing dense, cold brine that sinks beneath the marginal ice zones and initiates oceanic convection. Sea ice represents a natural barrier to surface navigation and so changes in sea ice cover have important consequences for future development of the Arctic. While sea ice is usually distinguishable from open ocean at optical wavelengths, cloud cover and the long polar night dictate the use of all-weather, day/night passive microwave radiometers for monitoring sea ice extent and concentration. As noted above, these radiometers measure the radiant energy emitted from the surface that, on one hand, can help identify ice type and age but, on the other hand, leads to complexities in designing more sophisticated instruments capable of sorting out whether the observed changes are due to different ice types populating a scene or because of change in the fractions of sea ice and open water in the scene. Moreover, the dimensions of the area sampled on the surface are often quite large (Hollinger and others [34] quote a field of view of 37 $\times$ 28 km for the SSMI 37 GHz vertically polarized channel). Consequently, approaches for estimating the concentration within a single pixel are required. A simple algorithm relies on the fact that the total emitted energy or equivalently the brightness temperature must equal the brightness temperature of the components in the scene times their respective concentrations within the pixel [35]. The component brightness temperatures are selected by tie points (such as a tie point for the brightness temperature of open water or first-year sea ice) which allows for a solution. More sophisticated algorithms attempt to better characterize regions where ice concentrations are low and where the data may be contaminated by weather effects. The results of these analyses are detailed measurements of ice extent which document the dramatic decrease in Arctic sea ice cover (Fig. 2.6). Graphs such as these represent some of the most compelling and straightforward evidence for changing climate at high latitudes.

Images such as those in Fig. 2.5 can also be used to document the coarse motion of the sea ice by tracking common features in repeat images. Better results are obtained with increasing resolution ranging from the several kilometer resolution obtainable with AVHRR to the very fine resolutions (tens of meters or less) achievable with SAR. Combined with airborne (Airborne Topographic Mapper flown as part of IceBridge) and space-borne (ERS-1/2, ICESat, Cryosat-2) altimeter estimates of ice thickness, circulation driven changes in ice thickness about Antarctica [36] and the total ice flux across the Arctic and out into the marginal seas can be computed. Based on ICESat estimates of sea ice freeboard, Kwok and others [37] estimate a 0.6 m thinning in Arctic multiyear ice for the period from 2003 to 2008.

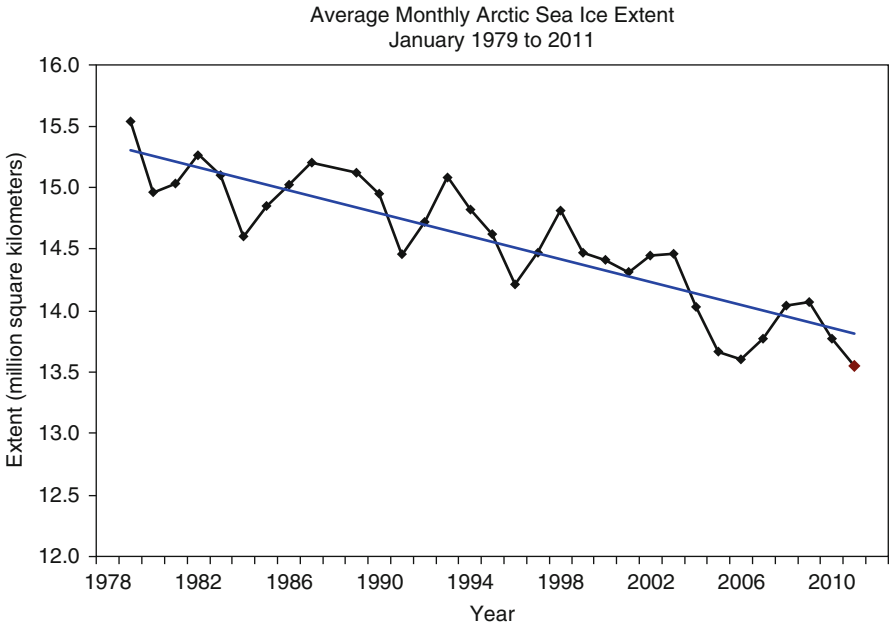

Fig. 2.6 Winter-time Arctic sea ice extent computed using passive microwave data. The decreasing trend illustrates the reduction in Arctic sea ice extent. There is a much more dramatic decline in ice extent during the summer months (Graph courtesy of the National Snow and Ice Data Center)

Regional Image Mapping of Glaciers and Ice Sheets

Airborne and space-borne image mapping of glaciers and ice sheets focuses on basic physical characteristics such as glacier termini, glacier snow lines, crevasse patterns, snow facies boundaries [38]. These properties have been successfully monitored with optical and microwave imaging instruments. As described in section "Early History of Cryospheric Remote Sensing," high latitude mapping began as early as 1962 with the launch of the Argon satellite. Shortly thereafter, the 1970s Landsat 1, 2, and 3 Multi-Spectral Scanner (MSS) images constitute an important glaciological resource [39, 40] and have been compiled into a series of beautiful folios edited by R. Williams Jr. and J. Ferrigno of the U.S. Geological Survey [see 41].

Compiling separate images into seamless, high-resolution digital maps of continental-scale areas is complicated by the data volume and the challenges in accurately estimating satellite orbits and instrument viewing geometries along orbit segments that might span from coast to coast. Initial successes in large-scale mapping were achieved through use of the moderate spatial resolution (1–2.5 km) and wide swath (2,400 km) Advanced Very High Resolution Radiometer (AVHRR) images [42] which helped reveal details about ice stream flow in West Antarctica [43]. After the original AVHRR mosaic of Antarctica, the United State Geological Survey (USGS) made subsequent improvements to the mosaic by eliminating more cloud, separating

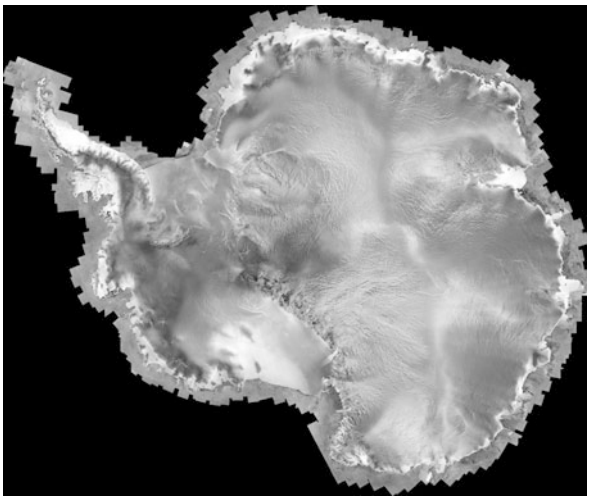

Fig. 2.7 Canadian RADARSAT-1 Antarctic Mapping Project synthetic aperture radar mosaic. The radar is sensitive to changes in the physical structure of the near surface snow. Bright coastal returns are scattered from subsurface ice lenses formed during fall freeze-up. Darker interior tones occur where snow accumulation is high. Other features such as ice streams and ice divides are visible (Map courtesy of K. Jezek. RADARSAT-1 data courtesy of the Canadian Space Agency)

the thermal band information to illustrate surface features more clearly, and correcting the coastline of the mosaic to include grounded ice while excluding thin, floating fast ice [44]. The European Earth Resources Satellite – 1 carried on board a synthetic aperture radar which allowed for large-scale regional mapping. Fahnestock and others [45] compiled a mosaic of Greenland which revealed the existence of a long ice stream in north east Greenland. In 1997, RADARSAT-1 synthetic aperture radar (SAR) data were successfully acquired over the entirety of Antarctica (Fig. 2.7). The coverage is complete and was used to create the first, high-resolution (25 m) radar image mosaic of Antarctica [46–48] The image was used to map the ice sheet margin [49] and to investigate patterns of ice flow across Antarctica resulting in the discovery of large ice streams that drain from Coates Land into the Filchner Ice Shelf. Other large-scale mapping has been completed with MODIS for both the Arctic and the Antarctic [50]. Most recently, Landsat imagery of Antarctica has been compiled into a single, easily accessible map-quality data set [51] and SPOT stereo imagery has been used to derive digital elevation models of ice sheets, ice caps, and glaciers [52].

InSAR Measurements of Glaciers and Ice Sheets Surface Velocity

Glaciers and ice sheets move under the load of their own weight. They spread and thin in a fashion dictated by their thickness, the material properties of ice, and the

environmental conditions operative on the glacier surface, sides and bottom. The rate and direction of motion reveals important information about the forces acting on the glacier, provides knowledge about the rate at which ice is pouring into the coastal seas, and enables scientists to predict how the ice sheet might respond to changing global climate.

Since the International Geophysical Year of 1957–1958 and before, scientists have placed markers on the ice sheet and then, using a variety of navigation techniques from solar observations to GPS, have remeasured their positions to calculate motion. More recently, scientists have used high-resolution satellite images to track the position of crevasses carried along with the glacier to compute surface motion. These approaches are time consuming and result in patchy estimates of the surface velocity field. During the early 1990s, researchers at the Jet Propulsion Laboratory showed that synthetic aperture radar (SAR) offered a revolutionary new technique for estimating the surface motion of glaciers [53]. Here, the SAR is operated as an interferometer. That is, the distance from the SAR to a point on the surface is computed by measuring the relative number of radar-wave cycles needed to span the distance between the radar and the surface. Later, another measurement is made from a slightly different position and the numbers of cycles is computed again. The difference in the number of cycles combined with control points is used to estimate relative displacement to about one quarter of a radar-wave cycle (just a few centimeters for RADARSAT-1). Given an estimate of surface topography, this enables measurement of even the slowest moving portions of glaciers [54, 55]. A related approach relies on the fact that images formed from coherent radar signals scattered off a rough surface will have a small-scale-speckly appearance. The speckle pattern is random over scene but it is stable from scene to scene over a short time. Tracking the speckle pattern over time enables another measurement of surface velocity and while less accurate than the interferometric phase approach, speckle retracking has the advantage of yielding estimates of two components of the velocity vector [56, 57]. Typically a mixture of phase interferometry and speckle retracking are used in glacier motion studies.

Surface topography can also be estimated using InSAR techniques in cases where the surface velocities are small, the period between repeat observations is short [58], when multiple interferometric pairs are available [59], or when multiple antennas enable acquisition of interferometric data in a single pass as was done with NASA's Shuttle Radar Topographic Mission [60]. Although the surface elevation accuracy of InSAR topography is typically on the order of a few meters, the results can be used to estimate local slopes and also in comparison with earlier data provide a rough estimate of mass change.

Surface elevation and velocity data are key to studies of glacier dynamics [61]. InSAR data have been used to investigate the relative importance of different resistive stresses acting on ice streams and to predict the future behavior of ice streams and glaciers currently in retreat [62, 63]. Measurements on mostly retreating glaciers in the Himalayas [64], Patagonia [65, 66], European Alps [67], and Alaska (Fig. 2.8) document changing surface elevation and internal dynamics, and, together with estimates of ice thickness and surface accumulation rate, can provide a direct estimate of glacier mass loss [68].

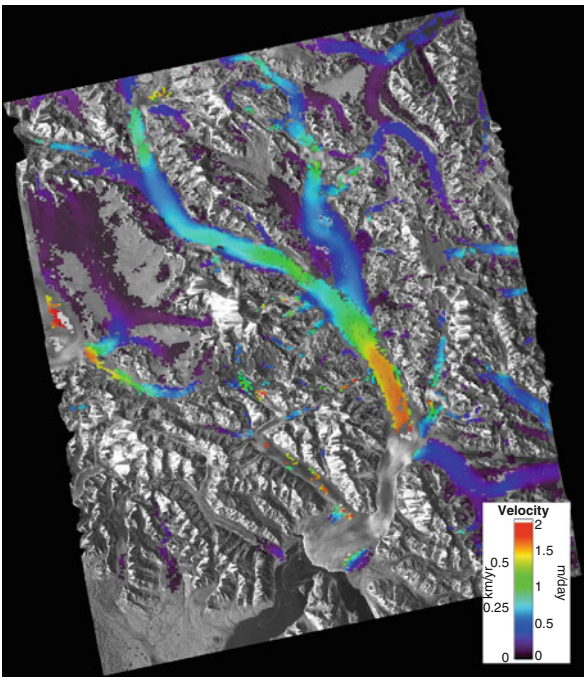

Fig. 2.8 Surface velocities on Hubbard Glacier Alaska measured using Japanese PALSAR L-band interferometric pairs. Hubbard Glacier is a tidewater glacier and ice from the advancing snout calves directly into Disenchantment Bay (*lower center*). Hubbard Glacier is one of the few in Alaska that is currently thickening and advancing (Image courtesy of E. W. Burgess and R. R. Forster, University of Utah)

Glaciers and Ice Sheets Mass Loss

Glaciers and ice sheets are reservoirs of freshwater with over 90% of Earth's freshwater bound in the Antarctic Ice Sheet [69], which when depleted have local, regional and global impacts. Indirect approaches for identifying whether ice sheets are losing mass include using proxy indicators such as surface melt area and duration – both measureable using passive microwave techniques [70, 71]. More directly, there are three primary remote sensing techniques currently used to assess the changing volume (or mass) of ice contained in glaciers [72]. The first involves an estimate of the difference between the annual net accumulation of mass on the surface of the glacier and the flux of ice lost from the terminus. The flux from the terminus is calculated using the measured ice thickness from airborne radar and the surface velocity, which is currently best estimated with InSAR [73]. The second approach is to measure surface elevation change. This has

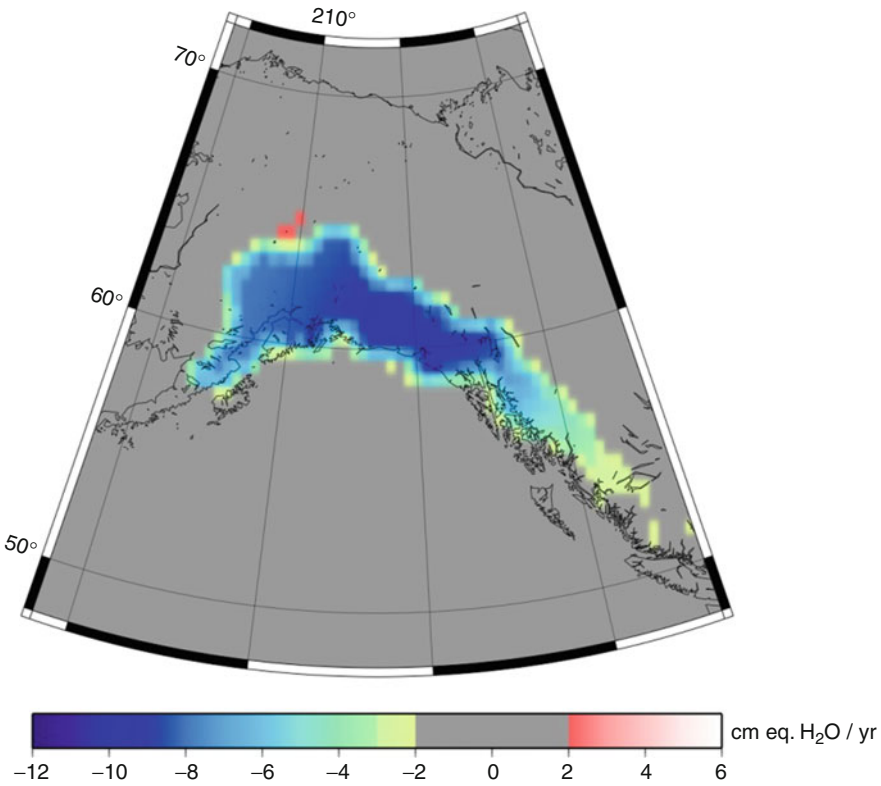

Fig. 2.9 Mass loss from Alaskan Glaciers in cm of water equivalent per year from GRACE (Image courtesy of S. Luthcke, NASA GSFC)

been accomplished with space-borne radar altimeters [74, 75] and airborne and space-borne lasers [76–78]. Finally, the changing glacial mass can be estimated directly by measuring changes in the gravity field as has been done with GRACE [79–81]. Figure 2.9 illustrates the estimated mass loss rate from Alaskan Glaciers as illustrated using GRACE data (Updated from [82]).

Recent analyses suggest these different techniques are yielding similar mass reductions for the Greenland Ice sheet [8, 83]. Thinning is primarily in the coastal regions where the rate of thinning has been increasing since the early 1990s and the current rates of mass loss estimated between 150 and 250 Gt/year. West Antarctica data indicate mass loss similar to Greenland, whereas East Antarctica retains a slightly positive (50 Gt/year) mass balance. Using surface mass balance estimates and GRACE gravity data, Rignot and others [84] report a combined ice sheet thinning rate of 475 $\pm$ 158 Gt/year. Cazenave and Llovel [8] conclude that for the period between 1993 and 2007 about 55% of total sea level rise can be attributed to melting of glaciers and ice sheets.

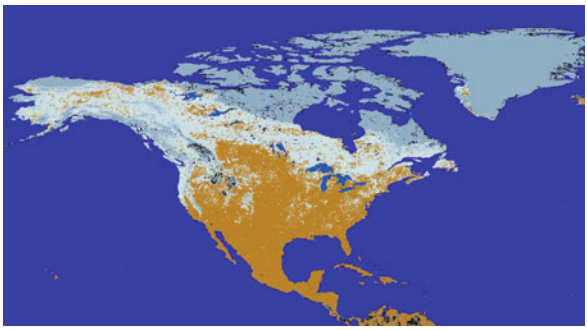

Fig. 2.10 Snow cover extent from NASA's MODIS. Increasing shades of *gray* indicate greater percentages of snow cover within each pixel. *Brown* denotes snow-free surface

The Seasonal Snow Pack

Seasonal snow cover plays an important role in regional hydrology and water resource management. Rapid melting of the seasonal snow pack across the northern Great Plains in April 1997 resulted in catastrophic flooding of the Red River. From a climate perspective, the bright snow surface also serves as an effective mirror for returning incoming solar radiation back into space thus modulating the planetary heat budget.

The spectral reflectivity differences between snow, cloud, and other land cover types enables the seasonal snow cover to be routinely mapped globally using visible and infrared sensors such as NOAA's AVHRR, NASA's MODIS, and ESA's MERIS instruments. Snow may be mapped based on visual inspection of multi-spectral imagery. Automatic snow detection is accomplished by computing the normalized difference between, for example, the MODIS visible band (0.545–0.565 μm) and the near infrared band (1.628–1.652 μm). Snow is detected when the normalized difference exceeds a threshold value of 0.4 and when other criteria on land and cloud cover are met [85] (Fig. 2.10). Based on analysis of the NOAA 35 year data record, Dery and Brown [86] conclude that springtime snow extent across the northern hemisphere declined by some 1.28×10^6 km^2 over a 35 year period.

Snow thickness and hence indirectly the mass of snow are key variables for estimating the volume of water available in a reservoir and potentially releasable as runoff. The most successful techniques to date have relied on passive-microwave-based algorithms. One approach for estimating snow thickness is to difference 19 and 37 GHz brightness temperature data that along with a proportionality constant yields an estimate of the snow thickness. The algorithm is based on the fact that 19 GHz radiation tends to minimize variations in ground temperature because it is less affected by the snow pack. The 37 GHz radiation is strongly scattered by the snow grains and brightness temperature at this frequency decreases rapidly with snow thickness/snow water equivalent. Factors which confuse this algorithm include topography and changes in ground cover [87].

Information about the seasonal onset of snowmelt can be obtained from microwave data. A few percent increase in the amount of free water in the snow pack causes the

Fig. 2.11 January 2010 NASA MODIS image of ice formed on the St. Lawrence River. Thin layers of new ice are distorted into swirls by the surface currents (*center left*). Thicker ice is held fast to the southern shore (Image courtesy of MODIS Rapid Response Team, NASA GSFC)

snow emissivity to approach unity resulting in a dramatic increase in passive microwave brightness temperature. This fact has been successfully used to track the annual melt extent on the ice sheets and also to track the springtime melt progression across the arctic. Higher resolution estimates of melt extent can be obtained with scatterometer and SAR data. These data generally show an earlier spring time date for the beginning of melt onset and a later date for the fall freeze [88].

Lake and River Ice

Lake and river ice form seasonally at mid and high latitudes and elevations. River ice forms under the flow of turbulent water which governs its thickness. The combination of ice jams on rivers with increased water flow during springtime snowmelt can result in catastrophic floods. Lake ice forms under less dynamic conditions resulting in a smoother ice surface that acts as an insulator to the underlying water. Hence lacustrine biology is strongly influenced by the formation of the ice canopy. The start of ice formation and the start of springtime ice break up are proxy indicators for changes in local climate as well as impacts on the ability to navigate these waterways.

Streams, rivers, lakes of all sizes dot the landscape. Locally, ice cover observations can be made from aircraft. Regionally or globally, river and lake ice monitoring is challenging because physical dimensions (long but narrow rivers) often require high resolution instruments like medium- to high-resolution optical data (Fig. 2.11) or SAR to resolve details [89]. Moreover, since the exact date of key processes, such as the onset of ice formation or river-ice breakup are unknown, voluminous data sets are required to support large-scale studies.

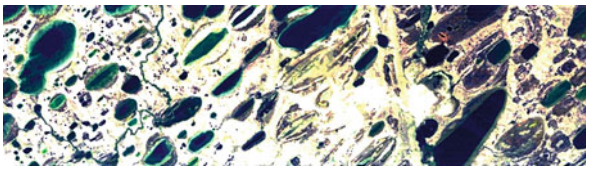

Fig. 2.12 EO-1 Hyperion satellite data acquired over the north coast of Alaska (70.5 N 156.5 W) and about 50 km inland from the coast, which is toward the *right* on this image. The image is 7.5 km wide (*top* to *bottom*). Color composite using channels 16 23 and 28

Permafrost

Permafrost presents one of the greatest challenges for regional remote sensing technologies [7, 90]. The near surface active layer, the shallow zone where seasonal temperature swings allow for annual freeze and thaw, is complicated by different soil types and vegetative cover. This combination tends to hide the underlying persistently frozen ground from the usual airborne and space-borne techniques mentioned above. Even in winter when the active layer is frozen, remote sensing of the permafrost at depth is extremely difficult because of the spatially variable electrical properties of the material. Thus far, the most successful airborne and space-borne remote sensing methods involve optical photography to identify surface morphologies as proxy indicators of the presence of permafrost. Patterned ground and pingos are examples of the types of features visible in optical imagery and that are diagnostic of underlying permafrost. SAR interferometry has been suggested as another tool that can be used to monitor terrain for slumping associated with thawing permafrost. Figure 2.12 shows E01 Hyperion satellite, visible-band data collected over the north slope of Alaska. Shallow, oval shaped lakes form in thermokarst, which develops when ice rich permafrost thaws and forms a hummocky terrain. Lakes and depressions left by drained lakes are densely distributed across the tundra. The long axis of the lake is oriented perpendicular to the prevailing wind direction. SAR intensity images have been used to determine that most of these small lakes freeze completely to the bottom during the winter months [91].

Recent Developments in Airborne Radar Ice Sounding of Glaciers

Today, airborne radars operating between about 5 and 500 MHz are the primary tools used for measuring ice sheet thickness, basal topography, and inferring basal properties over large areas. These radars are typically operated as altimeters and acquire profile data only along nadir tracks that are often separated by 5 or more kilometers. The along track resolution is met by forming a synthetic aperture and the vertical resolution of the thickness is met by transmitting high bandwidth signal.

Even though highly accurate thickness measurements can be achieved, information in the third cross-track dimension is absent.

While the surface properties of the ice sheets are becoming increasing well documented, the nature of the glacier bed remains obscured by its icy cover. Revealing basal properties, such as the topography and the presence or absence of subglacial water, is important if we are to better estimate the flux of ice from the interior ice sheet to the sea and to forecast anticipated changes of the size of the ice sheets. Recent experiments demonstrate how it is possible to go beyond airborne nadir sounding of glaciers and to produce three-dimensional images of the glacier bed. This development represents a major step forward in ice sheet glaciology by providing new information about the basal boundary conditions modulating the flow of the ice and revealing for the first time geomorphologic processes occurring at the bed of modern ice sheets. The approach relies on the application of radar tomography to UHF/VHF airborne radar data collected using multiple, independent antennas and receivers. Tomography utilizes phase and amplitude information from the independent receivers to isolate the direction of a natural target relative to the aircraft. Combined with the range to the target based on the echo travel time and position of the aircraft, tomographic methods yield swaths of reflectivity and topographic information on each side of the aircraft [92].

Cooperative Efforts to Observe, Monitor, and Understand the Cryosphere

Several cooperative, international scientific studies of the high latitudes have been organized. Beginning with the 1897 voyage of the Belgica to the Antarctic Peninsula and continuing to the 2007 International Polar Year, studies have relied on the most recent technologies to increase knowledge of the polar regions. To realize the benefit of the growing constellation of international satellites to the scientific objectives of the 2007 International Polar Year (IPY) (Fig. 2.13), the Global Interagency IPY Polar Snapshot Year (GIIPSY) project engaged the science community to develop consensus polar science requirements and objectives that could best and perhaps only be met using the international constellation of earth observing satellites [93]. Requirements focused on all aspects of the cryosphere and range from sea ice to permafrost to snow cover and ice sheets. Individual topics include development of high-resolution digital elevation models of outlet glaciers using stereo optical systems, measurements of ice surface velocity using interferometric synthetic aperture radar, and frequently repeated measurements of sea ice motion using medium resolution optical and microwave imaging instruments.

The IPY Space Task Group (STG), convened by the World Meteorological Organization (WMO), formed the functional link between the GIIPSY science community and the international space agencies. STG membership included representatives from the national space agencies of Italy, Germany, France, UK,

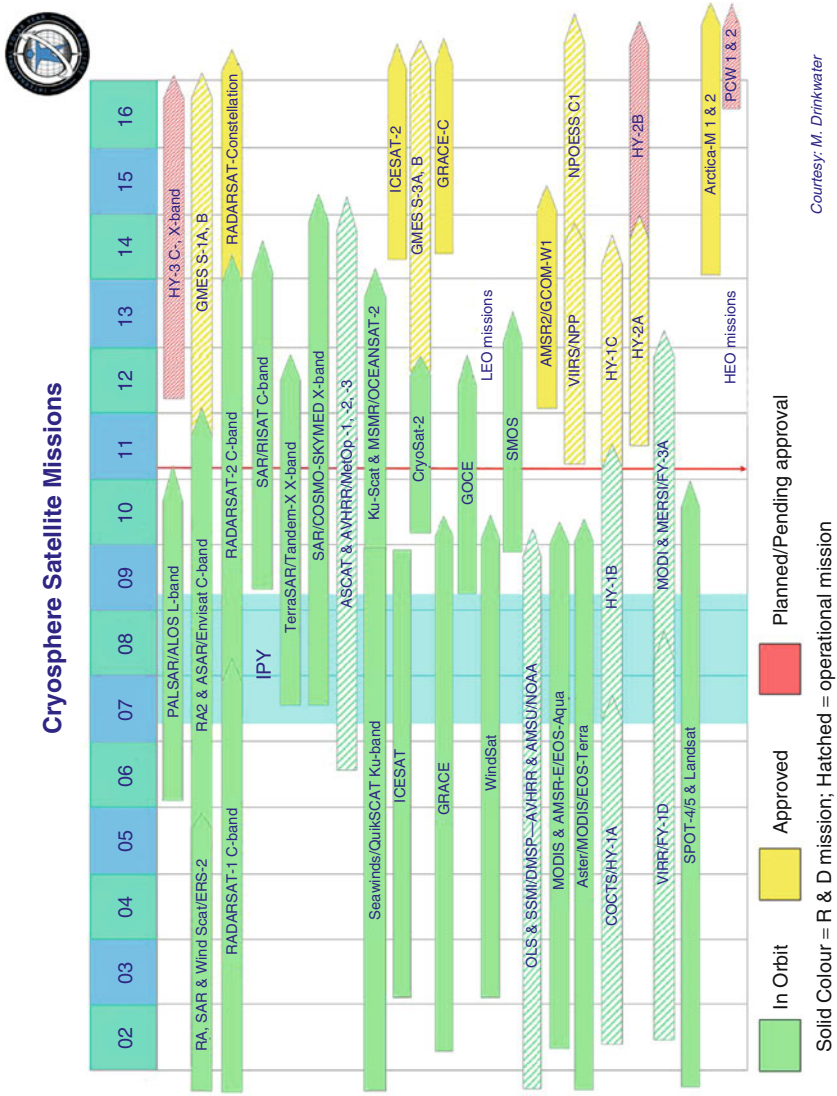

Fig. 2.13 Current, approved and planned satellites for studying and monitoring the Cryosphere (Figure courtesy of Mark Drinkwater, European Space Agency)

US, Canada, Russia, China, Japan, and the European Space Agency (ESA), which in itself represents 19 nations. The STG determined how best to satisfy GIIPSY science requirements in a fashion that distributed the acquisition burden across the space agencies and recognized the operational mandates that guide the activities of each agency.

The STG adopted four primary data acquisition objectives for its contribution to the IPY. These are:

- Pole to coast multi-frequency InSAR measurements of ice-sheet surface velocity
- Repeat fine-resolution SAR mapping of the entire Southern Ocean sea ice cover for sea ice motion
- One complete high resolution visible and thermal IR (Vis/IR) snapshot of circumpolar permafrost
- Pan-Arctic high and moderate resolution Vis/IR snapshots of freshwater (lake and river) freeze-up and breakup

The STG achieved most of these objectives including: acquiring Japanese, ALOS L-band, ESA Envisat and Canadian Radarsat C-band, and German TerraSAR-X (Fig. 2.14) and Italian COSMO_SKYMED X band SAR imagery over the polar ice sheets [94]; acquiring pole to coast InSAR data for ice sheet surface velocity; optically derived, high-resolution digital elevation models of the perimeter regions of ice caps and ice sheets; coordinated campaigns to fill gaps in Arctic and Antarctic sea ice cover; extensive acquisitions of optical imagery of permafrost terrain; observations of atmospheric chemistry using the Sciamachy instrument.

Future Directions

Emerging sensor and platform technologies hold great promise for future airborne and space-borne remote sensing of the cryosphere. Airborne programs are likely to continue to use large manned aircraft in a fashion similar to NASA's IceBridge program which integrates a sophisticated suite of instruments including lidars, radars, gravimeters, magnetometers, optical mapping systems, and GPS. But there will also be a steady shift toward smaller, more dedicated unmanned aerial vehicles capable of remaining on station for longer periods and fulfilling some of the temporal coverage requirements that are difficult to satisfy with larger aircraft requiring a substantial number of crewmen.

It is worth noting again that ice sounding radars are exclusively deployed on aircraft for terrestrial research. This is driven operationally by the challenges of ionospheric distortions and by governmental controls on frequency allocations available for remote sensing applications designed to limit interference with communications and other commercial uses of the frequency bands. Certainly the latter is not an issue for other planetary studies and in fact the Martian ice caps have been successfully sounded from the orbiting MARSIS and SHARAD radars [95].

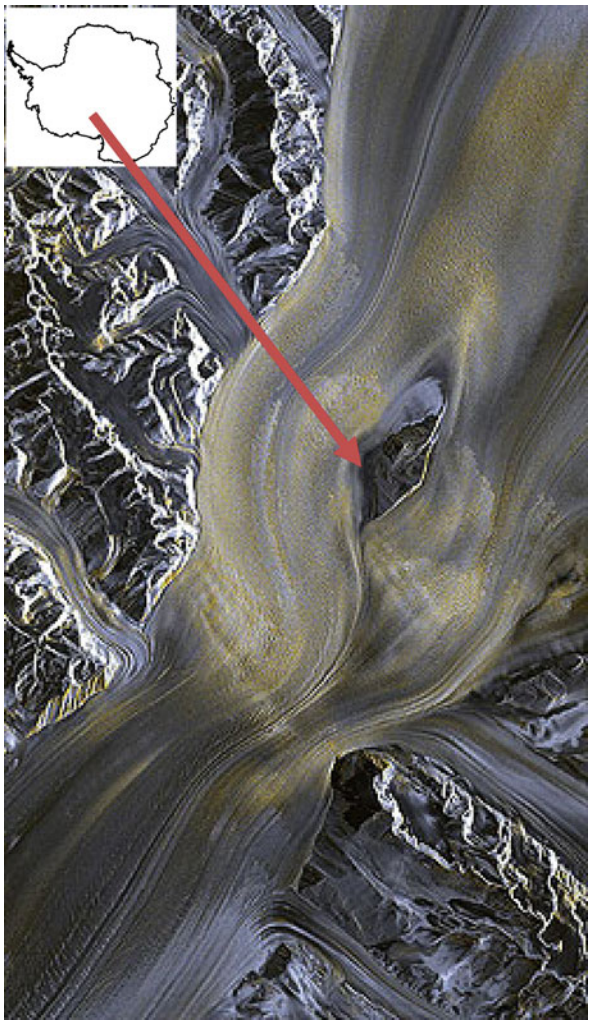

Fig. 2.14 German Aerospace Center TerraSAR-X observations of the Nimrod Glacier (inset map of Antarctica). Ice floes around a central nunatak and down toward the Ross Ice Shelf. Crevasses appear in conjunction with the interruption of flow by the nunatak. Cooperative use of Canadian, German, European Space Agency, Italian, and Japanese synthetic aperture radar (SAR) satellites along with ground segment and data processing capabilities provided by the United States yielded a rich and diverse SAR data set that will be a lasting legacy of the IPY (TerraSAR-X data courtesy of D. Floricioiu, German Aerospace Center. Inset coastline derived from RADARSAT-1 Antarctic Mapping Project map)

These extraterrestrial successes motivate continuing interest in deploying similar instrument for observing Earth's ice cover in the future.

As indicated in Fig. 2.13, there will be an ongoing constellation of satellites capable of collecting valuable cryospheric data. Here, coordination amongst the

different space faring nations will be key to realizing the greatest scientific benefit. Lessons about cooperation gleaned from the IPY can be profitably extended to the acquisition of data and the development of geophysical products beyond the polar regions to all sectors of the cryosphere. There could also be generally better integration of the atmospheric chemistry and polar meteorological communities, as well as incorporation of gravity and magnetic geopotential missions into the coordination discussions. It is also possible to envision discussion and collaboration on emerging technologies and capabilities such as the Russian Arktika Project [96] and advanced subsurface imaging radars. A primary objective of continued coordination of international efforts is securing collections of space-borne "snapshots" of the cryosphere through the further development of a virtual Polar Satellite Constellation [97]. A natural vehicle for adopting lessons learned from GIIPSY/STG into a more encompassing international effort could be the Global Cryosphere Watch [98] recently proposed by WMO to be in support of the cryospheric science goals specified for the Integrated Global Observing Strategy Cryosphere Theme [1].

Bibliography

Primary Literature

1. IGOS (2007) Integrated global observing strategy cryosphere theme report – for the monitoring of our environment from space and from Earth. WMO/TD-No. 1405. World Meteorological Organization, Geneva, 100p
2. Perovich D, Light B, Eicken H, Jones K, Runciman K, Nghiem S (2007) Increasing solar heating of the Arctic ocean and adjacent seas, 1979–2005: attribution and role in the ice-albedo feedback. Geophys Res Lett 34:L19505. doi:10.1029/2007GL031480
3. Perovich D, Richter-Menge J, Jones K, Light B (2008) Sunlight, water and ice: extreme arctic sea ice melt during the summer of 2007. Geophys Res Lett 35:L11501. doi:1029/2008GL034007
4. Ainley D, Tynan C, Stirling I (2003) Sea ice: a critical habitat for polar marine mammals. In: Thomas D, Dieckmann G (eds) Sea ice: an introduction to its physics, chemistry, biology and geology. Blackwell Science, Oxford, pp 240–266
5. Arrigo K (2003) Primary production in sea ice. In: Thomas D, Dieckmann G (eds) Sea ice: an introduction to its physics, chemistry, biology and geology. Blackwell Science, Oxford, pp 143–183
6. Lizotte M (2003) The microbiology of sea ice. In: Thomas D, Dieckmann G (eds) Sea ice: an introduction to its physics, chemistry, biology and geology. Blackwell Science, Oxford, pp 184–210
7. Grosse G, Romanovsky V, Jorgenson T, Water Anthony K, Brown J, Overduin P (2011) Vulnerability and feedbacks of permafrost to climate change. EOS 92(9):73–74
8. Cazenave A, Llovel W (2010) Contemporary sea level rise. Ann Rev Mar Sci 2:145–173
9. Prowse TD, Bonsal B, Duguay C, Hessen D, Vuglinsky V (2007) River and lake ice. In: Eamer J, Ahlenius H, Prestrud P, United Nations Environment Programme et al (eds) Global outlook for ice and snow. United Nations Environment Programme, Nairobi, pp 201–214. ISBN 978-92-807-2799-9

10. Kim Y, Kimball J, McDonald K, Glassy J (2011) Developing a global data record of daily landscape freeze/thaw status using satellite passive microwave remote sensing. IEEE Trans Geosci Remote Sens 49(3):949–960
11. McKinley AC (1929) Applied aerial photography. Wiley, New York, 341p
12. Mittelholzer W and others (1925) By airplane towards the north pole (trans: Paul E, Paul C). Hougton Mifflin, Boston, 176p
13. Wilkins H (1929) The Wilkins-Hearst Antarctic Expedition, 1928–1929. Geogr Rev 19(3):353–376
14. Wilkins H (1930) Further Antarctic explorations. Geogr Rev 20(3):357–388
15. Byrd RE (1930) Little America. G.P. Putman's Sons, New York, 422p
16. McDonald RA (1995) Corona: success for space reconnaissance, a look into the cold war and a revolution in intelligence. Photogramm Eng Remote Sens 61(6):689–720
17. Peebles C (1997) The Corona Project: America's First Spy Satellites. Naval Institute Press, Annapolis, 351p
18. Wheelon AD (1997) Corona: the first reconnaissance satellites. Phys Today 50(2):24–30
19. Richelson JT (1998) Scientists in black. Sci Am 278(2):48–55
20. Sohn HS, Jezek KC, van der Veen CJ (1998) Jakobshavn Glacier, West Greenland: 30 years of spaceborne observations. Geophys Res Lett 25(14):2699–2702
21. Zhou G, Jezek KC (2002) 1960s era satellite photograph mosaics of Greenland. Int J Remote Sens 23(6):1143–1160
22. Bindschadler RA, Vornberger P (1998) Changes in the West Antarctic ice sheet since 1963 from declassified satellite photography. Science 279:689–692
23. Kim K, Jezek KC, Sohn H (2001) Ice shelf advance and retreat rates along the coast of Queen Maud Land, Antarctica. J Geophys Res 106(C4):7097–7106
24. Kim K, Jezek K, Liu H (2007) Orthorectified image mosaic of the Antarctic coast compiled from 1963 Argon satellite photography. Int J Remote Sens 28(23–24):5357–5373
25. Waite AH, Schmidt SJ (1962) Gross errors in height indication from pulsed radar altimeters operating over thick ice or snow. Proc IRE 50(6):1515–1520
26. Bogorodsky VV, Bentley CR, Gudmandsen PE (1985) Radioglaciology. D. Reidel, Dordrecht, 254p
27. Fisher E, McMechan G, Gorman M, Cooper A, Aiken C, Ander M, Zumberge M (1989) Determination of bedrock topography beneath the Greenland ice sheet by three-dimensional imaging of radar sounding data. J Geophys Res 94(B3):2874–2882
28. Koenig L, Martin S, Studinger M (2010) Polar airborne observations fill gap in satellite data. EOS 91(38):333–334
29. Schanda E (1986) Physical fundamentals of remote sensing. Springer, Berlin, 187p
30. Hall D, Martinec J (1985) Remote sensing of ice and snow. Chapman and Hall, New York, 189p
31. Rees WG (2006) Remote sensing of snow and ice. Taylor and Francis Group, Boca Raton, 285p
32. Petrenko VF, Whitworth RW (1999) Physics of ice. Oxford University Press, Oxford, 373p
33. Carsey FD (ed) (1992) Microwave remote sensing of sea ice, A.G.U. geophysical monograph 68. American Geophysical Union, Washington, DC, 462p
34. Hollinger J, Peirce J, Poe G (1990) SSM/I instrument evaluation. IEEE Trans Geosci Remote Sens 28(5):781–790
35. Parkinson C, Gloersen P (1993) Global sea ice cover. In: Gurney R, Foster J, Parkinson C (eds) Atlas of satellite observations related to global change. Cambridge University Press, Cambridge, pp 371–383
36. Zwally HJ, Yi D, Kwok R, Zhao Y (2008) ICESat measurements of sea ice freeboard and estimates of sea ice thickness in the Weddell sea. J Geophys Res 113:C02S15. doi:10.1029/2007JC004284
37. Kwok R, Cunningham G, Wensnahan M, Rigor I, Zwally HJ, Yi D (2009) Thinning and volume loss of the Arctic ocean sea ice cover:2003–2008. J Geophys Res 114:C07005. doi:10.1029/2009JC005312

38. Williams R Jr, Hall D (1993) Glaciers. In: Gurney R, Foster J, Parkinson C (eds) Atlas of satellite observations related to global change. Cambridge University Press, Cambridge, pp 401–422
39. Swithinbank C (1973) Higher resolution satellite pictures. Polar Rec 16(104):739–751
40. Swithinbank C, Lucchitta BK (1986) Multispectral digital image mapping of Antarctic ice features. Ann Glaciol 8:159–163
41. U.S. Geological Survey (2010) Satellite image atlas of glaciers of the world. USGS Fact Sheet FS 2005-3056, 2p
42. Merson RH (1989) An AVHRR mosaic of Antarctica. Int J Remote Sens 10:669–674
43. Bindschadler R, Vornberger P (1990) AVHRR imagery reveals Antarctic ice dynamics. EOS 71:741–742
44. Ferrigno JG, Mullins JL, Stapleton JA, Chavez PS Jr, Velasco MG, Williams RS Jr (1996) Satellite image map of Antarctica, Miscellaneous investigations map series 1-2560. U.S Geological Survey, Reston
45. Fahnestock MR, Bindschadler RK, Jezek KC (1993) Greenland ice sheet surface properties and ice dynamics from ERS-1 SAR imagery. Science 262:1525–1530
46. Jezek KC (2008) The RADARSAT-1 Antarctic Mapping Project. BPRC Report No. 22. Byrd Polar Research Center, The Ohio State University, Columbus, 64p
47. Jezek KC (1999) Glaciologic properties of the Antarctic ice sheet from spaceborne synthetic aperture radar observations. Ann Glaciol 29:286–290
48. Jezek K (2003) Observing the Antarctic ice sheet using the RADARSAT-1 synthetic aperture radar. Polar Geogr 27(3):197–209
49. Liu H, Jezek K (2004) A complete high-resolution coastline of Antarctica extracted from orthorectified Radarsat SAR imagery. Photogramm Eng Remote Sens 70(5):605–616
50. Scambos TA, Haran T, Fahnestock M, Painter T, Bohlander J (2007) MODIS-based mosaic of Antarctica (MOA) data sets: continent-wide surface morphology and snow grain size. Remote Sens Environ 111(2–3):242–257
51. Bindschadler R, Vornberger P, Fleming A, Fox A, Mullins J, Binnie D, Paulsen S, Granneman B, Gorodetzky D (2008) The Landsat image mosaic of Antarctica. Remote Sens Environ 112(12):4214–4226
52. Korona J, Berthier E, Bernarda M, Rémy F, Thouvenot E (2008) SPIRIT. SPOT 5 stereoscopic survey of Polar Ice: reference images and topographies during the fourth International Polar Year (2007–2009). ISPRS J Photogramm Remote Sens 64(2):204–212. doi:10.1016/j.isprsjprs.2008.10.005
53. Goldstein RM, Englehardt H, Kamb B, Frohlich R (1993) Satellite radar interferometry for monitoring ice sheet motion: application to an Antarctic ice stream. Science 262:1525–1530
54. Kwok R, Fahnestock M (1996) Ice sheet motion and topography from radar interferometry. IEEE Trans Geosci Remote Sens 34(1):189–199
55. Joughin I, Kwok R, Fahnestock M (1996) Estimation of ice-sheet motion using satellite radar interferometry: method and error analysis with application to Humboldt Glacier, Greenland. J Glaciol 42(142):564–575
56. Gray AL, Short N, Matter KE, Jezek KC (2001) Velocities and ice flux of the Filchner Ice Shelf and its tributaries determined from speckle tracking interferometry. Can J Remote Sens 27(3):193–206
57. Joughin I (2002) Ice-sheet velocity mapping: a combined interferometric and speckle-tracking approach. Ann Glaciol 34(1):195–201
58. Eldhuset P, Andersen S, Hauge EI, Weydahl D (2003) ERS tandem InSAR processing for DEM generation, glacier motion estimation and coherence analysis on Svalbard. Int J Remote Sens 24(7):1415–1437
59. Rignot E, Forster R, Isaaks B (1996) Mapping of glacial motion and surface topography of Hielo Patagonico Norte, Chile, using satellite SAR L-band interferometry data. Ann Glaciol 23:209–216

60. Surazakov A, Aizen V (2006) Estimating volume change of mountain glaciers using SRTM and map-based topographic data. IEEE Trans Geosc Remote Sens 44(10): 2991–2995
61. Joughin I, Gray L, Bindschadler R, Price S, Morse D, Hulba C, Mattar K, Werner C (1999) Tributaries of West Antarctic ice streams revealed by RADARSAT interferometer. Science 286:283–286
62. Stearns L, Jezek K, Van der Veen CJ (2005) Decadal scale variations in ice flow along Whillans ice stream and its tributaries, West Antarctica. J Glaciol 51(172): 147–157
63. Beem L, Jezek K, van der Veen CJ (2010) Basal melt rates beneath the Whillans ice stream, West Antarctica. J Glaciol 56(198):647–654
64. Luckman L, Quencyand D, Beven S (2007) The potential of satellite radar interferometry and feature tracking for monitoring flow rates of Himalayan glaciers. Remote Sens Environ 111:172–181
65. Floricioiu D, Eineder M, Rott H, Yague-Martinez N, Nagler T (2009) Surface velocity and variations of outlet glaciers of the Patagonia Icefields by means of TerraSAR-X. In: Geoscience and remote sensing symposium, IGARSS 2009, vol 2, Cape Town, 12–17 Jul 2009, pp 1028–1031
66. Forster R, Rignot E, Isacks B, Jezek K (1999) Interferometric radar observations of the Hielo Patagonico Sur, Chile. J Glaciol 45(150):325–337
67. Paul F, Haeberli W (2008) Spatial variability of glacier elevation changes in the Swiss Alps obtained from two digital elevation models. Geophys Res Lett 35:L21502. doi:10.1029/2008GL034718
68. Yu J, Liu H, Jezek K, Warner R, Wen J (2010) Analysis of velocity field, mass balance, and basal melt of the Lambert Glacier system by incorporating Radarsat SAR interferometry and ICESat laser altimeter measurements. J Geophys Res 115:B11102. doi:10.1029/2010JB007456
69. Thomas RH (1993) Ice sheets. In: Gurney R, Foster J, Parkinson C (eds) Atlas of satellite observations related to global change. Cambridge University Press, Cambridge, pp 385–400
70. Bhattacharya I, Jezek K, Wang L, Liu H (2009) Surface melt area variability of the Greenland ice sheet: 1979–2008. Geophys Res Lett 36:L20502. doi:10.1029/2009GL039798
71. Liu H, Wang L, Jezek K (2006) Spatio-temporal variations of snow melt zones in Antarctic ice sheet derived from satellite SMMR and SSM/I data (1978–2004). J Geophys Res 111:F01003. doi:1029/2005JF0000318
72. Rignot E, Thomas R (2002) Mass balance of the polar ice sheets. Science 297(5586):1502–1506
73. Rignot E, Kanagaratnam P (2006) Changes in the velocity structure of the Greenland ice sheet. Science 311(5673):986–990
74. Zwally HJ, Giovinetto M, Li J, Cornejo H, Beckley M, Brenner A, Saba J, Yi D (2005) Mass changes of the Greenland and Antarctic ice sheets and shelves and contributions to sea-level rise: 1992–2002. J Glaciol 51(175):509–527
75. Wingham DJ, Shepherd A, Muir A, Marshall G (2006) Mass balance of the Antarctic ice sheet. Philos Trans R Soc A 364:1627–1635
76. Larsen CF, Motyka RJ, Arendt AA, Echelmeyer KA, Geissler PE (2007) Glacier changes in southeast Alaska and northwest British Columbia and contribution to sea level rise. J Geophys Res Earth 112:F01007
77. Thomas R, Frederick E, Krabill W, Manizade S, Martin C (2006) Progressive increase in ice loss from Greenland. Geophys Res Lett 33:L10503. doi:10.1029/2006GL026075
78. Herzfeld UC, McBride PJ, Zwally HJ, Dimarzio J (2008) Elevation change in Pine Island Glacier, Walgreen Coast Antarctica, based on GLAS (2003) and ERS-1(1995) altimeter data analyses and glaciological implications. Int J Remote Sens 29(19):5533–5553. doi:10.1080/01431160802020510

79. Chen J, Wilson C, Blankenship D, Tapley B (2009) Accelerated Antarctic ice loss from satellite gravity measurements. Nat Geosci 2. doi:10.1038/NGEO694
80. Luthcke SB, Zwally HJ, Abdalati W, Rowlands D, Ray R, Nerem R, Lemoine F, McCarthy J, Chinn D (2006) Recent Greenland ice mass loss by drainage system from satellite gravity observations. Science 314(5803):1286–1289
81. Velicogna I (2009) Increasing rates of ice mass loss from the Greenland and Antarctic ice sheets revealed by GRACE. Geophys Res Lett 36:L19503. doi:10.1029/2009GL040222
82. Luthcke S, Arendt A, Rowlands D, McCarthy J, Larsen C (2008) Recent glacier mass changes in the Gulf of Alaska region from GRACE mascon solutions. J Glaciol 54(188):767–777
83. Thomas R, Davis C, Frederick E, Krabill W, Li Y, Manizade S, Martin C (2008) A comparison of Greenland ice-sheet volume changes derived from altimetry measurements. J Glaciol 54(185):203–212
84. Rignot E, Velicogna I, van den Broeke MR, Monaghan A, Lenaerts J (2011) Acceleration of the contribution of the Greenland and Antarctic ice sheets to sea level rise. Geophys Res Lett 38:L05503. doi:10.1029/2011GL046583
85. Hall D, Riggs G, Salomonson V, DiGirolamo N, Bayr K (2002) MODIS snow-cover products. Remote Sens Environ 83:181–194
86. Dery S, Brown R (2007) Recent northern hemisphere snow cover extent trends and implications for the snow-albedo feedback. Geophys Res Lett 34:L22504. doi:10.1029/2007GL031474
87. Foster J, Chang A (1993) Snow cover. In: Gurney R, Foster J, Parkinson C (eds) Atlas of satellite observations related to global change. Cambridge University Press, Cambridge, pp 361–370
88. Forster R, Long D, Jezek K, Drobot S, Anderson M (2001) The onset of Arctic sea-ice snow melt as detected with passive and active microwave remote sensing. Ann Glaciol 33:85–93
89. Jeffries M, Morris K, Kozlenko N (2005) Ice characteristics and processes, and remote sensing of frozen rivers and lakes. In: Duguay C, Piertroniro A (eds) Remote sensing of northern hydrology, Geophysical monograph series 163. American Geophysical Union, Washington, DC, pp 63–90
90. Duguay C, Zhang T, Leverington D, Romanovsky V (2005) Satellite remote sensing of permafrost and seasonally frozen ground. In: Duguay C, Piertroniro A (eds) Remote sensing of northern hydrology, Geophysical monograph series 163. American Geophysical Union, Washington, DC, pp 91–142
91. Jeffries M, Morris K, Liston G (1996) Method to determine lake depth and water availability on the north slope of Alaska with spaceborne imaging radar and numberical ice growth modeling. Arctic 49(4):367–374
92. Jezek K, Wu X, Gogineni P, Rodriguez E, Freeman A, Fernando-Morales F, Clark C (2011) Radar images of the bed of the Greenland ice sheet. Geophys Res Lett 38:L01501. doi:10.1029/2010GL045519
93. Jezek K, Drinkwater M (2010) Satellite observations from the International Polar Year. EOS Trans AGU 91(14):125–126
94. Crevier Y, Rigby G, Werle D, Jezek K, Ball D (2010) A RADARSAT-2 snapshot of Antarctica during the 2007–08 IPY. Newsl Can Antarct Res Netw 28:1–5
95. Picardi G, Plaut JJ, Biccari D, Bombaci O, Calabrese D, Cartacci M, Cicchetti A, Clifford SM, Edenhofer P, Farrell WM, Federico C, Frigeri A, Gurnett DA, Hagfors T, Heggy E, Herique A, Huff RL, Ivanov AB, Johnson WTK, Jordan RL, Kirchner DL, Kofman W, Leuschen CJ, Nielsen E, Orosei R, Pettinelli E, Phillips RJ, Plettemeier D, Safaeinili A, Seu R, Stofan ER, Vannaroni G, Watters TR, Zampolini E (2005) Radar soundings of subsurface Mars. Science 310(5756):1925–1928. doi:10.1126/science.1122165
96. Asmus VV, Dyaduchenko VN, Nosenko YI, Polishchuk GM, Selin VA (2007) A highly elliptical orbit space system for hydrometeorological monitoring of the Arctic region. WMO Bull 56(4):293–296

97. Drinkwater MR, Jezek KC, Key J (2008) Coordinated satellite observations during the International Polar Year: towards achieving a Polar Constellation. Space Res Today 171:6–17
98. Goodison B, Brown J, Jezek K, Key J, Prowse T, Snorrason A, Worby T (2007) State and fate of the polar cryosphere, including variability in the Artic hydrologic cycle. WMO Bull 56(4): 284–292

Books and Reviews

Gloersen P, Campbell W, Cavalieri D, Comiso J, Parkinson C, Zwally H (1992) Arctic and Antarctic sea ice, 1978–1987: satellite passive microwave observations and analysis, NASA SP-511. NASA, Washington, DC, 290p

Parkinson C, Comiso J, Zwally H, Cavalieri D, Gloersen P, Campbell W (1987) Arctic sea ice, 1973–1976: satellite passive microwave observations, NASA SP-489. NASA, Washington, DC, 296p

Schnack-Schiel S (2003) The macrobiology of sea ice. In: Thomas D, Dieckmann G (eds) Sea ice: an introduction to its physics, chemistry, biology and geology. Blackwell Science, Oxford, pp 211–239

Weeks W, Hibler W (2010) On sea ice. University of Alaska Press, Fairbanks, 664p

Zwally H, Comiso J, Parkinson C, Campbell W, Carsey F, Gloersen P (1983) Antarctic sea ice, 1973–1976: satellite passive microwave observations, NASA SP-459. NASA, Washington, DC, 206p

Chapter 3
Aircraft and Space Atmospheric Measurements Using Differential Absorption Lidar (DIAL)

Russell De Young

Glossary

Absorption	The process in which incident radiant energy is retained or absorbed by a gas.
Absorption coefficient	The fraction of incident energy removed by absorption per unit length of travel of radiation through a gas.
Active remote sensing	A remote sensing system that transmits its own energy source and measures atmospheric properties from the returned signal.
Aerosol	A colloidal suspension of liquid or solid particles in air.
Aerosol extinction	The reduction of optical energy passing through the atmosphere due to scattering and absorption of that energy.
Atmospheric boundary layer	The bottom layer of the atmosphere that is in contact with the surface and is often turbulent with a capped stable layer of air or temperature inversion. The height is variable but is typically several kilometers during the day.
Depolarization ratio	Defined as the ratio of the backscattered lidar power in the cross-polarization plane to the backscattered power in the polarization plane (transmitted laser beam) induced by the atmospheric constituents.
DIAL	Differential absorption lidar is a lidar technique used to measure the atmospheric concentration of any gas as a function of altitude.

This chapter was originally published as part of the Encyclopedia of Sustainability Science and Technology edited by Robert A. Meyers. DOI:10.1007/978-1-4419-0851-3

R. De Young (✉)
NASA Langley Research Center, Mail Stop 401A, Hampton, VA 23681-0001, USA
e-mail: Russell.J.Deyoung@nasa.gov

J. Orcutt (ed.), *Earth System Monitoring: Selected Entries from the Encyclopedia of Sustainability Science and Technology*, DOI 10.1007/978-1-4614-5684-1_3,

Extinction coefficient	The fraction of incident radiant energy removed by extinction per unit of travel of radiation through the air.
In situ	Methods for obtaining information about atmospheric properties through direct contact with the atmosphere as opposed to remote sensing.
Lidar	Light Detection and Ranging is a technique for detecting and characterizing atmospheric properties using a pulsed laser.
Passive remote sensing	A remote sensing technique that relies on the use of the Sun, Moon, or Earth surface as a radiation source to measure atmospheric gas species by absorption of that radiation as it passes through the atmosphere.
Polarization	The property of light where the electric field vector is oriented in a single plane called plane polarization.
Primary trace atmospheric gas or particles	Substances that are directly emitted into the atmosphere from the surface, vegetation, or natural or human activities such as fires, industrial processes, and car emissions.
Relative humidity	The ratio of the vapor pressure of water to its saturation vapor pressure at the same temperature.
Scattering	The process by which atmospheric gases are excited to radiate by an external source of light and the resultant light is usually detected in a direction not aligned with the light source.
Scattering coefficient	The fraction of incident radiant energy removed by scattering per unit length of travel of radiation through the air.
Stratosphere	The region of the atmosphere from the top of the troposphere to a height of 10–17 km (the base of the mesosphere).
Troposphere	The region of the atmosphere from the Earth's surface to the tropopause at 10–20 km, depending on latitude and season, where most weather occurs.

Definition of the Subject and Its Importance

The study of the atmosphere has expanded greatly in the past decade due to concern about global climate change and air quality health effects. The natural atmospheric chemistry is complex but with anthropogenic emissions released into the

This chapter was originally published as part of the Encyclopedia of Sustainability Science and Technology edited by Robert A. Meyers. DOI:10.1007/978-1-4614-5684-1_1

atmosphere, the resulting complexity makes modeling very difficult. Chemical reactions generally increase with temperature and thus a warming climate may change the weather and climate in unpredictable ways. Also with increased regulations regarding air quality emissions, more attention is being directed toward atmospheric species measurements to assess the impact of specific emission regulations. As a result of these concerns, lidar has become a very valuable tool to directly measure the number density of specific atmospheric species as a function of altitude. This article will review the use of differential absorption lidar (DIAL) in current aircraft based missions and the potential for use of DIAL in orbiting spacecraft

A particular lidar technique called Differential Absorption Lidar (DIAL) has proven to be an especially powerful method to measure atmospheric species. It has been used both on the ground and in many aircraft to determine the concentration of gas species. There are presently no DIAL systems in space, but there are projections by NASA and other nations to place them in Earth orbit to measure critical gases over remote areas and for long periods of time. This article will discuss the DIAL technique, demonstrate its usefulness using airborne examples, and discuss the value of a space–based DIAL satellite system.

Introduction

The need for accurate atmospheric gas concentration measurements as a function of altitude has expanded as a result of predicted atmospheric changes associated with global climate change and the impact of air quality on human health. Both local natural and anthropogenic emissions can be transported around the Earth and thus have health impacts far from the emission sources. Lidar has proven to be a powerful technique for measuring the concentrations of many gas species related to health and climate change concern.

Differential Absorption Lidar (DIAL) from aircraft was first accomplished for ozone at NASA Langley Research Center in 1980 [1] and for water vapor in 1982 [2]. Currently DIAL systems are being flown by NOAA and European countries, but presently there are no DIAL systems deployed in space.

The DIAL system has the ability to address major questions concerning the atmosphere. DIAL systems can be deployed in fixed ground locations, in either piloted or unpiloted aircraft or in satellite platforms. Each has distinct advantages for addressing atmospheric research questions. Some of these questions are:

- How does urban pollution transport out of the boundary layer into the free troposphere and then to continental scales?
- How do atmospheric species chemically transform with transport age and reaction with other species?

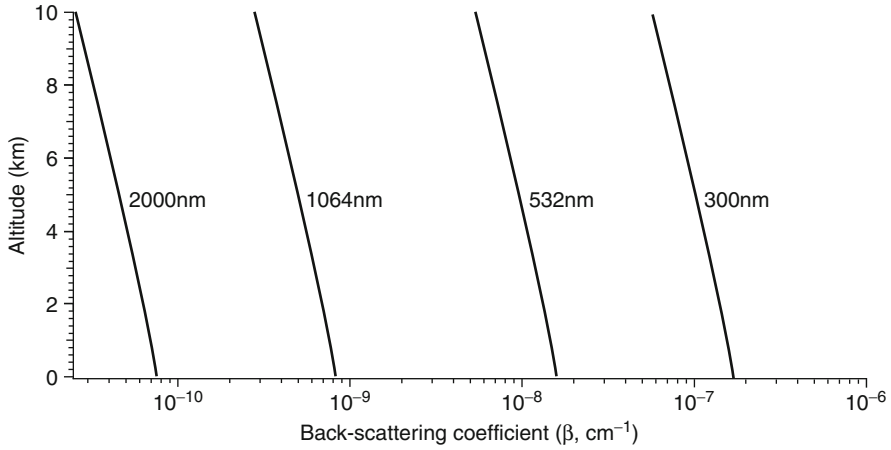

Fig. 3.1 Backscattering coefficient vs. altitude for different laser wavelengths and northern latitude standard atmosphere

- What vertical and horizontal resolution measurements are needed to substantially improve chemical weather models?
- What atmospheric species need to be measured simultaneously to understand atmospheric chemical transformation?
- What are the temporal and spatial water vapor scales needed to improve hurricane intensification and path forecasting?
- To what resolution do we need to measure atmospheric water vapor to make future weather predictions for every square kilometer and for 1 month in the future for the entire globe?
- Can climate change impacts be measured for chemical weather?

Atmospheric Backscattering and the DIAL Equation

The ability to use laser remote sensing relies on the characteristic of electromagnetic radiation scattering from atmospheric aerosols and molecules. The atmosphere consists primarily of nitrogen and oxygen molecules as well as highly variable aerosols. Scattering from molecules or Rayleigh scattering can be calculated as [3]

$$\beta = (3/8\pi)\beta_s(P/P_s)(T_s/T) \tag{3.1}$$

where β_s is the volume scattering coefficient (km^{-1}) for the laser wavelength used, P_s is 1013.25 millibars, T_s is 288.15 K, and T and P are the standard pressures and temperatures at altitude. Equation 3.1 describes the backscatter coefficient that scatters some laser radiation back to the DIAL receiver system. Figure 3.1 shows the results of Eq. 3.1 for several common laser wavelengths. The wavelengths at

355, 532, and 1,064 nm are associated with the Nd:YAG laser system while 2,000 nm is commonly used for CO_2 DIAL measurements. Several important properties are noted from the figure. The backscatter coefficient decreases by three orders of magnitude from 355 to 2,000 nm making the use of DIAL more difficult in the infrared. The backscatter is much higher at lower altitudes due to the increased atmospheric density but this also has a disadvantage in that optical detectors are easily saturated by the near field atmospheric lidar return causing signal-induced noise. In contrast the backscatter at 10 km is much less, but this is an advantage for aircraft deployed systems in that the near field signal is substantially reduced, thus reducing signal-induced noise in optical detectors [4].

Scattering also occurs from atmospheric aerosols, but aerosols are highly variable in spatial and temporal extent. Nevertheless, both aerosols and molecules contribute to the lidar backscatter signal.

The DIAL equation, giving the atmospheric number density N of any gas species, is derived from the lidar equation which is discussed in detail in [5–7] and given as

$$\begin{aligned} N(R) = {} & 1/(2(R_2 - R_1)(\sigma_{on} - \sigma_{off})) \\ & * \ln(P_{on}(R_1)P_{off}(R_2)/P_{off}(R_1)P_{on}(R_2)) \\ & - 1/(2(R_2 - R_1)(\sigma_{on} - \sigma_{off})) \\ & * \ln(\beta_{on}(R_1)\beta_{off}(R_2)/\beta_{off}(R_1)\beta_{on}(R_2)) \\ & - 1/(\sigma_{on} - \sigma_{off}) * (\alpha_{on} - \alpha_{off}) \end{aligned} \tag{3.2}$$

where the third term is a correction for scattering and absorption of interfering gas species as well as the finite difference (due to the on- and off-line wavelength difference) in the average extinction coefficient, α. If care is taken on the choice of wavelengths to avoid interfering gases and the difference between on- and off-line-wavelengths is small, then this term is negligible. The second term accounts for an inhomogeneous atmosphere where the backscatter coefficient, β, is different at ranges R_1 and R_2. Assuming a homogeneous atmosphere and a sufficiently small on- and off-line wavelength difference, then this term can be made negligible. The first term is the traditional DIAL equation. Here R_2–R_1 is the range cell defined by the digitization rate of the receiver digitizer. The differential absorption cross section, $\sigma_{on}-\sigma_{off}$, is the difference between the on- and off-line cross sections at the on- and off-line wavelengths. The "ln" term is the ratio of the on- and off-line powers received at either R_1 or R_2 ranges. Kuang [8] gives an example of a typical ozone DIAL analysis for a ground-based system with an aerosol correction procedure.

Figure 3.2 outlines the characteristics of the DIAL technique. A pulsed laser emits pulses at either the on- or off-line wavelength with a narrow divergence. The range of interest, R, is determined by ct/2 where c is the light velocity and t is the round trip time. At some point in the atmosphere, the laser divergence intersects the receiver field of view and due to atmospheric scattering, receives the power P(r). The range cell is usually set by the digitization rate, for example a rate of 5-MHz results in a 30-m range cell (R_2–R_1). The online wavelength corresponds to a well-

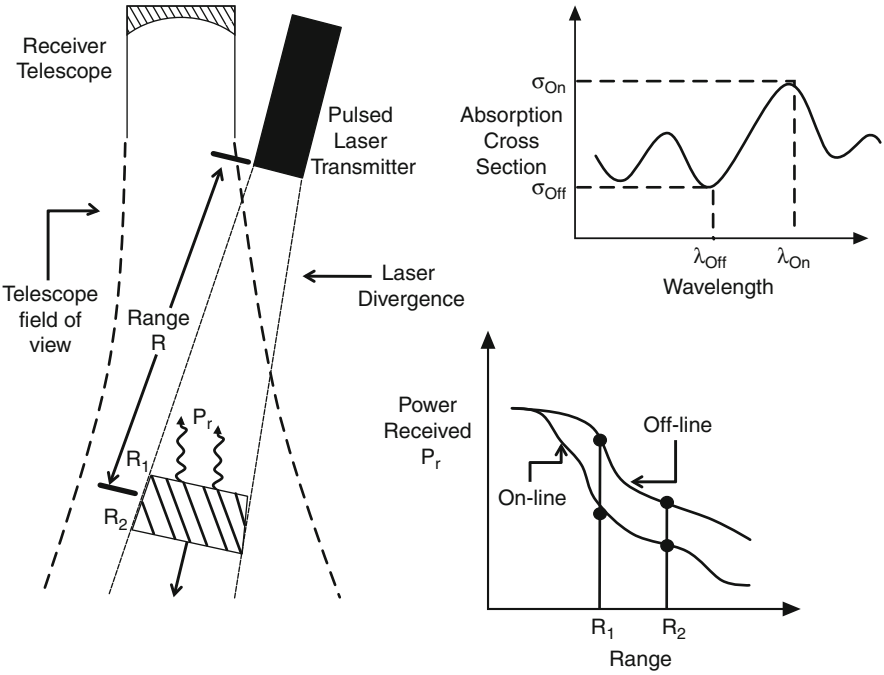

Fig. 3.2 Characteristics of the DIAL technique

known absorption feature of the particular gas species to be measured. Since the linewidth of the laser has some finite width, care is taken to determine the convolution of the laser linewidth with the absorption linewidth. The off-line is chosen near the online wavelength but in a region where there is no (little) absorption by the gas species of interest. Generally, the on- and off-line pulses are alternating at a repetition rate as high as possible to allow noise reduction by averaging without sacrificing horizontal resolution. The on- and off-line powers at each range cell R_2–R_1 are recorded at the receiver computer for postprocessing into curtain profiles of the particular gas species.

Several examples will now be described that illustrate the power of the DIAL technique to profile the atmosphere for different species from both aircraft and space platforms.

Airborne Ozone DIAL

NASA has a variety of aircraft that are regularly involved in atmospheric research. The most capable aircraft is the NASA DC-8 aircraft shown in Fig. 3.3, which has flown in research mission all over the world for the past 20 years. The DC-8 carries

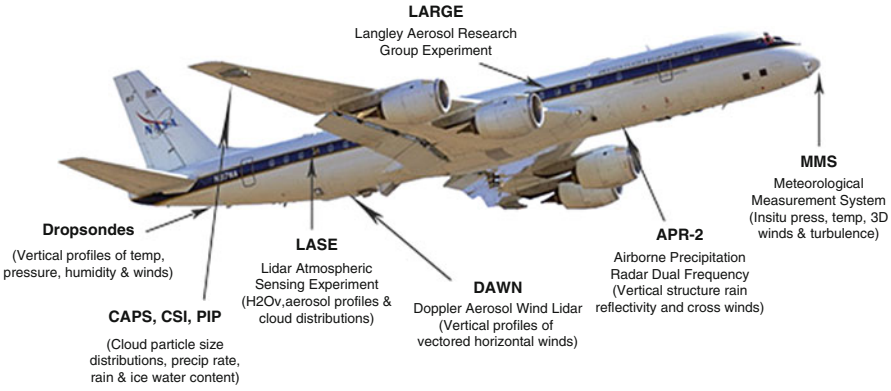

Fig. 3.3 The NASA DC-8 aircraft with several measurement systems listed including the water vapor DIAL system LASE

an ozone or water vapor DIAL system along with a dozen other instruments that probe the atmosphere resulting in a synergistic measurements platform.

Figure 3.4 shows a schematic of the NASA Langley ozone DIAL system on the DC-8 aircraft. There are two Nd:YAG lasers: one for the online (290 nm) and the other for the off-line (300 nm) wavelength. Each Nd:YAG laser pumps a corresponding dye laser which in turn is doubled into the ultraviolet spectral region at 300 or 290 nm with a pulse repetition rate of 40 Hz each and an on- and off-line separation of 350 μs. The on- and off-line laser pulse energy is split in two: One is transmitted in the zenith and the other in the nadir. As the aircraft flies, ozone profiles from the ground to the aircraft and from the aircraft to the stratosphere are simultaneously recorded. These two profiles can then be spliced together with the aircraft in situ ozone data, resulting in a complete ozone atmospheric profile. The ozone is usually presented in terms of mixing ratio or parts per billion by volume (ppbv). The vertical return signal is averaged to produce a resolution of 300 m and the horizontal resolution is 12 km.

The DIAL technique also has the advantage of retrieving data on clouds and aerosols. The residual dye laser energy at 599 nm (zenith) and at 583 nm (nadir) is vertically polarized and along with the residual 1,064-nm energy is transmitted with the UV ozone wavelengths. The visible wavelengths are received and sent through a cross polarizer to determine the percentage of backscattered depolarization. The resolution of the aerosol channel is 60 m in the vertical and 400 m in the horizontal.

An example is given to demonstrate the science derived and the capability of the DIAL technique for measuring atmospheric ozone. This example is from the NASA **A**rctic **R**esearch of the **C**omposition of the **T**roposphere from **A**ircraft and **S**atellites (ARCTAS) mission [9] and presents a complete DIAL data set for flight 15 on June 24, 2008.

Figure 3.5 shows the 8-h DC-8 flight track around Los Angeles, CA. The corresponding ozone atmospheric profile is shown for the flight track. The ozone

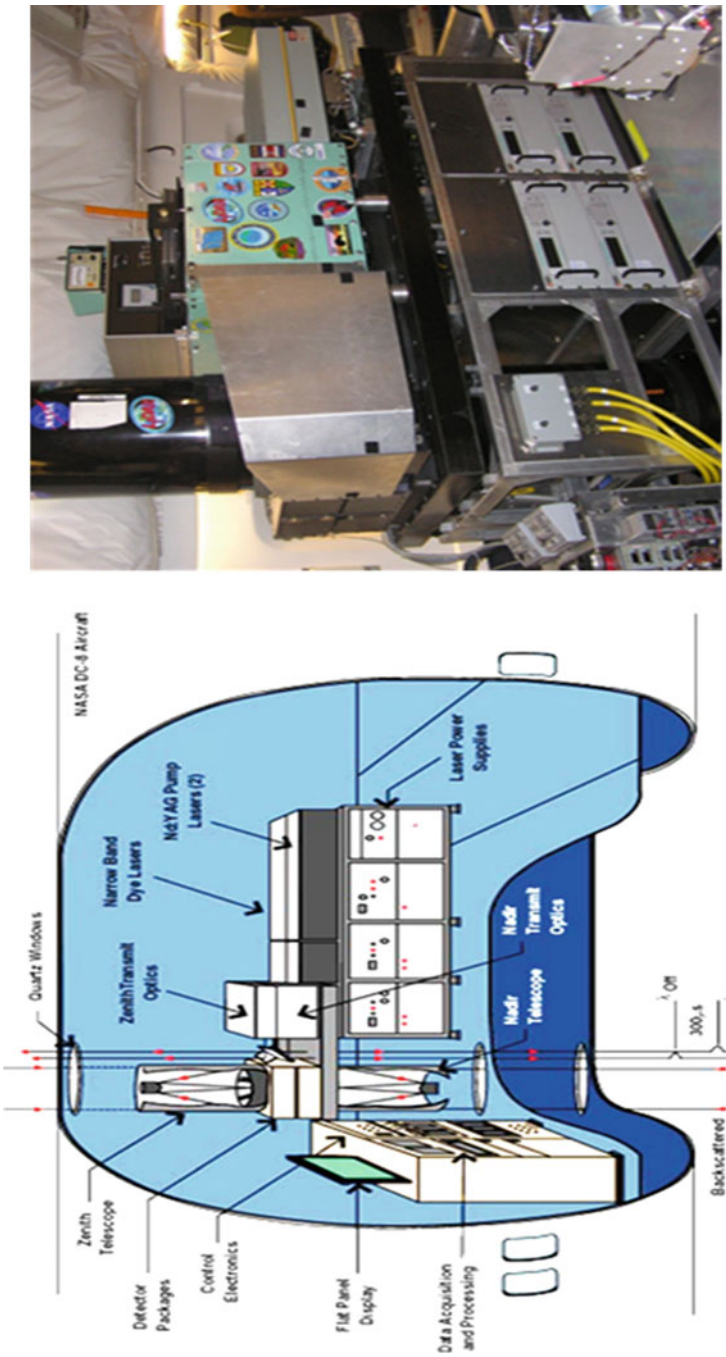

Fig. 3.4 Schematic and photo of the NASA Langley ozone DIAL system on the DC-8 aircraft

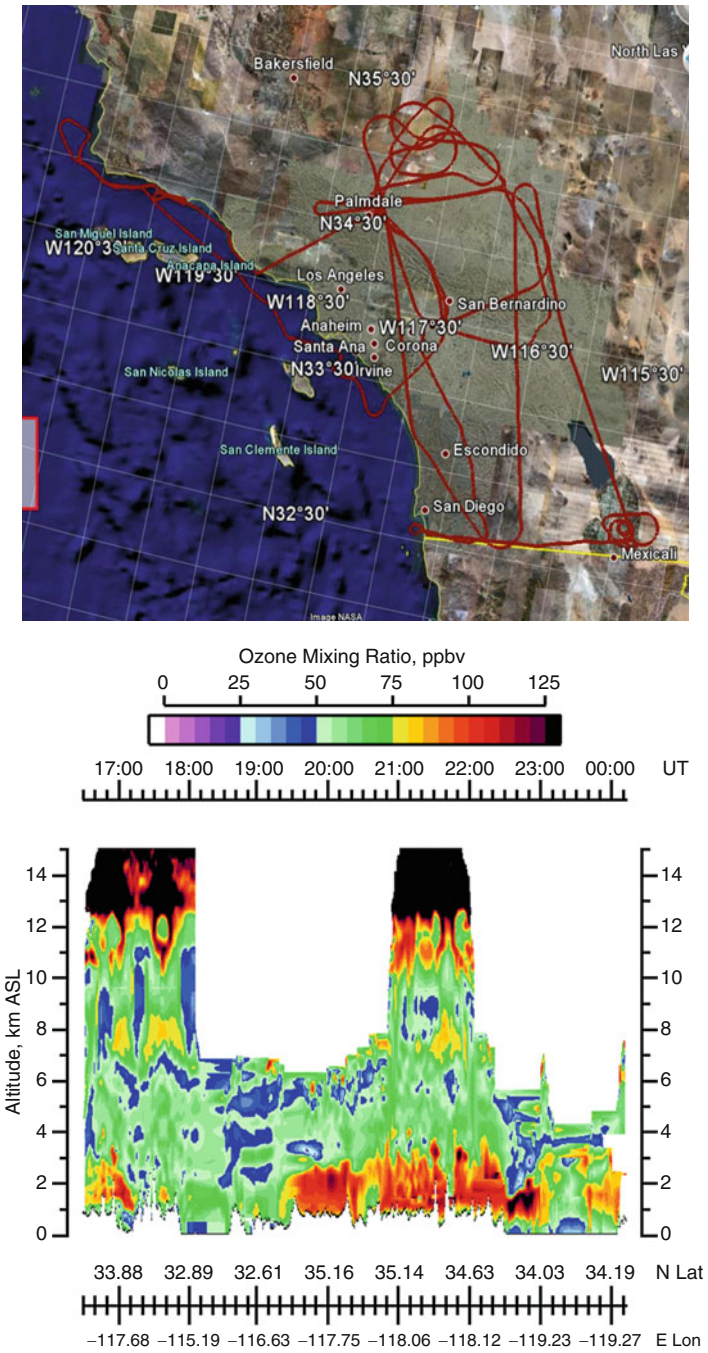

Fig. 3.5 The aircraft flight plan for ARCTAS campaign on June 24, 2008 and the corresponding DIAL ozone atmospheric profile in parts per billion by volume

concentration, as a function of altitude, is colored and corresponds to an ozone mixing ratio of 0–125 ppbv. This profile is interesting as it shows both stratospheric and boundary layer ozone. In the stratosphere the ozone is typically greater than 2,500 ppbv, so the figure shows the lower edge of the stratospheric ozone layer that protects life from harmful UV exposure from the Sun. The dynamics of the stratospheric/tropospheric boundary cause ozone filaments to bleed into the troposphere at 12 km as shown in the figure. The ground profile is shown in kilometers above sea level and in the mountains north of Los Angeles high ozone concentrations are observed. At the flight time, there were numerous fires in the mountain region generating both aerosols and ozone. Ozone concentrations above 100 ppbv are measured and seen to transport out into the Pacific Ocean where the ozone decreases as the flight track moves northwest. While this ozone was generated in remote areas, the ozone generated in urban areas as a result of anthropogenic emissions can have severe health effects especially above background levels of 40 ppbv (U.S. EPA primary ozone standard is 75 ppb) and DIAL has the ability to measure the atmospheric distribution of this ozone. Likewise, stratospheric ozone has been measured especially with regard to stratoshperic depletion in Antarctica due to chlorofluorocarbon emissions.

The residual laser energy at 1,064 and 591 nm (average of the two dye laser wavelengths) is transmitted along with the DIAL UV wavelengths to probe the aerosol distribution above and below the aircraft. If the aerosol size parameter $2\pi r/\lambda < 1$, where r is the aerosol radius and λ the lidar wavelength, then large backscattering occurs. The 1,064- and 591-nm wavelengths probe different aerosol size distributions. Figure 3.6 shows the aerosol backscattering ratio at both 1,064- and 591-nm wavelengths as a function of altitude. This ratio is the backscatter at either wavelength to the molecular atmospheric backscatter at the pressure altitude. If the ratio is zero, then there is no aerosol scattering, only molecular scattering. Most of the aerosol backscattering occurs near the ground which is the atmospheric source of aerosols. In the figure, high aerosol scattering occurs near the fire sites in the mountains but aerosols are also transported out over the ocean (at times past 22.50 UT) where they are hydrated by moisture and thus grow in size producing greater backscatter. It is interesting to note that there are no clouds detected in the profile, yet nowhere in the atmosphere is there pure molecular scattering. This has implications for climate change as aerosols can either reflect or absorb incident energy, affecting the energy balance of the global atmosphere.

The aerosol wavelength dependence (color ratio) is shown in Fig. 3.7. The color ratio is the ratio of 1,064 to 591-nm backscattering and gives an indication of relative aerosol size with larger ratios indicating larger aerosols. As seen during the flight time of 21:00–22:00, finer particles are emitted by these fires but as they rise they grow in size, probably due to hydration. The aerosols also tend to grow in size as they transport over the ocean after time 22:30.

Figure 3.7 also shows the aerosol depolarization at 591 nm derived from the aerosol scattering ratio. The laser is linearly polarized as it is transmitted into the atmosphere and two receiver channels are used to detect the atmospheric return, one capturing the linear polarized return and the other the orthogonal or depolarized return signal. The ratio of the depolarized signal to the transmitted linear polarized

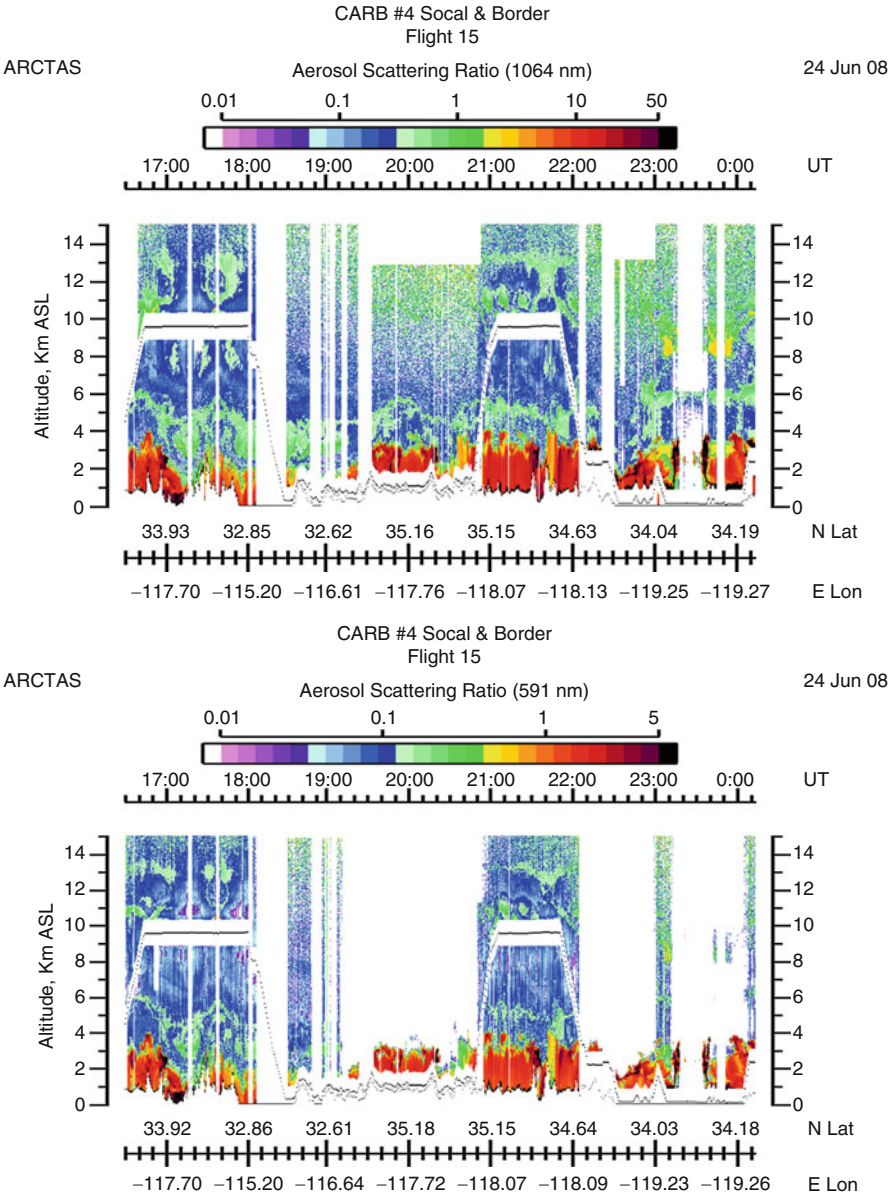

Fig. 3.6 The aerosol scattering ratio for 1,064 and 591 nm (average of the dye laser wavelengths) as a function of altitude. The ground profile above sea level is noted as well as the aircraft flight track

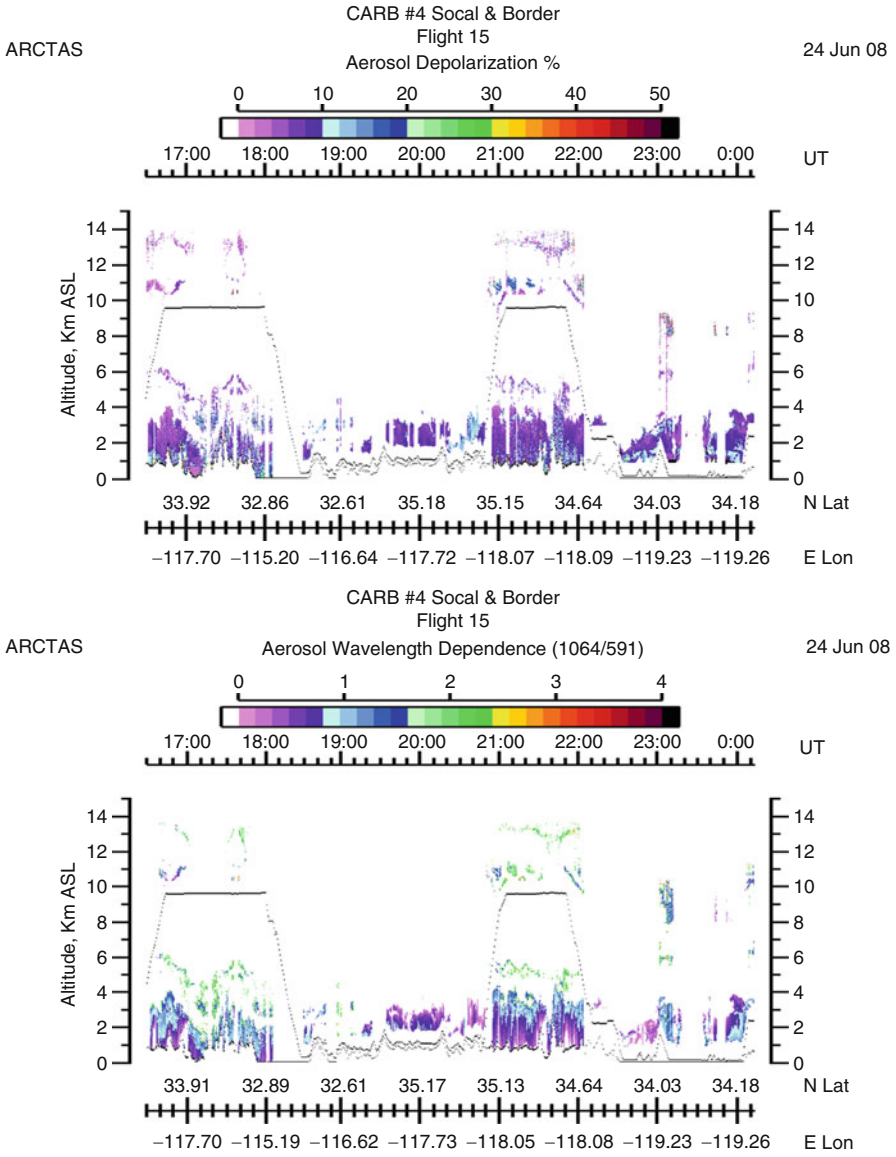

Fig. 3.7 The percent aerosol depolarization and the ratio of 1,064–591 nm backscatter is shown as a function of altitude

signal is the aerosol depolarization. Spherical aerosols backscatter light with little polarization change, but nonspherical aerosols generally depolarize the backscatter signal depending on their shape [10]. Thus, the depolarization gives some information on the structure and shape of the atmospheric aerosols and can distinguish

between liquid and solid phase aerosols. In the figure, the depolarization measured was generally between 3% and 9%. The fires at 17:00 UT appear to contain less dust (less depolarization) than fires at 21:00–22:00 UT, where the depolarization is higher, indicating the fires there lifted more dust into the fire plume.

This example of the DIAL technique for measuring ozone demonstrates the utility of DIAL. Here both the stratospheric and tropospheric ozone concentration can be determined simultaneously. Further the residual laser energy of the dye lasers is used to probe the aerosols at 591 and 1,064 nm, showing the importance of aerosols in the boundary layer as well as aerosol transport in the troposphere. This example shows the importance of measuring both ozone and aerosols simultaneously.

The ozone absorption cross section is broad in the ultraviolet spectral region (250–320 nm), allowing many different wavelength on- and off-line pairs to be used. Absorption cross section for ozone and a number of atmospheric gases of interest for atmospheric chemistry are shown by Schoulepnikoff [11]. For the stratosphere where ozone density is large, wavelength pairs near 320 are used in order to generate a significant return signal. Whereas in the troposphere where the ozone mixing ratio is lower, higher absorption is needed, thus wavelength pairs from 280 to 300 are used.

Airborne Water Vapor DIAL

Atmospheric water vapor is the most radiatively active gas in the atmosphere and as a result affects weather patterns, precipitation, clouds, and hurricanes. Water vapor and ozone affect the production of OH radicals which help determine tropospheric chemistry. At high relative humidities, aerosols grow hydroscopiclly and in turn reduce visibility. Water vapor has very high temporal and spatial variability in the atmosphere and radiosonde or space–based satellite passive instruments cannot fully characterize the global variability. Airborne and eventually space–based water vapor DIAL systems could characterize the water vapor distribution for climate change and real-time weather forecasting by providing high vertical and horizontal profiles of water vapor distributions for input into climate models. Like ozone DIAL, a water vapor DIAL system can also measure clouds and aerosols, which significantly improves our understanding of water vapor distribution dynamics. Clouds and aerosols are currently the largest source of uncertainty in global climate models and both play a major role in atmospheric chemistry.

Figure 3.8 shows a schematic and photo of the Laser Atmospheric Sensing Experiment (LASE) water vapor DIAL system on the NASA DC-8 aircraft. The LASE system uses a Ti:sapphire–based laser transmitter [12]. This laser is a 5-Hz double-pulsed (300-μs separation) Ti:sapphire laser that operates on the 817.2213-nm (vac) absorption line of water vapor and is pumped by a frequency-doubled flashlamp-pumped Nd:YAG laser. The laser wavelength is varied along the water vapor absorption line to create an on- and off-line DIAL wavelength pair.

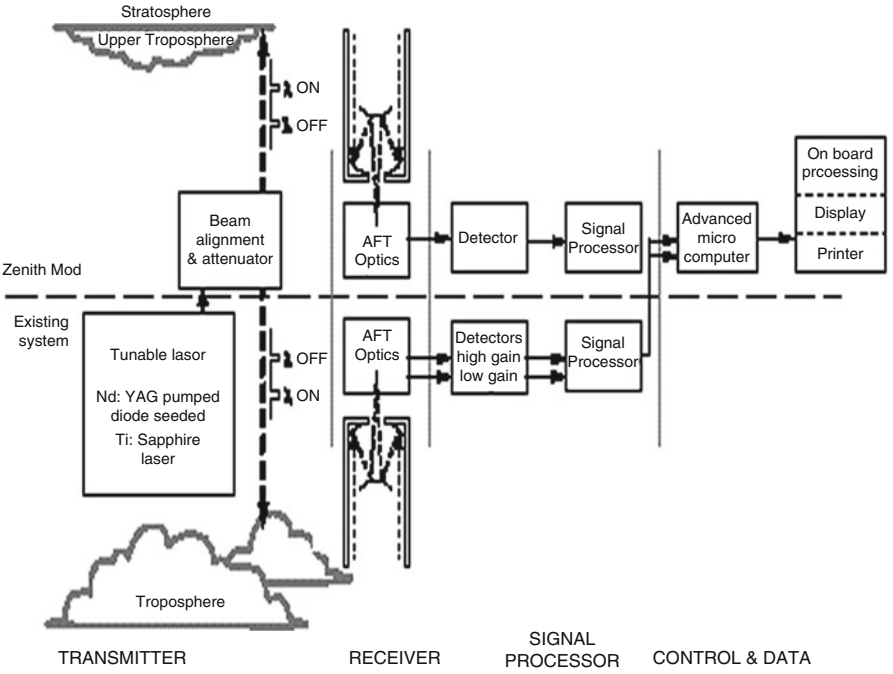

Fig. 3.8 The Laser Atmospheric Sensing Experiment (LASE) water vapor DIAL system schematic and photo of instrument on the NASA DC-8 aircraft

LASE can operate over two or three water vapor concentration regions to cover a large altitude region (dynamic range) in the troposphere. This unique method of operation permits rapid and more flexible absorption cross-section selection capability for water vapor measurements over the entire troposphere in a single pass.

The off-line wavelength is used to measure the aerosol scattering ratio and is selected for minimum absorption by water vapor. The wavelength of the laser is controlled by diode laser injection seeding that is frequency locked to the water vapor line using a water vapor absorption cell. The laser linewidth is less than 0.25 pm and the line stability is approximately 0.35 pm, much less than the pressure broadened atmospheric water vapor linewidth. The pulse energy ranges from 75 to 100 mJ and approximately 60% of the energy is transmitted in the nadir direction and 40% in the zenith direction. The beam divergence is typically 1 mrad and the telescope field of view is 1.5 mrad. The detector system consists of two silicon avalanche photodiodes (Si:APD) and three digitizers to cover a large signal dynamic range (10^6). The data system on the DC-8 will enable real-time and postflight analyses onboard the aircraft.

Atmospheric water vapor profiles are taken during night or day with a vertical resolution of 330 m and horizontal resolution of from 14 to 42 km. The aerosol resolution is 30 m in the vertical and 200 m in the horizontal. The accuracy of the water vapor measurement is 6% or 0.01 g/kg whichever is greater. The atmospheric in situ water vapor aircraft data can be spliced into the LASE DIAL data to produce a complete water vapor profile throughout the troposphere.

Figure 3.9 is a profile example from the Genesis and Rapid Intensification Processes (GRIP) DC-8 aircraft campaign from August 15 to September 30, 2010 [13]. This flight segment took place east of Denver, CO over a relatively flat agriculture area. In the figure, the boundary layer is shown below 2 km containing significant amounts of water vapor. Above the boundary layer the air mass is quite dry. Back trajectories have determined that this air mass came from the California fires occurring at that time, thus there is enhanced backscattering from smoke particles at 5 km. The aerosol scattering ratio is increased at the top of the boundary layer due to absorption of water by the aerosols, increasing their size, thus producing this thin layer of enhanced backscattering.

Figure 3.10 outlines the analysis process by which the DIAL raw data is transformed into useful data products [14]. The atmospheric return signals are combined with ground elevation data and DC-8 navigation and in situ water vapor data to create a composite water vapor return. There are three wavelength on- and off-line pairs used for different atmospheric water absorption conditions as well as three amplifier gains to increase the measurement dynamic range. This data is used to create an initial DIAL calculation for water vapor and also relative aerosol backscatter. Temperature, pressure, and relative humidity data from radiosondes on the DC-8 are used to calculate the effect of temperature and pressure on water vapor line boarding as well as aerosol scattering. The nadir and zenith profiles are combined with in situ water vapor data to produce a complete water vapor profile of the troposphere. The aerosol scattering analysis is done in an iterative process to create the aerosol scattering ratio with water correction.

Space-Based DIAL

Currently there are no space deployed Earth orbiting DIAL systems. There are simpler backscatter Earth orbiting lidar systems to measure clouds and aerosols.

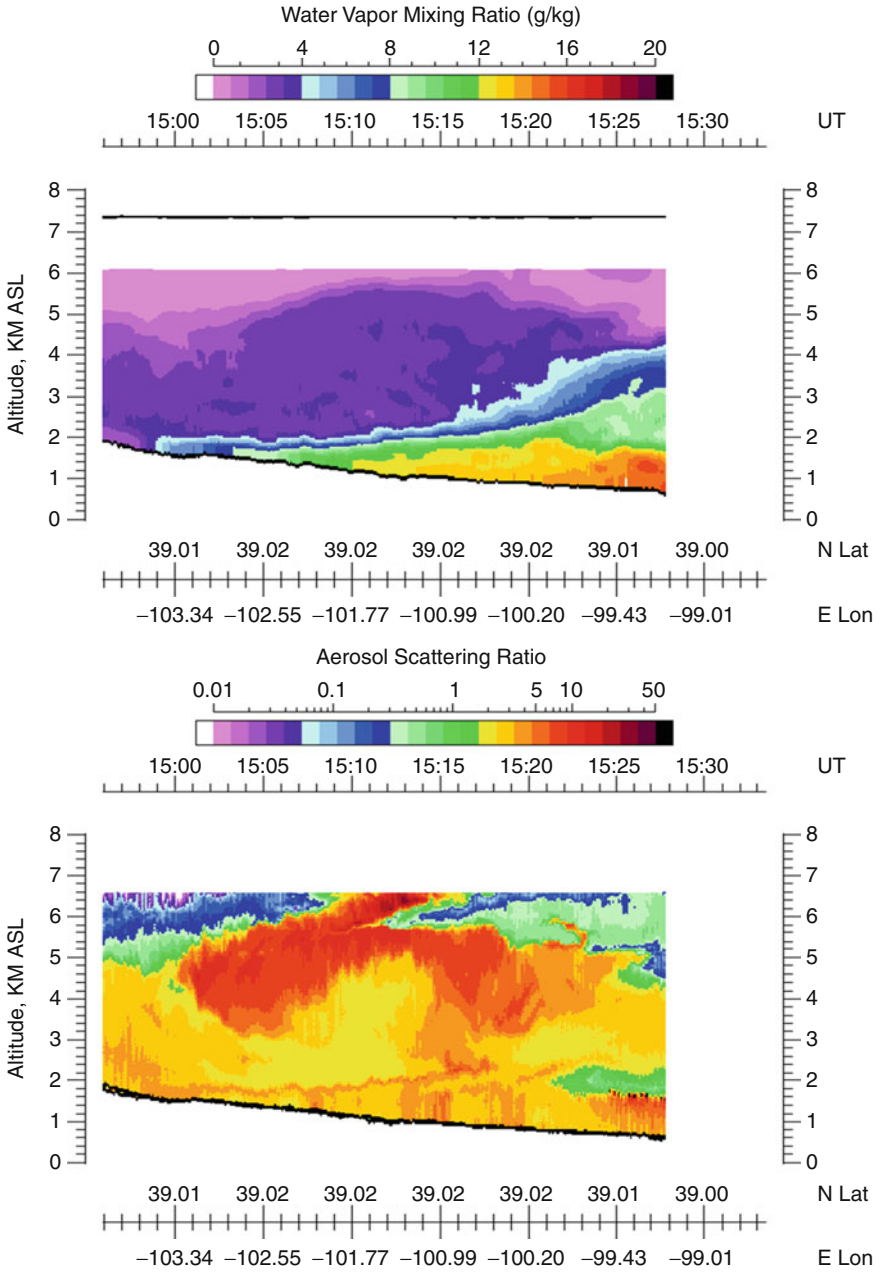

Fig. 3.9 Water vapor mixing ratio and the corresponding aerosol scattering ratio during the GRIP campaign [12]

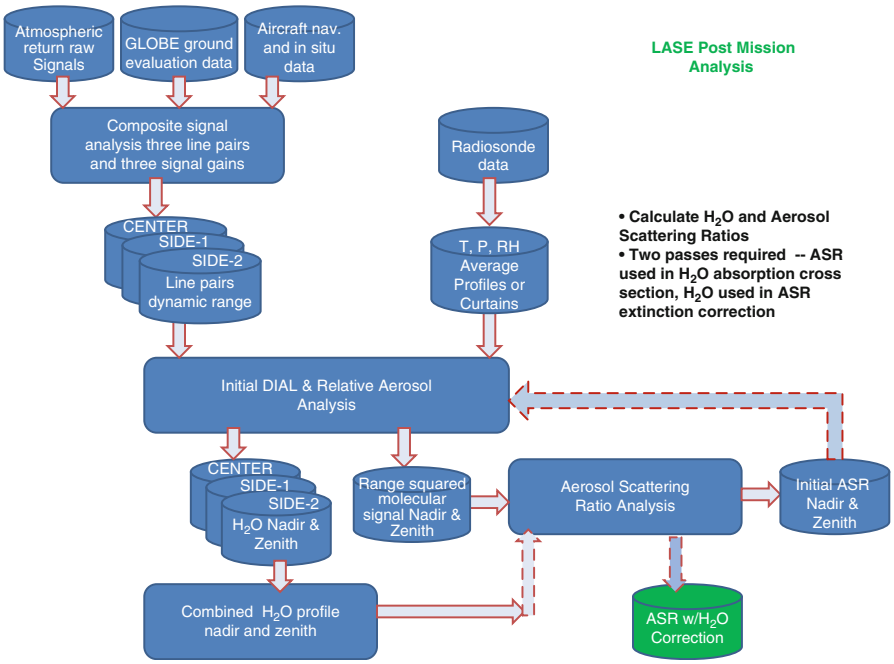

Fig. 3.10 The analysis by which the DIAL raw data is transformed into useful data products

The first of these was the Laser In-space Technology Experiment (LITE) which flew for 10 days on the Space Shuttle in 1994 [15]. This backscatter lidar used a flashlamp-pumped Nd:YAG laser with nonlinear conversion into 532 and 355 nm laser emission. Three beams were transmitted (1,064, 532, and 355 nm) and provided the first highly detailed global view of the vertical structure of clouds and aerosols from the surface through the middle stratosphere. The complexity of deploying a lidar in space is a daunting challenge and LITE performed extremely well demonstrating the utility of backscatter lidars in space even though its deployment was very short.

Another space-based lidar was the Ice Cloud and land Evaluation Satellite (ICESat) which was launched in 2003 and decommissioned in 2010 [16, 17]. The ICESat mission was designed to provide elevation data needed to determine ice sheet mass balance as well as cloud property information, especially for polar stratospheric clouds and aerosols. It provided topography and vegetation data around the globe, in addition to the polar-specific coverage over the Greenland and Antarctic ice sheets. It also provided planetary boundary layer heights which is an important parameter linking the surface to atmosphere dynamics, especially over the world's oceans. The satellite combined a precision surface lidar with a sensitive dual-wavelength cloud and aerosol lidar. The lasers emitted infrared and visible laser pulses at 1,064 (75 mJ) and 532 (35 mJ) nm wavelengths using three identical diode-pumped Nd:YAG lasers (6-ns TEM00 spatial mode). The repetition rate was 40 Hz. There was

a 1-m diameter beryllium telescope used in the receiver. As ICESat orbited, the laser produced a series of approximately 70-m diameter laser spots that are separated by nearly 170-m along the spacecraft's ground track. Aerosol data could also be retrieved.

ICESat was a major step forward for space-based lidars. It lasted for some 5 years and used diode laser pumping of the Nd:YAG laser transmitter. This is the only technique that can achieve the electrical-to-optical conversion to make space lasers practical. It was also low voltage technology minimizing corona discharge due to high voltage. It demonstrated the flexibility of taking multiple science measurements such as ice sheet height, cloud heights, atmospheric boundary layer height, and aerosol concentrations. It could be operated autonomously in the radiation and vacuum environment of space for many years until the pump diodes and other components eventually degraded. All this capability is directly related to future DIAL systems deployed in space.

The only current operational lidar satellite in orbit is the Cloud-Aerosol Lidar and Infrared Pathfinder Satellite Observations (CALIPSO) carrying a backscatter lidar instrument as shown in Fig. 3.11 [18]. The satellite was launched in 2006 to an orbit altitude of 705 km and after 5 years is still operational, gathering global data on clouds and aerosols.

The Nd:YAG laser transmitter has two wavelengths 1,064 and 532 nm each transmitting 110 mJ, 20-ns linearly polarized laser pulses. The 532-nm channel can measure depolarization with a polarization beam splitter resolving parallel and perpendicular return signal components. The repetition rate is 20.16 Hz. The beams form a footprint of 70-m diameter with 335-m spacing between footprints. The receiver telescope is 1-m diameter with a field of view of 90 m on the surface. Aerosol profiles can be retrieved from 40-km altitude to the surface with 60-m vertical and 5-km horizontal resolutions.

CALIPSO is providing the first multiyear global dataset of lidar aerosol and cloud profiles. Figure 3.12 is an example of one flight track on July 16, 2009 over the African Continent. The insert shows the orbit track from north to south. The aerosol and cloud 532-nm profile moves from left to right. CALIPSO has the ability to identify broad groups of aerosol types. In the upper left are aerosols emitted from volcanoes and in the center dust plumes are seen. Near the coast of Africa, biomass burning is taking place and smoke plumes are noted near 3-km altitude. Over the ocean, clouds are forming at the top of the boundary layer. A space–based DIAL system would acquire aerosol and cloud data very similar to these CALIPSO results.

Two future lidar missions are planned by the European Space Agency the ADM-Aeolus [20] (launch 2013) and Earthcare [21] (launch 2016) satellites. The aim of the Atmospheric Dynamics Mission (ADM-Aeolus) is to provide global observations of three-dimensional wind fields, which will improve current wind-profiling atmospheric modeling, operational weather forecasting, and climate research. ADM-Aeolus satellite (400-km sun synchronous) will gather data by the active doppler wind lidar (DWL) method, whereby laser (Aladin-Atmospheric LAser Doppler INstrument) pulses are transmitted in the atmosphere and then measure the backscattered Doppler shift of the received return signal, creating a wind profile showing the relative strength and direction of winds at different altitudes, as well as moisture and aerosol levels in

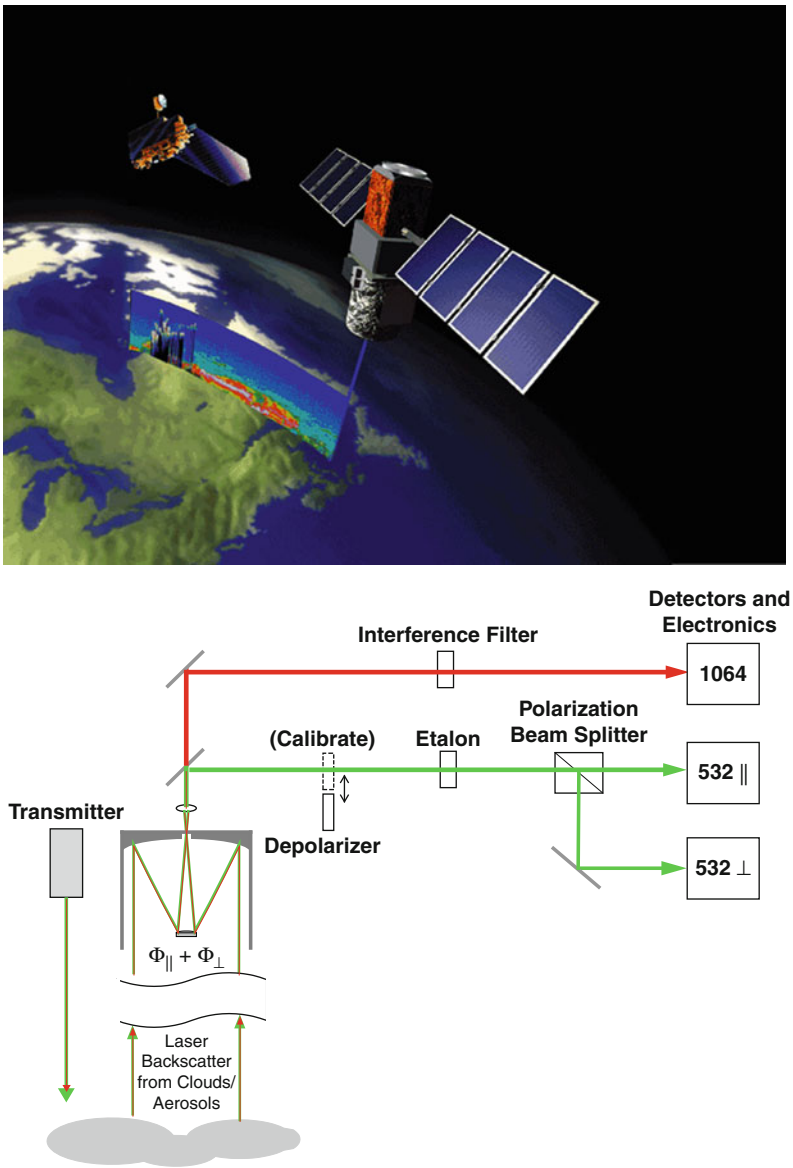

Fig. 3.11 The CALIPSO satellite showing a typical cloud and aerosol lidar retrieval. Also a schematic of the lidar optical system

the atmosphere. Wind speeds will be measured in the boundary layer (1-m/s resolution), in the free troposphere (2-m/s) with average wind velocities over 50-km tracks and 120 profiles per hour. The diode-pumped Nd:YAG laser is frequency tripled to 355 nm at 150-mJ pulse energy, 100-Hz pulse repetition rate, and 30-MHz laser

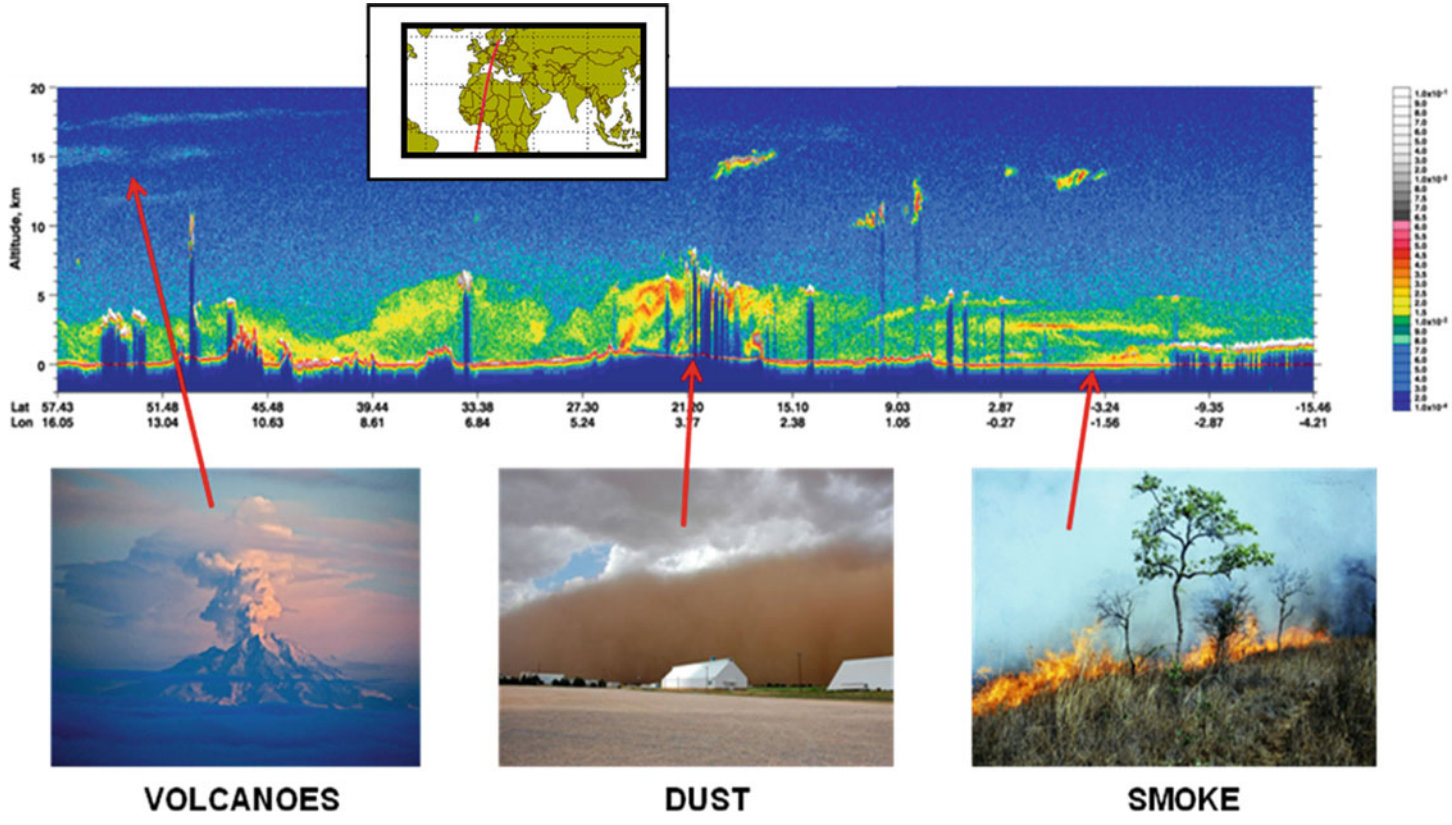

Fig. 3.12 CALIPSO image shows 532-nm attenuated backscatter profiles from 16 July 2009 (∼01:35 UTC until ∼01:55 UTC) [19]

linewidth (tunable over 10-MHz). The receiver has a Mie channel (aerosol and water droplets) with Fizeau spectrometer, and a Rayleigh channel (molecular scattering). The telescope is 1.5-m diameter.

The EarthCARE satellite (Earth Clouds, Aerosols, and Radiation Explorer) is a joint European-Japanese mission addressing the need for better understanding of the interactions between cloud, radiative and aerosol processes that play an important role in climate change by acquiring vertical profiles of clouds and aerosols, as well as the radiances at the top of the atmosphere. Cloud feedbacks are the main cause of uncertainty in predictions of future climate, and correct representation of clouds, aerosols, and radiation processes in models is needed. Current knowledge of the global profiles of aerosol and cloud properties is far too limited and the required profiles can only be provided by the high spectral resolution lidar. EarthCARE has been defined with the specific scientific objectives of quantifying aerosol-cloud-radiation interactions so they may be included correctly in climate and numerical weather forecasting models by providing:

- Vertical profiles of natural and anthropogenic aerosols on a global scale, their radiative properties and interaction with clouds.
- Vertical distribution of atmospheric liquid water and ice on a global scale, their transport by clouds and radiative impact.
- Cloud overlap in the vertical, cloud-precipitation interactions and the characteristics of vertical motion within clouds.
- The combination of the retrieved aerosols and cloud properties to derive the profile of atmospheric radiative heating and cooling.

The Atmospheric Lidar (ATLID) on the satellite is a high-spectral resolution with depolarization lidar system. The Nd:YAG laser produces 355-nm pulses at 30 mJ and a repetition rate of 74 Hz. High spectral purity demands a 50-MHz linewidth and stability of 50 MHz over a 1 month time in order to separate the Mie (100-m resolution) and Rayleigh (300 m) scattering atmospheric contributions by the high spectral resolution technique.

These backscatter lidar systems add to the technology base required by future space DIAL systems. The LITE system demonstrated that valuable aerosol and cloud data could be obtained from space. The ICESat mission used diode laser pumping, allowing efficient long-term lidar measurements from space. The CALIPSO mission is currently providing important long-term information on aerosols and clouds for climate models. In the future, ADM-Aeolus and ATLID EarthCARE missions will use large receiver telescopes and laser line narrowing techniques required to spectrally resolve atmospheric species by the DIAL technique for future missions.

While the DIAL technique is most often considered for measuring Earth's atmosphere, it could also be used for other planetary atmospheres such as Mars. A small lander could measure the water vapor concentration of the Mars atmosphere to help in the search for water-based life as life, as known on planet Earth, requires water. Although the atmospheric concentration of water vapor is very low, there is still

sufficient vapor to form hazes, ground fog, frost, and clouds. An exchange of water vapor exists between the ice cap at the northern pole and the atmosphere. The DIAL technique could be utilized to measure the processes that determine the distribution of water vapor and thus indicate where sources and sinks of water vapor exist. This could then lead to sites where life on Mars might be found.

Figure 3.13 shows a Tm:germanate fiber laser, tunable around 1.9 μm, which when coupled to a low mass lidar receiver, can fulfill the requirements for a water vapor Mars DIAL system. Laser diodes are used to pump a Te:germanate fiber that lases on a water vapor absorption line near 1.9 μm. The DIAL system is very compact and low mass yet capable of measuring the water vapor profile up to about 6 km. Figure 3.14 shows the pulsed laser energy as a function of laser diode pumping current. The on- and off-line wavelengths are indicated where the online experiences more atmospheric absorption than the off-line wavelength. Such small systems could easily be packaged and deployed at multiple locations to profile the planetary water vapor distribution [22, 23].

Future Directions

Ground- and aircraft-based DIAL systems are now in regular use profiling many atmospheric species as well as clouds and aerosols [24]. The open question is when and how will the DIAL technique be deployed in space for global Earth and other solar system bodies atmospheric observations. The CALIPSO lidar system cost about $300 million (FY 06 dollars) including launch, thus a DIAL system deployed in space would cost over $1 billion due to its increased complexity when compared to a backscatter lidar such as CALIPSO.

A number of studies have been published describing concepts and characteristics of space deployed DIAL systems for ozone [25] and water vapor [26, 27]. A concept for a space–based ozone DIAL system called ORACLE would deploy a UV DIAL system at 400 km with a laser pulse energy of 500 mJ and on- and off-line wavelengths of 308 and 320 nm, respectively. The ORACLE system would measure a single species, ozone, as well as clouds and aerosols. The receiver would have a 4.5 m^2 telescope. For daytime operation, the ozone concentration error would be ~10% for altitudes between 5 and 45 km. Such studies demonstrated the utility as well as technology progress needed to deploy an ozone DIAL system in space.

With such a large investment in a space–based DIAL system, there would be a need to profile many different atmospheric species, some not recognized as important today for both air quality and global climate change applications. In this concept, the DIAL system would rapidly tune to several different online wavelengths corresponding to the species of interest in the present atmospheric campaign. Thus the species involved in the major atmospheric chemical reactions would be profiled and then would be used to initialize global chemical weather models. The off-line wavelength would be used, as it is presently, to profile clouds

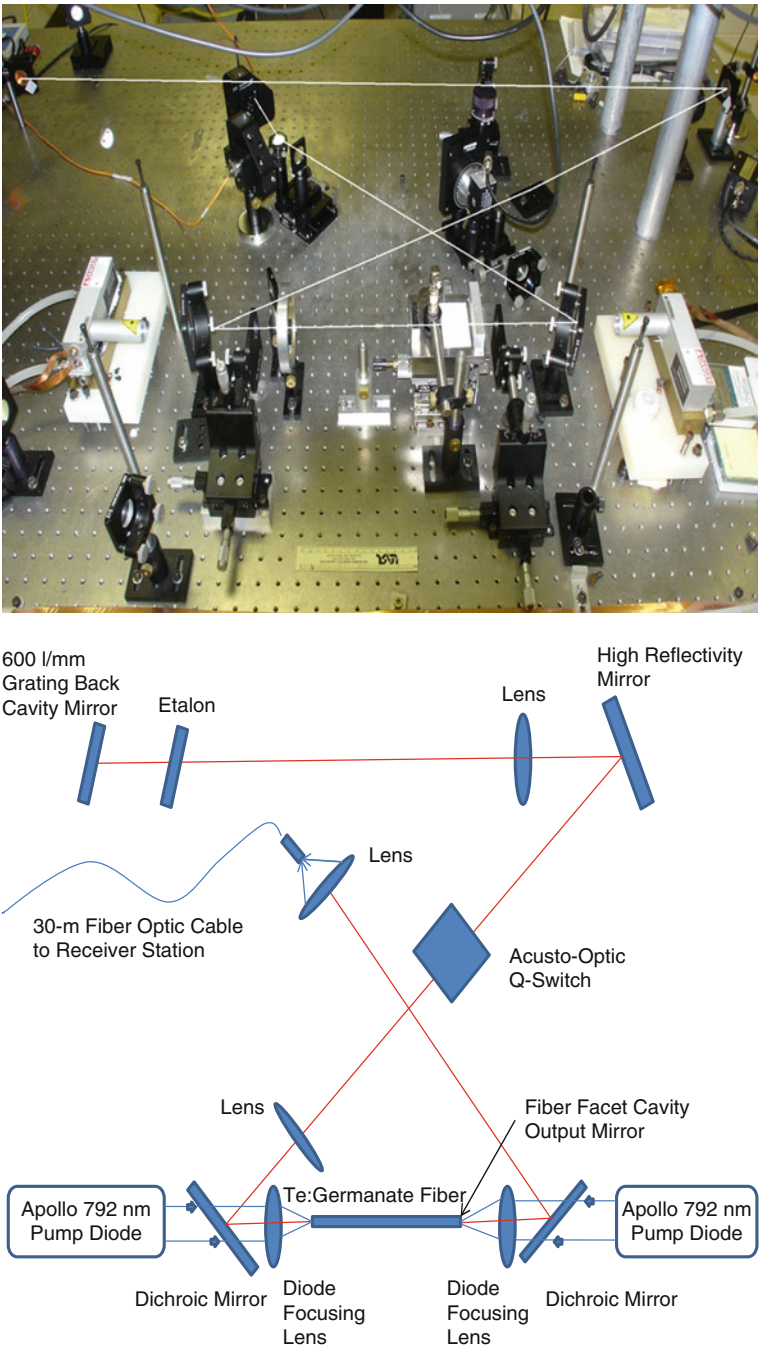

Fig. 3.13 Schematic and photo of the Tm:germanate fiber laser transmitter

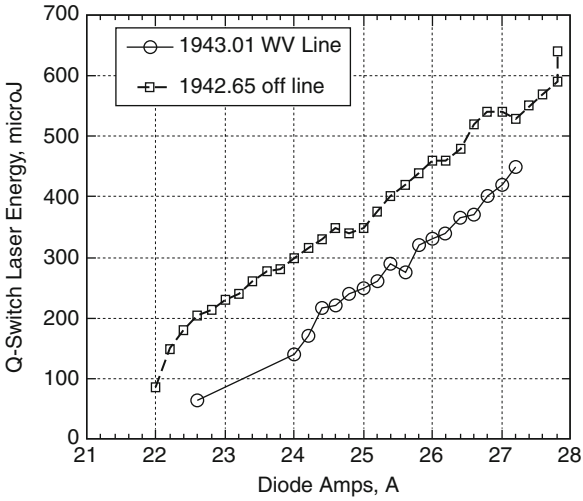

Fig. 3.14 Pulsed laser output vs. pump diode current

and aerosols. The laser transmitter would need to be reliably tuned to any online wavelength with narrow linewidth and broad tuning range to cover all molecular species of interest.

The DIAL laser transmitter would need to operate in the infrared spectral region from about 1 to 5 μm where there are many molecular absorption lines available for almost all atmospheric species of interest. The laser (orbit altitude 350–400 km) would need to generate 10-Hz pulse pairs at from 0.5 to 1.0-J energy per pulse. The receiver telescope would need to be about 5 m in diameter and the receiver optical system would need to be ~70% efficient [28]. Avalanche photo detectors (APDs) such as the HgCdTe are being developed which can photon count the return signal. Such a DIAL system could typically profile atmospheric ozone with horizontal resolution of 200 km, a vertical resolution of 2 km with 10% measurement accuracy. This would allow adequate profiling of regional and continental scale processes.

Future space–based DIAL systems will be driven by the science requirements that are related to the open questions with regard to climate change [29] and air quality [30, 31]. An example of how the above multiwavelength space–based DIAL system could impact an air quality global pollution field campaign can be demonstrated using the International Global Atmospheric Chemistry (IGAC) Lagrangian 2 K4 campaign [32]. In this field campaign, several aircraft were used to measure in situ concentrations of ozone, carbon monoxide, volatile organic compounds, NO_x (NO + NO_2), and NO_y (mainly in the form of PAN) created from Alaskan forest fires in 2004 and transported to Europe. These fires create polluted plumes that undergo chemical evolution and mixing with air masses of different origin such that their chemical composition can radically change. Ozone levels in such polluted plumes are of interest since it is a major health concern and also a major source of the OH radicals (most efficient cleansing agent in the atmosphere). Ozone is mainly produced by reactions involving oxidation of volatile organic compounds (VOCs), and carbon monoxide (CO) in the presence of nitrogen

Molecular Species	Measurement Need			
	Air quality	Oxidation efficiency	Climate	Stratosphere ozone depletion
O_3 (ozone)	■	■	■	■
CO (carbon monoxide)	■	■		
j (NO_2)	■	■		
j (O^1D)	■	■		
H_2O (water vapour)	■	■	■	■
HCHO (formaldehyde)	■	■		
VOCs (volatile organic compounds)	■	■		
Active nitrogen: NOx = NO + NO_2	■	■		■
Reservoir species: HNO_3	■	■	■	■
N_2O			■	
SO_2	■		■	
Active halogens: BrO, ClO, OClO				■
Reservoir species: HCl, $ClONO_2$				■
CO_2			■	
CH_4		■	■	■
OH	■			

Fig. 3.15 Important atmospheric molecular species that could be measured from space using DIAL and the corresponding measurement needed to profile these species

oxides (NO_x = NO + NO_2), and mainly destroyed by reactions involving water vapor and HO_x radicals. This long-range biomass burning plume was sampled in the troposphere over North America, the North Atlantic, and over Europe by three different aircraft. A photochemical trajectory model was used to examine the chemical processes responsible for the plume evolution. Six day modeled concentrations of O_3, CO, NO_y, NO, PAN, H_2O and temperature were compared to sparse in situ concentration measurements.

While campaigns such as the above are very costly and very infrequent, an orbiting IR tunable DIAL system could measure all the species giving a three-dimensional profile of the plume as it was transported toward Europe. The ability to accurately profile the chemical change as the plume aged demonstrates the unique and powerful ability to understand with high-resolution atmospheric chemical weather. Figure 3.15 shows the most important atmospheric molecular species to be profiled by DIAL and the corresponding need to measure these species [33–35]. An IR tunable DIAL system could potentially measure all these species from space producing a three-dimensional profile of the chemical evolution and transport of these species with high spatial and temporal resolution.

As interest in transport of atmospheric pollution species and associated pollution species precursors increases, there may develop a need to monitor fluxes of these atmospheric species as they are transported across national

boundaries. As noted above, the ADM-Aeolus satellite will have a lidar capable of measuring wind velocities as a function of altitude. This measurement can be combined with the IR DIAL space-based system resulting in the determination of molecular fluxes (#/cm^2-s) across national boundaries for regulatory and health monitoring purposes.

Differential absorption lidar systems have been deployed on the ground in aircraft and eventually in space. The essential components of a space–based DIAL system are now in place; efficient diode-pumped solid-state lasers, high pulse energy, narrow linewidth emission, large telescopes, autonomous operation, and radiation resistant long life operation. While more research needs to be invested in infrared tunable DIAL laser transmitters, nevertheless the ultimate utility of DIAL systems will be demonstrated in space deployed atmospheric measurement systems generating high spatial and temporal resolution atmospheric molecular profiles for chemical weather and health monitoring.

Bibliography

1. Browell EV, Carter AF, Shipley ST, Allen RJ, Butler CF, Mayo MN, Siviter JH, Hall WM (1983) NASA multipurpose airborne DIAL system and measurements of ozone and aerosol profiles. Appl Optics 22:522–534
2. Browell EV, Browell EV (1983) In: Killinger DK, Moorradian A, Killinger DK, Moorradian A (eds) Optical laser remote sensing. Springer, New York, pp 138–148
3. Bucholtz A (1995) Rayleigh scattering calculations for the terrestrial atmosphere. Appl Optics 34:2765–2773
4. Williamson CK, De Young RJ (2000) Method for the reduction of signal-induced noise in photomultiplier tubes. Appl Optics 39:1973–1979
5. Weitkamp C (2005) Lidar range resolved optical remote sensing of the atmosphere. Springer, New York
6. Kovalev VA, Eichinger WE (2004) Elastic lidar. Wiley, New Jersey
7. Browell EV (1989) Differential absorption lidar sensing of ozone. Proc IEEE 77:419–432
8. Kuang S, Burris JF, Newchurch MJ, Johnson S, Long S (2010) Differential absorption lidar to measure subhourley variation of tropospheric ozone profiles. IEEE Trans Geo Remote Sensing 49:557–571
9. http://www.espo.nasa.gov/arctas/
10. Flesia C, Mugnai A, Emery Y, Godin L, de Schoulepnikoff L, Mitev V (1994) Interpretation of lidar depolarization measurements of the Pinatubo stratospheric aerosol layer during EASOE. Geo Res Letts 21:1443–1446
11. Schoulepnikoff L, Van Den Bergh H, Calpini B (1998) Tropospheric air pollution monitoring LIDAR. In: Myers RA (ed) Encyclopedia of environmental analysis and remediation. Wiley, New York, pp 4873–4909
12. Ismail S, Browell EV (1994) Recent lidar technology developments and their influence on measurements of tropospheric water vapor. J Atmos Oceanic Tech 11:76–84
13. Ismail S (2011) GRIP Campaign data, private communication
14. Kooi S (2011) private communication
15. Winker DM, Couch RH, McCormick MP (1996) An overview of LITE: NASA lidar in-space technology experiment. Proc IEEE 84:164–179

16. Farrell SL, Laxon SW, McAdoo DC, Yi D, Zwally HJ (2009) Five years of arctic sea ice freeboard measurements from the ice, cloud and land elevation satellite. J Geophys Res 114: C04008. doi:2008JC005074/2008JC005074
17. Abdalati W, Zwally HJ, Bindschadler R, Csatho B, Farrell SL, Fricker HA, Harding D, Kwok R, Lefsky M, Markus T, Marshak A, Neumann T, Palm S, Schutz B, Smith B, Spinhirne J, Webb C (2010) The ICESat-2 laser altimetry mission. Proc IEEE 98:735–751
18. Winker DM, Pelon J, Coakley JA, Ackerman SA, Charlson RJ, Colarco PR, Flamant P, Fu Q, Hoff RH, Kittaka C, Kubar TL, Le Treut H, McCormick MP, Megie G, Poole L, Powell K, Trepte C, Vaughan MA, Wielicki BA (2010) The CALIPSO mission a 3D view of aerosols and clouds. Bull Am Met Soc. doi:10.1175/2010BAMS3009.1
19. Vaughan MA (2011) NASA Langley Research Center, private communication
20. Clissold P (ed) (2008) ADM-Aeolus, SP-1311, ESA Communication Production Office, The Netherlands, ISBN 978-92-9221-404-3
21. Le Hors L, Toulemont Y, Heliere A (2008) Design and development of the backscatter lidar ATLID for EARTHCARE. In: International Conference on Space Optics, Toulouse, 14–17 Oct 2008
22. Barnes NP, Walsh BM, Reichle D, De Young RJ (2009) Tm:fiber lasers for remote sensing. Opt Mat. doi:10.1016/j.optmat.2007.11.037, 31:1061-1064
23. De Young RJ, Barnes NP (2010) Profiling atmospheric water vapor using a fiber laser lidar system. Appl Optics 49:562–567
24. Browell EV (1995) Airborne lidar measurements. Rev Laser Eng 23:135–141
25. Ball DJ, Dudelzak AE, Rheault F, Browell EV, Ismail S, Stadler JH, Hoff RM, McElroy CT, Allan I, Carswell CTA, Hahn JF, Ulitsky A (1998) ORACLE (ozone research with advanced cooperative lidar experiment): joint NASA-CSA development of a space-base ozone DIAL. Proc SPIE 3494:223–226. doi:10.1117/12.332422
26. Ismail S, Browell EV (1989) Airborne and spaceborne lidar measurements of water vapor profiles: a sensitivity analysis. Appl Optics 28:3603–3615
27. Wulfmeyer V, Bauer H, Girolammo D, Serio C (2005) Comparison of active and passive water vapor remote sensing from space: an analysis based on the simulated performance of IASI and space borne differential absorption lidar. Remote Sens Environ 95:211–230
28. Ismail S, Peterson LD, Hinkle JD (2005) Applications of deployable telescopes for earth-observing lidar. In: Proceedings of the ESTO earth science technology conference, College Park, 27–28 June 2005
29. Chin M, Kahn RA, Schwartz SE (eds) (2009) CCSP 2009: atmospheric aerosol properties and climate impacts, Report by the U.S. Climate Change Science Program and the Subcommittee on Global Change Research, National Aeronautics and Space Administration, Washington, DC, 128 pp
30. Monks PS, Granier C, Fuzzi S, Stohl A, Williams ML, Akimoto H, Amanni M et al (2009) Atmospheric composition change – global and regional air quality. Atmos Environ 43:5268–5350
31. Browell EV, Ismail S, Grant WB (1989) Differential absorption lidar (DIAL) measurements from air and space. Appl Phys B 67:399–410
32. Real E, Law KS, Weinzierl B, Fiebig M, Petzold A, Wild O, Methven J, Arnold S, Stohl A, Huntrieser H, Roiger A, Schlager H, Stewart D, Avery M, Sachse G, Browell E, Ferrare R, Blake D (2007) Processes influencing ozone levels in Alaskan forest fire plumes during long-range transport over the North Atlantic. J Geo Res 112:D10S41. doi:10.1029/2006JD007576
33. Laj P, Klausen J, Bilde M, Pla-Duelmer C, Pappalardo G, Clerbaux C, Baltensperger U et al (2009) Measuring atmospheric composition change. Atmos Envir 43:5351–5414
34. Ismail S, Gervin J, Wood HJ, Peri F (2004) Remote sensing of tropospheric chemistry using lidars from geostationary orbit. Proc SPIE 5659:146–154
35. World Meteorological Organization (2007) WMO global atmospheric watch strategic plan: 2008–2015. Report 172

Chapter 4
Contemporary Sea Level Variations, Observations and Causes

Anny Cazenave

Glossary

Glacier	Large persistent ice body, generally formed in mountain areas by snow accumulation during winter and further compaction into ice.
Ice sheets	Ice bodies covering the Greenland and Antarctica continents.
Mean sea level	A measure of the average height of the ocean's surface with respect to a fixed reference surface.
Satellite altimetry	Space technique dedicated to the measurement of the height of the sea surface from a satellite-borne radar altimeter.
Sea level rise	Sea level rises in response to global warming. The components that cause sea level rise are ocean thermal expansion and freshwater mass addition to the oceans due to land ice melt and land water-storage decrease.
Steric sea level	Contribution to observed sea level due to temperature and salinity variations.
Thermal expansion	Volume change of ocean water response to a change in temperature.

This chapter was originally published as part of the Encyclopedia of Sustainability Science and Technology edited by Robert A. Meyers. DOI:10.1007/978-1-4419-0851-3

A. Cazenave (✉)
LEGOS, Laboratoire d'Etudes en Geophysique et Oceanographie Spatiales,
18 Avenue Edouard Belin, 31401 Toulouse, France
e-mail: Anny.cazenave@legos.obs-mip.fr

J. Orcutt (ed.), *Earth System Monitoring: Selected Entries from the Encyclopedia of Sustainability Science and Technology*, DOI 10.1007/978-1-4614-5684-1_4,

Definition of the Subject

Sea level change is a very sensitive index of climate change and variability. For example, as the ocean warms in response to global warming, seawaters expand, and thus sea level rises. When mountain glaciers melt in response to increasing air temperature, sea level rises because of freshwater mass input to the oceans. Similarly, ice mass loss from the ice sheets causes sea level rise. Corresponding increase of freshwater into the oceans changes water salinity, hence seawater density as well as ocean circulation that in turn affects sea level and its spatial variability. Modification of the land hydrological cycle due to climate variability and direct anthropogenic forcing leads to increased or decreased runoff, hence ultimately to sea level change. Hence local and regional climate changes may affect the sea level.

Introduction

Sea level variations spread over a very broad spectrum. The largest global-scale sea level changes (100–200 m in amplitude) occurred on geological timescales ($\sim$100 myr) and depended primarily on tectonics processes (e.g., large-scale change in the shape of ocean basins associated with seafloor spreading and mid-ocean ridges expansion). With the formation of long-live ice sheets (e.g., formation of the Antarctica ice sheet about 35 myr ago) global mean sea level dropped by about 60 m. Cooling of the Earth since about 3 myr ago has led to glacial/interglacial cycles driven by changes of the Earth's orbit and obliquity. Quasi-periodic growth and decay of the northern hemisphere ice caps on a timescale of tens of thousands of years have produced large oscillations of the global mean sea level, on the order of 100 m. On shorter (decadal to multi-centennial) timescales sea level fluctuations are mainly driven by natural forcing factors (e.g., solar radiation, volcanic eruptions) and internal variability the climate system (e.g., atmosphere-ocean perturbations such as El Nino-Southern Oscillation (ENSO), North Atlantic Oscillation (NAO), and Pacific Decadal Oscillation (PDO)). Since the beginning of the industrial era, sea level is also responding to anthropogenic global warming. In this chapter, only recent (last few decades) sea level variations and their causes are discussed.

Observations of Sea Level Change and Variability (Twentieth Century and Last Two Decades)

Twentieth Century

Our knowledge of the past century sea level change comes from tide gauge measurements located along continental coastlines and islands. The largest tide

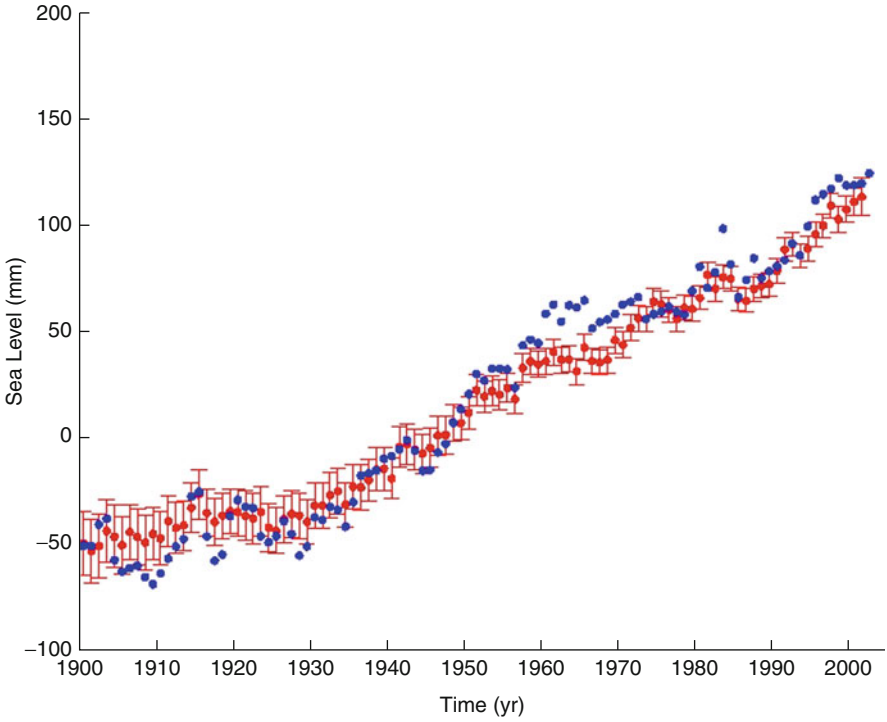

Fig. 4.1 Global mean sea level evolution (1900–2000) during the twentieth century (Data based on tide gauges; *red points* from Ref. [3]; *blue points* from Ref. [5])

gauge data base of monthly and annual mean sea level records is the Permanent Service for Mean Sea Level (PSMSL, www.psmsl.org) which contains data for the twentieth century from ~2,000 sites maintained by about 200 nations. The records are somewhat inhomogeneous in terms of data length and quality. For long-term sea level studies, only ~10% of this data set is useable because of data gaps. Tide gauges measure sea level relatively to the ground, hence monitor also ground motions. In active tectonic and volcanic regions, or in areas subject to strong ground subsidence due to natural causes (e.g., sediment loading in river deltas) or human activities (groundwater pumping and oil/gas extraction), tide gauge data are directly affected by the corresponding ground motions. Postglacial rebound, the visco-elastic response of the Earth to last deglaciation (also called Glacial Isostatic Adjustment (GIA)) is another process that gives rise to vertical land movement.

After the ~130 m sea level rise associated with the deglaciation that followed the Last Glacial Maximum ~20,000 years ago, geological, geochemical and archeological observations indicate that the mean sea level remained almost stable during the last 2–3 millennia [1, 2]. However, since the late nineteenth century tide gauge records have shown significant sea level rise. During the twentieth century, a mean rate of ~1.8 mm/year is reported [3–5]. Figure 4.1 shows tide gauge-based sea level evolution for the twentieth century.

Satellite Altimetry Era

Since the early 1990s, satellite altimetry has become the main tool for precisely and continuously measuring sea level with quasi-global coverage and a few days revisit time. Compared to tide gauges which provide sea level relative to the ground, satellite altimetry measures "absolute" sea level variations. The concept of the satellite altimetry measurement is simple: the onboard radar altimeter transmits microwave radiation toward the sea surface which partly reflects back to the satellite. Measurement of the round-trip travel time provides the height of the satellite above the instantaneous sea surface (called "range"). The quantity of interest in oceanography is the sea surface height above a fixed reference surface (typically a conventional reference ellipsoid). It is obtained by the difference between the altitude of the satellite above the reference (deduced from precise orbitography) and the range measurement. The estimated sea surface height needs be corrected for various factors due to ionospheric and atmospheric delay, and of biases between the mean electromagnetic scattering surface and sea at the air-sea interface. Other corrections due geophysical effects, such as solid Earth, and pole and ocean tides, are also applied. High-precision satellite altimetry started with the launch of Topex/Poseidon in 1992 and its successors Jason-1 and Jason-2 launched in 2001 and 2008, respectively. The precision of an individual sea surface height measurement based on these missions has reached the 1–2 cm level. Precision on the global mean rate of rise is currently of $\sim$ 0.4–0.5 mm/year. This value is based on error budget analyses of all sources of errors affecting the altimetry system or on comparisons with tide gauge-based sea level measurements (e.g., [6–10]). The temporal evolution of the global mean sea level from satellite altimetry since early 1993 is shown in Fig. 4.2. It is characterized by an almost linear increase (except for temporary anomalies associated with the 1997–1998 El Nino and the 2007–2008 and 2010–2011 La Ninas). Over this 18-year-long period, global mean sea level has been rising at a rate of $\sim 3.2 \pm 0.4$ mm/year. This rate is significantly higher than the mean rate recorded by tide gauges over the past decades.

Satellite altimetry has also revealed that sea level is not rising uniformly (Fig. 4.3). In some regions (e.g., Western Pacific), the rates of sea level rise have been faster than the global mean rate by a factor of up to 3 over the past two decades. In other regions rates have been slower than the global mean (e.g., Eastern Pacific).

Causes of Present-Day Sea Level Changes (Global Mean and Regional Variability)

Global Scale

The main factors causing current global mean sea level rise are thermal expansion of seawaters, land ice loss, and freshwater mass exchange between oceans and land

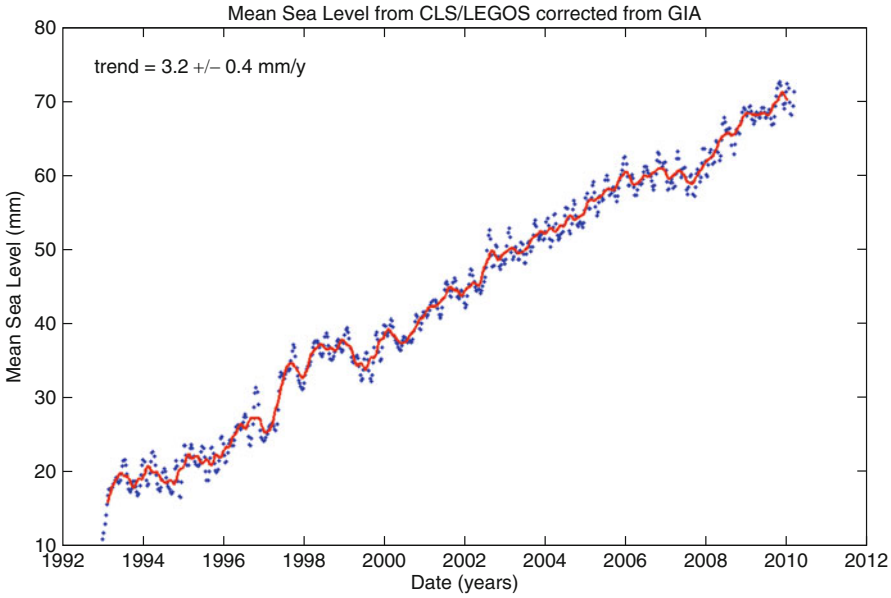

Fig. 4.2 Global mean sea level evolution from satellite altimetry (1993–2010) (Updated from Ref. [19])

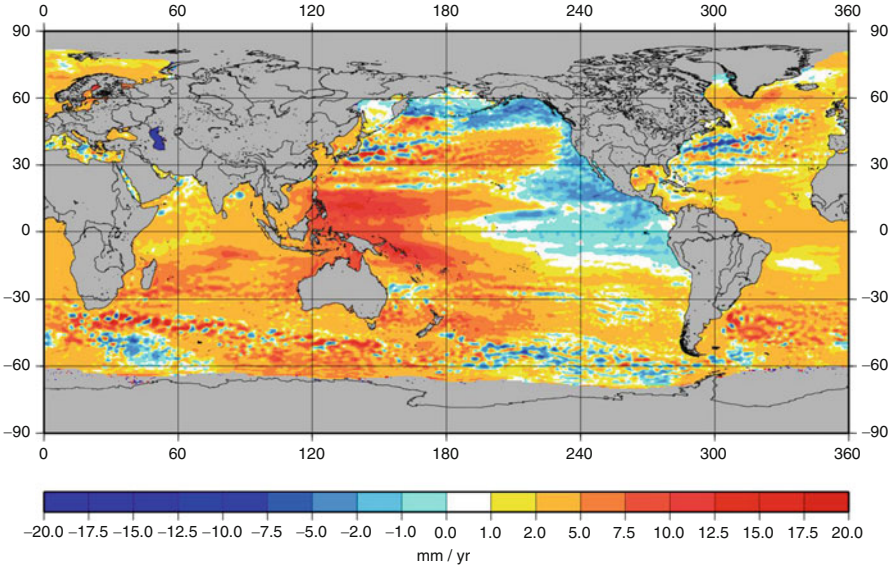

Fig. 4.3 Observed spatial trend patterns in sea level over the altimetry era (1993–2010) (Updated from Ref. [19])

water reservoirs. These contributions vary in response to natural climate variability and to global climate change induced by anthropogenic greenhouse gases emissions.

Ocean Warming

Analyses of in situ ocean temperature data collected over the past 50 years by ships and recently by Argo profiling floats [11] indicate that ocean heat content, and hence ocean thermal expansion, has significantly increased since 1950 (e.g., [12–14]). Ocean warming explains about 25% of the observed sea level rise of the last few decades (e.g., [15]). However, this value is likely a lower bound, due to the lack of hydrographic data in remote regions of the southern hemisphere and in the deep ocean (below 1,000 m). Recent reevaluation of ocean warming estimates to >40% this contribution to past decades sea level rise [16]. A steep increase was observed in thermal expansion over the decade 1993–2003 (e.g., [15, 17]), but since about 2003, thermal expansion has increased less rapidly [14, 18]. The recent slower rate of steric rise likely reflects short-term variability rather than a new long-term trend. On average, over the satellite altimetry era (1993–2010), the contribution of ocean warming to sea rise accounts for $\sim$ 30–40% [19, 20].

Glaciers Melting

Being very sensitive to global warming, mountain glaciers and small ice caps have retreated worldwide during the recent decades, with significant acceleration during the 1990s. From mass balance studies of a large number of glaciers, estimates have been made of the contribution of glacier's ice melt to sea level [21–24]. For the period 1993–2010, glaciers and ice caps have accounted for $\sim$ 30% to the observed sea level rise [19, 20].

Ice Sheets

If totally melted, Greenland and West Antarctica would raise sea level by about 7 m and 3–5 m, respectively. Thus even a small amount of ice mass loss from the ice sheets would produce substantial sea level rise, with adverse societal and economical impacts on vulnerable low-lying coastal regions. Since the early 1990s, different remote sensing observations (airborne and satellite radar and laser altimetry, Synthetic Aperture Radar Interferometry (InSAR), and since 2002, space gravimetry from the GRACE mission) have provided important observations of the mass balance of the ice sheets. These data indicate that Greenland and West Antarctica are loosing mass at an accelerated rate (e.g., [25, 26]). Most recent mass balance estimates from GRACE space gravimetry suggest for the 2002–2009 time span, averaged rates of ice mass loss of 240 Gt/year for Greenland and 150–200 Gt/year

for Antarctica (e.g., [27, 28]), in rather good agreement with INSAR (e.g., [29, 30]) and radar and laser altimetry results (e.g., [31]). The space-based observations unambiguously show ice mass loss acceleration in the recent years. For the period 1993–2003, <15% of the rate of global sea level rise was due to the ice sheets [21]. But their contribution has increased up to ~75% since 2003–2004, about equally split between Greenland and Antarctica (e.g., [29, 30]). Accelerated polar ice loss over the past few years has more than compensated recent slower rate of ocean thermal expansion, and as a result, sea level has continued to rise at almost the same rate (e.g., [32]). Although not constant through time, on average over 2003–2010, ice sheets mass loss explains ~25% of the rate of sea level rise [19, 20].

There is more and more evidence that recent negative ice sheet mass balance mainly results from rapid outlet glacier flow along some margins of Greenland and West Antarctica, and further iceberg discharge into the surrounding ocean (e.g., [33–38]). This process, known as dynamic thinning, is often observed in regions where glaciers are grounded below sea level (e.g., in the Amundsen Sea sector, West Antarctica). Thinning and subsequent breakup of floating ice tongues or ice shelves that buttressed the glaciers result in rapid grounding line retreat and accelerated glacier flow. Several recent observations have suggested that warming of subsurface ocean waters may trigger these dynamical instabilities [34–38].

Land Water Storage

Change in land water storage, due to natural climate variability and human activities (i.e., anthropogenic changes in the amount of water stored in soils, reservoirs and aquifers as a result of dam building, underground water mining, irrigation, urbanization, deforestation, etc.) is another potential contribution to sea level change. Model-based estimates of land water-storage change caused by natural climate variability suggest no long-term contribution to sea level for the past few decades, although interannual/decadal fluctuations have been significant. Since 2002, space gravimetry observations from the GRACE space mission now allow determination of the total (i.e., due to climate variability and human activities) land water contribution to sea level. GRACE data confirm that the land water signal is dominated by interannual variability with only a modest contribution (<10%) to the trend [39, 40]. On the other hand, intensive dam building along rivers during the second half of the twentieth century may have lowered sea level by ~ -0.5 mm/year [41], but groundwater pumping, in particular for irrigation, may have more or less counterbalanced this effect.

Sea Level Budget over 1993–2010

Although none of the climate factors discussed above evolve linearly with time, on average over the 1993–2010 time span, ocean warming, glaciers melting, and ice sheet mass loss have each contributed by roughly 30% to global mean sea level rise [19, 20].

Regional Scale

The regional variability in sea level trends is mainly due large-scale changes in the density structure of the oceans in response to forcing factors (e.g., heat and freshwater exchange at the sea-air interface) and changes of the ocean circulation [15]. The largest regional changes in sea level trends result from ocean temperature change (i.e., from nonuniform thermal expansion) but in some regions, change in water salinity is also important (e.g., [42, 43]).

Observations of ocean temperature over the past few decades show that trend patterns in thermal expansion are not stationary but fluctuate both in space and time in response to internal perturbations of the climate system such as ENSO, NAO, and PDO [15]. As a result, sea level trend patterns observed by satellite altimetry over the last 18 years are expected to be different from those of the last 50 years, as confirmed by past sea level reconstructions (e.g., [44, 45]).

Processes other than thermal expansion may also give rise to regional sea level variations. This is the case for the response of the solid Earth to the last deglaciation (GIA). The meltwater from the former ice sheets does not redistribute uniformly over the oceans because of several processes: self-gravitation between ice and water masses, ocean basin deformations associated with the viscoelastic response of the Earth to the changing load, and changes of the Earth's rotation due to water and ice mass redistribution [46, 47]. On-going ice mass loss of the Greenland and Antarctica ice sheets also leads to nonuniform sea level rise because of about the same processes [48, 49]. These regional sea level changes are broadscale but their regional fingerprint is different for each melting source (Greenland, Antarctica, glaciers). Amplification by up to 30% are expected far from the melting source while significant sea level drop should occur around the region which is losing ice.

Future Sea Level Rise

IPCC AR4 projections based on coupled climate models indicate that sea level should be higher than today's value by ~ 40 cm by 2100 (within a range of ± 20 cm due to model results dispersion and uncertainty on future greenhouse gases emissions) [50]. However this value is possibly a lower bound because it only accounts for future ocean warming, glaciers melting and changes in ice sheet surface mass balance. As discussed above, a large proportion of Greenland and West Antarctica ice mass loss results from coastal glacier flow into the ocean through complex dynamical instabilities. Such processes have begun to be understood only recently and thus were not taken into account in the IPCC AR4 sea level projections. Recent studies suggest that account of ice sheet fast dynamics will increase future sea level rise (e.g., [51]). But the exact global mean sea level elevation by the end of the 21st century remains quite uncertain. Present-day sea level rise is not uniform; this is also expected for the future. The regional sea level map for 2090–2100 provided by IPCC AR4

(average of 16 models for one emission scenario; Ref. [50]) shows higher than average sea level rise in the Arctic Ocean due to decrease in salinity in response to fresh water input and along a narrow band in the south Atlantic and south Indian oceans. Recent studies confirm this general behaviour (e.g., [52]).

Impacts of Sea Level Rise

Sea level rise is a major concern for populations living in low-lying coastal regions (about 25% of human beings) because it will give rise to inundation, wetland loss, shoreline erosion, and saltwater intrusion in surface water bodies and aquifers, and will raise water tables [53]. Moreover, in many coastal regions of the world, the effects of rising sea level act in combination with other natural and/or anthropogenic factors, such as decreased rate of fluvial sediment deposition in deltaic areas, ground subsidence due to tectonic activity or groundwater pumping, and hydrocarbon extraction [54].

Besides factors that modify shoreline morphology (e.g., sediment deposition in river deltas, change in coastal waves and currents), what does matter in coastal regions is relative sea level rise, i.e., the combination of sea level rise and vertical ground motions. In many coastal regions of the world, these two factors are currently of the same order of magnitude and most often of opposite sign (sea level rises and ground subsides). Accelerated ground subsidence is reported in many regions, either because of local groundwater withdrawal (Tokyo subsided by 5 m, Shanghai by 3 m, and Bangkok by 2 m during the last decades; Ref. [53]) or hydrocarbon extraction (e.g., Gulf Coast where ground subsidence in the range 5–10 mm/year is observed; Ref. [55]). Whatever the causes, ground subsidence directly interacts with and amplifies climate-related sea level rise (long-term trend plus regional variability). However, if sea level continues to rise at current rates and more likely accelerates, the climate factors (sea level rise) will become dominant. However, it remains difficult to quantify future sea level rise in specific regions where various factors interfere in a complex way.

Future Directions

Most recent developments indicate that sea level is currently rising slightly faster since the early 1990s than during the previous decades. Owing to the recent progress in understanding the causes of present-day sea level rise, the sea level budget for the period 1993–2010 can be nearly closed. Approximately 30–40% of the rate of sea level rise is due to ocean thermal expansion in response to ocean warming. Mass loss in mountain glaciers and ice sheets accounts for the remaining 60–70%. Sea level will continue to rise in the future decades because of expected increased global warming. However, the exact amount of sea level rise in the

coming decades is still an open question. The main source of uncertainty is the future behavior of the Greenland and Antarctica ice sheets in a warming climate. Improved understanding and modeling of the complex dynamical response of the ice sheets to global warming is among the priorities of the international climate research community. In parallel, observing change and variability of sea level and its different components using in synergy various in situ and space-based observing systems is another important goal.

The recently launched high-precision altimeter satellites of the Topex/Jason series and their expected successors will provide continuity in the monitoring of sea level variations from space on multidecadal timescale. In addition to ocean temperature and salinity measurements from the international Argo project, mass balance of the ice sheets from GRACE and other remote sensing techniques, GRACE-based land water-storage change and in situ and remote observations of mountain glaciers will provide invaluable observations for understanding the causes of sea level variations.

Sea level changes involve interactions of all components of the climate system (oceans, ice sheets and glaciers, atmosphere, land water reservoirs) on a wide range of spatial and temporal scales. Even the solid Earth through its visco-elastic response to water mass redistribution affects sea level. Systematic monitoring of oceans, cryosphere, and land waters from in situ and space-observation systems are thus crucial to validate climate models, and hence improve future sea level projections. Considering the highly negative impact of future sea level rise for society, the multidisciplinary aspects of sea level rise (observations, modeling, coastal impact studies) should remain a major area of future climate research.

Bibliography

Primary Literature

1. Lambeck K, Yokoyama Y, Purcell T (2002) Into and out of the last glacial maximum: sea level change during oxygen isotope stages 3 and 2. Quater Sci Rev 21:343–360
2. Kemp AC, Horton B, Donnelly JP, Mann ME, Vermeer M, Rahmstorf S (2011) Climate related sea level variations over the past two millennia. Proc Natl Acad Sci USA 108: 11017–11022
3. Church JA, White NJ (2006) A 20th century acceleration in global sea-level rise. Geophys Res Lett 33:L01602. doi:10.1029/2005GL024826
4. Holgate SJ, Woodworth PL (2004) Evidence for enhanced coastal sea level rise during the 1990s. Geophys Res Lett 31:L07305. doi:10.1029/2004GL019626
5. Jevrejeva S, Grinsted A, Moore JC, Holgate S (2006) Non linear trends and multiyear cycles in sea level records. J Geophys Res C09012. doi:1.1029/2005JC003229, 2006
6. Ablain M, Cazenave A, Valladeau G, Guinehut S (2009) A new assessment of the error budget of global mean sea level rate estimated by satellite altimetry over 1993—2008. Ocean Sci 5:193–201
7. Leuliette EW, Nerem RS, Mitchum GT (2004) Results of TOPEX/Poseidon and Jason-1 calibration to construct a continuous record of mean sea level. Mar Geod 27:79–94

8. Leutiette EW, Scharroo R (2010) Integrating Jason-2 into a multiple-altimeter climate data record. Mar Geod 33:504–517
9. Beckley BD, Lemoine FG, Lutchke SB, Ray RD, Zelensky NP (2007) A reassessment of global rise and regional mean sea level trends from TOPEX and Jason-1 altimetry based on revised reference frame and orbits. Geophys Res Lett 34:L14608. doi:10.1029/2007GL030002
10. Nerem RS, Chambers DP, Choe C, Mitchum GT (2010) Estimating mean sea level change from the TOPEX and Jason altimetermissions. Mar Geod 33(1):435–446
11. Roemmich D, Owens WB (2000) The ARGO project: global ocean observations for understanding and prediction of climate variability. Oceanography 13:45–50
12. Levitus S, Antonov JL, Boyer TP, Locarnini RA, Garcia HE, Mishonov AV (2009) Global ocean heat content 1955–2008 in light of recently revealed instrumentation. Geophys Res Lett 36:L07608. doi:10.1029/2008GL037155
13. Ishii M, Kimoto M (2009) Reevaluation of historical ocean heat content variations with varying XBT and MBT depth bias corrections. J Oceanogr 65:287–299
14. Lyman JM, Godd SA, Gouretski VV, Ishii M, Johnson GC, Palmer MD, Smith DM, Willis JK (2010) Robust warming of the global upper ocean. Nature 465:334–337. doi:10.1038/nature09043
15. Bindoff N, Willebrand J, Artale V, Cazenave A, Gregory J, Gulev S, Hanawa K, Le Quéré C, Levitus S, Nojiri Y, Shum CK, Talley L, Unnikrishnan A (2007) Observations: oceanic climate and sea level. In: Solomon S, Qin D, Manning M, Chen Z, Marquis M, Averyt KB, Tignor M, Miller HL (eds) Climate change 2007: the physical science basis. Contribution of working group I to the fourth assessment report of the intergovernmental panel on climate change. Cambridge University Press, Cambridge/New York
16. Domingues C, Church J, White N, Gleckler PJ, Wijffels SE et al (2008) Improved estimates of upper ocean warming and multidecadal sea level rise. Nature 453:1090–1093. doi:10.1038/nature07080
17. Lombard A, Cazenave A, Le Traon PY, Ishii M (2005) Contribution of thermal expansion to present-day sea level rise revisited. Global Planet Change 47:1–16
18. Llovel W, Guinehut S, Cazenave A (2010) Regional and interannual variability in sea level over 2002–2009 based on satellite altimetry, Argo float data and GRACE ocean mass. Ocean Dyn 60:1193–1204. doi:10.1007/s10236-010-0324-0
19. Cazenave A, Llovel W (2010) Contemporary sea level rise. Annu Rev Mar Sci 2:145–173
20. Church J et al (2011) The Earth's sea level and energy budgets from 1961 and 2008. Geophys Res Lett 38:L18601
21. Lemke P et al (2007) Observations: changes in snow, ice and frozen ground. In: Solomon S, Qin D, Manning M, Chen Z, Marquis M, Averyt KB, Tignor M, Miller HL (eds) Climate change 2007: the physical science basis. Contribution of working group I to the fourth assessment report of the intergovernmental panel on climate change. Cambridge University Press, Cambridge/New York
22. Kaser G, Cogley JG, Dyurgerov MB, Meier MF, Ohmura A (2006) Mass balance of glaciers and ice caps: consensus estimates for 1961–2004. Geophys Res Lett 33:L19501. doi:10.1029/2006GL027511
23. Meier MF, Dyurgerov MB, Rick UK, O'Neel S, Pfeffer WT, Anderson RS, Anderson SP, Glazovsky AF (2007) Glaciers dominate Eustatic sea-level rise in the 21st century. Science 317(5841):1064–1067
24. Cogley JC (2009) Geodetic and direct mass balance measurements: comparison and joint analysis. Ann Glaciol 50:96–100
25. Alley R, Spencer M, Anandakrishnan S (2007) Ice sheet mass balance, assessment, attribution and prognosis. Ann Glaciol 46:1–7
26. Allison I, Alley RB, Fricker HA, Thomas RH, Warner RC (2009) Ice sheet mass balance and sea level. Antarct Sci 21:413–426
27. Velicogna I (2009) Increasing rates of ice mass loss from the Greenland and Antarctica ice sheets revealed by GRACE. Geophys Res Lett 36:L19503

28. Chen JL, Wilson CR, Blankenship DD, Tapley BD (2009) Accelerated Antarctic ice loss from satellite gravity measurements. Nat Geosci. doi:10.1038/ngeo694, 2009
29. Rignot E, Bamber JL, Van Den Broecke MR, Davis C, Li Y et al (2008) Recent Antarctic ice mass loss from radar interferometry and regional climate modeling. Nat Geosci 1:106–110
30. Rignot E, Box JE, Burgess E, Hanna E (2008) Mass balance of the Greenland ice sheet from 1958 to 2007. Geophys Res Lett 35:L20502. doi:10.1029/2008GL035417
31. Zwally HJ et al (2011) Greenland ice sheet mass balance: distribution of increased mass loss with climate warming; 2003–07 versus 1992–2002. J Glaciol 57(201):88–102
32. Cazenave A, Dominh K, Guinehut S, Berthier E, llovel W, Ramillien G, Ablain M, Larnicol G (2009) Sea level budget over 2003–2008: a reevaluation from GRACE space gravimetry, satellite altimetry and Argo. Global Planet Change 65:83–88. doi:10.1016/j/gloplacha.2008.10.004
33. Howat IM, Joughin IR, Scambos TA (2007) Rapid changes in ice discharge from Greenland outlet glaciers. Science 315:1559–1561. doi:10.1126/science.1138478
34. Holland D, Thomas RH, De Young B, Ribergaard MH, Lyberth B (2008) Acceleration of Jakobshawn Isbrae triggered by warm subsurface ocean waters. Nat Geosci 1:659–664. doi:10.1038/ngeo316
35. Straneo F et al (2010) Rapid circulation of warm subtropical waters in a major glacial fjord in East Greenland. Nat Geosci 3:182–186
36. Joughin I, Das SB, King M, Smith BE, Howat IM, Moon T (2008) Seasonal speedup along the western flank of the Greenland ice sheet. Science 320:781–783
37. Pritchard HM, Arthern RJ, Vaughan DG, Edwards L (2010) Extensive dynamic thinning on the margins of the Greenland and Antarctic ice sheets. Nature. doi:10.1038/nature08471
38. Rignot EK, And KM, Velicogna I (2010) Rapid submarine melting of the calving faces of West Greenland glaciers. Nat Geosci 3:187–191
39. Ramillien G, Bouhours S, Lombard A, Cazenave A, Flechtner F, Schmidt R (2008) Land water contributions from GRACE to sea level rise over 2002–2006. Global Planet Change 60:381–392
40. Llovel W, Becker M, Cazenave A, Jevrejeva S, Alkama R, Decharme B, Douville H, Ablain M, Beckley B (2011) Terrestrial waters and sea level variations on interannual time scale. Global Planet Change 75:76–82. doi:10.1016/j.gloplacha.2010.10.008
41. Chao BF, Wu YH, Li YS (2008) Impact of artificial reservoir water impoundment on global sea level. Science 320:212–214. doi:10.1126/science.1154580
42. Lombard A, Garric G, Penduff T, Molines JM (2009) Regional variability of sea level change using a global ocean model at ¼ resolution. Ocean Dyn. doi:10.1007/s10236-009-0161-6
43. Wunsch C, Ponte RM, Heimbach P (2007) Decadal trends in sea level patterns: 1993–2004. J Clim 20(24). doi:10.1175/2007JCLI1840.1
44. Church JA, White NJ, Coleman R, Lambeck K, Mitrovica JX (2004) Estimates of the regional distribution of sea-level rise over the 1950 to 2000 period. J Clim 17(13):2609–2625
45. Llovel W, Cazenave A, Rogel P, Berge-Nguyen M (2009) 2-D reconstruction of past sea level (1950–2003) using tide gauge records and spatial patterns from a general ocean circulation model. Clim Past 5:1–11
46. Mitrovica JX, Tamisiea ME, Davis JL, Milne GA (2001) Recent mass balance of polar ice sheets inferred from patterns of global sea-level change. Nature 409:1026–1029
47. Peltier WR (2004) Global glacial isostasy and the surface of the ice-age Earth: the ICE-5 G (VM2) model and GRACE. Annu Rev Earth Planet Sci 32:111–149
48. Mitrovica JX, Gomez N, Clark PU (2009) The sea-level fingerprint of West Antarctic collapse. Science 323:753
49. Milne G, Gehrels WR, Hughes C, Tamisiea M (2009) Identifying the causes of sea level changes. Nat Geosci 2:471–478
50. Meehl GA et al (2007) Global climate projections. In: Solomon S, Qin D, Manning M, Chen Z, Marquis M, Averyt KB, Tignor M, Miller HL (eds) Climate change 2007: the physical science

basis. Contribution of working group I to the fourth assessment report of the intergovernmental panel on climate change. Cambridge University Press, Cambridge/New York
51. Pfeffer WT, Harper JT, O'Neels S (2008) Kinematic constraints on glacier contributions to 21st century sea level rise. Science 321:1340–1343
52. Slangen AB, Katsman CA, van de Wal RSW, Vermeersen LLA, Riva REM (2011) Towards regional projections of twenty-first century sea level change based on IPCC SRES scenarios. Clim Dyn. doi:10.1007/s00382-011-1057-6
53. Nicholls RJ (2007) The impacts of sea level rise. Ocean Challenge 15(1):13–17
54. Nicholls RJ, Cazenave A (2010) Sea-level rise and its impact on coastal zones. Science 328:1517–1520
55. Ericson JP, Vorosmarty CJ, Dingman SL, Ward LG, Meybeck L (2006) Effective sea level rise and deltas: causes of change and human dimension implications. Global Planet Change 50:63–82

Books and Reviews

Bigg G (2003) The oceans and climate. Cambridge University Press, Cambridge, MA
Church JA, Woodworth PL, Aarup T, Wilson WS (Eds) (2010) Understanding sea level rise and variability. Wiley-Blackwell
Cazenave A, Nerem S (2004) Present-day sea level change: observations and causes. Rev Geophys 42:RG3001. doi:8755-1209/04/2003RG000139
Cazenave A, Remy F (2011) Sea level and climate: measurements and cause of changes. Wiley Interdiscip Rev Clim Change 2:647–662
Church JA, White NJ, Aarup TG, Wilson WS, Woodworth PL, Domingues CM, Hunter JR, Lambeck K (2008) Understanding global sea levels: past, present and future. Sustain Sci. doi:10.1007/s11625-008-0042-4
Church JA, Woodworth PL, Aarup T, Wilson WS (eds) (2010) Understanding sea level rise and variability. Wiley-Blackwell, Chichester
Nerem S, Leuliette E, Cazenave A (2006) Present-day sea level change. C R Geosciences 338(14–15):1077–1083
Solomon S, Qin D, Manning M, Chen Z, Marquis M, Averyt KB, Tignor M, Miller HL (eds) IPCC 4th assessment report, 2007. Climate change 2007: the physical science basis. Contribution of working group I to the fourth assessment report of the intergovernmental panel on climate change. Cambridge University Press, Cambridge/New York

Chapter 5
Coral Reef Ecosystems

Helen T. Yap

Glossary

Coral reef	A geological structure of significant topographic relief above the sea floor, made of calcium carbonate and constructed by living organisms (mainly corals belonging to the order Scleractinia, phylum Cnidaria, and coralline algae).
Hermatypic	Refers to corals that are able to build reefs.
Holocene	A geologic age that corresponds to 10,000 years before the present, or "B.P."
Scleractinia	The order of hard or stony corals to which the reef builders belong, under the phylum Cnidaria.
Zooxanthellae	Golden brown single-celled algae that inhabit the gastrodermal cells of reef-building corals (belonging to the phylum Dinophyta, order Gymnodiniales).

Definition of the Subject and Its Importance

Coral reefs are geological structures of significant dimensions, constructed over millions of years by calcifying organisms. The present day reef-builders are hard corals belonging to the order Scleractinia, phylum Cnidaria. The greatest concentrations of

This chapter was originally published as part of the Encyclopedia of Sustainability Science and Technology edited by Robert A. Meyers. DOI:10.1007/978-1-4419-0851-3

H.T. Yap (✉)
The Marine Science Institute, University of the Philippines, Diliman,
1101 Quezon City, Philippines
e-mail: helentyap@yahoo.com; hty@upmsi.ph

J. Orcutt (ed.), *Earth System Monitoring: Selected Entries from the Encyclopedia of Sustainability Science and Technology*, DOI 10.1007/978-1-4614-5684-1_5,

coral reefs are in the tropics, with highest levels of biodiversity situated in reefs of the Indo-West Pacific region. These ecosystems have provided coastal protection and livelihood to human populations over the millennia. Human activities have caused destruction of these habitats, the intensity of which has increased alarmingly since the latter decades of the twentieth century. The severity of this impact is directly related to exponential growth rates of human populations especially in the coastal areas of the developing world. However, a more recently recognized phenomenon concerns disturbances brought about by the changing climate, manifested mainly as rising sea surface temperatures, and increasing acidification of ocean waters due to greater drawdown of higher concentrations of atmospheric carbon dioxide. Management efforts have so far not kept pace with the rates of degradation, so that the spatial extent of damaged reefs and the incidences of localized extinction of reef species are increasing year after year. The major management efforts to date consist of establishing marine protected areas and promoting the active restoration of coral habitats.

Introduction

Over the millennia, coral reef ecosystems have served as the basis of human survival and sustenance in many coastal areas in the tropics and subtropics. They are significant geologic formations that provide crucial protection from destructive forces of the sea. They also harbor the greatest diversity of animal phyla than any other habitat on the planet. But because of the finely tuned balance between primary production and energy consumption within the ecosystem, coral reefs are unable to sustain high levels of biomass extraction. Added to this, a range of human impacts from overfishing to pollution and direct destruction of the habitat has caused extensive degradation of these ecosystems since the latter decades of the twentieth century. This trend has been exacerbated by recently recognized effects of climate change. The main culprits are rising sea surface temperatures and increasing acidification of ocean waters, both of which exert adverse impacts on the physiology of the coral-zooxanthellae complex, thus hampering its ability to effectively recover from various environmental disturbances. The best management option at the present time is to put as many reefs as possible under protection, while providing for alternative means of livelihood to displaced fishers. The field of active coral restoration is still at an early stage and warrants further research.

Geology and Distribution

A reef is a "discrete carbonate structure formed by in situ or bound organic components that develops topographic relief upon the sea floor" [1]. The majority of coral reefs are located in the tropics [2, 3] (Fig. 5.1). The limit of their

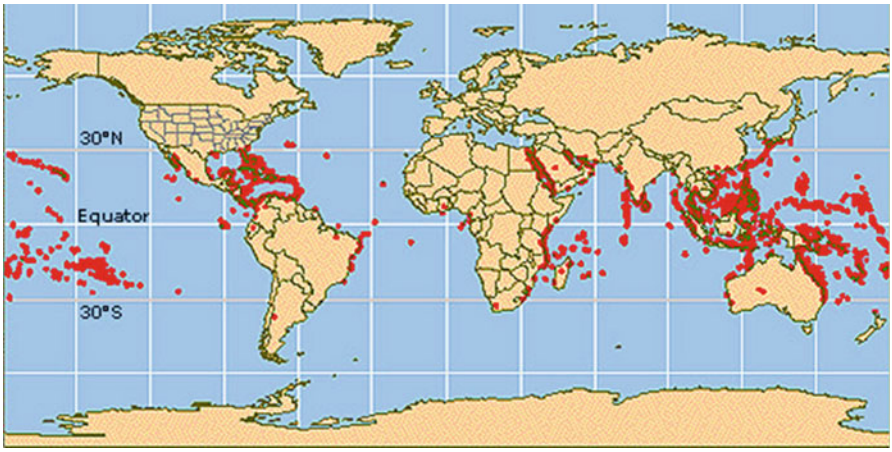

Fig. 5.1 Global distribution of coral reefs (Source: NOAA National Ocean Service Education Web Site, revised 25 March 2008, http://oceanservice.noaa.gov/education/, NOAA National Ocean Service, Communications and Education Division)

distribution is represented by Midway and Kure, for example, which are well-developed algal-coral atolls that lie north of 28°N latitude at the northwestern end of the Hawaiian chain. As summarized by Moberg and Folke [4], coral reefs are estimated to constitute from 0.1% to 0.5% of the ocean floor, with actual areal estimates ranging between 255,000 and 1,500,000 km^2. The coastlines of more than 100 countries are lined by coral reefs. Advances in methodology, particularly remote sensing, are helping to delineate more accurately the distribution and extent of coral reefs, and the proportions of the different components that constitute the bottom substrate (live coral, vegetation, nonliving cover such as rock and sand) [5]. However, remote sensing is still limited by the fact that only the visible range of the electromagnetic spectrum can penetrate the water column sufficiently down to depths occupied by coral reefs which are shallow-water ecosystems. Hence, this tool should be complemented by actual ground-truth surveys whenever possible [5].

The three main types of coral reefs are fringing reefs, barrier reefs, and atolls [2–4]. Other than these major categories, there are minor reef forms of various sizes and shapes, and situated at different depths of the ocean floor. For example, Moberg and Folke [4] mention platform reefs as a fourth category (Table 5.1). Fringing reefs develop close to the shore in relatively shallow waters. Among the longest expanses of reefs in the world is the fringing reef that lines the shores of the Red Sea [2], with a length, if stretched out, exceeding 2,500 miles (4,000 km). Barrier reefs are composed of a series of reef structures arranged roughly parallel to the coast, and separated from it by a fairly deep lagoon. The largest such aggregation of reefs in the world is the renowned Great Barrier Reef off the Queensland coast of Australia [2] with a length of more than 1,200 miles (almost 2,000 km). It varies in width from about 10 miles (16 km) to almost 200 miles (320 km). The total area of reef habitat that it encompasses is about 25,000 km^2 [6]. The various reef structures within the

Table 5.1 The four main reef types

Platform reefs	Fringing reefs	Barrier reefs	Atolls
Frequently found in the lagoons created by atolls and barrier reefs	Closely follow shorelines, narrow shallow lagoon	Separated from land by a relatively wide, deep lagoon	Horseshoe shaped or circular reef surrounding a central lagoon (often far from land in the open ocean)
In the Great Barrier Reef lagoon, Belize, Red Sea, Bahamas	Red sea, East Africa, Seychelles, and other Indo-Pacific islands, most Caribbean reefs	The Great Barrier Reef in Australia, Belize Barrier Reef, off Mayotte in the Western Indian Ocean	>95% of the atolls are in the Indo-Pacific, others are found outside Belize and in Western Atlantic

Source: From [4]

barrier reef are separated from each other by lagoons of different sizes. Atolls are annular reefs that encircle a lagoon. They may arise from the deep sea, or from the shallower depth of the continental shelf [2]. Platform reefs are carbonate structures of various shapes and sizes usually situated inside lagoons.

A major factor controlling reef growth is sea level rise [1]. It is to be noted, however, that the more relevant metric is *relative* sea level change, because the actual sea level in an area is a net result of both sea level change and tectonic movement of the land due to the presence of active faults [7, 8]. Thermal expansion of the ocean due to increasing heat content caused by climate change also contributes to sea level rise [9]. In terms of the effects of sea level changes on reef growth, more information exists for tropical Atlantic reefs compared to their counterparts in the Pacific [10]. Much geological research has focused on Holocene reefs. These are considered analogues of ancient reefs, and preserve records of eustatic changes in sea level and neotectonics. The measured vertical accretion rates during the Holocene display some variability (reviewed in [10]). Caribbean reefs had higher average rates, on the order of 6 m/ky, compared with Indo-Pacific reefs which have grown at an average rate of 4.4 m/ky. Reasons for this difference still remain unknown. In the Pacific, the Philippines, though it lies in the acknowledged center of shallow-water marine biodiversity, has been little studied compared to the Great Barrier Reef, the Ryukyus, and the islands of Hawaii and Polynesia. The study of Shen et al. [10] represents the first coral-based sea level record from the South China Sea. Reef accretion rate is estimated to have reached as high as 10–13 m/ky during the period 9.2–8.2 ka.

Amphitropical distributions are disjunct distributions where the population or species occurs subtropically on both sides of the equator [11]. Such patterns have been most commonly observed in fish. In the case of corals, however, disjunct distributions in central Indo-Pacific species are observed by Veron [11] to display no significant amphitropical component. Veron [11] also claims similarities between corals of Hawaii and those in the southeast Pacific on a larger scale. Dispersal is believed to play a key role in the speciation and distribution of coral species.

The tropical oceans consist of four major biogeographic regions [4]: the Indo-West Pacific (IWP), the Eastern Pacific, the Western Atlantic, and the Eastern Atlantic.

Knowledge about coral distributions is summarized as follows (quoted from [11]):

- There are areas of high diversity in the tropical western margins of the world's three great ocean basins, that of the Indian Ocean being relatively ill-defined.
- Within the Indo-Pacific, there is little generic variation within the center of high diversity.
- There is attenuation of species diversity latitudinally and longitudinally from these centers.
- Regions distant from centers of species diversity tend to have similar genera.
- Latitudinal attenuation occurs in the same or similar "drop-out" sequence in the northern and southern hemispheres.
- Latitudinal attenuation is highly correlated with sea surface temperature.
- The mean generic age of Caribbean corals is twice that of Indo-Pacific corals and centers of diversity have relatively young generic ages.

In a recent analysis of biogeographic patterns of corals and reef fish across the Pacific and Indian Oceans, Bellwood and Hughes [12] established a "remarkable congruence" between the two groups in terms of gradients in diversity. The peak in diversity for both corals and fish was observed in the Indo-Australian region, between 120°E and 170°E longitude. There was a steep decline across the Pacific toward its eastern boundary, where assemblages are notably more depauperate. There also was a decline westward across the Indian Ocean, though not as steep. A similar congruence for corals and fish was observed in terms of biodiversity patterns along latitudinal gradients. The peak in diversity was near the equator, with declines on either side at higher latitudes.

Biology and Ecology

The main builders of modern-day reefs are the hard or stony corals belonging to the order Scleractinia of the phylum Cnidaria [13]. They constitute the main framework structure, as well as act as fillers and cementers of the reef matrix together with the coralline algae. The basic unit of the coral is an anemone-like structure called the coral polyp. Large coral forms are often colonial, consisting of numerous polyps that have reproduced asexually by budding. However, there are a few solitary forms such as members of the genus *Fungia*, commonly known as "mushroom corals." Recent phylogenetic evidence indicates that deep-water coral species arose from shallow-water ancestors, following a long established process of diversification of marine taxa along a gradient from shallow to deeper habitats [14].

The majority of reef corals are in a symbiotic relationship with a dinoflagellate of the genus *Symbiodinium*. Dinoflagellates are golden brown single-celled algae

belonging to the phylum Dinophyta, order Gymnodiniales [13]. They have been given the name "zooxanthellae" [15]. They inhabit the gastrodermal cells of the coral polyp where they perform the basic function of photosynthesis. The products of photosynthesis are used primarily by the algae for their own metabolic maintenance and for reproduction. However, under favorable conditions the zooxanthellae produce an excess of photosynthetic products such as simple sugars, lipids and amino acids which are then translocated to the coral host cell [15]. The photosynthate is utilized by the coral to supply its own nutritional needs. In addition, this supplementary energy source fuels the all-important mechanism of calcification which is the basis of reef building [16]. The symbiotic algae also provide oxygen, a by-product of photosynthesis, which helps support the metabolism of the coral host. Because of a finely tuned balance between primary production and energy consumption of all species within the ecosystem, coral reefs have relatively low rates of net primary production [17]. Hence, they are unable to sustain high levels of biomass extraction.

Not all coral species harbor symbiotic algae, and are termed "azooxanthellate" [3]. It is the zooxanthellate forms that possess the in-house power unit, so to speak, which helps support calcification on a large scale. Hence, the majority of these are so-called hermatypic or reef-building corals. They are colonial in form, and this trait together with their symbiosis with algae is believed to confer on them a competitive advantage over other benthic invertebrates, and helps explain their dominance in tropical reefs [14].

The extant members of the order Scleractinia are evenly divided between zooxanthellate and azooxanthellate species [14]. Most azooxanthellate species are solitary (as opposed to colonial) and are nearly absent from reefs. However, they have wider geographic and bathymetric distributions than reef corals, extending up to aphotic depths in the ocean. Recent phylogenetic analyses indicate that they originated from ancestors that were symbiotic [14].

With respect to the zooxanthellate coral taxa, it is, ironically, the possession of this singular advantageous feature that has rendered them extremely susceptible to a relatively recent stress in the form of increasing ocean temperatures. This phenomenon is part of what has been recognized as global climate change [18]. Temperature stress, that is, water temperatures significantly above normal for prolonged periods, causes zooxanthellae to lose their pigment, or to be expelled by the host polyp. In both instances, there is a loss of photosynthetic capability of the coral-algae symbiotic complex with a resulting impairment in the ability to meet nutritional needs of both coral host and symbiont.

Scientific findings over the last few decades have established that there are a number of clades of zooxanthellae, originally thought to belong only to one species of the genus *Symbiodinium*. These clades are genetically distinct from one another. To date, there are eight known phylogenetic clades, with each clade containing multiple subclades or types [19, 20]. Scleractinian corals establish functional symbioses primarily with clades A-D. Their genetic distinction imparts different physiological properties to the various clades, properties that are manifested at the level of the host-zooxanthellae complex or "holobiont" [19–21],

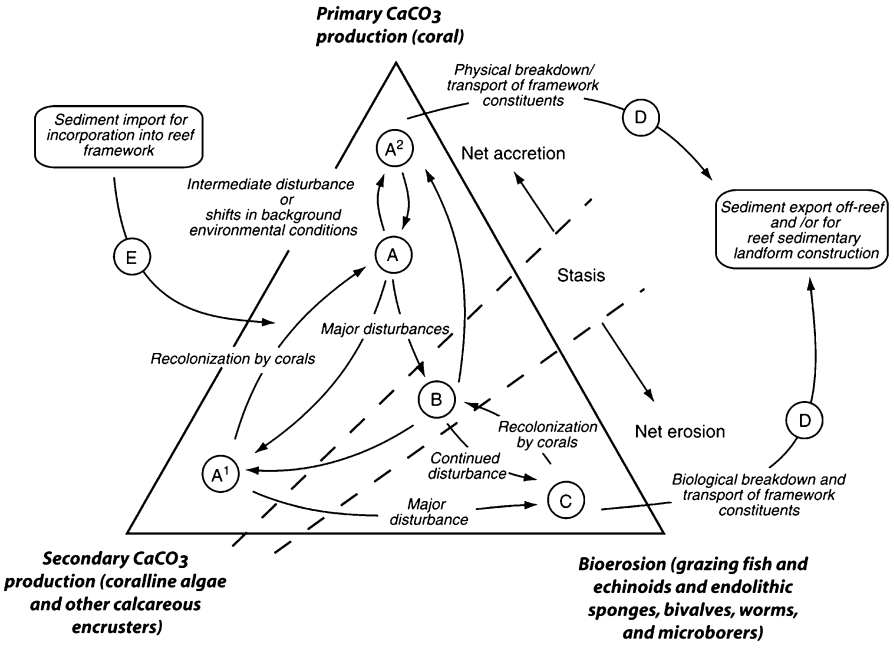

Fig. 5.2 Conceptual model depicting processes contributing to coral reef carbonate accretion or erosion, and the effects of environmental change (From [22])

notably the ability to adapt to various ambient temperature regimes. Hence, some zooxanthellate corals are able to tolerate increases in water temperature better than others. In some instances, the algae are not expelled by the host coral and are able to continue photosynthesizing, providing the latter with vital nourishment during stressful thermal conditions.

Reef accretion is due to a net positive balance of calcium carbonate production over calcium carbonate loss (Fig. 5.2, [22]). The major producers of calcium carbonate are the hard corals. Their skeletons constitute the main framework of the reef, which is a geological structure in three dimensions and which can measure thousands of meters across. There are other important calcifying organisms as well, notably the coralline algae. The remains of these and other calcifiers such as molluscs and foraminiferans serve to fill in the reef matrix over geologic time. Another source of calcium carbonate on the reef is the import of sediment from outside sources via water currents. The loss of calcium carbonate is due to erosion, dissolution, or export of sediment out of the reef. Erosion can be due to physical or biological processes. Important bioeroders are fish that graze on coral (notably parrotfish), sea urchins that scrape hard substrates in the process of feeding, sponges, molluscs, and worms that bore into coral skeletons, plus a variety of microborers.

Optimal Environmental Requirements

Because of the intimate symbiosis with algae, reef-building corals will survive and grow down to particular depth limits in the ocean due to specific light requirements for algal photosynthesis [15]. Most extensive reef structures occur in relatively shallow waters, typically down to depths of thirty (30) meters [15]. Hermatypic corals require high levels of aragonite supersaturation in order to maintain sufficient rates of calcification. Coral reef communities also thrive best in nutrient-poor waters [1].

Another critical environmental factor is temperature. The physiology of the coral-alga symbiotic complex functions optimally within specific temperature ranges, typically not lower than 18°C, with the limiting high temperatures believed to be sustained maxima of 30–34°C [1]. Although coral reefs achieve maximal development in the tropics, recent trends indicate that the highest summer temperatures in many tropical areas are probably exceeding the upper thermal tolerance limits of many coral species. The phenomenon of coral bleaching, whereby a coral colony becomes white because the symbiotic zooxanthellae either lose their pigments or are altogether expelled [23], is becoming more frequent [18].

Different coral species are adapted to a wide range of hydrodynamic regimes, from calm to turbulent. They may be found in a corresponding range of habitats from sheltered lagoons to reef slopes exposed to the open sea. However, they require a minimum of water circulation around the coral colony to ensure that wastes are carried away, and that a sufficient amount of oxygen is made available for respiration. A microscopic boundary layer exists around the surface of the coral colony that controls the diffusion of nutrients and gases between the external environment and the internal environment of the coral-alga symbiotic complex.

Because of their metabolic requirements, corals, just like all other organisms with aerobic respiration, need a minimum amount of dissolved oxygen in the water in order to survive. Hypoxic conditions that are generated by excessive microbial decay of organic matter, or by abnormally high water temperatures, can impair coral survival and health. Similarly, salinity, because of its effects on coral-algal physiology, must also be maintained within certain ranges (34–36 ppt) for optimal survival and growth of coral colonies [13]. If levels of salinity drop precipitously, as in periods of heavy rainfall coinciding with low tides, for example, corals in shallow areas can experience osmotic stress. If the period of immersion in low salinity water is protracted, then some colonies can experience mortality. Abnormally high salinity, above typical oceanic values of 35 ppt, can also inflict metabolic stress on corals. Exceptions, however, are coral populations in normally high salinity areas like the Red Sea [13] which have adapted over the millennia to such extreme conditions.

Waters around flourishing reef areas are characteristically oligotrophic, with relatively low nutrient concentrations. The coral-alga symbiotic complex is efficient in taking up nutrients from surrounding waters, utilizing them for photosynthesis, and recycling them back into the external medium through metabolism.

Important nutrients in reef areas are nitrate, ammonium, and phosphate. They exist in a fine balance with the living community, a balance that is easily disrupted by excessive influx of nutrients from external sources. An increased supply of nutrients favors the primary producers over the coral. Thus, depending on a particular situation, there would be increased abundances of zooxanthellae residing within coral colonies, of phytoplankton in the water column, or of algae inhabiting the bottom substrate. Algae compete with corals for space and light.

Biodiversity

Coral reefs are among the richest marine habitats in terms of species diversity [3, 11]. They are often alluded to as the "rainforests of the sea." The high species diversity is attributable to known factors, namely, the location of coral reefs in the tropical and subtropical latitudes with their attendant climatic regimes, and the complex topography afforded by the three-dimensional geological structure. The relatively high light intensities close to the equator support the levels of primary production that are needed to drive the multitude of trophic pathways in a typical coral reef ecosystem. The relatively small ranges of temperature fluctuations, as compared to temperate and higher latitudes, enable a sustained level of metabolism throughout the entire year for many species, including several reproductive episodes.

Recent analyses of the fossil record indicate that reefs were probably cradles of evolution during the Phanerozoic era (which covers about 500 million years from the present), with approximately 22% of examined genera originating in reef environments [24]. The class Anthozoa, which contains the reef-building scleractinian corals, contains the largest number of genera originating in reef environments. In addition to being sites of the appearance of new species, coral reefs are seen to have exported various taxa to other environments. The most likely explanation as to why reefs have played this role over their geologic history is their habitat complexity [24].

The complex three-dimensional structure of a typical reef provides a plethora of habitable space for a wide variety of organism types with a corresponding wide range of behaviors. In an analysis of a large contemporary data set, Bellwood and Hughes [12] determined that patterns in the diversity of corals and reef fish on a biogeographic scale were best explained by the availability of habitat area, a key feature of topographic complexity. The various species interact primarily via feeding or trophic pathways, although the picture has sadly been drastically altered by excessive human exploitation, in addition to other natural and anthropogenic impacts [25].

Coral reefs contain the greatest number of phyla of any habitat on earth, including 32 of the estimated total of 34 animal phyla [13]. The stony corals which build up the reef framework belong to the phylum Cnidaria, which also includes the hydroids and jellyfish, and the non-reef building soft corals. Another dominant component of the benthic community are the sponges belonging to the phylum Porifera. Other conspicuous invertebrates are represented by the phylum

Echinodermata which includes the starfish, sea urchins, sea cucumbers, and crinoids and the phylum Mollusca covering a huge variety of clams and shells, not to mention squid and octopus. The phylum Arthropoda includes the class Crustacea, a very large one that includes crabs, lobsters, and shrimps. It is a member of the subphylum Vertebrata, however (apart from the hard corals themselves), that captures the most attention from coral reef enthusiasts. The most renowned vertebrate group is the fishes which comprise thousands of species on a pristine reef. Other vertebrates that used to dominate coral reef habitats in different parts of the globe, but that are sadly depleted now [25] include the sea cows, turtles, and crocodiles. Even sea birds that were once plentiful around reef ecosystems are now dwindling in numbers.

Among reef habitats, the most diverse are found in the Indo-West Pacific region, particular around the islands of the Philippines, Indonesia, and Papua New Guinea [26–28]. These islands combined harbor more than 2,500 species of fish belonging in 165 families, more than 3,200 species of mollusc, and about 500 species of coral in almost 80 genera. A recent study involved mapping of the geographic ranges of 1,700 species of reef fish, 804 species of coral, 662 species of snail, and 69 species of lobster [27]. For all taxa, the peak in species richness was determined to be in what has come to be known as the "coral triangle" of Southeast Asia, namely, the islands mentioned above. Species richness then falls off rapidly toward the east across the Pacific, and less rapidly toward the west, across the Indian Ocean. Sites in the southern Philippines and central Indonesia were found to be in the top 10% richest locations.

In the analysis of Roberts et al. [27], 58 species of corals, or 7.2% of the total studied, had restricted geographic ranges. The values for fish, snails, and lobsters were 26.5%, 28.7%, and 53.6%, respectively. The implication of this finding is that many species may be vulnerable to localized extinctions, particularly if they are restricted to geographic locations receiving high levels of human impact. Areas with high degrees of endemism combined with significant levels of impact have been termed marine biodiversity "hotspots." A renowned example of a place which has a high degree of biodiversity but whose reefs are among the most threatened (and degraded) in the world is the Philippines [27, 28].

A recent study has shown that the Philippines harbors a higher concentration of species per unit area than Indonesia, with a rigorous pattern emerging for marine shore fishes [29]. The authors hypothesize a center of origin on the Eurasian plate, with geological events being responsible for allopatric speciation, in addition to island integration. The Philippine center of diversity has significant abundance of both widespread Indo-Pacific species as well as species whose distribution is limited to coral reefs.

Fisheries

Over the millennia, the greatest benefit provided to mankind by coral reef ecosystems has been in the form of harvest, primarily of finfish, in addition to

other vertebrates and invertebrates [25]. Human populations along the coast made extensive use of nearby reef areas that were situated typically in shallow water and often in sheltered lagoons or embayments, a fact that rendered them eminently accessible by even the most primitive means of transport such as rafts and hand-paddled canoes. Traditional methods involved the use of various kinds of nets, or of hook-and-line fishing.

There are over 4,000 species of teleost fishes known to be associated with coral reefs [30]. Approximately 10% of these are directly dependent on corals. They are either obligate coral dwellers, corallivores (i.e., they feed on coral tissue), or possess juvenile stages that always settle into live coral in the process of recruitment. The total global fisheries yield from coral reefs is estimated to be USD five billion annually [30].

In the central Philippines, which was recognized recently as among the richest in the world in terms of species diversity [29], the following fish families contribute substantially to fish catch [31]: Acanthuridae, Siganidae, Scaridae, Labridae, Haemulidae, Lethrinidae, Lutjanidae, Mullidae, Serranidae, Carangidae, Scombridae, Sphyraenidae, Belonidae, and Caesionidae. In terms of total potential fish yield, Alcala and Russ [31] suggest a figure of 350,000 metric tons annually for the entire country, based on an aerial estimate of 25,000 km^2 of reef area.

Physical Connectivity

Marine habitats such as coral reefs have the key distinguishing feature (when compared to terrestrial habitats) of being situated within a water medium, as opposed to air. The physical differences between water and air impart fundamental properties in terms of how the respective communities function, and how they are structured. One obvious difference is that water is considerably denser than air, and is capable of carrying a much larger quantity of material. Because of this, there is significant transport by water currents between habitats over a large range of distances, from microscopic (at the scale of molecular motion) to the macroscopic scale (up to hundreds of kilometers) [32].

Oceanic currents convey a whole spectrum of materials, from dissolved compounds, to particles (living and nonliving) to organisms of various sizes, from microscopic plankton to mammals weighing several tons. The relevant aspect for marine conservation and sustainability is the ecological process of recruitment, whereby gametes or larvae are carried away from particular habitats and transported to other areas at varying distances from the point of origin. Recruitment is a vital process for the maintenance and renewal of populations. Communities that suffer significant decreases in recruitment over appreciable amounts of time are in danger of diminishing or even disappearing altogether.

One of the first papers that advocated a study of surface oceanic currents in order to predict possible recruitment trajectories is that of Roberts [33]. The author, using

the Caribbean as an example, proposed that if larvae can be regarded as passively dispersing particles, then upstream reefs, if harboring healthy populations of reef species, may be considered sources supplying downstream areas. The effective distance by which recruitment can occur successfully would, theoretically, be dictated by the length of time during which a larva remains viable in the water column, or the duration of the pelagic larval phase [34]. In an extension of this perspective to management applications, downstream reefs receiving viable recruits in sufficient amounts would be less at risk of decimation even if exploitation rates were high. Upstream reefs, on the other hand, would be in greater need of protection. These ideas helped to inspire the vigorous movement that emerged in a number of countries that have coral reefs in their territorial waters to establish networks of marine reserves or protected areas premised, among other criteria, on the possible existence of connectivity based on oceanographic patterns. Marine protected areas (MPA's) are discussed in section "Marine Protected Areas".

Subsequently, a large number of studies have been conducted to confirm or refute these ideas [6]. One limitation is that the only means of directly determining the actual fate of individual larvae is by tagging and parentage techniques [6]. Other approaches are indirect, and include genetic analysis, the description of local population structure, and the application of biophysical modeling which combines the characterization of current patterns and hydrographic regimes with larval behavior of particular species.

Recent research indicates that the degree of larval retention within a natal reef, as well as the spatial extent of connectivity in both corals and fish appear to be independent of larval duration [6], contrary to previous expectations. In the case of corals, for both broadcast spawners as well as brooding species, both self-recruitment and inter-reef dispersal have been found to be significant. Dispersal can occur over distances as long as tens of kilometers. Broadcast spawners are corals that release gametes into the water column. The eggs and sperm may come from the same colony (hermaphroditic), or from colonies with separate sexes (gonochoric). Fertilization takes place in the water column. The entire series of developmental stages from cleavage, to formation of the embryo and then of the fully-formed larva all occur as part of the pelagic phase. Brooding species are corals where the egg remains inside the polyp, and is fertilized by sperm that find their way into the cavity. The larva develops inside the polyp and emerges after a period of time, fully formed, into the surrounding water.

In the case of reef fish, a number of methods indicate that, for a range of species, there are ecologically significant levels of self-recruitment at the scale of individual reefs or reef clusters [6]. Results have yielded an average of as high as 45–50% self-recruitment. The amount of self-recruitment does not seem to be related to the mode of spawning nor pelagic larval duration. For both corals and fish, the patterns of dispersal may be influenced more by the geographic setting, size, and location of reefs rather than by the biological characteristics or individual life histories of particular species. This finding, again, has implications for the design of networks of marine reserves, including their size, spatial arrangement, and the distances between them.

Ecological Goods and Services from Coral Reefs

Coral reefs have provided benefits to coastal human populations for thousands of years. Perhaps the greatest value that these ecosystems have is as a source of food. A variety of organisms continue to be harvested, notably the finfish which still possess considerable economic value, in addition to their contribution to basic sustenance of populations, particularly in developing countries. Despite their limited cover in proportion to the entire ocean floor (0.1–0.5%), almost a third of marine fish species in the entire world are found on coral reefs, and about 10% of fish consumed by humans are caught from reef areas [4].

Other vertebrate groups that have been the object of traditional fishing are the dugongs (Order Sirenia) and turtles [25]. Invertebrates that have been traditionally harvested from reefs for human consumption include sea urchins, sea cucumbers, molluscs, and crustaceans. A variety of species of seaweed are also used for food.

Coastlines that are lined by coral reefs are afforded natural protection from the destructive forces of the sea. The natural erosion that occurs within reef habitats due to physical abrasion by waves and currents produces sand which accumulates on beaches. Typically white sand is composed of pulverized coral, shells, coralline algae, and foraminiferans in varying proportions.

In some localities, corals are collected for building material in the construction of houses, roads, and other infrastructure. Other less common uses of reef organisms are as sources of pharmaceuticals.

Coral reefs have always been valued for their aesthetic beauty. In recent decades, they have supported a vigorous tourism and leisure industry that has extended its reach globally. Tourists would travel hundreds to thousands of kilometers to visit pristine reefs. The traffic usually emanates from the more affluent societies in Europe and North America, and heads in the direction of the Caribbean, the Red Sea, the Indian Ocean, and all the way to the high diversity reefs of the Indo-West Pacific.

Table 5.2 presents a general listing of goods and services derived from coral reefs [4].

Threats to Coral Reefs

Unfortunately, the degradation of coral reef habitats has become a worldwide trend [35, 36]. The current concern from the ecological and conservation perspective is how to prevent this trend from becoming irreversible. In the Indo-Pacific region, for example, which is the cradle of coral reef diversity, coral cover is estimated to already lie at least 20% below the best historical reference points [37]. The average loss of coral cover annually is estimated at 1%. This represents a figure of 1,500 km^2 of coral cover lost from the early 1980s to around 2003.

Table 5.2 Ecological goods and services derived from coral reef ecosystems

Goods		Ecological services					
			Biotic services				
Renewable resources	Mining of reefs	Physical structure services	Within ecosystems	Between ecosystems	Biogeochemical services	Information services	Social and cultural services
Sea food products	Coral blocks, rubble and sand for building	Shoreline protection	Maintenance of habitats	Biological support through "mobile links"	Nitrogen fixation	Monitoring and pollution record	Support recreation
Raw materials for medicines	Raw materials for production of lime and cement	Build up of land	Maintenance of biodiversity and a genetic library	Export of organic production, and plankton to pelagic food webs	CO_2/Ca budget control	Climate record	Aesthetic values and artistic inspiration
Other raw materials (seaweed and algae for agar, manure, etc.)	Mineral oil and gas	Promoting growth of mangroves and sea grass beds	Regulation of ecosystem processes and functions	–	Waste assimilation	–	Sustaining the livelihood of communities
Curio and jewelery	–	Generation of coral sand	Biological maintenance of resilience		–	–	Support of cultural, religious and spiritual values
Live fish and coral collected for the aquarium trade	–	–	–	–	–	–	–

Source: From [4]

Table 5.3 Families of reef-building coral species that are near threatened (NT) and/or threatened (Thr) according to Red List categories of the International Union for the Conservation of Nature (IUCN). Criteria are defined by population size reduction and changes in geographic range

Family	Total species	NT + Thr	Thr
Acroporidae	271	71.6%	49.5%
Agariciidae	45	38.1%	26.2%
Astrocoeniidae	15	18.2%	9.1%
Caryophylliidae	3	0.0%	0.0%
Dendrophylliidae	15	71.4%	50.0%
Euphylliidae	17	100.0%	64.3%
Faviidae	130	65.6%	20.0%
Fungiidae	46	27.3%	15.9%
Helioporidae	1	100.0%	100.0%
Meandrinidae	10	42.9%	42.9%
Merulinidae	12	36.4%	9.1%
Milleporidae	16	42.9%	35.7%
Mussidae	52	53.3%	26.7%
Oculinidae	16	70.0%	40.0%
Pectiniidae	29	50.0%	25.0%
Pocilloporidae	31	48.3%	31.0%
Poritidae	101	56.0%	34.1%
Rhizangiidae	1	0.0%	0.0%
Siderastreidae	32	42.3%	19.2%
Trachyphyliidae	1	100.0%	0.0%
Tubiporidae	1	100.0%	0.0%
Total	845		

Source: Modified from [38]

In a recent study, Carpenter et al. [38] compiled data on the status of all known zooxanthellate reef-building corals. These include 845 species from the order Scleractinia, plus reef-building species from other groups of the phylum Cnidaria, the octocorals and hydrocorals. There were sufficient data for 704 species so that conservation status could be assigned. Of these, 32.8%, or roughly one third, were in categories with elevated risk of extinction (Table 5.3). Following criteria from the International Union for Conservation of Nature (IUCN), these species were considered to be under serious threat of population declines within their established geographic ranges. A combination of natural and anthropogenic factors are responsible for the losses in coral cover in different parts of the world.

Since corals are the natural framework builders for the habitat of other reef species, notably fish, declines in coral cover and abundance are usually accompanied by similar decreases in the other biota as well. A study in the Indian Ocean, for example, documented changes in size structure, diversity, and trophic composition of reef fish communities following decreases in coral cover as a result of climate change [39].

Natural Threats

The recent literature highlights the phenomenon of global change, particularly change in the climate, as posing an increasing threat to the health of natural ecosystems, both terrestrial and aquatic [40]. The main culprit is commonly believed to be the large-scale release of carbon dioxide into the atmosphere due to the burning of fossil fuel which reached unprecedented levels since the beginning of the industrial revolution [41, 42]. Another cause for the release of large quantities of this gas is land use practices such as deforestation [42]. The presence of large amounts of carbon dioxide in the atmosphere has created the so-called greenhouse effect, whereby long-wave radiation emitted by the earth system is trapped instead of being released into outer space. The result is a net warming of the planet over time. Temperature has been determined to follow a significant upward trend since the start of the industrial era in the 1800s. Thus, although variations in temperature are a natural feature of the environment, and occur on a range of time scales ranging from diurnal and seasonal all the way to millions of years (corresponding to the geological epochs), the specific causes as to why it is now perceived to be a problem are human-related.

Monitoring long-term trends in sea surface temperature (SST) has been aided greatly by advances in technology, as exemplified by the suite of satellite products developed by the National Oceanic and Atmospheric Administration's (NOOA)-Coral Reef Watch [26]. Specifically, services have been derived from the 0.5°C (approximately 50 km) resolution twice-weekly product delivered by the Advanced Very High Resolution Radiometer (AVHRR). This product has been effective in detecting large-scale thermal stress in the ocean, and in relating this to coral bleaching events, for example. In the Indo-Pacific region, particularly the islands of the Philippines, Indonesia, and Papua New Guinea also known as the "Coral Triangle," an upward trend in SST has been established for the period 1985–2006, with an average rate of increase of 0.2°C per decade [26]. However, it should be noted that satellites detect the temperature of what is essentially the ocean's "skin," so that satellite-derived data should, wherever possible, be complemented by actual temperature measurements made on site at different depths of the reef [43].

With respect to estimates of warming of the entire global ocean, reliable data exist for the upper 300 m [44]. The majority of in situ measurements have been contributed by expendable bathythermograph (XBT) data. After accounting for multiple sources of uncertainty, a statistically significant linear warming trend has been obtained for the period 1993–2008 amounting to 0.64 Wm^{-2} (reflecting the entire surface area of the Earth) with a 90% confidence interval of 0.53–0.75 Wm^{-2} [44].

The increased levels of carbon dioxide in the atmosphere have resulted in another phenomenon that is detrimental to coral reefs. Because of increased partial pressure of the gas (PCO_2) which results in steeper diffusion gradients, there is greater drawdown into the ocean from the atmosphere. An international survey effort consisting of two research programs, the World Ocean Circulation Experiment and the Joint Global Ocean Flux Study, yielded an estimated oceanic uptake

of anthropogenically produced CO_2 for the period 1800–1994 of 118 ± 19 petagrams of carbon [42]. This amount represents about 48% of the total emissions from fossil fuel burning and cement manufacturing, indicating the magnitude of the oceanic sink. Furthermore, this value is projected to be about one third of the long-term potential of the ocean for carbon storage. A more recent estimate made in 2008 puts the value at 140 ± 25 petagrams of carbon, with the Southern Ocean being the primary conduit for entry [41].

Carbon dioxide reacts with seawater to form carbonic acid, decreasing oceanic pH [45]. If the PCO_2 concentrations in the ocean surface continue to increase in proportion to the increase in atmospheric concentrations of this gas, it is estimated that a doubling of the latter from preindustrial levels will result in a 30% decrease in carbonate ion concentration and a 60% increase in hydrogen ion concentration [42]. The result is increasing acidification of the oceans which is believed to pose a threat to calcifying organisms, including the hard corals [46]. The higher acidity values depress aragonite saturation state which is crucial in the net carbonate balance, and which can spell the difference between net accretion and net dissolution of calcium carbonate. Not only corals but other calcifying organisms such as shellfish, foraminiferans, and echinoderms are at risk [47], with significant consequences for the rest of the ecosystem. For example, trophic pathways will be altered if certain species decrease in abundance as a result of reduction in calcification rates, which imply diminution or weakening of protective shells or armor, thus compromising growth, reproduction and survival from predation.

A long-term study of growth rates of juvenile coral in the Caribbean suggests that corals $\leq$40 mm have actually grown more slowly than previously thought [48]. The period of decline in growth rate corresponds with observations of rising seawater temperature and depressed aragonite saturation state, implying effects of climate change. This finding does not bode well for the future viability of coral communities in the region because juvenile stages are critical for the successful establishment of populations of any species. On the other side of the world, in the Great Barrier Reef, experimental manipulations of temperature directly affected the metabolism of coral larvae, with higher temperatures increasing rates of development, and thus the onset of competency [49]. Thus, expected increases in sea surface temperatures will likely cause changes in larval dispersal ranges.

Another natural phenomenon that is perceived to be growing in severity is the occurrence of diseases in corals and other marine species [50, 51]. Although diverse communities of microbes normally inhabit the surfaces of coral colonies and all other types of surfaces on a reef [13] increasing experimental evidence combined with modeling indicates that environmental factors such as increasing water temperatures might promote a shift in dominance from antibiotic-producing beneficial microbes to pathogenic forms such as certain species of *Vibrio*. The loss of antibiotic protection would render corals more susceptible to disease and increase their risk of mortality [52]. Other causative agents of coral disease that have been identified include - *Aspergillus sydowii* (that attacks sea fans) and *Sphingomonas* sp. [51].

Predation on corals has long been considered an important natural threat to the survival of corals [1]. Two notable examples of this phenomenon involve the

crown-of-thorns (COT) starfish, *Acanthaster planci*, and the gastropod *Drupella*. Damage on a fairly large scale, up to hundreds of square meters on a number of reefs, has been documented due to active grazing by these two invertebrate predators. Cyclic fluctuations in populations of many species are considered natural, and are connected with changes in climate, food supply or a combination of these. With respect to COT outbreaks, however, the causes are presumed to relate to unnatural factors such as human overharvesting of natural predators and increases in planktonic food supply of the larvae [18, 53]. Recent evidence from the Great Barrier Reef, for example, suggests that nutrient enrichment of the waters (probably due to land-derived pollution) has triggered blooms of phytoplankton that serve as food for COT larvae, thus enhancing their survival and growth to adulthood [53].

Anthropogenic Threats

Up till recent times, the most severe impacts inflicted on coral reefs have been due to human activities, directly or indirectly [22, 54]. A recent review of anthropogenic threats to coral reefs worldwide is that of Wilkinson [36].

Water quality is generally influenced by levels of nutrients such as nitrogen and phosphorus, concentrations of total organic carbon, turbidity, and light attenuation [55]. Water quality, in general, has been documented to correlate directly with species richness of hard corals and of phototrophic octocorals [56]. Clarity of the water, as commonly measured in terms of Secchi depth for example, is a good indicator of water quality. Low water quality has been observed to be associated with proliferation of macroalgae. The most common cause of diminution in water quality is effluent from the land.

Land-derived impacts have been in existence ever since humans started to modify the land extensively for their use. In terms of documented effects on reefs, the most important activities are agriculture and deforestation. These activities involve the release of huge amounts of sediment which eventually find their way into coastal waters via run-off. Rivers, for instance, transport large amounts of sediment into the ocean. The sediment settles directly on the bottom, physically smothering benthic life-forms.

Another land-derived impact is pollution from both point and nonpoint sources. It can take the form of organic pollution, such as from sewage, and inorganic pollution – for example, heavy metals. Sewage in the water is ultimately degraded by bacteria to yield inorganic nutrients, primarily nitrogen and phosphorus. These elements fuel photosynthesis by both phytoplankton and benthic plants, resulting in high rates of primary production and an increase in biomass of the primary producers. The latter are effective competitors with hard corals for space and light.

In coral reef habitats, the nutrients of interest are nitrate, ammonium, and soluble reactive phosphate assimilated by plants [57]. In addition, dissolved organic forms of nitrogen and phosphorus are significant as well. They are remineralized into the

inorganic forms that are utilized by primary producers. Coral reefs that are close to sites of dense human habitation are susceptible to detrimental effects of nutrient pollution. The effects are aggravated if there is limited flushing, such as within embayments and lagoons.

Destructive fishing practices are another cause of major disturbances to coral reef communities [58]. In many parts of the developing world, the use of explosives to catch fish is still a significant problem. The use of the metabolic poison, sodium cyanide, to catch ornamental fish for the aquarium trade, also continues to be widespread [28]. Both categories of disturbance inflict direct harm on the habitat. Explosives cause catastrophic destruction of the reef substrate and all living organisms within the effective radius of the explosion. They leave behind telltale craters of varying size, depending on the blast, and expanses of rubble and broken coral.

Cyanide is usually dissolved in sea water and squirted directly into crevices and other places where the target fish shelter. It kills virtually all living organisms with which it comes into contact, including coral colonies which are common hiding places for fish. The dose of the poison applied is meant to merely stun the fish for ease of capture, because these are intended to be shipped live to prospective customers.

Another major impact is simply the excessive harvest or overfishing of organisms, be they finfish, invertebrates, or economically important species of algae. For coastal ecosystems in general, the ecological extinction of species due to excessive exploitation precedes the effects of other human-related impacts such as pollution and anthropogenic-related climate change [25]. Jackson et al. [25] hypothesize that it is the depletion of entire species groups, or even trophic levels, that paved the way for the occurrence of subsequent disturbances such as eutrophication, outbreaks of disease and the invasion of species.

Impacts on Reef-Associated Organisms

Decreases in diversity and/or abundance of hard corals have been accompanied by declines in other reef-associated species, notably the fish [30]. The families that are directly dependent on corals are most at risk. These include the butterflyfish (Chaetodontidae), the cardinalfish (Apogonidae), and the gobiids (Gobiidae). A recent empirical study demonstrated that live coral provides effective shelter to both adult and juvenile stages of the damselfish *Pomacentrus amboinensis* [59]. In contrast, juveniles attempting to shelter in bleached and dead coral were driven away by larger fish, thus exposing them to greater predation. They subsequently suffered higher mortality rates. In addition, factors associated with climate change and various human impacts will affect the biology and ecology of the fishes themselves. Temperature, for example, exerts a direct effect on fish physiology, and abnormally high levels can impair reproduction. The aggregate effects of perturbations to the coral

reef ecosystem will be manifested in changes in the diversity, abundance, and distribution of fish. Climate change per se can exert a direct influence by causing shifts in the geographic ranges of various fish species.

One of the most widely discussed phenomena in the scientific literature is that of the coral-algal phase transition or "shift," meaning that reef communities once dominated by scleractinian corals are now largely populated by macroalgae or turf algae [22, 60] or some other reef-associated species [61]. This phenomenon gained widespread attention in the Caribbean [25, 62] with the occurrence of mass mortalities of animals that normally graze on algae. Such grazers include sea urchins and herbivorous reef fish (scarids and acanthurids), and incidents of mortality have been attributed to disease or overfishing of these functional groups. The resulting depletion in populations of herbivores has been observed to correlate with explosions in abundance of macroalgae, which are competitors of hard corals for light and space. A recent study appears to confirm this belief for some Caribbean locations, where recovery of the sea urchin *Diadema antillarum* has occurred [63]. In sea urchin zones where there is significant grazing on algae, the survival of juvenile scleractinian corals was observed to be higher.

For coral reefs in other parts of the world, however, the shift from coral to macroalgal dominance does not appear to be as widespread as previously assumed [64]. Bruno et al. [64] compiled empirical data from reef surveys in the Indo-Pacific, the Great Barrier Reef, the Caribbean, and the Florida Keys. The results of their analysis indicate that the replacement of corals by macroalgae as the dominant benthic component on reefs is neither common nor geographically extensive as previously thought. Apart from a depletion of populations of grazers, nutrient pollution also contributes to algal blooms [65, 66]. Some evidence suggests that the effects of nutrient enrichment tend to be localized to reefs located near centers of dense human populations, and in areas where there is limited flushing of water, such as lagoons and embayments [57].

Management

Given the problems facing coral reefs enumerated above, it is clear that management action should operate on a range of scales, from highly localized to regional and global. It will have to encompass the whole gamut from reducing destructive fishing practices, to implementation of land use schemes that control sedimentation and pollution, and to activities such as restoring herbivore populations [37]. The global policy arena will also need to be involved as this is the effective scale at which global climate change can be addressed.

The field of coral reef management has seen uneven progress over the past decades [54, 62, 67]. Like in most other areas involving natural resources, the effectiveness of management has been diminished by the fact that responsibility for what is essentially a common domain has been fragmented and distributed over

a number of sectors, such as agriculture, fisheries, tourism, human settlements, and industry. The result of this is the often conflicting mandates of different government departments and agencies.

An emerging consensus is that human population growth has begun to far outstrip the capacity of the natural resource base to provide goods and services, and to absorb wastes [67]. This reality manifests itself more clearly in developing countries, where the inability of many citizens to maintain an adequate livelihood results in chronic want, hunger, and disease. In the case of developed countries, the better managed economic sectors (including manufacturing and trade), the superior infrastructure, and the more efficient social delivery system tend to compensate for the diminishing returns from natural resources. Nevertheless, the heavy burden of human demands on natural resources is true for coral reefs in both the developed and developing world.

For coral reef ecosystems, the most pressing goal of management action should be the protection of whatever levels of biodiversity are remaining. Ecological science has demonstrated the advantages of maintaining high species numbers in any natural habitat [61]. One benefit of high species diversity is that a number of different species can play similar ecological roles, a prime example in coral reefs being herbivory or grazing. This aspect is sometimes referred to as "redundancy." If one species becomes locally extirpated because of overfishing, for example, another species can continue its ecological function, thus maintaining the overall balance in the system in terms of fluxes of matter and energy. Examples of reef organisms with similar grazing functions are sea urchins (belonging to the genera *Diadema*, *Tripneustes* and *Salmacis*) and fish belonging to the families Acanthuridae, Chaetodontidae and Scaridae.

Protecting, and then enhancing, existing levels of diversity would necessarily require limits on the extraction of living resources. This would require strict regulation of fishing. If at all possible, fishing for subsistence should be discouraged, and alternative livelihoods developed for traditional fishers. All manner of destructive fishing should be banned, with the imposition of severe penalties.

Marine Protected Areas

The designation of marine protected areas (MPA's), where no extractive activity whatsoever is allowed, is by far the most widely advocated management tool for coral reefs [54, 67, 68]. The core argument for this type of intervention is compelling: If carefully selected areas are protected from human activities, particularly resource extraction, then natural ecological processes will be allowed to proceed without interruption. The expected result is a healthy, thriving community with increased abundance and diversity of many reef-associated species [69].

The natural behavior of the motile species, particularly the finfish, would cause them to move beyond the boundaries of an MPA into areas that are open for fishing. This so-called spillover should be of benefit to subsistence and, where applicable, commercial fishers. An additional benefit of functioning MPA's is in the form of "recruitment subsidy" whereby spawning populations of reef species that are under protection produce adequate quantities of gametes or larvae which are then carried beyond the MPA boundaries to replenish depleted stocks in openly exploited areas.

These two expected benefits of MPA's require further research and experimental testing [70], with available supporting evidence still somewhat sparse and ambiguous [68]. One study providing possible evidence of export of fish from a coral reef reserve is that of Abesamis and Russ [71] in the Philippines. The reserve has been maintained for over two decades, and the observed movement into surrounding areas was attributed to behavior of adult fish as they increased in size and density.

One documented effect of MPA's is increase in the populations of herbivores as a result of protection from fishing [72, 73]. Herbivores include invertebrates such as sea urchins, and fish such as parrotfish (family Scaridae) and surgeonfish (family Acanthuridae). In studies in the Philippines and the Bahamas, adequate populations of herbivores were found to be effective in keeping macroalgal cover in check [72, 73]. It is strongly advocated that the maintenance or restoration of herbivore populations within reef areas should be part of management, in addition to controlling nutrient pollution (see section "Improving Water Quality"). A recent study of a Caribbean marine reserve focused on coral population dynamics after the occurrence of two types of major disturbances, namely, bleaching and hurricane impacts. There was more effective recovery of corals within as compared to outside the reserve [72]. Coral cover increased significantly along with a corresponding reduction in macroalgal cover brought about by grazing of herbivorous parrotfishes. The latter had presumably increased in abundance due to effective protection.

The effects of marine reserves have not always been consistent, however, particularly in the face of large-scale disturbances such as those related to climate change. In a large-scale study of no-take areas (NTA's) spanning several countries across the Indian Ocean, there was little difference in the decline in coral cover between NTA's and areas open to fishing [39]. This finding suggests that management efforts should encompass spatial scales larger than the patchwork of MPA's along with their intervening, openly exploited areas. More attention should be given to reef areas that serve as regional refugia, and which act as viable sources of recruits even in the face of large-scale impacts.

To be effective in the long run, fisheries management must take a comprehensive approach, and combine the designation of MPA's with other interventions such as restrictions on gear types and catch size, as well as the provision of alternative forms of livelihood to fishers [74].

Improving Water Quality

Effective management action to maintain the health and diversity of coral reef communities must include the maintenance of good water quality [56]. Coral reef communities are known to thrive best under conditions of clear water, low nutrient levels, adequate sunlight, and moderate temperatures. The key intervention in this regard is the strict control of pollutant loading in coastal waters known to harbor sensitive ecosystems such as coral reefs, sea grass beds, and mangrove forests. Thus, all countries that possess these ecosystems in their territorial waters should enforce strict antipollution legislation.

Since another major land-derived stress is sediment loading, management must also address land-based activities that cause the mobilization of significant quantities of sediment and their release into coastal waters. The main sectors of concern would be agriculture (which also employs the use of chemicals in the form of fertilizers and pesticides), deforestation, and the building of coastal infrastructure (for urbanization and industry).

Restoration

The field of coral restoration has, as its current focus, the hard corals themselves, belonging to the order *Scleractinia*. These are the main structural components of present-day reefs, both as framework-builders and as fillers of the reef matrix (section "Biology and Ecology"). The science of coral restoration is still fairly young and very much at an experimental stage [75, 76]. Perhaps one of the earliest works alluding to the possibility of restoring damaged reef habitats by means of the transplantation of either branches or whole colonies of hard corals is that of Maragos [77] in Hawaii. Examples after that include investigations conducted in the Philippines on the survival and growth of transplanted coral fragments [78]. At the present time, the field has seen the entry of new experimental techniques geared toward augmenting live coral cover by increasing the abundance of either adults or recruits [75].

The main rationale for intervention in the form of restoration is if a damaged reef community has not recovered naturally over appreciable amounts of time. The causes of reef degradation are enumerated in section "Threats to Coral Reefs." Unfortunately, many reefs throughout the world are presently in a degraded state, showing little signs of natural recovery. The dominant cover in such reefs typically consists of macroalgae, turf algae, sponges, soft corals, hydroids, or any combination of these in various proportions. Coral restoration, by definition, is the attempt to bring a reef community back to a dominance by scleractinian corals within a relatively short period of time (as opposed to the decades it would take for a reef to recover naturally, if at all). Some experimental evidence indicates that the establishment of live coral cover can increase the local diversity of reef-associated species [79].

Before any attempt at restoration is initiated, a thorough assessment of the candidate site should be made. The causes of damage, both proximal and long term, should be identified and their current degrees of severity evaluated. It would be ideal if the causes of destruction are mitigated prior to intervention. For example, if causes of reef degradation involve poor water quality due to land-based pollution or sedimentation, then these issues should be resolved first. Similarly, if damage is caused by harmful fishing practices, then these should be controlled or eliminated. A further assessment of the candidate site for restoration should consider the prevailing environmental conditions such as suitability of the substrate, water clarity, salinity, and nutrient levels. These are factors that directly affect coral physiology and should be determined to be suitable for coral survival and growth before juveniles or transplants are introduced.

The most common approach in the past has been to transfer live whole colonies, or fragments of colonies from healthy coral populations to degraded sites within the same reef [76]. It is necessary to source material from within the same general area because long periods of transportation would inflict significant stress on the coral. This would potentially lead to unacceptable mortality rates of the transplants. The whole coral colony or transplant is translocated to what is essentially a new environment. One essential criterion for site selection is that the recipient site should show evidence of the existence of coral communities in the past, usually in the form of dead skeletons. This is an indication that the area could possibly support a new coral-dominated community again, provided that environmental conditions are not permanently inimical to the survival and growth of introduced corals.

Since the use of whole colonies or fragments of colonies usually causes some collateral damage to the source population, other strategies have been developed in recent years to avoid this. One strategy is to collect fragments found on the reef substrate and "rear" these under special conditions of high maintenance ("nurseries") until they reach a size suitable for reestablishment on the natural substrate. Another strategy being tested is to induce spawning of coral colonies under laboratory or hatchery conditions and collect the resulting larvae which can number in the tens of thousands. The larvae are induced to settle on material of a convenient size, such as plastic pins or concrete tiles. When the larvae metamorphose into juveniles, the latter are reared up to a size considered suitable for "outplanting" to the natural reef.

A major problem of coral restoration efforts is the relatively high mortality suffered by either recruits or transplants introduced into a degraded reef [80]. As mentioned above, a degraded reef surface is typically covered by a variety of organisms including turf algae, macroalgae, soft corals, sponges, and hydroids. These are forms that have proven to be able to adapt and thrive under the altered conditions that probably have led to the demise of the original hard coral inhabitants in the first place. Examples of such environmental conditions are increased turbidity and nutrient loading in the water. In addition to being tolerant of the new conditions, these organisms effectively compete with the hard coral recruits and transplants for space.

Coral transplants and recruits introduced into degraded reef environments have also been observed to suffer from predation (pers. obs.). Common predators that occur in the reefs of the Philippines and other similar geographic areas are the crown-of-thorns starfish, *Acanthaster planci*, and the gastropod *Drupella*. There are possibly other causes of coral mortality that are as yet undiscovered, and that have hampered progress in restoration.

Efforts at the present time are focused on developing cost-effective techniques that would minimize expenditure in terms of finances, manpower, and resources, and maximize output in terms of live coral material (juveniles or adults) that can be used in restoration interventions.

A parallel activity to restoration of the hard corals is restocking of other important reef invertebrates. A notable example is the giant clam (Family Tridacnidae) which is a major inhabitant of coral reefs, can grow to appreciable sizes, and can contribute to the carbonate budget of a reef by accreting fairly massive shells. Many species of giant clams have become rare or locally extinct in many reef areas throughout the world, primarily due to overharvesting. Scientific efforts have yielded a fair degree of success in terms of producing large numbers of juveniles under hatchery conditions and then reintroducing these into suitable reef sites [81]. Such established populations have been thriving for several decades in the Philippines, for example. A recent experiment has demonstrated that restocking denuded reef areas with live coral together with giant clams can significantly enhance fish abundance and diversity [82].

Future Directions

Coral reef ecosystems, particularly in the developing world, are clearly no longer able to support major extractive activities, including fishing, on a sustained basis. They are confronted with the twin challenges of limited biological productivity and demands from a relentlessly increasing human population. It is imperative that, as far as possible, coral reef areas all over the world be put under protection to conserve whatever is remaining of their biodiversity and ecological function. However, equally urgent attention should be paid to providing alternative livelihood to the numerous populations of coastal fishers who will be displaced once their traditional fishing grounds are declared off limits for protection. In addition to protecting nature, the fundamental obligation of resource management is to help ensure a decent quality of life for the human inhabitants.

A scrutiny of the existing global economic order would not be unwarranted in this respect, since many coastal populations in developing countries have been reduced to economic desperation. In the management of the use of coastal resources, the perspective should be extended beyond the limited confines of the coastal zone to the national, regional, and even global arenas. For example, it is about time that, in the spirit of interdisciplinary research, fiscal and trade policies

also be examined along with traditional ecological investigations. An inherent injustice may still be embedded in legal international structures that tend to disenfranchise the poor of the control over their own natural resources (not just fisheries) and over the generation of economic wealth from the proper use of these resources (including forest, agriculture, and mineral assets). Unless this aspect is properly addressed, impoverished populations all over the world will continue to deplete natural resources at unsustainable levels simply to ensure their own survival. The related issue of controlling human population growth rate would be a crucial consideration.

Alongside this basic initiative, vigorous efforts should be put in place to control or abate pollution, and to improve water quality. Coral reef communities are extremely sensitive to factors that diminish light availability, such as turbidity, and to abnormally high nutrient levels that promote the proliferation of weedy species such as phytoplankton and benthic algae.

The field of coral restoration is still very much at an experimental stage, with relatively few documented reports of success. It is worthwhile to continue research in this area, as certain coral species have proven to be resilient to variations in climatic factors such as light and temperature, and the enhancement of topographic complexity by coral transplantation has been demonstrated to increase species diversity on local scales.

Bibliography

Primary Literature

1. Wood R (1999) Reef evolution. Oxford University Press, Oxford
2. Ladd HS (1977) Types of coral reefs and their distribution. In: Jones OA, Endean R (eds) Biology and geology of coral reefs, vol IV, Geology 2. Academic, New York, pp 1–18
3. Veron JEN (2000) Corals of the world, vol 1–3. Australian Institute of Marine Science, Townsville
4. Moberg F, Folke C (1999) Ecological goods and services of coral reef ecosystems. Ecol Econ 29:215–233
5. Guild L, Lobitz B, Armstrong R, Gilbes F, Goodman J, Detres Y, Berthold R, Kerr J (2008) NASA airborne AVIRIS and DCS remote sensing of coral reefs. In: Proceedings of 11th International Coral Reef Symposium Session 17, Fort Lauderdale, pp 616–620
6. Jones GP, Almany GR, Russ GR, Sale PF, Steneck RS, van Oppen MJH, Willis BL (2009) Larval retention and connectivity among populations of corals and reef fishes: history, advances and challenges. Coral Reefs 28:307–325
7. Berdin RD, Siringan FP, Maeda Y (2004) Holocene sea-level highstand and its implications for the vertical stability of Panglao Island, southwest Bohol, Philippines. Quat Int 115–116:27–37
8. Maeda Y, Siringan F, Omura A, Berdin R, Hosono Y, Atsumi S, Nakamura T (2004) Higher-than present Holocene mean sea levels in Ilocos, Palawan and Samar, Philippines. Quat Int 115–116:15–26

9. Domingues CM, Church JA, White NJ, Gleckler PJ, Wijffels SE, Barker PM, Dunn JR (2008) Improved estimates of upper-ocean warming and multi-decadal sea-level rise. Nature 453:1090–1093
10. Shen C-C, Siringan FP, Lin K, Dai C-F, Gong S-Y (2010) Sea-level rise and coral reef development of northwestern Luzon since 9.9 ka. Palaeogeogr Palaeoclimatol Palaeoecol 292(3–4):465–473
11. Veron JEN (1995) Corals in space and time: biogeography and evolution of the Scleractinia. Comstock/Cornell, Ithaca
12. Bellwood DR, Hughes TP (2001) Regional-scale assembly rules and biodiversity of coral reefs. Science 292:1532–1534
13. Sheppard CRC, Davy SK, Pilling GM (2009) The biology of coral reefs. Oxford University Press, Oxford
14. Barbeitos MS, Romano SL, Lasker HR (2010) Repeated loss of coloniality and symbiosis in scleractinian corals. Proc Nat Acad Sci. doi:10.1073/pnas.0914380107
15. Muscatine L (1971) Endosymbiosis of algae and coelenterates. In: Lenhoff HM, Muscatine L, Davis LV (eds) Experimental coelenterate biology. University of Hawaii Press, Honolulu, pp 179–191
16. Muscatine L (1971) Calcification in corals. In: Lenhoff HM, Muscatine L, Davis LV (eds) Experimental coelenterate biology. University of Hawaii Press, Honolulu, pp 227–238
17. Yap HT, Montebon ARF, Dizon RM (1994) Energy flow and seasonality in a tropical coral reef flat. Mar Ecol Prog Ser 103:35–43
18. Veron JEN (2008) A reef in time. Belknap Press of Harvard University Press, Cambridge, MA/London
19. Berkelmans R, van Oppen MJH (2006) The role of zooxanthellae in the thermal tolerance of corals: a 'nugget of hope' for coral reefs in an era of climate change. Proc R Soc B 273:2305–2312
20. Mieog JC, Olsen JL, Berkelmans R, Bleuler-Martinez SA, Willis BL, van Oppen MJH (2009) The roles and interactions of symbiont, host and environment in defining coral fitness. PLoS One 4:e6364
21. LaJeunesse TC, Smith R, Walther M, Pinzon J, Pettay DT, McGinley M, Aschaffenburg M, Medina-Rosas P, Cupul-Magaña AL, Perez AL, Reyes-Bonilla H, Warner ME (2010) Host-symbiont recombination versus natural selection in the response of coral-dinoflagellate symbioses to environmental disturbance. Proc R Soc B. doi:10.1098/rspb.2010.0385
22. Perry CT, Spencer T, Kench PS (2008) Carbonate budgets and reef production states: a geomorphic perspective on the ecological phase-shift concept. Coral Reefs 27:853–866
23. Douglas AE (2003) Coral bleaching–how and why? Mar Pollut Bull 46:385–392
24. Kiessling W, Simpson C, Foote M (2010) Reefs as cradles of evolution and sources of biodiversity in the Phanerozoic. Science 327:196–198
25. Jackson JBC, Kirby MX, Berger WH, Bjorndal KA, Botsford LW, Bourque BJ, Bradbury RH, Cooke R, Erlandson J, Estes JA, Hughes TP, Kidwell S, Lange CB, Lenihan HS, Pandolfi JM, Peterson CH, Steneck RS, Tegner MJ, Warner RR (2001) Historical overfishing and the recent collapse of coastal ecosystems. Science 293:629–638
26. Peñaflor EL, Skirving WJ, Strong AE, Heron SF, David LT (2009) Sea-surface temperature and thermal stress in the Coral Triangle over the past two decades. Coral Reefs 28:841–850
27. Roberts CM, McClean CJ, Veron JEN, Hawkins JP, Allen GR, McAllister DE, Mittermeier CG, Schueler FW, Spalding M, Wells F, Vynne C, Werner TB (2002) Marine biodiversity hotspots and conservation priorities for tropical reefs. Science 295:1280–1284
28. Safina C (1997) Song for the blue ocean. Henry Holt, New York
29. Carpenter KE, Springer VG (2005) The center of the center of marine shore fish biodiversity: the Philippine Islands. Environ Biol Fish 72:467–480
30. Munday PL, Jones GP, Pratchett MS, Williams AJ (2008) Climate change and the future for coral reef fishes. Fish Fish 9:261–285

31. Alcala AC, Russ GR (2002) Status of Philippine coral reef fisheries. Asian Fish Sci 15:177–192
32. Soto I, Andréfouët S, Hu C, Muller-Karger FE, Wall CC, Sheng J, Hatcher BG (2009) Physical connectivity in the Mesoamerican Barrier Reef System inferred from 9 years of ocean color observations. Coral Reefs 28:415–425
33. Roberts CM (1997) Connectivity and management of Caribbean coral reefs. Science 278:1454–1457
34. Grahame J, Branch GM (1985) Reproductive patterns of marine invertebrates. Oceanogr Mar Biol Ann Rev 23:373–398
35. Nyström M, Folke C, Moberg F (2000) Coral reef disturbance and resilience in a human-dominated environment. Trends Ecol Evol 15:413–418
36. Wilkinson C (2008) Status of coral reefs of the world: 2008. Global Coral Reef Monitoring Network and Reef and Rainforest Research Center, Townsville
37. Bruno JF, Selig ER (2007) Regional decline of coral cover in the Indo-Pacific: timing, extent and subregional comparisons. PLoS One 2007(8):e711
38. Carpenter KE, Abrar M, Aeby G, Aronson RB, Banks S, Bruckner A, Chiriboga A, Cortes J, Delbeek JC, DeVantier L, Edgar GJ, Edwards AJ, Fenner D, Guzman HM, Hoeksema BW, Hodgson G, Johan O, Licuanan WY, Livingstone SR, Lovell ER, Moore JA, Obura DO, Ochavillo D, Polidoro B, Precht WF, Quibilan MC, Reboton C, Richards ZT, Rogers AD, Sanciangco J, Sheppard A, Sheppard C, Smith J, Stuart S, Turak E, Veron JEN, Wallace C, Weil E, Wood E (2008) One-third of reef-building corals face elevated extinction risk from climate change and local impacts. Science 321:560–563
39. Graham NAJ, McClanahan TR, MacNeil MA, Wilson SK, Polunin NVC, Jennings S, Chabanet P, Clark S, Spalding MD, Letourneur Y, Bigot L, Galzin R, Öhman MC, Garpe KC, Edwards AJ, Sheppard CRC (2008) Climate warming, marine protected areas and the ocean-scale integrity of coral reef ecosystems. PLoS One 3:e3039
40. Hughes TP, Baird AH, Bellwood DR, Card M, Connolly SR, Folke C, Grosberg R, Hoegh-Guldberg O, Jackson JBC, Kleypas J, Lough JM, Marshall P, Nyström M, Palumbi SR, Pandolfi JM, Rosen B, Roughgarden J (2003) Climate change, human impacts, and the resilience of coral reefs. Science 301:929–933
41. Khatiwala S, Primeau F, Hall T (2009) Reconstruction of the history of anthropogenic CO_2 concentrations in the ocean. Nature 462:346–349
42. Sabine CL, Feely RA, Gruber N, Key RM, Lee K, Bullister JL, Wanninkhof R, Wong CS, Wallace DWR, Tilbrook B, Millero FJ, Peng T-H, Kozyr A, Ono T, Rios AF (2004) The oceanic sink for anthropogenic CO_2. Science 305:367–371
43. Sheppard C (2009) Large temperature plunges recorded by data loggers at different depths on an Indian Ocean atoll: comparison with satellite data and relevance to coral refuges. Coral Reefs 28:399–403
44. Lyman JM, Good SA, Gouretski VV, Ishii M, Johnson GC, Palmer MD, Smith DM, Willis JK (2010) Robust warming of the global upper ocean. Nature 465:334–337
45. Feely RA, Sabine CL, Hernandez-Ayon JM, Ianson D, Hales B (2008) Evidence for upwelling of corrosive "acidified" water onto the continental shelf. Science. doi:10.1126/science.1155676
46. Hoegh-Guldberg O, Mumby PJ, Hooten AJ, Steneck RS, Greenfield P, Gomez E, Harvell CD, Sale PF, Edwards AJ, Caldeira K, Knowlton N, Eakin CM, Iglesias-Prieto R, Muthiga N, Bradbury RH, Dubi A, Hatziolos ME (2007) Coral reefs under rapid climate change and ocean acidification. Science 318:1737–1742
47. Brennand HS, Soars N, Dworjanyn SA, Davis AR, Byrne M (2010) Impact of ocean warming and ocean acidification on larval development and calcification in the sea urchin *Tripneustes gratilla*. PLoS One 5:e11372
48. Edmunds PJ (2007) Evidence for a decadal-scale decline in the growth rates of juvenile scleractinian corals. Mar Ecol Progr Ser 341:1–13

49. Heyward AJ, Negri AP (2010) Plasticity of larval pre-competency in response to temperature: observations on multiple broadcast spawning coral species. Coral Reefs. doi:10.1007/s00338-009-0578-5
50. Harvell CD, Kim K, Burkholder JM, Colwell RR, Epstein PR, Grimes DJ, Hofmann EE, Lipp EK, Osterhaus ADME, Overstreet RM, Porter JW, Smith GW, Vasta GR (1999) Emerging marine diseases – climate links and anthropogenic factors. Science 285:1505–1510
51. Rosenberg E, Ben-Haim Y (2002) Microbial diseases of corals and global warming. Environ Microbiol 4:318–326
52. Mao-Jones J, Ritchie KB, Jones LE, Ellner SP (2010) How microbial community composition regulates coral disease development. PLoS Biol 8(3):e1000345
53. Fabricius KE, Okaji K, De'ath G (2010) Three lines of evidence to link outbreaks of the crown-of-thorns seastar *Acanthaster planci* to the release of larval food limitation. Coral Reefs. doi:10.1007/s00338-010-0628-z
54. Bellwood DR, Hughes TP, Folke C, Nyström M (2004) Confronting the coral reef crisis. Nature 429:827–833
55. Lirman D, Fong P (2007) Is proximity to land-based sources of coral stressors an appropriate measure of risk to coral reefs? An example from the Florida Reef Tract. Mar Pollut Bull 54:779–791
56. De'ath G, Fabricius K (2010) Water quality as a regional driver of coral biodiversity and macroalgae on the Great Barrier Reef. Ecol Appl 20:840–850
57. Szmant AM (2002) Nutrient enrichment on coral reefs: is it a major cause of coral reef decline? Estuaries 25:743–766
58. Salvat B (ed) (1987) Human impacts on coral reefs: facts and recommendations. Antenne Museum E.P.H.E, French Polynesia
59. McCormick MI (2009) Behaviourally mediated phenotypic selection in a disturbed coral reef environment. PLoS One 4:e7096
60. Bahartan K, Zibdah M, Ahmed Y, Israel A, Brickner I, Abelson A (2010) Macroalgae in the coral reefs of Eilat (Gulf of Aqaba, Red Sea) as a possible indicator of reef degradation. Mar Pollut Bull. doi:10.1016/j.marpolbul.2009.11.017
61. Nyström M, Graham NAJ, Lokrantz J, Norström AV (2008) Capturing the cornerstones of coral reef resilience: linking theory to practice. Coral Reefs 27:795–809
62. Mumby PJ, Steneck RS (2008) Coral reef management and conservation in light of rapidly evolving ecological paradigms. Trends Ecol Evol 23:555–563
63. Idjadi JA, Haring RN, Precht WF (2010) Recovery of the sea urchin *Diadema antillarum* promotes scleractinian coral growth and survivorship on shallow Jamaican reefs. Mar Ecol Prog Ser 403:91–100
64. Bruno JF, Sweatman H, Precht WF, Selig ER, Schutte VGW (2009) Assessing evidence of phase shifts from coral to macroalgal dominance on coral reefs. Ecology 90:1478–1484
65. Burkepile DE, Hay ME (2009) Nutrient versus herbivore control of macroalgal community development and coral growth on a Caribbean reef. Mar Ecol Prog Ser 389:71–84
66. Smith JE, Hunter CL, Smith CM (2010) The effects of top-down versus bottom-up control on benthic coral reef community structure. Oecologia. doi:10.1007/s00442-009-1546-z
67. Sale PF (2008) Management of coral reefs: where we have gone wrong and what we can do about it. Mar Pollut Bull 56:805–809
68. Russ GR (2006) Yet another review of marine reserves as reef fishery management tools. In: Sale PF (ed) Coral reef fishes; dynamics and diversity in a complex ecosystem. Elsevier, Amsterdam, pp 421–443
69. Worm B, Barbier EB, Beaumont N, Duffy JE, Folke C, Halpern BS, Jackson JBC, Lotze HK, Micheli F, Palumbi SR, Sala E, Selkoe KA, Stachowicz JJ, Watson R (2006) Impacts of biodiversity loss on ocean ecosystem services. Science 314:787–790

70. Sale PF, Cowen RK, Danilowicz BS, Jones GP, Kritzer JP, Lindeman KC, Planes S, Polunin NVC, Russ GR, Sadovy YJ, Steneck RS (2005) Critical science gaps impede use of no-take fishery reserves. Trends Ecol Evol 20:74–80
71. Abesamis RA, Russ GR (2005) Density-dependent spillover from a marine reserve: long-term evidence. Ecol Appl 15:1798–1812
72. Mumby PJ, Harborne AR (2010) Marine reserves enhance the recovery of corals on Caribbean reefs. PLoS One 5:e8657
73. Stockwell B, Jadloc CRL, Abesamis RA, Alcala AC, Russ GR (2009) Trophic and benthic responses to no-take marine reserve protection in the Philippines. Mar Ecol Prog Ser 389:1–15
74. Worm B, Hilborn R, Baum JK, Branch TA, Collie JS, Costello C, Fogarty MJ, Fulton EA, Hutchings JA, Jennings S, Jensen OP, Lotze HK, Mace PM, McClanahan TR, Minto C, Palumbi SR, Parma AM, Ricard D, Rosenberg AA, Watson R, Zeller D (2009) Rebuilding global fisheries. Science 325:578–585
75. Edwards AJ, Gomez ED (2007) Reef restoration concepts and guidelines. Global Environment Facility (GEF) Coral Reef Targeted Research and Capacity Building for Management Programme, St. Lucia
76. Yap HT (2000) The case for restoration of tropical coastal ecosystems. Ocean Coast Manag 43:841–851
77. Maragos JE (1974) Coral transplantation: a method to create, preserve and manage coral reefs. Seagrant advisory report, UNIHI-SEAGRANT-AR-74-03 CORMAR-14
78. Alcala AC, Gomez ED, Alcala LC (1982) Survival and growth of coral transplants in Central Philippines. Kalikasan Philipp J Biol 11:136–147
79. Yap HT (2009) Local changes in community diversity following coral transplantation. Mar Ecol Progr Ser 374:33–41
80. Shaish L, Levy G, Katzir G, Rinkevich B (2010) Coral reef restoration (Bolinao, Philippines) in the face of frequent natural catastrophes. Restor Ecol. doi:10.1111/j.1526-100X.2009.00647.x
81. Gomez ED, Mingoa-Licuanan SS (2006) Achievements and lessons learned in restocking giant clams in the Philippines. Fish Res 80:46–52
82. Cabaitan PC, Gomez ED, Aliño PM (2008) Effects of coral transplantation and giant clam restocking on the structure of fish communities on degraded patch reefs. J Exp Mar Biol Ecol 357:85–98

Book and Review

Bradbury RH, Seymour RM (2009) Coral reef science and the new commons. Coral Reefs. doi:10.1007/s00338-009-0540-6

Chapter 6
Earth System Environmental Literacy

Sustainability Education: Challenges of Integrating Virtual Versus Real Nature in Science Education

Margaret Lowman

Glossary

Ecosystem services	Benefits provided by natural systems that do not necessarily require significant financial maintenance, including water purification, clean air, pollination, soil decomposition, biodiversity, and many others. In accounting, balance sheets often overlook these free services provided by Mother Nature.
Finite resources	In sustainability education, this involves those natural resources on planet Earth that require careful allocation into the future, such as fresh water, oil, and many others.
NEON	Acronym for a long-term environmental monitoring program funded by Congress and mandated to include both research and education components, entitled "National Ecological Observatory Network."

This chapter was originally published as part of the Encyclopedia of Sustainability Science and Technology edited by Robert A. Meyers. DOI:10.1007/978-1-4419-0851-3

M. Lowman (✉)
Nature Research Center, NC Museum of Natural Sciences and Professor,
North Carolina State University, 11 W. Jones Street, Raleigh, NC 27601, USA

TREE Foundation, Sarasota, FL, USA
www.natureresearch.org; www.treefoundation.org

J. Orcutt (ed.), *Earth System Monitoring: Selected Entries from the Encyclopedia of Sustainability Science and Technology*, DOI 10.1007/978-1-4614-5684-1_6,

Pedagogy	The art, science, or profession of teaching and indirectly, the process of implementing assessments or outcomes as part of educational research in order to improve teaching.
STEM	Acronym describing the major science subjects for education advancement, which include "science, technology, engineering, and mathematics."
Sustainability	When a system functions indefinitely with regard to present and future needs, such as when human and natural systems operate indefinitely through careful resource allocation.
Virtual versus real	In sustainability education, there is an underlying controversy between the importance of tools of teaching: newer techniques involve virtual tools (computers, handheld devices, simulated games, virtual field trips, and videos), whereas more conventional tools include real nature such as field trips, taxonomic collections, and hands-on natural science activities. Ideally, both virtual and real approaches contribute to effective learning.

Definition of Sustainability Education

> The best time to plant a tree is twenty years ago. The next best time is now. (African proverb)

If every citizen could read the above quote and understand its underlying ecological concepts, economic challenges, social services, and spiritual heritage, then it is likely that sustainability education would be achieved. The notion of a tree and its ecosystem services illustrate sustainability in the simplest yet most robust sense. To plant and grow a tree, economists struggle with volatile currencies; ecologists juggle development and conservation; religious leaders advocate stewardship; and social scientists examine equity in a world of declining resources. Sustainability education requires an integrated approach between ecology, risk analyses, economics, social sciences, biological sciences, political sciences, languages, biotechnology, physical sciences, health sciences, and religion. All these practitioners (and many others) contribute to sustainability education, an emerging discipline that requires an interdisciplinary synthesis of knowledge, translated into practice, to insure the future of life on Earth.

Introduction

Science education, also termed STEM (science, technology, engineering, and mathematics) is undergoing a revolution in America as well as overseas [1]. The clear links between our environment, human health, and economics have

triggered a serious effort to improve science literacy into the twenty-first century. As global environmental setbacks including climate change, famine, and biodiversity extinction loom, Earth's living systems are fast approaching a tipping point beyond which life on earth may cease to exist as it is known now [2]. Yet never before have humans had such high levels of technology to achieve solutions to global challenges. How to integrate these new technologies with science education is one of the major priorities facing both local and national governments. Neighborhoods and communities face the challenges of air quality and fresh water; entire nations prepare to adapt to rising sea levels and volatile food prices due to droughts; and around the globe, nations struggle with increasing levels of carbon dioxide in our atmosphere and oceans [3]. All of these issues directly link to the quality of sustainability education, which translates into training the next generation to understand the links between a healthy environment, human health, a sound economy, and shared use of finite natural resources.

It is daunting to link the future health of planet Earth with the importance of learning about how our Earth operates. But science or sustainability education in this sense has become a direct metric for our future survival. In America, professional groups including National Academy of Sciences, National Science Foundation, American Association for Advancement of Science, National Association of Environmental Educators, Boy and Girl Scouts of America, American Association of Museums, almost all scientific societies, and even grassroots organization such as Children and Nature Network, local Sierra Club chapters, and religious networks have embraced the challenge of raising science literacy. Furthermore, science literacy is adopted here to umbrella many different aspects of STEM literacy. Diverse components of science literacy included under this umbrella range from marine literacy, environmental literacy, physics literacy, mathematics literacy, and to ecological literacy. Sustainability goes one step further from the collective science literacies in that it requires the integration of both social and physical/biological sciences. But one common denominator emerges for all of these efforts relating to science or sustainability literacy – the notion of sustainability education embraces our knowledge of how to continue to live on planet Earth without exhausting our resources.

Ultimately, sustainability education may be best achieved by a blend of hands-on (i.e., real) and virtual science education experiences. Building bridges between virtual and real environments, among scientists and citizens, and spanning ecology and economics were some of the central issues in recent summits and conferences of educators and other professionals in Washington, DC during 2009–2010. This chapter reviews some of the emerging informal science education priorities for integrating tools both virtual and real, ultimately to create effective sustainability education.

Short History of Sustainability Education and Related Education Initiatives

Over the past decade, myriad conferences, conversations, workshops, and white papers have been produced on the topic of science education, and on raising America's STEM literacy as part of its global economic competitiveness [4–13]. It is well recognized that the conventional methods of large lectures, textbooks, and short laboratory sessions are not able to cover the overwhelming body of scientific knowledge, and even worse, this format does not inspire today's students to pursue careers in science or even to achieve a minimal level of scientific literacy. Educators and scientists alike recognize that innovative, new pedagogies need implementation immediately, if America can regain her leadership in technology and innovation, especially in fields that relate to sustainability such as energy, conservation, biodiversity, ecosystem services, and environmental justice. This commitment has gained center stage in editorials, publications, and conversations from the highest federal levels to the grassroots of small school PTAs; yet specific mechanisms for achieving a robust level of sustainability education have not yet been successfully documented. This remains a priority for both the current practitioners of STEM education, for educators, and for the stewards of natural resources, who recognize the need for interdisciplinary approaches in education to ensure sustainability for all.

Ecological Literacy

> There is one important difference between ecology and many other fascinating sciences and games: unsolved problems of chess, astronomy, or mathematics will not change if we ignore them. Our activity or lack of activity can alter the state of ecology. (Lawrence B. Slobodkin 2003)

Ecological or environmental literacy has been a cornerstone for both formal and informal science education [14]. In particular, the big challenge for ecology education is not a lack of information, but rather the need to provide the relevant context [15, 16] that will motivate the next generation of environmental scientists to collect, access, and interpret relevant information needed for ecological stewardship. A conceptual understanding of "healthy" ecosystems and related ecosystem services, ranging from food and energy to clean air and water, will be required – not only to serve as the foundation for sound economics, but also to sustain human health. Nature shapes, and is shaped, by communities where people live, and in this sense ecology education overlaps directly with sustainability education. When students bond with their natural surroundings, and then use virtual simulations to understand large-scale ecological processes and drivers, ecology education is achievable [17, 18].

During October 2010, a diverse group of organizations hosted a sustainability education summit, entitled Environmental Literacy for a Sustainable World (www.esa.org/eesummit). The mission of this summit was *not* to create a white paper to mail out to participants 6 months later, as is often the aftermath of conferences, but to create a decadal action plan embraced and activated by the participants to advance environmental literacy. One of the first notions of the summit was to agree that all the science literacies are closely related, and that the achievement of a sustainable world will only come about by raising the standards of ecological, environmental, and science literacy – or whatever the label. An open letter to government leaders about the importance of sustainability education was one of the first outcomes (for, e.g., 17 January 2011, www.heraldtribune.com). Additional action items include: (1) Produce a common set of 5–15 key concepts and principles that link human and natural systems for use by teachers and policy makers; (2) Engage communities to meet the challenges of an uncertain future; (3) Create a network of green-design built environments; create an "APP" (application for handheld mobile devices) that links personal behavior to the environment as an index of health; (4) Construct a "go-to" site for environmental materials, aka a technology infrastructure to inventory, synthesize and share best practices and programs; and others. These action items all have different timelines, with the ultimate goal of engaging diverse stakeholders in different elements of sustainability education by 2020.

Conservation Literacy

Like ecology, conservation biology represents another closely related discipline to sustainability, and hence the concepts and applications of an educational strategy will overlap. In the field of conservation biology, a lively debate about the creation of a conservation ethic started long ago with Aldo Leopold's seminal book, *The Sand County Almanac* [14]. Leopold articulated a value system with regard to land, "That land is a community is the basic concept of ecology, but that land is to be loved and respected is an extension of ethics. That land yields a cultural harvest is a fact long known, but latterly often forgotten."

The Society for Conservation Biology defined its goals and objectives as, "the education, at all levels, preparatory and continuing, of the public, of biologists, and of managers in the principles of conservation biology" [19]. Further, the Society's education committee articulated principles that seek to maintain Earth's biological diversity, ecological integrity, and ecological health. But the practitioners of conservation biology admit that their approach is very passive,

"Among conservation biologists the prevailing view of conservation education appears to rest on a deep-seated belief that the basic function of conservation education should be to disseminate knowledge that scientists generate, essentially to transport information to the public and key groups in the expectation that it will eventually precipitate more appropriate conservation-related behaviors" [20].

This is not unusual, and most scientists have adopted a "speak and they will listen" approach to STEM education. But in a world of declining and finite resources, a tipping point is fast being approached in the education circles, whereby the methodologies need to drastically change in order to inspire a science-literate community as stewards of global health. Sustainability education – if launched with appropriate integration of virtual and real natural systems [21], facts and "oh-wow" responses, local and global perspectives, and interdisciplinary approaches [22, 23] – is critical to succeed.

Biological Literacy

As a biologist by training, I have tracked the notion of biological literacy as a component of science education throughout my career [1]. The world has witnessed an amazing explosion of knowledge in biology – ranging from genomics and nanotechnology to global climate change and how sea-level rise will impact Earth's resources.

The relevance of biology education may be the most focused of all the "science literacies" to date due to extensive support from NSF, AAAS, Association of American Medical Colleges (AAMC), and Howard Hughes Medical Institute (HHMI). In its most recent "conversation" that included over 500 biological sciences faculty, administrators, students, and other practitioners, AAAS published a white paper called "Vision and Change" (www.visionand change.com) [1]. They summarized four academic concepts to implement change in biology education: (1) Integrate core concepts and competencies; (2) Focus on student-centered learning; (3) Promote a campus-wide commitment to change; and (4) Engage the biology community in the implementation of change. The outcome of the "conversation" was to encourage all biology educators to develop a coordinated and sustainable plan for implementation of principles that will improve the national standards of biology education.

Specific working groups to advance biology education (also termed "new biology") convened around different priorities needed for biology education: managing large, complex data sets; interdisciplinary approaches; making connections among different concepts and/or questions; and seek new inquiry-based learning activities rather than the conventional memorization and lecture-based approaches [1]. Advancing education in biological sciences directly impacts our nation's ability to respond to recent challenges, ranging from climate change to safe drinking water [10–12]. The core literacy concepts were delineated to include evolution, structure and function, information flow, and pathways and transformations of energy/matter, systems [1]. Core competencies were defined as the abilities to apply the process of science, use quantitative reasoning; use modeling/simulation; tap into the interdisciplinary nature of science; communicate/collaborate with other disciplines; and understand the relationship between science and society [1].

While these criteria were developed for biology education, many of the same elements would be relevant for sustainability education which concurrently embraces biology as well as other disciplines.

Sustainability Education in the Twenty-First Century

Achieving science literacy is vital in the twenty-first century. Sustainability education can be construed as that interdisciplinary platform whereby diverse members of global communities seek to understand the role of humans in their physical and social environments. As global environmental challenges loom at an unprecedented magnitude, "tipping points" that threaten to irreversibly damage Earth's living systems are fast approaching [16]. Yet, never before have humans had such a wealth of technology to achieve solutions at their disposal, allowing collaboration from virtually anywhere in the world, drawing ideas from multiple disciplines to process and analyze countless data points, and teaching the next generation to view our world in exciting, novel ways that inspire environmental stewardship.

In our teaching, environmental scientists must seek to balance cellular versus organismal biology, virtual models versus real-time data, and science blended with policy. Future stewards will need skills in assessing, predicting, managing, and communicating the dramatic ecological and societal risks and changes confronting us [1]. However, a major stumbling block in training the next generation of practitioners is the challenge of effectively integrating technology with in situ fieldwork. While most senior ecologists were inspired by their training in the field, younger scientists are more familiar with virtual ecosystems through gaming, social networking, and computer models, sometimes leading to so-called nature-deficit disorder. How can environmental practitioners blend "hands-on" fieldwork with "cutting-edge" technology? This conundrum is the subject of ongoing debate. Those born after 1980 spend more time indoors with electronic devices than going outdoors to experience nature first hand [17, 18].

On a positive note, new programs are emerging that successfully integrate virtual and real environments. The National Ecological Observatory Network (NEON) will conduct continental-scale environmental monitoring in situ, and their large databases will be accessible to students, citizen scientists, and policy makers ([20], see also www.neoninc.org). At the North Carolina Museum of Natural Sciences in North Carolina, the new Nature Research Center, with its mission "to engage the public in understanding the scientific research that affects their daily lives," will house state-of-the-art research laboratories, accessible to the public, a three-story Daily Planet immersion theater, broadcasting field science from remote sites via video-streaming, and dedicated virtual and real meet-the-scientist activities ([21], see also www.naturesearch.org) . These two examples illustrate the changing landscape for ecology education, and how technology can, and must, advance environmental literacy.

NEON

The National Ecological Observatory Network will take field measurements by scientists, citizens, and students collectively to a new level [24]. This continent-scale research platform will conduct long-term monitoring in America's major ecosystems, and create an important education outreach component as a parallel stream of the research program. Affectionately called the "ecologists' Hubble Telescope," this is the largest federally funded research project undertaken by the ecological community, and aspires to contribute data sets that will lead to best practices for solving environmental challenges in the future. Critical to NEON's success is the sustainability education and outreach component that have the potential to change how policy makers as well as citizens learn about sustainable solutions.

Citizen science has burgeoned in the past decade, in part due to Internet and handheld technological devices, but also because of a growing awareness that sustainability education is a community responsibility. Almost 20 years ago, the Jason Expedition (www.jason.org) pioneered distance learning for middle school youth, who not only visited marine and rain forest canopy environments, but also collected ecological data to share with other schools (e.g., [25]). Today, myriad programs including Project Budburst (www.budburst.org) and Project Nestwatch (www.nestwatch.org) rely on citizens' collecting data, which are collated at a central source for scientific use.

Planning for NEON took over a decade with hundreds of ecologists providing input. Projected to become fully operational by 2016, NEON's 20 field sites will be linked by high-capacity cyber infrastructure with the capacity to make forecasts about environmental changes. Important for sustainability education, these issues include six of the National Academies' grand challenges: biodiversity, climate change, ecohydrology, biogeochemistry, infectious disease, invasive species, and land use [26]. And even more critical to sustainability education is NEON's capacity to involve not just scientists – but also the public, students, teachers, and policy makers – to use the NEON interface for downloading data and learning by doing. NEON also pledges to prioritize science communication to diverse audiences [24] and foster the links between human health and healthy ecosystems. Will NEON's education vision be achieved, or will it become a pile of dusty papers on some university desks? Only time will tell, but NEON has the potential to advance sustainability education across an entire continent.

NRC

The Nature Research Center (NRC) at the North Carolina Museum of Natural Sciences is a new, 80,000-square foot wing of the existing 132-year-old Museum. While conventional museums focus on "what we know" about science, the new wing will engage the public in "how we know what we know" and in particular

Fig. 6.1 North Carolina's new Nature Research Center integrates cutting-edge research, education and technology for diverse audiences to foster environmental literacy

inspire the public to understand scientific research that affects their daily lives. The NRC goals are to conduct/communicate cutting-edge science, create exemplary role models to inspire diversity in the next generation of scientists, and integrate real and virtual science to engage youth about scientific discoveries. Four new labs will house scientists, educators, technology experts, students, and volunteers – all working together to understand how science works and communicate it to a diverse audience. In addition, the notion of scientists and educators and technology geeks all working together on the floor is unique to the Museum world, and seeks to assimilate "citizen science" into all components of research and education at the NRC. Many partners will insure a robust content for science communication – joint positions with the UNC system, partnerships with NOAA, NASA, National Geographic, and North Carolina government agencies, will all contribute to the creation of innovative science communication. The NRC has four unique learning platforms, facilitating the assessment of how different audiences learn best: (1) The Daily Planet, a high technology, immersion theater linked through the Ethernet highway to all classrooms in North Carolina and ultimately, around the world; (2) Citizen science labs, where participation in data collection by volunteers will contribute to answering important questions about our environment; scientific laboratories with glass walls allowing visitors to be involved in the research; (3) Investigate labs, where related research will be undertaken that involves school groups or other visitors; and (4) Hands-on exhibits where visitors are immersed in *how science works* (Fig. 6.1).

By "reinventing" the education pathways of conventional museums, the NRC hopes to inspire diverse students to become excited about science, and to inspire scientists to engage in successful education outreach, which links directly to creating a higher level of sustainability education.

Future Directions

The future is ours by design, but there is a need to seek interdisciplinary solutions and then communicate them with one voice. When baby boomers think back to their childhood, they can probably recall a favorite tree house, scout camping trip, or neighborhood picnics. In today's world, children are not allowed unsupervised time outdoors, due in part to parents' distrust of issues ranging from strangers to global security. But knowledge of real nature is essential to raise levels of environmental literacy, and in turn achieve a higher degree of sustainability education. Harking back to the African proverb in the beginning of this entry, many children do not have a clear concept of what is required to sustain a tree. But knowledge of nature is their best weapon if young people are ultimately to make good decisions about personal health, climate change, and land-use management.

Despite the gloom and doom notions surrounding environmental literacy and our human aspiration to attain a sustainable lifestyle, there are exemplary actions providing amazing examples of best practices. What are some of the diverse projects exemplifying sustainable education? Here is a selection of sustainability education activities, perhaps useful to implement in your own community!

1. *Strategies for Ecology Education, Diversity and Sustainability (SEEDS). Diverse People for a Diverse Science*. SEEDS is an education program of the Ecological Society of America (Fig. 6.2). Its mission is to diversify and advance the ecology profession through opportunities that stimulate and nurture the interest of underrepresented students to not only participate in ecology, but to lead. Focused mainly at the undergraduate level, with extension services for communities, high schools, graduate students, and international collaborations, the SEEDS program promotes an ecology profession with wide representation to ensure environmental understanding and a sustainable future for all. (www.esa.org/seeds)
2. *Urban Farming*. In partnership with a neighboring community garden, Mill Creek Farm (MCF) transformed a vacant West Philadelphia lot into a thriving urban farm and intergenerational educational center (Fig. 6.3). Now starting on their sixth field season, MCF engages and galvanizes the community by providing affordable and sustainable food to the surrounding neighborhoods, employing local high-school students, offering food justice education and much, much more. For more information (including a documentary and radio stories) visit: http://www.millcreekurbanfarm.org/

Fig. 6.2 At the Ecological Society of America's annual meetings, SEEDS students are mentored to insure a diverse community of ecologists

Fig. 6.3 Mill Creek Farm, near Philadelphia Pennsylvania, examplifies the growing popularity of sustainable urban farming

Fig. 6.4 At North America's first public canopy walkway in Florida, third graders conduct original research on forest canopies

3. *Sustainability Education for Incarcerated Youth*. For 19 years, high school science teacher DC Randle taught biology and environmental sciences to middle and high school youth in the Minnesota correction system. Defined as emotionally, behaviorally disordered students, they thrived under a curriculum that allowed them to rediscover nature. Using the natural resources around their facility, their science teacher provided a strong backbone for sustainability education to these at-risk youth.
4. *Local-to-Global Connections*. As part of a fund raiser for a local canopy walkway, Meg Lowman started leading field trips to the Amazon for underserved youth in Florida. Called the Florida-Peru Connection, the local community funded scholarships for local Boys and Girls Club and Girls Inc. students. In return, young people have visited America from Amazonian villages along the Rio Napo in Peru. The link between local and global is an important concept for sustainability, and experiencing other ecosystems and culture first hand had a significant impact on the perspectives of both the Amazon and the American communities who were part of the exchange. As a result of shared global views, both Florida and the Amazon share a canopy walkway for education, where children (and others) conduct research on the biodiversity of forests (Fig. 6.4). More information is listed at www.treefoundation.og
5. *Student Outreach in Science (SOS)*. Environmental studies students at New College of Florida developed sustainability outreach activities appropriate for elementary and middle school classes. They developed a skillset in science

communication, and then took their lessons to underserved schools in the districts, providing a student-teaching-student model that was well received by both the teachers and the students. Units ranged from climate change adaptation to growing local vegetables to invasive species to clean energy. Over 60 students at New College received the Sarasota County Conservation Education award based on their SOS program (www.canopymeg.com)

6. *Master of Arts in Sustainable Communities, Northern Arizona University* (http://home.nau.edu/sus/). Students are admitted from all kinds of backgrounds – from political science and sociology to science and engineering to humanities and business. Students build their own programs of coursework from the university's very broad array of courses relevant to sustainability (of economies and of societies as well as of natural resources and environment). More important, they each develop independent, community-based research/thesis projects. Many come to this program as working professionals while some are more conventional students coming straight from a bachelor's degree. Graduates from this program are indeed transforming many communities around the intermountain west. Another unique program at NAU is the Professional Science Master's in Climate Science and Solutions. http://climatesciencesolutions.nau.edu/
7. *Measuring the Sustainability of Food to Table*. Professor David Cleveland at University of California, Santa Barbara engaged his environmental studies students in measuring the energy budget of regional agriculture, from farm to table. This agrifood systems analysis has the potential to change small-scale and local agriculture, and educate students in sustainable practices at the same time. It also earned David the award of Campus Sustainability Champion [27]. http://es.ucsb.edu/profile/cleveland
8. *Young Voices on Climate Change*. Author Lynn Cherry, finding resistance to teaching climate science, is producing inspiring, empowering short films to break down those barriers. The *Young Voices on Climate Change* documents inspiring success stories of kids shrinking their carbon footprint and fighting climate change. When climate change science is preceded with the showing of these films, youth and adults alike are more receptive to embracing the seriousness of environmental change rather than denying. Young people listen to others their own age and, in these films their peers model the skills, motivation, and confidence necessary to reduce CO_2 emissions.(www.YoungVoicesonClimateChange.com)
9. *Sustainability between Connecticut and Jamaica*. Eastern Connecticut State University recently had approved a new major in Sustainable Energy Studies – one interesting program associated with students in this new major has been the service-learning project taking students to Jamaica to develop a small wind power system for the school in Lucea, Jamaica. The university has a long-standing relationship with Jamaican public schools because of our program to get their normal school teachers to complete their bachelor's degree in USA. This type of global experience in sustainability education is part of Eastern's two Strategic Plan Initiatives – Liberal Arts Work and Global Citizenship.

Check out: http://www.diversityweb.org/DiversityDemocracy/vol14no2/loxsom.cfm?utm_source=pubs&utm_medium=blast&utm_campaign=divdemvol14no2

10. *The Perennials Collaborative*. The emerging generation of sustainability leaders brings new ideas for sustainability initiatives. Samir Doshi at University of Vermont and colleagues have undertaken a collective, action-oriented community project to inspire "Perennials," those visionary leaders who (like perennial plants) have roots in communities and become forces of vision and change. Doshi's team is making a documentary, web site, and hosting community workshops throughout the country, especially in at-risk areas such as Appalachia, to inspire more actions for sustainability. (www.perennialscollaborative.com).

America is at a crossroads for education in science, technology, engineering, and mathematics (STEM). Currently, a company can hire nine Mexicans or eight Indian engineers at the same cost as one American; 93% of middle school students learn physical sciences form a noncertified teacher; and Americans spend more on potato chips than the entire federal R&D budget for energy [6]. It is no wonder that America currently ranks 48th in terms of global STEM education. Recent reports by the National Academies of Science, Engineering and other focus groups have assessed America's current STEM education, and listed actions that federal policy makers could take to enhance STEM and allow America to increase her global competitiveness [5, 6]. Such actions include increasing America's economy by vastly improving K-12 STEM education; doubling federal investments in STEM research to fuel our economy, provide security, and foster sustainability; and encourage citizen science to raise STEM literacy. Will these actions be implemented, or will the Academies' report be overlooked? Only time will tell, but STEM and ultimately sustainability education collectively will invariably determine the quality of life for the next generation.

Bibliography

Primary Literature

1. Brewer CA, Smith D (2010) Vision and change in undergraduate education: a call to action. American Association for the Advancement of Sciences, Washington, DC, p 79
2. Pooley E (2010) The climate war. Harper Collins, New York
3. Braasch G (2007) Earth under fire. University of California Press, Berkeley, CA, USA, 286 pp
4. Council on Undergraduate Research (CUR) (2007) Developing and sustaining a research-supportive curriculum: a compendium of successful practices. CUR, Washington, DC
5. National Academy of Sciences (NAS) (2008) Rising above the gathering storm. National Academy of Sciences Press, Washington DC, USA
6. National Academy of Sciences (NAS) (2010) Rising above the gathering storm, revisited: rapidly approaching category 5. National Academies Press, Washington, DC
7. National Research Council (NRC) (1996) National science education standards. National Academies Press, Washington, DC

8. National Research Council (NRC) (1997) Science teaching reconsidered: a handbook. National Academies Press, Washington, DC
9. National Research Council (NRC) (1999) Transforming undergraduate education in science, mathematics, engineering, and technology. National Academies Press, Washington, DC
10. National Research Council (NRC) (2010a) Research at the intersection of the physical and life sciences. National Academies Press, Washington, DC
11. National Research Council (NRC) (2010b) Synthetic biology – building a nation's inspiration: interdisciplinary research team summaries. National Academies Press, Washington, DC
12. National Research Council (NRC) (2010c) Expanding underrepresented minority participation: America's science and technology talent at the crossroads. Committee on Underrepresented Groups and the Expansion of the Science and Engineering Workforce Pipeline. National Academies Press, Washington, DC
13. National Science Foundation (NSF) (1996) Shaping the future: new expectations for undergraduate education in science, mathematics, engineering, and technology. NSF, Washington, DC
14. Leopold A (1949) A sand county almanac. Oxford University Press, New York, NY, USA
15. National Research Council (2000) How people learn: brain, mind, experience, and school. National Academies Press, Washington, DC
16. National Science Foundation (2009) Advisory Committee for Environmental Education and Research. NSF, Washington, DC
17. Louv R (2006) Last child in the woods – saving our children from nature-deficit disorder. Algonquin Press, Chapel Hill
18. Lowman MD, Burgess E, Burgess J (2006) It's a jungle up there – more tales from the treetops. Yale University Press, New Haven
19. Trombulak SC, Omland KS, Robinson JA, Lusk JJ, Fleischner TL, Brown G, Domroese M (2004) Principles of conservation biology: recommended guidelines for conservation literacy from the education committee of the Society for Conservation Biology. Conserv Biol 18:1180–1190
20. Bride I (2006) The conundrum of conservation education and the conservation mission. Conserv Biol 20:1337–1339
21. Lowman M, Mourad T (2010) Bridging the divide between virtual and real nature. Front Ecol Environ 8(7):339
22. Balmford A, Cowling RM (2006) Fusion or failure? The future of conservation biology. Conserv Biol 20:692–695
23. Brewer C (2006) Translating data into meaning: education in conservation biology. Conserv Biol 20:689–691
24. Lowman M, D'Avanzo C, Brewer C (2009) A national ecological network for research and education. Science 323:1172–1173
25. Burgess E, Burgess J, Lowman MD (2003) Lowman and thousands of Jason X school students. 2003. Observations of a Coleopteran herbivore on a bromeliad in the Peruvian Amazon. J Bromel Soc 53:221–224
26. National Research Council (2001) Grand challenges in environmental sciences. National Academies Press, Washington, DC
27. Cleveland DA, Radko CN, Muller NM, Watson TD, Rekstein NJ, Van H, Wright M, Hollingshead SE (2011) Effect of localizing fruit and vegetable consumption on greenhouse gas emissions and nutrition, Santa Barbara County. Environ Sci Technol 45:4555–4562

Chapter 7
Gravity Recovery and Climate Experiment (GRACE): Detection of Ice Mass Loss, Terrestrial Mass Changes, and Ocean Mass Gains

Victor Zlotnicki, Srinivas Bettadpur, Felix W. Landerer, and Michael M. Watkins

Glossary

Equivalent water thickness	Since time changes in the gravity field are caused by time changes in mass distributions, equivalent water thickness ("EWT") is the variable thickness of a thin layer of water (thin relative to both the radius of the Earth and the horizontal scale of the signals) draping the Earth that would correspond to the observed changes in gravity. The conversion from gravitational spherical harmonics to water thickness (and vice versa) is unique and well defined, regardless of what actually causes the gravitational changes. The concept is not used when studying changes in the solid Earth, such as glacial isostatic adjustment or earthquakes.
Glacial isostatic adjustment (GIA)	Also known as postglacial rebound, it is the viscoelastic response of the mantle and lithosphere to the removal of the great ice sheets that covered parts of the Earth and peaked

This chapter was originally published as part of the Encyclopedia of Sustainability Science and Technology edited by Robert A. Meyers. DOI:10.1007/978-1-4419-0851-3

V. Zlotnicki (✉)
Climate, Oceans and Solid Earth Science Section, Jet Propulsion Laboratory, California Institute of Technology, 4800 Oak Grove Dr, Pasadena, CA 91109-8099, USA
e-mail: victor.zlotnicki@jpl.nasa.gov

S. Bettadpur
Center for Space Research, University of Texas-Austin, Austin, TX 78759, USA

F.W. Landerer
Jet Propulsion Laboratory, California Institute of Technology, Pasadena, CA 91109-8099, USA

M.M. Watkins
Jet Propulsion Laboratory, California Institute of Technology, 4800 Oak Grove Dr, Pasadena, CA 91109-8099, USA

J. Orcutt (ed.), *Earth System Monitoring: Selected Entries from the Encyclopedia of Sustainability Science and Technology*, DOI 10.1007/978-1-4614-5684-1_7,

	21,000 years ago [65]. The deglaciation was essentially complete 6,000 years ago. The lithosphere rises where the ice sheets used to be, but sinks in other locations.
Ionosphere	A set of layers at altitudes between approximately 80 and 1,000 km above the Earth's surface, with electrons and electrically charged atoms. The ionosphere leads to a delay to electromagnetic radiation, which is frequency-dependent and changes with local time and solar activity. The GRACE KBR system uses two frequencies to correct for this path delay.
KBR	K-band microwave ranging system measures the distance between the two GRACE satellites using two frequencies, 24 and 32 GHz.
Mascons	Mass concentrations. The term was coined by Muller and Sjogren [60] to describe mass concentrations in the lunar nearside, beneath the center of the surface features termed "mare" (pl. "maria"). Today the term "mascons" refers to an alternative method to solve the GRACE gravity fields in terms of distributed spherical caps or point masses, instead of using the spherical harmonic representation.
Newton's law of gravitation	It states that every point mass attracts every other point mass with a force that is directly proportional to the product of their masses and inversely proportional to the square of the distance between them: $F = G.m_1.m_2/r^2$, where m_1 and m_2 are the masses, r is the distance between them, and G is the universal gravitational constant, $G \approx 6.6738 \times 10^{-11}$ $m^3/kg/s^2$. This law is at the heart of the GRACE measurements, since any specific mass on the Earth is in general at a different distance from the two spacecrafts, causing a slight difference in the gravitational acceleration they impart to the spacecraft, and thus causing a slight but measurable relative acceleration between the spacecrafts.
Satellite	Is an object, natural (like the Moon) or artificial (each GRACE satellite) that orbits around another large object, in this case the Earth. "Orbits" means that the centripetal acceleration due to the speed of the satellite equals the gravitational acceleration between the satellite and the larger object it orbits around; in this manner the satellite neither falls toward Earth, nor escapes its gravitational pull. In practice, the GRACE satellites do fall slightly toward the Earth while they orbit around it, whereas the Moon slowly increases its distance to the Earth.
Spherical harmonics	Are a set of functions of latitude and longitude that form an infinite, orthogonal, normalized set of basis functions whose sum, with appropriate scale coefficients, completely

describes any other function defined in terms of spherical coordinates. Spherical harmonics satisfy Laplace's equation, as does the gravitational potential outside the Earth. Laplace's equation states that the sum of the second derivatives of the gravitational potential with respect to each of the three directions of space at a point must add up to zero if there are no masses at that point.

Definition of the Subject and Its Importance

The gravity field of the Earth, caused by the distribution of masses inside and on the surface of the Earth, changes in time due to the redistribution of mass. Such mass fluxes can be due both to natural processes (such as the seasonal water cycle, ocean dynamics, or atmospheric variations), as well as due to human actions, such as the systematic withdrawal of groundwater for human consumption. The ability to measure such changes globally is of great significance for understanding the environmental dimension of sustainability.

Until the launch of the GRACE satellite pair in 2002, such time changes in mass redistribution could only be measured globally as time changes in the longest wavelengths of the gravity field, on the order of 10,000 km and longer, from the orbit perturbations of artificial Earth satellites, or very locally at individual points on the Earth using long-term gravimeter deployments.

The GRACE satellite pair has provided the first global measurements at horizontal resolutions from 300 km to global, and time scales from 10 days to interannual. These measurements have been used to assess the mass variability in the oceans, terrestrial water storage, and loss of ice mass in glaciers and ice sheets. Long-term trends, episodic variations such as result from large earthquakes, and seasonal changes have all been measured with unprecedented accuracy and detail.

Introduction

Imagine the ability to weigh Greenland every month over several years: It would tell us whether Greenland is losing ice, how fast, and whether the loss is accelerating. Imagine the ability to weigh the total water content every month over several years in the soil of Northern India, where the groundwater supplies hundreds of millions of people: It would tell us whether that precious resource is being used at a sustainable rate or depleted. Imagine the ability to measure how

much water the ocean basins are gaining: It would allow us to separate the two key components of sea-level rise, the addition of mass and the thermal expansion due to increased ocean temperature. As we will see below, these are no longer imaginary possibilities but actual findings using data from a satellite pair called GRACE, or Gravity Recovery and Climate Experiment. The GRACE satellite pair was launched on March 17, 2002 to measure monthly changes in the gravity field of the Earth with exquisite accuracy. It is from these monthly changes in the gravitational attraction of large bodies of water, ice, and rock that we can "weigh" changes from month to month in Greenland, groundwater, and even the oceans. GRACE also yields a very accurate measurement of the time-averaged gravity field, a useful quantity for studies of tectonics and of the time-averaged ocean circulation. There is a well-known inherent ambiguity in interpreting changes in gravity: The data type can localize the changed mass horizontally, but it alone cannot distinguish whether the mass change comes from the surface or deeper layers, from the ocean, or from an earthquake that moved the sea floor. Additional information is needed to identify the source of the mass changes unambiguously. This entry reviews the basis of the GRACE measurements, some technical details that clarify the strengths and limitations of the GRACE data, and provides illustrative examples of the applications in hydrological, cryospheric, oceanic, and geophysical sciences. Given the wide variety of phenomena GRACE can tell us about, this entry cannot be an exhaustive review of the more than 700 peer-reviewed publications on GRACE published through the end of 2010. Also, while the GRACE satellite pair carries global position systems (GPS) antennas and hardware for use in "GPS occultation" soundings of the atmosphere, we focus the discussion on results obtained from the gravity data derived from GRACE.

The measurement of gravity from satellite orbit perturbations (that is, from departures of the satellite's path from a classical Keplerian ellipse) has been in existence for many decades. It started immediately at the dawn of the space age, with measurements of the Earth's pear shape [62]. Tracking satellites from terrestrial observatories or from GPS satellites, using radiometric or laser ranging methods, provided important information on the long-wavelength, static (long-term mean) gravity field through the next 3 decades. Precise measurement of time-variable gravity from those techniques was only possible, however, for the Earth's oblateness parameter (J2). Long-term measurements of the J2 parameter were used [24, 27] to identify and explain a steadily decreasing trend in the flattening of the Earth, due to GIA, and associate the departures from that steady trend with interannual climatic variability, such as the El Nino-Southern Oscillation phenomenon. See also [8, 22, 23]. The advent of the German CHAMP mission in mid-2000 improved the situation; CHAMP determined gravity changes at continental (several thousand kilometers) scales and annual and longer periods. The GRACE mission results provided a true paradigm shift, providing an unprecedented global and accurate measurement to 300-km spatial resolution, continuously since 2002.

What Is GRACE

GRACE, launched on March 17, 2002, is a joint mission of the US and German space agencies, the National Aeronautics and Space Administration (NASA) and the Forschungszentrum der Bundesrepublik Deutschland für Luft- und Raumfahrt (DLR). GRACE was the first mission flown under the NASA Earth System Science Pathfinder (ESSP) Program, with Principal Investigator (PI) from the Center for Space Research at the University of Texas, and the co-PI from the Helmholtz Center Potsdam, German Research Centre for Geosciences (GFZ) [89]. Mission management and implementation are the responsibility of the NASA Jet Propulsion Laboratory (JPL), a NASA center managed by the California Institute of Technology. Mission operations are performed by DLR, with co-funding by the European Space Agency (ESA). DLR was also responsible for the launch services. JPL led the development of the satellite system in partnership with Astrium GmBH and Space Systems Loral (SS/L). Astrium was the prime contractor for major elements of the two satellites based on the CHAMP (CHAllenging MiniPayload) satellite heritage, while SS/L was the prime contractor for the attitude control system and microwave instrument electronics. JPL also provided the key microwave range-rate sensors between the satellite pair, and the Global Positioning System (GPS) receivers.

Almost all Earth-viewing spaceborne instruments measure electromagnetic radiation, either naturally emitted or reflected by the Earth's surface (passive), or the returns of signals emitted toward the Earth by the instrument itself (active). GRACE is fundamentally different: The satellite pair senses gravity through the changes in the intersatellite distance. The two satellites fly along the same orbit (Fig. 7.1). Currently (as of July 2011), the pair flies 454 km above the Earth's surface (at launch, it was 502 km), separated by 206 km. Imagine the satellite pair passing over a mountain. As the lead satellite "feels" the increased gravitational attraction of the upcoming mountain, it accelerates toward that mass excess. Due to Newton's law of gravitational attraction (whereby the force acting on a mass is inversely proportional to the squared distance to the attracting mass) that acceleration toward the mountain is larger for the lead satellite than for the trailing one, whose distance to the mountain is larger. As a consequence, the distance between the two satellites increases, if ever so slightly. When the mountain is in-between the satellites, both are attracted toward the mountain, so the intersatellite distance decreases. A highly precise microwave ranging system (called "KBR," or K-band ranging system) aboard each satellite beams radio signals toward the other satellite and measures those changes in distance: This measurement forms the basis of the computation of the gravitational field. The measurement is so precise that it detects changes of a few microns in range or approximately 0.1 μm/s in velocity every 5 s. To picture that level of accuracy, it is approximately equivalent to measuring the distance between Los Angeles and San Diego to an accuracy of a (fine) human hair's width.

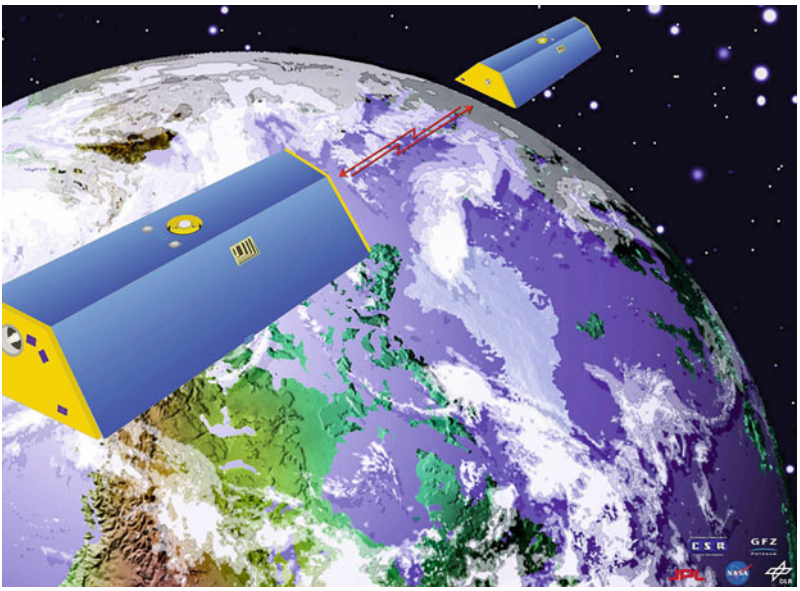

Fig. 7.1 Artist's conception of the GRACE satellite pair in orbit. In reality, each satellite is 3.123-m long, the distance between the pair ranges between approximately 175 and 230 km, and the altitude has been slowly decaying from 502 km at launch to 454 km currently (July 2011), relative to a distance of 6,378 km from the center of the Earth. The orbital inclination is 89°

The key science instrument in each GRACE satellite is the microwave K-band ranging instrument. Each satellite transmits signals to the other at two frequencies, (24 and 32 GHz, called "K" and "Ka" bands, respectively) in order to correct for ionospheric path delay. The K-band ranging assembly consists of an ultra-stable oscillator, the microwave electronics, a K-band ranging horn, sampler, and the instrument processing unit (IPU). The ultra-stable oscillator serves as the frequency and clock reference for the GRACE satellites. The K-band ranging horn transmits and receives K-band carrier signals to and from the other GRACE satellite. The IPU is the nerve center for the science instruments in the spacecraft, providing the digital signal processing functions for the K and Ka band signals, as well as for the GPS signals. It also provides various clocks for the satellite operations and performs data processing for the star camera attitude (directions). The K-band ranging system was manufactured by JPL with equipment from Space Systems/Loral and the Applied Physics Laboratory.

The intersatellite range-change measurement must be corrected for the effect of forces other than gravity, such as drag or solar radiation pressure. To do so, both satellites carry accelerometers located very close to each satellite's center of mass. The accelerometers were built by ONERA, the French Aerospace Lab. An approximate orientation of the spacecraft is provided by the star cameras (two aboard each satellite). Used both for science and for attitude and orbit control, they determine each satellite's orientation by tracking their orientation with reference to the stars.

They were developed by the Danish Technical University, Copenhagen, Denmark. In order to provide precise synchronization of the ranging data between the two satellites, and in order to geo-locate the science data, both satellites carry Global Positioning System (GPS) units developed by JPL. There are three GPS antennas: One is used to collect navigation data, the two other antennas are used for backup navigation and atmospheric occultation data collection. The GPS units provide an additional piece of information essential to the computations: time-tagging events to better than 0.1 ms.

Other instrument assemblies aboard the spacecraft include a Coarse Earth and Sun sensor, used for approximate position and orientation whenever GRACE is in "safe mode" (when a serious anomaly in the satellite cannot be automatically corrected on board, the satellite is put into "safe mode" by the onboard computer, to ensure only the satellite's vital functions remain on, while the failure is being analyzed on the ground); a Center of Mass Trim Assembly, to adjust the satellite's center of mass with respect to the proof mass of the accelerometers; solar cell arrays, covering the outer shell of the satellites to generate power for the electronics, and nickel-hydrogen cell batteries to store and release power as needed; telemetry and telecommand subsystems for the satellites to communicate with Earth via radio systems in the microwave S-band spectrum. Each satellite uses a separate set of S-band frequencies for transmission and reception. Both, the power and telemetry as well as the telecommand subsystems, were supplied by Astrium.

The satellite's "attitude," or orientation and orbit control, is controlled by a system consisting of sensors, actuators, and software. Two kinds of attitude actuators are available. A reaction control system with a set of twelve 10-mN thrusters uses gaseous nitrogen stored in the two tanks along the main satellite axis. Fine corrections of orientation are adjusted using six 30-Amp-m^2 magnetorquers, to minimize the satellite fuel consumption. Each GRACE satellite can adjust its orbit by firing its two orbit-control thrusters (also gaseous nitrogen propellant) mounted on the rear-panel of the satellite, each of which provides 40 mN of thrust. The attitude and orbit-control system was designed by Space Systems Loral and implemented by Astrium and its subcontractors.

Further information on the spacecraft can be found at http://grace.jpl.nasa.gov/files/GRACE_Press_Kit.pdf, and details on the mission, its subsystems, and current operational status are available at the GRACE mission homepage: http://www.csr.utexas.edu/grace/.

Spherical Harmonics; Equivalent Water Thickness; Mascons; and Spatial Resolution

The gravitational potential of the Earth, sensed by a satellite at altitude h, is formally expressed as the sum of spherical harmonic functions [8]

$$T(\theta,\ \varphi) = \frac{GM}{(a+h)} \sum_{l=0}^{\infty} \sum_{m=0}^{l} \left(\frac{a}{a+h}\right)^{l} (C_{lm} \cos(m\phi) + S_{lm} \sin(m\phi))\ P_{lm} \cos(\theta) \tag{3.1}$$

where T is the "anomalous" potential (the difference between the true potential and a reference value) at colatitude θ, longitude ϕ. The dimensionless C_{lm}'s and S_{lm}'s are called Stokes' coefficients; the P_{lm} are Legendre functions of degree l, order m, $m \leq l$, GM is the product of the universal gravitational constant G times the mass of the Earth, M, and a is a mean radius of the Earth. All other quantities (geoid height, gravity acceleration anomaly, or disturbance, etc.) have similar expansions, whose coefficients are related to those in Eq. 7.1 through functions of the degree l and dimensional constants. The l = 0, m = 0 coefficient in the expansion is exactly 1.0, and accounts for the total mass of the Earth system, conventionally regarded as a constant. The l = 1 terms are zero if the analysis is done in a reference frame where its origin is the instantaneous center of mass of the Earth system. The n = 2, m = 0 term accounts of the Earth's oblateness, and is of order 10^{-3} relative to the central term. All other harmonic coefficients are of order 10^{-6} or smaller. Representation of the geographic features of small spatial extent requires the expansion to be carried to higher degree-l.

The GRACE data analysis problem reduces to the extraction of the Stokes coefficients from residuals of the GRACE tracking data calculated using prior best knowledge of the Earth's gravity field and its variations. A global distribution of the mission data is required before the gravity field parameters can be estimated. It takes approximately 1 month for the GRACE data to provide uniform, global coverage. The Earth's gravity field variations are therefore represented by monthly piece-wise constant spherical harmonic coefficients of the anomalous geopotential, represented to a fixed maximum degree/order. The GRACE mission data products are these Stokes coefficients, delivered monthly for the entire mission lifetime. The long-term mean estimates provide the determination of the static gravity field, and the monthly deviations represent the time-variability of the mass flux at the longer time scales.

However, hydrologists, oceanographers, and cryospheric scientists are less interested in the gravitational C_{lm}'s and S_{lm}'s coefficients, but rather in estimates of time changes in surface mass, or ocean bottom pressure. Let the surface mass density σ be the vertical integral of the density ρ through the Earth's surface layer (containing the atmosphere, the oceans, and the water/snow/ice stored on land), where we assume all time changes are concentrated. Using the above series, with h = 0, σ is

$$\Delta\sigma(\theta,\phi) \approx \frac{a\rho_E}{3} \sum_{l=0}^{l\max} \sum_{m=0}^{l} \frac{(2l+1)}{(1+k_l)} W_l P_{lm}(\cos\theta) \times [\Delta C_{lm} \cos(m\varphi) + \Delta S_{lm} \sin(m\varphi)] \tag{3.2}$$

where ρ_E is the mean density of the Earth, a is its radius, and the k_l are so-called load Love numbers representing the elastic response of the solid Earth to surface loading [96]. The W_l is an isotropic filter that strongly downweighs high degree l terms, which are often contaminated with noise amplified by the downward continuation effect, discussed below. More general filters, nonisotropic filters and irregular area-averaged filters, are discussed by Swenson and Wahr [84], while a decorrelation filter which removes North–South "striping" from GRACE maps was first discussed by Swenson and Wahr [85], then optimized for ocean studies by Chambers [10]. Equation 7.2 allows us to convert the C_{lm}, S_{lm} to a surface mass distribution, typically expressed in centimeters of equivalent water thickness ("cm EWT"). In the above formula, the maximum spherical harmonic degree indicated is l_{max}; in practice, there is little signal above spherical harmonic degree 60 in the monthly GRACE fields, although some solutions are given to $l_{max} = 120$. An order of magnitude estimate for the spatial half-wavelength associated with a particular degree l is given by the approximation 40,000 km/(2l) so $l = <60$ implies half-wavelengths longer than ~330.

Two sets of coefficients require special handling. The coefficients of degree 1 orders 0 and 1, which indicate the position of the center of mass of the Earth (which varies in time) relative to an Earth-fixed coordinate origin, are not measured by GRACE. Swenson et al. [87] realized that by assuming that we know the component of n = 1 from an ocean model, it is possible to use the GRACE data and the ocean information to derive degree 1 coefficients. Degree 1 coefficients can also be derived from satellite laser and Doppler ranging data [25]. The coefficients of degree 2 order 0 are poorly determined in the GRACE data, and it is now a standard practice to replace them by coefficients estimated from satellite laser ranging [23]. See also [9].

Another way to describe the gravity field uses "mascons" (mass concentrations, see "Glossary"). In this approach, either small spherical caps or point masses are assumed to cover the Earth's surface, and one solves directly for the mass of each local mascon from the intersatellite range-rate or acceleration data, rather than for the global Stokes coefficients. When the solution is unconstrained, such that no a priori correlation is imposed on neighboring mascons, nor any smoothing is imposed on the Stokes coefficients, there is little difference in the result [79]. However, there are advantages in imposing correlations between neighboring mascons when one knows that, for example, a set is in one hydrological basin and the nearby set is in another one, uncorrelated to the first. In addition, the mascon basis functions more conveniently allow higher spatial resolution at higher latitudes where ground tracks are spaced more densely.

GRACE data products can be obtained from several public sources. Because of small differences in the processing strategy, the results differ in small but significant ways, and it is a good practice to check the results from two centers for a particular application. The GRACE Science Data System consists of three centers, the Center for Space Research (UTCSR) at the University of Texas-Austin [5], the Geoforschungzentrum in Potsdam, Germany, and the Jet Propulsion Laboratory in Pasadena. These three centers provide spherical harmonic solutions through http://podaac.jpl.nasa.gov and a mirror archive at http://isdc.gfz-potsdam.

de/; gridded versions of their data, with additional corrections applied (for example, the decorrelation filters of Chambers [10] or Swenson and Wahr [85], can be found at http://grace.jpl.nasa.gov. Additional sources include NASA's Goddard Space Flight Center (GSFC) [79] who supply mascon solutions, the Centre National d'Etudes Spatiales (CNES) in France [7, 46] who supply 10-day SH solutions, the Institut für Geodäsie und Geoinformation at the University of Bonn (ITG-Bonn), Germany who supply both monthly and daily SH solutions [58], and Delft University of Technology, Netherlands [49] who supply monthly SH solutions.

Background Fields

Since the satellite motion is a nonlinear function of the gravitational potential, the derivation of a monthly set of either Stokes coefficients or mascons involves the solution of a very large nonlinear least squares problem. Nongravitational influences are modeled using the data collected by the accelerometer. The satellite orientation is also important because the range-change measurements are made to a reference point displaced from the center of mass of the satellite, to which the dynamical equations of motion refer. To make the solution computationally tractable, one solves not for the full gravity field, but for the difference from an initial guess (a nominal, a priori model). The a priori model is the sum of an earlier estimate of the time-averaged gravity field, plus the disturbances due to the Sun, Moon, and other planets, plus the gravitational effects of solid Earth and ocean tides, plus the time-varying mass of the atmosphere derived from European Center for Medium Range Weather Forecast (ECMWF) model output, plus the time-varying effects of non-tidal ocean mass redistribution derived from a numerical ocean model driven by ECMWF [28], plus a model of the "pole tide" (both Earth and ocean), which is not actually a tide but the result of a perturbation of the Earth's rotation. All the components of the a priori model are collectively called "background models," and the solution depends to some extent on their fidelity. The equations of motion of the satellites are integrated numerically with time steps of a few seconds, the background models are interpolated to those times, the observable position of the satellites and intersatellite range rate are computed from the models and compared to the observed values, and the residual differences are then used in the least squares solutions. These residual differences reflect both the processes not modeled in the background (e.g., land-surface hydrology, or ice sheet mass changes) as well as processes erroneously modeled in the background (e.g., atmospheric or tidal variability). The residual differences, aggregated over a month, are then used in the least squares solution for the anomalous geopotential for that month. In addition to the desired gravitational model for a month, a large number of instrument- and spacecraft-dependent "nuisance parameters" are adjusted which include biases, bias drifts, clock offsets, orbits of the GRACE satellites and the GPS satellites, etc.

Note that the tides, atmospheric and oceanic mass redistributions, as well as land hydrology, all have energy at periods much shorter than a month, the typical time span of one GRACE gravity solution. The models therefore remove this energy, which could otherwise be aliased into longer period variations in the retrieved gravity fields.

For ocean studies, the monthly averaged ocean model is added back to the solution. At this writing, adding a background model of the land hydrological mass changes, which has been shown to improve the solution, is being considered to become part of the gravity field processing for an upcoming data release.

Ambiguity; Downward Continuation; Data Accuracy

Gravity data provided by in-situ or airborne instruments (called gravimeters) have long been used in both exploration and research geophysics to help define buried structures that exhibit density variations (e.g., ore deposits). Two measurement effects are well known by those practitioners: the ambiguity of interpretation ("nonuniqueness" of a solution), and the problem of "downward continuation" of a measurement taken at some altitude.

Consider a sphere of density ρ_1 and radius r_1 at depth $h_1 > r_1$. This sphere would produce the same gravitational attraction at the surface as another sphere of density ρ_2 and the same radius r_1 but at depth h_2, exactly "under" the first sphere, so long as they satisfied the ratios $\rho_1/\rho_2 = (h_2/h_1)^2$. While this is harder to see in more complex shapes, it illustrates well the ambiguity in the interpretation: It is not possible to assign a mass uniquely to a buried structure without some additional data or constraints [66]. The main assumption to aid the interpretation of GRACE data is that monthly changes in gravitational attraction are produced primarily by movement of water within and among Earth reservoirs: the cryosphere, the oceans, and the soil [96], except in those regions where glacial isostatic adjustment (GIA) and earthquakes produce strong signals. This assumption is generally valid: While large mountain ranges produce large signals in the time-mean gravity field, their effect in the time-varying gravity field over a few years or even decades is negligible (Fig. 7.2). Indeed, as will be shown below, maps of the time-variable gravity do not show strong signals where the time-averaged gravity field has its stronger signals. In the case of GRACE, ambiguity arises when trends in mass displacements from GIA [due to the lithosphere's slow adjustment to the loss of the ice load that peaked 21,000 calendar years ago [65] and was essentially complete 6,000 years ago] can confound the signals due to trends in present-day ice or hydrological mass changes. Large earthquakes can also cause prominent signals in GRACE data as the lithosphere moves and adjusts following a quake.

To understand downward continuation, consider a simple plane, one-dimensional geometry. The gravity field above the x-axis, due to a mass distribution

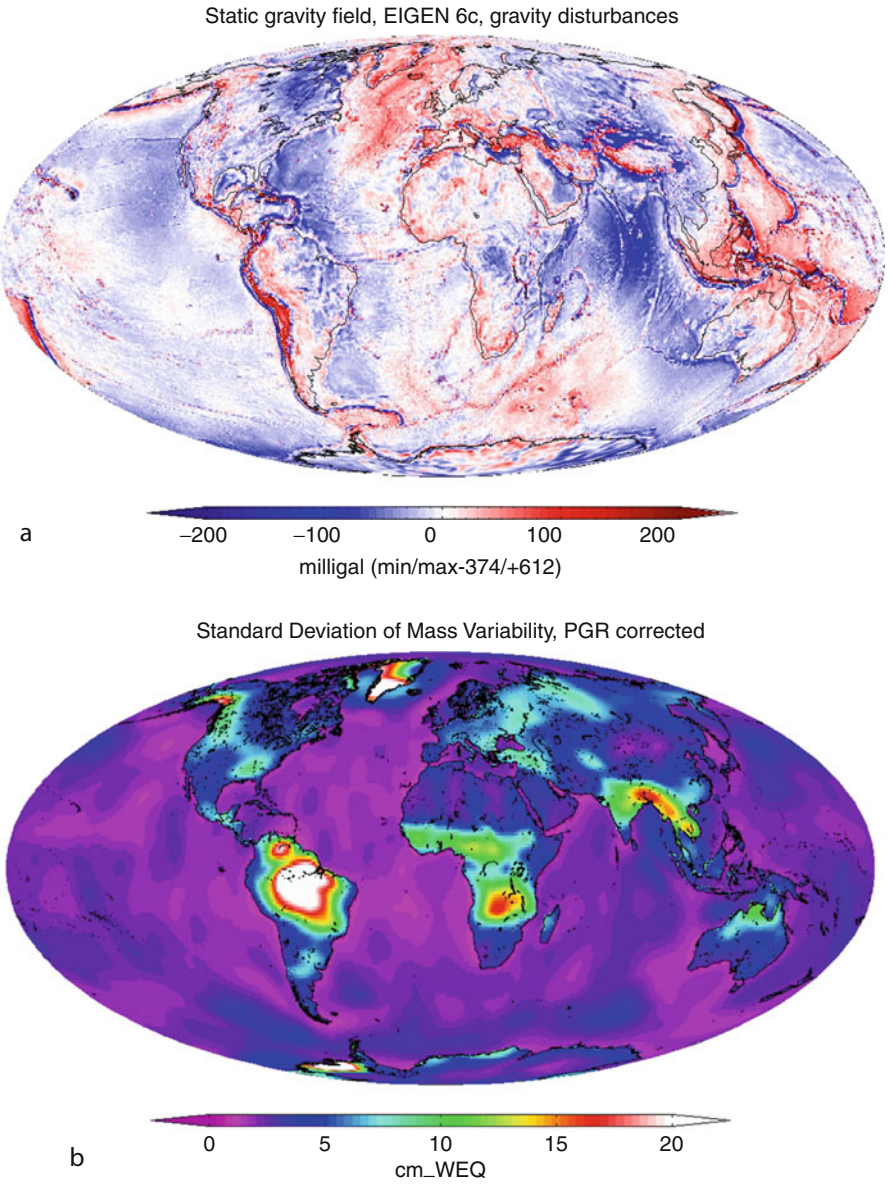

Fig. 7.2 (**a**) The static gravity field EIGEN6c, which combines GRACE and in situ data. The quantity displayed is the "gravity disturbance," which is the difference between actual gravity acceleration at a point and a reference value, which includes the longest wavelengths of gravity, at the same point. The short length-scale-features in this map are closely related to surface topography, whether on land or at the sea floor. (Data from the International Centre for Global Earth Models, Potsdam, Germany http://icgem.gfz-potsdam.de/ICGEM.) (**b**) The standard deviation of monthly maps of changes of mass which give rise to changes in the gravity field derived from GRACE, expressed in centimeters of equivalent water thickness (see section "Spherical Harmonics. Equivalent Water Thickness. Mascons. Spatial Resolution"; here abbreviated as "WEQ" = "EWT"). Data cover the time period Jan 2003 to Dec 2010. A destriping decorrelation filter has been applied; land data are further smoothed with a 300 km Gauss filter, while ocean data are smoothed with a 500 km Gauss filter. The trends due to glacial isostatic adjustment have been

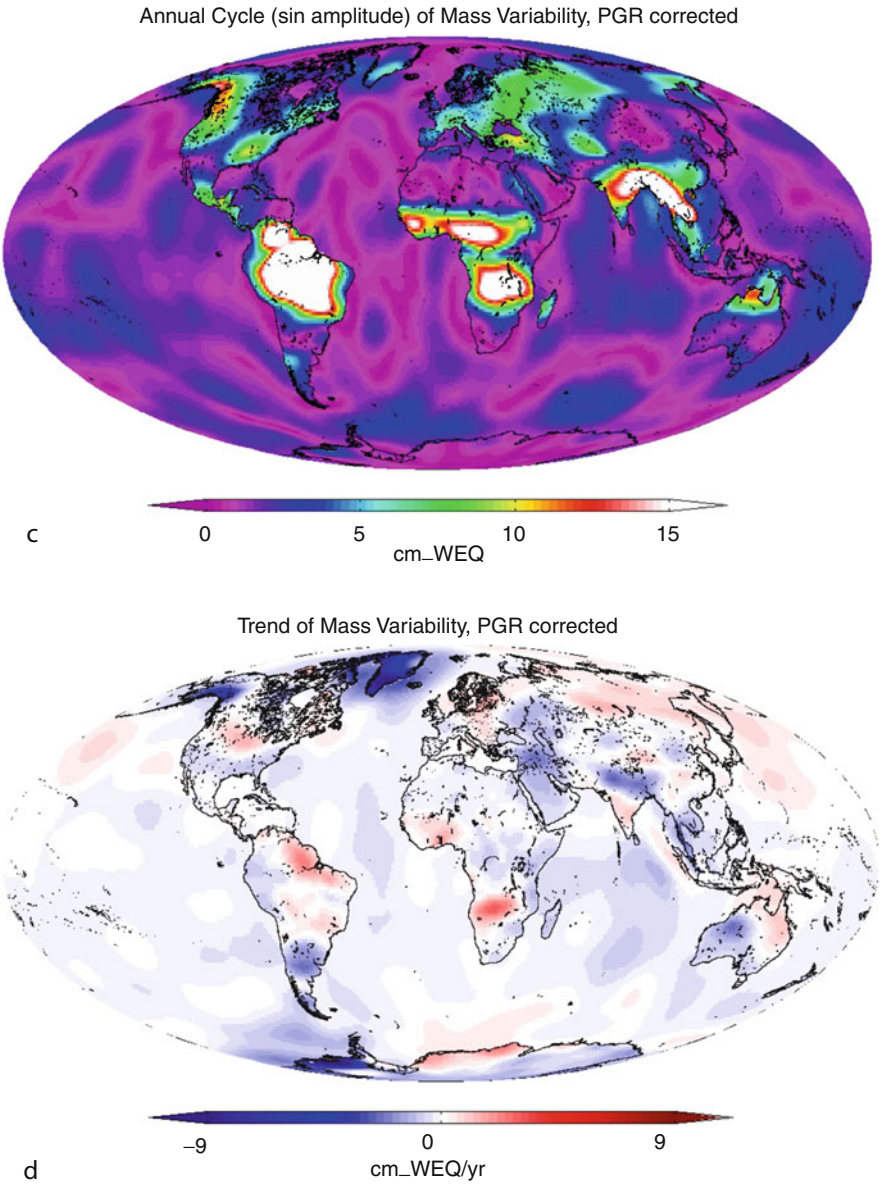

Fig. 7.2 (continued) removed from the data using the model of (Paulson et al. [65]). Note that there is essentially no correlation between this map and Fig. 7.2a; by contrast, here the largest signals are at low latitudes, West Antarctica, Greenland, and the Gulf of Alaska, indicating that by and large monthly changes in gravity are indeed associated with changes in the surface water and ice mass redistribution (Data from http://grace.jpl.nasa.gov). (**c**) The amplitude of a (sinusoidal) annual cycle fit to the data of Fig. 7.2b. Note the differences from Fig. 7.2b, for example, Antarctica where the annual cycle is almost absent, or Greenland where it is minimal. (**d**) Trend of the data in Fig. 7.2b. Note that the strongest negative (decreasing mass) trends are in Greenland, West Antarctica, and Alaska

below the x-axis, satisfies the following equation, a consequence of Laplace's equation which governs the gravity field away from its source masses

$$G(\lambda, z) = G(\lambda, 0)^{*}\exp\left(\frac{-2\pi z}{\lambda}\right) \tag{3.3}$$

where G(λ, z) is the Fourier component of the gravity acceleration distribution g(x, z) with wavelength λ, and z is the altitude above a plane that is (just) above all masses. The exponential in Eq. 7.3 is the plane equivalent of the factor $(a/(a+h))^{l}$ in the spherical harmonic expansion (Eq. 7.1). As a consequence, if we measure g(x, z) at altitude z, short wavelength features of the gravity distribution g(x, 0) are attenuated by the factor $\exp(-2\pi z/\lambda)$; for $\lambda \gg z$, this factor tends to 1 while for $\lambda \ll z$, the factor tends to zero. The "downward continuation" problem arises when we measure at altitude z where short wavelengths are attenuated, but wish to know the signal magnitude at z = 0. This would require an exponential amplification of the weak signals, but it would also produce an exponential magnification of the inevitable noise present in the data. Filter applications to solve or at least mitigate this problem were discussed in section "Spherical Harmonics. Equivalent Water Thickness. Mascons. Spatial Resolution."

The accuracy of GRACE data at a particular point in space and time is the result of several factors: propagation of measurement errors through the processing, loss of signal due to smoothing or destriping which makes the values at a geographical position include "leakage" from neighboring positions (smoothing) and even far away locations (destriping), and the ambiguity associated with the signals of GIA and large earthquakes. The effect of measurement errors depends on latitude (smaller at higher latitudes), and smoothing radius (smaller with larger radii); for example, smoothing with a 750 km Gaussian, but not applying any destriping filter, leads to errors in the mass anomalies ranging between 8 mm of equivalent water near the poles to over 28 mm at the Equator [97].

Applications in Land Hydrology

Over land, repeat GRACE gravity data are interpreted as changes in total water stored in groundwater, soil moisture, vegetation, surface water, snow, and ice, a vertical integration over all relevant layers; this quantity is called terrestrial water storage (TWS). The main complicating issue that arises is the effect of destriping and smoothing filters on the hydrological signals. This effect can be estimated by applying the same filters to output of a land-surface hydrology model (LSM), then computing a gain factor as a least squares ratio between the time series of change in TWS of the filtered and unfiltered model outputs [43].

GRACE gravity data in Northern India, interpreted as TWS, revealed a steady, large-scale mass loss beyond the natural variability simulated by a land hydrology

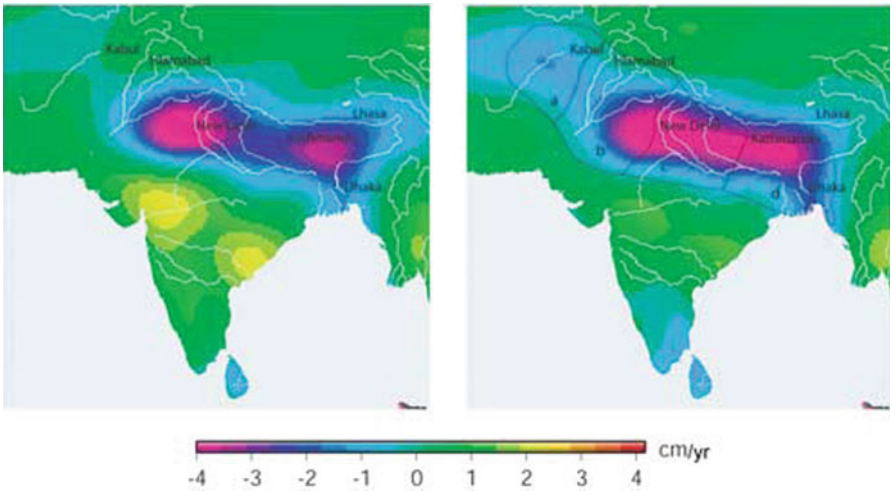

Fig. 7.3 *Left*: Mass loss detected by GRACE in Northern India, in centimeter of equivalent water thickness (From [90]). *Right*: after subtracting from the *left* map the prediction of the Community Land Model (*CLM*) hydrology model, a measure of natural variability. Thus, the *right* map depicts the anthropogenic withdrawal of groundwater in the region. See [90] for details

model [90], which resulted from the excessive extraction of groundwater (Fig. 7.3). When the GRACE data were combined with hydrological models to remove natural variability, the authors concluded the region had lost groundwater at a rate of 54 $\pm$ 9 km^3/year between April 2002 and June 2008 and noted that continued extraction of groundwater at that rate could lead to a major water crisis (see also [78]). GRACE data also showed groundwater depletion in California: During a drought period that lasted from October 2003 to March 2010, California's Sacramento and San Joaquin River Basins lost water at a rate of 31.0 $\pm$ 2.7 mm/year equivalent water height, or a total volume of 30.9 km^3. Adding other data and a hydrological model, the authors concluded that most of the loss, 20.3 km^3, occurred in the Central Valley [30]. While the authors concluded that such a water loss is unsustainable over many years, the most recent data show a return to pre-drought conditions starting in 2009, likely due to significantly increased precipitation.

Australia's recent record droughts motivated many studies using GRACE data. LeBlanc et al. [45] investigated the devastating drought which started in 2001 in the Murray-Darling Basin in southeast Australia. They combined GRACE with in situ and simulated hydrological data to show that groundwater levels continued to decline 6 years after the 2001 onset of the drought, for a total groundwater loss of 104 km^3 between 2001 and 2007; the drought continued even though annual precipitation in the region returned to average during 2007. Combining GRACE data, numerical model output, and various atmospheric datasets, Garcia-Garcia (2011) [31] showed that interannual changes in the seasonal signal in TWS were intricately related both to the El Nino-Southern Oscillation (ENSO) and the Indian

Ocean Dipole (IOD) phenomena, with positive phases of the IOD related to anomalously low precipitation in southeastern Australia due to a reduced tropical moisture flux, and that the sustained water storage reduction over central and southern Australia during 2006–2008 was associated with three consecutive positive IOD events. See also [3].

GRACE data over the largest drainage basin in the world, the Amazon, were used to observe two extreme seasons: the very dry 2002–2003 and the extremely wet 2009 seasons, during which (March 2009) TWS in the entire basin was $\sim 624 \pm 32$ Gt above the 2002–2009 time average [20]; the authors note that this huge TWS excess is roughly equal to the water consumption for 1 year in the USA. Not surprisingly, the GRACE data were consistent with precipitation data from the Global Precipitation Climatology Project. The authors also note the close correlation between these interannual TWS changes in the Amazon and El Nino-Southern Oscillation (ENSO) events as measured by a widely used ENSO index based on Sea Surface Temperature in the eastern tropical Pacific. The 2002–2003 dry season was tied to 2002–2003 El Niño and the 2009 flood to La Niña conditions. See also [1, 34].

Swenson and Wahr [86] combined GRACE with radar and laser altimetry, scatterometer, and precipitation data to asses water level changes in several lakes in the Great Rift Valley, East Africa, and to separate the effects of climatic variability from those of water resources management at the downstream dams of Lake Victoria. Comparing the water level drops from Lakes Victoria, Tanganyika, and Malawi, the authors concluded that about half of the decrease in Lake Victoria was due to climate forcing, and half to water management; this conclusion for the period 2003–2009 was consistent with previous findings for earlier time periods. See also [2, 4].

An innovative application used GRACE TWS data to evaluate precipitation products from two global analyses – Global Precipitation Climatology Project (GPCP) and Climate Prediction Center Merged Analysis of Precipitation (CMAP) – [83]. Both GPCP and CMAP merge in situ rain gauge data with satellite data. At high latitudes, the uncertainty in these products is significantly higher than at lower latitudes, due to gauge "undercatch," a systematic underestimation by the in situ data, which is empirically corrected for. The authors used GPCP and CMAP to estimate precipitation, and the output of a land hydrology model to estimate evapotranspiration and runoff. They concluded that the gauge undercatch correction used by GPCP may be overestimated and pointed out the usefulness of the GRACE data in assessing precipitation estimates – and their biases – over large regions with sparse in situ gauge data.

The correlation of interannual variability of stored water over land and interannual changes in sea level, corrected for thermal expansion, was found to be ~ 0.6 [50, 51].

Perhaps the most promising use of GRACE data in land hydrology applications is its rigorous assimilation into numerical land-surface hydrology models (LSMs), together with a variety of other data such as snow water equivalent or soil moisture, and forcing fields such as precipitation. The reason is that the output of such models allows the separation of the various vertical components that add up to the total

TWS and can provide information at scales finer than the resolution of GRACE, both in space and time. Zaitchik et al. [101] used an ensemble Kalman filter and smoother applied to the catchment land-surface model (CLSM) to study the Mississippi River basin and its four main subbasins. They found that the model with GRACE data assimilation had improved skill over the model without assimilation; skill was determined by the correlation with measured groundwater and with gauged river flow for the four subbasins and for the overall Mississippi River. They then evaluated model performance for eight smaller watersheds, all smaller than the scale of GRACE observations. In seven of eight cases, GRACE data assimilation increased the correlation between changes in TWS and gauged river flow, evidence of the potential to downscale GRACE data to finer spatial scales in hydrological applications. See also [54, 82].

Applications in Cryospheric Studies

When using the time variability GRACE data to study large glaciers and continental ice sheets, the change in gravity is interpreted as a change in ice mass; the change in equivalent water thickness, integrated over the relevant surface area and multiplied by the density of water, yields the change in Gigatons (Gt) of ice. Two complicating issues arise: glacial isostatic adjustment (GIA) and the effect of GRACE filtering and destriping on the estimates. These same issues certainly arise in hydrological and oceanographic studies, but they are more prominent in cryospheric studies for two reasons: firstly, for most hydrological studies, GIA is a small signal relative to the hydrological trend, or simply, the trend is not the main point of the study but rather interannual changes in the hydrological signal, while in cryospheric studies, the trend is the desired signal; secondly, the effect of the smoothing and destriping filters for hydrological studies can be estimated by applying the same filters to output of a land-surface hydrology model (LSM). No such calculation can be performed for changes in ice mass, since currently no adequate, reliable ice sheet models exist. The GIA correction is relatively small for Greenland, but it is as large as the overall ice mass trend for Antarctica. Therefore, uncertainties in the GIA model propagate directly into uncertainties of the estimated ice loss for Antarctica. The solution to the scaling issue requires having external knowledge about the location of the small regions where ice melt is concentrated. This information could come from the Ice, Cloud, and land Elevation Satellite (ICESat) laser altimeter, or from Interferometric Synthetic Aperture Radar (InSAR), then building a model of spatial ice mass loss based on this information, and finally computing a scaling factor in a similar manner as for hydrological signals. For both the Greenland and Antarctic ice sheets, the mass loss is concentrated in coastal outlet glaciers and ice streams, and this information is used to construct a model of ice loss to which the destriping and smoothing filters are applied to derive necessary gain factors.

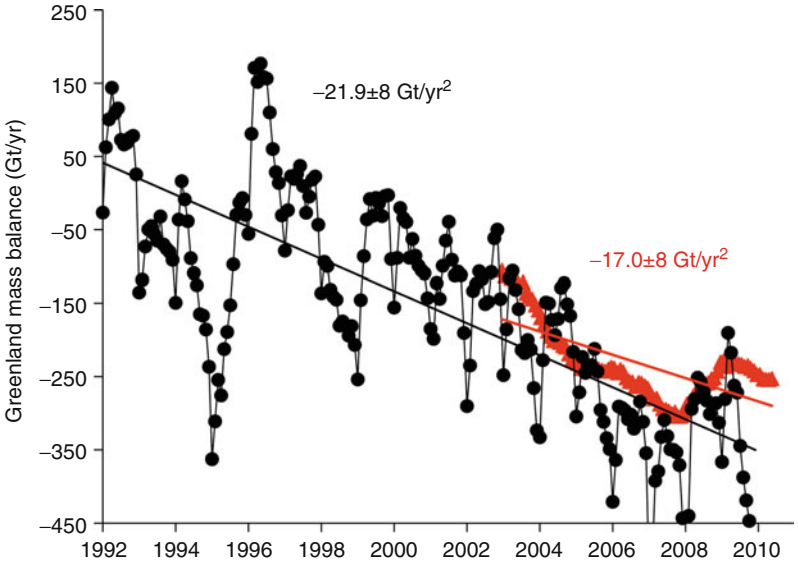

Fig. 7.4 Decreasing trends in Greenland mass, obtained from two methods: Mass Balance method (*black circles*) and GRACE (*red triangles*). See text in section "Applications in Cryospheric Studies" for details. Note the excellent agreement of these two totally independent methods between 2003 and 2010. Because this plot depicts changes in the trend, the GRACE result is unaffected by uncertainties in modeling GIA, a constant trend (From E. Rignot, 2011, personal communication based on [75])

Needless to say, "whether ice sheets and glaciers are melting, and whether such melting is accelerating" are topics of great scientific and social interest.

GRACE data revealed that Greenland's ice lost mass at an accelerated pace: While 137 Gt/year of ice were lost in 2002–2003, the rate increased to 286 Gt/year in 2006–2009, an acceleration of -30 ± 11 Gt/year^2 in 2002–2009 ([93]; see also [17]). The same study estimated the mass loss from Antarctica to have accelerated from 104 Gt/year in 2002–2006 to 246 Gt/year in 2006–2009, an acceleration of -26 ± 14 Gt/year^2. It is important to note that, while the trends are affected by the accuracy of GIA estimates, the accelerations are not because the GIA process is a trend without notable acceleration over the time periods considered. The Antarctic ice loss is mostly concentrated in West Antarctica. These results were bolstered by another study, which covered the time period 1992–2009 [75], and combined GRACE data over 2002–2009 with the "mass-budget method" (MBM) over the longer time span. In the MBM, Interferometric Synthetic Aperture Radar is used to compute glacier velocities while radio echo sounding is used to compute ice thickness; from this combination, perimeter loss is derived, and the perimeter loss is then differenced from net accumulation computed from the sum of snowfall minus surface ablation reconstructed from a regional atmospheric model. During the common time period of 2002.9–2009.5, the GRACE data and the MBM results agree within their error bars (Fig. 7.4). For Greenland, the mass losses estimated

from MBM and GRACE differ by ±20 Gt/year, within their respective errors of ±51 Gt/year and ±33 Gt/year, and the accelerations in mass loss agree even better: 19.3 ± 4 Gt/year^2 with MBM and 17.0 ± 8 Gt/year^2 with GRACE. For Antarctica, the mass loss rates differ by ±50 Gt/year, within the error bar of ±150 Gt/year for MBM and ±75 Gt/year for GRACE, while the accelerations are 13.2 ± 10 Gt/year^2 with GRACE data and 15.1 ± 12 Gt/year^2 with MBM (the 18-year MBM estimates of the accelerations are 21.9 ± 1 Gt/year^2 for Greenland and 14.5 ± 2 Gt/year^2 for Antarctica, indicating that the GRACE period is probably too short to estimate long-term accelerations due to strong interannual variability). This study estimates that during 2006, the Antarctic mass loss using the MBM was 200 ± 150 Gt/year, comparable to Greenland's 250 ± 40 Gt/year. The total contribution from both ice sheets amounted to 1.3 ± 0.4 mm/year sea-level rise during 2006. See also [15, 17, 19, 38, 77, 80, 92]. These studies show that most of the Antarctic ice mass loss is concentrated on the West Antarctic Ice Sheet, especially the Peninsula, and that East Antarctica has experienced a small but measurable mass increase during the GRACE years.

Focusing on smaller regions, GRACE data showed that the Greenland ice loss was largest in the southeast at the beginning of the GRACE period, but in the last few years the rates have decreased in this region, while they increased in the northwest [21, 40]. The Canadian Arctic Archipelago, off the northwestern shore of Greenland, was studied using GRACE and two other independent approaches: surface mass-budget modeling plus an estimate of ice discharge and repeat satellite laser altimetry from ICESat [32]. It was found that the three approaches gave comparable results: Between the periods 2004–2006 and 2007–2009, the rate of mass loss increased from 31±8Gt/year to 92 ± 12 Gt/year, although the authors recognize that the time series is rather short to establish reliable long-term trends. On even smaller spatial scales, ice mass loss bordering the Gulf of Alaska and northwestern Canada was studied [54] using a mascon approach to localize GRACE signals better. It was found that although there was an overall −84±5Gt/year mass loss (0.23±0.01 mm/year in equivalent sea-level rise) between April 2003 and September 2007, the spatial and temporal variabilities were very large, and choosing another time period (April 2003 to September 2006) gave a very different trend value. See also [16, 19]. Overall, the variability observed with GRACE agrees well with regional patterns of glacier mass loss determined from aircraft altimetry and in situ data. On even smaller spatial scales, large ice mass losses in the Patagonia ice field were documented [18, 39], the latter using a mascon approach. See also [56].

Permafrost regions also received attention. Landerer et al. [44] studied the Eurasian pan-Arctic region during 2003–2009 and concluded that changes in discharge were not due to melting of excess ground ice, but rather to changes in precipitation. However, increases of water storage, while driven by precipitation, were partially co-located with regions of discontinuous permafrost, which has warmed significantly over the last decades and changes in the terrestrial hydrological dynamics are thus likely.

Applications in Ocean Studies

GRACE data for ocean studies have been interpreted in three ways: as the time-averaged geoid, as the time-varying but globally averaged total mass of the oceans, and as the time-varying spatial pattern of ocean bottom pressure (OBP). In many cases, the data have been used together with satellite radar altimetric measurements of sea surface height (SSH). In both cases, the signals are described as changes in centimeters of water height, since 1 millibar of OBP is approximately equal to the weight of 1 cm of water.

Ocean dynamic topography is the difference between an SSH map from radar altimetry and an estimate of the geoid, the equipotential surface of the Earth's gravity field that best approximates mean sea level. Slopes in the dynamic topography imply gravitational forces acting on the ocean, forces that drive surface ocean currents. A mean dynamic topography (MDT) is a multi-year time-averaged dynamic topography, and reflects the stationary component of the surface ocean circulation. GRACE data improved our knowledge about the geoid enormously relative to preexisting models. MDTs based on SSH and GRACE only [94] were used to study the double celled gyre of the South Atlantic ocean. In combination with surface drifter and other in situ data, as well as dynamic constraints imposed by the ocean surface momentum balance [57], these new MDTs were also used to study small scale zonal striations in the ocean; GRACE constrained the longer wavelengths and the drifter data the finer space scales. See also [76]. These MDTs are now being improved with the use of data from the Gravity field and steady-state Ocean Circulation Explorer (GOCE) [42].

Time changes in the total mass of the ocean, and their relation to land-ice melt, are a topic of great climatic and societal interest. SSH increases measured by radar altimeters reflect both increases in ocean mass and thermal expansion due to increased temperatures. In addition to radar altimetry and GRACE, an in situ observing system using Argo floats (www.argo.ucsd.edu) has been measuring temperature and salinity in the upper 1,000–2,000 m of the ocean, with good coverage since 2005. In principle, it is possible to derive the thermal expansion component from Argo, and therefore, the sum of the mass component from GRACE and the thermal expansion component from Argo should add up to the altimetrically observed SSH (assuming that the current thermal expansion is small below 2,000 m). In practice, each observing system has its strengths and weaknesses (for example, GRACE data near land tend to be contaminated by large land hydrological signals; Argo coverage prior to 2005 is spotty). However, the three datasets now agree within error estimates, both on seasonal time scales and in terms of their trend [47, 48]. In fact, a discrepancy in earlier estimates of this balance [53] helped identify a problem in the in situ data [98]. See also [12, 14, 74]. The interannual variability in the spatial distribution of GRACE-derived oceanic mass change and that derived from altimetry minus Argo has also been studied [51].

GRACE data over the oceans have been compared with in situ bottom pressure recorders (BPR). BPR sites are few relative to the vastness of the oceans, they are seldom occupied for longer than a year or two without changing instruments, and

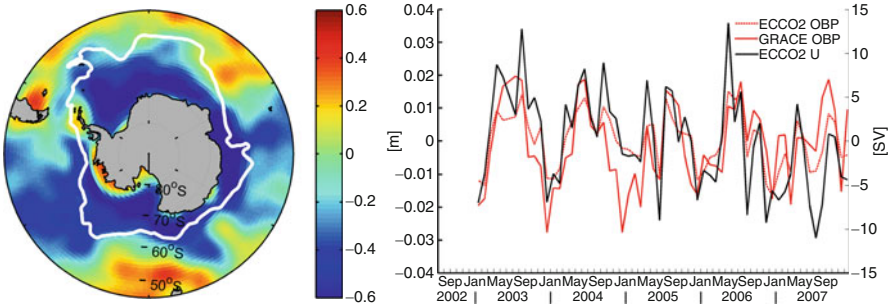

Fig. 7.5 *Left*: Correlation of Drake Passage Transport in the ECCO2 numerical ocean model with GRACE-derived ocean bottom pressure (*OBP*). The *white line* indicates the Southern ACC front of the Antarctic Circumpolar Current. *Right*: Time series of Drake transport and OBP averaged along the Southern ACC front, both from ECCO2 and GRACE. Note that the correlation is not only over seasonal time scales but also the interannual variability is captured (Data and plots from Carmen Boening, 2010, personal communication)

the instruments drift, especially when first installed at the bottom of the ocean. Hence, the comparisons have focused on subannual signals. The general conclusion is that there is good agreement at mid-to-high latitudes where the signal exceeds 1 cm RMS, and poor agreement at tropical and lower latitudes, where the bottom pressure signal is weaker and GRACE errors are larger [55, 59, 64, 73].

Large-scale mass exchanges among the Pacific, Atlantic, and Indian Ocean basins between August 2002 and December 2008 were identified in GRACE data and a numerical ocean model [11]. These exchanges occurred both over seasonal and interannual time scales. Changes in transport of the Antarctic Circumpolar Current were observed through changes in OBP in both GRACE and numerical ocean models [102] and (Fig. 7.5); an exchange of water between the Southern Ocean and the Pacific was also observed [70].

A declining trend in GRACE-derived OBP in the Arctic was correlated to corresponding changes observed with an in situ bottom pressure gauge and, more importantly, to mass changes due to decreasing upper ocean salinities near the North Pole and in the Makarov Basin [59]. (Data subsequent to the publication of that paper has shown the basin reverting to its previous state.) In addition to this interannual variability, annual oscillations of about 2 cm OBP in the Arctic ocean, with maximum in late summer to early fall, were observed with GRACE and modeled as a response to runoff and precipitation minus evaporation that agrees in phase with the data and is 10% larger [69].

A record increase in OBP (from GRACE) and SSH (from the Jason-2 radar altimeter) was observed in late 2009 to early 2010 over a large mid-latitude region of the South East Pacific, diagnosed as a response to wind stress curl associated with a strong and persistent anticyclone in late 2009, which was likely related to the concurrent Central Pacific El Nino [6]. While all previously described results focused on large regions, a 20 cm seasonal signal in the small Gulf of Thailand was observed with GRACE, altimetric SSH and a nearby tide gage [99].

A promising use of the time-varying spatial distribution of OBP from GRACE is its incorporation into numerical ocean models as a data constraint. Steps in this direction were taken by Siegismund et al. [81] and Quinn and Ponte [71] who compared GRACE with OBP in numerical ocean models in order to assess the errors that should be assigned to the GRACE data in order to assimilate it into a numerical ocean model.

The availability of GRACE data made it possible to reevaluate the impact of self-attraction and loading produced by the global redistribution of seawater and land water, as well as in the analysis of tide gage data, which typically disregard these effects (tidal models do include self-attraction and loading) [76]. The authors used continental water mass storage from a hydrological model, Greenland and Antarctica seasonal signals from GRACE, and ocean bottom pressure from a numerical ocean model, and found that the amplitude of the seasonal cycle due to self-attraction and loading at tide gages ranges between 2 and 18 mm. See also [95].

Tides are an area of special interest both as a dealiasing correction to GRACE and radar altimetry data, and more importantly because they have climatic effects; for example, they affect outflows of Antarctic Bottom Water in the Ross Sea by increasing the benthic layer thickness during spring tide [63]. Four global tidal models were assessed in terms of their ability to reduce tidal residuals (identified by their frequency) in the GRACE intersatellite range-rate data [72]; aside from power at the solar semidiurnal tide frequency in low latitudes due to errors in the model of atmospheric tides, the authors found power at the frequencies of nonlinear shallow-water tides indicating areas of needed improvement in global ocean tidal models. Going one step further, Egbert et al. [29] assimilated mass anomalies inferred from GRACE into a hydrodynamic tidal model around Antarctica focused on the M2, S2, and O1 constituents. They showed that after GRACE data assimilation, the model better matched independent tide gage and ICESat laser altimetry data over the Filchner, Ronne and Ross Ice Shelves. See also [36].

Applications in Solid Earth Studies

GRACE time-variable gravity data have been applied in two areas of solid earth science: glacial isostatic adjustment (GIA, also known as postglacial rebound), and large earthquakes. The data processing for these applications is rather different from the previous examples that focus on surface mass changes. In the case of GIA, spatial trends in gravity potential as observed by GRACE are combined with in situ GPS data, ICESat laser altimetry and other data in least squares inversions to separate the contributions to observed surface deformations caused by GIA from those caused by present-day ice mass changes. In the case of large earthquakes, the preferred data type have been the along-track intersatellite range rates, because these can better localize signals with small spatial extent that occur over a short time period.

Tide-gauge, GPS, and GRACE data were combined in a simultaneous inversion for a self-consistent model of GIA and regional sea-level change estimates for the Fennoscandia region [37]; the final models were consistent in peak uplift values (9.5±0.4 mm/year), but located the peak uplift several degrees to the east of previously published results toward the middle of the northern Gulf of Bothnia; this work identified a background uniform gravity rate required for simultaneously fitting the data which could be due either to errors in the GRACE data or to errors in other models used as part of the inversion. A regional study of the Antarctic Peninsula using GRACE mascon and GPS data [38] found that simultaneous solution for ice loss and GIA crustal motions is possible, provided the linear trends in crustal uplift are robustly determined by the GPS stations with adequate spatial coverage of the regions with active GIA uplift and ice loss. A global study [100] combined GRACE and GPS data with ocean bottom pressure from a data-assimilative numerical ocean model to separate the contributions of present-day change (in terms of the thickness of ice and water) from that of GIA; these authors find a measurable GIA uplift signal in Greenland, where GIA models predict a negligible signal. Wu et al.[100] have revised their published estimate of Greenland ice mass loss from 104 Gt/year in their original paper to 140 Gt/year by adding to the inversion more realistic constraints on the ice distribution (X. Wu, 2011, personal communication). See also [13, 41, 68, 91].

Three large earthquakes were studied with GRACE data: (1) the 2004 Sumatra-Andaman earthquake with magnitude M_w 9.2, (2) the somewhat weaker 2010 Maule (Chile) earthquake (M_w 8.8), and (3) the 2011 earthquake off the Pacific coast of Tohoku, Japan (M_w 9.0). At this writing, published results are available for the first two.

The time series (May 2003 to April 2007) of localized gravity changes derived directly from the intersatellite range-rate data, using so-called Slepian functions every 15 days, allowed [33] to find step-like time behavior (coseismic) and exponential-like time behavior (postseismic relaxation) stemming from the 26 December 2004 Sumatra-Andaman earthquake. The authors used seismic and geodetic data to estimate the coseismic slip and evaluated postseismic relaxation mechanisms that fit the GRACE data with alternate asthenosphere viscosity models. They also observed a prominent positive post-earthquake gravity change around the Nicobar Islands, attributable to seafloor uplift. See also [26]. Small changes in the GRACE satellites' intersatellite range were detected after the Maule, Chile earthquake (Mw 8.8, about 4 times lower energy release than the Sumatra-Andaman earthquake) on February 27, 2010 [35] A gravity anomaly of −5 μGal over 500 km was found east of the epicenter after the earthquake. Based on coseismic models, the long-wavelength negative gravity change is primarily the result of crustal dilatation as well as surface subsidence in the onland region. Finite fault coseismic models predicted a much smaller offshore positive gravity anomaly, due to partial compensation of the gravity changes because of surface uplift and interior deformation. The authors noted that gravity data from GRACE fill in the seldom-observed long-wavelength part of the spectrum of earthquake deformations (for large earthquakes), a complement to surface geodetic measurements and seismic data.

Future Directions

The GRACE mission successfully demonstrated the usefulness of space-based time-varying gravity data in a variety of applications. It is clear that time-varying gravity data can monitor some of the effects and consequences of climate change and anthropogenic activity (ice loss; groundwater loss, the mass component of sea-level rise). Given this utility, it is not surprising that there is much interest in Europe, the USA, and in other countries to launch future missions devoted to measuring time-variable gravity. A mission called e-Motion was proposed to the European Space Agency, but was not selected in 2011. In the USA and Germany, a "follow-on" or "gap-filler" mission, very similar to the first-generation GRACE satellites, has been approved and is scheduled to launch in 2016. Several improvements due to lessons learned from GRACE, as well as an experimental laser link between the two satellites will be implemented. In the USA, the National Research Council's Decadal Survey of Earth Sciences (NRC 2007) recommended a GRACE-II mission, which would be a significant improvement to the GRACE capabilities, and is planned to launch in the 2020 decade. Much discussion for the next decade centers around launching coordinated pairs of satellites, sponsored by different countries, to improve the spatial and temporal resolution of the retrieved signals.

Acknowledgments This work was performed in part at the Jet Propulsion Laboratory, California Institute of Technology, under contract with the National Aeronautics and Space Administration, and at the Center for Space Research, University of Texas-Austin.

Bibliography

Primary Literature

1. Alsdorf D, Han S-C, Bates P, Melack J (2010) Seasonal water storage on the Amazon floodplain measured from satellites. Remote Sens Environ 114:2448–2456
2. Awange JL, Sharifi M, Ogonda G, Wickert J, Grafarend EW, Omulo M (2007) The falling Lake Victoria water levels: GRACE, TRIMM and CHAMP satellite analysis of the lake basin. Water Resources Manage. doi:10.1007/s11269-007-9191-y
3. Awange JL, Sharifi MA, Baur O, Keller W, Featherstone WE, Kuhn M (2009) GRACE hydrological monitoring of Australia: current limitations and future prospects. J Spat Sci 54:23–36
4. Becker M, Llovel W, Cazenave A, Guentner A, Cretaux J-F (2010) Recent hydrological behavior of the East African great lakes region inferred from GRACE, satellite altimetry and rainfall observations. C R Geosci 342:223–233. http://dx.doi.org/10.1016/j.crte.2009.12.010
5. Bettadpur S (2007) CSR Level-2 processing standards document for product release 04 GRACE. The GRACE Project. Center for Space Research, University of Texas at Austin, pp 327–742. http://podaac.jpl.nasa.gov/gravity/grace

6. Boening C, Lee T, Zlotnicki V (2011) A record high ocean bottom pressure in the South Pacific observed by GRACE, J Geophys Res Lett 38:L04602. doi:10.1029/2010GL046013
7. Bruinsma S, Lemoine J-M, Biancale R, Vale's N (2010) CNES/GRGS 10-day gravity field models (release 2) and their evaluation. Adv Space Res 45:587–601. doi:10.1016/j.asr.2009.10.012
8. Cazenave A, Mercier F, Bouille F, Lemoine J-M (1999) Global-scale interactions between the solid Earth and its fluid envelopes at the seasonal time scale. Earth Planet Sci Lett 171:549–559
9. Chambers DP (2006a) Observing seasonal steric sea level variations with GRACE and satellite altimetry. J Geophys Res 111 (C3). doi:10.1029/2005JC002914
10. Chambers DP (2006) Evaluation of new GRACE time-variable gravity data over the ocean. Geophys Res Lett 33(17)
11. Chambers DP, Willis JK (2009) Low-frequency exchange of mass between ocean basins. J Geophys Res 114:C11008. doi:10.1029/2009JC005518
12. Chambers DP, Wahr J, Nerem RS (2004) Preliminary observations of global ocean mass variations with GRACE. Geophys Res Lett 31:L13310. doi:10.1029/2004GL020461
13. Chambers DP, Wahr J, Tamisiea ME, Nerem RS (2010) Ocean mass from GRACE and glacial isostatic adjustment. J Geophys Res 115:B11415. doi:10.1029/2010JB007530
14. Chen JL, Wilson CR, Tapley BD, Famiglietti JS, Rodell M (2005) Seasonal global mean sea level change from satellite altimeter, GRACE, and geophysical models. J Geodesy 79:532–539. doi:10.1007/s00190-005-0005-9
15. Chen JL, Wilson CR, Tapley BD (2006) Satellite gravity measurements confirm accelerated melting of Greenland ice sheet. Science 313. doi:10.1126/science.1129007
16. Chen JL, Tapley BD, Wilson CR (2006) Alaskan mountain glacial melting observed by satellite gravimetry. Earth Planet Sci Lett 248:353–363
17. Chen JL, Wilson CR, Tapley BD (2006) Satellite gravity measurements confirm accelerated melting of Greenland ice sheet. Science 313:1958–1960
18. Chen JL, Wilson CR, Tapley BD, Blankenship DD, Ivins E (2007) Patagonia icefield melting observed by GRACE. Geophys Res Lett 34(22):L22501. doi:10.1029/2007GL031871
19. Chen JL, Wilson CR, Blankenship DD, Tapley BD (2009) Accelerated Antarctic ice loss from satellite gravity measurements. Nat Geosci 2:859–862. doi:10.1038/NGEO694
20. Chen JL, Wilson CR, Tapley BD (2010) The 2009 exceptional Amazon flood and interannual terrestrial water storage change observed by GRACE. Water Resour Res 46:W12526. doi:10.1029/2010WR009383
21. Chen JL, Wilson CR, Tapley BD (2011) Interannual variability of Greenland ice losses from satellite gravimetry. J Geophys Res-Solid Earth 116:B07406. http://dx.doi.org/10.1029/2010JB007789)
22. Cheng M, Tapley B (1999) Seasonal variations in low degree zonal harmonics of the Earth's gravity field from satellite laser ranging observations. J Geophys Res 104(B2):2667–2681
23. Cheng MK, Tapley BD (2004) Variations in the Earth's oblateness during the past 28 yeas. J Geophys Res 109:B09402. doi:10.1029/2004JB003028
24. Cox CM, Chao BF (2002) Detection of a large-scale mass redistribution in the terrestrial system since 1998. Science 297:831–833
25. Cretaux J-F, Soudarin L, Davidson FJM, Gennero M-C, Berge-Nguyen M, Cazenave A (2002) Seasonal and interannual geocenter motion from SLR and DORIS measurements: comparison wit with surface loading data. J Geophys Res 107. doi:10.1029/2002JB001820
26. de Linage C, Rivera L, Hinderer J, Boy J-P, Rochester Y, Lambrotte S, Biancale R (2009) Separation of coseismic and postseismic gravity changes for the 2004 Sumatra-Andaman earthquake from 4.6 yr of GRACE observations and modelling of the coseismic change by normal-modes summation. Geophys J Int 176:695–714
27. Dickey JO, Marcus SL, deViron O, Fukumori I (2002) Recent Earth oblateness variations: unraveling climate and postglacial rebound effects. Science 298:1975–1977

28. Dobslaw H, Thomas M (2007) Simulation and observation of global ocean mass anomalies. J Geophys Res 112:C05040. doi:10.1029/2006JC004035
29. Egbert GD, Erofeeva SY, Han S-C, Luthcke SB, Ray RD (2009) Assimilation of GRACE tide solutions into a numerical hydrodynamic inverse model. Geophys Res Lett 36:L20609. doi:10.1029/2009GL040376
30. Famiglietti JS, Lo M, Ho SL, Bethune J, Anderson KJ, Syed TH, Swenson SC, de Linage CR, Rodell M (2011) Satellites measure recent rates of groundwater depletion in California's central valley. Geophys Res Lett 38:L03403. doi:10.1029/2010GL046442
31. Garcia-Garcia D, Ummenhofer CC, Zlotnicki V (2011) Australian water mass variations from GRACE data linked to Indo-Pacific climate variability. Remote Sens Environ 115:2175–2183. http://dx.doi.org/10.1016/j.rse.2011.04.007
32. Gardner AS, Moholdt G, Wouters B, Wolken GJ, Burgess DO, Sharp MJ, Cogley JG, Braun C, Labine C (2011) Sharply increased mass loss from glaciers and ice caps in the Canadian Arctic Archipelago. Nature 473:357–360. doi:10.1038/nature10089
33. Han S-C, Sauber J, Luthcke SB, Ji C Pollitz FF (2008) Implications of postseismic gravity change following the great 2004 Sumatra-Andaman earthquake from the regional harmonic analysis of GRACE intersatellite tracking data. J Geophys Res 113:B11413. doi:10.1029/2008JB005705
34. Han S-C, Kim H, Yeo I-Y, Yeh P, Oki T, Seo K-W, Alsdorf D, Luthcke SB (2009) Dynamics of surface water storage in the Amazon inferred from measurements of inter-satellite distance change. Geophys Res Lett 36:L09403. http://dx.doi.org/10.1029/2009GL037910
35. Han S-C, Sauber J, Luthcke S (2010) Regional gravity decrease after the 2010 Maule (Chile) earthquake indicates large-scale mass redistribution. Geophys Res Lett 37:L23307. doi:10.1029/2010GL045449
36. Han S-C, Ray RD, Luthcke SB (2010) One centimeter-level observations of diurnal ocean tides from global monthly mean time-variable gravity fields. J Geodyn 84:715–729. doi:10.1007/s00190-010-0405-3
37. Hill EM, Davis JL, Tamisiea ME, Lidberg M (2010) Combination of geodetic observations and models for glacial isostatic adjustment fields in Fennoscandia. J Geophys Res 115: B07403. doi:10.1029/2009JB006967
38. Horwath M, Dietrich R (2009) Signal and error in mass change inferences from GRACE: the case of Antarctica. Geophys J Int 177:849–864. doi:10.1111/j.1365-246X.2009.04139.x
39. Ivins ER, Watkins MM, Yuan D-N, Dietrich R, Casassa G, Rlke A (2011) On-land ice loss and glacial isostatic adjustment at the Drake Passage: 2003–2009. J Geophys Res 116: B02403. doi:10.1029/2010JB007607
40. Khan SA, Wahr J, Bevis M, Velicogna I, Kendrick E (2010) Spread of ice mass loss into northwest Greenland observed by GRACE and GPS. Geophys Res Lett 37:6501. doi:10.1029/2010GL042460
41. King MA, Altamimi Z, Boehm J, Bos M, Dach R et al (2010) Improved constraints on models of glacial isostatic adjustment: a review of the contribution of ground-based geodetic observations. Surv Geophys 31:465–507. http://dx.doi.org/10.1007/s10712-010-9100-4
42. Knudsen P, Bingham R, Andersen O, Rio M-H (2011) A global mean dynamic topography and ocean circulation estimation using a preliminary GOCE gravity model. J Geodesy. doi:10.1007/s00190-011-0485-8
43. Landerer FW, Swenson SC (2011) Accuracy of scaled GRACE terrestrial water storage estimates. Water Resour Res, in press
44. Landerer FW, Dickey JO, Güntner A (2010) Terrestrial water budget of the Eurasian pan-Arctic from GRACE satellite measurements during 2003–2009. J Geophys Res 115:D23115. doi:10.1029/2010JD014584
45. Leblanc MJ, Tregoning P, Ramillien G, Tweed SO, Fakes A (2009) Basin-scale, integrated observations of the early 21st century multiyear drought in southeast Australia. Water Resour Res 45:W04408. doi:10.1029/2008WR007333

46. Lemoine JM, Bruinsma S, Loyer S, Biancale R, Marty JC, Perosanz F, Balmino G (2007) Temporal gravity field models inferred from GRACE data. Adv Space Res 39(10):1620–1629
47. Leuliette EW, Miller L (2009) Closing the sea level rise budget with altimetry, Argo, and GRACE. Geophys Res Lett 36:L04608. doi:10.1029/2008GL036010
48. Leuliette EW, Willis JK (2011) Balancing the sea level budget. Oceanography 24:122–129. http://dx.doi.org/10.5670/oceanog.2011.32
49. Liu X, Ditmar P, Siemes C, Slobbe DC, Revtova E, Klees R, Riva R, Zhao Q (2010) DEOS Mass Transport model (DMT-1) based on GRACE satellite data: methodology and validation. Geophys J Int 181:769–788. doi:10.1111/j.1365-246X.2010.04533.x
50. Llovel W, Becker M, Cazenave A, Cretaux JF, Ramillien G (2010) Global land water storage change from GRACE over 2002–2009; inference on sea level. CR Geosciences 342:179–188. http://dx.doi.org/10.1016/j.crte.2009.12.004
51. Llovel W, Guinehut S, Cazenave A (2010) Regional and interannual variability in sea level over 2002–2009 based on satellite altimetry Argo float data and GRACE ocean mass. Ocean Dyn 60:1193–1204. doi:10.1007/s10236-010-0324-0
52. Lo M-H, Famiglietti JS, Yeh PJ-F, Syed TH (2010) Improving parameter estimation and water table depth simulation in a land surface model using GRACE water storage and estimated base flow data. Water Resources Res 46:W0551. http://dx.doi.org/10.1029/2009WR007855
53. Lombard A, Garcia D, Ramillien G, Cazenave A, Biancale R, Lemoine JM, Flechtner F, Schmidt R, Ishii M (2007) Estimation of steric sea level variations from combined GRACE and Jason-1 data. Earth Planet Sci Lett 254:194–202. doi:10.1016/j.epsl.2006.11.035
54. Luthcke SB, Arendt AA, Rowlands DD, McCarthy JJ, Larsen CF (2008) Recent glacier mass changes in the Gulf of Alaska region from GRACE mascon solutions. J Glaciol 54(188):767–777. http://dx.doi.org/10.3189/002214308787779933
55. Macrander A, Böning C, Boebel O, Schröter J (2010) Validation of GRACE gravity fields by in-situ data of ocean bottom pressure. In: Flechtner F, Gruber T, Güntner A, Mandea M, Rothacher M, Schöne T, Wickert J (eds) System Earth via geodetic-geophysical space techniques. Springer, Berlin. http://dx.doi.org/10.1007/978-3-642-10228-8_14
56. Matsuo K, Heki K (2010) Time-variable ice loss in Asian high mountains from satellite gravimetry. Earth Planet Sci Lett 290:30–36. doi:10.1016/j.epsl.2009.11.053
57. Maximenko N, Niiler P, Rio M-H, Melnichenko O, Centurioni L, Chambers D, Zlotnicki V, Galperin B (2009) Mean dynamic topography of the ocean derived from satellite and drifting buoy data using three different techniques. J Atmos Ocean Technol. doi:10.1175/2009JTECHO672.1, http://www.springerlink.com/content/r882426635467007/
58. Mayer-Gürr T, Eicker A, Kurtenbach E, Ilk K-H (2010) ITG-GRACE: global static and temporal gravity field models from GRACE data. Adv Technol Earth Sci 2010(Part 2):159–168. doi:10.1007/978-3-642-10228-8_13
59. Morison J, Wahr J, Kwok R, Peralta-Ferriz C (2007) Recent trends in Arctic Ocean mass distribution revealed by GRACE. Geophys Res Lett 34:L07602. doi:10.1029/2006GL029016
60. Muller PM, Sjogren WL (1968) Mascons: lunar mass concentrations. Science 161:680–684
61. Nerem RS, Wahr J (2011) Recent changes in the Earth's oblateness driven by Greenland and Antarctic ice mass loss. Geophys Res Lett 38:L13501. doi:10.1029/2011GL047879
62. O'Keefe JA, Eckels A, Squires RK (1959) The gravitational field of the earth. Astron J 64:245
63. Padman L, Howard SL, Orsi AH, Muench RD (2009) Tides of the northwestern Ross Sea and their impact on dense outflows of Antarctic Bottom Water. Deep-Sea Res Pt II Oceanography 56:818–834. http://dx.doi.org/10.1016/j.dsr2.2008.10.026
64. Park J, Watts DR, Donohue K, Jayne S (2008) A comparison of in situ bottom pressure array measurements with GRACE estimates in the Kuroshio extension. Geophys Res Lett 35: L17601. doi:10.1029/2008GL034778
65. Paulson A, Zhong S, Wahr J (2007) Inference of mantle viscosity from GRACE and relative sea level data. Geophys J Internat 171:497–508

66. Parker RL (1975) Theory of ideal bodies for gravity interpretation. Geophys J Roy Astron Soc 42(2):315–334
67. Peltier WR (2004) Global glacial isostasy and the surface of the ice-age Earth: the ICE-5G (VM2) model and GRACE. Annu Rev Earth Planet Sci 32:111–149. doi:10.1146/annurev.earth.32.082503.144359
68. Peltier WR, Luthcke SB (2009) On the origins of earth rotation anomalies: New insights on the basis of both "paleogeodetic" data and gravity recovery and climate experiment (GRACE) data. J Geophys Res 114:B11405. doi:10.1029/2009JB006352
69. Peralta-Ferriz C, Morison J (2010) Understanding the annual cycle of the Arctic Ocean bottom pressure. Geophys Res Lett 37:L10603. doi:10.1029/2010GL042827
70. Ponte RM, Quinn KJ (2009) Bottom pressure changes around Antarctica and wind-driven meridional flows. Geophys Res Lett 36:L13604. doi:10.1029/2009GL039060
71. Quinn KJ, Ponte RM (2008) Estimating weights for the use of time-dependent gravity recovery and climate experiment data in constraining ocean models. J Geophys Res 113:C12013. doi:10.1029/2008JC004903
72. Ray RD, Luthcke SB, Boy J-P (2009) Qualitative comparisons of global ocean tide models by analysis of intersatellite ranging data. J Geophys Res 114:C09017. doi:10.1029/2009JC005362
73. Rietbroek R, LeGrand P, Wouters B, Lemoine J-M, Ramillien G, Hughes CW (2006) Comparison of in situ bottom pressure data with GRACE gravimetry in the Crozet-Kerguelen region. Geophys Res Lett 33:L21601. doi:10.1029/2006GL027452
74. Rietbroek R, Brunnabend S-E, Dahle C, Kusche J, Flechtner F, Schröter J, Timmermann R (2009) Changes in total ocean mass derived from GRACE, GPS, and ocean modeling with weekly resolution. J Geophys Res: Oceans 114:C11004. doi:10.1029/2009JC005449
75. Rignot E, Velicogna I, van den Broeke MR, Monaghan A, Lenaerts J (2011) Acceleration of the contribution of the Greenland and Antarctic ice sheets to sea level rise. Geophys Res Lett 38:L05503. doi:10.1029/2011GL046583
76. Rio MH, Guinehut S, Larnicol G (2011) New CNES-CLS09 global mean dynamic topography computed from the combination of GRACE data, altimetry, and in situ measurements. J Geophys Res 116:C07018. doi:10.1029/2010JC006505
77. Riva REM, Gunter BC, Urban TJ, Vermeersen BLA, Lindenbergh RC, Helsen MM, Bamber JL, van de Wal RSW, van den Broeke MR, Schutz BE (2009) Glacial isostatic adjustment over Antarctica from combined ICEsat and GRACE satellite data. Earth Planet Sci Lett 288:516–523. http://dx.doi.org/10.1016/j.epsl.2009.10.013
78. Rodell M, Velicogna I, Famiglietti JS (2009) Satellite-based estimates of groundwater depletion in India. Nature 460:999–1002. http://dx.doi.org/10.1038/nature08238
79. Rowlands DD, Luthcke SB, McCarthy JJ, Klosko SM, Chinn DS, Lemoine FG, Boy J-P, Sabaka TJ (2010) Global mass flux solutions from GRACE: a comparison of parameter estimation strategies—mass concentrations versus stokes coefficients. J Geophys Res 115:B01403. doi:10.1029/2009JB006546
80. Sasgen I, Martinec Z, Bamber J (2010) Combined GRACE and InSAR estimate of West Antarctic ice mass loss. J Geophys Res (Earth Surface) 115:F04010. doi:10.1029/2009JF001525
81. Siegismund F, Romanova V, Köhl A, Stammer D (2011) Ocean bottom pressure variations estimated from gravity, nonsteric sea surface height and hydrodynamic model simulations. J Geophys Res 116:C07021. doi:10.1029/2010JC006727
82. Sun AY, Green R, Rodell M, Swenson S (2010) Inferring aquifer storage parameters using satellite and in situ measurements: estimation under uncertainty. Geophys Res Lett 37:L10401. http://dx.doi.org/10.1029/2010GL043231
83. Swenson S (2010) Assessing high-latitude winter precipitation from global precipitation analyses using GRACE. J Hydrometeorol 11:405–420. doi:10.1175/2009JHM1194.1

84. Swenson S, Wahr J (2002) Methods for inferring regional surface-mass anomalies from gravity recovery and climate experiment (GRACE) measurements of time-variable gravity. J Geophys Res 107(B9):2193. doi:10.1029/2001JB000576
85. Swenson S, Wahr J (2006) Post-processing removal of correlated errors in GRACE data. Geophys Res Lett 33:L08402. doi:10.1029/2005GL025285
86. Swenson S, Wahr J (2009) Monitoring the water balance of Lake Victoria, East Africa, from space. J Hydrol 370(1–4):163–176. doi:10.1016/j.jhydrol.2009.03.008
87. Swenson S, Chambers DP, Wahr J (2008) Estimating geocenter variations from a combination of GRACE and ocean model output. J Geophys Res 113. doi:10.1029/2007JB005338
88. Tamisiea ME, Hill EM, Ponte RM, Davis JL, Velicogna I, Vinogradova NT (2010) Impact of self-attraction and loading on the annual cycle in sea level. J Geophys Res 115:C07004. doi:10.1029/2009JC005687
89. Tapley BD et al (2004) GRACE measurements of mass variability in the Earth system. Science 305:503–505. doi:10.1126/science.1099192
90. Tiwari VM, Wahr J, Swenson S (2009) Dwindling groundwater resources in Northern India, from satellite gravity observations. Geophys Res Lett 36:L18401. doi:10.1029/2009GL039401
91. Tregoning P, Ramillien G, McQueen H, Zwartz D (2009) Glacial isostatic adjustment and nonstationary signals observed by GRACE. J Geophys Res 114:B06406. doi:10.1029/2008JB006161
92. van den Broeke M, Bamber J, Ettema J, Rignot E, Schrama E, van de Berg WJ, van Meijgaard E, Velicogna I, Wouters B (2009) Partitioning recent Greenland mass loss. Science 326:984. doi:10.1126/science.1178176
93. Velicogna I (2009) Increasing rates of ice mass loss from the Greenland and Antarctic ice sheets revealed by GRACE. Geophys Res Lett 36:L19503. doi:10.1029/2009GL040222
94. Vianna ML, Menezes V V (2011) Double-celled subtropical gyre in the South Atlantic Ocean: means, trends, and interannual changes. J Geophys Res 116:C03024. doi:10.1029/2010JC006574
95. Vinogradova NT, Ponte RM, Tamisiea ME, Quinn KJ, Hill EM, Davis JL (2011) Self-attraction and loading effects on ocean mass redistribution at monthly and longer time scales. J Geophys Res-Oceans 116. http://dx.doi.org/10.1029/2011JC007037
96. Wahr J, Molenaar M, Bryan F (1998) Time variability of the Earth's gravity field: hydrological and oceanic effects and their possible detection using GRACE. J Geophys Res 103:30205–30229. doi:10.1029/98JB02844
97. Wahr J, Swenson S, Velicogna I (2006) Accuracy of GRACE mass estimates. Geophys Res Lett 33:L06401. doi:10.1029/2005GL025305
98. Willis JK, Lyman JW, Johnson GC, Gilson J (2008) In situ data biases and recent ocean heat content variability. J Oceanic Atmosph Technol 26:846–852. doi:10.1175/2008JTECHO608.1
99. Wouters B, Chambers DP (2010) Analysis of seasonal ocean bottom pressure variability in the Gulf of Thailand from GRACE. Glob Planet Chang 74:76–81. doi:10.1016/j.gloplacha.2010.08.002
100. Wu X, Heflin MB, Schotman H, Vermeersen BLA, Dong D, Gross RS, Ivins ER, Moore AW, Owen SE (2010) Simultaneous estimation of global present-day water transport and glacial isostatic adjustment. Nat Geosci 3:642–646. doi:10.1038/NGEO938
101. Zaitchik BF, Rodell M, Reichle RH (2008) Assimilation of GRACE terrestrial water storage data into a land surface model: results for the Mississippi river basin. J Hydrometeorol 9:535–548. doi:10.1175/2007JHM951.1
102. Zlotnicki V, Wahr J, Fukumori I, Song Y-T (2007) Antarctic circumpolar current transport variability during 2003–2005 from GRACE. J Physical Oceanog 37(2):230–244

Books and Reviews

Cazenave A, Chen J-L (2010) Time-variable gravity from space and present-day mass redistribution in the Earth system. Earth Planet Sci Lett 298(2010):263–274. doi:10.1016/j.epsl.2010.07.035

Chambers DP, Schröter J (2011) Measuring ocean mass variability from satellite gravimetry. J Geodyn 52:333–343. doi:10.1016/j.jog.2011.04.004

Dickey J et al (1997) Satellite gravity and the geosphere. US National Research Council, National Academy Press, Washington, DC

Chapter 8
Heat Content and Temperature of the Ocean

Rui M. Ponte

Glossary

CTD (conductivity-temperature-depth)	Instrument used to obtain vertical profiles of salinity, temperature, and pressure in the ocean at resolutions up to 1 m.
Heat content	Amount of energy contained in thermal motion associated with any volume of matter, which is proportional to its temperature and specific heat.
Mixed layer	Near-surface layer where turbulent mixing primarily induced by atmospheric forcing produces homogeneous conditions of temperature, salinity, and other water properties.
Objective analysis	General mathematical procedure by which the value of a variable of interest at a given location and time is derived from similar observations at other times and/or places (also sometimes referred to as optimal interpolation).
Potential temperature	Temperature attained by a fluid parcel if measured at a given standard pressure (typically 1,000 hPa corresponding approximately to atmospheric pressure at the ocean surface).
Specific heat	Amount of energy per unit mass necessary to change the temperature of a given substance by 1°C, with typical values for seawater around 4,000 J/kg/°C.

This chapter was originally published as part of the Encyclopedia of Sustainability Science and Technology edited by Robert A. Meyers. DOI:10.1007/978-1-4419-0851-3

R.M. Ponte (✉)
Atmospheric and Environmental Research, Inc, 131 Hartwell Avenue,
Lexington, MA 02421, USA
e-mail: rponte@aer.com

J. Orcutt (ed.), *Earth System Monitoring: Selected Entries from the Encyclopedia of Sustainability Science and Technology*, DOI 10.1007/978-1-4614-5684-1_8,

Thermistor	Sensor that uses known thermal dependences of electrical resistance to determine temperature.
Thermocline	Region of enhanced vertical temperature gradients separating well-mixed layers near the surface from the layers with weak thermal stratification found in the deep ocean.
XBT (eXpendable BathyThermograph)	Instrument used to obtain essentially continuous recordings of temperature with depth, from the surface to about 700 m, which can be deployed from a ship underway and without having to be retrieved.

Definition of the Subject

The global ocean is a vast body of water covering approximately two thirds of Earth's surface and having an average depth around 4,000 m. Temperatures in the ocean can range from a balmy 30°C in the surface layers of the tropics to an icy cold −2°C in polar regions and at abyssal depths. Apart from the strong spatial variability, water temperatures at a place also change on all time scales, from hours to decades. Variability in surface water temperatures affects air-sea heat exchange and is an important factor determining the nature and strength of ocean–atmosphere coupling. Changes in ocean temperatures imply expansion or contraction of the water column and can thus have a major impact on sea level. And given the large heat capacity of seawater compared to that of air and the large mass of the oceans compared to that of the atmosphere, relatively small fluctuations in oceanic temperatures imply substantial changes in heat content, which are essential for properly accounting for the planet's energy balance. As such, taking the temperature of the oceans and determining changes in its heat content is an essential diagnostic of the state of Earth's climate and the overall health of our planet.

The task of monitoring seawater temperatures is made very difficult by the vastness of the global oceans and by the remote and harsh environment in which measurements must be taken. Original temperature observations date back at least a few centuries and were made by dropping thermometers in the water, first at the surface and then also at depth. Developments mainly in the second half of the twentieth century have led to a number of different sensor technologies, including continuous vertical profiling instruments deployed on various platforms (ships, moored instruments, autonomous floats), acoustic tomography, as well as space remote sensing techniques. Despite significantly improved data gathering capabilities, considerable challenges remain in observing the oceans globally and at sufficient temporal and spatial resolution. The sampling problem is a daunting one, and the historical temperature database is fraught with other issues as well

regarding lack of metadata, unknown instrumental biases, and consistency between shifting technologies. A number of developing observing systems, together with advancements in modeling and data synthesis capabilities, promise to deliver a more accurate chart of ocean temperature and heat content in the years ahead.

Introduction

Measurements of seawater temperatures must have started with the appearance of the first thermometers in the seventeenth century. As early as the eighteenth century, Benjamin Franklin was making use of a thermometer as a rudimentary navigation aid to chart the changes in temperature across the Gulf Stream [1]. With the development of commercial shipping and the birth of well-funded military naval fleets, routine ship measurements of near-surface temperature were well under way in the nineteenth century. Dedicated scientific efforts to sample the oceanic temperature structure, not just at the surface but also at depth, had to wait until the second half of the nineteenth century, however. The global Challenger expeditions in the 1870s [2] and later the Meteor expeditions in the 1920s [3] signaled the birth of oceanography as a science. By this time, the importance of knowing the physical and chemical properties of seawater had become all too clear.

Temperature is a key parameter for determining water density, along with salinity and pressure. As it warms and cools, seawater expands and contracts by an amount determined by its coefficient of thermal expansion, which increases with temperature, pressure, and salinity (e.g., [4]) and can vary significantly from place to place in the ocean. Density changes tend to be more sensitive to temperature at depth, where pressure is largest, and in the tropics, where the waters are warmest. As horizontal differences in density determine pressure gradients and currents, temperature is of crucial dynamical importance when trying to infer the ocean circulation and how it changes in time.

The impact of temperature on density (or correspondingly volume) also means that changes in ocean thermal properties are directly related to changes in sea level. As described in most basic oceanographic texts (e.g., [4]), by knowing the fluctuations in temperature throughout the water column, their integrated effects on volume can be calculated and represent the so-called thermosteric component of sea level variability. (Salinity also affects volume and gives rise to halosteric changes in sea level. Steric sea level signals refer to the combined effects of temperature and salinity.) Interpretation, analysis, and prediction of sea level change are thus tightly related to accurate knowledge of temperatures over all ocean depths.

Last but not least, seawater temperatures give a measure of how much thermal energy or heat content is contained in the ocean. Oceanic heat content is a quantity of major relevance for climate and is a particular focus of this entry. Given the difference in the specific heat of water and air, heating or cooling a given amount of

seawater requires approximately four times more energy than for the same mass of air. More importantly, because the density of water is approximately 1,000 times larger than the density of air, the ocean's heat capacity and thermal inertia are vastly larger than those of the atmosphere. As such, the oceans can serve as a large reservoir of heat in the climate system. Being a dynamic fluid with an active circulation, the oceans continually transport and redistribute heat and participate in important heat exchanges with the atmosphere as well as the cryosphere. Knowledge of oceanic temperature fields can thus hold vital information on the past, present, and future state of Earth's climate.

By the time the classic oceanography text by Sverdrup et al. [5] was published, summarizing much of what was known about the oceans at the time, the crude characteristics of the oceanic temperature structure were beginning to take shape. Apart from the clear decrease of near-surface temperature with latitude away from the tropics, mimicking that of surface air temperatures, other major features, well known to us today and seen in the example of Fig. 8.1, were already apparent. The presence of a near-surface layer with homogenized temperature and other properties was established early on. This so-called surface mixed layer owed its existence to high turbulence and mixing induced primarily by air-sea fluxes at the upper boundary, and its thickness, which could reach several hundred meters, was very much dependent on location. Below the mixed layer, a region of rapid decrease in temperature with depth was present in most of the oceans. The rapid transition between the warm surface layers and the cold abyss, nominally called the thermocline, exhibited a fairly complex dependence on region and could extend over various thicknesses and up to depths of 1,000 m. Much colder deep and bottom waters beneath the thermocline tended to be less stratified with depth and also more homogeneous in latitude and longitude, without the marked latitudinal dependence of the upper layers.

The initial picture that emerged from the first scientific expeditions in the nineteenth and twentieth centuries was necessarily one of essentially steady conditions, given the paucity of data with a few snapshots taken along a handful of sections. Ever since those original efforts, the quest for determining temperature distributions in space and time over the vast global oceans has been an endeavor with almost epic overtones. In what follows, a brief description of the panoply of instruments and methods used to measure temperature and heat content is attempted within a historical timeline, from the earliest to the most modern period. Such a voyage through the world of instrumentation and data gathering sets the stage for a discussion of what is presently known about ocean temperature and heat content, starting with the near-surface layers and progressing down to the abyssal depths. The main focus is on the thermal structure at large spatial scales (100 km and longer) and its variability on time scales of months to centuries relevant for climate. Although much progress has been achieved in recent decades, considerable challenges remain and some possible pathways for the future are traced at the end.

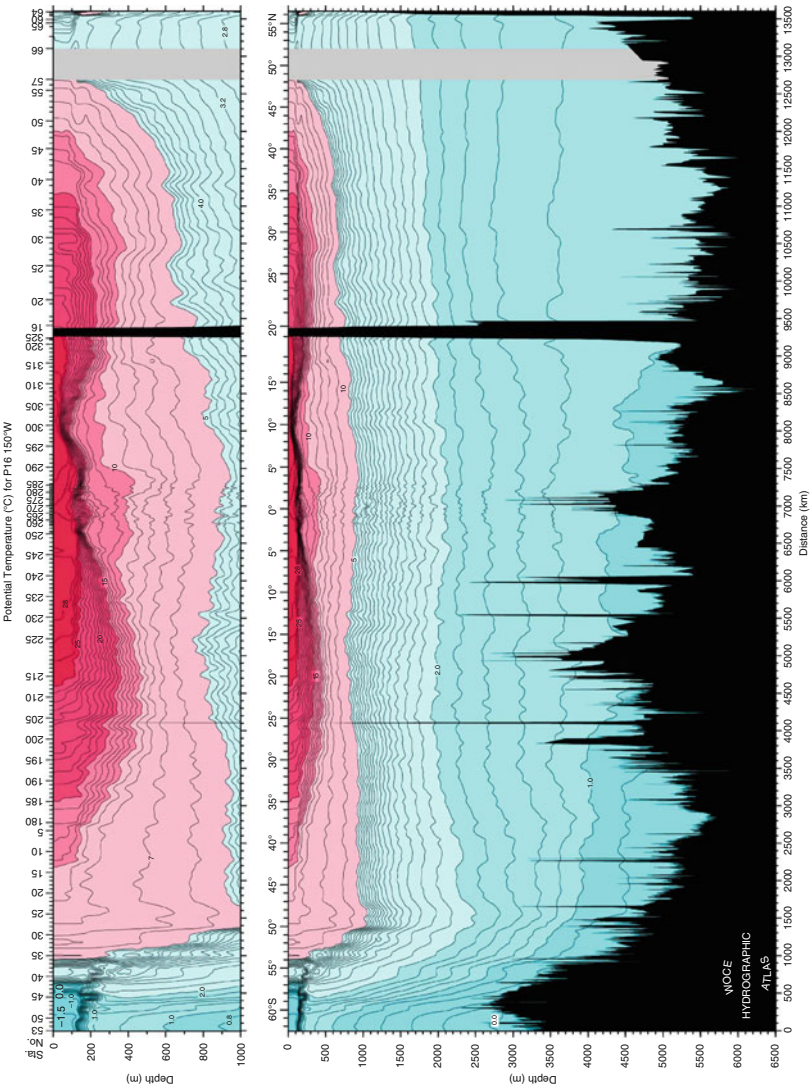

Fig. 8.1 Latitude-depth cross-section of potential temperature along approximately 150°W in the Pacific. *Contour lines* are drawn every 1°C (0.2°C) for temperatures warmer (colder) than 5°C. Different *color shading* is shown at intervals of 5°C, with temperatures getting progressively colder from *red* to *blue shades*, and with the *darkest red* representing the range 25–30°C. *Bottom panel* shows the full water column, with the *top panel* focusing on the *upper* 1,000 m for added detail. Bathymetry is shaded in *black*, with the land feature reaching the surface near 20°N being the Hawaiian Islands (Reproduced from Talley [6])

Brief History of Temperature Observations

Conventional thermometers were the first instruments used to sample oceanic temperatures [5]. The bulk of the data was taken at the surface, either by dropping the thermometers in the water or by using a bucket to collect water for measurement. Some subsurface measurements were obtained by using insulated bottles that would maintain collected water samples at their ambient temperatures, with minimal exchanges of heat with surroundings during ascent. For subsurface sampling, however, most scientific surveys through the first half of the twentieth century were made using reversible thermometers [5], which were set to sample at some predetermined depth levels. The technology was simple and reliable but expensive. Furthermore, only point measurements in time and space were possible with reversible thermometers.

Continuous sampling devices were experimented with early on but their use did not become widespread until the second half of the twentieth century [7]. First thermographs used standard thermometry and various methods for continuous data recording and were mainly deployed in the hulls or intake pipes of ships. Such instruments had no pressure sensors and thus no ability to determine depth, and data gathering was confined mainly to the top few meters of the ocean. The first useful attempts to continuously record temperature and depth are reported by Spilhaus [8, 9]. The original bathythermograph (BT) followed a completely mechanical design and its reliability made it one of the most extensively used instruments for ocean surveying in the 1950s and 1960s [10]. Its depth range was quite limited, however, allowing measurements only in approximately the upper 150 m.

An important development was the appearance of the expendable BT (XBT), which used thermistor technology to measure temperature over approximately the upper 700 m of the ocean [10]. Without a pressure sensor, the depth of measurement was inferred from the elapsed time since deployment and the "known" free fall rates, as established by the manufacturer of the instruments. Because of its relatively low cost and its easy use and operation from a ship underway, the XBT became the workhorse of the in situ observing system for a long time. A great deal of what is known about the upper ocean temperature and heat content variability is owed to millions of XBT profiles carried out mostly from merchant ships and other ship-of-opportunity vessels. As such, XBT sampling tended to be best along most traveled shipping routes, particularly between Europe and North America (see Fig. 8.2). By any measure, large chunks of ocean were rarely visited by XBT surveys and the deep ocean was totally out of reach. The method of assigning depths to XBT temperature profiles based on instrument free fall rates also led to the introduction of complicated biases, which are still being dealt with to date [12, 13].

In parallel with XBT development, the need for high-accuracy profiling instruments that could sample the ocean all the way to the bottom led to the development of the conductivity-temperature-depth (CTD) sensor. Various different versions were produced mainly in the 1950s and 1960s, and CTD use quickly became the standard in all the major scientific campaigns (e.g., [7]). Compared to

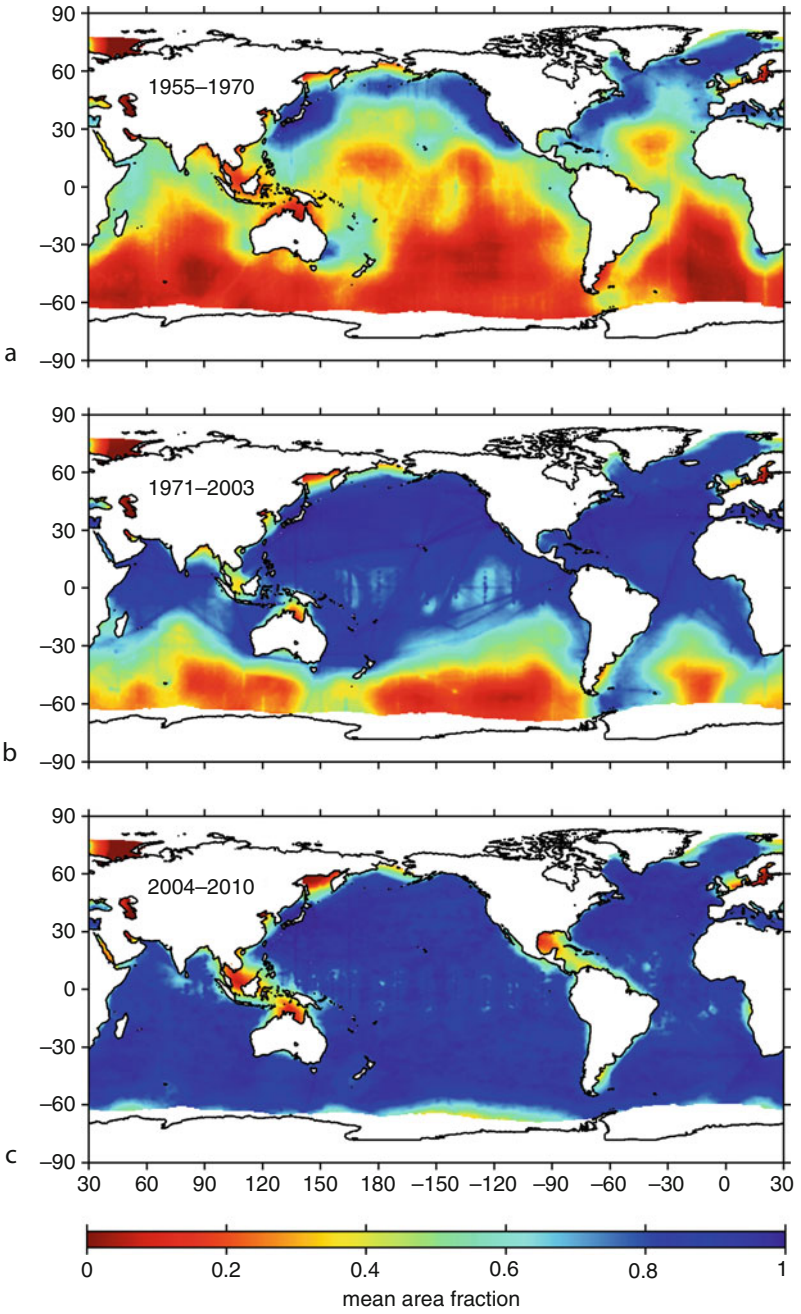

Fig. 8.2 Estimate of the annual mean sampling for the *upper* 750 m expressed as the fractional area of data coverage, provided by John Lyman as an update to the results discussed in Lyman and Johnson [11]. (**a**) Coverage prior to 1970 is very poor over most of the global oceans. (**b**) Substantial improvements in the period 1971–2003 come from XBT surveys, mostly in the Northern Hemisphere and along ship routes clearly seen as tracks in the plot. (**c**) The increase in coverage for the most recent period shown (2004–2010) reflects data collected by the Argo system

XBT deployments, which could be carried out with the ship underway, CTD casts required dedicated ship time, but CTD precisions were significantly better than those possible with XBT sensors, and including pressure sensors ensured an accurate mapping of the thermal structure in the vertical. The CTD instrument has continued to evolve and current versions have accuracies better than 0.001°C and vertical resolutions of about 1 m. (Temperature variability at submeter scales is a topic in its own right and much of the work that led to the CTD sensor has evolved into several instruments capable of measuring thermal microstructure at millimeter scales; interested readers can learn more about microstructure instrumentation by consulting for example [7, 14, 15] and their cited references.)

Traditional CTD surveys, involving basin-wide sections of full-depth casts made at variable horizontal spacings (typically a few tens of kilometers, as in the example of Fig. 8.1), together with XBT profiles along major shipping lanes, continued to be the main method of observing oceanic thermal structures until the end of the twentieth century. But even as the World Ocean Circulation Experiment (WOCE) became a reality [16], focus was still on obtaining a single realization of the global temperature field. Only a few sections were meant to be sampled repeatedly to assess the full temporal variability. Costs of operating research ships from which CTD casts could be performed continued to be a major impediment for truly global coverage. Even after several decades of XBT and CTD measurement campaigns, extensive oceanic regions, particularly in the Southern Hemisphere, remained severely under-sampled by the end of the twentieth century (Fig. 8.2).

The march toward a truly global observing system took another major step with the implementation of the Argo system of profiling floats in the last decade [17, 18]. Following years of research and development in autonomous float technology, major international cooperation under the Argo Project led to the seeding of the global ocean with more than 3,000 floats (Fig. 8.3) with the capability of profiling temperature and other properties between depths of 2,000 m and the surface approximately every 10 days. Measurements are relayed by satellite while the floats are at the surface in between each cycle of ascent and descent. Coverage is almost global, apart from the lack of data in high latitudes and ice-covered regions, where current Argo technology does not work (Fig. 8.3). Shallow and marginal seas are also not part of the sampling Argo strategy. In a short number of years since their deployment, Argo floats have produced more than 300,000 profiles and have provided more samples than all the data ever collected before in many regions.

Despite all the efforts to measure subsurface temperature, it is at the surface that coverage is most adequate in both space and time (e.g., [19]). A major factor in the density of observations at the surface has been the space-based remote sensing techniques established since the 1980s (e.g., [20, 21]). Given the dependence of surface infrared and microwave radiation on sea surface temperature, satellite radiometers measuring at these frequency bands can be used to retrieve sea surface temperature. Many other factors like atmospheric clouds and water vapor impact the radiation reaching the instrument and have to be corrected. For these purposes, increasingly complex validation and calibration methods have been developed over the last 30 years. Many of such efforts rely on in situ measurements from ships, surface

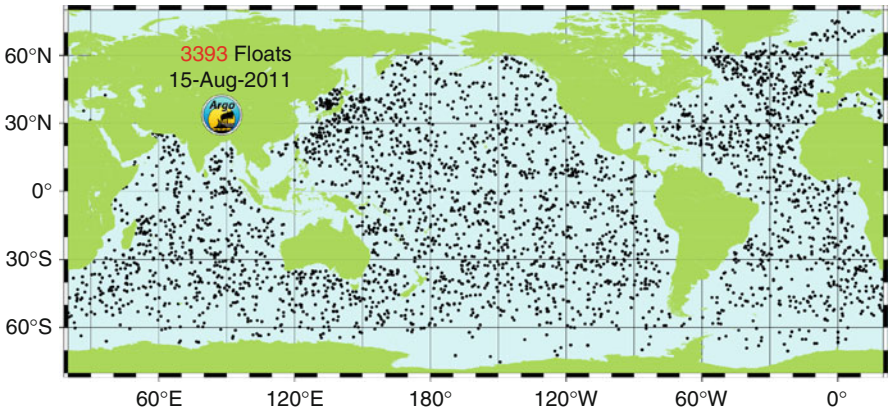

Fig. 8.3 Distribution of Argo floats as of August 2011 as estimated by the Argo Project (Reproduced from the Argo Project web site). Global coverage of the oceans involves more than 3,000 floats. High northern and southern latitudes and shallow and marginal seas remain poorly sampled

buoys, and drifters. However dense in space and time, satellite measurements strictly measure the temperatures right at the surface and their interpretation in terms of near-surface temperatures remains an issue of research [21].

For subsurface thermal information, aside from profiling measurements by XBT, CTD, and Argo instruments, a number of other in situ programs are also useful to mention. Surface and subsurface moorings of various types have been deployed, which usually include thermistor chains. Operational programs are in place in the tropical Pacific and Atlantic [22, 23] with a similar system currently under implementation in the tropical Indian Ocean [24]. Many research projects with local or regional focus provide occasional temperature measurements (e.g., [16, 25]), and a few long-term stations have also been maintained in places like Bermuda and Hawaii [26, 27]. In any case, traditional ship-based XBT and CTD surveys and more recently the Argo floats provide the bulk of information on ocean temperature and heat content over the last decades.

Apart from direct temperature measurements, several other indirect observing methods have been recently developed. Indirect thermometry can make use of the relationship between temperature and any other oceanic variable that can be accurately measured. Such is the case with the strong dependence of sea level on thermosteric height, which is directly related to integrated temperature over the water column. Measuring variability in sea level using satellite altimetry can complement in situ temperature observations in efforts to infer changes in heat content [28, 29]. As with many indirect methods, ancillary observations are needed. As sea level also depends on salinity through changes in halosteric height, measurements of salt content can help in isolating the temperature effects. In addition, changes in sea level can be due to changes in the mass of the water column and the ability to measure the total mass content either using in situ bottom

pressure recorders or satellite gravity techniques can lead to improved inferences of heat content based on sea level observations, as discussed by Ponte [30] and Jayne et al. [31].

Temperature has also a strong effect on sound speed. Such dependence is the basis for the acoustic thermometry ideas proposed by Munk and Forbes [32] and others. Sound travel times can be inverted to estimate variability in averaged temperature and heat content along ray paths connecting any source and receiver pair. Plans to establish acoustic monitoring for the global oceans are revisited in Dushaw et al. [33] but presently current data sets are confined to a few experiments carried out mostly in the North Pacific, between Hawaii and the North American coast [34]. Long-range acoustic thermometry can work over many thousands of kilometers and thus can average noisy mesoscale fields over large oceanic volumes at the expense of lack of horizontal resolution of any temperature or heat content features. Although the vertical resolution is limited, acoustic measurements can provide much needed temperature estimates at depths presently not sampled at all by the Argo system.

From Raw Observations to Scientific Analyses

From a pure observational perspective, the diversity of instruments and observing platforms involved in temperature data gathering at any one time, the shifts in technology throughout many decades of observations, the lack of detailed information about many historical data sets (e.g., types of XBT instruments used, depth at which near-surface temperatures are taken), the various parties involved in collecting observations, among other factors, make archiving and quality controlling the data a laborious and difficult task. Major efforts in the USA have been pursued at NOAA's National Oceanographic Data Center and are well documented in the World Ocean Database series produced by NOAA roughly every 4 years, with the last edition released in 2009 (e.g., [35, 36]). Other more regional compilations are also available (e.g., [37]), and no central archive includes all the collected temperature data. Data processing tasks commonly involve statistical checks for outliers, elimination of duplicate observations, correcting for depth biases, along with many subjective criteria for flagging "suspicious" observations. More restricted data compilations based on specific hydrographic programs like WOCE [38] allow for better quality control and accuracy. In the end, researchers must decide what data to use and to discard (e.g., [38, 39]) and scientific analysis and results can depend on such choices (e.g., [37, 40, 41]).

Apart from data quality issues, the irregular and sparse sampling in both space and time makes quantitative study of temperature and heat content variability for climate inference far from a trivial task. Most studies rely on objective analysis/optimal interpolation methods (e.g., [42, 43]) to fill in data gaps in both space and time and reduce the observations to regularly gridded fields in latitude and longitude

at given standard depth levels, which are more prone to scientific analysis. Objective analysis methods require assumptions about the nature of the fields being estimated (e.g., their degree of smoothness in space) and the statistics of the data (e.g., spatial and temporal correlation scales of data noise), which can influence how each data point is weighted to provide an estimated value at places where no data are available. As with data use, subjective choices are often involved and can lead to differences in results, particularly for regions where data are very sparse and estimates become more dependent on the details of the objective analysis method used. The series of World Ocean Atlas from NOAA (e.g., [44]) are a widely used example of a mean and seasonal temperature climatology produced from objective analysis applied to the wide variety of temperature measurements contained in the World Ocean Database [35, 36].

More advanced methods of data interpolation involve the use of ocean general circulation models (GCM), which embody the most complete description of the dynamic relations among all relevant observables (temperature, salinity, velocity, sea level) under strict laws of fluid motion and conservation principles of heat, momentum, and other quantities. Various data assimilation or state estimation techniques (e.g., [43, 45]) allow optimal combination of the information embedded in GCM codes with that contained in observations of all types. The use of such computationally intensive methods for climate analyses has been common practice in meteorology (e.g., [46]) and is becoming more common in oceanography (e.g., [47–49]) after rapid developments in ocean GCMs and data gathering capabilities, as well as in computing power, in the last decade. Most techniques involve minimization of an "objective" function that evaluates model-data misfits and thus require knowledge about data error statistics, which determine how tightly the model is allowed to fit the data. Books by Daley [43], Wunsch [45], and several others discuss the various basic approaches to data assimilation available. For the purposes of analyzing oceanic temperature and heat content variability in a climate context, it is helpful to use methods that produce temperature evolutions consistent with all the flow fields, air-sea fluxes, and other boundary and initial conditions. As discussed by Wunsch et al. [48], fitting the temperature observations must be achieved if possible through dynamically consistent adjustments in currents, atmospheric forcing, model physics, and other factors, and without introducing unphysical jumps in the temperature evolution, which would imply the violation of basic heat conservation principles.

Estimates of temperature fields, obtained either through objective analysis or model-data synthesis methods of the sort described above, provide the basis for a variety of climate analyses, including studies of air-sea interaction, sea level change, planetary heat balance, and many other topics. In the context of this entry, the focus is on oceanic heat content variability. Changes in heat content per unit area are just proportional to changes in temperature ΔT over a layer of thickness H and given by $\rho C_p H \Delta T$, where ρ is the density of seawater and C_p is its specific heat at constant pressure [4]. For typical values of $\rho \sim 1{,}028$ kg/m^3 and $C_p \sim 4{,}000$ J/kg/°C, increasing the mean temperature of the water column ($\sim$4,000 m) by 1°C implies a change in heat content of around 1.6×10^{10} J/m^2.

To achieve such warming over 1 year, an anomalous heat flux of ~500 W/m^2 would have to be applied. By the same token, an error in the annual change in mean temperature of 0.001°C amounts to an error in implied heat flux of 0.5 W/m^2. For comparison, present estimates of the planetary heat flux imbalance under possible global warming scenarios are of the order of 1 W/m^2 [50]. Thus, very small changes in oceanic temperatures can imply large changes in heat content, in terms of Earth's heat balance and climate, and accurate global measurements of ocean temperatures, from the surface to the bottom, and from the tropics to the polar regions, are deemed essential in this context.

Spatial and Temporal Patterns of Variability on Climate Scales

A vast literature documents numerous attempts at describing the temperature and heat content variability in the global oceans, either from straightforward analysis of the temperature observations (e.g., [51]), from objective analysis methods using only temperature or also other types of data (e.g., [29]), or from data-constrained model solutions based on the most sophisticated assimilation methods (e.g., [52]). In this section, a summary of the current state of knowledge on the subject is presented, focusing on the advances made in most recent years. Information on the upper ocean layers is considerably richer in detail than on the deeper layers, as the amount of data quickly dwindles with increasing depth. Temperature and heat content analyses are discussed interchangeably. The simple relation between temperature and heat content discussed in the previous section can be used to approximately convert between the two variables.

Spatial and temporal coverage of the near-surface ocean is far better than at any other depth level, given the early practices of surface measurements from ships and more recently the global daily coverage brought by the advent of the satellite era. These widely different measurement techniques have been combined to produce records of what is commonly called sea surface temperature (SST). What SST values represent is, however, not a trivial issue because of the presence of vertical temperature gradients very near the surface. Much of the in situ data comes without precise information on the depth of measurement, which can be anywhere from near the surface to a few meters below it. In turn, satellite sensors sample the upper few microns or millimeters, depending on whether infrared or microwave instruments are used. As such, satellite values can be influenced by strong diurnal effects affecting the skin layer and can also differ substantially from "bulk" SST properties representing an average of the upper few meters (~10 m) of the ocean. A detailed account of many of these issues, including various definitions of SST and how in situ and satellite data are being used to improve present and past SST records, can be found in Donlon et al. [21] and references therein.

Despite all the inherent ambiguities, SST records constitute one of the most important oceanic datasets for climate studies. Historical data compilations

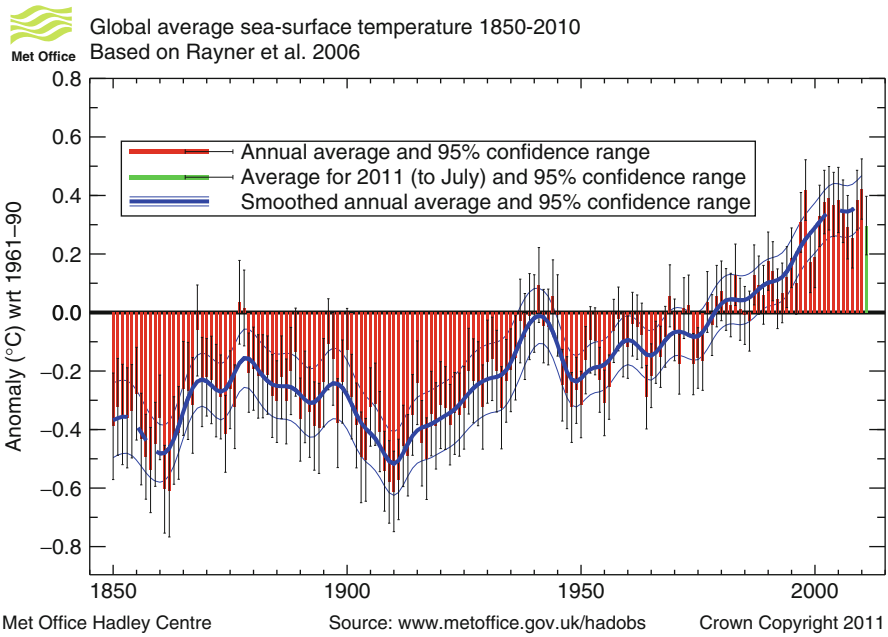

Fig. 8.4 Global mean sea surface temperature for the period 1850–2009 (anomalies relative to 1961–1990) based on Rayner et al. [54] and produced by the UK Met Office Hadley Center (http://www.metoffice.gov.uk/hadobs)

(e.g., [19]) provide estimates of SST since the middle of the nineteenth century, although the earlier periods have much sparser data coverage (e.g., [53]). When global mean estimates are attempted, a record of increasing SST over the last century emerges from most studies, consistent with a warming planet [20, 54, 55]. As can be seen in Fig. 8.4, present global mean SST estimates are almost 1°C warmer than in the early twentieth century. Apart from a long-term warming trend, variability at all time scales is present in the annual mean values. Considerable uncertainties are involved, however. Time-varying instrumental biases are a particular concern (e.g., [56]) and efforts to correct such errors are likely to continue (e.g., [57]).

While global mean SST is an essential climate index, just like surface air temperature, numerous climate variables and processes are related to SST spatial variations, from the intensity and quantity of tropical cyclones, which depend on tropical warm waters to form and grow, to the onset of deep convection in the ocean, which can happen in the presence of cold, dense surface waters at high latitudes. A great deal of effort has thus been devoted to understanding major spatial and temporal patterns of SST variability in relation to air-sea fluxes, ocean and atmosphere dynamics, and their connection to climate variability. Deser et al. [53] review major modes of interannual and multi-decadal variability with clear SST signatures, including the El Niño-Southern Oscillation, the Pacific Decadal Oscillation, the North

Atlantic Oscillation, and the Atlantic Multi-Decadal Oscillation. As one parameter controlling air-sea transfers, knowledge of SST is key to making long-range climate forecasts (e.g., [58]). In addition, the existence of century-long time series of SST with some spatial information provides essential surface boundary conditions for atmospheric model simulations of the past climate and allows for model calibration and validation (e.g., [46, 59]).

Depending on region and time of year, SST observations can provide a window on mixed layer temperatures and can thus yield information on heat content in the near-surface layers of the ocean, assuming the mixed layer depth is known. Ultimately, for a full and quantitative description of heat content variability, subsurface temperature observations are needed. Until the implementation of the Argo system, a great majority of temperature profiles were based on XBT casts and confined to the upper 700 m. Multi-decadal analyses of large-scale temperature and heat content variability have thus focused on these depths. Early observations are, however, quite thin and time series studies are restricted to the period since the 1950s. Apart from the presence of a strong seasonal cycle, which is mainly confined to the upper 100–200 m of the water column (e.g., [60, 61]) and driven by heat exchange with the atmosphere, the main interest has been on determining variability in temperature and heat content at scales of years to decades.

Numerous temperature analyses have produced estimates of mean oceanic heat content anomalies for depths 0–700 m (e.g., [37, 41, 62]). Several such time series, all using mostly the same available data but different processing procedures, are reproduced in Fig. 8.5 [63]. Most analyses indicate warming and increasing heat content of the upper ocean over the last three decades, in agreement with analyses of SST (see Fig. 8.4). The long-term warming has been related to anthropogenic influences by several studies (e.g., [64, 65]). Superposed on the general warming are interannual and decadal signals that can be caused by natural climate variability, including the impact of volcanism and variable solar radiation [65–68]. The spread among all series is considerable, however, and this can be an issue particularly if one is interested in studying their year-to-year evolution. Differences in the series can also affect the quantitative determination of long-term trends. Differences are not confined to the period before the 1990s when coverage is sparse (see Fig. 8.2) and methodologies to fill in data gaps can be influential. Other factors, including quality control and bias correction procedures, can affect the estimates, even over most well-covered periods [41].

Recent discovery of several systematic biases in XBT and Argo data [13, 40, 69] has led to various updates in mean heat content series. The estimates in Fig. 8.5 include several of these bias corrections, which imply major differences in temporal evolution with previously published results (e.g., [70]). Efforts to understand the differences in Fig. 8.5 are ongoing (e.g., [41, 63]) and likely to continue in the foreseeable future. Multi-instrument approaches to estimating heat content, such as combining in situ temperature and altimeter sea level [29] or comparing XBT and CTD temperature estimates [69] can be useful when trying to rid the observing system of systematic errors in the various data streams, which are difficult to detect otherwise. Ultimately

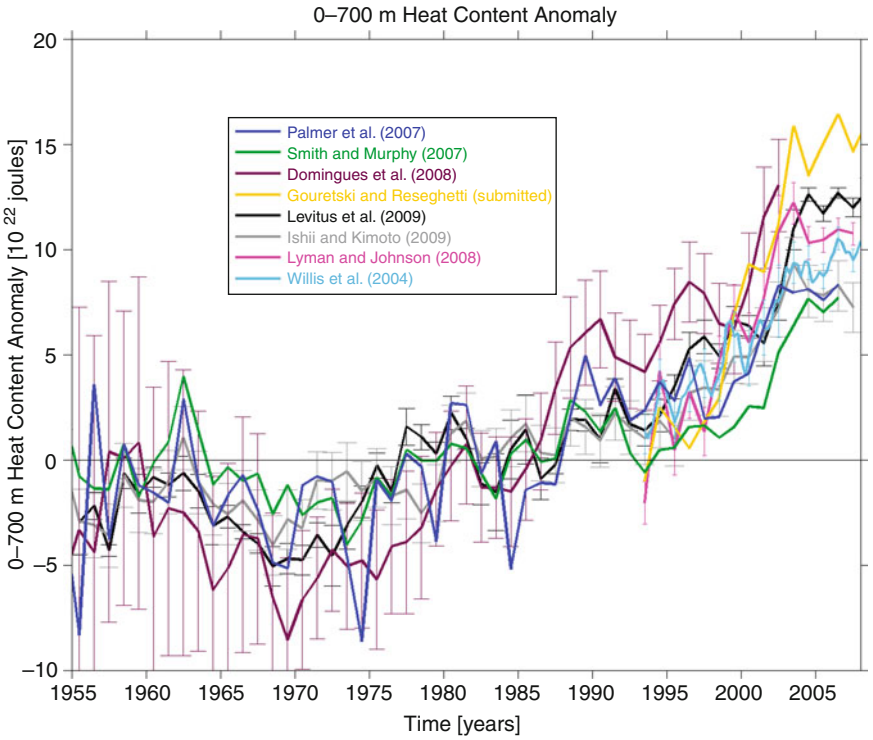

Fig. 8.5 Anomalies in upper ocean (0–700 m) heat content relative to the mean over the period 1955–2002. Various curves are from several data-based estimates (Reproduced from Fig. 8.2 of Palmer et al. [63]). The spread among all the curves is caused by several factors, including the specific data used, the applied bias corrections, and the objective analysis methods for smoothing and interpolation

the synthesis of all data sets using models and data assimilation can bring out similar benefits (e.g., [52, 71]).

If knowledge of spatial mean temperature and heat content variability, with all the averaging and noise reduction involved, suffers from significant uncertainties, robust information on spatial patterns of variability is even more problematic because of very poor data coverage in extensive areas such as the Southern Ocean (Fig. 8.2). Even for the more recent Argo period, significant observational gaps are still present in ice-covered regions and marginal seas (Fig. 8.3). Some of the earliest estimates of variability were based on differences over a few pentadal periods or on time series for whole oceanic basins, to allow for meaningful averages [72, 73]. More recently, state estimation/data assimilation methods have been brought to bear on the problem (e.g., [48, 74]).

Long-term trends in upper ocean heat content (0–700 m), calculated over approximately the last three decades from a number of different analyses and methods summarized in Carton and Santorelli [52], are shown in Fig. 8.6. Although the

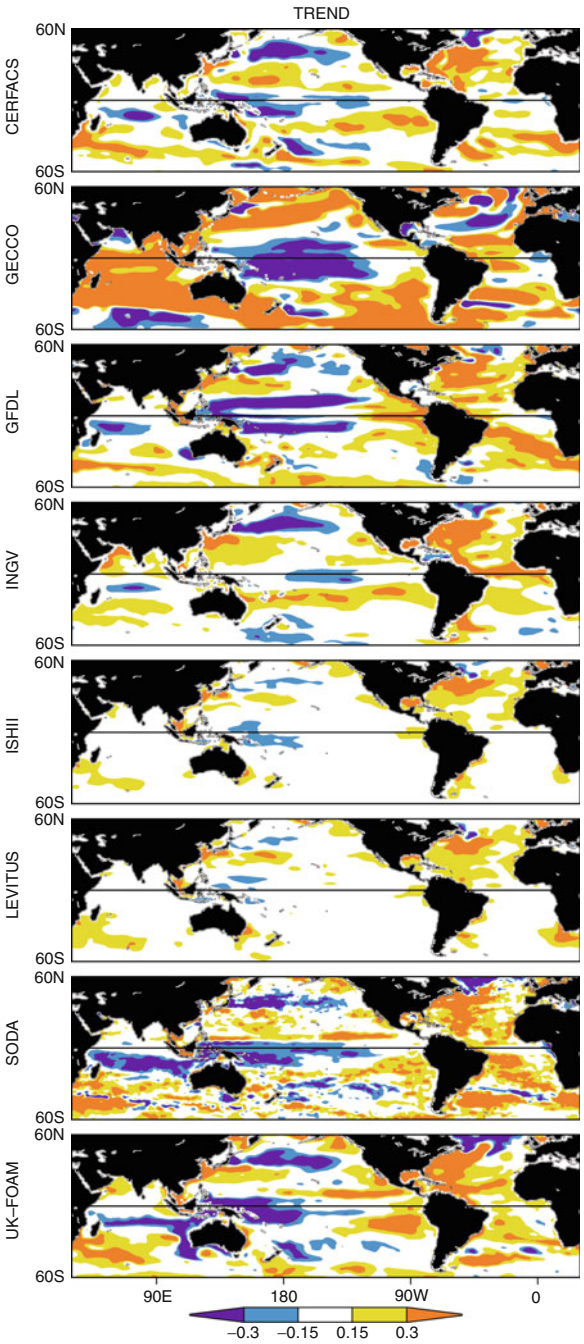

Fig. 8.6 Linear trends for heat content in the upper ocean (0–700 m) reproduced from Fig. 8.2 of Carton and Santorelli [52] and corresponding to several different analyses for approximately the period 1960–2005. Apart from the "Levitus" and "Ishii" fields, which are purely derived from observations, all others involve ocean models and data assimilation schemes. Details of all the analyses are given in Carton and Santorelli [52] and references therein. Coloring represents regions where values are outside the range $\pm$ 1.5 $\times$ 10^8 J/m^2/decade

warming trend in global mean heat content is clear in Fig. 8.5, the spatial patterns in Fig. 8.6 include both places of warming and cooling. Complex spatial and time variability patterns in ocean temperature fields are also evident in the acoustic measurements analyzed by Dushaw et al. [34]. The oceans are far from warming at the same rate everywhere. Despite considerable differences among all analyses, which can be taken as a crude measure of their uncertainty, there is a general tendency for warming in places like the Atlantic and parts of the south and north Indian Ocean, as well as cooling over the equatorial Pacific and parts of the North Pacific.

The inhomogeneous patterns of warming and cooling in Fig. 8.6 reflect the complexity of air-sea heat transfers and oceanic heat transports, both in the horizontal and in the vertical. Aside from the long-term (multi-decadal) scales represented in the trends in Fig. 8.6, heat content variability at all time scales permeates the available records (e.g., [52]). As with SST, some of the spatial patterns in upper ocean heat content can be related to primary modes of natural climate variability reviewed by Deser et al. [53]. Changes in major circulation systems such as the meridional overturning circulation in the North Atlantic [66] or the Antarctic Circumpolar Current in the Southern Ocean [75] can be involved. Achieving a full understanding of the mechanisms responsible for past upper ocean heat content variability is hampered, however, by the poor observational base. As societal focus shifts to the determination and understanding of regional climate variability and how it affects human life at a local level, the need to determine spatial patterns of variability in heat content will only grow in the future. Maintaining some of the recently implemented in situ and satellite observing capabilities is a minimum requirement to be able to monitor heat content variability both at the regional and global level.

As the focus of analysis descends to layers below the XBT maximum sampling depth of 700 m, the amount of historical observations diminishes considerably. Only the most recent period after the implementation of the Argo system, from 2003 onward, provides reasonable near-global coverage up to depths of around 2,000 m. The short record length precludes a comprehensive treatment of variability at all climate scales of interest, but the density and quality of the data provide for good estimates of spatial variability, both horizontally and vertically. Analyses of Argo data by von Schuckmann et al. [61] for the period 2003–2008 and comparisons with mean climatological temperature values confirm long-term warming tendencies, particularly in the North Atlantic, found by Levitus [72], Levitus et al. [76], and Antonov et al. [77] and show that temperature variability on interannual and decadal time scales can reach to 2,000 m and deeper, well below the XBT sampling range. The spatial and time structure of interannual temperature signals is quite complex, however.

Figure 8.7 reproduced from von Schuckmann et al. [61] shows an example of year-to-year zonally averaged temperature anomalies for the Atlantic Ocean, given as a function of depth and latitude. Typical amplitudes range between $\pm 0.2^{\circ}$C, alternating sign on relatively long ($\sim$1,000 km) meridional scales. Aside from the long-term warming already noted, other time scales are involved. Spatially, anomalies in Fig. 8.7 can show vertical coherence, with the same sign extending

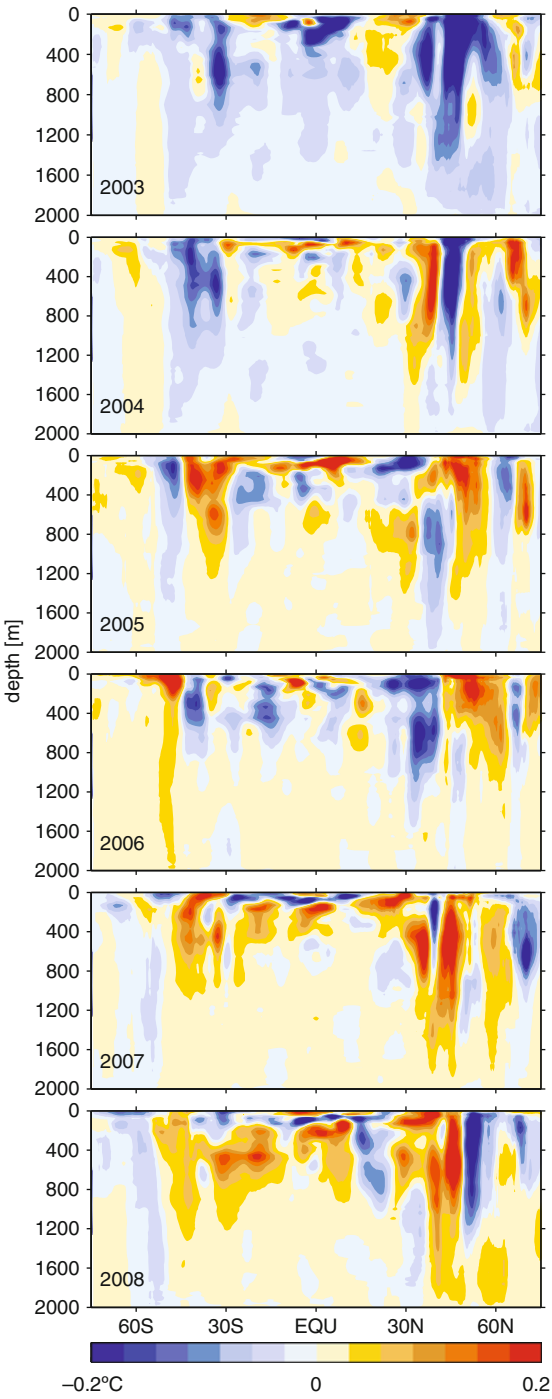

Fig. 8.7 Mean annual temperature anomalies for the period 2003–2008, calculated from Argo data as described in detail by von Schuckmann et al. [61]. Values represent zonal averages for the Atlantic basin (Reproduced from Fig. 8.9 of von Schuckmann et al. [61])

over most of the sampled water column, or considerable vertical structure including reversals of sign with depth. In addition, strongest anomalies are not always found at the surface, and sizable variability is apparent at all sampled depths, with deepest variability present at mid- and high latitudes. A variety of processes can be related to the temperature signals in Fig. 8.7, including changes in the position of subtropical and subpolar temperature fronts, strong air-sea interaction and onset of deep convection in the high latitudes, and changes in the strength of the horizontal circulation. von Schuckmann et al. [61] discuss some of the mechanisms behind the variability in Fig. 8.7 with references to other relevant works. In any case, only now is the observational system becoming dense enough to begin putting together a detailed temporal evolution of the three-dimensional temperature fields. A full understanding of these observations will likely come with the accumulation of good quality data and dedicated modeling and data synthesis efforts in the future (e.g., [49, 78]).

Below the Argo sampling maximum depth of 2,000 m, not even the most recent years are well sampled at all. Yet these very poorly observed layers represent approximately half of the volume of the global oceans. Most of the current knowledge about basin-scale temperature structures and variability in the deep/abyssal oceans comes from high-quality full-depth CTD casts obtained as part of global programs like WOCE [16] and earlier campaigns such as those during the International Geophysical Year in the late 1950s (e.g., [51]). Some attempts at including depths up to 3,000 m in calculations of heat content have been confined to highly averaged estimates in time and space (e.g., [76]). Most analyses, particularly for abyssal layers, tend to examine individual basin sections that have been reoccupied at various times, thus providing snapshots separated by several years to decades (e.g., [51, 79–82]). The observed changes in temperature are then used to infer variability, presumed to be long term and large scale in character, but great care must be taken to properly interpret such sparse observations.

Figure 8.8 shows an example of decadal temperature changes in the abyssal eastern South Indian Ocean from Johnson et al. [81]. Differences between temperature measurements taken in 1994–1995 and 2007 range between ±0.2°C, with strongest warming observed in latitudes south of 50S. Large variations are seen all the way to the bottom, well below 2,000 m. The warming in the Australian-Antarctic Basin below 3,500 m amounts to a mean change of +0.1°C and is statistically significant and generally consistent with other observational evidence [81]. Such a warming is equivalent to a heat flux imbalance of 0.9 W/m^2, which is substantially larger than values of 0.1 W/m^2 typically associated with geothermal heat flux at the ocean bottom [83]. Causes of the increase in temperature in Fig. 8.8 are thus likely related to changes in bottom circulation and water mass properties connected to surface processes around Antarctica, where bottom dense waters are formed through strong heat losses to the atmosphere and subsequently descend to great depths before spreading northward.

Abyssal temperature changes similar to those in Fig. 8.8 have been observed in many other ocean basins. For example, Fukusawa et al. [79], Kawano et al. [84], and Johnson et al. [80] document deep and abyssal warming across several sections of the

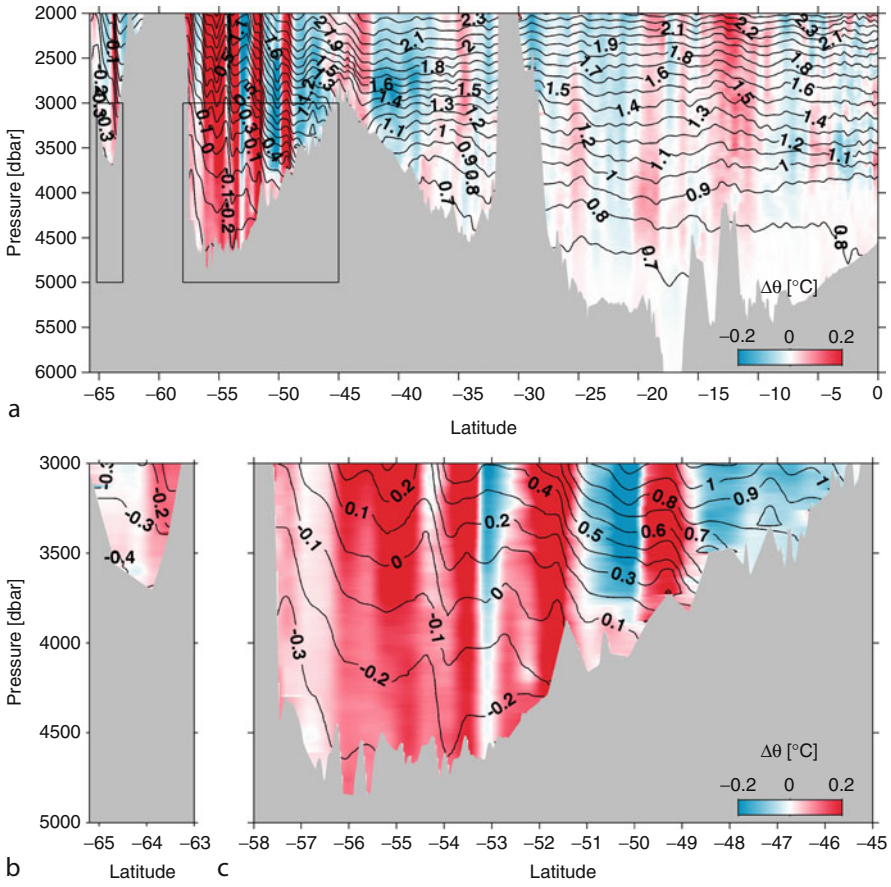

Fig. 8.8 Mean values of potential temperature (*contours*) and differences in potential temperature between the periods 1994–1995 and 2007 as a function of latitude and pressure (in decibars, which are approximately equivalent to depth in meters). Section covers most of the Southern Hemisphere, from Antarctica to the equator, at longitudes between 82E and 95E to the west of Australia. Panels (**b**) and (**c**) zoom in on the *boxes* drawn in (**a**) corresponding to abyssal waters in the Princess Elizabeth Trough and the Australian-Antarctic Basin southern most region. Full details are provided in Johnson et al. [81] (Reproduced from Fig. 8.4 of Johnson et al. [81])

North and South Pacific. Abyssal changes tend to be larger and decrease in range from south to north, with section mean changes in potential temperature as large as 0.01°C [80]. Similar warming of about 0.04°C is found in the bottom 1,500 m of the Brazil Basin in the South Atlantic [85]. As with the findings in the Indian Ocean shown in Fig. 8.8, these temperature changes in the abyssal Pacific and Atlantic oceans cannot be explained solely by effects of geothermal heat flux and are likely related to anomalies advected from the south, where sources of bottom water are located [29, 79, 80, 85].

Although changes in abyssal temperatures are relatively small compared to the changes in the upper ocean (cf. Figs. 8.7 and 8.8), these changes involve large volumes of water and can amount to substantial signals in global oceanic heat content. Estimates of multi-decadal changes in global mean heat content for depths 0–3,000 m can differ by 25% from those based on the upper 700 m only (e.g., [76]). Contributions from abyssal depths may be smaller but not negligible. For example, if the observed abyssal warming in the western South Atlantic is reflective of global mean changes, it would imply decadal changes in heat content in the abyssal ocean close to 50% of those observed in the upper ocean [85]. Similarly, abyssal temperature changes and corresponding steric height effects could account for significant sea level signals on basin scales. Observed warming in the bottom waters of the South Indian Ocean implies changes in sea level as large as 4 cm over nearly a decade [81]. For comparison, global mean rates of sea level rise have been around 3 cm/decade in recent years (e.g., [86]).

Given that most deep and abyssal observations are confined to a few sections for each basin, the spatial extent of the observed long time scale signals at depths is not known. Thus, global means or even basin means are difficult to estimate [76, 82] and the impact of deep and abyssal temperature changes on large-scale heat content and sea level remains the subject of speculation. Besides the extremely sparse sampling in space, examining snapshots of the temperature field every few years or decades presents other sampling issues. Fluctuations over a range of time scales, from hours to decades, can be present even at depth. As can be seen in the example in Fig. 8.8, differences of any two temperature sections contain numerous relatively small-scale features, which are generally related to the presence of eddies with time scales of a few months or shorter and with temperature signatures reaching all the way to the bottom. This eddy "noise" is large enough to make much of the differences in Fig. 8.8 and in many other similar studies statistically insignificant (e.g., [80, 81]). Much denser observations in both space and time are needed to improve statistical robustness and be able to discern whether observed changes are truly long term or the effect of short time scales, which cannot be resolved in the present records. By the same token, for the deep ocean, dynamical interpolations and extrapolations of the data in time and space using model and estimation techniques assume increased importance [48, 49]. These efforts provide the ability to use information from all observations, not just temperature, including data collected at other depths, to provide "best" estimates of the temperature variability in space and time.

Future Directions

Significant investment at the international level will be needed to sustain the current array of in situ and satellite systems (primarily Argo and altimetry) relevant to ocean heat content and temperature monitoring. At the same time, the severe under-sampling of many regions of the global oceans, including the high latitudes

covered by sea ice and the deep layers below 2,000 m not sampled by Argo system, continues to be a problem in the quest to achieve truly global measurements of ocean temperatures and heat content at appropriate temporal resolutions for climate monitoring and other purposes. As society grapples with the need to assess current climate conditions and predict their evolution on decadal and longer time scales, future developments in ocean monitoring capabilities gain increased significance. Several paths for action are foreseen, with some of the seeds of an improved observing and estimating system already in place.

The development of float technology promises to extend the capabilities of the Argo system to ice-covered and deep waters [18, 87]. At the same time, efforts are underway to improve sampling of the marginal and coastal seas (e.g., [88, 89]). In all these areas, apart from the use of autonomous Argo-type floats, other observing platforms and technologies are expected to contribute to the collection of temperature data. Programs that use marine mammals for profiling at some high latitude regions (e.g., [90]) could be expanded. Gliders [91, 92] can provide routine profiling with considerably more control on sampling patterns than Argo-type floats and technology improvements could lead to operational glider deployments in many regions in the future. Moored instrumentation at all depths will be involved, as part of calibration programs or monitoring of "choke" points where variability and transports of ocean properties such as heat and freshwater require specific in situ observations.

Besides temperature measurements, other observing systems indirectly relevant for the determination of ocean heat content will see substantial advances over the next decade. High-precision satellite altimetry has reached quasi-operational status with the launch of Jason-2 and the scheduled launch of Jason-3 for 2014. A number of other missions scheduled to fly over the next few years will deliver denser surface height observations in space and time [93]. Potential breakthrough sampling is the goal of the Surface Water and Ocean Topography mission, which is still in the initial stages of planning [94]. Similarly, measurements of the variable gravity field from space with higher accuracies than presently possible should complement developments in altimetry to deliver better estimates of full-depth integrated changes in heat content [31]. In terms of in situ observations, acoustic thermometry [32] has been successfully exploited in the North Pacific [34] and the Arctic [95]. Expanded acoustic measurements discussed by Dushaw et al. [33] promise to deliver much needed coverage of deep layers over basin scales. Such measurements can also contribute to the monitoring of temperature change and heat transport variability across important "choke points" in the ocean, as in the ongoing program in Fram Strait [33].

Within the coming years, concerted and stepped up efforts to create an integrated global observing system will deliver improved measurements of temperature as well as many other oceanic parameters (salinity, velocity, bottom pressure, etc.) which are all indirectly linked to the determination of ocean heat content. Appropriate synthesis of all these diverse measurements, providing interpolation and extrapolation of the observations under rigorous physical conservation principles, can only be achieved with the use of models and state estimation techniques (e.g., [78]). In the future, as is established practice with the atmosphere (e.g., [46]), global estimates of temperature

and heat content will come from the implementation of such systems. Similar machinery can be applied to the efficient design of observing systems that maximize collection of relevant information for the purposes of climate monitoring, analysis, and prediction [96]. Glider technologies begin to provide the possibility of adaptive sampling procedures, under which instruments are continuously directed at making measurements at times and places deemed important for determining the evolution of a given parameter of interest.

The combination of developments in observing, modeling, and estimating systems promises to deliver a revolution in the way ocean temperatures and heat content are determined in the near future. The impact on many areas of ocean and climate science will be hard to miss, from making it possible to relate sea level change to increased heat transfer from the atmosphere or melting of ice sheets, to providing better understanding of the variable Earth's radiation balance and hydrological cycle.

Acknowledgments The author is indebted to J. Carton, G. Johnson, J. Kennedy, J. Lyman, M. Palmer, K. von Schuckmann, and S. Walker for help with the figures reproduced here. The support of NASA and the National Oceanographic Partnership Program is gratefully acknowledged.

Bibliography

Primary Literature

1. Stommel H (1965) The Gulf stream: a physical and dynamical description, 2nd edn. University of California Press, Berkeley, 248 pp
2. Thomson CW (1877) The voyage of the Challenger, vol 2, The Atlantic. Macmillan, London, 396 pp
3. Wüst G, Defant A (1936) Atlas zur Schichtung und Zirkulation des Atlantischen Ozeans. Schnitte und Karten von Temperatur, Salzgehalt und Dichte. In: Wissenschaftliche Ergebnisseder Deutschen Atlantischen Expedition auf dem Forschungs-und Vermessungsschiff "Meteor" 1925–1927, 6: Atlas, 103 plates
4. Gill AE (1982) Atmosphere–ocean dynamics. Academic, New York, 662 pp
5. Sverdrup HU, Johnson MW, Fleming RH (1942) The oceans: their physics, chemistry and general biology. Prentice-Hall, New York
6. Talley LD (2007) In: Sparrow M, Chapman P, Gould J (eds) Hydrographic atlas of the world ocean circulation experiment (WOCE), vol 2, Pacific Ocean. International WOCE Project Office, Southampton
7. Baker DJ Jr (1981) Ocean instruments and experiment design. In: Warren BA, Wunsch C (eds) Evolution of physical oceanography. MIT Press, Cambridge
8. Spilhaus AF (1938) A bathythermograph. J Mar Res 1:95–100
9. Spilhaus AF (1940) A detailed study of the surface layers of the ocean in the neighborhood of the Gulf Stream with the aid of rapid measuring hydrographic instruments. J Mar Res 3:51–75
10. Snodgrass JM (1968) Instrumentation and communications. In: Brahtz JF (ed) Ocean engineering: goals, environment, technology. Wiley, New York, pp 393–477
11. Lyman JM, Johnson GC (2008) Estimating annual global upper-ocean heat content anomalies despite irregular in situ ocean sampling. J Climate 21:5629–5641

12. Hanawa K, Rual P, Bailey R, Sy A, Szabados M (1995) A new depth-time equation for Sippican or TSK T-7, T-6, and T-4 expendable bathythermographs (XBT). Deep-Sea Res I 42:1423–1451
13. Willis JK, Lyman JM, Johnson GC, Gilson J (2009) In situ data biases and recent ocean heat content variability. J Atmos Ocean Tech 26:846–852
14. Gregg MC (1998) Estimation and geography of diapycnal mixing in the stratified ocean. In: Imberger J (ed) Physical processes in lakes and oceans, vol 54. Amer Geophys Union, Washington, DC, pp 305–338
15. Thorpe SA (2004) Recent developments in the study of ocean turbulence. Ann Rev Earth Planet Sci 32:91–109
16. Siedler G, Church J, Gould J (2001) Ocean circulation and climate: observing and modelling the global ocean. Academic, Boston
17. Roemmich D, Johnson GC, Riser GCS, Davis R, Gilson J, Owens WB, Garzoli SL, Schmid C, Ignaszewski M (2009) The argo program: observing the global ocean with profiling floats. Oceanography 22:34–43
18. Freeland, H, Roemmich D, Garzoli S, LeTraon PY, Ravichandran M, Riser S, Thierry V, Wijffels S, Belbéoch M, Gould J, Grant F, Ignazewski M, King B, Klein B, Mork K, Owens B, Pouliquen S, Sterl A, Suga T, Suk M, Sutton P, Troisi A, Vélez-Belchi P, Xu J (2010) Argo – A decade of progress. In: Hall J, Harrison DE, Stammer D (eds) Proceedings of the OceanObs'09: sustained ocean observations and information for society, vol 2, Venice, 21–25 Sep 2009
19. Woodruff SD, Diaz HF, Kent EC, Reynolds RW, Worley SJ (2008) The evolving SST record from ICOADS. In: Brönnimann S, Luterbacher J, Ewen T, Diaz HF, Stolarski RS, Neu U (eds) Climate variability and extremes during the past 100 years, vol 33, Advances in global change research. Springer, Dordrecht, pp 65–83
20. Reynolds RW, Smith TM (1994) Improved sea surface temperature analyses using optimal interpolation. J Climate 7:929–948
21. Donlon C, Robinson IS, Casey KS, Vasquez-Cuervo J, Armstrong E, Arino O, Gentlemann CL, May DA, LeBorgne P, Piolle J, Barton I, Beggs H, Poulter DJS, Merchant CJ, Bingham A, Heinz S, Harris A, Wick GA, Emery B, Minnett PJ, Evans R, Llewellyn-Jones D, Mutlow CT, Reynolds R, Hawamura H, Rayner NA (2007) The global ocean data assimilation experiment high-resolution sea surface temperature pilot project. Bull Am Met Soc 88:1197–1213
22. McPhaden MJ, Busalacchi AJ, Cheney R, Donguy J-R, Gage KS, Halpern D, Ji M, Julian P, Meyers G, Mitchum GT, Niller PP, Picau J, Reynolds RW, Smith N, Takeuchi K (1998) The tropical ocean-global atmosphere (TOGA) observing system: a decade of progress. J Geophys Res 103:14169–14240
23. Bourlès B, Lumpkin R, McPhaden MJ, Hernandez F, Nobre P, Campos E, Yu L, Planton S, Busalacchi A, Moura AD, Servain J, Trotte J (2008) The PIRATA program: history, accomplishments, and future directions. Bull Am Met Soc 89:1111–1125
24. McPhaden MJ, Meyers G, Ando K, Masumoto Y, Murty VSN, Ravichandran M, Syamsudin F, Vialard J, Yu L, Yu W (2009) RAMA: the research moored array for African-Asian-Australian monsoon analysis and prediction. Bull Am Meteorol Soc 90:459–480
25. Send U, Weller RA, Wallace D, Chavez F, Lampitt RL, Dickey T, Honda M, Nittis K, Lukas R, McPhaden M, Feely R (2010) OceanSITES. In: Hall J, Harrison DE, Stammer D (eds) Proceedings of OceanObs'09: sustained ocean observations and information for society, vol 2, Venice, 21–25 Sep 2009. ESA Publication WPP-306, doi:10.5270/OceanObs09.cwp.78
26. Michaels AF, Knap AH (1996) Overview of the U.S. JGOFS BATS and hydrostation S program. Deep-Sea Res 43(2–3):157–198
27. Karl DM, Lukas R (1996) The Hawaii ocean time-series (*HOT*) program: background, rationale, and field implementation. Deep-Sea Res II 43:129–156
28. White WB, Tai C-K (1995) Inferring interannual changes in global upper ocean heat storage from TOPEX altimeter. J Geophys Res 100:24943–24954
29. Willis JK, Roemmich D, Cornuelle B (2004) Interannual variability in upper ocean heat content, temperature, and thermosteric expansion on global scales. J Geophys Res 109:C12036. doi:10.1029/2003JC002260

30. Ponte RM (1999) A preliminary model study of the large-scale seasonal cycle in bottom pressure over the global ocean. J Geophys Res 104:1289–1300
31. Jayne SR, Wahr JM, Bryan FO (2003) Observing ocean heat content using satellite gravity and altimetry. J Geophys Res 108:3031. doi:10.1029/2002JC001619
32. Munk WH, Forbes AMG (1989) Global ocean warming: an acoustic measure? J Phys Oceanogr 19:1765–1778
33. Dushaw B, Au W, Beszczynska-Möller A, Brainard R, Cornuelle B, Duda T, Dzieciuch M, Fahrbach E, Forbes A, Freitag L, Gascard J-C, Gavrilov A, Gould J, Howe B, Jayne S, Johannessen OM, Lynch J, Martin D, Menemenlis D, Mikhalevsky P, Miller JH, Munk WH, Nystuen J, Odom R, Orcutt J, Rossby T, Sagen H, Sandven S, Simmen J, Skarsoulis E, Stephen R, Vinogradov S, Wong KB, Worcester PF, Wunsch C (2010) A global ocean acoustic observing network. In: Hall J, Harrison DE, Stammer D (eds) Proceedings of OceanObs'09: sustained ocean observations and information for society, vol 2, Venice, 21–25 Sep 2009. ESA Publication WPP-306, doi:10.5270/OceanObs09.cwp.25
34. Dushaw BD, Worcester PF, Munk WH, Spindel RC, Mercer JA, Howe BM, Metzger K Jr, Birdsall TG, Andrew RK, Dzieciuch MA, Cornuelle BD, Menemenlis D (2009) A decade of acoustic thermometry in the North Pacific Ocean. J Geophys Res 114:C07021. doi:10.1029/2008JC0051
35. Boyer TP, Antonov JI, Baranova OK, Garcia HE, Johnson DR, Locarnini RA, Mishonov AV, O'Brien TD, Seidov D, Smolyar IV, Zweng MM (2009) World ocean database 2009. In: Levitus S (ed) NOAA atlas NESDIS 66. US Gov Printing Office, Washington, DC, p 219, DVDs
36. Johnson DR, Boyer TP, Garcia HE, Locarnini RA, Baranova OK, Zweng MM (2009) World ocean database 2009 documentation. In: Levitus S (ed) NODC internal report 20. US Government Printing Office, Washington, DC, p 175
37. Ishii M, Kimoto M (2009) Reevaluation of historical ocean heat content variations with time varying XBT and MBT depth bias corrections. J Oceanogr 65:287–299
38. Gouretski VV, Koltermann KP (2004) WOCE global hydrographic climatology [CD-ROM], Ber Bundesamt Seeschiffahrt Hydrogr Rep 35. Bundesamt Seeschiffahrt Hydrogr, Hamburg, pp 52
39. Worthington LV (1981) The water masses of the world ocean: some results of a fine-scale census. In: Warren BA, Wunsch C (eds) Evolution of physical oceanography. MIT Press, Cambridge
40. Gouretski VV, Kolterman KP (2007) How much is the ocean really warming? Geophys Res Lett 34:L01610. doi:10.1029/2006GL027834
41. Lyman JM, Good SA, Gouretski VV, Ishii M, Johnson GC, Palmer MD, Smith DM, Willis JK (2010) Robust warming of the global upper ocean. Nature 465:334–337
42. Bretherton FP, Davis RE, Fandry CB (1976) Technique for objective analysis and design of oceanographic experiments applied to MODE-73. Deep-Sea Res 23:559–582
43. Daley R (1991) Atmospheric data analysis. Cambridge University Press, Cambridge, 457 pp
44. Locarnini RA, Mishonov AV, Antonov JI, Boyer TP, Garcia HE (2010) World ocean atlas 2009, volume 1: Temperature. In: Levitus S (ed) NOAA Atlas NESDIS 68. U.S. Government Printing Office, Washington, DC, pp 184
45. Wunsch C (1996) The ocean circulation inverse problem. Cambridge University Press, Cambridge
46. Kalnay E, Kanamitsu M, Kistler R, Collins W, Deaven D, Gandin L, Iredell M, Saha S, White G, Woollen J, Zhu Y, Leetmaa A, Reynolds R, Chelliah M, Ebisuzaki W, Higgins W, Janowiak J, Mo KC, Ropelewski C, Wang J, Jenne R, Joseph D (1996) The NCEP/NCAR 40-year reanalysis project. Bull Am Meteor Soc 77:437–470
47. Carton JA, Giese BS, Grodsky SA (2005) Sea level rise and the warming of the oceans in the simple ocean data assimilation (SODA) ocean reanalysis. J Geophys Res 110:C09006. doi:10.1029/2004JC002817

48. Wunsch C, Ponte RM, Heimbach P (2007) Decadal trends in sea level patterns: 1993–2004. J Climate 20:5889–5911
49. Köhl A, Stammer D, Cornuelle BD (2007) Interannual to decadal changes in the ECCO global synthesis. J Phys Oceanogr 37:313–337
50. Hansen J, Nazarenko L, Ruedy R, Sato M, Willis J, Del Genio A, Koch D, Lacis A, Lo K, Menon S, Novakov Y, Perlwitz J, Russell G, Schmidt GA, Tausnev N (2005) Earth's energy imbalance: confirmation and implications. Science 308:1431–1435
51. Roemmich D, Wunsch C (1984) Apparent changes in the climatic state of the deep North Atlantic Ocean. Science 307:447–450
52. Carton JA, Santorelli A (2008) Global decadal upper-ocean heat content as viewed in nine analyses. J Climate 21:6015–6035
53. Deser C, Alexander MA, Xie S-P, Phillips AS (2010) Sea surface temperature variability: patterns and mechanism. Annu Rev Mar Sci 2:115–143
54. Rayner NA, Brohan P, Parker DE, Folland CK, Kennedy JJ, Vanicek M, Ansell TJ, Tett SFB (2006) Improved analyses of changes and uncertainties in sea surface temperature measured in situ since the mid-nineteenth century: the HadSST2 dataset. J Climate 19:446–469
55. Smith TM, Reynolds RW, Peterson TC, Lawrimore J (2008) Improvements to NOAA's historical merged land-ocean surface temperature analysis (1880–2006). J Climate 21:2283–2296
56. Thompson DWJ, Kennedy JJ, Wallace JM, Jones PD (2008) A large discontinuity in the mid-twentieth century in observed global-mean surface temperature. Nature 453:646–649
57. Rayner NA, Kaplan A, Kent EC, Reynolds RW, Brohan P, Casey KS, Kennedy, JJ, Woodruff SD, Smith TM, Donlon C, Breivik LA, Eastwood S, Ishii M, Brandon T (2010) Evaluating climate variability and change from modern and historical SST observations. In: Hall J, Harrison DE, Stammer D (eds) Proceedings of OceanObs'09: sustained ocean observations and information for society, vol 2, Venice, 21–25 Sep 2009. ESA Publication WPP-306, doi:10.5270/OceanObs09.cwp.71
58. Chen D, Cane MA, Kaplan A, Zebiak SE, Huang DJ (2004) Predictability of El Niño over the past 148 years. Nature 428:733–736
59. Compo GP, Whitaker JS, Sardeshmukh PD (2006) Feasibility of a 100 year reanalysis using only surface pressure data. Bull Am Met Soc 8:175–190
60. Antonov JI, Levitus S, Boyer TP (2004) Climatological annual cycle of ocean heat content. Geophys Res Lett 31:L04304. doi:10.1029/2003GL018851
61. von Schuckmann K, Galliard F, Le Traon P-Y (2009) Global hydrographic variability patterns during 2003–2008. J Geophys Res 114. doi:10.1029/2008JC005237
62. Levitus S, Antonov JI, Boyer TP, Locarnini RA, Garcia HE, Mishonov AV (2009) Global ocean heat content 1955–2008 in light of recently revealed instrumentation problems. Geophys Res Lett 36:L07608. doi:10.1029/2008GL037155
63. Palmer MD, Antonov J, Barker P, Bindoff N, Boyer T, Carson M, Domingues CM, Gille S, Gleckler P, Good S, Gourtetski V, Guinehut S, Haines K, Harrison DE, Ishii M, Johnson GC, Levitus S, Lozier MS, Lyman JM, Meijers A, von Schuckmann K, Smith D, Wijffels S, Willis J (2010) Future Observations for Monitoring Global Ocean Heat Content. In: Hall J, Harrison DE, Stammer D (eds) Proceedings of OceanObs'09: sustained ocean observations and information for society, vol 2, Venice, 21–25 Sep 2009. ESA Publication WPP-306, doi:10.5270/OceanObs09.cwp.68
64. Levitus S, Antonov JL, Wang J, Delworth TL, Dixon KW, Broccoli AJ (2001) Anthropogenic warming of earth's climate system. Science 292:267–270
65. Barnett TP, Pierce DW, AchutaRao KM, Gleckler PJ, Santer BD, Gregory JM, Washington WM (2005) Penetration of human-induced warming into the world's oceans. Science 309:284–287
66. Lozier MS, Leadbetter S, Williams RG, Roussenov V, Reed MSC, Moore NJ (2008) The spatial pattern and mechanisms of heat content change in the North Atlantic. Science 319:800–803

67. Church JA, White NJ, Arblaster JM (2005) Significant decadal-scale impact of volcanic eruptions on sea level and ocean heat content. Nature 438:74–77
68. White WB, Dettinger MD, Cayan DR (2003) Sources of global warming of the upper ocean on decadal period scales. J Geophys Res 108:3248. doi:10.1029/2002JC001396
69. Wijffels SE, Willis J, Domingues CM, Barker P, White NJ, Gronell A, Ridgway K, Church JA (2008) Changing eXpendable BathyThermograph fallrates and their impact on estimates of thermosteric sea level rise. J Climate 21:5657–5672. doi:10.1175/2008JCLI2290.1
70. Domingues CM, Church JA, White NJ, Gleckler PJ, Wijffels SE, Barker PM, Dunn JR (2008) Improved estimates of upper-ocean warming and multi-decadal sea-level rise. Nature 453:1090–1093. doi:10.1038/nature07080
71. Stammer D, Köhl A, Awaji T, Balmaseda M, Behringer D, Carton J, Ferry N, Fischer A, Fukumori I, Giese B, Haines K, Harrison DE, Heimbach P, Kamachi M, Keppenne C, Lee T, Masina S, Menemenlis D, Ponte R, Remy E, Rienecker M, Rosati A, Schröter J, Smith D, Weaver A, Wunsch C, Xue Y (2010) Multi-model ensemble ocean synthesis in support of climate diagnostics. In: Hall J, Harrison DE, Stammer D (eds) Proceedings of OceanObs'09: sustained ocean observations and information for society, vol 2, Venice, 21–25 Sep 2009. ESA Publication WPP-306, doi:10.5270/OceanObs09.cwp.85
72. Levitus S (1989) Interpentadal variability of temperature and salinity at intermediate depths of the North Atlantic Ocean, 1970–74 versus 1955–59. J Geophys Res 94:6091–6131
73. Levitus S, Antonov J, Boyer TP, Stephens C (2000) Warming of the world ocean. Science 287:2225–2229
74. Köhl A, Stammer D (2008) Decadal sea level changes in the 50-year GECCO ocean synthesis. J Climate 21:1876–1890
75. Böning CW, Dispert A, Visbeck M, Rintoul SR, Schwarzkopf FU (2008) The response of the Antarctic circumpolar current to recent climate change. Nature Geosci 1:864–869
76. Levitus S, Antonov JI, Boyer TP (2005) Warming of the world ocean, 1955–2003. Geophys Res Lett 32:L02604. doi:10.1029/2004GL021592
77. Antonov JI, Levitus S, Boyer TP (2005) Thermosteric sea level rise, 1955–2003. Geophys Res Lett 32:L12602. doi:10.1029/2005GL023112
78. Wunsch C, Heimbach P, Ponte RM, Fukumori I, The ECCO-GODAE Consortium Members (2009) The global general circulation of the ocean estimated by the ECCO-consortium. Oceanography 22:88–103
79. Fukasawa M, Freeland H, Perkin R, Watanabe T, Uchida H, Nishina A (2004) Bottom water warming in the North Pacific Ocean. Nature 427:825–827. doi:10.1038/nature02337
80. Johnson GC, Mecking S, Sloyan BM, Wijffels SE (2007) Recent bottom water warming in the Pacific Ocean. J Climate 20:5365–5375. doi:10.1175/2007JCLI1879.1
81. Johnson GC, Purkey SG, Bullister JL (2008) Warming and freshening in the abyssal southeastern Indian Ocean. J Climate 21:5351–5363. doi:10.1175/2008JCLI2384.1
82. Purkey SG, Johnson GC (2010) Warming of global abyssal and deep Southern Ocean waters between the 1990s and 2000s: contributions to global heat and sea level rise budgets. J Climate 23:6336–6351
83. Stein C, Stein S (1992) A model for the global variation in oceanic depth and heat flow with lithospheric age. Nature 359:123–129
84. Kawano T, Fukasawa M, Kouketsu S, Uchida H, Doi T, Kaneko I, Aoyama M, Schneider W (2006) Bottom water warming along the pathway of lower circumpolar deep water in the Pacific Ocean. Geophys Res Lett 33:L23613. doi:10.1029/2006GL027933
85. Johnson GC, Doney SC (2006) Recent western South Atlantic bottom water warming. Geophys Res Lett 33:L14614. doi:10.1029/2006GL026769
86. Cazenave A, Nerem RS (2004) Present-day sea level change: observations and causes. Rev Geophys 42:RG3001. doi:10.1029/2003RG000139
87. Klatt O, Boebel O, Fahrbach E (2007) A profiling float's sense of ice. J Atmos Ocean Technol 24(7):1301–1308

88. Poulain P, Barbanti R, Font J, Cruzado A, Millot C, Gertman I, Griffa A, Molcard A, Rupolo V, LeBras S, Petit de la Villeon L (2007) MedArgo: a drifting profiler program in the Mediterranean Sea. Ocean Sci 3:379–395
89. Malone T, DiGiacomo P, Muelbert J, Parslow J, Sweijd N, Yanagi T, Yap H, Blanke B (2010) Building a global system of systems for the coastal ocean. In: Hall J, Harrison DE, Stammer D (eds) Proceedings of OceanObs'09: sustained ocean observations and information for society, vol 2, Venice, 21–25 Sep 2009. ESA Publication WPP-306, doi:10.5270/OceanObs09.cwp.59
90. Charrassin JB, Hindell M, Rintoul SR, Foquet F, Sokolov S, Biuw M, Costa D, Boehme L, Lovell P, Colman R, Timmermann R, Meijers A, Meredith M, Park Y-H, Bailleul F, Goebel M, Tremblay Y, Bost C-A, McMahon CR, Field IC, Fedak MA, Guinet C (2008) Southern Ocean frontal structure and sea-ice formation rates revealed by elephant seals. Proc Nat Aca Sci 105:11634–11639. doi:10.1073/pnas/0800790105
91. Rudnick DL, Davis RE, Eriksen CC, Fratantoni DM, Perry MJ (2004) Underwater gliders for ocean research. J Mar Tech Soc 38:73–84
92. Eriksen CC, Perry MJ (2009) The nurturing of seagliders by the National Oceanographic Partnership Program. Oceanography 22:146–157
93. Wilson S, Parisot F, Escudier P, Fellous J-L, Benveniste J, Bonekamp H, Drinkwater M, Fu L, Jacobs G, Lin M, Lindstrom E, Miller L, Sharma R, Thouvenot E (2010) Ocean surface topography constellation: the next 15 years in satellite altimetry. In: Hall J, Harrison DE, Stammer D (eds) Proceedings of OceanObs'09: sustained ocean observations and information for society, vol 2, Venice, 21–25 Sep 2009. ESA Publication WPP-306, doi:10.5270/OceanObs09.cwp.92
94. Durand M, Fu L-L, Lettenmaier DP, Alsdorf DE, Rodríguez E, Esteban-Fernandez D (2010) The surface water and ocean topography mission: observing terrestrial surface water and oceanic submesoscale eddies. Proc IEEE 98(5):766–779
95. Gavrilov AN, Mikhalevsky PN (2006) Low frequency acoustic propagation loss in the Arctic Ocean: results of the arctic climate observations using underwater sound experiment. J Acoust Soc Am 119:3694–3706
96. Heimbach P, Forget G, Ponte RM, Wunsch C, Balmaseda M, Awaji T, Baehr J, Behringer D, Carton J, Ferry N, Fischer A, Fukumori I, Giese B, Haines K, Harrison DE, Hernandez F, Kamachi M, Keppenne C, Köhl A, Lee T, Menemenlis D, Oke P, Remy E, Rienecker M, Rosati A, Smith D, Speer K, Stammer D, Weaver A (2010) Observational requirements for global-scale ocean climate analysis: lessons from ocean state estimation. In: Hall J, Harrison DE, Stammer D (eds) Proceedings of OceanObs'09: sustained ocean observations and information for society, vol 2, Venice, 21–25 Sep 2009, ESA Publication WPP-306, doi:10.5270/OceanObs09.cwp.42

Books and Reviews

Hall J, Harrison DE, Stammer D (eds) (2010) Proceedings of OceanObs'09: sustained ocean observations and information for society, vol 2, Venice, 21–25 Sep 2009. ESA Publication WPP-306

Koblinsky C, Smith N (eds) (2001) Ocean observations for the 21st century. GODAE Office/BoM, Melbourne

Peixoto JP, Oort AH (1992) Physics of climate. American Institute of Physics, New York

Sparrow M, Chapman P, Gould J (2007) The world ocean circulation experiment (WOCE) hydrographic atlas, 4 volumes. International WOCE Project Office, Southampton

Warren BA, Wunsch C (1981) Evolution of physical oceanography. MIT Press, Cambridge

Chapter 9
Hurricane and Monsoon Tracking with Driftsondes

Philippe Drobinski, Philippe Cocquerez, A. Doerenbecher, Terrence Hock, C. Lavaysse, D. Parsons, and J.L. Redelsperger

Glossary

African easterly jet (AEJ)	Wind jet developing at about 600-hPa pressure level (about 4,200 m) and 5°N latitude over the African continent.
African easterly waves (AEWs)	Synoptic scale, westward propagating waves embedded in the AEJ.
AMMA	African Monsoon Multidisciplinary Analysis (AMMA) program, initiated in 2002 with an intensive field campaign in 2006, and focusing on the physical changes in the environment of the West African monsoon and their impacts on society.

This chapter was originally published as part of the Encyclopedia of Sustainability Science and Technology edited by Robert A. Meyers. DOI:10.1007/978-1-4419-0851-3

P. Drobinski (✉) • C. Lavaysse
Institut Pierre Simon Laplace/Laboratoire de Météorologie Dynamique, École Polytechnique/UPMC/ENS/CNRS, Palaiseau 91128, France
e-mail: philippe.drobinski@lmd.polytechnique.fr

P. Cocquerez
Sous-direction Ballon, Centre National d'Études Spatiales, Toulouse, France
e-mail: cocquerez@cnes.fr

A. Doerenbecher • J.L. Redelsperger
Centre National de Recherches Météorologiques, Météo-France/CNRS, Toulouse, France

T. Hock • D. Parsons
Atmospheric Technology Division, National Center for Atmospheric Research, 3450 Mitchell Lane, Boulder, CO 80307, USA
e-mail: hock@ucar.edu

J. Orcutt (ed.), *Earth System Monitoring: Selected Entries from the Encyclopedia of Sustainability Science and Technology*, DOI 10.1007/978-1-4614-5684-1_9,

Boundary layer pressurized balloon (BLPB)	Balloon drifting in the atmospheric boundary layer and carrying an instrumented gondola which collects measurements of the typical meteorological variables.
Concordiasi	International project of the THORPEX-International Polar Year aiming at a better understanding of the climate of Antarctica.
Driftsonde	Stratospheric drifting balloon launching dropsondes over high-impact weather, providing vertical profiles of meteorological data.
Hurricane	A hurricane is a tropical cyclone, occurring in the North Atlantic Ocean or the Northeast Pacific Ocean. A tropical cyclone is a storm system characterized by a large low-pressure center and numerous thunderstorms that produce strong winds and heavy rain.
HyMeX	Hydrological cycle in the Mediterranean experiment (HyMeX) program aiming at improving the understanding of running-water cycle in the Mediterranean region with a particular focus on the evolution and predictability of hydro-meteorological extreme events in the perspective of climate change.
Mesoscale convective system (MCS)	Complex of thunderstorms normally persisting for several hours or more.
Saharan air layer (SAL)	Surges of hot, dry air that cascade into the Atlantic from the Sahel region of Africa.
THORPEX	Global program of the World Meteorological Organization (WMO) aiming at accelerating improvements in the prediction of high-impact weather.
T-NAWDEX	THORPEX-North Atlantic Waveguide and Downstream impact Experiment.
T-PARC	THORPEX Pacific Asian Regional Campaign.
West African monsoon	Rainy phase of a seasonal change in atmospheric circulation over West Africa. The other major monsoon systems are the Asia-Australian monsoons in the sampled environment.

Definition of the Subject

Tropical cyclones (TCs) are a typical weather threat. The threat can apply to humans, their properties, and activities. Their prediction, particularly their trajectory and intensity, remains difficult. In addition, TCs develop above the tropical oceans where the coverage by in situ observations is poor and within cloud clusters (mesoscale convective systems MCS) that limit the ability of numerical weather

prediction (NWP) models to assimilate satellite data [18]. Improved forecast of TCs trajectories is a huge benefit in terms of material costs of evacuations and damage, not being able to quantify saved life.

The deployment of additional observations to improve understanding and forecasting TCs started very early in the USA, from the early 1980s. This approach is called adaptive observation and was initiated by the National Oceanic and Atmospheric Administration (NOAA). The philosophy of adaptive observation is the adjustment of the usual (so-called routine) observing network in order to deal with some particularly threatening weather situations to come. This adaptation aims at improving the numerical weather prediction (NWP) through the deployment of additional observations. When incorporated in the models, thanks to data assimilation procedures, these added observations decrease the uncertainty on the modeled state of the atmosphere (analysis). Subsequent numerical weather forecasts are likely to be improved. This improvement is expressed with respect to the NWP system that would not incorporate the additional data.

Any type of observation can be used. All time and space scales may be considered. Historically, the adaptive observation focused on the synoptic scales, for TCs first, then for mid-latitudes winter storms [15, 22]. The terms "adaptive observation" or "observation targeting" may be used in various senses that may be misleading. Adaptive observation first refers to the observing strategy itself, which is a real-time observation practice in close link with NWP.

An adaptive observing strategy requires a constant monitoring of the weather situation. The typical strategy is implemented following five stages:

- Case identification (weather threat) using forecasts
- Computation of objective targeting guidance to help the decision process (where and when to deploy)
- Design of the deployment and decision making, transmitting the deployment instructions to the observation providers (observing platforms)
- Deployment of additional observations (data collection, transmission)
- Assimilation (this stage is automatic and do not imply any specific effort)
- A posteriori evaluation of the data impact (in research mode, optional, often ignored)

The Hurricane Synoptic Flow was the first regular seasonal TC targeting campaign, conducted by NOAA, on the North Atlantic hurricane basin (1982–1996). The research aircraft P3 deployed dropsondes along a circular navigation around the cyclone [5]. The choice of deployment was essentially subjective, but the campaign was a success. From 1997 to 2011, the NOAA Hurricane Synoptic Surveillance has combined subjectively and objectively guided deployments [1] of dropsondes in the Gulf of Mexico, Eastern Pacific, and Western Atlantic. In Asia, the annual campaigns DOTSTAR [25] that started in 2003 allow the improvement of the observing system in the Western Pacific with dropsondes released from Taiwanese jet aircrafts. Again, the choices of deployments are based on both subjective and objective analyses. From an NWP impact point of view, observations that are deployed in the close TCs' environment produce the best results in terms of TC trajectory prediction [11]. However, this conclusion holds for already formed and named TCs. Another issue is to better monitor tropical environment in which TCs may appear, develop, and strengthen.

Introduction

More recently, in West Africa, drifting balloons launched from Zinder (Niger) (Fig. 9.1) into the stratosphere (about 50 hPa) dropped 124 dropsondes over wide swaths of Africa and the Atlantic Ocean between end of August and end of September 2006, in order to document the meteorological environment of mesoscale convective systems (MCS) and TCs in the Atlantic [6]. This deployment of the so-called driftsonde system was performed in the frame of the African Monsoon Multidisciplinary Analysis (AMMA) program, initiated in 2002 with an intensive field campaign in 2006, and focusing on the physical changes in the environment of the West African monsoon and their impacts on society [20]. MCSs are the main precursors of TCs in the Atlantic (e.g., [2]), and may even contribute to tropical cyclogenesis in the Pacific (e.g., [10]). It is believed that scale interaction processes drive the tropical cyclogenesis that occurs over the Atlantic off the West African coast during late summer. This interaction involves:

- The African Easterly Jet (AEJ) develops at about 600-hPa pressure level and 4°N-5°N latitude because heating of the West African land mass during summer creates a surface temperature and moisture gradient between the Gulf of Guinea and the Sahara, and the atmosphere responds by generating vertical wind shear to maintain thermal wind balance.
- The African easterly waves (AEWs) which are synoptic scale, westward propagating disturbances produced by barotropic and baroclinic instabilities embedded in the AEJ.
- The Saharan air layer (SAL).
- The westward propagating MCSs.

It is already known that some Atlantic tropical cyclones have their origin in MCSs propagating over the African continent [23]. For example, Hill and Lin [13] related the genesis of Hurricane Alberto (2000) to a MCS initiated over the Ethiopian highlands. Lin et al. [17] documented this case study and identified

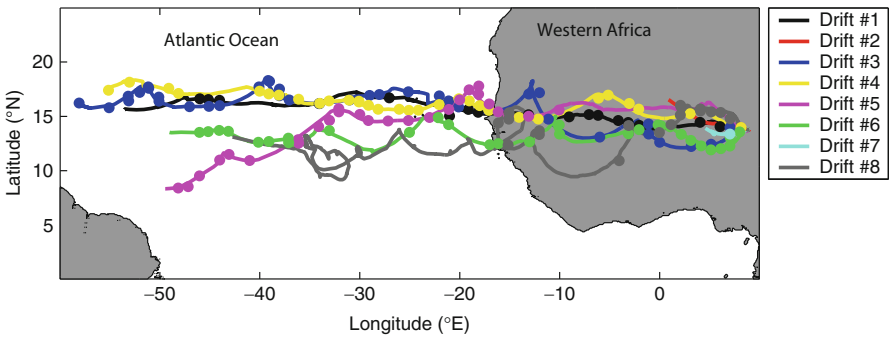

Fig. 9.1 Trajectories of the eight driftsondes launched from Zinder (Niger) between August 28 and September 22, 2006. The *dots* indicate the location of a dropsonde

three successive convective genesis and lysis periods before the final cyclogenesis event off the Guinea coast. Berry and Thorncroft [3] also showed that the MCSs associated with the pre-Alberto disturbance were embedded in an AEW. The SAL may significantly impede the development of incipient tropical waves or disturbances and can even weaken preexisting tropical cyclones.

During the AMMA, the driftsondes sampled squall lines in the troughs of AEW and the southeastern edge of the tropical storm Florence, hurricanes Gordon and Helene. In addition to tracking potential hurricanes, the driftsondes gathered bird's-eye data on surges of hot, dry air that cascade into the Atlantic from the Sahel region of Africa. These surges carry huge amounts of dust as far west as Florida, influencing air chemistry, upper-ocean biology, and Atlantic weather systems. Although driftsondes have been tested over the last few years, this was the first time they were used in weather research and prediction. Based on this new type of dataset, this entry aims at illustrating and analyzing the potential of such observation system for tracking high-impact weather system such as cyclone and hurricanes in area generally void of in situ data, and provides additional observation for real-time forecast improvement.

Section"The Driftsonde Observations" presents the driftsonde system which was first used in the frame of a large scientific research program. Section"Analysis of the Driftsonde Trajectories and the Respective Synoptic Environment" describes the synoptic environment (including AEW activity) of the meteorological processes (MCS and tropical storm initiation) investigated with the series of vertical profiles provided by the dropsondes. Section "Analyses of AEW with the Driftsondes" describes the AEW activity and spatial pattern in relation with the dropsonde location. Section"Conclusion" concludes the description of the driftsonde system, lists the ongoing research activity using the driftsonde data collected during AMMA, and proposes perspectives for the use of such observation system.

The Driftsonde Observations

The concept of using driftsondes to take measurements over remote but scientifically important locations around the globe comes from THORPEX, a global program of the World Meteorological Organization (WMO) to accelerate improvements in the prediction of high-impact weather. A driftsonde is composed of a drifting stratospheric balloon and a gondola carrying dropsondes.

For the AMMA project, the drifting stratospheric balloons were developed by the Centre National d'Études Spatiales (CNES) whereas the dropsondes were designed at the National Center for Atmospheric Research (NCAR) and their development was funded by the National Science Foundation (NSF) and the National Oceanic and Atmospheric Administration (NOAA). To build the driftsonde system, scientists and engineers at NCAR and CNES had to overcome many hurdles. Each driftsonde had to be robust enough to endure days of extreme stratospheric cold (averaging −60°C) as well as the intense sunlight of the high,

thin atmosphere. For the balloon deployment to be affordable and practical, the system also required low-cost, lightweight, off-the-shelf instruments capable of operating reliably in low pressure and in temperature extremes with very low power. Each gondola held about 35 dropsondes designed by NCAR (the number of dropsondes could differ between the driftsondes) carried on the ballooning systems designed by CNES. In order to make the driftsonde concept practical, NCAR developed a highly compact instrument package, roughly the size of a small bottle of water but weighing only about 140 g. Called MIST (Miniature In situ Sounding Technology), it weighs less than half as much as older dropsondes, which were designed at NCAR in the 1990s. Although driftsondes have been tested over the last few years, this was the first time they were used in weather research and prediction.

The Zinder site, located 740 km east of Niamey, was selected in order to study the AEW, that serve as seedlings for hurricanes during the late African monsoon period (August–September). Dozens of these waves moved across Africa into the Atlantic between about 10°N and 20°N. A small number developed into tropical storms. During July–September 2006 period, a total of 27 AEWs were objectively analyzed (compared with 31 in 2004 and 28 in 2005). July was very different from the later months with six out of seven of the first waves forming close to the longitude of Niamey or west of it. In August, the AEWs were initiated further east, between 10°E and 20°E, but AEWs over Niamey were still weak. Starting at the end of August and going into September, the AEWs became more coherent with stronger amplitudes over most of tropical North Africa. Interestingly, several AEWs also appeared to start further east, between 20°E and 30°E at this time. It should also be noted that all seven of the AEWs that became named tropical cyclones (Chris – AEW number 6; Ernesto – AEW number 13; Debby – AEW number 14; Florence – AEW number 18; Gordon – AEW number 19; Helene – AEW number 20; Isaac – AEW number 23; see [14]) were initiated east of Niamey and six of these occurred after the middle of August. After being launched from Zinder, each balloon drifted from Africa toward the Caribbean at heights of around 20 km height, where light easterly winds prevail. The trajectories exhibited cycloid-like patterns due to the presence of near-inertial waves [12] (Fig. 9.1). At least twice per day (0000 and 1200 UTC), each gondola released a dropsonde that fell by parachute, sensing the weather conditions during its 20-min descent and radioing data back to the gondola and then, by satellite, to the operation center in Paris. Whenever promising weather system developed, the operation center signaled the gondola to release additional dropsondes as often as in 3-h intervals. Eight driftsondes were released from Zinder during the late African monsoon period coinciding with the peak period for hurricane formation over the tropical Atlantic (August–September) and 124 sondes were successfully dropped from the eight driftsondes with 15 vertical profiles from the last dropsondes of driftsonde 8 sent to the GTS for assimilation. However, the number of successfully dropped sondes differed between driftsondes. Table 9.1 summarizes the operation during the driftsonde deployment. Table 9.1 shows that the most successful flights corresponded to driftsondes 1, 3, 4, 5, 6, and 8. However, the synoptic environment documented with driftsonde 1 was not of high scientific interest. Driftsonde 8 trajectory was particularly

Table 9.1 Summary of driftsonde operations

Driftsonde number dropsondes	First dropsonde coordinates and date	Last dropsonde coordinates and date	Number of successful
1	(6.04°E,14.05°N) – August 28 1406 UTC	(−44.03°E,16.47°N) – September 2 1217 UTC	8
2	(8.13°E,13.93°N) – August 29 2118 UTC	(8.13°E,13.93°N) – Augember 29 2118 UTC	1
3	(7.04°E,13.99°N) – September 1 2351 UTC	(−58.07°E,16.22°N) – September 9 1312 UTC	33
4	(8.14°E,13.97°N) – September 4 1942 UTC	(−55.14°E,17.40°N) – September 11 1110 UTC	14
5	(−10.07°E,15.58°N) – September 9 0807 UTC	(−50.09°E, 8.39°N) – September 13 1808 UTC	25
6	(8.00°E,13.57°N) – September 9 2055 UTC	(−46.03°E,13.52°N) – September 18 0005 UTC	26
7	(7.03°E,13.37°N) – September 12 2358 UTC	(7.03°E,13.37°N) – September 12 2358 UTC	1
8	(6.10°E,15.36°N) – September 16 0603 UTC	(−15.07°E,15.33°N) – September 22 1742 UTC	16

complex and difficult to manage since the flight period corresponded to the weakening of the 50 hPa easterly winds due to a change of the Madden Julian oscillation (MJO) phase. So driftsonde 8 did not allow the tracking of any interesting meteorological event. In the following, we thus analyze in detail the data collected with driftsondes 3–6. They documented in an unprecedented way AEW initiating continental mesoscale convective systems (MCS) evolving over the ocean into tropical storm like Florence and hurricanes like Gordon and Helene, some of them skirting with the US Atlantic and Gulf coasts and all experiencing extra-tropical transition.

Analysis of the Driftsonde Trajectories and the Respective Synoptic Environment

Figure 9.2 shows the space-time "distances" of the dropsondes from the center of tropical storms Florence, Gordon, and Helene. The closest in space and time from the storm center is the best. Figure 9.2a shows that driftsonde 1 approaches Helene track at less than 500 km about a week in advance, whereas driftsondes 3 and 4 followed tropical storm Florence dropping several sondes less than 500 km from the storm track. Gordon track was sampled by driftsonde 4 1 day after its passage (Fig. 9.2b) whereas Helene track was sampled by driftsonde 6 less than 1 day after its passage (Fig. 9.2c).

Figure 9.3 displays the Meteosat Second Generation (MSG) 10.8 μm channel brightness temperature which indicates that convective activity as well as the

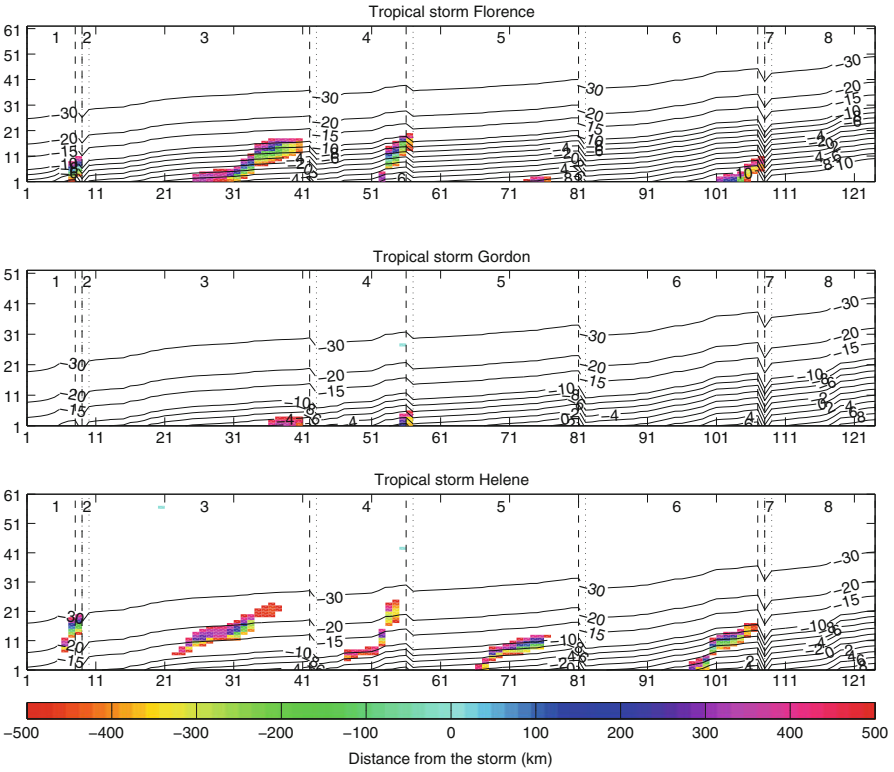

Fig. 9.2 Space (color code) and time (iso-contours) "distances" of the dropsondes from the center of tropical storms (TS) Florence (**a**), Gordon (**b**), and Helene (**c**) (color code). The abscissa corresponds to the number of space-time coordinate information available for the TS trajectory. The ordinate corresponds to the number of successful dropsondes available for the whole field campaign. The numbers at the top of the figure indicate the identification number of the driftsonde. Only distances smaller than 500 km are shown, the positive (negative) sign indicates that the sonde is dropped ahead (behind) of the center of the storm. The iso-contours are shown for −30, −20, −15, −10, −8, −6, −4, −2, 0, 2, 4, 6, 8, and 10 days, the positive (negative) sign indicate that the sonde is dropped before (after) the storm

filtered 700 hPa wind field is shown with arrows (the absence of arrows indicate winds weaker than 1 m s^{-1}). It shows that driftsonde 3 drifts in the vicinity of an MCS propagating westward over the continent at about 15 m s^{-1}. At about 40°W, tropical depression Florence is forming. Figure 9.4 (first column) shows a time versus height cross section of wind speed, temperature, and humidity constructed with the vertical profiles obtained by the sondes dropped from driftsonde 3. Figure 9.4a shows evidence of a strong wind tongue between 4 and 5 km height corresponding to the AEJ. Figure 9.4i shows the moist African planetary boundary layer between Julian days 245 and 248 (September 2–5, 2006) (75% relative humidity) extending up to about 1 km height. Above the planetary boundary layer, layers of saturated air between 5 and 8 km height reveal the proximity of

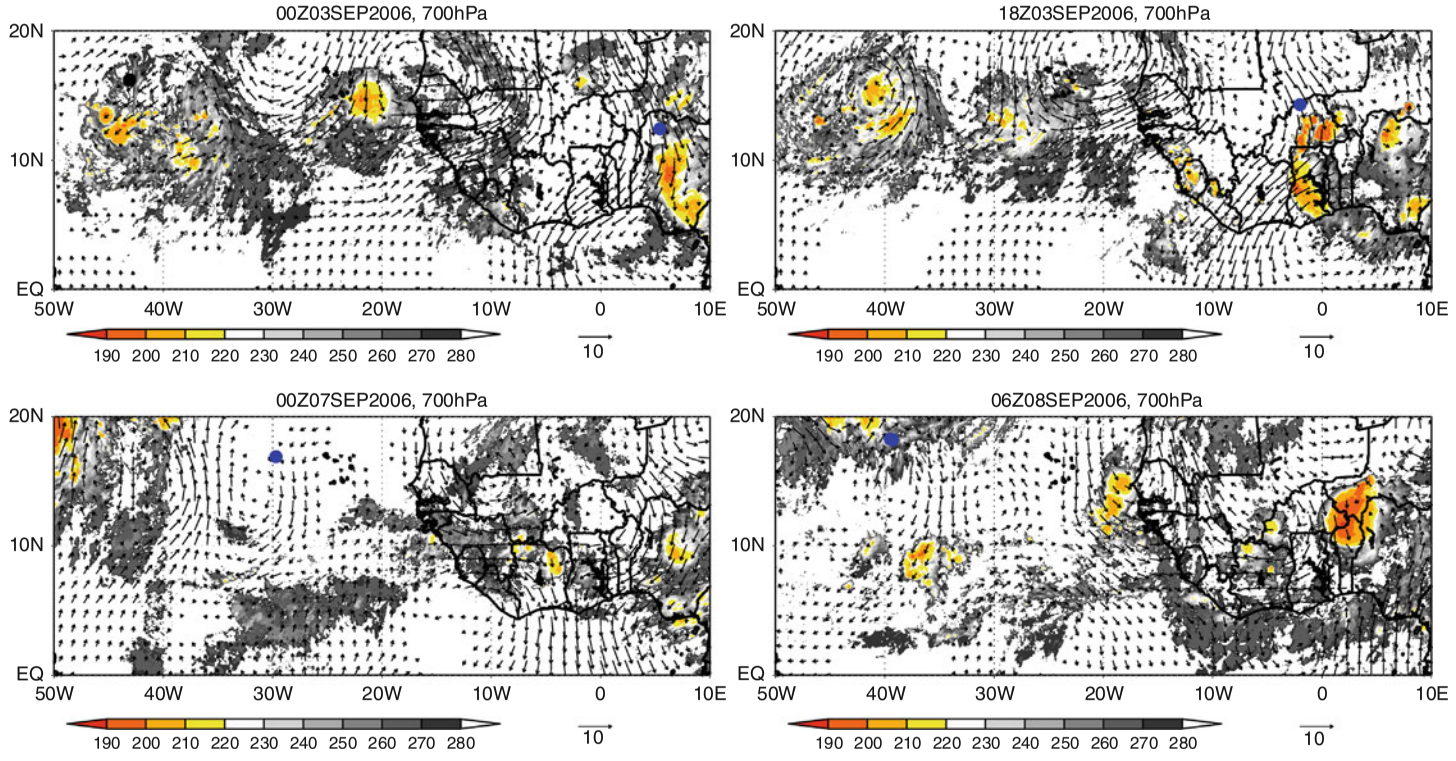

Fig. 9.3 Meteosat Second Generation (MSG) 10.8 μm channel brightness temperature which indicates convective activity with superimposed filtered 700 hPa wind field shown with *arrows* (the absence of arrows indicate winds weaker than 1 m s^{-1}) on September 3, 2006, (Julian day 246) at 0000 UTC (**a**), on September 3, 2006, (Julian day 246) at 1800 UTC (**b**), on September 7, 2006, (Julian day 250) at 0000 UTC (**c**) and on September 8, 2006, (Julian day 251) at 0600 UTC (**d**). The black and blue filled dots indicate the locations of dropsondes from driftsondes 1 and 3, respectively

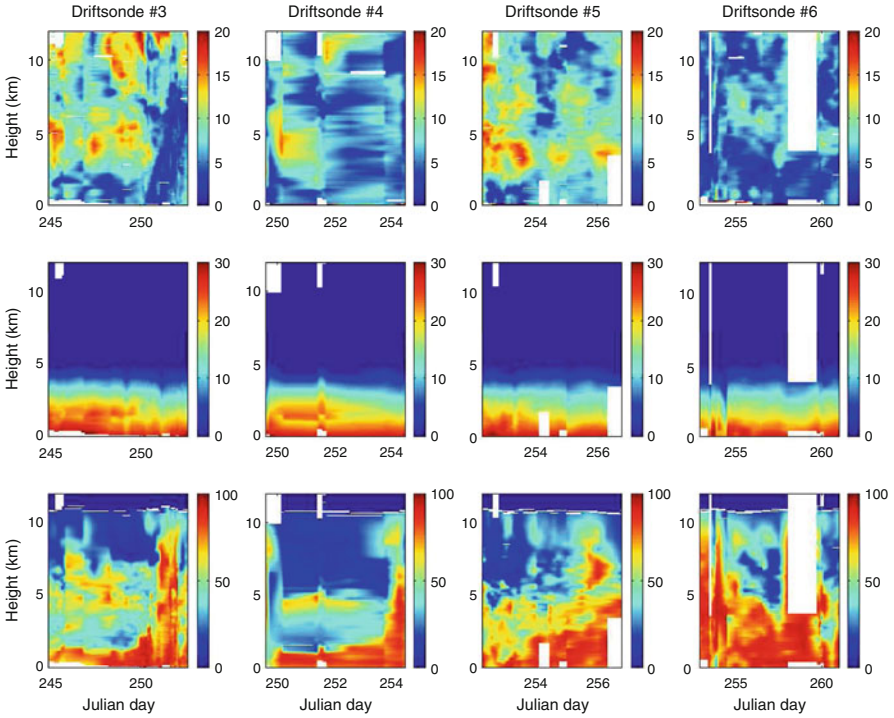

Fig. 9.4 Time versus height cross section of wind speed (*first row*, panels **a**, **b**, **c**, and **d**), temperature (*second row*, panels **e**, **f**, **g**, and **h**) and humidity (*third row*, panels **i**, **j**, **k**, and **l**) constructed with the vertical profiles obtained by the sondes dropped from driftsonde 3 (first column; blue trajectory in Fig. 9.1), 4 (second column; yellow trajectory in Fig. 9.1), 5 (third column; purple trajectory in Fig. 9.1), and 6 (fourth column; green trajectory in Fig. 9.1)

the convective activity. On Julian day 250 (September 7, 2006), dropsondes are released from driftsonde 3 few hundreds of kilometers downstream of Florence, located at about 50°W, which in the meantime has been classified as a tropical storm (it becomes a hurricane on September 10, 2006). The near-surface wind decreases in the disturbed environment near tropical storm Florence as shown in Fig. 9.4a while the planetary boundary layer humidity and depth increase (up to about 90% relative humidity and up to 3 km during day 250) before reaching the disturbed environment near Florence where very intense convection occurs (Fig. 9.4i). Figure 9.4b is similar to Fig. 9.4a for driftsonde 4. However, the much lower number of successful dropsondes does not allow the documentation of fine-scale structures over the Atlantic Ocean. It however shows a disturbed environment similar to driftsonde 3 less than 200 km south of the developing tropical storm Gordon at about 55°W (not shown) and Julian day 254 with large humidity extending up to the tropopause and weak near-surface winds. The existence of weak-surface winds is surprising since one may associate naturally developing tropical storms with large evaporation and thus strong winds. The vertical profiles

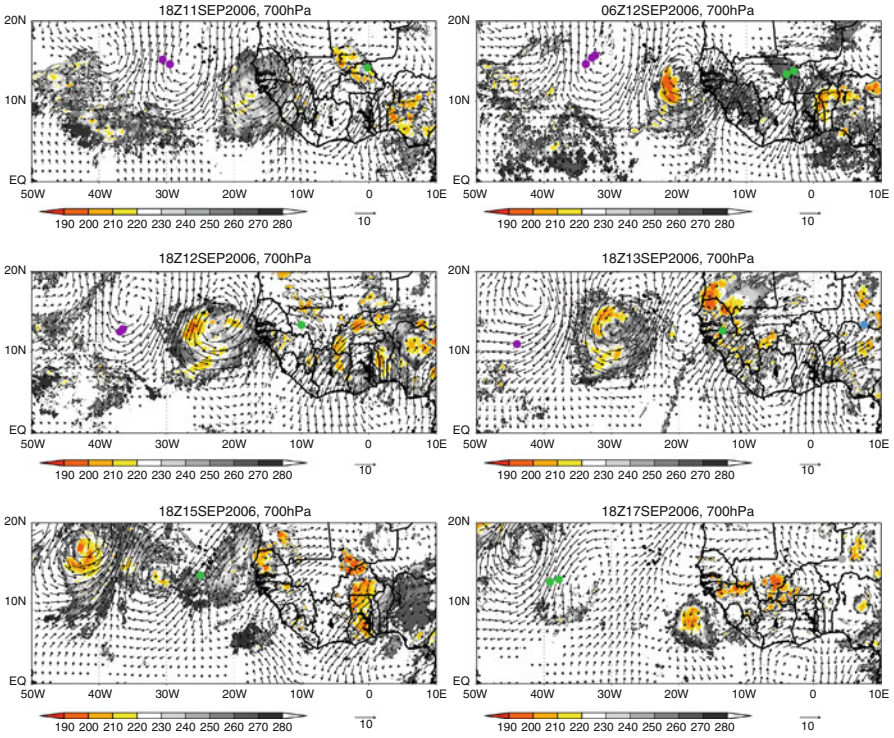

Fig. 9.5 Meteosat Second Generation (MSG) 10.8 μm channel brightness temperature which indicates convective activity with superimposed filtered 700 hPa wind field shown with *arrows* (the absence of *arrows* indicate winds weaker than 1 m s^{-1}) on September, 11, 2006, (Julian day 254) at 1800 UTC (**a**), on September 12, 2006, (Julian day 255) at 0600 UTC (**b**), on September 12, 2006, (Julian day 255) at 1800 UTC (**c**), on September 13, 2006, (Julian day 256) at 1800 UTC (**d**), on September 15, 2006, (Julian day 258) at 1800 UTC, (**e**) and on September 17, 2006, (Julian day 260) at 1800 UTC (**f**). The *purple*, *green*, and *cyan filled dots* indicate the locations of dropsondes from driftsondes 5, 6, and 7, respectively

of relative humidity documented by the dropsondes of driftsonde 4 around Julian day 250 also show evidence of very low humidity values just above the planetary boundary layer (around 20% relative humidity) and at about 5–6 km height (below 10% relative humidity) corresponding the AEJ (Fig. 9.4). The low level dry layer was identified as a strong dry air outflow from the Sahara by the Meteosat-8/Goes-10 combined Saharan air layer product. The very dry air conveyed by the AEJ originated in the upper levels (200–250 hPa) on the anticyclonic side of the polar jet stream at 50°N as diagnosed by the method proposed by Roca et al. [21].

Figure 9.5 is similar to Fig. 9.3 between September 11, 2006, and September 17, 2006. Driftsondes 5 and 6 represented by purple and green filled dots, respectively, sensing the atmosphere ahead and downstream the tropical storm Helene which initiates on September 11, 2006, at 1800 UTC over the coast of Senegal and moves westward at a propagation speed of about 8 m s^{-1}. Figure 9.4 shows that after the

formation of three successive storms in about 2 weeks, all evolving into hurricane category, driftsondes 5 and 6 probe a much more disturbed environment than for Florence, with higher convective activity both over the continent and the ocean with nearly saturated air observed up to 5 km along the driftsonde tracks. The AEJ tends to weaken during driftsonde 6 flight.

Analyses of AEW with the Driftsondes

As AEWs are the dominant synoptic weather systems in West Africa and the tropical Atlantic during boreal summer and are an important component of the regional climate by modulating West African rainfall including mesoscale convective systems (MCSs) which can be precursors of tropical cyclones in the Atlantic, the respective locations of the dropsonde and AEW are now investigated.

A method based on the wavelet analysis with a Morlet mother wavelet [24] of the meridional wind field at 700 hPa is used to detect AEW activity. The sum of the spectral density between 3 and 5 days period allows to perform an index which estimates the wave activity over each grid points. The spatial average of this index is then computed to observe the large-scale AEWs activity. This method has been proposed by Lavaysse et al. [16]. Figure 9.6 shows the longitude/latitude field of the mean AEW index averaged between August 15 and September 30, 2006, as well as the Hovmöller space-time diagram of the 2–6 day bandpass filtered meridional wind at 700 hPa averaged between 5°N and 20°N. Using this method, we detect in 2006 three periods of large AEW activity over West Africa and the tropical Atlantic (i.e., 50°W, 10°E and 5°N, 20°N): middle of July, middle of August, and middle of September. This is in accordance with other methods of AEW as the variance of the 700 hPa meridional wind filtered in the 3–5 days band period, and the 700 hPa curvature vorticity method by Berry et al. [4] and illustrated by Janicot et al. [14]. These results are also in accordance following different analyses as ECMWF and national centers for environmental predictions (NCEP) (not shown) and different geopotential levels (700 or 850 hPa). During the period of driftsonde operations (i.e., August 29 to September 23, 2006), the AEW activity shows two distinct periods. Driftsonde 1 (black trajectory, Fig. 9.1) flies during a period of low AEW activity preceding the initiation of Helene tropical storm on September 3, 2006, at 40°W also during the period of low AEW activity. The AEW activity increases on September 1, 2006, over West Africa. The area of large waves activity propagates westward in association with the westward propagation of the filtered meridional wind. Driftsonde 3 (blue trajectory) follows the ridge sector of the strengthening wave train (Fig. 9.3) but the AEW activity abruptly decreases when the waves reach the ocean (around 20°W). A similar scenario occurs for driftsonde 4 (yellow trajectory). Around September 7, 2006, AEW activity is maximum over West Africa. In the same time, driftsonde 5 (purple trajectory) is launched (Table 1). Ten sondes are dropped in the ridge sector of the AEW over West Africa (Fig. 9.5).

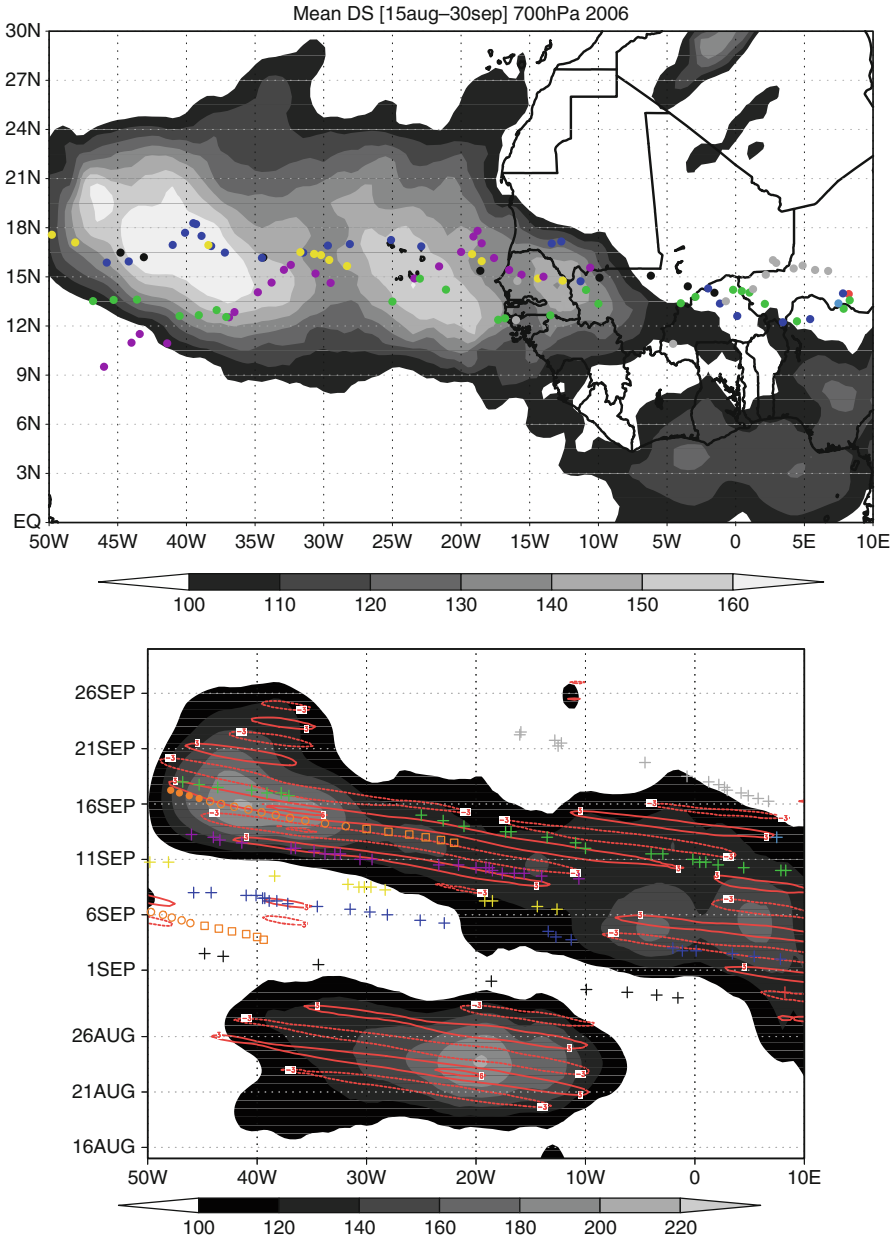

Fig. 9.6 *Left panel*: Mean AEW index with the location of the dropsondes superimposed. *Right panel*: Hovmöller space-time diagram of the 2–6 day bandpass filtered NCEP-2 meridional wind at 700 hPa (*red contour* for +1 m s^{-1}) and AEW index (*gray shading*) averaged between 5°N and 20°N. Superimposed are the locations of the dropsondes of the eight driftsondes ("+" marker with same color code as in Fig. 9.1) and the 1-day averaged location of the tropical storms Florence and Gordon (*squares*, *circles*, and *filled circles* when classified as tropical depression, tropical storm, and hurricane, respectively). Gordon is not visible since forming at about 55°W, that is, out of the abscissa scale

Above the coast, the westward propagation speeds of the driftsonde and the AEW are different thus on September 11, driftsonde 5 drops sondes in the trough sector of the AEW ahead of the ridge sector. Driftsonde 5 is particularly interesting when flying over the continent because of its proximity to the trough of the AEW associated with large convective activity. This AEW-MCS system is the precursor of tropical storm Florence initiating around September 12, at 20°W. This storm propagates along a maximum of the mean AEW activity index with the largest value over the tropical Atlantic (September 15 at 42°W; Fig. 9.6). Driftsonde 6 (green trajectory) covers the largest longitudinal cross section with a first drop at 7°E and the last drop at 47°W. Driftsonde 6 remains over the same ridge sector along the whole operation period and provides temporal-longitudinal evolution of the activity and characterization of the ridge.

Conclusion

It is worth emphasizing that all the driftsondes deployed during AMMA were still on probation. This status explains the late dissemination of the data on the GTS (driftsonde 8, only) and the technically mitigated success. The driftsonde system has gradually reached the stage of maturity. During T-PARC, 16 driftsondes were launched from Hawaii during August 2008 [9]. About 250 dropsondes were targeted eventually that correspond to a 64% success rate. The launch site of the pre-Concordiasi test-campaign was in the Seychelles in February 2010 and 3 driftsondes with limited dropsondes were deployed. Finally, Concordiasi test-campaign took place from September to December 2010 [19] over Antarctica. More than 620 dropsondes were deployed from a fleet of 13 driftsondes launched at McMurdo station. The mission success rate was close to 95%, most of the data were disseminated on the GTS.

Whenever the dropsonde data are disseminated or not, the evaluation of the NWP-wise benefit of deploying these observing platforms requires some specific impact studies. These imply to compare the quality of forecasts when the NWP system processes the dropsondes' data or not. The data collected over West Africa and the Atlantic Ocean during AMMA have been used to evaluate numerical weather prediction of the late 2006 African monsoon [8]. They will also be used for a posteriori analysis of their added value for numerical weather forecast. The evaluation of NWP impact of T-PARC driftsondes has not been carried out yet, though many phenomenological studies have been carried out. The evaluation of Concordiasi is currently being done. As the NWP benefit is gained as soon as the data are assimilated in operational NWP systems, the exact assessment of this benefit triggers a limited motivation. Indeed, this evaluation is crucial to correctly assess the NWP efficiency of data targeting with such platforms.

Future Directions

The idea of a network of high atmosphere balloons distributed in the stratosphere and dropping sondes on demand has existed for more than a decade. Some projects have emerged with the advent of THORPEX. Many of them were intractable. The driftsonde system, which appeared to be one of the less ambitious projects, eventually emerged in AMMA 2006. The system has been improved in T-PARC 2008 and for Concordiasi in 2010. The system will be upgraded in 2011–2013, but this last technical step will prevent the system to be deployed in the joint T-NAWDEX/HyMeX framework in 2012–2014 (T-NAWDEX stands for THORPEX-North Atlantic Waveguide and Downstream impact Experiment and HyMeX means Hydrological Cycle in the Mediterranean Experiment). In this last field campaign, the challenge would have been to deploy driftsondes above the Atlantic Ocean, from the USA. The objective was to sample the whole Atlantic, upstream from Europe and the Mediterranean region. Hopefully, the new generation system will probably be deployed in further future specific observation campaigns.

In near future and NWP-wise, the main interest of the driftsonde system is its ability to sample a whole atmospheric environment in which a weather threat is likely to emerge. This mode is especially effective if driftsondes are deployed in a network of several units. This is typically the level of targeting that should be achieved for adaptive observation. Indeed, several factors contribute to the suboptimality of single-use (single weather event) driftsondes' deployment.

- The release of driftsonde is a delicate art, highly dependent on environmental conditions. The system has a limited capacity to respond to a very specific request (short time and very localized area).
- After having drift above the area of interest as defined for the targeted event, the balloon is lost to its initial targeting mission.
- Controlling the trajectory is currently not possible. In the cases and T-PARC and AMMA (summer) the trajectories showed rather zonal despite a few fluctuations. But during the probe campaign for Concordiasi in the Seychelles (February 2010), the trajectories were poorly predictable and let the balloons drift out of the Tropics.

However, regular sampling of regions void of any observations can be very profitable for weather forecasting. Furthermore, deployment in areas (space-time) where the flow is periodic preserves driftsondes' fleet on the region of interest: around the globe intertropical circulation in summer or polar vortex in winter. The specific impact remains to be shown clearly with the existing datasets. This should be a prerequisite to any further deployment and the time left by the upgrade of the driftsonde system should be used to demonstrate the usefulness of these data in some global prediction systems.

Finally, there are other aerostats that may be more suitable for adaptive deployment in response to the possible occurrence of some weather event in particular. Boundary layer pressurized balloon (BLPB) is one example. The BLPB is a balloon drifting in the atmospheric boundary layer and carrying an instrumented gondola

which collects measurements of the typical meteorological variables. The proof of concept will be given during the HyMeX special observing periods. In the HyMeX field campaigns, the BLPBs will be deployed above the marine surroundings of some intense convective systems that occur at the periphery of the Mediterranean basin [7].

Acknowledgments We are thankful to J. Fox, K. Romberg, J. VanAndel, H. Cole, C. Martin, G. Granger, D. Flanigan, and D. Lauritsen (NCAR) for assistance in operation of the driftsonde system. Based on French initiative, AMMA was built by an international scientific group and is currently funded by a large number of agencies, especially from France, UK, Germany, USA, and Africa. It has been the beneficiary of a major financial contribution from the European Community's Sixth Framework Research Program. Detailed information on scientific coordination and funding is available on the AMMA International website http://www.amma-international.org.

Bibliography

1. Aberson SD (2003) Targeted observations to improve operational tropical cyclone track forecast guidance. Mon Wea Rev 131:1613–1628
2. Avila LA, Pasch RJ (1992) Atlantic tropical systems of 1991. Mon Wea Rev 120:2688–2696
3. Berry GJ, Thorncroft C (2005) Case study of an intense African easterly wave. Mon Wea Rev 133:752–766
4. Berry GJ, Thorncroft C, Hewson T (2007) African easterly waves during 2004 – analysis using objective techniques. Mon Wea Rev 135:1251–1267
5. Burpee RW, Franklin JL, Lord SJ, Tuleya RE, Aberson SD (1996) The impact of omega dropwindsondes on operational hurricane track forecast models. Bull Am Meteorol Soc 77:925–933
6. Drobinski P, Parsons D, Cocquerez P, Cardonne A, Cole H, Fox J, Lefevre JP, Redelsperger JL, Romberg K, VanAndel J, Vénel S (2006) Des ballons stratosphriques traquent la mousson africaine. La Météorologie 55:2–3
7. Drobinski P, Basdevant C, Doerenbecher A, Pannekoucke O, Fesquet C, Verdier N, Vargas A (2010) Balloon deployment during the HyMeX (Hydrological in the Mediterranan EXperiment) project. 38th COSPAR Scientific Assembly, Bremen
8. Drobinski P, Karbou F, Bauer P, Cocquerez P, Lavaysse C, Hock T, Parsons D, Rabier F, Redelsperger JL, Vénel S (2011) Driftsonde observations to evaluate numerical weather prediction of the late 2006 African monsoon. J Appl Meteorol Climatol (submitted)
9. Elsberry RL, Harr PA (2008) Tropical cyclone structure (TCS-08) field experiment science basis, observational platforms, and strategy. Asia-Pacific J Atmos Sci 44:209–231
10. Frank NL (1970) Atlantic tropical systems of 1969. Mon Wea Rev 98:307–314
11. Harnisch F, Weissmann M (2010) Sensitivity of typhoon forecasts to different subsets of targeted dropsonde observations. Mon Wea Rev 138:2664–2680
12. Hertzog A, Vial F, Mechoso CR, Basdevant C, Cocquerez P (2002) Quasi-Lagrangian measurements in the lower stratosphere reveal an energy peak associated with near-inertial waves. Geophys Res Lett 29:1229. doi:10.1029/2001GL014083
13. Hill CM, Lin YL (2003) Initiation of a mesoscale convective complex over the Ethiopian Highlands preceding the genesis of Hurricane Alberto (2000). Geophys Res Lett 30:1232. doi:10.1029/2002GL016655
14. Janicot S, Thorncroft CD, Ali A, Asencio N, Berry G, Bock O, Bourles B, Caniaux G, Chauvin F, Deme A, Kergoat L, Lafore JP, Lavaysse C, Lebel T, Marticorena B, Mounier F, Nedelec P, Redelsperger JL, Ravegnani F, Reeves CE, Roca R, de Rosnay P, Schlager H, Sultan B,

Tomasini M, Ulanovsky A (2008) ACMAD forecasters team: large-scale overview of the summer monsoon over West Africa during the AMMA field experiment in 2006. Ann Geophys 26:2569–2595
15. Joly A, Browning KA, Bessemoulin P, Cammas J-P, Caniaux G, Chalon J-P, Clough SA, Dirks R, Emanuel KA, Eymard L, Gall R, Hewson TD, Hildebrand PH, Jorgensen D, Lalaurette F, Langland RH, Lematre Y, Mascart P, Moore JA, Persson PO, Roux F, Shapiro MA, Snyder C, Toth Z, Wakimoto RM (1999) Overview of the field phase of the Fronts and Atlantic Storm-Track Experiment (FASTEX) project. Bull Am Meteorol Soc 125:3131–3163
16. Lavaysse C, Diedhiou A, Laurent H, Lebel T (2006) African easterly waves and convective activity in wet and dry sequences of the West African Monsoon. Clim Dyn 27:319–332
17. Lin YL, Robertson KE, Hill CM (2005) Origin and propagation of a disturbance associated with an African easterly wave as a precursor of Hurricane Alberto (2000). Mon Wea Rev 133:3276–3298
18. McNally T (2002) A note on the occurrence of cloud in meteorologically sensitive areas and the implications for advanced infrared sounders. Q J Roy Meteorol Soc 128:2551–2556
19. Rabier F, Bouchard A, Brun E, Doerenbecher A, Guedj S, Guidard V, Karbou F, Peuch V-H, El Amraoui L, Puech D, Genthon C, Picard G, Town M, Hertzog A, Vial F, Cocquerez P, Cohn SA, Hock T, Fox J, Cole H, Parsons D, Powers J, Romberg K, VanAndel J, Deshler T, Mercer J, Haase JS, Avallone L, Kalnajs L, Mechoso CR, Tangborn A, Pellegrini A, Frenot Y, Thpaut J-N, McNally A, Balsamo G, Steinle P (2010) The Concordiasi project in Antarctic. Bull Am Meteorol Soc 91:69–86
20. Redelsperger JL, Thorncroft CD, Diedhiou A, Lebel T, Parker DJ, Polcher J (2006) African monsoon multidisciplinary analysis: an international research project and field campaign. Bull Am Meteorol Soc 87:1739–1746
21. Roca R, Lafore JP, Piriou C, Redlesperger JL (2005) Extratropical dry-air intrusions into the West African monsoon midtroposphere: an important factor for the convective activity over the Sahel. J Atmos Sci 62:390–407
22. Szunyogh I, Toth Z, Zimin A, Majumdar SJ, Persson A (2002) On the propagation of the effect of targeted observations: the 2000 Winter Storm Reconnaissance Program. Mon Wea Rev 130:1144–1165
23. Thorncroft C, Hodges K (2001) African easterly wave variability and its relationship to Atantic tropical cyclone activity. J Clim 14:116–1179
24. Torrence C, Compo GP (1998) A practical guide to wavelet analysis. Bull Am Meteorol Soc 79:61–78
25. Wu C-C, Chen J-H, Lin P-H, Chou K-H (2007) Targeted observations of tropical cyclone movement based on the adjoint-derived sensitivity steering vector. J Atmos Sci 64:2611–2626

Chapter 10
Large-Scale Ocean Circulation: Deep Circulation and Meridional Overturning

Stephen R. Rintoul

Glossary

Antarctic bottom water	A dense water mass formed near the Antarctic continental margin that spreads northward to ventilate the abyssal ocean.
Argo floats	Autonomous profiling floats that drift with ocean currents at 1–2 km depth and periodically measure temperature and salinity while rising to the sea surface, where the data is transferred by satellite.
Barotropic	The depth-independent component of ocean currents. Direct current measurements are needed to determine the barotropic flow.
Baroclinic	The depth-dependent component of ocean currents. The baroclinic flow can be estimated from measurements of ocean density.
Deep western boundary current	Strong deep flows intensified along the western boundary of the basins.
Eddy	The small-scale, time-variable component of the ocean circulation (also mesoscale eddy).
Ekman transport	Wind-driven transport of the surface layer of the ocean to the right (left) of the wind in the northern (southern) hemisphere.

This chapter was originally published as part of the Encyclopedia of Sustainability Science and Technology edited by Robert A. Meyers. DOI:10.1007/978-1-4419-0851-3

S.R. Rintoul (✉)
Antarctic Climate and Ecosystems Cooperative Research Centre, Wealth from Oceans National Research Flagship, CSIRO Marine and Atmospheric Research,
GPO Box 1538, Hobart, TAS 7001, Australia
e-mail: Steve.Rintoul@csiro.au

J. Orcutt (ed.), *Earth System Monitoring: Selected Entries from the Encyclopedia of Sustainability Science and Technology*, DOI 10.1007/978-1-4614-5684-1_10,

Geostrophic flow	The large-scale flow of the oceans is in geostrophic balance, where horizontal pressure gradients are balanced by the Coriolis force.
Glider	Like an Argo float with wings, an autonomous instrument that varies its buoyancy allowing it to move both vertically and horizontally, measuring water properties.
Hydrographic sections	Ship transects along which measurements are made of seawater properties (e.g., temperature, salinity, carbon, nutrients).
Meridional	In the north–south direction.
Meridional overturning circulation	A basin-integrated view of the net north–south flow in the ocean basins.
North Atlantic deep water	Deep water formed in high latitudes of the North Atlantic that spreads to the south in a deep western boundary current.
Ocean conveyor belt	A highly simplified conceptual representation of the large-scale overturning circulation of the oceans.
Overturning circulation	A global-scale network of ocean currents consisting of sinking of dense water in a small number of deep water formation regions and a compensating return flow of water in the upper ocean.
Potential vorticity	A property of a fluid related to its rotation rate and stratification, which is approximately conserved by the large-scale ocean circulation. Analogous to angular momentum.
Sverdrup	A unit of the volume of water carried by ocean currents ($1\ \mathrm{Sv} = 10^6\ \mathrm{m}^3\ \mathrm{s}^{-1}$).
Thermohaline circulation	A term sometimes used as a synonym for the overturning circulation, or more specifically the portion of the overturning circulation driven by exchange of heat and moisture (i.e., thermohaline forcing) at the sea surface.
Ventilation	The transfer of surface waters to the interior ocean, resulting in renewal of oxygen levels and other properties of the subsurface ocean.
Water mass	A volume of the ocean with similar water mass properties.
Water mass formation	The process by which surface water acquires a characteristic set of water mass properties through air–sea interaction, and transfers these properties into the ocean interior when the water mass sinks.
Zonal	The east–west direction.

Definition of the Subject

Roughly half the world ocean volume lies below 2,000 m depth. This deep half of the ocean is cold ($<3°C$), indicating that the abyssal ocean is filled with waters that sink in high latitudes, where cold surface waters are found [1]. The deep ocean circulation transports the cold waters that sink in the polar regions throughout the deep ocean basins. The transfer of surface water to the deep ocean must be balanced by an inflow of water in the upper ocean to the deep water formation regions, to conserve mass. The result is an "overturning circulation ," in which the export of cold deep waters from the source regions is balanced by a return flow of warmer water in the upper ocean. The large temperature contrast between the upper and lower limbs of the overturning circulation makes this flow pattern an efficient means of transporting heat. The large-scale overturning circulation is the primary means by which the ocean stores and transports quantities of relevance to the Earth's climate system and biogeochemical cycles, including heat, freshwater, carbon, and nutrients. The evolution of climate is therefore influenced strongly by the overturning circulation.

The deep ocean, once thought to be largely quiescent, is now recognized to include energetic flows in many locations. The classical description of the deep ocean circulation includes deep boundary currents along the western boundaries of ocean basins, and quieter flows in the ocean interior. Observations from long-term moorings and deep floats have illustrated a more dynamic deep ocean environment, with energetic variability observed at a wide range of space and timescales, including narrow jets, eddies, and recirculating gyres.

The deep and overturning circulations are difficult to observe with existing tools. Most of the knowledge of deep currents has been inferred from the distribution of properties measured along hydrographic transects occupied by ships. The coverage of the deep ocean by full-depth hydrographic sections remains sparse in space and time. In addition, the property distributions reflect the integrated response to a combination of advective and diffusive processes and their interpretation in terms of deep circulation can be ambiguous. Direct measurements of deep currents, for example from current meter moorings, are even less common. The deep ocean circulation, therefore, remains largely unobserved. However, new tools are now making it feasible to obtain sustained measurements of the deep ocean.

Introduction

The conceptual framework developed by Stommel [2] still guides present thinking about the nature of the deep ocean circulation. Deep water that sinks in the polar regions of the ocean must flow away from the source regions. Stommel recognized that on a rotating earth these deep currents will be intensified along the western boundary of the ocean basins, forming "deep western boundary currents" (DWBCs). The sinking in the deep water formation regions was presumed to be

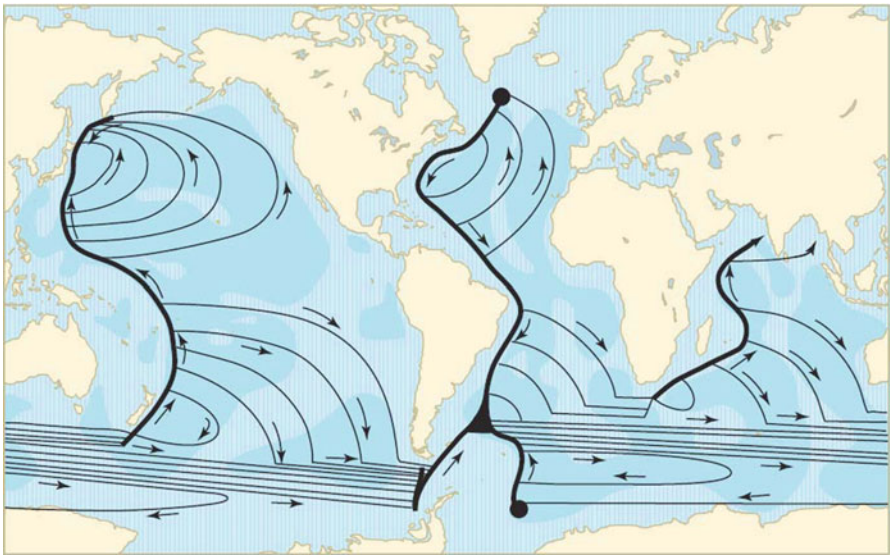

Fig. 10.1 The abyssal circulation according to Stomme's model [2]. Sources of deep water in the northern North Atlantic and Antarctica are denoted by *black dots*. These water masses are carried away from the source regions by a network of deep western boundary currents that feed weak poleward flows in the interior of each ocean basin (Reprinted from [4], as modified by [56], with permission)

balanced by weak upwelling distributed uniformly over the rest of the global ocean. The "stretching" of water columns produced by this upwelling requires that fluid must move poleward in the ocean interior to conserve potential vorticity. Stommel and Arons [3, 4] used these concepts to map the expected circulation pattern in the deep ocean, consisting of concentrated deep flows along the boundary of each basin and weak poleward flow in the interior (Fig. 10.1).

Both the upwelling and the interior flow are too weak to measure directly. Efforts to test this model of the deep circulation have therefore focused on measurements of the deep western boundary currents [5]. Swallow and Worthington [6, 7] used neutrally buoyant floats to confirm the presence of a deep southward flow along the western boundary of the North Atlantic. Warren and others used measurements of water properties collected by ships and direct velocity measurements from current meter moorings to identify DWBCs in each of the ocean basins [8–10]. In particular, the fact that the DWBCs carry waters that have recently been in contact with the atmosphere, and hence are rich in gases like oxygen and chlorofluorocarbons, means that tracer measurements provide a powerful tool for mapping the deep circulation.

In the modern ocean, deep water is only formed in a few locations in the high-latitude North Atlantic and over the Antarctic continental shelf. The density of seawater depends on both temperature and salinity. To sink from the sea surface to the deep ocean, surface waters must become sufficiently cold and salty to be denser

than the water below. The surface waters in the high-latitude North Pacific are so fresh that even when cooled to the freezing point, they remain too buoyant to sink [11]. Even in the North Atlantic and the Southern Ocean, deep water is only formed in a few particular regions where air-sea heat loss and the release of brine during sea ice formation result in a sufficient increase in density to cause surface waters to sink.

The flow of deep water away from the source regions is balanced by a return flow of warmer, lighter water in the upper ocean. These counter flows, linked by formation of dense water at high latitude, form an overturning cell. The northward transport of warm water in the upper ocean and compensating southward transport of cold water at depth results in a poleward transport of heat in the Atlantic basin. The large temperature contrast between the upper and lower limb of the overturning makes this circulation pattern an efficient means of transporting heat. In fact, at midlatitudes the ocean and atmosphere make roughly equal contributions to the poleward redistribution of heat absorbed in the tropical regions. The overturning circulation is also an important player in the biogeochemical cycles of carbon, nutrients, and other properties.

Various terms have been used to refer to the overturning circulation . Because deep water formation depends on density, and hence on temperature and salinity, the circulation is often referred to as the thermohaline circulation. However, as discussed below, it is not clear that the overturning is driven solely or primarily by the exchange of heat and moisture and so the term "thermohaline" is potentially misleading. In addition, the phrase has been used by many authors to mean different things, adding to the confusion [12]. In the Atlantic, the term "meridional overturning circulation (MOC)" is commonly used. However, the global-scale overturning circulation involves zonal as well as meridional flows, and the zonally averaged perspective inherent in the term MOC is itself potentially misleading. Therefore, the more general term overturning circulation is used here.

Another term, the "great ocean conveyor belt," was introduced by Wally Broecker [13, 14]. He highlighted the link between glacial cycles and variations in the strength of the overturning circulation. In particular, the addition of freshwater from melting continental ice sheets during the transition from glacial to interglacial conditions made surface waters in the North Atlantic too buoyant to sink, slowing the heat transport by the ocean conveyor, and cooling northern hemisphere climate. The switching on and off of the conveyor was linked to temperature changes in Greenland as large as 10°C over periods as short as a decade or two. Broecker's work highlighted the role of the "ocean conveyor" in global climate and renewed interest in the forcing of the circulation and its sensitivity to changes in forcing (in particular, freshwater input).

Broecker's "conveyor belt" picture was intended to serve as a logo or metaphor for the much more complex, three-dimensional, and time-variable circulation now commonly referred to as the overturning circulation, rather than as a realistic depiction of the flow. The actual flow paths involved in the global overturning circulation are much more complex, including narrow boundary currents, recirculation gyres, small-scale eddies, and jets. The deep circulation is steered by the topography of the seafloor and can also be influenced by the deep expression of circulation features in the upper ocean, such as boundary currents and eddies.

The large capacity of the ocean to store heat has a significant influence on climate. For example, more than 93% of the extra heat energy stored by the Earth system over the last 50 years is found in the ocean [15, 16]. The extra heat stored in the ocean has caused a rise in sea level, as a consequence of thermal expansion of the water column. Most of the extra heat stored in the ocean has accumulated in the upper 700 m. However, there is increasing recognition that the deep ocean makes a significant contribution to ocean heat storage and sea-level rise [17]. Accounting for the contribution of the deep ocean is necessary to explain the observed record of past sea-level rise (e.g., [18]) and to close the overall energy budget of the earth [17]. In addition, the warming projected by climate models for a given level of greenhouse gas forcing (called the climate sensitivity) is sensitive to the amount and depth of ocean heat storage [19]. Observations of the deep ocean are therefore needed to improve climate projections and to understand changes in sea level and the planetary energy budget.

Progress in understanding the deep circulation has been slowed by the technical challenge of observing the deep ocean. While new instruments like Argo profiling floats have revolutionized the ability to observe the upper 2 km of the ocean, providing the first year-round, broad-scale measurements of the ocean, no equivalent yet exists for the deep ocean. Deep ocean observing systems still rely heavily on traditional oceanographic platforms like ships and moorings. Because research vessels and long-term deep water moorings are expensive, the spatial and temporal coverage of deep ocean observations remains very limited. The deep ocean is now recognized to be more energetic and to include flows on smaller spatial scales than once believed, characteristics that increase the challenge of observing the deep circulation and its variability.

Deep Water Masses and Circulation

Sources of Deep and Bottom Water

To sink from the sea surface to the deep ocean, surface waters must become sufficiently dense, hence cold and/or salty. These conditions are met in only a handful of places in the present day ocean. Warm, saline waters move north in the upper layers of the Atlantic Ocean, gradually losing heat to the atmosphere, until ultimately sinking in the Norwegian, Greenland, and Iceland seas. These dense waters spill through gaps in the ridge system isolating the northern seas from the North Atlantic. Mixing with ambient waters during the descent into the deep North Atlantic increases the volume and modifies the properties of the dense overflows. Deep convection in the Labrador Sea produces somewhat lighter and warmer water which contributes to the deep waters in the basin. Collectively these dense waters supplied to the basin are known as North Atlantic Deep Water (NADW).

An even denser water mass, known as Antarctic Bottom Water (AABW), is formed in several locations around the margin of Antarctica. Heat lost to the atmosphere cools the ocean and, if the sea temperature reaches the freezing point of about −1.8°C, results in the formation of sea ice. Salty brine released when sea ice forms increases the density of the underlying water and makes an important contribution to the formation of dense shelf waters. As the dense waters flow off the shelf and sink into the deep ocean, they entrain about three times their volume of ambient waters [20]. The mixture of dense shelf waters and entrained fluid forms AABW. The primary sources of AABW are the Weddell Sea in the Atlantic sector, the Ross Sea in the Pacific sector, and the Adélie/Wilkes Land coast south of Australia [20–22].

NADW and AABW are examples of water masses, volumes of water with similar physical and chemical properties, reflecting a common origin. Water masses acquire their characteristic properties (e.g., temperature, salinity, and dissolved gas concentrations) through exchange between the surface ocean and the atmosphere. When water masses sink from the sea surface, they carry these characteristic properties with them into the ocean interior. These properties gradually evolve as the water masses are carried away from the source regions by ocean currents, as a result of mixing with water masses with different characteristics, but mixing is relatively weak in the ocean and water mass properties tend to be retained for long distances. Maps of water properties can thus be used to trace the spreading paths of water masses. In fact, given the difficulty of directly observing deep ocean currents, much of what is known about the deep circulation has been inferred from the distribution of water mass properties.

For example, surface waters in contact with the atmosphere are rich in dissolved gases like oxygen and chlorofluorocarbons (CFCs). The distribution of oxygen and CFC reflects the flow paths of deep water away from the source regions. Figure 10.2 shows the distribution of CFC-11 in the North Atlantic, illustrating the spreading pathway of the recently ventilated North Atlantic Deep Water [23]. At 24°N in the Atlantic, high CFC concentrations are observed in the deep ocean in the western basin, with the highest values observed adjacent to the boundary. A map of the inventory of CFC-11 in the NADW shows a plume of high CFCs spreading southward along the western boundary from the deep water formation regions in the Greenland –Iceland-Norwegian and Labrador Seas (Fig. 10.2b). Figure 10.3 shows a similar plot for the Southern Ocean, illustrating the three main sources of Antarctic Bottom Water in the Weddell and Ross Seas and the Adélie/Wilkes Land coast and the system of boundary currents exporting AABW to lower latitudes [20]. As seen in the North Atlantic, the highest concentrations are observed along the western boundary of each ocean basin. NADW and AABW supply roughly equal amounts ($10 - 15 \times 10^6\ m^3\ s^{-1}$) of dense water to the deep ocean [24] and AABW occupies roughly twice the volume of NADW [25].

No dense water is formed in the northern Indian and Pacific basins. The north Indian Ocean is limited to relatively low latitudes and so strong cooling of the ocean does not occur there. The Pacific extends to high latitudes and enough heat is lost to freeze the sea surface in winter. However, the surface waters of the Pacific are so

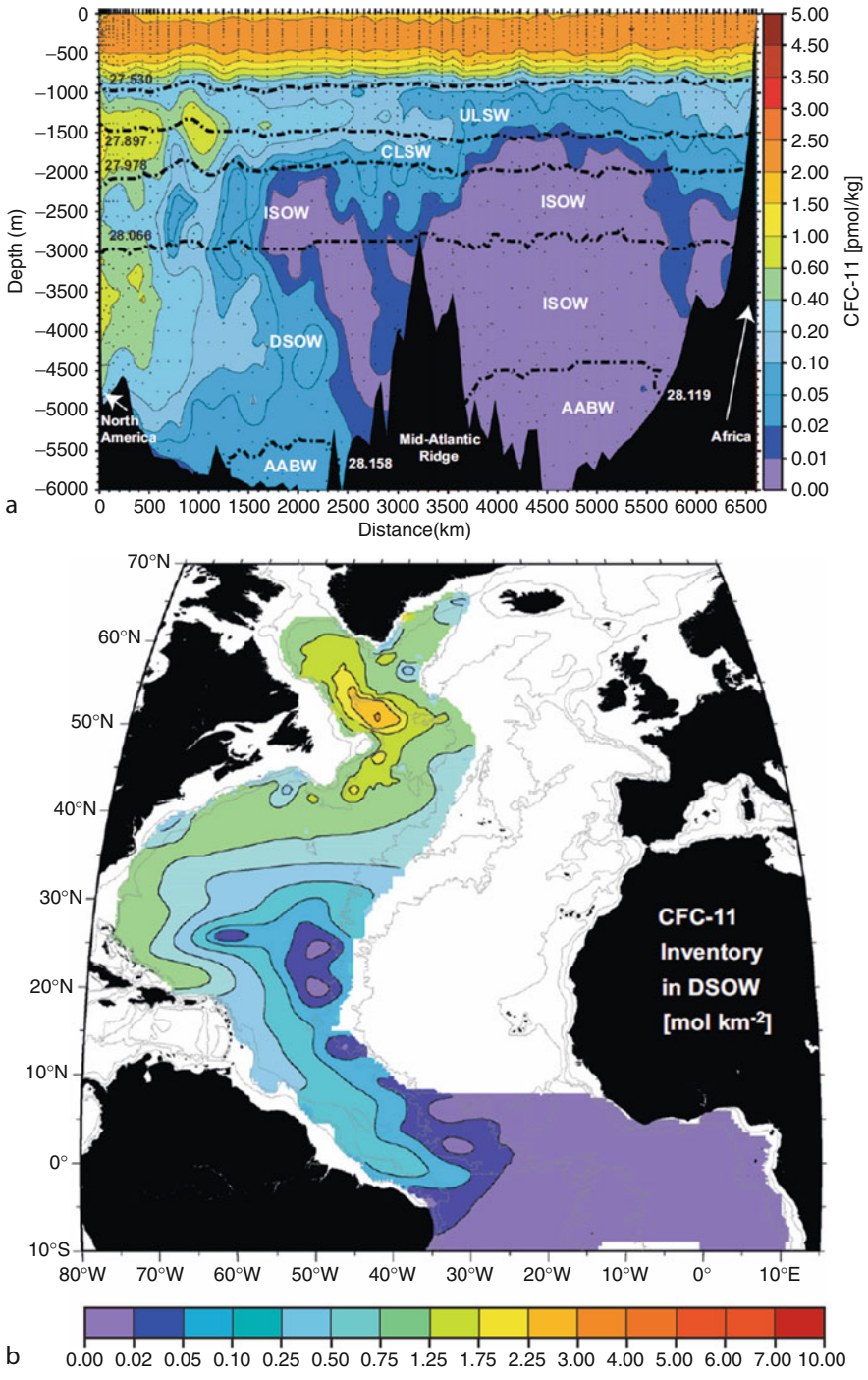

Fig. 10.2 (**a**) Vertical section of chlorofluorocarbon – 11 (CFC-11, [pmol kg^{-1}]) in the North Atlantic at 24°N. The initials indicate different water masses; *dashed lines* indicate surfaces of constant density. The neutral density surfaces defining the water mass boundaries are plotted as bold *dashed lines*. (**b**) The inventory of CFC-11 (molkm_2) in the density layer corresponding to dense overflow waters exported from the Greenland–Iceland–Norwegian Seas through the Denmark Straits (DSOW) (From [23], used with permission)

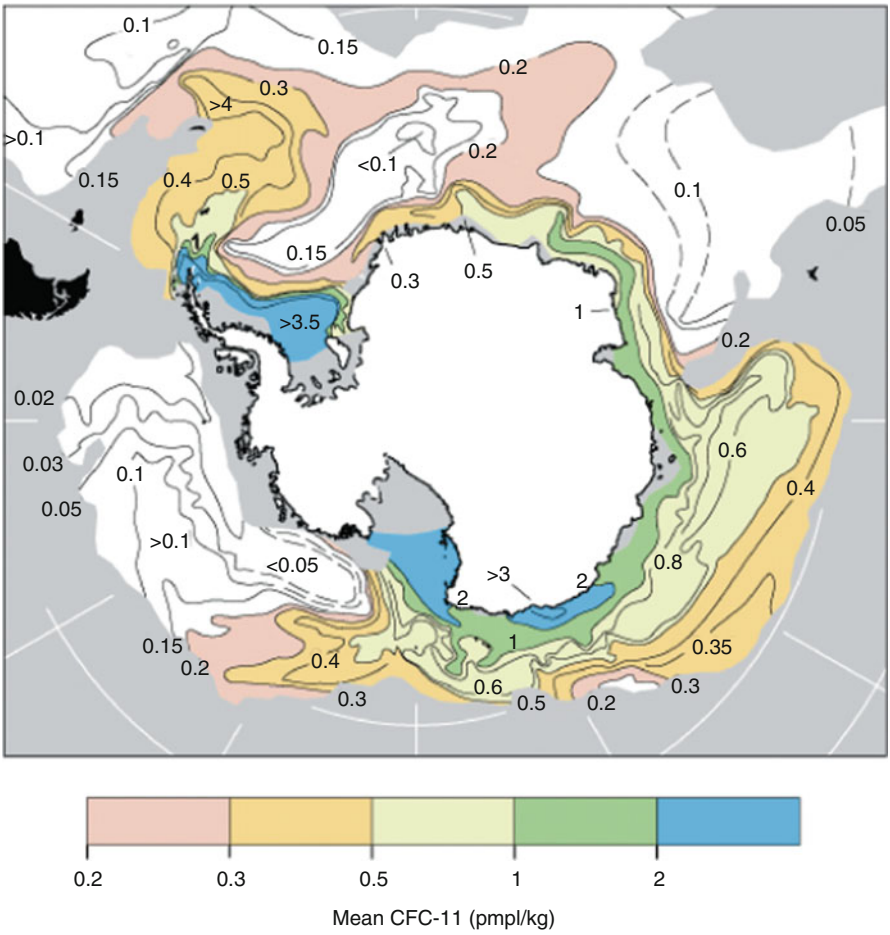

Fig. 10.3 Inventory of CFC-11 in the Antarctic bottom water layer. High concentrations (*blue*) near the Weddell Sea, Ross Sea, and Adélie/Wilkes Land Coast indicate the three major sources of Antarctic bottom water (Adapted from [20])

fresh that even when cooled to the freezing point they are too buoyant to sink into the deep ocean [11]. These basins are therefore ventilated from the south, by a mixture of NADW exported from the Atlantic and AABW formed in the Southern Ocean, called Circumpolar Deep Water (CDW) [26]. This can be seen clearly in the distribution of oxygen in the deep ocean in these basins. High oxygen values spread northward from the Southern Ocean at 4,000 m depth in the Pacific, with the strongest penetration seen to the east of the large bathymetric obstacle imposed by the Tonga–Kermadec Ridge (Fig. 10.4). Oxygen values are low in the North Pacific and spatial gradients are small, indicating relatively weak flow there. The oxygen distribution at 33°S in the Indian Ocean shows that the lowest oxygen values are observed at mid-depth,

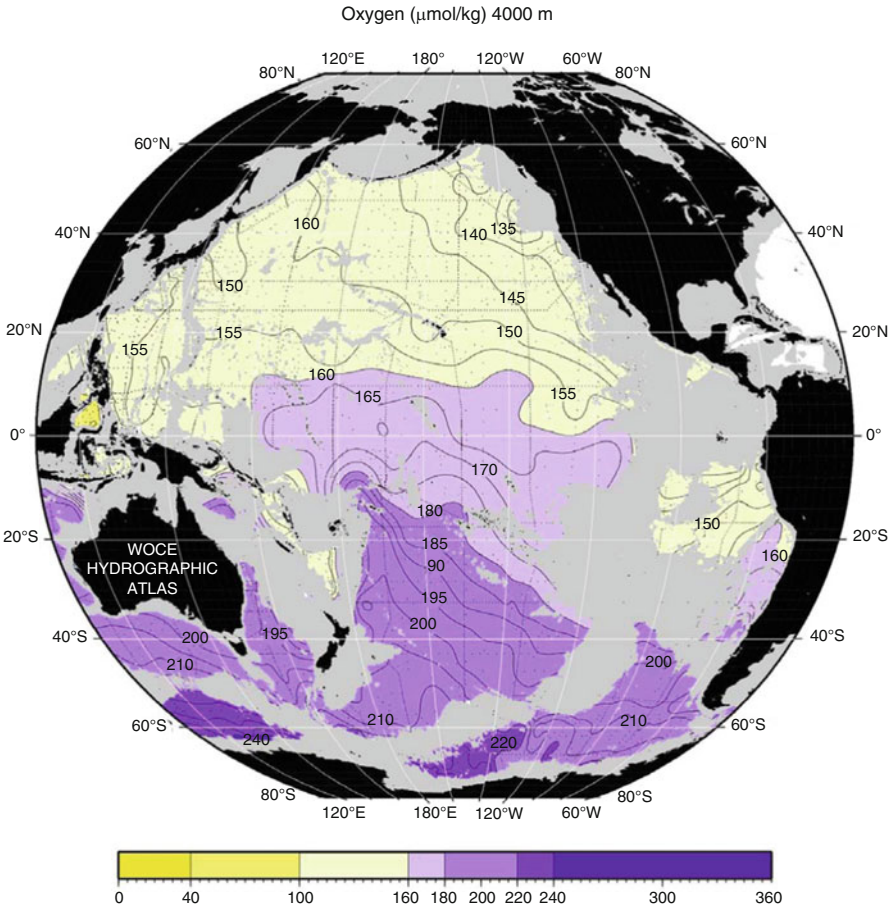

Fig. 10.4 Oxygen concentration at 4,000 m depth in the Pacific, illustrating the inflow of relatively oxygen-rich Circumpolar Deep Water in a deep western boundary current to the east of New Zealand. From the WOCE Pacific Atlas; used with permission

sandwiched between the well-ventilated upper ocean waters that have been in recent contact with the atmosphere and relatively oxygen-rich deep waters spreading northward into the basin along the western sides of the deep basins (Fig. 10.5).

Deep Ocean Circulation

The distribution of water mass properties in the deep ocean reflects the formation and spreading of dense water formed at high latitudes in the North Atlantic and

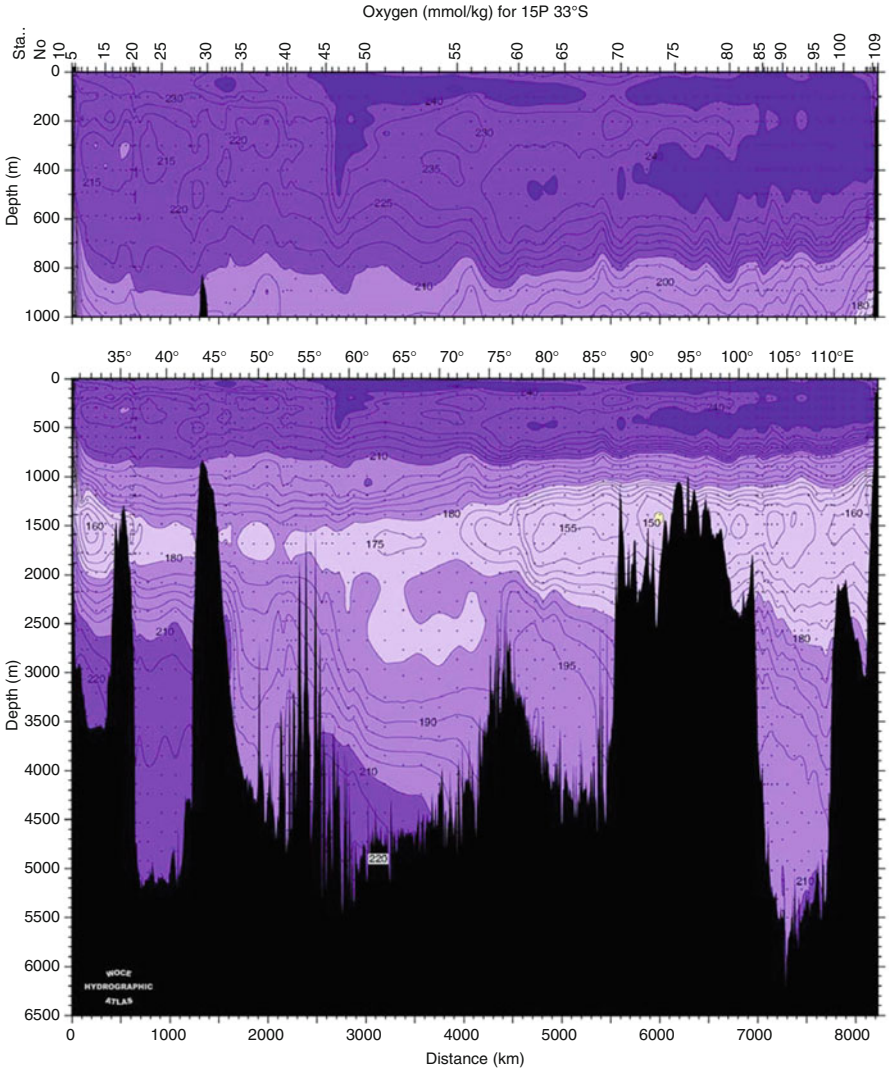

Fig. 10.5 Oxygen concentration at 33°S in the Indian Ocean. Abyssal waters are relatively rich in oxygen, with the highest values seen near the seafloor on the western side of each deep basin, reflecting the presence of deep western boundary currents (From WOCE Pacific Atlas; used with permission)

Southern Oceans. More specifically, the property distributions indicate the dominant role played by deep western boundary currents in the deep circulation. Maps of deep ocean properties like Figs. 10.2, 10.3, 10.4 also illustrate several other important aspects of the deep circulation: The flow is strongly steered by bathymetric features like the mid-ocean ridges and fracture zones; water properties gradually

evolve along the flow path as a result of mixing; and water mass properties often change more abruptly near sills between basins (e.g., the Samoa Passage near 10 S, 175 W, Fig. 10.4), suggesting enhanced mixing in these regions.

The transport of the deep western boundary currents have been measured at a number of locations in the Atlantic and at a few locations in the Indian and Pacific basins, from long-term moored experiments or hydrographic sections. Hogg [27] provides a useful summary of measurements that existed at that time. A DWBC carrying NADW southward can be identified throughout the Atlantic (e.g., Fig. 10.2b). AABW and CDW formed from a mixture of AABW and NADW flows northward along the western boundary of most of the deep basins surrounding Antarctica, as seen in Figs. 10.3 and 10.5.

Such measurements confirm the existence of the DWBCs expected from the Stommel's theory. However, as observations of the deep ocean have increased in number and duration, it has become clear that the deep circulation is more complex than illustrated in Fig. 10.1. Energetic eddies are common in the vicinity of the deep boundary currents, produced by dynamical instabilities of the currents. Stable transport estimates therefore require time series of sufficient duration to average over the eddy signal. In addition, momentum fluxes associated with these eddies drive recirculating gyres offshore of many DWBCs (e.g., [28, 29]). The presence of the deep recirculation gyres complicates efforts to measure the net transport of the DWBCs associated with the large-scale overturning circulation: few moored arrays span both the DWBC and the offshore gyres, as required to separate the recirculating and throughflow components of the DWBC.

The weak poleward flow expected from Stommel's deep circulation theory has proven even more elusive to observe. The first attempts to use neutrally bouyant floats to measure the interior flow instead discovered mesoscale eddies [30, 31]. Stommel's theory assumed a flat-bottomed ocean. The presence of seafloor bathymetry both steers the deep flow and can affect the dynamics of the deep circulation by driving vertical motions near the seafloor and hence meridional motion, analogous to the poleward flow caused by upwelling at the top of the deep layer in the Stommel model. In a basin with realistic bathymetry, therefore, one would not necessarily expect to see uniform poleward flow in the interior. Neutrally buoyant floats were used to study the deep flow in the Brazil Basin during the World Ocean Circulation Experiment [32]. Rather than weak poleward flow, the floats revealed alternating east–west (zonal) flows, with short north–south (meridional) scales, in the interior of the basin. The zonal flows in the interior were interpreted to be consistent with the idea that mixing (and therefore upwelling) was limited to the rough topography around the rim of the basin (as directly observed during the experiment, [33]). With no upwelling in the interior, there is no vortex stretching and no requirement for meridional flow in order to conserve potential vorticity. Zonal flows in the ocean interior have since been observed in many parts of the ocean [34].

Global Overturning Circulation

The DWBCs that dominate the circulation of the deep ocean form the lower limb of the global overturning circulation. To balance the sinking of dense water in the North Atlantic and Southern Ocean, an equal volume of water in the upper ocean must flow toward the sinking regions in the upper limb of the overturning circulation. The shallow and deep branches of the OC must be linked by upwelling (and therefore mixing) somewhere in the ocean interior. While the existence of a global-scale circulation pattern linking the high-latitude sources of deep water to lower latitudes, and the upper layers of the ocean to the deep sea, has been recognized for many years, a quantitative understanding of the structure and dynamics of the overturning circulation was lacking.

Role of the Overturning Circulation in Climate and Biogeochemical Cycles

The OC is a primary mechanism for the transport and storage of heat and freshwater and carbon by the ocean and therefore has a substantial impact on climate variability and change [35]. For example, in the North Atlantic the ocean carries about 1×10^{15} W of heat to the north, helping to moderate the climate of western Europe. The relative contribution of deep and shallow overturning cells to the net meridional transport of heat and freshwater varies between the ocean basins [36, 37]. Changes in the OC have been linked to past climate variations, including abrupt changes caused by a slowing of the overturning, and climate models suggest the circulation will both respond to and modulate climate change in the future (e.g., [38]). In particular, large inflows of freshwater produced from melting of ice during the transition out of glacial cycles are believed to have made the surface waters of the North Atlantic so buoyant that dense water was no longer formed [14]. The resulting slowdown of the overturning circulation and reduction in heat transport led to rapid cooling. Climate models project a slowdown of the overturning circulation of about 30% over the next century, as a result of warming and freshening of the surface layers of the ocean, although the magnitude and sensitivity to change of the overturning varies widely between models.

The OC also plays an important role in the global cycles of carbon, nutrients, and other properties. Sinking of organic matter transfers nutrients and carbon from the surface to the deep ocean. Upwelling of deep water as part of the OC, particularly in the Southern Ocean, returns nutrients to the surface ocean to support phytoplankton growth [39]. Models suggest that nutrients upwelled and exported by the Southern Ocean support 75% of global primary production north of 30°S [39]. Changes in the overturning circulation would therefore be expected to influence global primary productivity and ecosystem function [40]. Deep water is also rich in carbon and the efficiency with which the ocean sequesters carbon dioxide from the atmosphere depends on a balance between the outgassing from upwelled deep water and the physical and biological processes acting to transport carbon into the ocean

interior [41]. Projections of future climate change are sensitive to the rate of carbon uptake by the ocean in climate models and therefore sensitive to the overturning circulation. Atmospheric observations and coarse-resolution ocean model studies have suggested that the carbon sink in the Southern Ocean has "saturated" in recent decades, as a result of an increase in strength of the overturning circulation (and hence increased outgassing of natural carbon from the deep ocean) in response to stronger winds [41]. This result, however, may significantly change when ocean eddy feedback processes are resolved [42]. The upwelling of carbon-rich deep water will also affect the carbon saturation state and pH of surface waters, with implications for calcifying organisms and marine ecosystems.

Seasonal and interannual climate variability is largely independent of the deep ocean and OC. But as the timescale of climate variability increases, the deep ocean becomes an increasingly important player. For example, a number of recent studies have shown that sea surface temperature variations on multi-decadal timescales are influenced by the overturning circulation (see [43] for a summary). These multi-decadal anomalies in Atlantic sea surface temperature (SST), known as the Atlantic Multi-decadal Oscillation, have in turn been linked to regional climate anomalies, persistent drought, hurricane frequency, and fisheries production (see [44–46] and references therein). On these timescales, the evolution of climate tends to be dominated by the slow dynamics of the ocean rather than the atmosphere [47, 48], suggesting that it may be possible to exploit ocean information to improve the prediction of these phenomena. For example, advection of salinity anomalies by the OC can result in decadal variability of the OC and its heat transport, and therefore in anomalies of sea surface temperature that drive decadal variability in the overlying atmosphere [45].

Conceptual Models of the Overturning Circulation

Observations of the deep circulation (section Deep Ocean Circulation) reveal features both consistent with (e.g., DWBCs) and at odds with (e.g., lack of evidence of poleward flow in the interior) the simple pattern (Fig. 10.1) expected from Stommel's model for the deep circulation. The limited deep observations available to date also reveal a variety of small-scale, energetic flows that complicate efforts to observe and understand the overturning. The connections between the upper and lower limbs of the overturning and the nature of the interior flows have been particularly difficult to quantify and understand. Nevertheless, a more complete conceptual model of the overturning circulation has gradually evolved over the past 25 years.

In the absence of other information, Stommel assumed the sinking at high latitudes was balanced by uniform upwelling elsewhere. A consequence of uniform upwelling was that much of the return to the upper ocean must take place in the Pacific, the largest ocean basin. There must therefore be exchange pathways in the upper ocean to return fluid upwelled in the Pacific and Indian Oceans to the Atlantic to complete the loop. Broecker and Peng [49] were the first to refer to the resulting

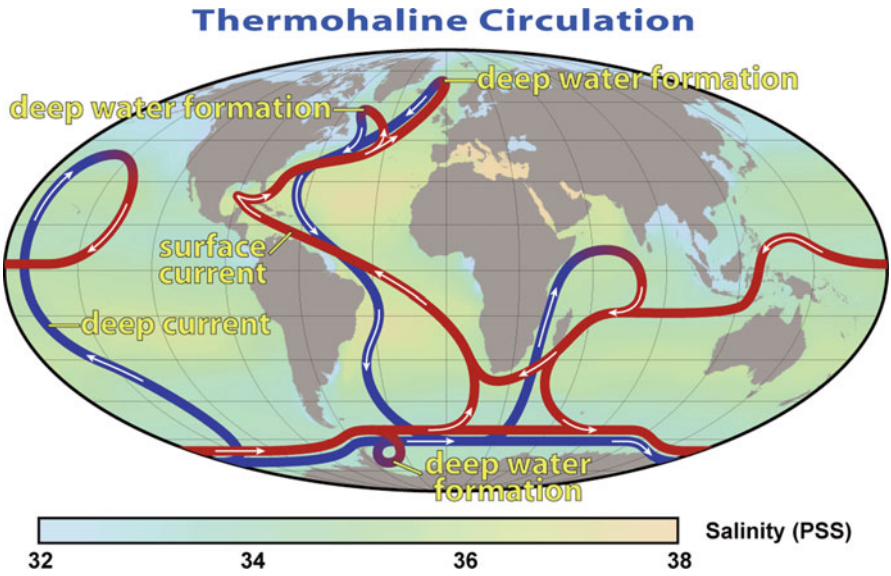

Fig. 10.6 An illustration of Broecker's "Great Ocean Conveyor Belt," modified to include sinking of dense water near Antarctica and the interbasin connection provided by the Antarctic Circumpolar Current around Antarctica. *Red arrows* indicate flows of warm water in the upper ocean; *blue arrows* the flow of deep water (Illustration by Robert Simmon, NASA; used with permission)

global circulation pattern as a "conveyor belt" and to attempt to illustrate the circulation with a two-layer schematic. Gordon's [50] version of this schematic included a more realistic representation of the regional currents and interbasin exchanges involved in the global cell, and was the first to include estimates of the transports carried by the various branches. A visually compelling cartoon of the two-layer schematic published by Broecker [13] with the title "Great Ocean Conveyor Belt" grabbed the imagination of many and was used in Broecker [14] to illustrate the role of the overturning circulation in glacial–interglacial cycles. Figure 10.6 shows a version of the Broecker conveyor belt, modified to include the Antarctic sources of deep water and the interbasin connection provided by the Antarctic Circumpolar Current.

A series of authors have sought to add to the realism of Broecker's schematic diagram, while retaining the power of a simple representation of the flow. Richardson [51] provides a very useful overview of the history of such diagrams. Here a few of the major contributions are highlighted. Gordon ([52]; figure reproduced in [51]) used a novel three-dimensional representation of the oceans to represent the global nature of the overturning circulation, including the major interbasin exchanges, alternating flows at different depths in each basin, and the upwelling and mixing that link the upper and lower limbs. Schmitz [53, 54] revised and colored Gordon's scheme. Lumpkin and Speer [55] (Fig. 10.7) further revised this schematic and added estimates of the transport of the major current branches.

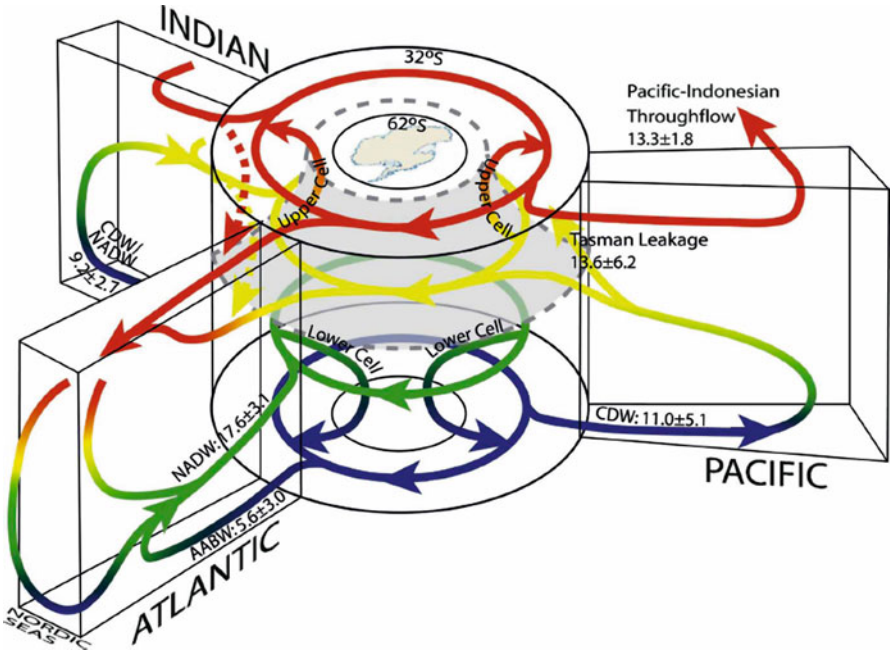

Fig. 10.7 A schematic view of the global overturning circulation. Color indicates approximate density ranges. *Red*: upper; *yellow*: intermediate; *green*: deep; *blue*: bottom. *Dashed arrows* indicate Indian-to-Atlantic westward exchange between Africa and the ACC (Format adapted from Gordon [52] and Schmitz [53, 54]; from [55]; used with permission)

Several authors have refined two-dimensional schematics of the overturning. In particular, the reports by Schmitz [53, 54] include a number of multilayer pictures of the global overturning, an example of which is shown in Fig. 10.8. These schematics were constructed by summarizing the results of a large number of regional and global studies and are particularly notable because they are quantitative, with an internally consistent set of transport estimates provided for each branch of the circulation. Finally, the schematic of Lumpkin (modified by Speich, 2009, personal communication) is a recent attempt to convey the global overturning in a more realistic fashion, including the major pathways, recirculating gyres, interbasin exchanges, water mass transformations, and eddies (Fig. 10.9).

A number of recent results have called aspects of the "conveyor belt" view of the overturning circulation into question [56]. The fact that an overturning circulation exists in the ocean is clearly supported by ocean observations, model studies and theory. However, it is becoming increasingly clear that it is inappropriate to think of this flow as a continuous, steady "belt" of flow connecting the ocean basins. (This was of course obvious from the start to the authors of early schematics of the overturning circulation, but the conveyor belt metaphor has at times been interpreted more literally than intended, perhaps a victim of its own success.) For example, the DWBC in the Atlantic is apparently not as continuous as once believed [57].

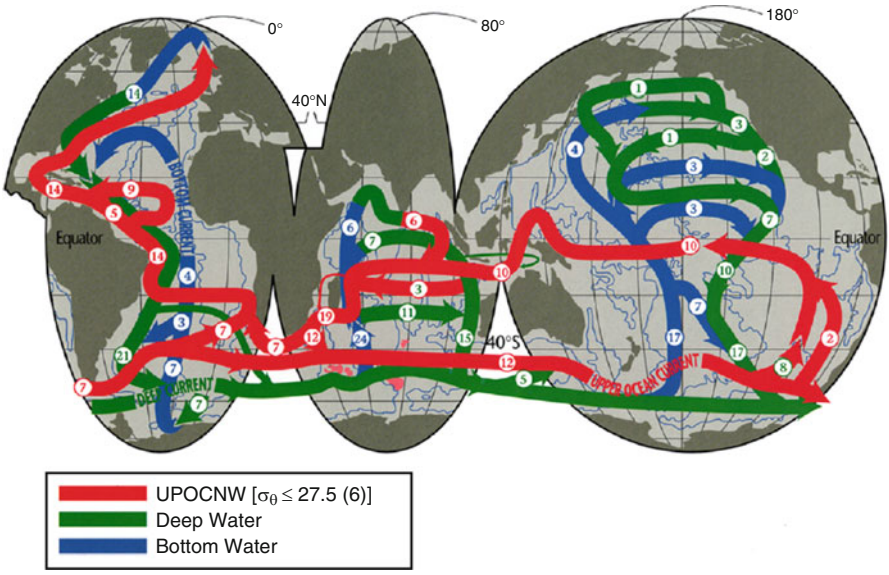

Fig. 10.8 A three-layer schematic of the global interbasin circulation by Schmitz [54]. Values in circles represent transport in Sverdrups. UPOCNW designates upper ocean water, a combination of upper layer water and intermediate water (From [54]; used with permission)

Eddies detrain and re-entrain fluid into the boundary current and into recirculation gyres, diluting waters in the boundary current and spreading the flow over a larger fraction of the interior of the basin. Floats have also revealed the importance of interior pathways [58]. The fact that local, time-varying processes (e.g., wind forcing, eddies, and recirculation gyres) can influence the transport of the DWBC means that variations in the strength of the current with time, or with latitude, do not provide an unambiguous indication of changes in the production of dense water in the source regions, as once assumed [56]. Moreover, evidence is growing that both the upper and lower limbs of the overturning are sensitive to wind and buoyancy forcing and to mixing. For example, it is not clear whether it is more appropriate to think of the overturning circulation as "pushed" by formation of dense water or "pulled" by upwelling driven by winds in the Southern Ocean and by vertical mixing [59]. Attribution of the cause of changes in the overturning is difficult because variations may reflect the response to a range of physical processes (e.g., eddies and wind) in addition to buoyancy forcing at high latitudes, as believed when the "conveyor belt" concept was developed.

Observations of the Overturning Circulation

The transport of properties by the OC depends on the rate of overturning and the difference in property concentration between the upper and lower limbs of

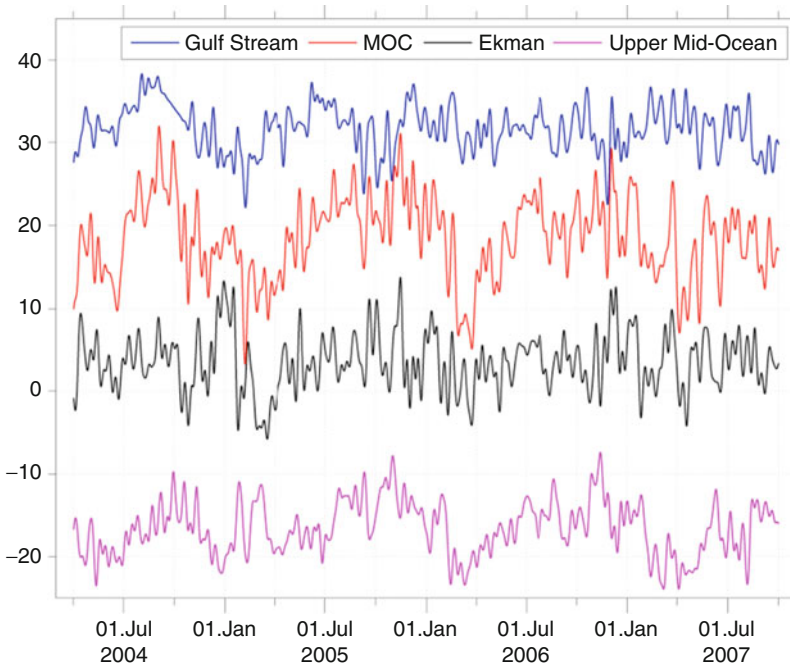

Fig. 10.9 Transport of the overturning circulation at 24 N in the Atlantic. Gulf Stream transport through the Florida Straits (*blue*), Ekman transport (*black*), upper mid-ocean transport (*magenta*), and overturning transport (*red*). Transports in Sv, positive northward. Florida Straits transport is based on electromagnetic cable measurements. Ekman transport is based on scatterometer winds. The upper mid-ocean transport is the vertical integral of the transport per unit depth down to 1,100 m. Overturning transport is the sum of Florida Straits, Ekman, and upper mid-ocean transport. The mean ± standard deviation of Gulf Stream, Ekman, upper-mid ocean, and overturning transports are 31.7 ± 2.8 Sv, 3.5 ± 3.4 Sv, −16.6 ± 3.2 Sv, and 18.5 ± 4.9 Sv, respectively (From [61]; used with permission)

the overturning; in many locations, the horizontal gyres also contribute to the meridional transport of heat and other properties. Therefore observations of the property transport by the OC must extend throughout the full depth and breadth of the ocean basins. With present technology, this is generally not feasible because of the expense of deploying a coherent array of current meter moorings across vast regions of the ocean. However, while continuous, direct measurements of the global OC are not yet possible, new approaches have been developed to allow monitoring of the OC at particular locations. An important achievement in the last decade is the first multiyear time series of the meridional mass transport contributing to the overturning circulation in the Atlantic sector.

For example, an array of instruments has been deployed to measure the overturning circulation crossing 26.5°N in the Atlantic [60–62]. Figure 10.9 shows a 3.5 year time series of the transport of individual components of the OC: the Gulf Stream at Florida Straits, the interior flow in the upper ocean, and the

Ekman transport. The mean overturning is 18.5 Sv (1 Sv = 10^6 m^3 s^{-1}), with a standard deviation of 4.9 Sv and a standard error of 1.5 Sv. The fact that the sum of the individual components approximately conserves mass provides additional confidence that the transport estimates are robust [62]. The measurements reveal significant high-frequency variability of the OC on several timescales, underscoring the need for both continuous sampling to avoid aliasing and for long time series to detect trends. The continuous time series is providing new insights into the dynamics of the OC, including identification of the mechanisms responsible for variability of the OC on different timescales (e.g., [63]).

The 26.5°N array exploits the fact that the net geostrophic transport between two points on a latitude circle can be determined from measurements of the pressure difference between the two points. Therefore the volume transport in the interior can be estimated from measurements on either side of the basin, without the need for a coherent array of instruments spanning the basin. This works well at 26.5 N in the Atlantic because of the particular geometry of the basin there. The strong flows in the boundary currents over the continental slope on the western side of the basin need to be measured directly.

The end-point monitoring approach has also proved effective at 16°N in the Atlantic, where the time series of North Atlantic Deep Water export is now more than 9 years long [64, 65]. Flows in the eastern basin contribute little to the net transport. The near-rectangular geometry of the western Atlantic basin allows the OC to be monitored with a small number of instruments and thus is very cost-effective. As found at 26.5°N, the transport of the lower limb of the OC is highly variable on short timescales (Fig. 10.10). Despite the large high-frequency variability, the time series is of sufficient duration to detect a weakening trend (significant at 85%), corresponding to a 3 Sv reduction in the NADW export over the duration of the record.

The demonstration that continuous measurements of the basin-scale overturning circulation can be made using a small number of instruments is a remarkable achievement. However, the subtropical North Atlantic represents a special case where the near-rectangular geometry of the ocean basins means that the end-point monitoring approach can capture most of the flow. Array design studies using general circulation models [66, 67] have identified some of the requirements for a basin-scale observing system for the overturning circulation. Where barotropic flows make a significant contribution to the mass and heat transport, they need to be measured directly and cannot be inferred from observations at the end points of a section. Where western boundary currents are broad (e.g., over sloping topography), extensive, and expensive, moored arrays may be required to resolve them. Complex bathymetry and barotropic flows in the ocean interior also need to be resolved, for example at subpolar latitudes where the gyre circulation makes a significant contribution to the net heat flux. For accurate estimates of property transports, these measurements need to be horizontally coherent to capture the correlations of velocity and temperature that are responsible for heat transport. In other words, at most latitudes, direct observations of the overturning circulation require massive moored arrays that are not feasible with present technology and resources.

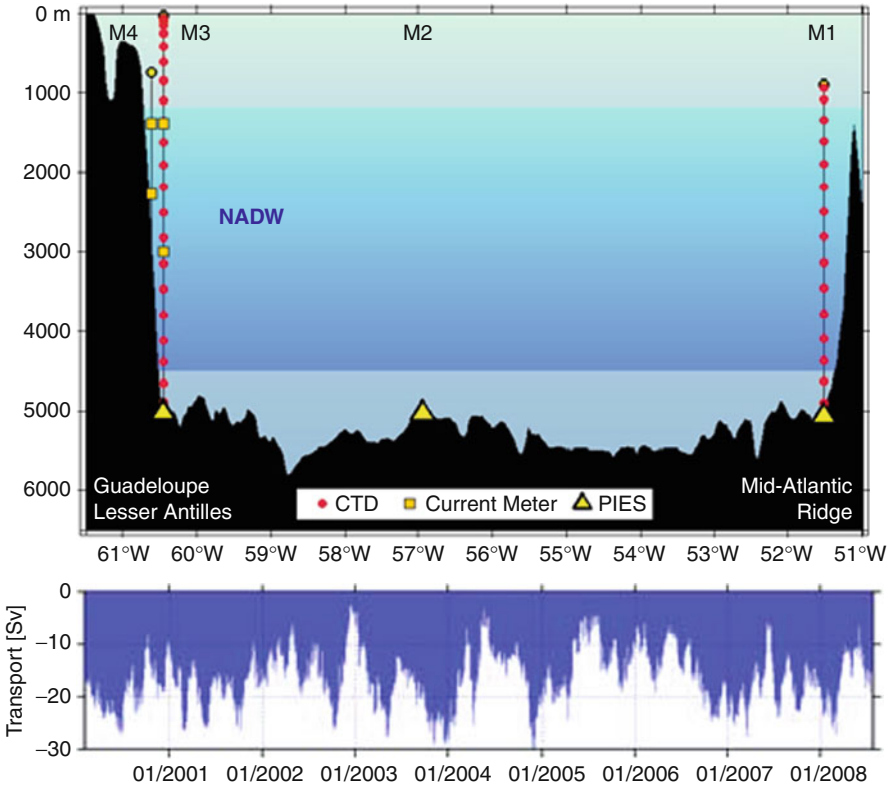

Fig. 10.10 Top: the 9°N array in the western basin of the Atlantic. Lines with red dots indicate end-point moorings; *yellow diamonds* indicate inverted echo sounders with pressure sensors (PIES). Bottom – Absolute transport of NADW through the array from end-point moorings with density sensors. The long-term mean is 14.9 Sv (southward) (From [65], used with permission)

While basin integrals of the OC are not yet feasible at most latitudes, major currents contributing to the overturning circulation have now been measured at several locations, in particular in the dense overflows and along the deep western boundary current carrying NADW southward [60, 68, 69]. These measurements have generally spanned the overflow or deep western boundary current, but not the flows in the interior of the basin. The presence of recirculation gyres offshore of the DWBC, usually not resolved by the moored arrays, often makes it difficult to use these measurements to infer the overall strength (or throughflow) of the OC [69]. However, they do provide robust estimates of a primary pathway of the deep limb of the overturning. The DWBC estimates can be combined with measurements in the ocean interior (e.g., from hydrographic sections) to estimate the OC and net meridional transport. They also provide valuable constraints for ocean state estimates and for the testing of ocean models.

Some current measurements have been made of the DWBC systems in the Indian and Pacific, but they are typically of less than 2-years duration and often lack the supplementary information needed to estimate the basin-wide overturning. As a consequence, estimates of the strength of the OC in the other ocean basins vary over a wide range (e.g., [70–73]). Examples of DWBC measurements include the flows carrying Antarctic Bottom Water (AABW) northward adjacent to the Kerguelen Plateau [74], into the Argentine Basin [75], through the Vema Channel to the Brazil Basin [76], and crossing the equator to enter the North Atlantic [77]; the flow entering the Indian Ocean through the Madagascar [78] and Perth Basins [79]; and the Pacific DWBC at 30°S [80], the Samoa Passage [81] and at 5°N [82].

Observations of Change in the Deep Ocean

In climate models, deep ocean heat uptake has been found to be well correlated with the climate sensitivity of the model, with greater ocean heat uptake implying a larger commitment to future warming and sea-level rise [83, 84]. In fact, the degree to which the deep ocean takes up heat may be the largest uncertainty in determining climate sensitivity [19]. A similar argument applies to the ocean uptake of carbon dioxide. Hence deep ocean measurements are central to reducing uncertainty in projections of global warming and sea-level rise. Observations suggest that warming of the deep ocean has contributed about 20% of the total increase in ocean heat content over the last decade or so [17].

While time series measurements are sparse in the deep ocean, there is increasing evidence of changes in properties and circulation. For example, the Antarctic Bottom Water (AABW) exported from the Southern Ocean to ventilate the abyss of each ocean basin has warmed in recent decades [17, 85–90] (Fig. 10.11). The changes in deep ocean temperature are sufficient to account for a significant fraction of the global energy imbalance [16, 18, 72, 87]. Reference [17] has estimated that the warming below 4,000 m depth and below 1,000 m south of the Subantarctic Front contributes about 0.09 W m^{-2} to the global heat budget (compared to 0.5 ± 0.18 W m^{-2} for the 0–700 m layer of the ocean [91]). This contribution to the planetary energy budget will grow in importance as the anthropogenic warming signal propagates to increasing depth with time. The warming below 4,000 m contributes about 0.1 mm $year^{-1}$ to global sea-level rise, while the warming below 1,000 m in the Southern Ocean contributes about 1 mm $year^{-1}$ of sea-level rise there. These new studies complement previous results [16, 92, 93], indicating significant warming between 700 and 3,000 m in the North Atlantic Ocean. The dynamical mechanism responsible for the observed abyssal warming is not yet known, but a recent study has highlighted the importance of wave-like motions that can rapidly transfer anomalies over large distances [94]. In this case, the warming of the deep North Pacific was traced back to changes in air-sea heat exchange at the sea surface off the coast of Antarctica, south of Australia.

The possibility that increased freshwater input to the high latitude ocean could cause a slowing of the thermohaline circulation and changes in climate has focused

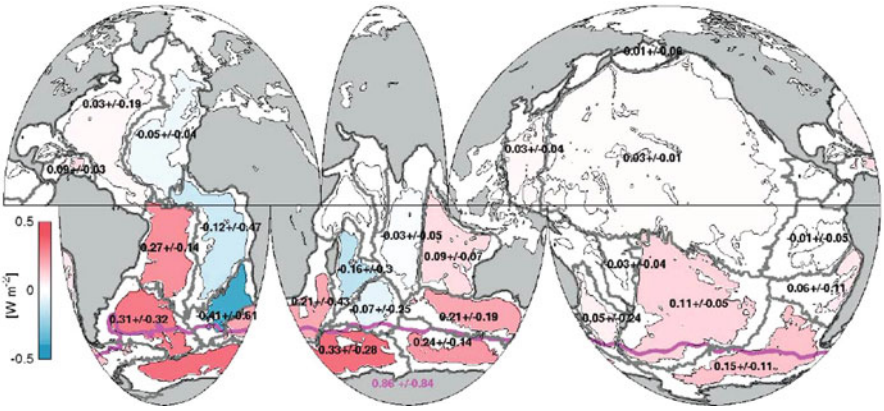

Fig. 10.11 Mean local heat fluxes through 4,000 m implied by abyssal warming below 4,000 m from the 1990s to the 2000s, with 95% confidence intervals. Basin boundaries (*thick gray lines*) and 4000 m isobaths (*thin gray lines*) are shown. The local contribution to the heat flux through 1,000 m south of the SAF (*maroon line*) implied by deep Southern Ocean warming from 1,000 to 4,000 m is also given (*maroon number*) with its 95% confidence interval (From [17]; used with permission)

considerable interest on the high-latitude freshwater budget. Changes in upper ocean salinity have been observed in each of the ocean basins, with an increase in salinity in the subtropical evaporation zones and a decrease at higher latitudes that is consistent with a more vigorous hydrological cycle and increased supply of meltwater at high latitudes [91, 95–97]. Numerous studies documented a freshening of North Atlantic Deep Water between the mid-1960s and the mid-1990s, when an atmospheric circulation pattern known as the North Atlantic Oscillation (NAO) evolved to an extreme positive state (e.g., [98]). The freshening reversed in the mid-1990s. Weakening of westerly winds in the mid-1990s to mid-2000s caused a reduction of deep convection in the Labrador Sea, a slowing and contraction of the subpolar gyre, and a northward advance of warm saline subtropical waters [99–104]. The NAO-induced upper ocean changes were rapidly transferred to deeper levels, causing an increase in temperature and salinity of deep waters [105–107].

While measurements are sparse in the Southern Ocean, several recent studies have detected changes in the salinity of Antarctic Bottom Water [86, 108–112]. The Ross Sea and Adélie Land regions supply about 40% of the total input of AABW [21]. Most of the AABW exported from both sources passes through the Australian Antarctic Basin, making it a good place to monitor changes in properties of the AABW formed in the Indian and Pacific sectors. The deep temperature–salinity relationship has changed throughout the basin in recent decades, with a shift toward fresher and lighter bottom water observed in the deepest 1,000 m of the water column [113]. References [110, 114, 115] suggest that the most likely source of the additional freshwater is basal melt of glacial ice in the Pacific sector. Enhanced

basal melting there has been linked to warmer ocean temperatures [116]. In contrast, in the Weddell Sea the situation is ambiguous, with freshening of bottom water in the west [117] and a slight increase in the salinity of deep water in the east [89].

The evidence from the North Atlantic and the Southern Ocean suggests that the dense water sinking in both hemispheres responds to changes in the high latitude freshwater balance, and rapidly transmits this climate signal to the deep ocean. However, in only a few places are the observations sufficiently frequent to avoid aliasing of interannual variability. Expanded arrays of continuous measurements of deep ocean properties are needed to better understand the OC and its response to changes in forcing.

An Observing System for the Deep Ocean and Overturning Circulation

Measuring the OC poses a significant challenge. The OC extends throughout the global ocean, reaches from the sea surface to the sea floor, and consists of both intense narrow boundary currents and broad flows in the ocean interior. In essence, measuring the OC and associated heat and freshwater transport requires observations of the global, full-depth, three-dimensional, time-varying flow of the ocean. The tools to do this do not yet exist. Indeed, the deep ocean remains essentially unmeasured by the present ocean observing system, at least in a continuous sense. Nevertheless, substantial progress has been made in recent years, as discussed above. Building on this foundation, the international community recently developed a strategy for sustained observations of the deep ocean and overturning circulation [118], in the context of a decadal review of the status and prospects for global ocean observations known as OceanObs09 [119, 120]. In the following, the strategy for deep ocean observations developed by that community effort is summarized.

Building Blocks for an Observing System for the OC and Deep Ocean

An observing system for the transport of the OC and deep currents needs to rely on a combination of approaches. For some science questions (e.g., quantifying the transport of the OC), focused arrays of instruments are needed in key pathways of the circulation; for others (e.g., quantifying ocean heat content and its contribution to sea-level rise), broad-scale measurements are needed to track the evolving inventory of climate-relevant variables. In this section, the tools available for

sampling the transport and inventory of the deep ocean are described; the following section outlines an initial strategy for their deployment.

Much of the transport of the OC is carried in narrow boundary currents and therefore direct velocity measurements are needed there. Both the surface-intensified but deep-reaching western boundary currents of the subtropical and subpolar gyres, and the deep western boundary currents that dominate the abyssal flow need to be measured. Boundary current transports can be observed using current meter arrays incorporating point measurements and profiling instruments (e.g., acoustic Doppler current profilers (ADCPs)), cables, pressure gauges, and C-PIES (an Inverted Echo Sounder ((IES)) equipped with a pressure sensor (P) and a current meter (C); the combination provides a cost-effective means of monitoring the ocean, especially in the vicinity of strong currents [121]).

The full-depth volume transport in the interior of deep basins can be inferred from deep hydrographic measurements near the end points (from moorings, ships, gliders, or in some cases C-PIES), using the geostrophic relationship, supplemented by additional measurements over the sloping topography at the basin boundaries or mid-ocean ridges. Estimates of the transport of other properties (e.g., heat, freshwater, carbon), on the other hand, require knowledge of the covariance between velocity and concentration and cannot, in general, be made from end-point measurements alone. Given the prohibitive cost of a coherent "picket fence" of tall moorings spanning ocean basins (and the lack of moored sensors for some properties of interest), repeat hydrographic sections are in most cases the only approach available for estimating property fluxes over the full ocean depth. In some locations, where a close relationship exists between an integral property (e.g., acoustic travel time) and a single mode of variability of vertical profiles of temperature and salinity, property fluxes can be measured using a coherent array of C-PIES.

While the main focus of the entry is on the deep ocean, the OC of course includes flows in the upper ocean as well. To measure the OC, measurements of boundary currents and interior flows in the upper ocean are needed, including the wind-driven Ekman transport in the surface layer. Strategies for measuring the upper ocean are summarized in [119, 120].

Measurements of the evolving inventory of heat, freshwater, carbon, and other properties rely heavily on deep repeat hydrography [122]. Hydrographic sections remain the only tool available to sample the deep ocean over broad scales and the only way to collect samples for biological and biogeochemical analyses. The signal of change will appear first and be most prominent near the dense water overflows and along the main pathways of the deep circulation; hence these areas need to be sampled more frequently. Moored instruments provide the only means to obtain continuous time series of ocean currents and water properties and are therefore a key part of the armory, despite their relatively high cost and therefore limited spatial distribution. Repeat glider transects can also contribute to this goal. Remote sensing from satellites (e.g., altimetry and gravity measurements) or by acoustic means (e.g., acoustic tomography and thermometry) can provide integral constraints on ocean heat content [123]. However, each of these tools has

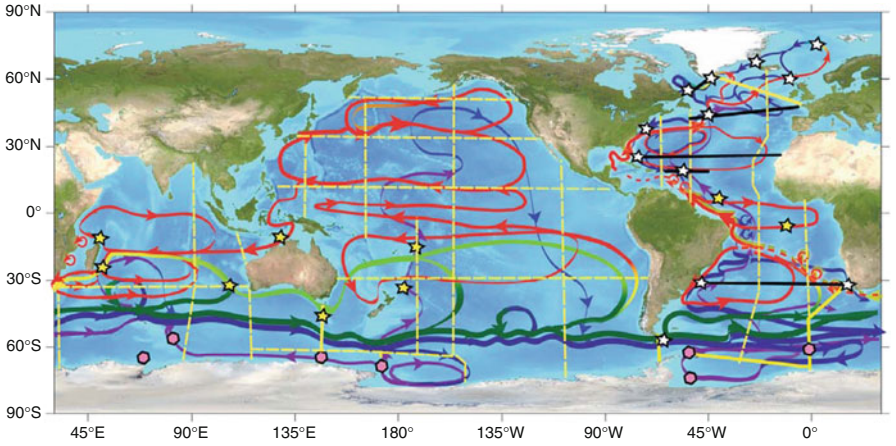

Fig. 10.12 Schematic of the global ocean overturning circulation. *Red* indicates upper ocean flow, *blue* and *purple* are deep flows, and *yellows* and *greens* represent transitions between depths. The proposed observing system includes repeat hydrography (*dashed yellow lines*; *solid bold yellow lines* indicate higher frequency repeat lines); basin-scale arrays of moorings and repeat hydrography for main transport lines (*bold black lines*); and moored arrays across deep boundary currents and interbasin exchanges (stars) and in the primary AABW outflows (hexagons). *White stars* indicate locations of existing arrays; *yellow stars* indicate recommended new arrays. For clarity, some components of the proposed observing system are omitted (e.g., floats and broad-scale mooring array, see [129]). Base map from S. Speich, adapted from R. Lumpkin (From [118]; used with permission)

limitations and as a result, changes in full-depth ocean heat content and other properties over most of the ocean can still not be measured accurately.

Because the reliance is on a variety of incomplete or indirect measurements to observe the overturning circulation and deep currents, analysis approaches such as inverse methods or state estimation are often required to combine the observations in a dynamically consistent manner and to interpolate between sparse observations.

A Strategy for a Deep Ocean Observing System

An initial strategy for sustained observations of the OC and deep ocean was articulated by Rintoul et al. [118] and is summarized here and in Fig. 10.12. For further detail, see [118] and references therein.

To understand the response of the OC and associated property transports to changes in forcing, measurements are needed at several latitudes to allow the meridional coherence of the OC to be assessed and understood. The partitioning of the meridional heat transport between the overturning and horizontal gyre circulations, for example, differs strongly with latitude [124]. Model studies

suggest that the meridional coherence of the AOC has different timescales at different latitudes, with stronger decadal variability in the subpolar regime and stronger high-frequency variability in the subtropics [125, 126]. Other model studies suggest that measurements at a single latitude in each basin of the Atlantic might be sufficient to detect OC changes on multidecadal scales, but that measurements at additional latitudes are needed to capture interannual to decadal variability and to understand the role that interocean and interbasin exchanges play in the OC and climate [124, 127].

Basin-wide monitoring of the Atlantic OC and meridional heat and freshwater transport is therefore needed in the subpolar and subtropical North Atlantic, at low latitudes, and in the South Atlantic. Based on relevance, feasibility, and the value of continuing existing time series, arrays at 47°N, 26.5°N, 9°N, and 35°S are recommended. The existing monitoring arrays at 26.5°N and 9°N need to be maintained. At 47°N and 35°S, interior measurements of water properties and velocity are needed, as well as boundary arrays and end-point monitoring. Closure of the Labrador Basin with a full-depth transport and flux array is also recommended to monitor the production and export of Labrador Sea Water, an important contributor to the Atlantic OC and a region known to be sensitive to climate variability such as the North Atlantic Oscillation.

Measurements of key components of the OC and deep circulation need to be made in additional locations, where basin-wide monitoring is not possible. Existing long-term measurements of dense overflows and boundary currents in the Atlantic must be continued (see Table 1 of [60] for the location of these measurements). A new array is needed at Cape Farewell to measure the combined flux of the Denmark Strait and Faroe Bank Channel overflows [128]. Monitoring of the boundary currents in the South Atlantic needs to be enhanced [129]. The major pathways for interbasin exchanges (the Southern Ocean and Indonesian Throughflow) need to be monitored [130–132]. The southern hemisphere dense overflows and boundary currents carrying ventilated water northward also need to be measured for a complete understanding of the global OC [133].

Repeat hydrography will remain the backbone of the broad-scale deep ocean observing system [122]. The recommended repeat hydrographic lines are shown in Fig. 10.12; these lines have been identified as high priority by the Global Ocean Ship-based Hydrographic Investigations Program (GO-SHIP) and commitments for future occupations exist for most of these sections. On each section, top-to-bottom measurements of temperature, salinity, oxygen, carbon, nutrients, and transient tracers are needed. More frequent sections are recommended near the dense water overflows and boundary currents, where the signal of change is evolving more rapidly (see [122] for the rationale and recommended sampling frequency for specific sections).

The repeat hydrography program , while essential, is still far from adequately sampling the deep ocean, given the infrequent sampling in space and time. The OceanSITES network of long-term time series stations will make an important contribution [134] and needs to be well-integrated with other deep-ocean observing systems, such as observatories established for geophysics or other applications.

In addition to maintaining the existing observing systems for deep ocean velocity, heat, salt, and carbon, there is a critical need to develop new, cost-effective, technologies for observing the deep ocean. Profiling floats capable of deeper profiling would allow broad-scale, sustained sampling of deep ocean properties for the first time. As well as the technological advances necessary to achieve this, design studies are needed urgently to determine the appropriate investment and deployment strategy for deep floats. Deep gliders could also make an important contribution and prototypes are being tested now that are designed to profile to 6,000 m depth. Near-continuous time series are needed to avoid aliasing and to determine the spectrum of deep variability. The OceanSITES network will make a significant contribution to this goal. Development of long-term moorings with the ability to transfer data to the surface (e.g., using expendable data capsules, acoustics, or other means) is needed to allow time series to be measured in remote ocean locations in a cost-effective manner [129]. Development of new sensors and platforms to measure carbon and other biogeochemical parameters is essential to improve the ability to track the evolving ocean inventory of carbon and acidification.

Status and Prospects

The observing system depicted in Fig. 10.12 is at various stages of readiness and commitment. Most of the hydrography lines have commitments for ongoing repeats, with a repeat time of 5–10 years. Several lines at high latitude are being repeated more frequently (indicated as solid lines in Fig. 10.12; see [122] for details). The moored arrays identified in Fig. 10.12 are, from a technology standpoint, ready to go now. More than 20 moored arrays and repeat lines have already been established in the Atlantic basin, as described in more detail in [60]. Many of these have a multiyear commitment. Each of the Southern Ocean sites identified by hexagons in Fig. 10.12 has been sampled with a moored array of at least 1-year duration in the last decade. The three Weddell Sea sites have been maintained for more than 8 years and are still underway. There are fewer established, long-term moored arrays in the other ocean basins, although pilot experiments are planned or are underway for most of the sites indicated in Fig. 10.12.

Overall, a large fraction of the recommended observing system for the deep ocean and OC already exists or is being developed – in particular, those components that rely on existing technology. On the other hand, the tools available today leave vast blind spots in the deep observing system: there are no means of making broad-scale, sustained measurements of the properties and circulation of the deep ocean. Three particular elements that are under development would make this possible: Floats capable of profiling throughout the full ocean depth; gliders capable of full-depth, basin-scale missions; and long-endurance moorings with data telemetry capability. For the nonphysical parameters (e.g., carbon, nutrients, biological variables), new sensors suitable for deployment on autonomous vehicles and moorings are urgently needed.

Future Directions

The overturning circulation and deep ocean strongly influence phenomena of direct relevance to sustainability, including climate change and variability, sea level, temperature and precipitation patterns over land, global biogeochemical cycles, and marine productivity. Despite its importance, observations of the deep ocean remain scarce, limiting the ability to understand and predict the overturning and deep circulations, their response to changes in forcing, and the impact of change. However, substantial progress has been made in recent years, including the first time-series measurements of the strength of the overturning circulation in the Atlantic, the discovery of new current pathways in the deep ocean, evidence for widespread changes in the deep ocean, and a deeper appreciation of the role of the deep ocean and overturning in the climate system. Building on these advances, the community has recently articulated a strategy for sustained observations of the deep ocean and overturning. New tools are needed before a comprehensive observing system for the deep ocean can be established and many of these technologies are under development. An ongoing challenge is the need to complete the transition from a collection of distinct observing elements to an integrated, coherent observing system.

Acknowledgments Many of the ideas presented here were developed as part of a community-wide effort to develop plans for a sustained deep ocean observing system, as input to the OceanObs09 process.

Bibliography

Primary literature

1. Worthington LV (1981) The water masses of the world ocean: some results of a finescale census. In: Warren BA, Wunsch C (eds) Evolution of physical oceanography. MIT Press, Cambridge, MA, pp 43–69
2. Stommel H (1958) The abyssal circulation. Deep-Sea Res 5:80
3. Stommel H, Arons AB (1960) On the abyssal circulation of the world ocean–I. Stationary planetary flow patterns on a sphere. Deep-Sea Res 6:140–154
4. Stommel H, Arons AB (1960) On the abyssal circulation of the world ocean – II. An idealized model of the circulation pattern and amplitude in oceanic basins. Deep-Sea Res 6:217–218
5. Warren BA (1981) Deep circulation of the world ocean. In: Warren BA, Wunsch C (eds) Evolution of physical oceanography. MIT Press, Cambridge, MA, pp 6–41
6. Swallow JC, Worthington LV (1957) Measurements of deep currents in the western North Atlantic. Nature 179:1183–1184
7. Swallow JC, Worthington LV (1961) An observation of a deep countercurrent in the western North Atlantic. Deep-Sea Res 8:1–19
8. Warren BA (1974) Deep flow in Madagascar and Mascarene basins. Deep-Sea Res 21:1–21

9. Warren BA (1977) Deep western boundary current in eastern Indian Ocean. Science 196:53–54
10. Warren BA (1978) Bottom water transport through Southwest Indian ridge. Deep-Sea Res 25:315–321
11. Warren BA (1983) Why is no deep water formed in the Pacific? J Mar Res 41:327–347
12. Wunsch C (2002) What is the thermohaline circulation? Science 298:1179
13. Broecker WS (1987) The biggest chill. Nat Hist Mag 97:74–82
14. Broecker WS (1991) The great ocean conveyor. Oceanography 4(2):79–89
15. Baringer MO, Arndt DS, Johnson MR (2010) State of the climate in 2009. Bull Am Meteorol Soc 91, S1
16. Levitus S, Antonov J, Boyer T (2005) Warming of the world ocean, 1955–2003. Geophys Res Lett 32:L02604. doi:10.1029/2004GL021592
17. Purkey SG, Johnson GC (2010) Warming of global abyssal and deep Southern Ocean waters between the 1990s and 2000s: Contributions to global heat and sea-level rise budgets. J Climate 23:6336–6351
18. Domingues CM, Church JA, White NJ et al (2008) Improved estimates of upper-ocean warming and multi-decadal sea-level rise. Nature 453:1090
19. Boe J, Hall A, Qu X (2009) Deep ocean heat uptake as a major source of spread in transient climate change simulations. Geophys Res Lett 36:L22701
20. Orsi AH, Johnson GC, Bullister JB (1999) Circulation, mixing and production of Antarctic bottom water. Prog Oceanog 43:55–109
21. Orsi AH, Smethie WM, Bullister JB (2002) On the total input of Antarctic waters to the deep ocean: a preliminary estimate from chlorofluorocarbon measurements. J Geophys Res C8:3122
22. Rintoul SR (1998) On the origin and influence of Adelie land bottom water. In: Jacobs S, Weiss R (eds) Ocean, ice and atmosphere: interactions at the Antarctic continental margin, vol 75, Antarctic Research Series. American Geophysical Union, Washington, pp 151–171
23. LeBel DA, Smethie WM, Rhein M et al (2008) The formation rate of North Atlantic deep water and eighteen degree water calculated from CFC-11 inventories observed during WOCE. Deep-Sea Res Part I-Oceanogr Res Pap 55(8):891–910
24. Orsi AH, Jacobs SS, Gordon AL et al (2001) Cooling and ventilating the abyssal ocean. Geophys Res Lett 28:2923–2926
25. Johnson GC (2008) Quantifying Antarctic bottom water and North Atlantic deep water volumes. J Geophys Res – Oceans 113(C5):C05027
26. Rintoul SR (2006) Circumpolar deep water. In: Encyclopedia of the Antarctic. Routledge, New York, pp 240–242
27. Hogg NG (2001) Quantification of the deep circulation. In: Siedler G, Church J, Gould J (eds) Ocean circulation and climate. Academic, San Diego, pp 259–270
28. McCartney MS (1992) Recirculationg components to the deep boundary current of the northern North Atlantic. Prog Oceanogr 29:283–383
29. Schmitz WJ, McCartney MS (1993) On the North Atlantic circulation. Rev Geophys 31:29–49
30. Crease J (1962) Velocity measurements in deep water of the western North Atlantic – summary. J Geophys Res 67:3173–3176
31. Swallow JC (1971) ARIES current measurements in western North Atlantic. Philos Trans R Soc Lond Ser A-Math Phys Sci 270:451–460
32. Hogg NG, Owens WB (1999) Direct measurement of the deep circulation within the Brazil Basin. Deep-Sea Res Part II-Top Stud Oceanogr 46(1-2):335–353
33. Ledwell JR, Montgomery ET, Polzin KL et al (2000) Evidence for enhanced mixing over rough topography in the abyssal ocean. Nature 403:179–182
34. Maximenko NA, Melnichenko OV, Niiler PP et al (2008) Stationary mesoscale jet-like features in the ocean. Geophys Res Lett 35:L08603

35. Bryden HL, Imawaki S (2001) Ocean heat transport. In: Siedler G, Church J, Gould J (eds) Ocean circulation and climate. Academic, New York, pp 455–474
36. Talley LD (2003) Shallow, intermediate, and deep overturning components of the global heat budget. J Phys Oceanogr 33:530–560
37. Talley LD (2008) Freshwater transport estimates and the global overturning circulation: shallow, deep and throughflow components. Prog Oceanogr 78:257–303
38. Alley RB, Marotzke J, Nordhaus WD, Overpeck JT, Peteet DM, Pielke RA Jr, Pierrehumbert RT, Rhines PB, Stocker TF, Talley LD, Wallace JM (2003) Abrupt climate change. Science 299:2005–2010
39. Sarmiento JL (2004) High-latitude controls of thermocline nutrients and low biological productivity. Nature 427:56–60
40. Schmittner A (2005) Decline of the marine ecosystem caused by a reduction in the Atlantic overturning circulation. Science 343:628–633
41. Le Quéré C et al (2007) Saturation of the southern ocean CO_2 sink due to recent climate change. Science 316:1735–1738. doi:10.1126/science.1136188
42. Böning CW, Dispert A, Visbeck M, Rintoul SR, Schwarzkopf F (2008) Response of the Antarctic circumpolar current to recent climate change. Nat Geosci. doi:10.1038/ngeo362
43. Latif M et al (2010) Dynamics of decadal climate variability and implications for its prediction. In: Hall J, Harrison DE, Stammer D (eds) Proceedings of OceanObs'09: sustained ocean observations and information for society, vol 2. ESA Publication WPP-306, Venice, 21–25 Sept 2009
44. Hurrell J et al (2010) Decadal climate prediction: opportunities and challenges. In: Hall J, Harrison DE, Stammer D (eds) Proceedings of OceanObs'09: sustained ocean observations and information for society, vol 2. ESA Publication WPP-306, Venice, 21–25 Sept 2009
45. Latif M et al (2006) A review of predictability studies of Atlantic sector climate on decadal time scales. J Clim 19:5971–5987
46. Zhang R, Delworth TL (2006) Impact of Atlantic multidecadal oscillations on India/Sahel rainfall and Atlantic Hurricanes. Geophys Res Lett 33(17). doi:82410.1029/2006GL026267
47. Latif M (1998) Dynamics of interdecadal variability in coupled ocean-atmosphere models. J Clim 11:602–624
48. Bjerknes J (1964) Atlantic air-sea interaction. In: Advances in geophysics, 10th edn. Academic, New York, pp 1–82
49. Broecker WS, Peng T-H (1982) Tracers in the sea. Eldigio Press, Palisades, p 690
50. Gordon AL (1986) Interocean exchange of thermocline water. J Geophys Res 91(C4):5037–5046
51. Richardson PL (2008) On the history of meridional overturning circulation schematic diagrams. Prog Oceanogr 76:466–486
52. Gordon A (1991) The role of thermohaline circulation in global climate change. In: Lamont–Doherty geological observatory 1990 and 1991 report, Lamont–Doherty Geological Observatory of Columbia University, Palisades, pp 44–51
53. Schmitz WJ Jr. (1996a) On the world ocean circulation: volume I, some global features/North Atlantic circulation. Woods Hole Oceanographic Institution technical report WHOI-96-03, 141 pp
54. Schmitz WJ Jr. (1996b) On the world ocean circulation: volume II, the pacific and Indian oceans/a global update. Woods Hole Oceanographic Institution technical report WHOI-96-08, 237 pp
55. Lumpkin R, Speer K (2007) Global ocean meridional overturning. J Phys Oceanogr 37:2550–2562
56. Lozier MS (2010) Deconstructing the conveyor belt. Science 328:1507–1511
57. Dengler M, Schott FA, Eden C, Brandt P, Fischer J, Zantopp RJ (2004) Break-up of the Atlantic deep western boundary current into eddies at 8° S. Nature 432:1018–1020
58. Bower AS, Lozier MS, Gary SF, Böning CW (2009) Interior pathways of the North Atlantic meridional overturning circulation. Nature 459:243–247

59. Visbeck M (2007) Oceanography: power of pull. Nature 447:383
60. Cunningham S et al (2010) The present and future system for measuring the atlantic meridional overturning circulation and heat transport. In: Hall J, Harrison DE, Stammer D (eds) Proceedings of OceanObs'09: sustained ocean observations and information for society, vol 2. ESA Publication WPP-306, Venice, 21–25 Sept 2009
61. Cunningham SA, Kanzow T, Rayner D, Baringer MO, Johns WE, Marotzke J, Longworth HR, Grant EM, Hirschi JJM, Beal LM, Meinen CS, Bryden HL (2007) Temporal variability of the Atlantic meridional overturning circulation at 26.5°N. Science 317(5840):935–938. doi: 10.1126/science.1141304
62. Kanzow T et al (2007) Flow compensation associated with the OC at 26.5°N in the Atlantic. Science 317:938–941
63. Bryden HL, Mujahid A, Cunningham SA, Kanzow T (2009) Adjustment of the basin-scale circulation at 26° N to variations in Gulf stream, deep western boundary current and Ekman transports as observed by the rapid array. Ocean Sci 5:421–433
64. Send U et al (2010) A global boundary current circulation observing network. In: Hall J, Harrison DE, Stammer D (eds) Proceedings of OceanObs'09: sustained ocean observations and information for society, vol 2. ESA Publication WPP-306, Venice, 21–25 Sept 2009
65. Send U et al (2002) Monitoring the Atlantic meridional overturning circulation at 16 N. CLIVAR Exchanges 25:31–34
66. Hirschi J et al (2003) A monitoring design for the Atlantic meridional overturning circulation. Geophys Res Lett 30(7). doi:10.1029/2002GL016776
67. Baehr J et al (2004) Monitoring the meridional overturning circulation in the North Atlantic: a model-based array design study. J Mar Res 62(3):283–312
68. Schott FA, Fisher J, Dengler M, Zantopp R (2006) Variability of the deep western boundary current east of the grand banks. Geophys Res Lett 33:L21S07. doi:10.1029/2006GL026563
69. Bryden HL, Johns WE, Saunders PM (2005) Deep western boundary current east of Abaco: mean structure and transport. J Mar Res 63:35–57
70. Ganachaud A, Wunsch C (2000) Improved estimates of global ocean circulation, heat transport and mixing *from* hydrographic data. Nature 408(6811):453–457
71. Talley LD, Reid JL, Robbins PE (2003) Data-based meridional overturning streamfunctions for the global ocean. J Clim 16(4). doi:10.1175/2787.1
72. Palmer MD, Bryden HL, Hirschi J, Marotzke J (2004) Observed changes in the south indian ocean gyre circulation, 1987–2002. Geophys Res Lett 31:L15303. doi:10.1029/2004GL020506
73. Sloyan BM, Rintoul SR (2001) The southern ocean limb of the global deep overturning circulation. J Phys Oceanog 31(1):143–173
74. Fukamachi Y, Rintoul SR, Church JA, Aoki S, Sokolov S, Rosenberg M, Wakatsuchi M (2010) Strong export of Antarctic bottom water east of the Kerguelen plateau. Nat Geosci 3:327–331. doi:10.1038/ngeo842
75. Whitworth AB, Whitworth T III, Nowlin WD, Pillsbury RD, Moore MI, Weiss RF (1991) Observations of the Antarctic circumpolar current and deep boundary current in the southwest Atlantic. J Geophys Res 96:15105–15118
76. Hogg NG, Siedler G, Zenk W (1999) Circulation and variability at the southern boundary of the Brazil basin. J Phys Oceanogr 29:145–157
77. Hall MM, McCartney M, Whitehead JA (1997) Antarctic bottom water flux in the equatorial western Atlantic. J Phys Oceanogr 27:1903–1926
78. Warren BA, Whitworth T, LaCasce JH (2002) Forced resonant undulation in the deep Mascarene Basin. Deep-Sea Res II 7–8:1513–1526
79. Sloyan BM (2006) Antarctic bottom and lower circumpolar deep water circulation in the eastern Indian Ocean. J Geophys Res 111:C02006. doi:10.1029/2005JC003011
80. Whitworth T III, Warren BA, Nowlin WD Jr, Rutz SB, Pillsbury RD, Moore MI (1999) On the deep western-boundary current in the Southwest Pacific basin. Prog Oceanogr 43:1–54

81. Rudnick DL (1997) Direct velocity measurements in the Samoan passage. J Geophys Res – Oceans 102:3293–3302
82. Kawabe M, Yanagimoto D, Kitagawa S (2006) Variations of deep western boundary currents in the Melanesian basin in the western North Pacific. Deep-Sea Res I 53:942–959
83. Raper SCB, Gregory JM, Stouffer RJ (2002) The role of climate sensitivity and ocean heat uptake on AOGCM transient temperature response. J Clim 15:124–130
84. Meehl GA, Washington WM, Collins WD et al (2005) How much more global warming and sea level rise? Science 307:1769–1772
85. Johnson GC, Doney SC (2006) Recent western South Atlantic bottom water warming. Geophys Res Lett 33:L14614. doi:10.1029/2006GL026769
86. Johnson GC, Purkey SG, Bullister JL (2008) Warming and freshening in the abyssal southeastern Indian Ocean. J Clim 21:5351–5363. doi:10.1175/2008JCLI2384.1
87. Johnson GC, Mecking S, Sloyan BM, Wijffels SE (2007) Recent bottom water warming in the Pacific Ocean. J Clim 20:5365–5375. doi:10.1175/2007JCLI1879.1
88. Fukasawa M, Freeland H, Perkin R, Watanabe T, Uchida H, Nishina A (2004) Bottom water warming in the North Pacific Ocean. Nature 427:825–827
89. Fahrbach E, Hoppema M, Rohardt G, Schröder M, Wisotzki A (2004) Decadal-scale variations of water mass properties in the deep Weddell Sea. Ocean Dyn 54:77–31
90. Kawano T et al (2006) Bottom water warming along the pathway of lower circumpolar deep water in the Pacific Ocean. Geophys Res Lett 33:L23613. doi:10.1029/2006GL027933
91. Bindoff N, Willebrand J, Artale V, Cazenave A, Gregory J, Gulev S, Hanawa K, Le Quere C, Levitus S, Nojiri Y, Shum CK, Talley L, Unnikrishnan A (2007) Observations: oceanic climate change and sea level. Climate change 2007: the physical science basis. In: Solomon S, Qin D, Manning M, Chen Z, Marquis M, Averyt KB, Tignor M, Miller HL (eds) Contribution of working group i to the fourth assessment report of the intergovernmental panel on climate change. Cambridge University Press, Cambridge, 385–432.79
92. Levitus S, Antonov JI, Wang J, Delworth TL, Dixon KW, Broccoli AJ (2001) Anthropogenic warming of earth's climate system. Science 292:267–270
93. Hansen J, Nazarenko L, Ruedy R, Sato M, Willis J, Del Genio A, Koch D, Lacis A, Lo K, Menon S, Novakov T, Perlwitz J, Russell G, Schmidt GA, Tausnev N (2005) Earth's energy imbalance: confirmation and implications. Science 308:1431–1435
94. Masuda S, Awaji T, Sugiura N et al (2010) Simulated rapid warming of abyssal North Pacific waters. Science 329:319–322
95. Durack PJ, Wijffels SE (2010) Fifty-Year trends in global ocean salinities and their relationship to broad-scale warming. J Clim 23:4342–4362
96. Roemmich D, Gilson J (2009) The 2004–2008 mean and annual cycle of temperature, salinity, and steric height in the global ocean from the Argo Program. Prog Oceanogr 82:81–100. doi:10.1016/j.pocean.2009.03.004
97. Hosoda S, Sugo T, Shikama N, Mizuno K (2009) Global surface layer salinity change detected by argo and its implication for hydrological cycle intensification. J Oceanogr 65:579–586
98. Dickson B, Yashayaev I, Meincke J, Turrell B, Dye S, Holfort J (2002) Rapid freshening of the deep North Atlantic Ocean over the past four decades. Nature 416:832–837
99. Hátún H, Sandø AB, Drange H (2005) Influence of the Atlantic subpolar Gyre on the thermohaline circulation. Science 309:1841–1844
100. Häkkinen S, Rhines PB (2004) Decline of subpolar North Atlantic circulation during the 1990s. Science 304:555–559
101. Bersch M, Yashayaev I, Koltermann KP (2007) Recent changes of the thermohaline circulation in the subpolar North Atlantic. Ocean Dyn 57:223–235
102. Holliday NP, Hughes SL, Bacon S, Beszczynska-Moeller A, Hansen B, Lavın A, Loeng H, Mork KA, Østerhus S, Sherwin T, Walczowski W (2008) Reversal of the 1960s to 1990s freshening trend in the northeast North Atlantic and Nordic Seas. Geophys Res Lett 35:L03614. doi:10.1029/2007GL032675

103. Sarafanov A, Falina A, Sokov A, Demidov A (2008) Intense warming and salinification of intermediate waters of southern origin in the eastern subpolar North Atlantic in the 1990s to mid-2000s. J Geophys Res 113:C12022. doi:10.1029/2008JC004975
104. Hakkinen S, Rhines PB (2009) Shifting surface currents in the northern North Atlantic Ocean. J Geophys Res – Oceans 114:C04005
105. Sarafanov A, Sokov A, Demidov A, Falina A (2007) Warming and salinification of intermediate and deep waters in the Irminger Sea and Iceland Basin in 1997–2006. Geophys Res Lett 34:L23609. doi:10.1029/2007GL031074
106. Yashayaev I (2007) Hydrographic changes in the Labrador Sea, 1960–2005. Prog Oceanogr 73:242–276
107. Sarafanov A (2009) On the effect of the North Atlantic Oscillation on temperature and salinity of the subpolar North Atlantic intermediate and deep waters. ICES J Mar Sci 66:1448–1454
108. Whitworth T III (2002) Two modes of bottom water in the Australian–Antarctic basin. Geophys Res Lett 29(5):1073. doi:10.1029/2001GL014282
109. Jacobs SS (2004) Bottom water production and its links with the thermohaline circulation. Antarct Sci 16(4):427–437
110. Jacobs SS (2006) Observations of change in the Southern Ocean. Philos Trans R Soc A 364:1657–1681. doi:10.1098/rsta.2006.1794
111. Aoki S, Bindoff NF, Church JA (2005) Interdecadal water mass changes in the Southern Ocean between 30E and 160E. Geophys Res Lett 32(L07607):1–5, ISSN 0094-8276
112. Aoki S, Rintoul SR, Ushio S, Watanabe S, Bindoff NL (2005) Freshening of the Adelie land bottom water near 140°E. Geophys Res Lett 32:L23601. doi:10.1029/2005GL024246
113. Rintoul SR (2007) Rapid freshening of Antarctic bottom water formed in the Indian and Pacific Oceans. Geophys Res Lett 34:L06606. doi:10.1029/2006GL028550
114. Jacobs SS, Guilivi CF, Merle P (2002) Freshening of the Ross Sea during the late 20th century. Science 297:386–389
115. Rignot E, Jacobs SS (2002) Rapid bottom melting widespread near Antarctic ice sheet grounding lines. Science 296:2020–2023
116. Shepherd A, Wingham D, Rignot E (2004) Warm ocean is eroding West Antarctic ice sheet. Geophys Res Lett 31:L23402. doi:10.1029/2004GL021106
117. Heywood KJ, Thompson AE, Fahrbach E, Mackensen A, Aoki S (2009) Cooling and freshening of the Weddell Sea outflow. Geophys Res Abstracts, 11: EGU2009-4336. EGU General Assembly 2009
118. Rintoul SR et al (2010) Deep circulation and meridional overturning. In: Hall J, Harrison DE, Stammer D (eds) Proceedings of OceanObs'09: sustained ocean observations and information for society, vol 1. ESA Publication WPP-306, Venice, 21–25 Sept 2009
119. Hall J, Harrison DE, Stammer D (eds) Proceedings of OceanObs'09: sustained ocean observations and information for society, vol 1. ESA Publication WPP-306, Venice, 21–25 Sept 2009
120. Hall J, Harrison DE, Stammer D (eds) Proceedings of OceanObs'09: sustained ocean observations and information for society, vol 2. ESA Publication WPP-306, Venice, 21–25 Sept 2009
121. Meinen CS, Watts DR, (2000) Vertical structure and transport on a transect across the North Atlantic Current near 428 N. J Geophys Res 105(21869):21891
122. Hood M et al (2010) Ship-based repeat hydrography: a strategy for a sustained global program. In: Hall J, Harrison DE, Stammer D (eds) Proceedings of OceanObs'09: sustained ocean observations and information for society, vol 2. ESA Publication WPP-306, Venice, 21–25 Sept 2009
123. Dushaw B et al (2010) A global ocean acoustic observing network. In: Hall J, Harrison DE, Stammer D (eds) Proceedings of OceanObs'09: sustained ocean observations and information for society, vol 2. ESA Publication WPP-306, Venice, 21–25 Sept 2009
124. Kieke D et al (2007) Changes in the pool of Labrador Sea water in the subpolar North Atlantic. Geophys Res Lett 34:L06605. doi:10.1029/2006GL028959

125. Bingham RJ et al (2007) Meridional coherence of the North Atlantic meridional overturning circulation. Geophys Res Lett 34(L23606). doi:10.1029/2007GL031731
126. Biastoch A et al (2008) Causes of interannual-decadal variability in the meridional overturning circulation of the midlatitude North Atlantic Ocean. J Clim 21(24):6599–6615
127. Baehr J, Stroup A, Marotzke J (2009) Testing concepts for continuous monitoring of the meridional overturning circulation in the South Atlantic. Ocean Model 9:147–153
128. Bacon S, Saunders PM (2009) The deep western boundary current at cape farewell: results from a moored current meter array. J Phys Oceanogr 40:815–829
129. Garzoli S et al (2010) Progressing towards global sustained deep ocean observations. In: Hall J, Harrison DE, Stammer D (eds) Proceedings of OceanObs'09: sustained ocean observations and information for society, vol 2. ESA Publication WPP-306, Venice, 21–25 Sept 2009
130. Gordon A et al (2010) Interocean exchange of thermocline water: indonesian throughflow; "Tassie" leakage; Agulhas leakage. In: Hall J, Harrison DE, Stammer D (eds) Proceedings of OceanObs'09: sustained ocean observations and information for society, vol 2. ESA Publication WPP-306, Venice, 21–25 Sept 2009
131. Weijer W et al (1999) Impact of interbasin exchange on the Atlantic overturning circulation. J Phys Oceanogr 29:2266–2284
132. Caltabiano A (2007) A monitoring system for heat and mass transports in the South Atlantic as a component of the Meridional Overturning Circulation, Estancia San Ceferino, Buenos Aires, Argentina, May 8, 9, and 10, 2007. In: Workshop report. 2007, International CLIVAR Project Office: Southampton, p 38
133. Rintoul S et al (2010) Southern ocean observing system (SOOS): rationale and strategy for sustained observations of the southern ocean. In: Hall J, Harrison DE, Stammer D eds) Proceedings of OceanObs'09: sustained ocean observations and infomation for society, vol 2. ESA Publication WPP-306, Venice, 21–25 Sept 2009
134. Send U et al (2010) OceanSITES. In: Hall J, Harrison DE, Stammer D (eds) Proceedings of OceanObs'09: sustained ocean observations and information for society, vol 2. ESA Publication WPP-306, Venice, 21–25 Sept 2009

Books and Reviews

Pickard GL, Emery WJ (1990) Descriptive physical oceanography: an introduction, 5th edn. Pergamon, Elsevier Science Ltd., Oxford, U.K. ISBN 008 0379532
Siedler G, Church J, Gould J (eds) (2001) Ocean circulation and climate, vol 77, International Geophysics Series. Academic, San Diego
Tomczak M, Godfrey JS (2003) Regional oceanography: an introduction, 2nd edn. xi+390p., figs., tabls., ind., 25 cm, Pergamon, Elsevier Science Ltd., Oxford, U.K. ISBN: 8170353068
Warren B, Wunsch C (eds) (1981) Evolution of physical oceanography. MIT Press, Cambridge, MA

Chapter 11
Long-Term Ecological Research Network

Robert B. Waide and McOwiti O. Thomas

Glossary

Biodiversity	Variation of life at all levels of biological organization.
Disturbance	A relatively discrete event in time and space that alters populations, communities, and ecosystems, including their attendant processes.
Ecology	The study of the relationship of organisms or groups of organisms to their environment.
Ecosystem dynamics	The observed changes in the characteristics of an ecosystem over time.
Ecosystem	The organisms living in a particular area in combination with the physical elements of the environment in which they live.
Episodic	Limited in duration or temporary.
Invisible present	Relating to an observation whose importance cannot be evaluated for lack of context.
Scale	Refers to differences in the spatial or temporal extent of a set of observations or measurements.
Synthesis	The creation of new knowledge by combining observations from diverse sources.
Transformative research	Scientific investigations whose results lead to radical changes in understanding of fundamental concepts.

This chapter was originally published as part of the Encyclopedia of Sustainability Science and Technology edited by Robert A. Meyers. DOI:10.1007/978-1-4419-0851-3

R.B. Waide (✉) • M.O. Thomas
Long Term Ecological Research Network Office, University of New Mexico, Albuquerque, NM 87131-0001, USA
e-mail: rwaide@lternet.edu; tmcowiti@lternet.edu

J. Orcutt (ed.), *Earth System Monitoring: Selected Entries from the Encyclopedia of Sustainability Science and Technology*, DOI 10.1007/978-1-4614-5684-1_11,

Definition of the Subject

The Long-Term Ecological Research (LTER) Network is the largest and longest-lived ecological network in the United States. Designed to provide long-term data from a broad range of key ecosystems, the LTER Network represents a unique national resource to address pressing environmental issues such as climate change, loss of biodiversity, and changes in patterns of land use. LTER is recognized internationally as one of the best organized and most successful large groups conducting research in ecology. With over 1,500 scientists, educators, and students, the network spans 26 sites located in 16 states in the contiguous United States, Alaska in the Arctic, Antarctica, and islands in the Caribbean and the Pacific Ocean (Fig. 11.1).

The network's formal vision is a society in which long-term ecological knowledge contributes to the advancement of the health, productivity, and welfare of the global environment, thereby advancing human well-being [2]. Within this vision, LTER's mission is to provide the scientific community, policy makers, and society with the knowledge and predictive understanding necessary to conserve, protect, and manage the nation's ecosystems, their biodiversity, and the services they provide. The LTER Network achieves this mission by using long-term observations and experiments to generate and test ecological theory at local to regional scales.

The National Science Foundation (NSF) created the LTER program in 1980. For three decades, the network has generated rigorous, site-based scientific research that has led to important regional and continental syntheses. LTER provides the scientific expertise, research platforms, and long-term datasets necessary to document and analyze environmental change.

Introduction

Because some of the most interesting and important ecological phenomena take place over long periods, long-term observations or experiments are necessary to truly understand their impacts. Processes such as climate change, recovery after disturbances such as forest fires, and changes in land cover are ecological processes that must be studied over the time scale of their occurrence (see, e.g., [3, 4]). Consequently, studies over sufficiently long time periods and large geographical scales are necessary to permit generalizations and theory about long-term events – such as deforestation, acid deposition, grazing, fire, and changes in trace gas fluxes [5].

In the concluding summary to a special report entitled "Long Term Ecological Research: An International Perspective," Risser [6] noted that long-term ecological studies are especially useful under four conditions: (1) the phenomena being studied are long term in their dynamics; (2) are episodic in nature, rare, complex, or subtle, such that long-term experiments are needed to isolate their dynamics and the control processes; (3) are poorly understood and cannot be predicted from short time scales; or (4) when long-term records are needed to make policy decisions.

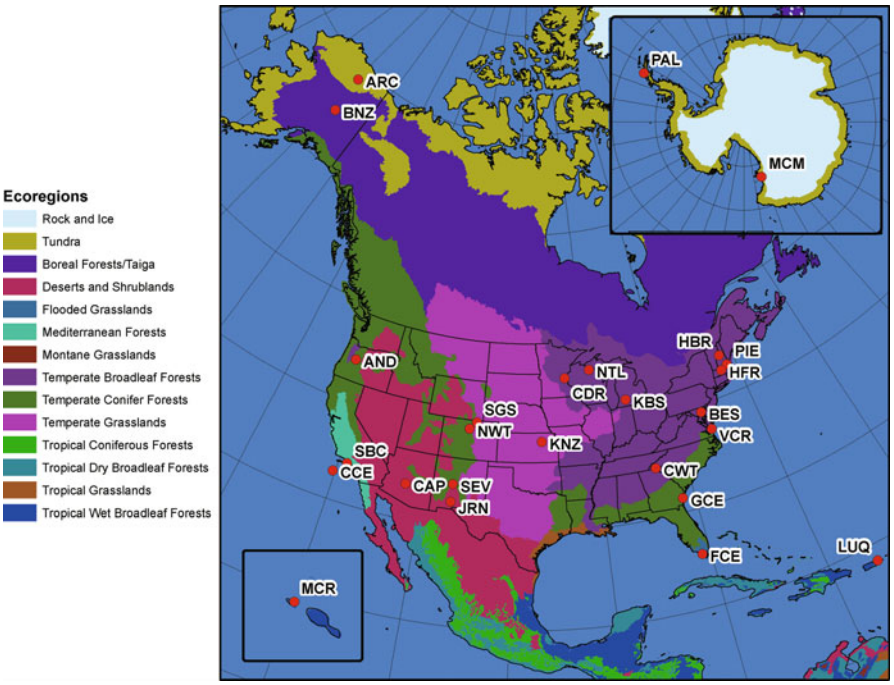

Fig. 11.1 Locations of current LTER sites within global ecoregions. Site names, acronyms, and home institutions are as follows: Andrews Experimental Forest LTER (AND) – Oregon State University; Arctic LTER (ARC) – The Ecosystems Center, Marine Biological Laboratory; Baltimore Ecosystem Study (BES) – Cary Institute of Ecosystem Studies; Bonanza Creek LTER (BNZ) – University of Alaska – Fairbanks; California Current Ecosystem (CCE) – Scripps Institution of Oceanography; Cedar Creek Natural History Area LTER (CDR) – University of Minnesota; Central Arizona – Phoenix (CAP) – Arizona State University; Coweeta LTER (CWT) – University of Georgia; Florida Coastal Everglades (FCE) – Florida International University; Georgia Coastal Ecosystems (GCE) – University of Georgia; Harvard Forest (HFR) – Harvard University; Hubbard Brook Experimental Forest LTER (HBR) – Cornell University; Jornada Basin (JRN) – New Mexico State University; Kellogg Biological Station (KBS) – Michigan State University; Konza Prairie LTER (KNZ) – Kansas State University; Luquillo Experimental Forest LTER (LUQ) – University of Puerto Rico; McMurdo Dry Valleys (MCM) – Ohio State University; Moorea Coral Reef (MCR) – University of California-Santa Barbara; Niwot Ridge LTER (NWT) – University of Colorado; North Temperate Lakes (NTL) – University of Wisconsin-Madison; Palmer Station (PAL) – The Ecosystems Center, Marine Biological Laboratory; Plum Island Ecosystems (PIE) – The Ecosystems Center, Marine Biological Laboratory; Santa Barbara Coastal (SBC) – University of California-Santa Barbara; Sevilleta LTER (SEV) – University of New Mexico; Shortgrass Steppe (SGS) – Colorado State University; Virginia Coast Reserve (VCR) – University of Virginia (Courtesy of Jamie Hollingsworth; data from The Nature Conservancy [1])

Although important, such long-term studies are generally rare, with only a few examples all across the globe (Fig. 11.2). According to Risser [6] long-term ecological studies are rare because: (1) long-term studies may not be considered innovative science, making their continuous funding difficult; (2) sites where the

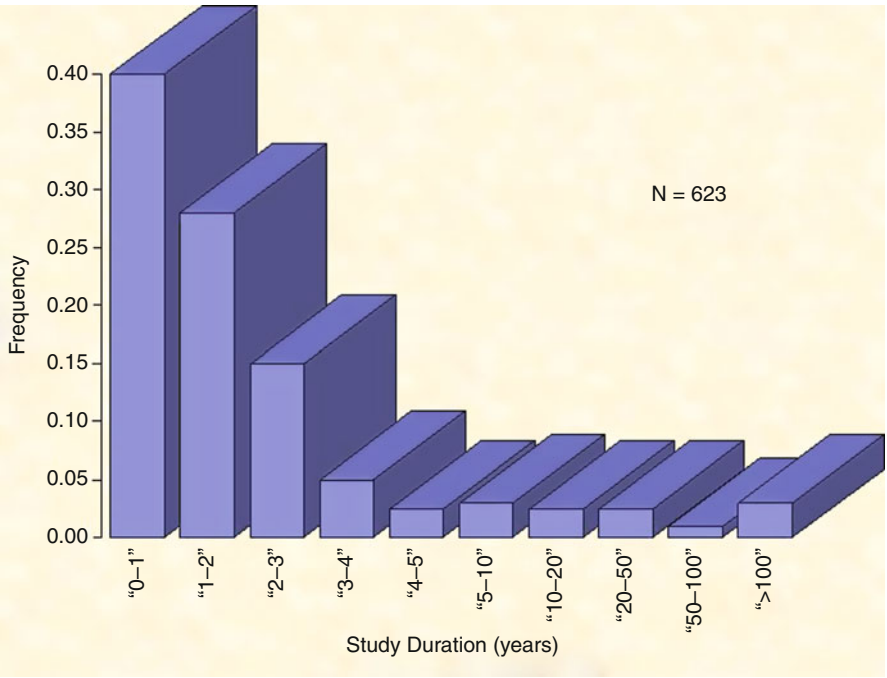

Fig. 11.2 Frequency distribution of a random sample of observational and experimental studies published in the journal Ecology between 1977 and 1987 (From Gosz et al. [7]. Data from Tilman [8])

measurements are taken may change, making the long-term results meaningless or difficult to interpret; (3) experimental designs may be too ambiguous for consistent long-term measurements or may not include adequate auxiliary studies to unravel controlling processes; (4) resources or incentives may be inadequate for dedicated scientists or research leaders to continue the studies; (5) new instrumentation may render the original methodology obsolete, coupled with insufficient attention to calibrating the old and new technologies; (6) new scientific advances may make the original question or hypothesis uninteresting or may provide a definitive answer, making the studies unnecessary.

It was this dearth of reliable information on key long-term ecological processes that prompted NSF to create the LTER Network in 1980 (see section "Major Milestones in LTER" in this document for a brief history of LTER's formation). Acting on the recommendations of three working groups comprising members of the ecological community [9–11], the Division of Environmental Biology at NSF constructed a call for proposals designed to "(1) initiate the collection of comparative data at a network of sites representing major biotic regions of North America and (2) evaluate the scientific, technical, and managerial problems associated with such long-term comparative research" [12]. Although the early emphasis of the LTER program was on expanding the time scale at which ecological research was

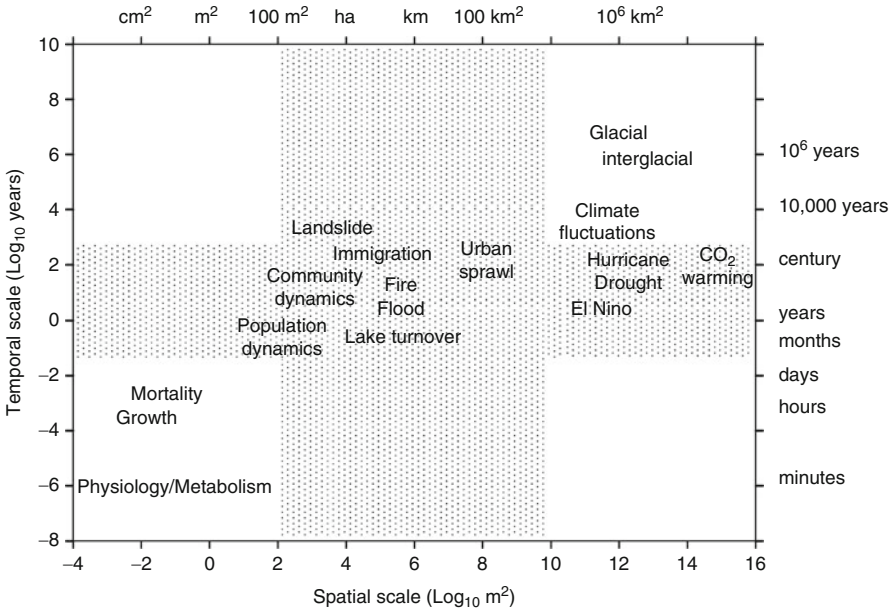

Fig. 11.3 Temporal and spatial domains of the LTER program focus on biological phenomena and physical events that operate on year to century time scales and plot to regional spatial scales (Redrawn from Magnuson et al. [13], with permission)

conducted, a concomitant expansion of the spatial scale of research was also expected (Fig. 11.3). This broadening perspective led to the twin concepts of the "invisible present" and the "invisible place."

Time and the Invisible Present

Magnuson [4] coined the term "invisible present" to describe ecological processes that result in significant change over decades but are hidden to the investigator conducting short-term studies. Ecologists working in this "invisible present" are not able to place current conditions in perspective without additional data from a longer span of time. Magnuson noted that short-term observations often could not identify cause and effect relationships because of inherent time lags of a year or longer between cause and effect. For example, changes in biomass accumulation in a forest as a result of disturbance may take years or decades to perceive. In short-term observational studies, it is rare to actually observe infrequent but important events. However, it is common to observe responses of an ecological system to an event that occurred long before observations began. Short-term manipulative studies often observe a system in transition rather than the complete trajectory to a new system state.

A good example of the importance of long-term data on the interpretation of ecological processes is given by observations of the ice cover records of Lake Mendota, WI (Fig. 11.4, [14]). The duration of ice cover in a single winter (1997–1998 in the example) might seem unremarkable without any other context. However, examination of successively longer segments of the 142-plus years of ice duration data provides the context to see the importance of that single year. A 10-year segment of data reveals that duration of ice cover in 1997–1998 was significantly less than the other 9 years of record [15], and that duration of ice cover varies considerably from year to year. A relationship between ice cover and an important feature of global climate, the southern ocean oscillation index [16, 17], is evident in the 50-year data segment, with 1997–1998 and other El Niño years having shorter durations of ice cover. The general warming trend in the data only becomes apparent within the complete record. What's more, the end of the little ice age about 1890 [18, 19] is reflected in the decrease in the duration of ice cover on Lake Mendota. The single observation from 1997 to 1998, viewed in the context of the complete data set, is revealed to be the year of shortest ice duration in the entire 142-year record. Thus, the long-term nature of this set of observations provides a clear context to interpret patterns at multiple temporal scales.

Space and the Invisible Place

In the same way that a point in time requires long-term temporal context for complete understanding, so a point in space requires a broad-scale spatial context [20]. Interpretation of observations at a single site (the invisible place) requires a spatial context that often spans multiple scales. In the LTER Network, observational or experimental studies are often designed and implemented at the plot scale, where the plot may encompass less than 1 m^2 or an entire watershed. Most LTER site research focuses on plot to landscape scales (Fig. 11.3), but the use of remote sensing and modeling approaches, the steady development of networked interactions among sites [21], and the growth of the long-term approach internationally provides the means to expand the research focus to regional, continental, and global scales [20].

The study of glacial lakes at the North Temperate Lake's LTER site in northern Wisconsin illustrates a typical approach to linking ecological elements in a broader spatial context. Although lakes in this landscape have many shared characteristics, the relative position of lakes connected along elevation gradients explains much significant dissimilarity, even in areas of slight relief. Lakes that are higher in the landscape are smaller, clearer, more dilute chemically, less diverse, and less affected by human use [22]. This pattern pertains to other lake districts throughout the northern hemisphere.

LTER scientists use two general approaches to extend results from small-scale and short-term studies to regional and broader scales [23]. An empirical approach

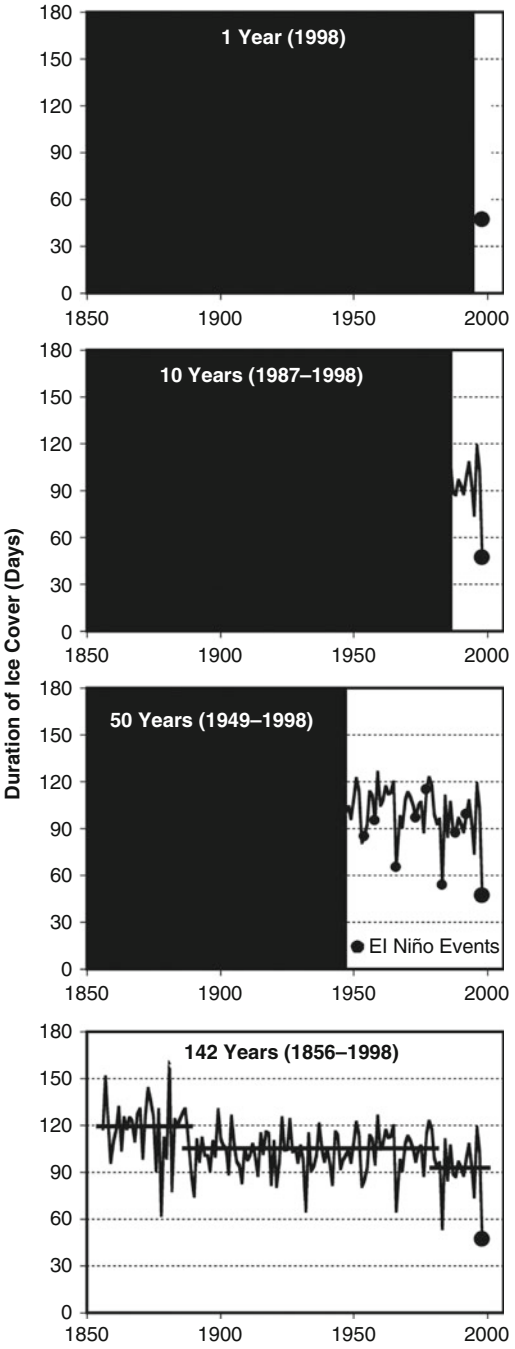

Fig. 11.4 Observations of ice cover records of Lake Mendota demonstrate the importance of broad temporal scale in rendering the present visible (From Magnuson et al. [14])

correlates values of ecological processes with aspects of the physical environment that are measurable at broad spatial scales using specialized tools including remotely sensed imagery. For example, Kratz et al. [24] compared patterns of spatial and temporal variability across 12 LTER sites using normalized difference vegetation indices (NDVI) from Landsat scenes. They found that variability within sites for a given year was considerably greater than variability among sites, indicating that studies of spatial heterogeneity must be coupled with long-term data to achieve an understanding of long-term dynamics at landscape and regional scales.

A second approach uses mechanistic models to simulate interactions among ecological processes measured at sites and predict patterns at broader scales [23]. Data from the LTER Network facilitate construction of mechanistic models in two important ways. Coordination among sites within the network produces consistent, multidisciplinary data sets over a broad geographic range. The existence of data on slow ecosystem processes, which govern long-term ecosystem dynamics, allows estimation of rate constants needed to model these dynamics. One example of the interaction between long-term data and mechanistic models is the photosynthesis and evapotranspiration model (PnET) developed by Aber and colleagues to predict ecosystem processes at regional scales [23]. The PnET models form a nested hierarchy of three models estimating (1) gross and net carbon (C) gain on a daily time step, (2) net C and water fluxes at variable time steps, and (3) biomass, litter fall, decomposition, and nitrogen (N) cycling. Together the three models allow prediction of the integrated function of ecosystems. Predictions from the models have been compared with long-term C, water, and nutrient balance data from the Harvard Forest and Hubbard Brook LTER programs. Discrepancies between predictions and empirical data instruct model improvement and guide site research. The PnET models allow regional scale prediction of integrated ecosystem characteristics over a wide range of future environmental conditions and previous land use histories [23].

Networks of integrated research sites provide the opportunity to examine continental scale ecological patterns and the drivers of those patterns. One multi-site, long-term experiment (the Long-Term Intersite Decomposition Experiment or LIDET) manipulated substrate quality across a broad range of vegetation and climate conditions to understand the factors controlling decomposition. Results from standardized measurements at 26 sites (17 LTER sites) indicated that decomposition of low-quality litter across a broad range of environmental conditions was slower than had been previously thought [25] and that significant variability resulted from ecosystem-specific factors such as the composition of the decomposer community. Studies such as these led LTER scientists to develop a conceptual framework for continental-scale research based on connectivity of flows of materials, organisms, and information across scales [26]. This framework emphasizes the importance of coordinated approaches across different research networks at continental and global scales.

Coordination of long-term ecological research at a global scale was initiated in 1993 through the formation of the International Long Term Ecological Research

Network [27], which now has research networks in 40 countries. As a founding member of this global network, the US LTER Network continues to play a central role in developing research to address global ecological issues. In addition, many LTER sites perform observations and conduct experiments as part of global networks focused on specific research questions. For example, LTER sites are engaged in global comparisons of forest structure through the Center for Tropical Forest Science at the Smithsonian Tropical Research Institute. This network includes 40 plots in 21 countries encompassing 4.5 million individual trees of 8,500 species.

Major Milestones in LTER

Scientific investigation at and among LTER sites is dynamic and evolves continuously in response to increasing knowledge and new opportunities. The commitment of LTER sites to long-term observations and experiments does not imply rigidity in focus and approach. The ability of LTER researchers to respond nimbly to new opportunities results from a flexible network structure with a minimum of requirements and uniform site activities. This flexibility would not be possible in a more monolithic network design. Thus, during the first decade of LTER (the 1980s), key concepts of long-term ecological research were explored and clarified. In the 1990s, there was an increased emphasis on large spatial scales and multiple interactions of ecological processes, species, and element cycles. In addition, interactions with physical and social scientists also increased. The third decade of the LTER program focused on synthesis. Using data and knowledge gained over the preceding 20 years, the LTER Network sought to reach new levels of understanding of long-term and large-scale ecological patterns and processes. This summary of the intellectual evolution of LTER provides context for a description of the major milestones in the development of LTER research.

Formation of the Network

The seeds of LTER were planted by the National Science Foundation (NSF) when it sponsored three workshops (in 1977, 1978, and 1979) to initiate and maintain close consultation with the ecological sciences community. At these workshops, the philosophy of collaborative research was developed and a centralized working hypothesis approach to collaboration proposed. Five core areas of research (Box 11.1) were defined to orient long-term ecological research projects toward question/hypothesis formulation and resolution over long time and broad spatial scales.

Box 11.1 Core Research Areas

The core areas are five research themes that are common to research at all sites and thus central to the coordination of network science. Core areas were originally selected by NSF to ensure appropriate breadth in LTER research programs and to guard against divergence among sites over time. Combined, the five core areas describe most of the major structural components of ecosystems. Although discussions about adding new core areas (e.g., biodiversity, social patterns and processes) have taken place within the LTER Network, none of these have been officially adopted.
The core areas are:

1. *Pattern and control of primary production* – Plant growth in most ecosystems forms the base or "primary" component of the food web. Spatial and temporal patterns of production and the controls of these patterns are major factors in structuring ecosystems.
2. *Spatial and temporal distribution of populations selected to represent trophic structure* – Populations of organisms are dynamic over space and time, and long-term trends in populations can be important indicators of environmental change.
3. *Movement of organic matter* – The sequestration of carbon by primary producers and its eventual fate in ecosystems have important implications for trophic dynamics, nutrient cycling, and global climate.
4. *Movement of inorganic matter* – Nitrogen, phosphorus, and other mineral nutrients are cycled through the ecosystem by way of decay and disturbances such as fire and flood. Availability of these nutrients exerts important controls over ecosystem structure and function.
5. *Disturbance patterns* – Disturbances often shape ecosystems by periodically reorganizing physical or community structure, resulting in significant changes in ecosystem services available to humans.

Major Milestones in the First LTER Decade

1980 – NSF selected an initial set of six sites (North Temperate Lakes, H.J. Andrews Experimental Forest, Coweeta Hydrological Laboratory, Konza Prairie, North Inlet Marsh, and Niwot Ridge) funded at $250,000 per year. Lead scientists from each site met in Washington, DC, and constituted a steering committee to begin the tasks of LTER communication, coordination, and accommodation of mutual goals.

1981 – Dick Marzolf (Konza Prairie) was elected the first Chair of the Steering Committee and NSF awarded a network coordination grant to Kansas State

Box 11.2 The LTER Network Office

The LTER Network Office (LNO) was established in 1983 through a coordination grant awarded by NSF to Oregon State University to support and coordinate network and site activities of the LTER Network. In 1989, NSF awarded another coordination grant to enlarge and establish LNO at the University of Washington-Seattle. The office officially moved to the University of New Mexico in 1997, and added the position of Executive Director. Robert B. Waide, formerly co-principal investigator of the Luquillo LTER program, was the first Executive Director of the LNO. With a core staff of 18 people and an annual budget of $1.5 million, the LNO's current service mandate includes:

- Providing an efficient computational and communication infrastructure for LTER research and education
- Developing and deploying state-of-the-art techniques in information management
- Maintaining a strong public outreach program
- Coordinating interactions with other scientific networks, agencies, and entities
- Providing administrative support
- Contributing to an efficient and effective environment in which site, cross-site, and synthetic research and education can be conducted

University (with Marzolf as PI). Subsequently, a second competition added five new sites to the network (Central Plains Experimental Range (now called Shortgrass Steppe), Okefenokee, Illinois Rivers, Cedar Creek Natural History Area, and Jornada Basin).

1982 – LTER held the first Data Management workshop and the first LTER Meteorological Committee (now Climate Committee) meeting, while the Steering Committee created a policy for workshops supported under the coordination grant.

1983 – NSF conducted the first national review of the LTER Program and the LTER Network Office (Box 11.2) was established through a coordination grant awarded by NSF to Oregon State University (with Jerry Franklin as PI).

1985 – LTER held its first All Scientists Meeting (Box 11.3) at Lake Itasca, MN.

1986 – NSF announced the third call for proposals for long-term ecological research sites; the LTER Intersite Climate Committee (formerly Meteorological Committee) developed standards for meteorological measurements at LTER sites [28, 29].

1987 – Five new sites (Arctic Tundra, Bonanza Creek Experimental Forest, Hubbard Brook Experimental Forest, Kellogg Biological Station, and Virginia

Box 11.3 All Scientists Meetings

Triennial All Scientist Meetings are used by the LTER Network to promote team building for cross-site research and synthesis. These 3–4 day meetings focus the LTER scientific community on new challenges, result in the formation of new research collaborations, help to integrate new sites and scientists into the LTER community, and provide the only opportunity for community-wide discussions of the future of the LTER program. In contrast to the usual scientific conference, an All Scientists Meeting focuses less on the presentation of individual research results and more on brainstorming, discussion, and synthesis of results from researchers addressing similar questions in different ecosystems. Moreover, All Scientists Meetings present excellent opportunities to share expertise, to transfer technology among sites, and to generate new scientific concepts, approaches, and experiments.

The most recent meeting in 2009 was attended by nearly 800 participants including many graduate students and broad representation for the International LTER community. The program included six plenary talks, 75 working group meetings, over 400 posters, four evening mixers, and pre-meetings for information managers, graduate students, education representatives, international attendees, and the LTER Executive Board.

Coast Reserve) joined the network; the LTER Intersite Climate Committee summarized climate information at the first 11 LTER sites [30]; and NSF announced the fourth call for long-term ecological research proposals.

1988 – Three new sites (Luquillo Experimental Forest, Sevilleta National Wildlife Refuge, and Harvard Forest) were added to the program, while two (Illinois Rivers and Okefenokee) were withdrawn (Box 11.4); the NSF Advisory Committee on Scientific and Technological Planning for LTER identified scientific issues addressed by the sites and recommended network-wide capabilities to address them; and the minimum standard installation (MSI) for LTER site data management was developed.

1989 – NSF conducted a second national LTER Program review and awarded a coordination grant to enlarge and establish the LTER Network Office at the University of Washington-Seattle (with Jerry Franklin as PI); an LTER working group developed the "Global Change Research Action Plan"; acquisition of satellite imagery and aerial photography for all sites began; an LTER-Chinese Ecological Research Network (CERN) exchange was developed; and the first LTER Network Strategic Plan resulted from the 1989 LTER Coordinating Committee Meeting at Harvard Forest ("A long-range Strategic Plan for the Long Term Ecological Research Network").

Box 11.4 Evaluation of LTER Sites

NSF funds each LTER site independently for 6-year periods, with renewal of awards based on proposals describing accomplishments and plans for future activities. Renewal proposals are reviewed by special panels of experts convened by NSF. The review panel may recommend continued funding, preparation of an addendum addressing specific points, or probation. An LTER site that is placed on probation receives only 2 years of funding and must write a new proposal addressing shortcomings for the next renewal cycle 2 years later. If the new proposal addresses criticisms successfully, 4 more years of funding are awarded. If not, the site is provided with terminal funding to close operations. The purpose of the probation process is to ensure that NSF's long-term investment is protected from transient problems, such the death or retirement of leading investigators, while still maintaining high standards of rigor in peer review. Four sites have been terminated during the 30-year history of the LTER program.

NSF also conducts mid-term program reviews as an essential part of NSF's ongoing evaluation cycle of the LTER program. Midway through the funding period, external peer review teams visit each site to evaluate the quality of science, education, and outreach as well as how well the site is managed and how integrated the sites are with the entire LTER Network [31]. The site reviews also serve as opportunities for site scientists and staff to get constructive criticism from the review team and to identify potential problems that require correction [32].

Major Milestones in the Second LTER Decade

1990 – The LTER Coordinating Committee developed site data management policy guidelines; LTER held its second All Scientists Meeting at Estes Park, CO.

1991 – Following an NSF Antarctic research proposal competition, a new site, Palmer Station LTER, Antarctica, was added to the network supported by funds from Polar Programs and Environmental Biology divisions; Geographic Information Systems (GIS) working group analyzed the status of LTER Network technical supplements and assessed future technical needs; and Global Positioning Systems (GPS) units were acquired for shared LTER site use and GPS training provided for representatives from all sites.

1992 – The LTER Coordinating Committee, at the request of NSF, developed an 8-year vision ("LTER 2000") for the creation of a global environmental research network based upon approaches established in the LTER Program.

1993 – A second Antarctic site, McMurdo Dry Valleys, was selected for the LTER Network; the NSF commissioned a 10-year review of the LTER Program;

the third LTER All Scientists Meeting was held at Estes Park, CO; an International LTER Summit at the Estes Park meeting led to the establishment of the International LTER (ILTER) Network, with Jerry F. Franklin (U.S. LTER Chair) as Steering Committee Chair; the LTER Network Internet (gopher) server was established at the Network Office; the LTER All-Site Bibliography, Core Data Set Catalog, and Personnel Database were developed and put online in searchable form; and the North Inlet LTER site was withdrawn, leaving 18 sites in the network.

1994 – In response to the 10-year review of the LTER Program, NSF conducted a special competition for cross-site and international comparisons and synthesis; nine grants ranging from $109,353 to $200,000 were made to LTER and non-LTER sites in the United States, Ireland, Scotland, Costa Rica, Argentina, and Russia; NSF announced a special competition for augmentation of LTER projects (Box 11.5) for regionalization, comprehensive site histories, and increased disciplinary breadth; LTER established a World Wide Web site at the Network Office; the first International LTER (ILTER) Steering Committee meeting was held at Rothamsted, U.K.; and NSF signed Memoranda of Agreement with the U.S. Forest Service and the National Biological Survey to cooperate/collaborate in LTER Program research.

1995 – Jerry Franklin retired after 12 years of service as Chair of the Coordinating Committee and was replaced by James Gosz; LTER established a National Advisory Board; NSF announced 13 new awards for cross-site comparisons and synthesis at LTER and non-LTER sites; the LTER Publications Committee developed a plan for publication of Network research synthesis volumes; and NSF/DOE/NASA/USDA Joint Program Awards, Terrestrial Ecology and Global Change (TECO), were awarded to seven LTER recipients, including researchers at Bonanza Creek, Cedar Creek, Central Plains, Harvard Forest, H.J. Andrews, and Jornada.

1996 – The first LTER site synthesis volume (Palmer LTER) was published by the American Geophysical Union (AGU).

1997 – A special competition resulted in addition of two new urban LTER sites (Central Arizona Phoenix and Baltimore Ecosystem Study); the Network Office officially began operation from the University of New Mexico.

1998 – An NSF competition resulted in a former Land Margin Ecological Research (LMER) site (Plum Island Ecosystem) joining the network; the LTER Network signed a contract to produce a Science Synthesis Series with Oxford University Press; Schoolyard LTER Supplements ($15,000 per year to each site) were added to LTER grants.

1999 – NSF provided funding supplements to enhance Internet connectivity at LTER sites; the LTER Social Science Committee was created; the LTER Network Office, the National Center for Ecological Analysis and Synthesis, the San Diego Supercomputer Center, and University of Kansas collaborated on the “Knowledge Network for Biocomplexity”; and a synthesis volume, “Standard Soil Methods for Long Term Ecological Research,” was published by Oxford University Press.

Box 11.5 Augmented LTER Sites

In 1996, NSF began an experiment that involved augmenting two LTER sites at a funding level that was double the network standard. The two sites, North Temperate Lakes in Wisconsin and Coweeta in the southern Appalachian mountains, were selected based on competitive proposals [33]. The successful proposals contained significant commitments to involve social and economic sciences and plans for developing regional-scale research.

The increased funding gave these sites the opportunity to focus on complex interactions between humans and ecological processes across a range of scales and to make significant advances in understanding the spatial, temporal, and decision-making components of land use and land-use change, and to build regional, national, and international collaborations.

The site augmentation experiment led to several significant findings by the participating sites. For example, North Temperate Lake researchers found that the economically optimal phosphorus input to lakes is often far less than estimates based on assumptions that lakes are linear, equilibrium systems with no stochastic factors and no time delays. By calculating the net economic value of water quality (based on the economics of farming, value of housing near the lake, and the recreational economy derived from boating, fishing, etc.), the researchers showed that the economically optimal phosphorus loading (which maximizes net costs and benefits to society as a whole) was about one third the current loading rate of the lake. These analyses show that the total economic value (i.e., the net benefit from all uses of the watershed, including agriculture, lakeshore property values, fishing, and other recreation) generated by the Lake Mendota watershed would increase substantially if less fertilizer were used.

At Coweeta, a spatially explicit model of land-use change over a 40-year period (1950–1990) identifying physical and human factors and determining land-use patterns for representative areas across the region showed that land-cover changes were more frequent at lower elevations and near roads. Bird diversity declined with forest patch size, which in turn influenced plant community composition. Some plant groups (e.g., *Liliaceae* and *myrmecochores*) with diaspores dispersed by ants were scarce or absent in patches subjected to intensive past land use. Land-use history was more important than patch size in explaining variation in abundance and composition of seed-dispersing ants. Fish density and diversity, in particular, were more affected by upstream than streamside deforestation. The "legacy effect" and the relative importance of upstream process pointed the way toward large-scale and long-term restoration given the implication that localized efforts often had little effect.

The discovery of these dramatic effects of land-use patterns and environmental heterogeneity on populations and communities led the Coweeta LTER to begin a new 30-year study in 2000 of stream regions forecast to differ over time in type and risk of development.

Major Milestones in the Third LTER Decade

2000 – Three new coastal sites joined the network (Georgia Coastal Ecosystem, Florida Coastal Everglades, and Santa Barbara Coastal); the fourth LTER (and first ILTER) All Scientists Meeting was held in Snowbird, Utah, in association with the annual meeting of the Ecological Society of America; and LTER entered into a collaborative relationship with the Organization of Biological Field Stations.

2001 – NSF conducted a 20-year review of the LTER Network; LTER celebrated its twentieth Anniversary; and the LTER Education Strategic Plan was published.

2002 – The first of what became an annual series of NSF-LTER Mini Symposia was held in Washington, DC; the LTER Network Information System Advisory Committee (NISAC) was formed; and the LTER Strategic Plan ("LTER 2000–2010: A Decade of Synthesis") was published.

2003 – The Cooperative Agreement for the LTER Network Office at the University of New Mexico was renewed; the fifth LTER All Scientists' Meeting was held in Seattle, Washington, in association with the Estuarine Research Federation; a Special Issue of *BioScience* focused on the Long-Term Ecological Research Network; the LTER Coordinating Committee approved a formal set of bylaws for the LTER Network; and the U.S. International Committee was formed.

2004 – The first LTER children's book, "My Water Comes from the Mountains," was published; two new sites (California Current Ecosystem and Moorea Coral Reef) joined the LTER Network; and the LTER Network received a grant from NSF to conduct network-level strategic planning.

2005 – The first LTER Graduate Student Collaborative Research Symposium took place at Andrews Experimental Forest; and the LTER Network Office "Strategic Plan" and "Implementation Plan" were published.

2006 – Jim Gosz stepped down after 10 years as Chair of the LTER Coordinating Committee and was replaced by John Magnuson; the Sixth LTER All Scientists' Meeting was held at Estes Park, CO; and the LTER Coordinating Committee approved a new LTER governance structure consisting of a Science Council and an Executive Board (Box 11.6).

2007 – Phil Robertson was elected Chair of the LTER Executive Board and Science Council; the "Decadal Plan for LTER," incorporating an integrated research plan, a description of the EcoTrends project, a Strategic Plan for Education, a Strategic Plan for Cyberinfrastructure, a new governance plan, and the "Integrative Science for Society and the Environment" document, was published; and "Principles and Standards for Measuring Primary Production" was published as part of the LTER series by Oxford University Press.

2008 – The LTER Network and the National Phenological Network signed a MOU for cooperation in phenological monitoring and assessment.

2009 – The seventh LTER All Scientists Meeting was held at Estes Park, CO; the LTER Network Office core funding was renewed and a separate award was made by NSF to facilitate synthesis and the development of network cyberinfrastructure.

Box 11. 6 Governance Structure

The Network is governed by bylaws enacted in 2003 by the *Coordinating Committee*, at that time the governing body of the LTER Network. The bylaws established a new governance structure consisting of an elected *Chair* and an *Executive Board* comprising nine rotating site representatives and one non-voting member selected to provide expertise on information management. Site representatives are the lead principal investigators of each LTER site. The Chair and the *Executive Director* of the LTER Network Office are ex officio members of the Executive Board. The *Science Council*, with a membership that includes two representatives from each site and the chairs of each Standing Committee, establishes the scientific direction and vision of the LTER Network. The voting membership of the Science Council (the 26 lead principal investigators from each site) reserves ultimate authority for decisions affecting the network. Ten *Standing Committees* (Climate, Communications, Education, Graduate Students, Information Management, International, Network Information System, Networks Coordination, Publications, and Social and Economic Science) support and inform the governance process. A *Network Office*, (see Box 2) funded separately by the National Science Foundation, facilitates research, education, information management, and governance activities (Fig. 11.5).

2010 – The LTER Network received the Distinguished Scientist Award from the American Institute of Biological Sciences (AIBS); NSF initiated a 30-year review of the LTER Program; and LTER created a Communications Committee and a Networks Coordination Committee.

2011 – Scott Collins was elected Chair of the LTER Executive Board and Science Council.

The LTER Network Today

Twenty-six research sites and a central coordinating office constitute the LTER Network at present, and more than 1,500 scientists are involved in research at these sites. The annual budget of the LTER program approaches $30 million (Fig. 11.6). The Network includes a wide range of ecosystem types spanning broad ranges of environmental conditions and human domination of the landscape. The geographic distribution of sites ranges from Alaska to Antarctica and from the Caribbean to French Polynesia and includes agricultural lands, alpine tundra, barrier islands, coastal lagoons, cold and hot deserts, coral reefs, estuaries, forests, freshwater

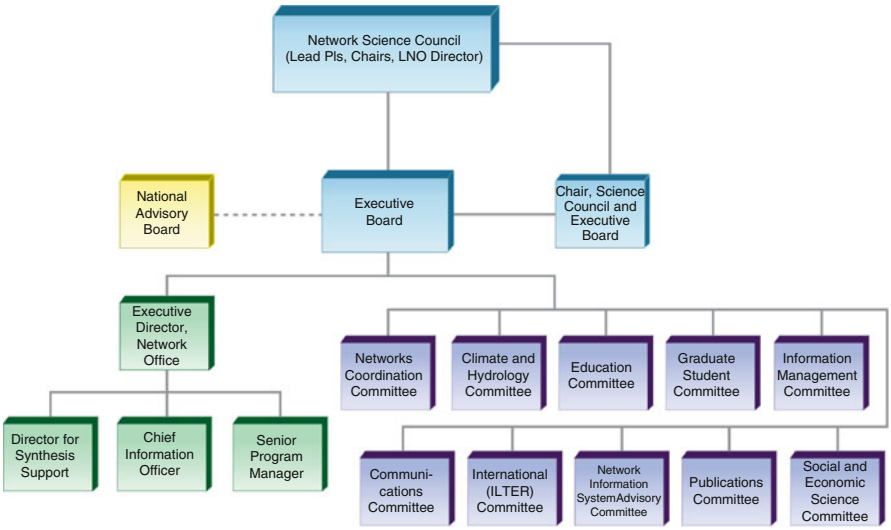

Fig. 11.5 Organizational chart for the LTER Network (Courtesy of Phil Robertson)

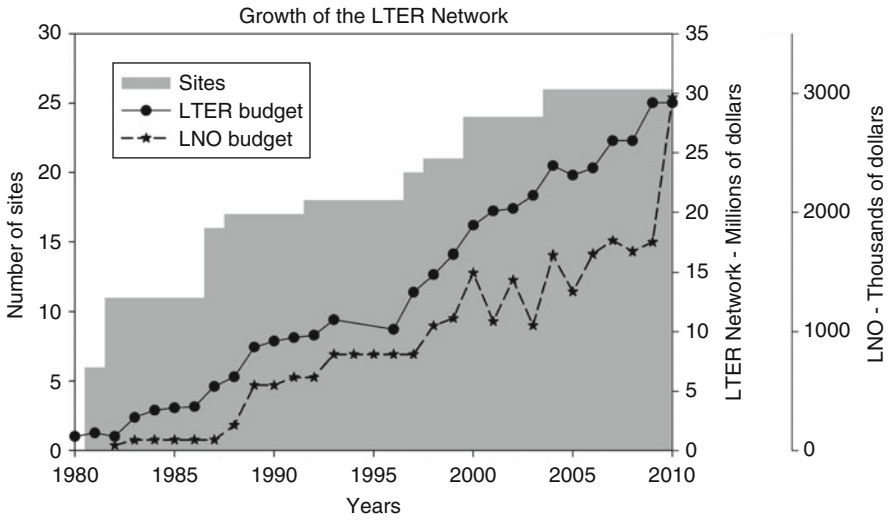

Fig. 11.6 Growth of the LTER Network

wetlands, grasslands, kelp forests, lakes, open ocean, savannas, streams, and urban landscapes. Collectively, the sites in the LTER Network provide opportunities to contrast marine, coastal, and continental regions, the full range of climatic gradients existing in North America, and aquatic and terrestrial habitats in a range of ecosystem types. All sites are sufficiently large to incorporate moderate to large landscape mosaics, and most sites include human-manipulated as well

as natural ecosystems. Most sites embody considerable within-site variability in habitats and ecosystem processes and attempt to characterize this variability in the context of broad regional gradients covering hundreds of kilometers.

In accordance with the factors driving the development of long-term ecological research in the United States, the LTER Network has adopted a central, organizing intellectual aim: to understand long-term patterns and processes of ecological systems at multiple spatial scales. To achieve this aim, the LTER Network focuses on six interrelated goals [7]:

Understanding: Gaining ecological understanding of a diverse array of ecosystems at multiple spatial and temporal scales.

The mission of the LTER Network begins with research based at individual sites, each of which has a unique theme. This site-based focus has allowed for key scientific advances at each of the sites, while the common focus on long-term research in a diverse array of ecosystems and landscapes has facilitated broad comparisons and syntheses across sites. Together the network of sites covers a wide range of subjects at multiple temporal and spatial scales.

Synthesis: Using the network of sites to create general ecological knowledge through the synthesis of information gained from long-term research and development of theory.

The products of LTER research extend beyond the accumulation of knowledge about diverse, individual ecosystem types. At a higher level, synthesis of this site-based knowledge across the network provides the broader scientific understanding from which new theory is derived and general applications can be developed.

Information Dissemination: Creating well-designed, documented databases that are accessible to the broader scientific community. Long-term research demands long-term data. The creation, curation, and dissemination of long-term databases are needed to assure that the data resources needed by researchers will continue to be available. These databases must include the additional information required to interpret data (i.e., metadata) as well as the data themselves. By adopting policies that promote the timely sharing of data (both inside and outside the LTER Network), the data can be used in a variety of ways not anticipated by the original collector such as regional, national, and global syntheses, thus providing a resource for the broader scientific community.

Legacies: Creating a legacy of well-designed and documented long-term observations, experiments, and archives of samples and specimens.

Many ecological phenomena change at decadal to century and longer time scales, and it is essential to maintain experiments and observations across periods appropriate to the questions addressed. The orderly transfer of experiments and interim results from one generation of scientists to the next requires a research design and setting that allows for multiple samplings (some unanticipated), long-term protection from competing uses, and meticulous documentation of experimental protocols. Also essential is a means to store protocols and observations in a manner that is

secure and consistently accessible to the scientific community for use in syntheses and cross-site comparisons (both inside and outside the LTER Network).

Training: Developing a cadre of scientists who are equipped to conduct long-term, collaborative research to address complex ecological problems.

One of the major lessons from the first 30 years of LTER has been that success both within sites and within the network requires a nontraditional approach to ecological research. This approach is characterized by a commitment to long-term measurements that may yield only a few useful initial results but that are essential to understanding long-term change, by a willingness to work as part of large teams that may have priorities that are different than one's own, by a desire to interact closely with others in order to share ideas and data, and by the need to develop a broad interdisciplinary perspective. Disseminating this approach through the involvement of graduate and undergraduate students, postdoctoral and international scientists, and K-12 educators, students, and the general public can ensure the success of long-term ecology in the future.

Outreach: Providing knowledge to the broader ecological community, general public, resource managers, and policy makers to address complex environmental challenges.

Humanity faces increasingly numerous and serious environmental problems that range from local to global in extent, and that must be tackled by institutions at local to international scales. The LTER Network and emerging ILTER networks provide the most comprehensive and diverse system of sites for ecological observations on the globe, and research of the LTER Network has repeatedly demonstrated the ability of long-term ecological science to address these environmental challenges. Increasingly, LTER research is finding applications in the work of federal, state, and local agencies that manage environmental resources. The synoptic and detailed knowledge of individual LTER sites, and the opportunities for multidimensional comparisons among sites, also represents significant opportunities for other disciplines including social sciences, earth sciences, and basic biological sciences that must be pursued. Finally, knowledge from this breadth of views permits us to identify and anticipate new issues and challenges, test existing ideas about causation, and help provide the science that underpins the processes of open, participatory, and forward-looking decision making.

Achievements of the LTER Network

> "At each of the Network's 26 sites we know an extraordinary amount about organisms and processes important at the site, about the way the site's ecosystems respond to disturbance, and about long-term environmental change. A growing number of cross-site observations and experiments is also revealing much about the way that key processes, organisms, and ecological attributes are organized and behave across major environmental gradients. In total, research in the LTER portfolio is contributing substantially to both our basic knowledge of ecological interactions and our ability to forecast change and to test ecological theory." (p(i), [34])

LTER's long-term research and monitoring has led to important new discoveries and had a transformative effect on science and society. Hobbie [35] listed the benefits resulting from the existence of the network: value added to research sites in the network because of long-term stability; value added to ecological science because long-term sites provide ecology with sustained intellectual attention to fundamental ecological issues; LTER data bases, which are important resources for the broader scientific community; cross-site synthesis, enabling hundreds of scientists to ask similar questions in a wide variety of habitats and increasing the possibilities for creative breakthroughs from interdisciplinary collaboration; education and training of teachers and students as an integral part of research programs; cooperative research with government agencies (e.g., in national parks, wildlife refuges and reserves, and experimental forests); contributions to society through advice on public policy and environmental management; and the establishment of an international LTER Network that now numbers 40 countries, facilitating collaboration in addressing environmental challenges in different parts of the world.

In 2010, the LTER Network received the Distinguished Scientist award from the American Institute of Biological Sciences for its contributions to the biological sciences. LTER research is featured in two of NSF's "Sensational 60" transformative scientific discoveries or advances [36]. Results from LTER research are embodied in over 10,000 peer-reviewed publications [35], a book series from Oxford University Press, and summaries on network (www.lternet.edu) and site web sites. Since 1993, the LTER research model has been adopted by 40 other member countries of the International Long Term Ecological Research Network.

Research

Progress in achieving the LTER Mission begins with the work of individual scientists, students, and educators at the 26 LTER sites. It is their work at the site level that forms the foundation of knowledge, data, observational and experimental legacies, and training that will ensure a lasting impact of the overall LTER program. Data and knowledge gained from intensive field experience are also key to development of syntheses of site-level information into models that allow prediction of long-term change and responses to human and other disturbances. Site-level synthesis activities often lead to new insights that feed back to affect the future course and evolution of site-level research.

Network infrastructure also promotes and facilitates cross-site and regional analyses, leading to larger-scale syntheses and to development and testing of ecological theory. In this work, the maintenance of a network database and protocols for data discovery and acquisition are particularly important. These efforts add to the basic body of scientific knowledge of long-term, large-scale ecological phenomena and, because students are deeply involved both at the site level and in intersite and network-level syntheses, they help to increase the numbers of people with appropriate expertise in both research and environmental problem solving.

Ultimately, both site and network-level activities feed back to the development of scientific capital, which includes well-trained scientists, a well-informed citizenry, and the basic data and understanding that underpin them. This accumulation of scientific capital also leads to new research and new applications of LTER research, including new forms of support for both research and education. Growth of scientific capital also includes interactions with new scientific disciplines, leading to expansion of the scope and applications of LTER research.

Research at LTER Sites The LTER Network comprises sites chosen competitively on the basis of research excellence, quality and duration of existing data sets, and strength of the commitment to long-term research and site security. The 26 sites that constitute the network at present represent a wide variety of research emphases and approaches. As part of their commitment to the LTER program, each site conducts a series of measurements and experiments directed toward the understanding of the five core areas as well as studies addressing ecological issues specific to the site. The most common scientific approaches include observation, experimentation, comparative analysis, retrospective study, and modeling, although emphases differ among sites. A sampling of key research results from LTER sites provides an idea of the potential impact of LTER research.

The Ecosystem Value Of Dead Wood – H. J. Andrews LTER scientists revealed the importance of dead trees to diversifying animal habitat and sustaining the flow of vital nutrients in forests and streams by tracking how fallen and standing deadwood changes as forests age. These studies profoundly influenced forest management by prioritizing the retention of dead wood in forests and streams.

Arctic Warming – Arctic LTER scientists discovered how Arctic warming is increasingly thawing frozen ground (permafrost), creating hot spots of erosion, nutrient release into rivers, and decomposition of ancient organic carbon. This information is essential for managers and policymakers grappling with how to mitigate and adapt to future climate change.

Fire and Climate – Through long-term studies of fire cycles and their links to climate, Bonanza Creek scientists have documented an increase in fire severity brought on by climate warming that will likely shift the Alaskan boreal forest from a spruce- to a broadleaf-dominated landscape.

New Climate Pattern – Long-term observations allowed California Current Ecosystem scientists to define a new climate pattern called the North Pacific Gyre Oscillation (NPGO), which links physical ocean changes, such as fluctuations in salinity and nutrients, with biodiversity and ecosystem processes in the eastern North Pacific. This climate pattern may affect marine ecosystems around the world.

Biodiversity Matters – Cedar Creek scientists discovered that the number of plant species in an ecosystem – its biodiversity – has a profound and surprisingly strong effect on ecosystem function. Long-term experiments have shown that ecosystems with greater plant species diversity are more productive and stable.

Integrative Research – Central Arizona-Phoenix scientists spearheaded efforts to integrate ecological and social research in urban ecosystems. Such interdisciplinary research has changed the way scientists and citizens perceive the natural environment in cities, transformed environmental education at all levels, and informed problem solving in cities.

Future Nitrogen Cycling – Drawing on two decades of research, Coweeta researchers discovered that warmer temperatures increase peak nitrate loading to forest streams during the growing season. These findings suggest that climate warming will triple the nitrogen export from forests, reducing water quality and long-term forest productivity.

Productivity Paradox – Florida Coastal Everglades scientists revealed how human-induced nutrient enrichment in the Everglade and Caribbean wetlands affect the "productivity paradox" in which an extraordinarily high level of algal growth supports far fewer aquatic animal consumers than expected. Understanding this dynamic is critical to the restoration of the Everglade ecosystems.

Sea-Level Rise – Georgia Coastal Ecosystem scientists predicted how rising sea levels will impact coastal marshes and reduce the benefits they provide society, such as clean water and fish habitat. Analyses have shown that new marshes created by rising waters do not fully offset the loss of existing marshes.

Legacies Shape Ecosystems – Using its century-long studies, Harvard Forest scientists have documented the persistent influence of human and natural history in shaping modern forest ecosystems. Ancient land use practices and prior forest conditions continue to influence a forest's potential to grow trees, respond to disturbance and stress, and support diverse plants and animals.

Shifting Songbirds – Hubbard Brook scientists have produced the longest continuous songbird record in North America and discovered that changing habitat, land use practices, and climate in eastern forests, tropical forests, and migratory routes drive the abundance of these beloved forest musicians.

Grassland Tipping Points – Jornada LTER scientists discovered that grasslands, shrublands, and other ecosystems have "tipping points," where dramatic and rapid changes can occur once certain thresholds are reached. A better understanding of these thresholds is paramount to management and protection of grasslands and other ecosystems.

Agriculture and Climate Change – Kellogg Biological Station researchers discovered and quantified how different crop management practices can interact to provide novel opportunities for greenhouse gas mitigation by agriculture. These discoveries inform agricultural greenhouse gas policies worldwide.

Sensitive to Change – Using long-term data on plant productivity and novel experiments to manipulate rainfall, Konza Prairie scientists demonstrated that grasslands are among the most sensitive ecosystems to changes in the water cycle. This research helps forecast the impact of climate change on the carbon balance of individual plants to whole ecosystems.

Tropical Carbon Cycling – Luquillo Experimental Forest scientists discovered that carbon cycling in tropical forests is highly sensitive to climate. Relatively small increases in temperature can decrease the ability of tropical forests to store carbon recently captured by photosynthesis, thus accelerating climate change.

Chain Reaction – McMurdo Dry Valleys scientists documented how even small variations in climate can drive major changes in polar ecosystems: Seemingly slight changes in temperature can set off a cascade of magnified responses that affect stream flow, nutrient cycling, and biodiversity.

Diversity Matters – Coral reef ecosystems are highly sensitive to disturbances and climate change. Moorea Coral Reef research documented how genetic and species diversity among corals and their symbionts helps corals to rapidly adapt to changing environmental conditions such as warming seawater and ocean acidification.

Early Warning Signs – Niwot Ridge research indicates that alpine ecosystems provide important early warning signs of global climate change. Alpine plants and animals survive on the razor's edge of environmental tolerances, making them more sensitive to changes in climate than downstream ecosystems.

Tracking Ice Cover – By synthesizing long-term records of lake and river ice cover throughout the Northern Hemisphere, North Temperate Lake scientists discovered long-term climate-induced reductions in ice cover on freshwater ecosystems over the past 150 years.

Penguins and Climate Change – Palmer Station scientists have documented a 75% reduction in Adélie penguin populations since 1980 and determined the cause to be altered cloud cover, winds, snowfall, sea ice cover, and other climate changes.

Tipping Points – Plum Island Ecosystem scientists discovered regionally specific "tipping points" beyond which marshes can no longer keep up with rising sea levels, and that human alteration of watersheds can either enhance or compromise a marsh's ability to survive in the face of rising sea levels.

Underwater Forests – Giant kelp provides critical food and shelter for a wide diversity of economically important organisms. An interdisciplinary team of Santa Barbara Coastal scientists discovered that kelp plants disperse their reproductive spores over surprisingly great distances, furthering our understanding of how these important ecosystems establish and survive.

Climate and Disease – Long-term observations and experiments by Sevilleta LTER scientists revealed an important link between human hanta virus outbreaks and the population dynamics of small mammals in the southwestern United States as affected by changes in climate systems such as El Niño. The discipline of the

ecology of infectious diseases that this research helped to establish is now a transformative area of ecological research.

Plague and Prairie Dogs – For over two decades, Short Grass Steppe scientists have observed black plague spreading through populations of the black-tailed prairie dog, an endangered species candidate. The effects of the resulting die-offs ripple through other populations including other rodents, flowering plants, pollinators, and large herbivores.

Dynamic Coastal Landscapes – By tracking long-term shifts in land cover on undeveloped coastal barrier ecosystems, Virginia Coast LTER scientists have learned how sea-level rise and storms interact to create a highly dynamic landscape. While the locations of lagoons, marshes, and other coastal ecosystems have changed over time, they have not experienced a net reduction in the area they cover.

Cross-Site Research and Synthesis In addition to transformative site–based research, LTER scientists conduct synthetic studies focused on general ecological principles underlying diverse ecosystems [22, 26, 35, 37–47]. Johnson et al. [21] demonstrated the evolution of the LTER program from a collection of research sites with common goals to a highly connected research network. A few examples illustrate the breadth of LTER cross-site research.

EcoTrends – The EcoTrends Project [47] is a collaborative effort among state and federal agencies and institutions in the United States to make long-term ecological data easy to access, analyze, and compare within and across sites (see http://www.ecotrends.info). The project is designed to promote and enable the use and synthesis of long-term data to examine critical trends (e.g., climate, land cover, and habitat availability) in the Earth's ecosystems. In addition to ecological data collected by participating sites, the EcoTrends database includes ancillary data from other sources. For example, LTER investigators obtained human population and economic data from 1790 to 2000, which was one of the four types of data being synthesized in the EcoTrends Project. The "Human Population and Economy" dataset contains over 200 separate variables suitable for describing changes in population and economic structure since the end of the eighteenth century. The dataset was collected for each of the more than 250 counties associated with the 21 continental North American LTER sites plus the Luquillo site in Puerto Rico. These datasets, tools, and information are available to anyone who would like to view trends in ecological variables for one or multiple sites or pursue additional statistical analyses of within-site and cross-site comparisons.

Climate Database (CLIMDB) and Hydrology Database (HYDRODB) – LTER sites have generally followed established LTER Climate Committee guidelines (see [29]) for collecting baseline meteorological data. Standardized measurements provided a basis for coordinating meteorological measurements at two or more sites

and enabled intersite comparisons, but access to comparable datasets from multiple sites was often problematic because most sites, while making climate data accessible online, displayed them in different formats and aggregated them using different methods. Similarly, sites that conducted long-term hydrologic measurements needed to establish access to their long-term datasets for streamflow, precipitation, and ambient air temperature, in addition to the hydrologic data. LTER developed ClimDB and HydroDB in response to the science-based need for standardized measurements, format, and aggregation of these data. LTER sites, along with USGS, and USDA Forest Service sites, contribute climate (http://www.fsl.orst.edu/climhy/) and hydrological (http://www.fsl.orst.edu/hydrodb/) data, which are stored in centralized servers that provide open access to long-term meteorological and stream flow records from these research sites.

Long-Term Intersite Decomposition Experiment Team (LIDET) – Sixteen LTER sites participated in a 10-year, 28-site experiment to test the effect of substrate quality and macroclimate on long-term decomposition and nutrient dynamics – particularly the degree to which these two factors control the formation of stable organic matter and nitrogen after extensive decay. Reciprocal litter transplants of 27 species were conducted at sites in North and Central America. Decomposition rates were strongly affected by substrate quality, but climate also resulted in strong and consistent effects [25]. Large-scale patterns were better explained by variables including both moisture availability and temperature. In general, roots decomposed more slowly than leaves, but ratios of aboveground to belowground decomposition rates varied across ecosystem types. Predictions of decomposition rates were possible using uncomplicated models based on litter quality and climate, but ecosystem-specific factors also contributed to observed differences (see http://andrewsforest.oregonstate.edu/research/intersite/lidet.htm for more information).

Lotic Intersite Nitrogen Experiment (LINX) – The Lotic Intersite Nitrogen Experiment was a collaborative study of nitrogen cycling in streams involving simulation modeling, field tracer (^{15}N) additions, and intersite comparison. The central hypothesis was that the considerable variability among streams in uptake, retention, and cycling of nitrogen is controlled by key hydrodynamic, chemical, and metabolic characteristics that determine water retention, degree of nitrogen deficiency, and energy flow through food webs in stream ecosystems. LINX I ran from September 1996 through August 2001 and resulted in 26 publications, 7 theses and dissertations, and 69 presentations. The study demonstrated that the smallest streams had the highest uptake of inorganic nitrogen, and that small streams were potentially significant sources of atmospheric nitrogen via nitrification.

LINX II was a 5-year project that began in September 2001 and ended in 2006. Data from tracer experiments across 72 streams and eight regions representing several biomes showed that biotic uptake and denitrification were less efficient at removing stream nitrate in streams with high nitrate concentrations. As a result, high nitrate streams export a disproportionate amount of nitrate to receiving waters. In addition, these patterns suggest that small streams become less important as nitrate sinks as nitrate concentration increases [48].

In addition to the specific cross-site and intersite research mentioned above, LTER sites also participate in numerous long-term interdisciplinary and multi-site syntheses with both LTER and non-LTER organizations. These include studies of above- and belowground productivity, carbon dioxide (CO_2) and climate change, biodiversity, disease control, microbial ecology, remote sensing, and geographical information systems, the adsorption of trifluoroacetate (TFA) in soils, among others.

National and International Networking – As a global leader in long-term and broad-scale ecological research, the LTER Network establishes linkages with existing and developing long-term ecological research programs in the United States and abroad. These relationships range from exchanges at the individual scientist and site research program levels, to participation in national and international meetings, to global-scale research planning and collaboration.

Nationally, LTER develops innovative partnerships with leading ecological research organizations and synthesis centers; facilitates the advancement of current ecological science and innovative research technologies; develops strong multidisciplinary science and public education programs; and pursues a multi-agency approach to develop databases of long-term research in key biomes and along major gradients.

Internationally, LTER assists in the establishment of networks for long-term ecological research worldwide; creates opportunities for collaboration between US and International LTER sites and networks; develops and operates a communication and data-sharing system among an international network of sites; facilitates the establishment of a global network of environmental research sites; and participates in other international scientific efforts.

Education

Education and outreach efforts are integral aspects of the LTER program. As a network of sites with a preponderance of academic scientists, graduate and undergraduate education is central to the goals of the network. Students at both graduate and undergraduate levels are routinely engaged in collecting LTER data, performing experiments, and analyzing results. This participation forms an important part of their educational experience, and hence education and research are highly integrated in most LTER programs. The network has many examples of former undergraduate students that have become research scientists in the LTER program.

In addition, LTER provides a unique opportunity to address the educational needs of teachers and students from grades K-12. As a long-term program, LTER has the potential to provide continuous opportunities for students to participate and learn throughout their entire academic life.

The LTER Network has adopted a strategic vision for education and outreach with three components. The first component addresses the structure needed to enable LTER research to have a public impact. This structure includes leadership within the network, a distributed organization that provides resources for sites to implement education programs at the local level, and cyberinfrastructure that enables broad collaboration among local education projects and between researchers and educators.

The second element of the LTER vision for education establishes the goal of conducting programs in research and development that address environmental science literacy by respecting and including the diverse perspectives that exist within the LTER Network. The final aspect of the LTER vision addresses inclusion of key constituent groups, including K-12 teachers and administrators, undergraduate and graduate students and professors, and end citizens active in LTER communities.

K-12 Schoolyard LTER Program In 1998, LTER formally expanded its education efforts to include K-12 students and teachers, mainly through the Schoolyard LTER (SLTER – http://schoolyard.lternet.edu/) program, which is funded through supplements by NSF's Division of Environmental Biology (DEB). The SLTER approach emphasizes the connection to local communities, for which an LTER site can serve as a "schoolyard" for understanding ecology and environmental science. The sites design their own programs in relation to the ecological research conducted at the site and the particular needs and resources of the local school district and community ([49], http://schoolyard.lternet.edu/LTEREduHandbook.pdf). SLTER funds support a wide range of education activities, including field trips and lab work for students, teacher professional development workshops, teaching supplies, community outreach, and program and research coordination. The schoolyard approach is particularly consistent with the development of empathy for their local environment ("Environmental Empathy") as discussed by Sobel [50] as a basis for teaching elementary age students. All the 26 LTER sites participate in the SLTER program.

As the SLTER program matured, LTER scientists devised the idea for a Children's Book Series to supplement SLTER activities – thus using children's science literature to overcome "ecophobia" while fostering environmental empathy [51]. The series currently includes three titles: "My Water Comes From The Mountains" by Tiffany Fourment (Note: the title has since been modified to reference specific mountains, e.g., "My Water Comes From The Rocky Mountains" and "My Water Comes From The San Juan Mountains"), "The Lost Seal" by Diane McKnight; and "Sea Secrets" by Mary M. Cerullo and Beth E. Simmons. Each book is richly illustrated with scenes derived from the story, with many artworks and sidebar comments by elementary school children.

Graduate and Undergraduate Education The LTER science community includes academic and government scientists and educators, graduate and undergraduate students, and professional staff. The research conducted at the sites is diverse, encompassing all aspects of ecology and ecosystem science, as well as investigations in atmospheric science, hydrology, and geomorphology. As centers of excellence in ecological research, LTER sites hosted by universities, government agencies, and nonprofit research institutions also provide important training grounds for the next

generation of scientists and leaders. LTER offers opportunities for graduate and undergraduate training and education. Many undergraduate and graduate students are supported directly from LTER awards each year and others use LTER facilities and equipment in support of their research programs. In addition, the LTER Network, through its association with other networks worldwide, provides opportunities for the international interchange of students and faculty.

In addition to typical university-based training, many LTER sites are involved in NSF-funded Integrative Graduate Education and Research Traineeship (IGERT) programs, and serve as hosts for Undergraduate Mentoring in Environmental Biology (UMEB) and Research Experience for Undergraduates (REU) site activities. The programs integrate field and laboratory techniques with education, providing the students with deeper understanding of the scientific process in ecology.

Most LTER sites or their home institutions participate in the REU and UMEB programs, which offer opportunities for students at both LTER and non-LTER institutions to work with LTER scientists. Participating sites fund REU students through separate grants and supplements or out of project funds. REU students receive stipends and course credit and work closely with scientist mentors on ongoing site research programs or specially designed projects. The UMEB program provides stipends to minority students during the summer and academic year to undertake independent research projects in environmental biology under the direction of departmental faculty. Students in the program come from a wide variety of disciplines including chemistry, geophysics, and biology. Some sites provide similar opportunities through private foundations and other sources.

LTER Education in the Future The LTER Network has adopted the goal of advancing the theory and practice of ecological and environmental education at all levels and in all areas of LTER expertise. The LTER sites and network are uniquely poised to promote education at the program, institution, state, and national levels. This work builds on, and is linked closely to, LTER scientific expertise in its five core research areas and its long-term, comparative approach. LTER education addresses some of the most important but vexing objectives for ecological and environmental education; that is, it uses outdoor, inquiry-based teaching and learning to build ecological literacy; it creates effective strategies for interdisciplinary and collaborative learning about ecology and it teaches about local ecosystems while fostering an understanding of distant ones as well. Strategic objectives for future LTER education programs [2] include:

1. Expanded resources for education and outreach at both site and network levels by developing new funding sources and improving coordination with existing education and outreach programs
2. Increased participation by LTER sites in education and outreach through collaboration, coordination, training, and exchange of best practices among sites

3. Preparation and dissemination of new instructional materials designed and developed through strategic partnerships with constituent organizations, with particular attention to the needs of traditionally underrepresented groups
4. Development of metrics to evaluate and guide education and outreach activities at site and network levels
5. Increased use of appropriate cyber technologies to improve indication among partners and to disseminate educational and outreach materials more effectively
6. Regular adaptive assessment by external evaluators to monitor progress of LTER education and outreach programs and to design new approaches when necessary

Data and Information

Long-term research and synthesis demands the long-term stewardship and ready accessibility of data. The creation, curation, and dissemination of long-term databases are needed to assure that the data resources needed by researchers will continue to be available. In addition, by adopting policies that promote the timely sharing of data (both inside and outside the LTER Network), scientists can use the data in a variety of ways not anticipated by the original collector, including for regional, national, and global syntheses, thus providing a rich resource for the broader scientific community [2].

LTER has led the ecological community in developing protocols and practices for documenting, curating, and sharing data. The strategic goals for LTER information management are (1) to provide sources of high-quality, well-documented, and error-checked data at each site that support local science, stimulate synthesis and the creation of new knowledge, and facilitate transformative network-wide research at broad scales; (2) to improve existing data practices and information management systems at sites to make them uniformly easy to use, sustainable, and consistent with LTER protocols; (3) to develop a central network-level data discovery and integration platform comprising databases and servers connected through web services for single-portal data publication, discovery, and access; (4) to improve information flow between LTER and other networks; and (5) to evaluate recent developments in computer science, information technology and design, cybersecurity, community standards, and communication and collaboration technology for potential application in LTER Network and site information management.

The recent proliferation of long-term collaborative research programs has created a parallel need for scientific information systems that allow data, information, and knowledge to flow across disciplinary and cultural boundaries [52]. Scientific information systems expand the potential for scientific inquiry and are leading to a paradigm shift in biology [53] most evident to date in the genomic community [54]. Other disciplines, including ecology, are primed for similar dramatic changes driven in part by new tools and approaches to managing data. The success of long-term studies is measured both on the generation of new knowledge and the creation of data and information that will facilitate subsequent studies.

Future Directions

LTER is moving increasingly toward research that integrates ecological and social sciences (Fig. 11.7), having realized that fundamental questions related to the services that society receives from ecosystems, how these services are perceived, how perceptions affect behavior, and how behavioral changes affect ecosystem form and function are central to understanding the sustainability of ecosystems on which society depends. By blending ecological and social science theories, methods, and interpretations, LTER is better able to understand and forecast environmental changes at a time when no ecosystem on Earth is free from human influence. The *Decadal Plan for LTER* [34] laid out a plan for integrated, network-level research to address crucial long term social-ecological questions in three thematic areas: (1) land and water use change – the dynamics of urban, exurban, and working systems; (2) climate change, variability, and extreme events; and (3) nutrient mobilization and species introductions. These questions are interdisciplinary in nature, and were developed after extensive discussions and consultations among teams of biophysical and social scientists, educators, and information managers. The questions are also multi-scale, and require observations and experiments at multiple sites to test hypotheses at scales ranging from regional to continental.

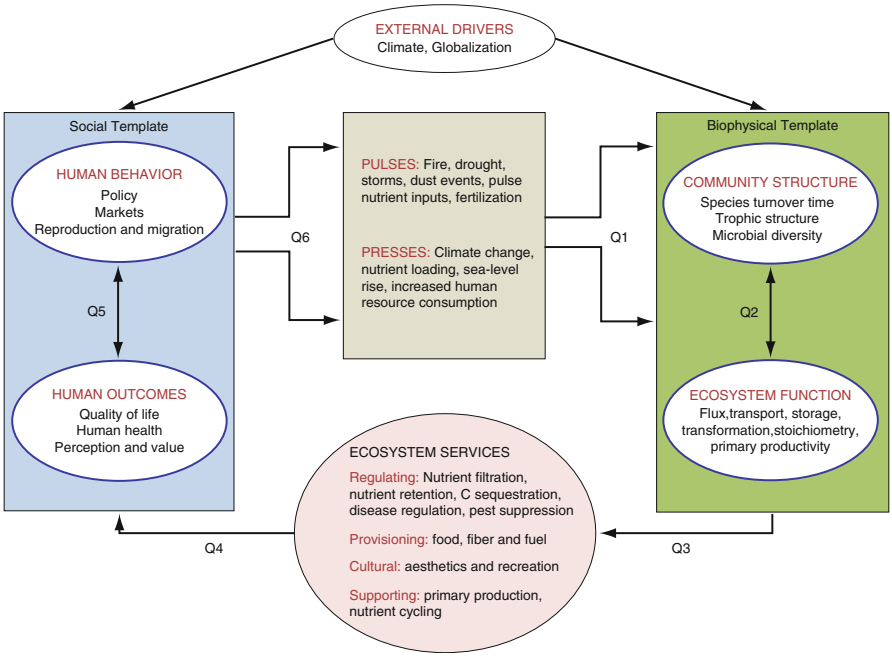

Fig. 11.7 Integrated science for society and the environment, a framework for future LTER research (From Collins et al. [55])

In fact, LTER is uniquely positioned to address these questions for a variety of reasons related to their long-term nature, the geographic distribution of network sites, the core strength of the network's biophysical science, its considerable and growing strength in the area of coupled human-natural systems, and its commitment to K-12 education and leadership in environmental cyberinfrastructure. Nevertheless, LTER recognized that it will require new long-term social-ecological observations, experiments, and modeling to address these questions effectively; advanced environmental cyberinfrastructure to collect, store, retrieve, visualize, and integrate the resulting complex data streams; partnerships with other environmental observatory networks to achieve this integration and facilitate synthesis; and education initiatives to train the next generation of environmental scientists to address transdisciplinary issues, and to enhance environmental literacy among the public.

Specific details of how the Decadal Plan's goals are to be achieved are constantly being worked out by Network science, education, and cyberinfrastructure teams, who identify individual questions, design observations, experiments, and modeling activities to address them, and the corresponding education and cyberinfrastructure needs for the resulting transdisciplinary research initiative. Science teams are presently developing four projects to advance the goals of the LTER Decadal Plan. The first of these projects is an effort to develop future scenarios to understand the vulnerability and resilience of regional landscapes to climate and land use change. Vulnerability to future climate change is also the theme of a second working group that will examine the affects of sea-level rise, increased storm surge, ocean acidification, and increases in water temperature, loss of sea ice, and changes in fresh water inflows on coastal LTER sites. Another working group is developing an experimental approach to evaluate the sensitivities of inland social-ecological systems to climate change to be conducted on a continental scale. Finally, a fourth group will examine how changes in the global cryosphere will affect ecosystem services such as planetary cooling, sea-level regulation, carbon storage, soil insulation, and water storage. Together, these four developing projects reflect the future direction of the LTER program.

Bibliography

Primary Literature

1. The Nature Conservancy, http://conserveonline.org/work spaces/ecoregional.shapefile/documents/terrestrial-ecoregional- boundaries-tnc/. Accessed 22 Apr 2011
2. Long Term Ecological Research Network (2011) Strategic and implementation plan. University of New Mexico. http://intranet2.lternet.edu. Accessed 13 Mar 2011
3. Likens GE (1983) A priority for ecological research. Bull Ecol Soc Am 64:234–243
4. Magnuson JJ (1990) Long-term ecological research and the invisible present. Bioscience 40:495–501

5. Callahan JT (1984) Long-term ecological research. Bioscience 34:363–367
6. Risser PG (1991) Summary. In: Risser PG (ed) Long term ecological research: an international perspective, vol 47, SCOPE. Wiley, New York, pp 287–290
7. Gosz JR, Waide RB, Magnuson JJ (2010) Twenty-eight years of the US-LTER program: experience, results, and research questions. In: Müller F, Baessler C, Schubert H, Klotz S (eds) Long-term ecological research: between theory and application. Springer, Dordrecht/New York, pp 59–74
8. Tilman D (1989) Ecological experimentation: strengths and conceptual problems. In: Likens GE (ed) Long-term studies in ecology: approaches and alternatives. Springer, New York, pp 136–157
9. National Science Foundation (1977) Long-term ecological measurements: report of a conference, Woods Hole. http://intranet2.lternet.edu
10. National Science Foundation (1978) Pilot Program for long-term observation and study of ecosystems in the United States: report of a second conference on long-term ecological measurements, Woods Hole. http://intranet2.lternet.edu
11. National Science Foundation (1979) Long-term ecological research concept statement and measurement needs: summary of a workshop at the Institute of Ecology, Indianapolis. http://intranet2.lternet.edu
12. National Science Foundation (1979) A new emphasis in long-term research. Washington, DC. http://intranet2.lternet.edu/sites/intranet2.lternet.edu/files/documents/LTER_History/Historical_Documents/LTER_rfp_1980.pdf
13. Magnuson JJ, Kratz TK, Frost TM, Bowser TJ, Benson BJ, Nero R (1991) Expanding the temporal and spatial scales of ecological research and comparison of divergent ecosystems: roles for LTER in the United States. In: Risser PG (ed) Long-term ecological research. an international perspective, vol 47, SCOPE. Wiley, Chichester, p 294
14. Magnuson JJ, Kratz TK, Benson BJ (2006) Long-term dynamics of lakes in the landscape: long-term ecological research on North Temperate Lakes. Oxford University Press, New York, p 400
15. Robertson DM (1989) The use of lake water temperature and ice cover as climatic indicators. PhD dissertation, University of Wisconsin-Madison, Wisconsin
16. Quinn WH, Zopf DO, Short KS, Kuo Yang RTW (1978) Historical trends and the statistics of the southern oscillation, El Niño, and Indonesian droughts. Fish Bull 76:663–677
17. Mysak LA (1986) El Niño, interannual variability and fisheries in the northeast Pacific Ocean. Can J Fish Aquat Sci 43:464–497
18. Wahl EW, Lawson TL (1970) The climate of the mid-nineteenth century United States compared to the current normals. Mon Weather Rev 98:259–265
19. Lamb HH (1977) Climate: present, past, and future. In: Climatic history and the future. Methuen, New York
20. Swanson FJ, Sparks RE (1990) Long-term ecological research and the invisible place. Bioscience 40:502–508
21. Johnson JC, Christian RR, Brunt JW, Hickman CR, Waide RB (2010) Evolution of collaboration within the U.S. Long-Term Ecological Research Network. Bioscience 60:931–940
22. Kratz TK, Deegan LA, Harmon ME, Lauenroth WK (2003) Ecological variability in space and time: insights gained from the US LTER Program. Bioscience 53:57–67
23. Rastetter EB, Aber JD, Peters DPC, Ojima DS, Burke IC (2003) Using mechanistic models to scale ecological processes across space and time. Bioscience 53:68–76
24. Kratz TK, Cunningham GL, Dahlgren RA, Frost TM, Halfpenny JC, Hansen JD, Heisey D, Inouye RS, Kaufman DW, McKee A, Yarie J, Magnuson JJ, Rapport DJ, Gaudet CL, Calow P, Bayley P, Benson BJ, Berish CW, Bledsoe CS, Blood ER, Bowser CJ, Carpenter SR (1995) Temporal and spatial variability as neglected ecosystem properties: lessons learned from 12 North American ecosystems. In: Rapport D, Calow P (eds)

Evaluating and monitoring the health of large-scale ecosystems. Springer, New York, pp 359–383
25. Gholz HL, Wedin DA, Smitherman SM, Harmon ME, Parton WJ (2000) Long-term dynamics of pine and hardwood litter in contrasting environments: toward a global model of decomposition. Glob Change Biol 6:751–766
26. Peters DP, Groffman PM, Nadelhoffer KJ, Grimm NB, Collins SL, Michener WK, Huston MA (2008) Living in an increasingly connected world: a framework for continental-scale environmental science. Front Ecol Environ 6:229–237
27. Franklin JF (1994) The U.S. long-term ecological research program: present, future, and international. In: Nottrott RW, Franklin JF, VandeCastle JR (eds) International networking in long-term ecological research. Proceedings of an international summit. U.S. LTER Network Office, University of Washington, Seattle, pp 22–31
28. Swift LW Jr, Ragsdale HL (1985) Meteorological data stations at long-term ecological research sites. In: Proceedings of the forest environmental measurements conference, Oak Ridge, 23–28 Oct 1983. Reidel, Holland
29. Greenland D (1986) Standardized meteorological measurements for Long-Term Ecological Research sites. Bull Ecol Soc Am 67:275–277
30. Greenland D, Kittel T (1987) A climatic analysis of long term ecological research sites. http://intranet.lternet.edu/archives/documents/Publications/climdes/
31. Crowl TA, Kane M, Gholz H (2010) NSF completes 2009 LTER site reviews and initiates a 30-year review of the LTER program. In: Network news. http://news.lternet.edu/article303.html
32. Corman JR, Gholz H (2008) NSF concludes 2007 LTER mid-term site reviews. In: Network news. http://news.lternet.edu/article152.html
33. Anonymous (2003) The value of LTER site augmentation. Network News 16(1):12–16. http://intranet2.lternet.edu/
34. U.S. Long Term Ecological Research Network (LTER) (2007) The decadal plan for LTER: integrative science for society and the environment. In: LTER network office publication series no. 24, Albuquerque
35. Hobbie JE (2003) Scientific accomplishments of the Long Term Ecological Research Program: an introduction. Bioscience 53:17–20
36. National Science Foundation (2010) NSF sensational 60. http://www.nsf.gov
37. Magnuson JJ, Wynne RH, Benson BJ, Robertson DM (2000) Lake and river ice as a powerful indicator of past and present climates. Verh Internat Verein Limnol 27:2749–2756
38. Carpenter SR, Gunderson LH (2001) Coping with collapse: ecological and social dynamics in ecosystem management. Bioscience 51:451–457
39. Knapp AK, Smith MD (2001) Variation among biomes in temporal dynamics of above ground primary production. Science 291:481–484
40. Foster DR, Swanson FJ, Aber JD, Burke IC, Brokaw N, Tilman D, Knapp AK (2003) The importance of land-use legacies to ecology and conservation. Bioscience 53:77–88
41. Grimm NB, Redman CL (2004) Approaches to the study of urban ecosystems: the case of central Arizona – Phoenix. Urban Ecosyst 7:199–213
42. Seastedt TR, Bowman WD, Caine TN, McKnight DM, Townsend A, Williams MW (2004) The landscape continuum: a model for high-elevation ecosystems. Bioscience 54:111–121
43. Suding K, Collins S, Gough L, Clark C, Cleland E, Gross K, Milchunas D, Penings S (2005) Functional- and abundance-based mechanisms explain diversity loss due to N fertilization. Proc Natl Acad Sci USA 102:4387–4392
44. Gragson TL, Grove M (2006) Social science in the context of the Long Term Ecological Research Program. Soc Nat Resour 19:93–100

45. Parton W, Silver WL, Burke IC, Grassens L, Harmon ME, Currie WS, King JY, Adair EC, Brandt LA, Hart SC, Fasth B (2007) Global-scale similarities in nitrogen release patterns during long-term decomposition. Science 315:361–364
46. Smith MD, Knapp AK, Collins SL (2009) A framework for assessing ecosystem dynamics in response to chronic resource alterations induced by global change. Ecology 90:3279–3289
47. Peters, DPC, Laney CM, Lugo AE, Collins SL, Driscoll CT, Groffman PM, Grove JM, Knapp AK, Kratz TK, Ohman MD, Waide RB, Yao J (2011) Long-term trends in ecological systems: a basis for understanding responses to global change. In: USDA agricultural research service publication no. XX, Washington, DC (in press)
48. Mulholland PJ, Helton AM, Poole GC, Hall RO Jr, Hamilton SK, Peterson BJ, Tank JL, Ashkenas LR, Cooper LW, Dahm CN, Dodds WK, Findlay S, Gregory SV, Grimm NB, Johnson SL, McDowell WH, Meyer JL, Valett HM, Webster JR, Arango C, Beaulieu JJ, Bernot MJ, Burgin AJ, Crenshaw C, Johnson L, Merriam J, Niederlehner BR, O'Brien JM, Potter JD, Sheibley RW, Sobota DJ, Thomas SM (2008) Stream denitrification across biomes and its response to anthropogenic nitrate loading. Nature 452:202–205
49. Bestelmeyer S, Dailey S, Elser M, Hembree P, Landis C, O'Connell K, Simmons B, Sommer S, Steiner S (2005) Handbook for LTER education. http://schoolyard.lternet.edu
50. Sobel D (1996) Beyond ecophobia: reclaiming the heart in nature education. The Orion Society and the Myrin Institute, Great Barrington
51. McKnight DM (2010) Overcoming "ecophobia": fostering environmental empathy through narrative in children's science literature. Front Ecol Environ 8:e10–e15. http://www.ceeauniba.net/files/e10.pdf. doi:1890/100041
52. Brunt JW, McCartney P, Baker KS, Stafford SG (2002) The future of ecoinformatics in long term ecological research. In: Rishe N (ed) Paper presented at the the 6th world multiconference on systemics, cybernetics and informatics conference, Orlando
53. Baker KS, Benson BJ, Henshaw DL, Blodgett D, Porter JH, Stafford SG (2000) Evolution of a multisite network information system: the LTER information management paradigm. Bioscience 50(11):963–978
54. Robbins RJ (1996) BioInformatics: essential infrastructure for global biology. J Comput Biol 3:465–478
55. Collins SL, Carpenter SR, Swinton SM, Ornstein D, Childers DL, Gragson TL, Grimm NB, Grove JM, Harlan SL, Kaye JP, Knapp AK, Kofinas GP, Magnuson JJ, McDowell WH, Melack JM, Ogden LA, Robertson GP, Smith MD, Whitmer AC (2011) An integrated conceptual framework for long-term social-ecological research. Front Ecol Environ 9:351–357

Books and Reviews

American Institute of Biological Sciences (2003) A special section on the US long term ecological research network. Bioscience 53(1):17–98

Bowman WD, Seastedt TR (eds) (2001) Structure and function of an alpine ecosystem: Niwot Ridge, Colorado, Long-Term Ecological Research Network series. Oxford University Press, New York

Chapin FS III, Oswood MW, Van Cleve K, Viereck LA, Verbyla DL (eds) (2006) Alaska's changing boreal forest, Long-Term Ecological Research Network series. Oxford University Press, New York

Coleman DC (2010) Big ecology:the emergence of ecosystem science. University of California Press, Berkeley/Los Angeles

Ecological Society of America (2008) Special issue: continental-scale ecology in an increasingly connected world. Front Ecol Environ 6(5):227–281

Fahey TJ, Knapp AK (eds) (2007) Principles and standards for measuring primary production, Long-Term Ecological Research Network series. Oxford University Press, New York

Foster DR, Aber JD (eds) (2004) Forests in time: the environmental consequences of 1,000 years of change in New England. Yale University Press, New Haven

Gragson TL, Grove M (2006) Social science in the context of the Long Term Ecological Research Program. Soci Nat Resour 19:93–100

Greenland D, Goodin DG, Smith RC (eds) (2003) Climate variability and ecosystem response at long-term ecological sites, Long-Term Ecological Research Network series. Oxford University Press, New York

Havstad KM, Huenneke LF, Schlesinger WH (eds) (2006) Structure and function of a Chihuahuan Desert ecosystem: the Jornada Basin long-term ecological research site, Long-Term Ecological Research Network series. Oxford University Press, New York

Knapp AK, Briggs JM, Hartnett D, Collins SL (eds) (1998) Grassland dynamics: long-term ecological research in tallgrass prairie, vol 1, Long-Term Ecological Research Network series. Oxford University Press, New York

Lauenroth WK, Burke IC (eds) (2008) Ecology of the shortgrass steppe: a long-term perspective, Long-Term Ecological Research Network series. Oxford University Press, New York

Magnuson JJ, Kratz TK, Benson BJ (eds) (2005) Long-term dynamics of lakes in the landscape: long-term ecological research on north temperate lakes, Long-Term Ecological Research Network series. Oxford University Press, New York

Michener WK, Waide RB (2008) The evolution of collaboration in ecology: lessons from the United States Long Term Ecological Research Program. In: Olson GM, Zimmerman A, Bos N (eds) Scientific collaboration on the Internet. MIT Press, Cambridge, MA, pp 297–310

Porter JH (2010) A brief history of data sharing in the U.S. Long Term Ecological Research Network. Bull Ecol Soc Am 91:14–20

Priscu JC (ed) (1998) Ecosystem dynamics in a polar desert: the McMurdo Dry Valleys. American Geophysical Union, Washington, DC

Redman C, Foster D (eds) (2008) Agrarian landscapes in transition: comparisons of long-term ecological and cultural change, Long-Term Ecological Research Network series. Oxford University Press, New York

Robertson GP, Coleman DC, Bledsoe CS, Sollins P (eds) (1999) Standard soil methods for long-term ecological research, vol 2, Long-Term Ecological Research Network series. Oxford University Press, New York

Ross RM, Hofmann EE, Quetin LB (eds) (1996) Foundations for ecological research west of the Antarctic Peninsula, vol 70, Antarctic research series. American Geophysical Union, Washington, DC

Shachak M, Gosz J, Pickett STA, Perevolotski (eds) (2005) Biodiversity in drylands: toward a unified framework, Long-Term Ecological Research Network series. Oxford University Press, New York

Zimmerman A, Nardi B (2010) Two approaches to big science: an analysis of LTER and NEON. In: Parker JN, Vermeulen N, Penders B (eds) Collaboration in the new life sciences. Ashgate, Burlington, pp 65–84

Chapter 12
Ocean Acidification

Maria Debora Iglesias-Rodriguez

Glossary

Acclimation	Organisms' physiological, morphological, and behavioral changes associated with environmental selection pressure. These are typically changes in size, growth rates, production rates of metabolites, or reproduction rates.
Adaptation	Change in population composition and numbers in response to environmental selection pressure. Adaptation is largely driven by the inherent genomic properties of a population (e.g., gene richness, genomic complexity, genetic diversity). In order for a population to adapt, a subset of its members (genotypes/ecotypes) may change in relative abundance.
Anthropocene	Period since the beginning of industrialization when the release of CO_2 and other by-products of human activities have had a profound effect on the Earth's ecosystems.
Biological pump	The biological processes (e.g., photosynthesis, calcification) that contribute to the downward flux of carbon from the ocean surface to the deep sea.
Biota	Animals and plants associated with a specific geographical region.

This chapter was originally published as part of the Encyclopedia of Sustainability Science and Technology edited by Robert A. Meyers. DOI:10.1007/978-1-4419-0851-3

M.D. Iglesias-Rodriguez (✉)
School of Ocean and Earth Science, National Oceanography Centre, University of Southampton, European Way, SO14 3ZH Southampton, UK
e-mail: debora.iglesias-rodriguez@noc.soton.ac.uk; dir@noc.soton.ac.uk

J. Orcutt (ed.), *Earth System Monitoring: Selected Entries from the Encyclopedia of Sustainability Science and Technology*, DOI 10.1007/978-1-4614-5684-1_12,

Calcification	Deposition of the soluble mineral phase of calcium carbonate ($CaCO_3$). In the marine environment, calcifiers include plants (e.g., coccolithophores, green and red algae, calcareous dinoflagellates) and animals (e.g., foraminifera, pteropods, fish, bivalves, gastropods, corals, echinoderms, crustacea, sponges).
Calcium carbonate saturation horizon	The depth of the ocean below which the saturation state of calcium carbonate is below 1, and therefore dissolution increases dramatically. This depth is also termed lysocline and it is dependent upon temperature and pressure.
Ocean acidification	Period of accelerated decline in ocean pH as a result of increasing formation of carbonic acid from rising dissolved carbon dioxide in seawater as a result of human activities.
pH	pH is defined as $-\log_{10}[H^+]$ and represents a measure of the acidity of a solution. A pH of 7 is neutral, a pH below 7 indicates that the solution is acid, and a pH above 7 indicates that the solution is alkaline. The pH scale is logarithmic, which means that each unit change in pH equals a tenfold change in acidity. The average surface ocean pH is ~8.1.
Saturation state of calcium carbonate (Ω)	The product of the concentration of dissolved calcium and carbonate ions in seawater divided by the stoichiometric solubility product ($\Omega = [Ca^{2+}][CO_3^{2-}]/K^*_{sp}$) of the biomineral produced by an organism, that is, aragonite or calcite. When $\Omega > 1$, the water is in supersaturated state with respect to calcite or aragonite, and carbonate precipitates; when $\Omega < 1$ the water is in undersaturated state with respect to calcite or aragonite and these minerals dissolve; when $\Omega = 1$ the water is in saturated state with respect to calcite or aragonite and there is no precipitation or dissolution of carbonate.

Definition of the Subject and Its Importance

The oceans play a central role in the maintenance of life on Earth. Oceans provide extensive ecosystems for marine animals and plants covering two-thirds of the Earth's surface, are essential sources of food, economic activity, and biodiversity, and are central to the global biogeochemical cycles. The oceans are the largest

reservoir of carbon in the Planet, and absorb approximately one-third of the carbon emissions that are released to the Earth's atmosphere as a result of human activities. Since the beginning of industrialization, humans have been responsible for the increase in one greenhouse gas, carbon dioxide (CO_2), from approximately 280 parts per million (ppm) at the end of the nineteenth century to the current levels of 390 ppm. As well as affecting the surface ocean pH, and the organisms living at the ocean surface, these increases in CO_2 are causing global mean surface temperatures to rise. As CO_2 increases in the atmosphere, the concentration of CO_2 in seawater increases proportionally as the gas diffuses into the ocean. Part of the dissolved CO_2 reacts with water (H_2O) to form carbonic acid (H_2CO_3) in a process termed ocean acidification [1, 2]. While the levels of CO_2 are not exceptional in the history of the Earth, the rate of increase in CO_2 is thought to be at least an order of magnitude faster than has occurred for 65 million years [3]. This rapid rate of change requires marine biota to adapt rapidly and a concern is whether, to what extent, and how marine animals and plants will be able to adapt (evolutionary selection of individuals) to changes in carbon chemistry as a result of ocean acidification. Changes in acclimation such as adjustments of physiology in marine biota (e.g., changes in photosynthesis, respiration, nitrogen fixation, and calcification) in response to ocean acidification have the potential to alter marine biogeochemical cycles. For example, changes in carbon acquisition via photosynthesis will affect the efficiency of the biological pump to sequester carbon. While the chemistry of ocean acidification is relatively well characterized and there is conclusive evidence that oceans have experienced increases in CO_2 parallel to those in the atmosphere, much less is known about the biological effects of these changes. The effects of ocean acidification are already seen in corals and other marine organisms but the responses appear to be species-specific and in some cases strain-specific (see [4] and references herein). Given that ocean acidification is a global-scale phenomenon, identifying its effects presents a challenge to science and requires joint coordinated international efforts across physical, chemical, and biological oceanography.

Introduction

The oceans provide services to humans, which are of great value to the functioning of societies. Oceans are a major ecosystem providing a significant global food source, for example, fisheries provide up to 20% of protein in Southeast Asian countries, western coastal Africa, and western and northern Europe [5]. The oceans have absorbed about one-third of the anthropogenic carbon emissions, which in part ameliorates global warming induced by human activity. However, this capacity to absorb CO_2 is challenged by the accelerated increase in human activities such as the increasing burning of fossil fuels, cement production, agriculture, and deforestation. These activities have influenced atmospheric CO_2 concentrations significantly since

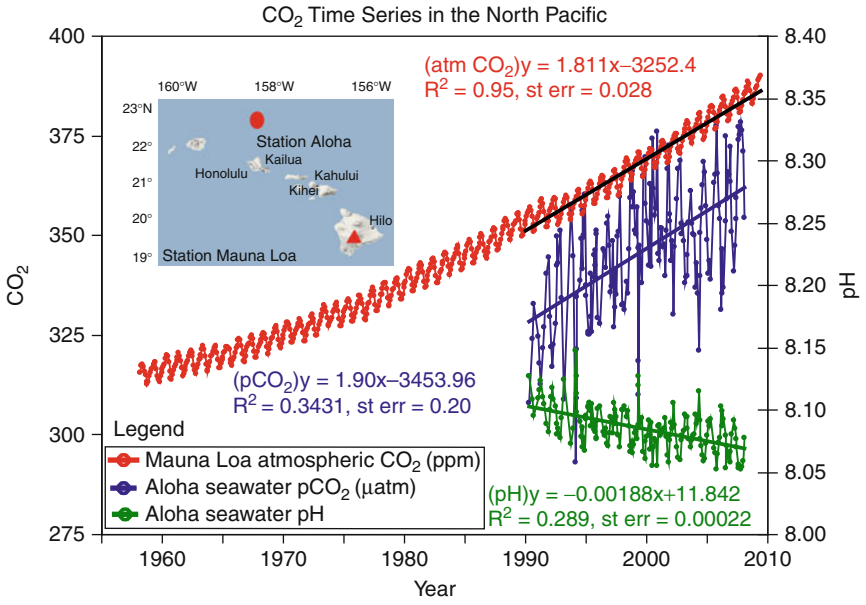

Fig. 12.1 Time series of atmospheric CO_2 at Mauna Loa (in ppm) and surface ocean pH and pCO_2 (µatm) at Ocean Station ALOHA in the subtropical North Pacific Ocean. Mauna Loa data: Dr. Pieter Tans, NOAA/ESRL (http://www.esrl.noaa.gov/gmd/ccgg/trends); HOTS/Aloha data: Dr. David Karl, University of Hawaii (http://hahana.soest.hawaii.edu) (Modified after Feely et al. [11])

the beginning of industrialization. Over this period, known as the Anthropocene, the speed of CO_2 increase is thought to be at least ten times faster than that experienced by the Earth for 65 million years [3]. As a result, the concentration of CO_2 in the atmosphere has been increasing from preindustrial levels of ~280 parts per million (ppm) to about 390 ppm at present. Projections according to the Intergovernmental Panel on Climate Change (IPCC) business-as-usual emission scenarios suggest that by the end of the century, atmospheric CO_2 could reach 800 ppm.

Observations in the geological record show that some marine biota have been able to adapt and thrive during fluctuations in atmospheric CO_2 while others have been severely affected by CO_2 changes [6–8]. Major extinction events have been associated with drastic changes in CO_2 and other climate-related factors. For example, during the Cretaceous-Tertiary (K/T) event, which took place ~65.5 million years ago, there was a large-scale mass extinction in a geologically short time period associated with major environmental changes including dramatic increases in temperature and CO_2 [9, 10]. However, to what degree CO_2 and temperature drive the observed extinctions remains an open question.

The accelerated rate of increase in the concentration of atmospheric CO_2 and the parallel rise in dissolved CO_2 in seawater (and the associated chemical changes) (Fig. 12.1) can affect marine life. For example, increases in CO_2 can potentially disrupt the acid base balance in tissues, fluids, and cells of marine organisms.

In organisms relying on building calcium carbonate ($CaCO_3$) structures like shells or skeletons, CO_2 increases can interfere with carbonate mineralization (please see section "Chemical Changes Associated with Ocean Acidification"). The extent to which marine biota can adapt to changes in carbonate chemistry and pH by evolutionary selection of individuals is critically dependent upon the genetic and physiological make up of their populations. Under IPCC carbon emission scenarios, surface ocean pH could decline by 0.3–0.4 units from preindustrial values to the end of this century [2]. Therefore, these fast changes (on geological terms, a century is a short time) may impede species to adapt to the new conditions. In coastal ecosystems the range of variation in CO_2 and temperature can be very broad, depending on biological activity and physical changes such as photosynthesis, respiration, tides, wave effect, etc. For example, an increase in bacterial respiration rates consumes oxygen and produces CO_2 such that acidity increases, sometimes dramatically. Therefore organisms living in these fast-changing environments (e.g., on sediments, where biological activity changes depending on the amount of organic carbon deposition) must be adapted and able to switch their physiology as pH and chemistry changes in their immediate environment. However, offshore and open ocean ecosystems are likely to be particularly susceptible to ocean acidification given that their exposure to fluctuations in pH and carbonate chemistry is much less pronounced than in coastal ecosystems. Therefore, abrupt changes in pH due to ocean acidification caused by human activities might occur more rapidly than the ability of some organisms to adapt while others will maintain their population numbers and health.

Biogeochemical Considerations: The Marine Carbon Cycle

The oceans represent the largest reservoirs of carbon in the Earth [12, 13]. In marine ecosystems, the magnitude and direction of carbon fluxes between the atmosphere, the upper ocean, and the ocean interior are critically dependent upon physical and chemical, as well as biological processes such as photosynthesis, which consumes CO_2, and respiration, decomposition, and calcification (CO_2-producing processes) (please see section "Chemical Changes Associated with Ocean Acidification") (Fig. 12.2). Photosynthesis also contributes to a large fraction of the annual global supply of oxygen, and removes nutrients (e.g., nitrate, phosphate, silicate, iron), which can be limiting in different parts of the ocean. Any change in functional properties of marine systems such as photosynthesis is going to have a profound effect on biogeochemical feedbacks and the ecosystem structure. Additionally, there is a vertical zonation of CO_2 sequestration at the surface and acidification of the deep sea because the organic matter produced by photosynthesis at the ocean surface is transferred to the deep sea where it is reoxidized into CO_2 by respiration, therefore increasing acidity. A change in photosynthetic activity will therefore impact upon the rates of consumption of CO_2 but also the rate of O_2 production.

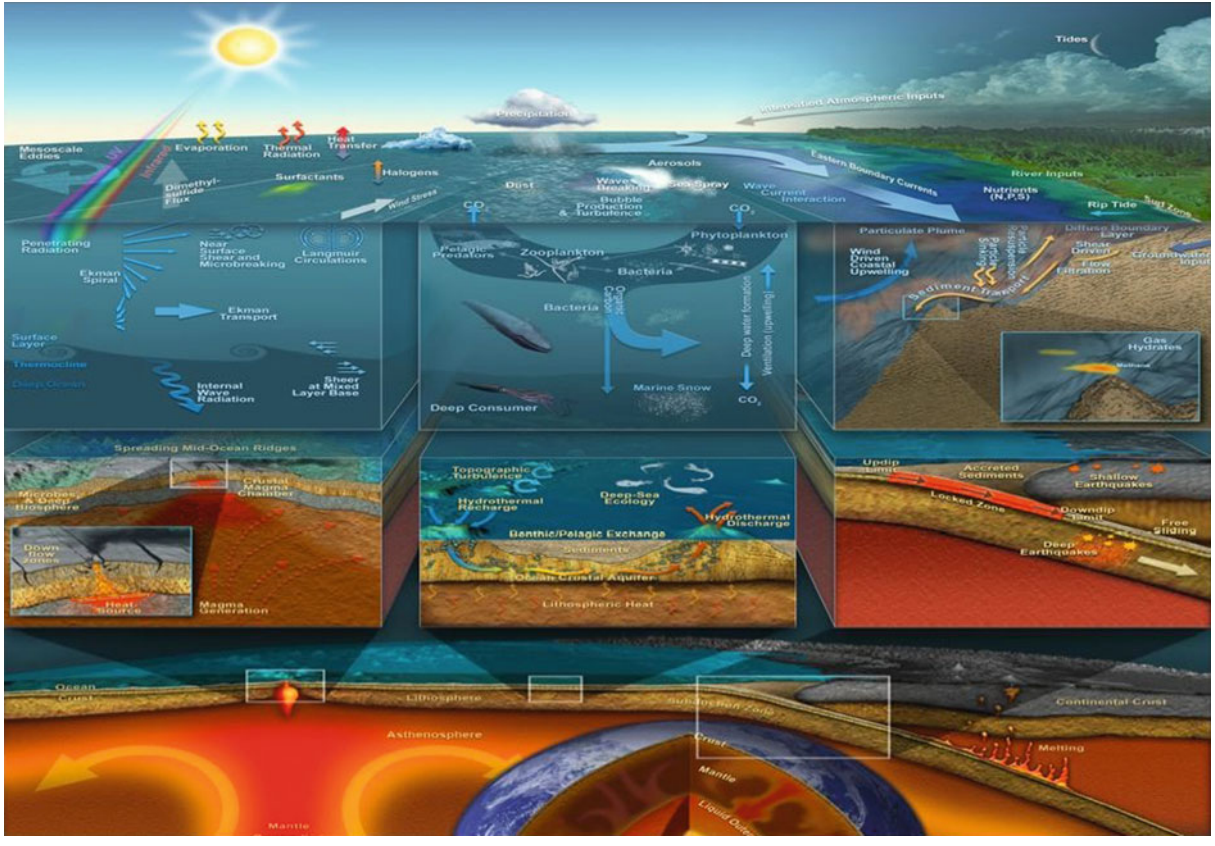

Fig. 12.2 The biological, chemical, and physical complexity of the oceans. Illustration designed by John Delaney and Mark Stoermer, and created by the Center for Environmental Visualization (CEV) for the NEPTUNE Program

Additionally, a decline in oxygen is predicted as a consequence of expected increases in temperature driven by climate change and altered ocean circulation [14–16] (O_2 solubility declines by ~6% for a 1°C increase in temperature). If the oceans experience a decrease in oxygenation, it will likely have an effect on respiration rates of marine animals and plants and on biological processes, which rely on oxygen. For example, any changes in the O_2:CO_2 ratios are likely to impact upon the functioning of enzymes catalyzing oxygenation and/or carboxylation reactions. One such example is the enzyme ribulose-1,5-biphosphate carboxylase/oxygenase, the most abundant enzyme on Earth, which controls fluxes of carbon at the ocean surface. Loss of oxygen from the oceans caused by warming could therefore have severe effects on marine biota, particularly those populating future oxygen minimum zones [16].

Chemical Changes Associated with Ocean Acidification

Since the beginning of industrialization, rising atmospheric CO_2 has caused increasing dissolution of CO_2 in seawater, which has lowered the average surface ocean pH by about 0.1 units [1]. Although a change in 0.1 pH units may seem small, this number represents ~30% increase in the concentration of hydrogen ions [H^+], which cause acidification of the seawater. The surface waters of the oceans are in fact alkaline (pH > 7), with an average pH of about 8.1, although there are spatial and seasonal variations due to inherent properties of the water, biological impacts, and weather and ocean physics. Carbon dioxide plays an important role in controlling the seawater pH, and any increases in the atmospheric CO_2 reach equilibration with the seawater phase in timescales of months. The main components of the carbonate system of seawater, the sum of which constitutes dissolved inorganic carbon (DIC), are CO_2, bicarbonate (HCO_3^-), carbonate (CO_3^{2-}), and carbonic acid (H_2CO_3) (Fig. 12.3), and their relative proportions are controlled by chemical equilibria, which are influenced by exchanges of CO_2 across the air-sea interface, and these are critically dependent upon changes in biological activity at the surface, and physical processes (e.g., wind, temperature changes) (Fig. 12.2) [18]:

$$CO_{2(aq)} + H_2O \Leftrightarrow H_2CO_3 \Leftrightarrow H^+ + HCO_3^- \Leftrightarrow 2H^+ + CO_3^{2-}$$

The relative proportion of these components of the DIC of seawater changes in response to increasing atmospheric CO_2 levels. Ocean acidification is a well-recognized consequence of rising atmospheric CO_2 as seen in the well-documented time series of the Hawaii Ocean Time-Series (HOT) station ALOHA, which illustrates the direct impact of changes in atmospheric CO_2 partial pressure

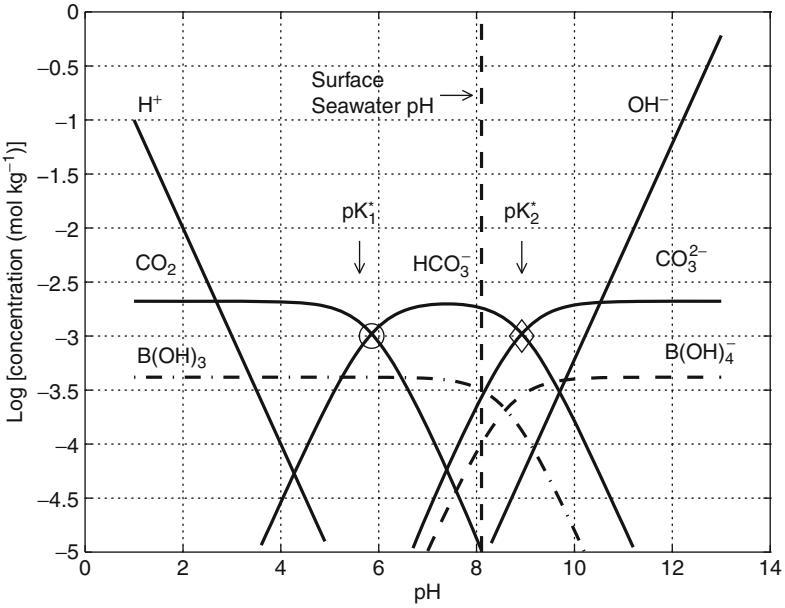

Fig. 12.3 Typical concentrations of dissolved inorganic carbon species in seawater as a function of pH. In addition to CO_2, HCO_3^-, CO_3^{2-}, H^+, and OH^-, this figure includes boric acid [$B(OH)_3$] and tetrahydroxyborate [$B(OH)_4^-$], as they contribute to the alkalinity of seawater (From [17])

(pCO_2) on seawater pCO_2 in parts per million (ppm) (Fig. 12.1). For surface open ocean conditions, about 93% of the total carbon is in the form of the bicarbonate ion (HCO_3^-), ~6% as carbonate (CO_3^{2-}), and ~1% remains as $CO_{2(aq)}$ and H_2CO_3. While the formation of H_2CO_3 is extremely slow (tens of seconds), the interconversion between HCO_3^- and CO_3^{2-} is extremely fast. These equilibria are shifted when atmospheric CO_2 concentrations increase and CO_2 dissolved in seawater forms a weak acid called carbonic acid (H_2CO_3), therefore causing the acidity of seawater to increase. A major fraction of this weak acid dissociates into hydrogen ions (H^+) and bicarbonate ions (HCO_3^-) ($H_2CO_3 \Leftrightarrow H^+ + HCO_3^-$). A small portion of the H^+ reacts with carbonate ion (CO_3^{2-}) to produce HCO_3^- ions. Therefore, an increase in dissolution of CO_2 in seawater causes a rise in the concentrations of H^+, H_2CO_3, and HCO_3^- and a decline in pH and in the concentration of CO_3^{2-}.

Three major biological processes affect the fluxes and direction of CO_2 between the sea surface and the atmosphere: photosynthesis, respiration, and calcification. Photosynthesis acts as a sink of CO_2 to produce organic carbon and oxygen ($6CO_2 + 6H_2O \Rightarrow C_6H_{12}O_6 + 6O_2$), while respiration produces CO_2 as a by-product ($C_6H_{12}O_6 + 6O_2 \Rightarrow 6CO_2 + 6H_2O$). The process of calcification uses CO_3^{2-} ($CO_3^{2-} + Ca^{2+} \Rightarrow CaCO_3$). However, given that the seawater concentration of

HCO_3^- is more than an order of magnitude greater than that of CO_3^{2-}, it is likely that organisms lacking a mechanism for concentrating CO_3^{2-} may use HCO_3^- as their ultimate carbon source for calcification ($2HCO_3^- + Ca^{2+} \Rightarrow CaCO_3 + CO_2 + H_2O$). Therefore, calcification is a source of CO_2 to the surrounding environment (about 0.6 moles of CO_2 are released for each mole of $CaCO_3$ precipitated) [19].

The process of calcification has received great attention over the last decade because a decline in carbonate ions could affect the health of organisms dependent on the use of these ions for the formation of their $CaCO_3$ plates and skeletons. The term $\Omega = ([Ca^{2+}][CO_3^{2-}]/K'_{sp}$, where K'_{sp} is the solubility product constant for $CaCO_3$, defines the saturation state of $CaCO_3$ and controls the formation and dissolution of calcium carbonate:

$$\text{dissolution} \rightarrow CaCO_3 \Leftrightarrow Ca^{2+} + CO_3^{2-} \leftarrow \text{biomineralization}$$

Given that the concentration of Ca^{2+} is five times that of DIC in seawater, Ω is largely dependent upon the concentration of CO_3^{2-}. Both $CaCO_3$ and CO_2 solubility increase with decreasing temperature and increasing pressure, and there is a critical depth controlling the formation and dissolution of $CaCO_3$: the saturation horizon or lysocline. Below the lysocline, seawater is undersaturated and $CaCO_3$ will start to dissolve, and above the lysocline $CaCO_3$ will be preserved. Waters are considered to be undersaturated when Ω is below 1 and supersaturated with respect to $CaCO_3$ when Ω is above 1. As temperature and pressure affect Ω, because increasing CO_2 dissolution at the surface decreases the carbonate ion concentration, the saturation horizons become shallower with increasing human activities releasing CO_2 to the atmosphere.

Biological Effects of Ocean Acidification

By the end of the century atmospheric CO_2 levels could reach more than 800 ppm [20], such that by 2100, the acidity of the ocean surface would have increased by about 150% relative to the beginning of industrialization. Although these levels are not unprecedented in the history of the Earth, the fast rate of change over the last 250 years [3] may affect some marine animals and plants in adapting to these abrupt changes in climate. When the carbonate saturation in seawater drops below 1 some $CaCO_3$ producing animals and plants may no longer be able to sustain calcification.

Metabolic Considerations: Advantages and Constraints of Elevated CO_2

Metabolically, CO_2 is not toxic but the shifts in carbonate chemistry associated with ocean acidification require organisms to regulate their physiology, and this adjustment is often associated with some metabolic cost [8, 21, 22]. An extreme case

scenario of elevated CO_2 is termed hypercapnia, which has been investigated experimentally in marine organisms although some of these experiments were carried out with unrealistically high CO_2 concentrations (much higher than those projected up to 2100). An analog in humans is respiratory hypercapnia (caused by buildup of CO_2 caused by hypoventilation) and metabolic acidosis, a condition whereby human blood, which is maintained at pH 7.35–7.50, drops below 7.35 (alkalosis occurs when blood pH increases to values above 7.45). A drop below the 7.35 is life threatening in humans despite pH being alkaline. It is however unlikely that marine organisms will suffer from acute poisoning due to a drastic drop in pH at expected future CO_2 levels.

In the metabolic compartments of organisms, CO_2, HCO_3^-, CO_3^{2-}, and oxygen (O_2), among other molecules, are maintained at different ratios depending on the rates and the energetic and catalytic requirements at the sites of photosynthesis (which uses CO_2 and/or HCO_3^-), calcification (which uses HCO_3^- and/or CO_3^{2-}), and respiration (which uses O_2). Therefore, while changes in the relative proportions of the carbon sources will exert a control on key metabolic processes, the balance between photosynthesis, respiration, and the resulting effects on food web feedbacks are also dependent upon other climate-relevant factors (e.g., temperature, light, nutrient availability, group competition, evolutionary processes).

Metabolically, elevated CO_2 could represent an advantage in CO_2 transfer across membranes. Typically, the average pH inside the cell and its compartments (e.g., the cytosol, nucleoplasm, mitochondria, and plastid stroma) is between 7.1 and 7.8 [23], which is lower than the mean surface open ocean pH (~8.1). As molecules crossing the plasma membrane need to be converted into the preferred electrochemical form, a decreased pH could arguably be energetically beneficial in CO_2 or HCO_3^- utilization across the external membrane of the cell. While the increase in CO_2 and HCO_3^- caused by ocean acidification seems to enhance photosynthetic carbon fixation, the parallel decrease in CO_3^{2-} ions requires the coordinated action of a consortium of enzymes at the site of calcification, internally (e.g., inside marine phytoplanktonic $CaCO_3$-producing cells called coccolithophore) and externally (e.g., in corals). The extent to which organisms can maintain calcification rates is critically dependent upon the efficiency of membrane processes transferring ions to maintain $[Ca^{2+}]$, pH, and, thus, $[CO_3^{2-}]$ and $[HCO_3^-]$ at levels that promote calcification.

Generally, increasing dissolved CO_2 has been found to enhance its removal by photosynthetic carbon fixation in phytoplankton by about 10% [24]. Increases in photosynthesis have been observed in diatoms [25, 26], coccolithophores [8, 27, 28]. Sea grasses [29, 30] seem to be in most cases either unaffected or enhanced by ocean acidification. However, different phytoplankton groups exhibit different sensitivities to increased CO_2 concentrations and this is likely due to whether CO_2 and/or bicarbonate are used for photosynthesis, to the cellular carbon requirements, and to other factors such as temperature. An example of this is a field manipulation experiment varying both temperature and CO_2, which appeared to control phytoplankton population composition [26]. Ocean acidification appears to cause

a decline in Fe availability to phytoplankton [31] and shifts in the proportion of nutrients in seawater driven by ocean acidification can influence community structure, nutrient utilization, and productivity [32, 33]. Nitrogen fixation, a functional property of cyanobacteria appears to be enhanced by elevated CO_2 in *Trichodesmium* sp. [34, 35].

Effect of Ocean Acidification on Calcifiers

Calcification, together with photosynthesis, is probably the most important physiological process affected by the increase in seawater CO_2 concentrations. Calcification is a widespread and resilient phenomenon in the history of Earth that is essential to most life forms. Calcification refers to the deposition of the soluble mineral phase of $CaCO_3$ and, in the marine environment, calcifiers include photosynthetic organisms (e.g., coccolithophores, green and red algae, calcareous dinoflagellates) and animals (heterotrophs (foraminifera), pteropods, fish, bivalves, gastropods, corals, echinoderms, crustacea, sponges). This process represents a source of CO_2 to the surrounding water and potentially to the atmosphere via the following equation: $Ca^{2+} + 2HCO_3^- \Rightarrow CaCO_3 + CO_2 + H_2O$ (please see section "Chemical Changes Associated with Ocean Acidification" for details). However, the effect of calcification (CO_2 source) can be counteracted by that of photosynthesis (CO_2 sink) in photosynthetic organisms like coccolithophores. It has been proposed that if the ratio of $CaCO_3$ to particulate organic carbon (the latter a product of photosynthesis) is below 1.5, then the calcifier is a sink of CO_2, but if this ratio increases to values above 1.5, the calcifier is considered a source of CO_2 to the environment [19]. While calcification is one mechanism by which carbon is exported to depth and it is a carbon sink as the formation of $CaCO_3$ removes carbon from the seawater into solid phase, it is however a source of CO_2.

Polymorph mineralogy and elemental chemistry of marine carbonates should be considered in predicting the responses of marine calcifiers to ocean acidification [36]. In the marine environment there are two main polymorphs of $CaCO_3$: calcite and aragonite. It is well established that aragonite is more soluble than calcite, and that the solubility of calcite increases with its Mg-content. Magnesium tends to substitute for calcium in the calcite lattice, forming "low-Mg calcite" when % $MgCO_3$ is less than 4, and "high-Mg calcite" when it is greater than 4 [37]. There are other forms of pelagic carbonates, for example, magnesium carbonate ($MgCO_3$) and strontium carbonate ($SrCO_3$), although most carbonate is buried in the form of $CaCO_3$. Although these additional carbonate forms make a smaller contribution to the $CaCO_3$ budget, they should be taken into account to assess the susceptibility of marine carbonates to CO_2-induced ocean acidification and whether or to what extent these proportions change.

In calcifiers, any change in the saturation state of the two main polymorphs of $CaCO_3$ – calcite and aragonite – is of particular concern because the making of their shells and skeletons is dependent on the availability of CO_3^{2-}. Calcifying organisms include planktonic plants and animals that drift in the water (e.g., coccolithophores, foraminifera, pteropods, and fish) and benthic organisms, which live at the bottom of the ocean (e.g., green and red algae, bivalves, gastropods, corals, echinoderms, crustacea, foraminifera, serpulid worms, bryozoa, and sponges). Generally, marine calcification seems to decline with decreasing carbonate ions although there is significant variability in the magnitude and direction of the slope (e.g., [8, 21, 22, 27, 28, 38–55]). However there are varying physiological responses to ocean acidification. For example, manipulations of CO_2 in seawater showed enhanced productivity under CO_2 up to 560 ppm, but severely reduced productivity under CO_2 regimes approaching 1,000 ppm [56]. The calcification response to ocean acidification remains unresolved in a group of $CaCO_3$-producing microscopic plants, the coccolithophores where significant variation has been observed between and even within species [8, 27, 28, 41, 44, 52, 57, 58]. Interestingly, studies suggest that increases in calcification in response to CO_2 occur with a metabolic cost. For example, in an investigation of susceptibility of calcifiers to ocean acidification, 6 of 18 species investigated actually began to dissolve (on a net basis) under high CO_2 and the gross morphology (and presumably function) of many of the shells was modified under high CO_2 [22]. In another study, growth rates of coccolithophores declined significantly under elevated CO_2 [8], suggesting that energetic demand may be significant, for example, in maintaining elevated pH at the site of calcification.

Calcifiers must adapt to the rapid rates of change in $CaCO_3$ saturation because the formation of their skeletons is critically dependent upon the availability of CO_3^{2-}, which is favorable when the seawater is supersaturated with calcium carbonate. This is why increasing CO_2 concentration and declining pH are detrimental to calcification [24]. This is particularly important in polar ecosystems, given that the solubility of CO_2 in seawater increases with decreasing temperature. Undersaturation with respect to aragonite by the year 2032 in the Arctic Ocean [59], and by 2050 in the Southern Ocean [60], may cause additional disruptions to many components of the marine food web. An increase in temperature associated with rising CO_2 will undoubtedly have consequences on metabolic rates. Although there are limited experiments on the combined effects of CO_2 and temperature (and other climate-related variables), it is known that their combined impacts can be different from those on its own [47, 61, 62]. One example is the relative effect of temperature and CO_2 on coral bleaching, the process by which the photosynthetic organisms living in symbiosis with corals, zooxanthellae, decline in numbers or produce less pigments [63, 64]. Therefore, understanding better the synergistic effects of climate-driven variables is central to managing ecosystems and making robust predictions to future climate scenarios.

Changes in pH over the History of the Earth

Marine organisms have adapted to fluctuations in atmospheric CO_2 throughout their evolutionary history. One of the best preserved calcifying groups, the coccolithophores, exhibits high diversities and abundances within a wide range of pCO_2, temperature, and Mg:Ca regimes, suggesting that they are an ecophysiologically versatile group [65]. Other groups including corals, mollusks, brachiopods, foraminifera, bryozoans, and echinoderms appear to have experienced changes in diversity and abundance though since their onset in the geological record [66–72]. Using coccolithophores as an example of one of the best preserved groups in the geological record, their identification in the late Triassic suggests that these algae evolved coccolithogenesis soon after their genetic differentiation at the Permian-Triassic (P/T) boundary [65, 73]. Their origin and further fast diversification is associated with a long-term decline in atmospheric pCO_2 [73] and a decrease in seawater Mg:Ca that promoted their predominantly low-Mg calcitic mineralogy [22].

During their evolution, deep sea dwellers have adapted to unique living conditions, with typically very stable temperatures and pressures, and relatively constant CO_2 concentrations (with the exception of volcanic CO_2 vents and zones of exceptionally high respiration rates). While deep sea ecosystems are generally exposed to little fluctuations in environmental factors including pH, the ocean surface and coastal regions are subjected to seasonal variations in pH, exposures to corrosive waters due to seasonal upwelling, and other short-term and often small-scale perturbations (e.g., [53, 74]). These unique ecosystems provide a natural laboratory where to test environmental impacts and adaptation of organisms to environmental selection pressure.

Distinct adaptations are reflected in the geological record revealing that organisms have been relatively resilient to changes in ocean pH [6] and Ca^{2+} levels [7]. However there have been periods of rapid environmental change, such as at the Cretaceous/Tertiary (K/T) boundary, which was accompanied by mass extinction of calcareous phytoplankton [9], and at the P/T boundary, which is associated with selective extinction of a range of calcifying marine organisms [10]. Whether marine calcifiers will adapt (evolutionary selection of specific groups) to future carbonate chemistry conditions (and associated changes in temperature and other factors) is presently at the centre of the debate in the ocean acidification community. At present, there is insufficient information to even speculate about possible biogeochemical shifts originating from distinct adaptations (evolutionary selection) or changes in the functional properties of organisms (acclimation) (e.g., change in photosynthetic carbon fixation, calcification, fertilization success, and larval development).

Geographic Variability in pH

While ocean acidification is a global-scale phenomenon, there are areas that already have naturally low pH conditions representative of projected scenarios. These

include polar regions (Arctic and Southern Oceans), coastal zones exposed to river inputs, effects of terrigenous material, and near-coastal seasonal upwelling.

There is plenty of evidence showing ocean acidification although there is temporal and spatial variability in carbonate chemistry [1, 2, 42, 60, 74–81]. It is also well established that the uptake of anthropogenic CO_2 is a major cause for long-term increases in DIC and decreases in $CaCO_3$ saturation state [4, 82]. However, temperature is one important factor determining the solubility of CO_2 in seawater as CO_2 solubility increases with decreasing temperature. Therefore, polar waters have inherently higher CO_2 content and polar ecosystems are potentially more vulnerable to further increases in CO_2 caused by ocean acidification. It has been suggested that the high latitude oceans (Arctic and Southern Oceans) will experience aragonite undersaturation by the middle of the century [36, 60, 83, 84]. Saturation of $CaCO_3$ is also affected by pressure such that deeper waters tend to have lower Ω. Shoaling of the aragonite and calcite saturation horizons is another effect associated with ocean acidification. Shallower undersaturated waters have been observed in the North Pacific [85], and Chukchi Sea and Arctic Ocean [86, 87], which makes organisms living in them potentially more vulnerable. Many of the organisms producing skeletons or body parts of solid-phase $CaCO_3$ are known to be sensitive to the concentration of CO_3^{2-} in ambient seawater, which determines $CaCO_3$ saturation. At present, most surface waters in the global ocean are supersaturated with respect to aragonite and calcite ($\Omega > 1$), but a decrease in these values will affect organisms with optimal carbonate precipitation rates above these saturation states.

Seasonal Upwelling Events

Upwelling is a process by which cold, dense, and typically nutrient-rich waters move toward the ocean surface, replacing warmer and nutrient-poor waters. Therefore, during these events, large areas and the organisms inhabiting them experience exposure to high CO_2. In 2008, Feely and colleagues [74] showed results indicating that the continental shelf of the west coast of North America may already be undersaturated with respect to aragonite resulting from the combined impacts of coastal upwelling and ocean acidification (Fig. 12.4). In this region, the seasonal upwelling of subsurface waters along the coast brings CO_2-enriched waters from depth to the surface ocean. The observations of this study suggest that these upwelled waters are enriched with anthropogenic CO_2 from gas exchange and vertical mixing as well as being inherently high in CO_2. Therefore, the CO_2 concentrations in these upwelled waters is much greater than those in preindustrial times. These acidified waters could have a detrimental effect on aragonite-producing organisms as these waters are undersaturated with respect to aragonite. Given that upwelling is a seasonal common phenomenon in many coastal regions, the enhanced acidity of upwelled waters could be affecting coastal ecosystems in other

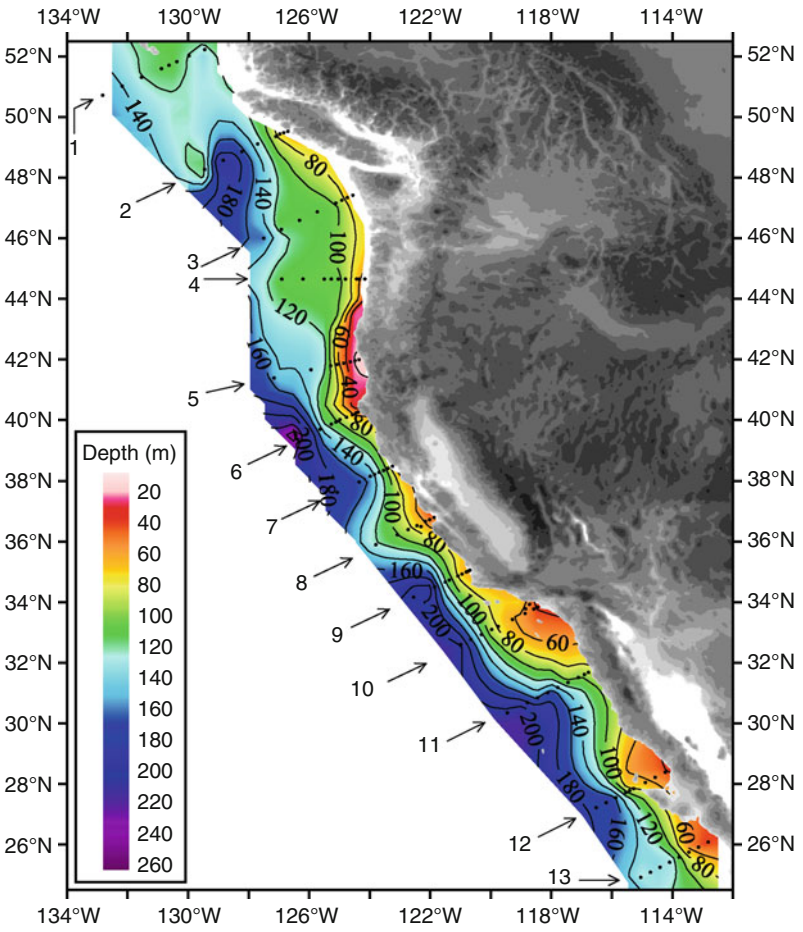

Fig. 12.4 The depths of undersaturated water (aragonite saturation < 1.0; pH < 7.75) on the continental shelf of western North America from Queen Charlotte Sound, Canada to San Gregorio Baja California Sur, Mexico. On transect lines 5 the corrosive water reaches all the way to the surface in the inshore waters near the coast. The *black dots* represent station locations [74]

upwelling regions. What remains to be tested is whether organisms experiencing these events seasonally have local adaptations to overcome these pronounced alterations in carbonate chemistry.

Future Directions

An international effort in monitoring changes in atmospheric and oceanic CO_2 concentrations, the ocean uptake of anthropogenic CO_2 and the natural CO_2

exchange under climate change and rising atmospheric CO_2 is already underway. This represents a huge step forward in assessing local, regional, and global effects, and identifying regions of particular susceptibility to changes in pH in coastal and open ocean environments.

The majority of studies on the causes and effects of ocean acidification have focused on short-term laboratory experiments with just a few field manipulations. Longer-term experiments that represent more realistic adaptations are needed to validate measured responses to abrupt exposures to acidified conditions, which are typically used in the laboratory. The emerging molecular technology will determine the extent to which organisms adapt to changes over long timescales, for example, by making use of existing and ongoing genome projects. Information at the most fundamental level of biological organization – the genome level – will provide first-hand information about how organisms evolve and how some functions are acquired and some others are lost. Information at all levels of organization, from global through ecological to molecular (genes, proteins), will enhance our ability to predict the fate of the ocean and the organisms inhabiting them a high CO_2 world.

Bibliography

Primary Literature

1. Caldeira K, Wickett ME (2003) Anthropogenic carbon and ocean pH. Nature 425:365
2. Caldeira K, Wickett ME (2005) Ocean model predictions of chemistry changes from carbon dioxide emissions to the atmosphere and ocean. J Geophys Res 110:C09S04, doi:10.1029/2004JC002671
3. Ridgwell A, Schmidt DN (2010) Past constraints on the vulnerability of marine calcifiers to massive carbon dioxide release. Nat Geosci 3:196–200
4. Doney SC, Fabry VJ, Feely RA, Kleypas JA (2009) Ocean acidification: the other CO_2 problem. Ann Rev Mar Sci 1:169–192. doi:10.1146/annurev.marine.010908.163834
5. Cooley SR, Doney SC (2009) Anticipating ocean acidification's economic consequences for commercial fisheries. Environ Res Lett 4:024007. doi:10.1088/1748-9326/4/2/024007
6. Gibbs SJ, Bown PR, Sessa JA, Bralower TJ, Wilson PA (2006) Nannoplankton extinction and origination across the Paleocene-Eocene thermal maximum. Science 314:1770–1773
7. Tyrrell T, Zeebe RE (2004) History of carbonate ion concentration over the last 100 million years. Geochim Cosmochim Acta 68:3521–3530
8. Iglesias-Rodrıguez MD, Halloran PR, Rickaby REM, Hall IR, Colmenero-Hidalgo E, Gittins JR, Green DRH, Tyrrell T, Gibbs SJ, von Dassow P, Rehm E, Armbrust VE, Boessenkool KP (2008) Phytoplankton calcification in a high CO_2 world. Science 320:336–339
9. MacLeod N, Rawson PF, Forey PL, Banner FT, Boudagher-Fadel MK, Bown PR, Burnett JA, Chambers P, Culver S, Evans SE, Jeffret C, Kaminski MA, Lord AR, Milner AC, Milner AR, Morris N, Owen E, Rosen BR, Smith AB, Taylor PD, Urquart E, Young JR (1997) The Cretaceous-tertiary biotic transition. J Geol Soc 154:265–292
10. Knoll AH, Bambach RK, Payne JL, Pruss S, Fischer WW (2007) Paleophysiology and end-Permian mass extinction. Earth Planet Sci Lett 256:295–313
11. Feely RA et al (2008) PICES Press 16(1):22–26
12. Sarmiento JL, Gruber N (2002) Sinks for anthropogenic carbon. Phys Today 55:30–36

13. Archer D (2005) Fate of fossil fuel CO_2 in geological time. J Geophys Res 110: C09S05, doi:10.1029/2004JC002625
14. Garcia HE, Boyer TP, Levitus S, Locarnini RA, Antonov JI (2005) Climatological annual cycle of upper ocean oxygen content anomaly. Geophys Res Lett 32:L09604. doi:10.1029/2004GL022286
15. Brierley AS, Kingsford MJ (2009) Impacts of climate change on marine organisms and ecosystems. Curr Biol 19:R602–R614. doi:10.1016/j.cub.2009.05.046
16. Keeling RF, Körtzinger A, Gruber N (2010) Ocean deoxygenation in a warming world. Ann Rev Mar Sci 2:199–229
17. Zeebe RE, Wolf-Gladrow D (2001) CO_2 in seawater: equilibrium, kinetics, isotopes. Elsevier Oceanography Series, 65, Amsterdam, pp 346
18. Sabine CL, Feely RA, Gruber N, Key RM, Lee K, Bullister JL, Wanninkhof R, Wong CS, Wallace DWR, Tilbrook B, Millero FJ, Peng T-H, Kozyr A, Ono T, Rios AF (2004) The oceanic sink for anthropogenic CO_2. Science 305:367–371
19. Frankignoulle M, Canon C, Gattuso J-P (1994) Marine calcification as a source of carbon dioxide: positive feedback of increasing atmospheric CO_2. Limnol Oceanogr 39:458–462
20. Intergovernmental Panel on Climate Change (2001) Climate change 2001: impacts, adaptation and vulnerability. In: McCarthy JJ et al (eds) Contribution of Working Group II to the Third Assessment Report of the Intergovernmental Panel on Climate Change. Cambridge University Press, New York
21. Wood HL, Spicer JI, Widdicombe S (2008) Ocean acidification may increase calcification rates, but at a cost. Proc Roy Soc Lon B 275:1767–1773
22. Ries JB, Cohen AL, McCorkle DC (2009) Marine calcifiers exhibit mixed responses to CO_2-induced ocean acidification. Geology 37:1131–1134
23. Venn AA, Tambutté E, Lotto S, Zoccola D, Allemand D, Tambutté S (2009) Imaging intracellular pH in a reef coral and symbiotic anemone. Proc Natl Acad Soc 106:16574–16579
24. Raven JA, Caldeira K, Elderfield H, Hoegh-Guldberg O, Liss P, Riebesell U, Shepherd J, Turley C, Watson A (2005) Ocean acidification due to increasing atmospheric carbon dioxide. The Royal Society policy Document 12/05, London
25. Tortell PD, Rau GH, Morel FMM (2000) Inorganic carbon acquisition in coastal Pacific phytoplankton communities. Limnol Oceanogr 45:1485–1500
26. Tortell PD, Payne CD, Li Y, Trimborn S, Rost, B, Smith, WO, Riesselman, C, Dunbar, RB, Sedwick, P, and DiTullio, GR (2008) CO_2 sensitivity of Southern ocean phytoplankton. Geophys Res Lett 35: L04605, 5 pp, doi:10.1029/2007GL032583
27. Riebesell U, Zondervan I, Rost B, Tortell PD, Zeebe RE, Morel FMM (2000) Reduced calcification of marine plankton in response to increased atmospheric CO_2. Nature 407:364–367
28. Shi D, Xu Y, Morel FMM (2009) Effects of the pH/pCO_2 control method on medium chemistry and phytoplankton growth. Biogeosciences 6:1199–1207
29. Palacios SL, Zimmerman RC (2007) Response of eelgrass Zostera marina to CO_2 enrichment: possible impacts of climate change and potential for remediation of coastal habitats. Mar Ecol Prog Ser 344:1–13
30. Zimmerman RC, Kohrs DG, Steller DL, Alberte RS (1997) Impacts of CO_2 enrichment on productivity and light requirements of Eelgrass. Plant Physiol 115:599–607
31. Shi D, Xu Y, Hopkinson BM, Morel FMM (2010) Effect of ocean acidification on iron availability to marine phytoplankton. Science 327:676–679
32. Tortell PD, DiTullio GR, Sigman DM, Morel FMM (2002) CO_2 effects on taxonomic composition and nutrient utilization in an equatorial Pacific phytoplankton assemblage. Mar Ecol Prog Ser 236:37–43
33. Blackford JC (2010) Predicting the impacts of ocean acidification: challenges from an ecosystem perspective. J Mar Syst 81:12–18. doi:10.1016/j.jmarsys.2009.12.016

34. Barcelos e Ramos J, Biswas H, Schulz KG, LaRoche J, Riebesell U (2007) Effect of rising atmospheric carbon dioxide on the marine nitrogen fixer. Trichodesmium Glob Biogeochem Cycles 21: GB2028, 6 pp, doi:10.1029/2006GB002898
35. Hutchins DA, Fu F-X, Zhang Y, Warner ME, Feng Y, Portune K, Bernhardt PW, Mulholland MR (2007) CO_2 control of Trichodesmium N2 fixation, photosynthesis, growth rates, and elemental ratios: Implications for past, present, and future ocean biogeochemistry. Limnol Oceanogr 52:1293–1304
36. Feely RA, Orr J, Fabry VJ, Kleypas JA, Sabine CL, Landgon C (2009) Present and future changes in seawater chemistry due to ocean acidification. In: McPherson BJ, Sundquist ET (eds) Carbon sequestration and its role in the global carbon cycle. AGU Monograph, Washington, DC
37. Morse JW, Andersson AJ, Mackenzie FT (2006) Initial responses of carbonate-rich shelf1369 sediments to rising atmospheric pCO_2 and "ocean acidification": role of high Mg-calcites. Geochim Cosmochim Acta 70:5814–5830
38. Gattuso J-P, Frankignoulle M, Bourge I, Romaine S, Buddemeier RW (1998) Effect of calcium carbonate saturation of seawater on coral calcification. Glob Planet Change 18:37–46
39. Kleypas JA, Buddemeier RW, Archer D, Gattuso J-P, Langdon C, Opdyke BN (1999) Geochemical consequences of increased atmospheric carbon dioxide on coral reefs. Science 284:118–120
40. Kleypas JA, Buddemeier RW, Gattuso J-P (2001) The future of coral reefs in an age of global change. Int J Earth Sci 90:426–437
41. Zondervan I, Zeebe RE, Rost B, Riebesell U (2001) Decreasing marine biogenic calcification: a negative feedback on rising atmospheric pCO_2. Glob Biogeochem Cycles 15:507–516
42. Feely RA, Sabine CL, Lee K, Millero FJ, Lamb MF, Greeley D, Bullister JL, Key RM, Peng T-H, Kozyr A, Ono T, Wong CS (2002) In situ calcium carbonate dissolution in the Pacific Ocean. Glob Biogeochem Cycles 16:1144
43. Leclercq N, Gattuso J-P, Jaubert J (2002) Primary production, respiration, and calcification of a coral reef mesocosm under increased CO_2 partial pressure. Limnol Oceanogr 47:558–564
44. Zondervan I, Rost B, Riebesell U (2002) Effect of CO_2 concentration on the PIC/POC ratio in the coccolithophore Emiliania huxleyi grown under light-limiting conditions and different daylengths. J Exp Marine Biol Ecol 272:55–70
45. Guinotte JM, Buddemeier RW, Kleypas JA (2003) Future coral reef habitat marginality: temporal and spatial effects of climate change in the Pacific basin. Coral Reefs 22:551–558
46. Langdon C, Broecker WS, Hammond DE, Glenn E, Fitzsimmons K, Nelson SG, Peng T-S, Hajdas I, Bonani G (2003) Effect of elevated CO_2 on the community metabolism of an experimental coral reef. Glob Biogeochem Cycles 17:1–14. doi:10.1029/2002GB001941
47. Reynaud S, Leclercq N, Romaine-Lioud S, Ferrier-Pages C, Jaubert J, Gattuso JP (2003) Interacting effects of CO_2 partial pressure and temperature on photosynthesis and calcification in a scleractinian coral. Glob Chang Biol 9:1660–1668
48. Langdon C, Atkinson MJ (2005) Effect of elevated pCO_2 on photosynthesis and calcification of corals and interactions with seasonal change in temperature/irradiance and nutrient enrichment. J Geophys Res 110: C09S07, doi:10.1029/2004JC002576
49. Guinotte JM, Orr J, Cairns S, Freiwald A, Morgan L, George R (2006) Will human induced changes in seawater chemistry alter the distribution of deep-sea scleractinian corals? Front Ecol Environ 4:141–146
50. Kleypas JA, Feely RA, Fabry VJ, Langdon C, Sabine CL, Robbins LL (2006) Impacts of ocean acidification on coral reefs and other marine calcifiers: a guide for future research, report of a workshop, St. Petersburg, FL, USA, 18–20 Apr 2005, sponsored by NSF, NOAA, and the US Geological Survey http://www.ucar.edu/communications/Final_acidification.pdf
51. Gazeau F, Quiblier C, Jansen JM, Gattuso J-P, Middelburg JJ, Heip CHR (2007) Impact of elevated CO_2 on shellfish calcification. Geophys Res Lett 34: L07603, doi:10.1029/2006GL028554

52. Fabry VJ, Seibel BA, Feely RA, Orr JC (2008) Impacts of ocean acidification on marine fauna and ecosystem processes ICES. J Mar Sci 65:414–432
53. Hall-Spencer JM, Rodolfo-Metalpa R, Martin S, Ransome E, Fine M, Turner SM, Rowley SJ, Tedesco D, Buia M-C (2008) Volcanic carbon dioxide vents show ecosystem effects of ocean acidification. Nature 454:96–99. doi:10.1038/nature07051
54. Nienhuis S, Palmer AR, Harley CDG (2010) Elevated CO_2 affects shell dissolution rate but not calcification rate in a marine snail. Proc Roy Soc B: Biol Sci 277(1693):2553–2558. doi:10.1098/rspb.2010.0206
55. Rodolfo-Metalpa R, Martin S, Ferrier-Pages C, Gattuso J-P (2010) Response of the temperate coral *Cladocora caespitosa* to mid- and long-term exposure to pCO_2 and temperature levels projected for the year 2100 AD. Biogeosciences 7:289–300
56. Anthony KRN, Kline DI, Diaz-Pulido G, Dove S, Hoegh-Guldberg O (2008) Ocean acidification causes bleaching and productivity loss in coral reef builders. Proc Natl Acad Soc 105:17442–17446
57. Langer G, Nehrke G, Probert I, Ly J, Ziveri P (2009) Strain specific responses of *Emiliania huxleyi* to changing seawater carbonate chemistry. Biogeosciences 6:2637–2646, http://www.biogeosciences.net/6/2637/2009/
58. Müller MN, Schulz KG, Riebesell U (2010) Effects of long-term high CO_2 exposure on two species of coccolithophores. Biogeosciences 7:1109–1116
59. Steinacher M, Joos F, Frölicher TL, Plattner G-K, Doney SC (2009) Imminent ocean acidification in the Arctic projected with the NCAR global coupled carbon cycle-climate model. Biogeosciences 6:515–533, www.biogeosciences.net/6/515/2009/
60. Orr JC, Fabry VJ, Aumont O, Bopp L, Doney SC et al (2005) Anthropogenic ocean acidification over the twenty-first century and its impact on calcifying organisms. Nature 437:681–686
61. Findlay HS, Wood HL, Kendall MA, Spicer JI, Twitchett RJ, Widdicombe S (2009) Calcification, a physiological process to be considered in the context of the whole organism. Biogeosciences Discuss 6:2267–2284, www.biogeosciences-discuss.net/6/2267/2009/
62. Walther K, Sartoris FJ, Bock C, Pörtner HO (2009) Impact of anthropogenic ocean acidification on thermal tolerance of the spider crab *Hyas araneus*. Biogeosciences 6:2207–2215
63. Kleppel GS, Dodge RE, Reese CJ (1989) Changes in pigmentation associated with the bleaching of stony corals. Limnol Oceanogr 34:1331–1335
64. Herfort L, Thake B, Taubner I (2008) Bicarbonate stimulation of calcification and photosynthesis in two hermatypic corals. J Phycol 44:91–98
65. Bown PR, Lees JA, Young JR (2004) In: Thierstein HR, Young JR (eds) Coccolithophores –from molecular processes to global impact. Springer, Berlin, p 481
66. Vinogradov AP (1953) The elementary chemical composition of marine organisms. Sears Foundation for Marine Research, New Haven
67. Weber JN (1969) The incorporation of magnesium into the skeletal calcites of echinoderms. Am J Sci 267:537–566
68. Lipps JH (1970) Plankton evolution. Evolution 24:1–21
69. Comperse EL, Bates JM (1973) Determination of calcite: aragonite ratios in mollusc shells by infrared spectra. Limnol Oceanogr 18:326–331
70. Wilkinson BH (1979) Biomineralization, paleoceanography, and the evolution of calcareous marine organisms. Geology 7:524–527
71. Zhuravlev AY, Wood RA (2008) Eve of biomineralization: controls on carbonate mineralogy. Geology 36:923–926
72. Zhuravlev AY, Wood RA (2009) Controls on carbonate skeletal mineralogy: global CO_2 evolution and mass extinctions. Geology 37:1123–1126
73. de Vargas C, Aubry M-P, Probert I, Young J (2007) In: Thierstein HR, Young JR (eds) Coccolithophores – from molecular processes to global impact. Springer, Berlin, p 251
74. Feely RA, Sabine CL, Hernandez-Ayon JM, Ianson D, Hales B (2008) Evidence for upwelling of corrosive "acidified" water onto the continental shelf. Science 320:1490–1492

75. Bates NR (2007) Interannual variability of the oceanic CO_2 sink in the subtropical gyre of the North Atlantic Ocean over the last 2 decades. J Geophys Res 112:C09013. doi:10.1029/2006JC003759
76. Bates NR, Peters AJ (2007) The contribution of atmospheric acid deposition to ocean acidification in the subtropical North Atlantic Ocean. Mar Chem 107:547–558
77. Chung SN, Lee K, Feely RA, Sabine CL, Millero FJ, Wanninkhof R, Bullister JL, Key RM, Peng T-H (2003) Calcium carbonate budget in the Atlantic Ocean based on water column inorganic carbon chemistry. Glob Biogeochem Cycles 17:1093
78. Feely RA, Sabine CL, Lee K, Berelson W, Kleypas J et al (2004) Impact of anthropogenic CO_2 on the $CaCO_3$ system in the oceans. Science 305:362–366
79. Sabine CL, Feely RA (2007) The oceanic sink for carbon dioxide. In: Reay D, Hewitt N, Grace J, Smith K (eds) Greenhouse gas sinks. CABI, Oxfordshire, pp 31–49
80. Santana-Casiano JM, Gonzalez-Davila M, Rueda MJ, Llinas O, Gonzalez-Davila EF (2007) The interannual variability of oceanic CO_2 parameters in the northeast Atlantic subtropical gyre at the ESTOC site. Glob Biogeochem Cycles 21:GB1015. doi:10.1029/2006GB002788
81. Watson AJ, Schuster U, Bakker DCE, Bates NR, Corbière A, González-Dávila M, Friedrich T, Hauck J, Heinze C, Johannessen T, Körtzinger A, Metzl N, Olafsson J, Olsen A, Oschlies A, Padin XA, Pfeil B, Santana-Casiano JM, Steinhoff T, Telszewski M, Rios AF, Wallace DWR, Wanninkhof R (2009) Tracking the variable North Atlantic sink for atmospheric CO_2. Science 326:1391–1393
82. Dore JE, Lukas R, Sadler DW, Church MJ, Karl DM (2009) Physical and biogeochemical modulation of ocean acidification in the central North Pacific. Proc Natl Acad Soc USA 106:12235–12240
83. Cao L, Caldeira K (2008) Atmospheric CO_2 stabilization and ocean acidification. Geophys Res Lett 35:L19609, 5 pp, doi:10.1029/2008GL035072
84. Gehlen M, Gangstø R, Schneider B, Bopp L, Aumont O, Ethe C (2007) The fate of pelagic $CaCO_3$ production in a high CO_2 ocean: a model study. Biogeosciences 4:505–519
85. Feely RA, Byrne RH, Acker JG, Betzer PR, Chen CTA et al (1988) Winter summer variations of calcite and aragonite saturation in the northeast Pacific. Mar Chem 25:227–241
86. Bates NR, Mathis JT, Cooper L (2009) The effect of ocean acidification on biologically induced seasonality of carbonate mineral saturation states in the Western Arctic Ocean. J Geophys Res Oceans 114:C11007, doi:10.1029/2008JC004862
87. Yamamoto-Kawai M, McLaughlin FA, Carmack EC, Nishino S, Shimada K (2009) Aragonite undersaturation in the Arctic Ocean: effects of ocean acidification and sea ice melt. Science 326:1098–1100

Books and Reviews

Feely RA, Fabry VJ, Dickson AG, Gattuso J-P, Bijma J, Riebesell U, Doney S, Turley C, Saino T, Lee K, Anthony K, and Kleypas J (2010) An international observational network for ocean acidification, OceanObs white paper (https://abstracts.congrex.com/scripts/jmevent/abstracts/FCXNL-09A02a-1664525-1-Feely-cwp2c04. pdf)

Houghton JT, Ding Y, Griggs DJ, Noger M, van der Linden PJ, Xiaosu D (2001) Climate change 2001: the scientific basis. In: Contrinbution of Working Group I to the Third Assessment Report of the Intergovernmental Panel on Climate Change 2001. Cambridge University Press, Cambridge, 944 p

Kleypas JA, Feely RA, Fabry VJ, Langdon C, Sabine CL, Robbins LL (2006) Impacts of ocean acidification on coral reefs and other marine calcifiers: a guide for future research. Report of St. Petersburg Workshop, FL, sponsored by NSF, NOAA, and U.S. Geological Survey, 88 p

Schubert R, Schellnhuber H-J, Buchmann N, Epiney A, Grieβhammer R, Kulessa M, Messner D, Rahmstorf S, Schmid J (2006) The future oceans – warming up, rising high, turning sour. German Advisor Council on global change, Special Report, Berlin, 110 p
Zeebe RE, Zachos JC, Caldeira K, Tyrrell T (2008) Oceans: carbon emissions and acidification. Science (Perspectives) 321:51–52

Documents

EPOCA. http://epoca-project.eu/
European geosciences union position statement on ocean acidification http://www.egu.eu/statements/egu-position-statement-on-ocean-acidification.html
IMBER. http://www.imber.info/
JSOST (Joint Subcommittee on Ocean Science and Technology; National Science and Technology Council). http://ocean.ceq.gov/about/jsost.html
National oceanic and atmospheric administration ocean acidification website. http://www.pmel.noaa.gov/co2/OA/
NSTC Joint subcommittee on ocean science and technology (2007) Charting the course for ocean science in the United States for the next decade, An ocean research priorities plan and implementation strategy, 26 Jan 2007, 84 p
Ocean Carbon and Biogeochemistry (OCB). http://www.us-ocb.org/ and http://www.whoi.edu/sites/oceanacidification
The Ocean Acidification Network. http://www.ocean-acidification.net/

Chapter 13
Ocean Evaporation and Precipitation

Luis Gimeno, Raquel Nieto, Anita Drumond, and Ana María Durán-Quesada

Glossary

Atmospheric rivers	The analysis of timescales shorter than climatic reveals that there are three to five major conduits of atmospheric circulation in each hemisphere, each of which is responsible for the transport of large amounts of water in narrow streams from the tropics through the midlatitudes toward the higher latitudes. These conduits were termed "atmospheric rivers" [10] because the way that the moisture that is transported is comparable with the way that water is transported in a terrestrial river such as the Amazon.
Clausius–Clapeyron equation	This is an equation that relates the saturation vapor pressure of air over liquid water as a function of temperature.
The El Niño–Southern Oscillation (ENSO)	*The El Niño–Southern Oscillation* is a quasiperiodic climatic pattern that occurs throughout the tropical Pacific Ocean. It is characterized by variations in the temperature of the surface of the tropical eastern Pacific Ocean (El Niño) coupled with variations in air pressure at the Earth's surface in the tropical Pacific (the Southern Oscillation). Warmer (colder) waters than normal over the eastern Tropical Pacific characterize an El Niño (La Niña) event, and this anomalous oceanic phenomenon is accompanied by a higher (lower) air pressure at the Earth's surface in the western Pacific.

This chapter was originally published as part of the Encyclopedia of Sustainability Science and Technology edited by Robert A. Meyers. DOI:10.1007/978-1-4419-0851-3

L. Gimeno (✉) • R. Nieto • A. Drumond • A.M. Durán-Quesada
Environmental Physics Laboratory (EPhysLab), Universidade de Vigo, Ourense, Spain
e-mail: l.gimeno@uvigo.es

J. Orcutt (ed.), *Earth System Monitoring: Selected Entries from the Encyclopedia of Sustainability Science and Technology*, DOI 10.1007/978-1-4614-5684-1_13,

Evapotranspiration	Evapotranspiration is a term that describes the transport of water into the atmosphere from different surfaces, including from the soil (soil evaporation), and from vegetation (transpiration).
Feedback mechanisms	These are processes such that when a system generates output, that output serves as input to an earlier stage in the operation of the system. This input to earlier stages causes a system to behave in a self-controlling manner. Feedback mechanisms can either amplify ("positive feedback") or diminish ("negative feedback") the effects of a change.
Hadley cell	This is a pattern of circulation that occurs in the tropical atmosphere, and involves a rising motion near the equator, a poleward flow at the upper troposphere (about 10–15 km above the surface), descending motion in the subtropics, and equatorward flow near the surface, which then completes the cell.
Inter tropical convergence zone	This is a band of cloudiness and precipitation that encircles the Earth near the equator where the northerly and southerly trade winds converge.
Low-level jet	This is the name given to a narrow zone of strong winds above the boundary layer (about 1,500 m above the surface), and is responsible for most of the moisture that is transported in tropical areas.
Monsoon	Seasonal precipitation caused by changes in atmospheric circulation associated with the asymmetric heating of land and sea.
South Pacific convergence zone	This is a band of low-level convergence, cloudiness, and precipitation that extends southeastward from the Indian–Pacific warm pool.
Surface freshwater flux	The difference between rates of evaporation and precipitation per unit area
Teleconnections	The relationship between, and the influence of, weather patterns in distant locations.
Thermocline	The oceanic depth at which the rate of decrease of temperature with depth is at a maximum. The thermocline may be considered to be the zone of separation between the oceanic mixed layer, which is influenced by atmospheric fluxes, and the deep ocean.
Walker circulation	This is a conceptual model of the zonal/vertical airflow in the tropical troposphere, caused by differences in the distribution of heat over the Earth's surface. Over the Pacific Ocean, low-level winds flow from the Eastern Pacific (characterized by high pressure) toward Indonesia (lower pressure), where the air then ascends to the high troposphere, before it then flows from Indonesia toward the Eastern Pacific, where it descends again.

Definition of the Subject and Its Importance

In view of the threat of global climate change, the proper understanding of the intensity of the hydrological cycle and of its development over time is one of the most important challenges of the century, at least in the area of the geosciences. The hydrological cycle can essentially be summarized to be the evaporation of moisture in one location, offset by precipitation elsewhere. The rate of evaporation exceeds the rate of precipitation over the oceans, which are therefore a net source of moisture; this moisture is then transported to the landmasses, which are a net sink for moisture, where precipitation exceeds evapotranspiration. In consequence, surface runoff enters rivers and other watercourses, which discharge into the ocean, thereby completing the cycle. Taken as a whole, the hydrological cycle is characterized by the evaporation of about half a million cubic kilometers of water per year, the bulk of which (86%) is from the ocean, with only 14% originating in the continents [1]. The vast majority of the water that evaporates from the oceans (90%) is precipitated back into them, while the remaining 10% is transported to the continents, where it precipitates. About two-thirds of this precipitation is recycled over the continents and only one-third runs off directly into the oceans. Ultimately, despite the small continental recycled component, all the water used in natural ecosystems and in human activity originates in the oceans. Because societies depend for their continued existence on the security of water resources, it is extremely important to understand the processes that govern the evaporation of water from the oceans (in the domain of oceanography) [2], the transport of moisture in the atmosphere (meteorology) [3], and the effects of these processes on the hydrological cycle (hydrology) [4], all within the context of the current paradigm of global climate change [5].

Introduction

Oceanic evaporation occurs when water molecules change phase from liquid to vapor at the air–sea interface. The rate at which this process occurs depends essentially on three variables: the available heat energy, the difference in humidity between the air and the surface, and the wind speed. The heat energy permits the water molecules to escape from the liquid with a latent energy that is then released during condensation. A gradient in humidity between the air and the surface of the sea is also necessary, because evaporation can only occur when the humidity of the air is lower than that of the evaporating surface of the sea. The wind influences the evaporation through the removal of water vapor from the evaporating surface by the turbulent movement of air, which then facilitates the evaporation by maintaining a vertical humidity gradient from the surface to the overlying air.

An assessment of the major oceanic sources of evaporation may be made conceptually using bulk parameterization and similarity theory [6]. The rate of evaporation (*Evp*) may be computed using

$$Evp = CeUdq$$

where *dq* is the difference between the saturation specific humidity at the sea surface and the near-surface atmospheric specific humidity; *U* is the near-surface wind speed; and *Ce* is a turbulent exchange coefficient that is controlled by the wind speed, the atmospheric stability, and the difference in temperature between the air and the sea. Evaporation should be prevalent in those oceanic regions with a high sea surface temperature, in sharp contrast with the air temperature, and where strong winds allow the humidity produced by the evaporation to be removed quickly, thereby preserving a clear contrast in the humidity between the air and the surface.

It is very difficult to estimate rates of evaporation, due to the very great uncertainties involved and because the rates themselves are so seldom measured. Usually, these rates are instead estimated from bulk flux formulae, which mean that it is possible to check the global distribution of evaporation over the oceans and to compare rates between different areas. One of the best estimates of evaporation is provided by the OAFlux data [7], which is produced by combining several reanalysis and satellite data sets. Figure 13.1 shows a picture of the annual and seasonal global distribution of evaporation. The global distribution of evaporation is approximately zonally oriented, with greater evaporation over the subtropical latitudes of the global oceans and less over the equatorial cold tongues and at higher northern and southern latitudes. It is also clear that more evaporation takes place over the regions of the oceanic western boundary currents and their extensions, including the Gulf Stream, the Kuroshio, the eastern Australian Current, the Agulhas Current, and the Falkland/Brazilian Current. These patterns show seasonal intensifications/reductions as a result of differences in wind speed, air–sea humidity gradient, and temperature.

Regions with the highest rates of evaporation coincide neither with those with the greatest amount of atmospheric water vapor nor with those with the highest precipitation. This is because water vapor has a residence time in the atmosphere of about 10 days [8] and can be transported fairly efficiently by general circulation. Figure 13.2 shows the main atmospheric fluxes of water vapor. An understanding of the processes of moisture transport requires a knowledge of the ways in which water vapor, which accounts for approximately 0.25% of the total mass of the atmosphere, is distributed (Fig. 13.3). The concentration of water vapor varies greatly, both in space and over time. The general global distribution of water vapor largely mirrors that of temperature because the equilibrium vapor pressure depends on temperature (Clausius−Clapeyron equation, C–C). Therefore, the greatest variations in the amount of water vapor occur with increasing height above the surface; specifically, concentrations of water vapor decrease markedly with increasing height. Important variations also occur close to the surface, where the

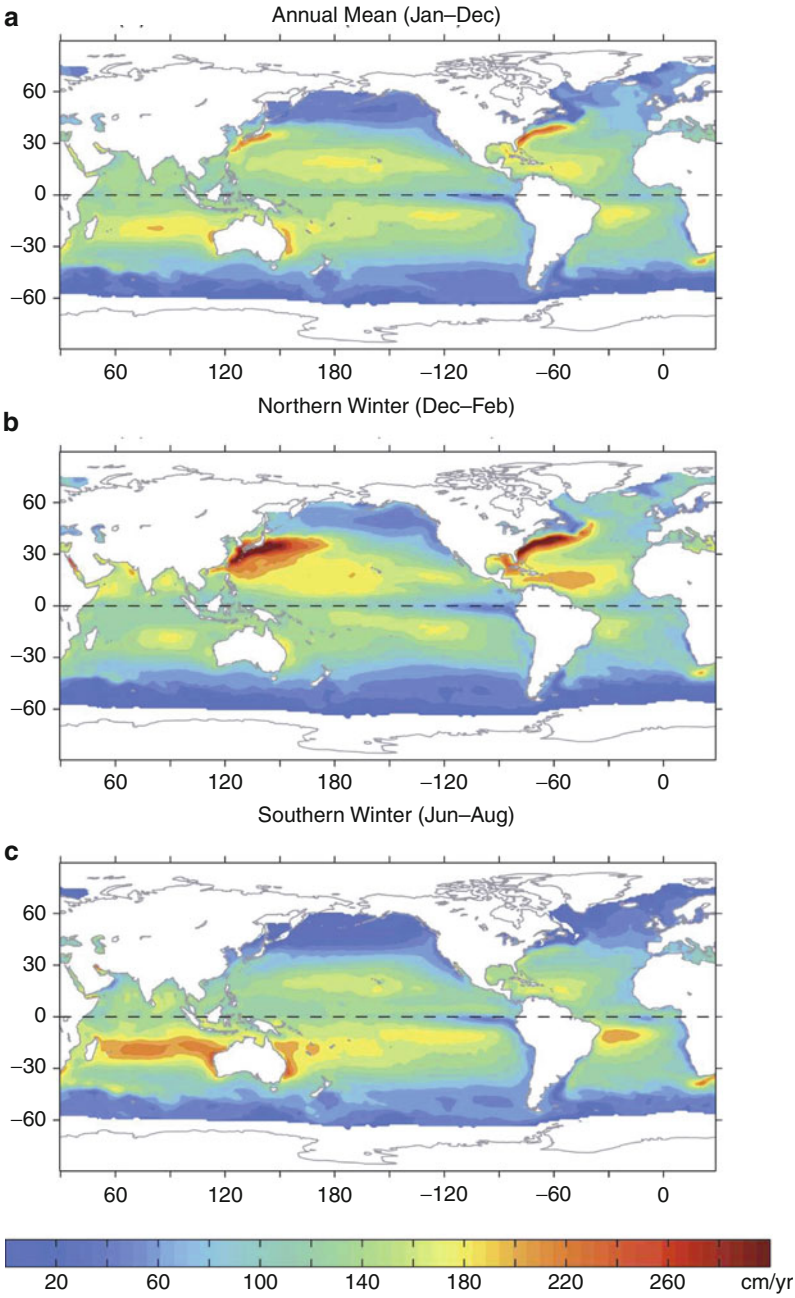

Fig. 13.1 Mean global evaporation showing (**a**) the annual mean values, and the mean values for (**b**) the northern winter (December–March), and (**c**) the austral winter (June–September). The mean values were constructed using data from the period 1958–2005 (From Yu [3])

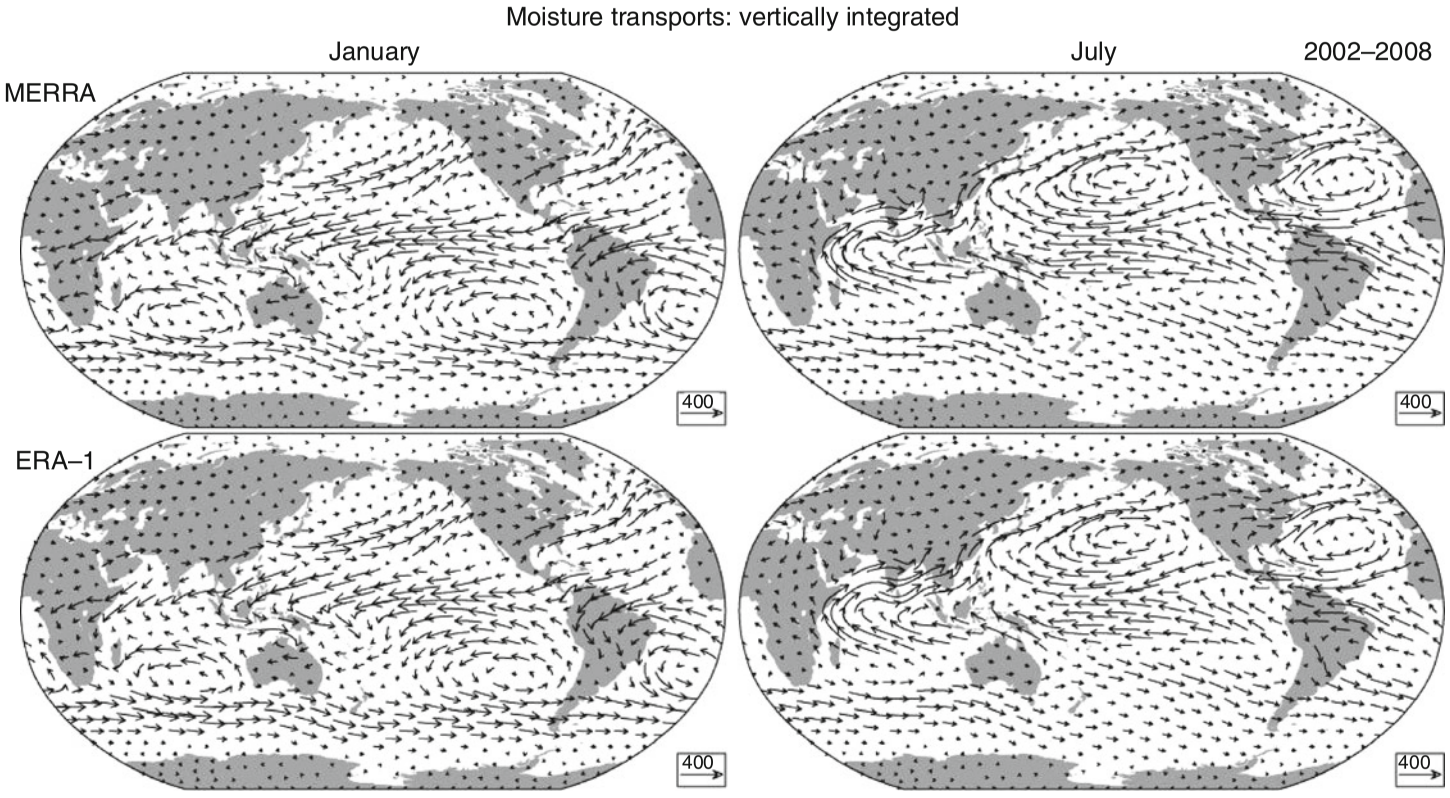

Fig. 13.2 Vertically integrated atmospheric moisture (including liquid and ice) transport for 2002–2008 from MERRA (*top*) and ERA-I (*bottom*) for January (*left*) and July (*right*). The units are kg m^{-1} s^{-1}; the *vector* key is given in the insert (From Trenberth et al. [9])

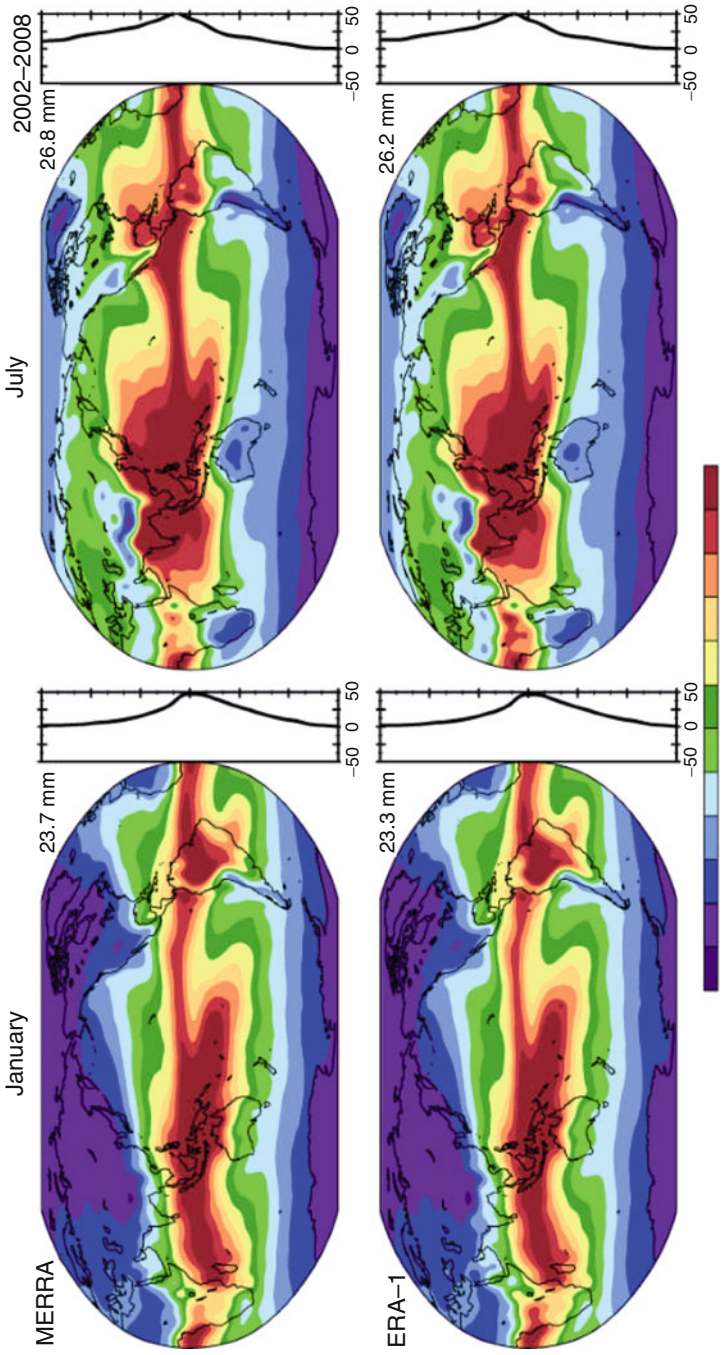

Fig. 13.3 Maps of total column atmospheric water for January (*left*) and July (*right*) for MERRA (*top*) and ERA-I (*bottom*) in mm for 2002–2008 (From Trenberth et al. [9])

concentrations vary by more than three orders of magnitude, from 10 ppm by volume in the coldest parts of the Earth's atmosphere, to as much as 5% by volume in the warmest [1]. Most of the Earth's water vapor is concentrated in the tropical atmosphere, which contains more than three times as much water as the extratropical atmosphere. The C–C equation describes the water-holding capacity of the atmosphere as a function of temperature, so the largest average values of total column water vapor (TCWV) occur over the tropical Pacific warm pool, where the highest large-scale values of sea surface temperature (SST) are typically found, and a strong gradient of TCWV occurs with latitude (typically, a 7% change in TCWV results from 1°C change in temperature).

Just as the distribution of evaporation differs from that of atmospheric water vapor, so it is also dissimilar to the distribution of precipitation (Fig. 13.4), which depends both on the supply of moisture and on the atmospheric instability that forces the air to rise. The distribution of precipitation is thus more similar to that of TCWV, especially in the tropics where atmospheric convergence tends to occur at low levels, in close association with the highest SSTs, although with much more structure due to known overturning circulations such as those associated with the Hadley cell and monsoons. In extratropical regions, the similarities between the distributions of TCWV and precipitation are much less clear. In these regions, precipitation is controlled by baroclinic instability due to strong meridional gradients of air temperature and the supply of moisture to strong, relatively narrow streams from the tropics through the mid- to the higher latitudes, which are sometimes referred to as "atmospheric rivers" [10]. It is these streams that provide most of the long-distance transport of moisture, accounting for 95% of the meridional flux of water vapor at 35° latitude [11].

In the following sections, the path of the atmospheric moisture is traced from its evaporation in the oceans to its precipitation in the continents, where water is needed to supply ecosystems and human socioeconomic activities.

Distribution of Evaporation from the Ocean and Precipitation

Once in the atmosphere, moisture is transported by general circulation and then falls to the surface as precipitation. In order to quantify this process of the transport of atmospheric water vapor, it is essential to identify the sources of the evaporation. Unfortunately, however, few direct measurements of evaporation have ever been made. In the absence of reliable measurements from around the globe, indirect methods must instead be used. One means of measuring evaporation involves a diagnosis of the vertically integrated moisture flux by referring to atmospheric data. Global maps that show the flux of moisture can provide a good indication of the major movements of the main moist air masses. Moreover, any divergence or convergence of that flux must reflect a net evaporation or precipitation, and indicate regions that act as sources of or sinks for atmospheric moisture [12].

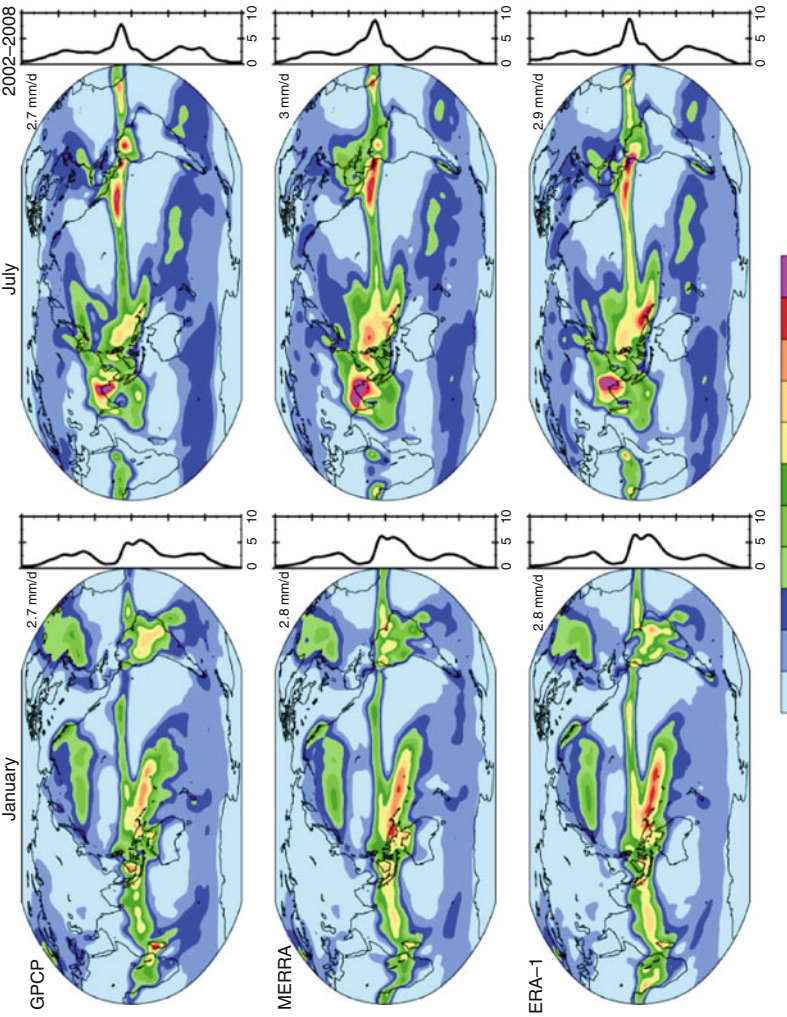

Fig. 13.4 Maps of precipitation for January (*left*) and July (*right*) for GPCP (*top*), MERRA (*middle*), and ERA-I (*bottom*) in millimeter per day for 2002–2008. The values shown at the *top right* of each map are the global means, and the zonal means are given to the *right* of each map (From Trenberth et al. [9])

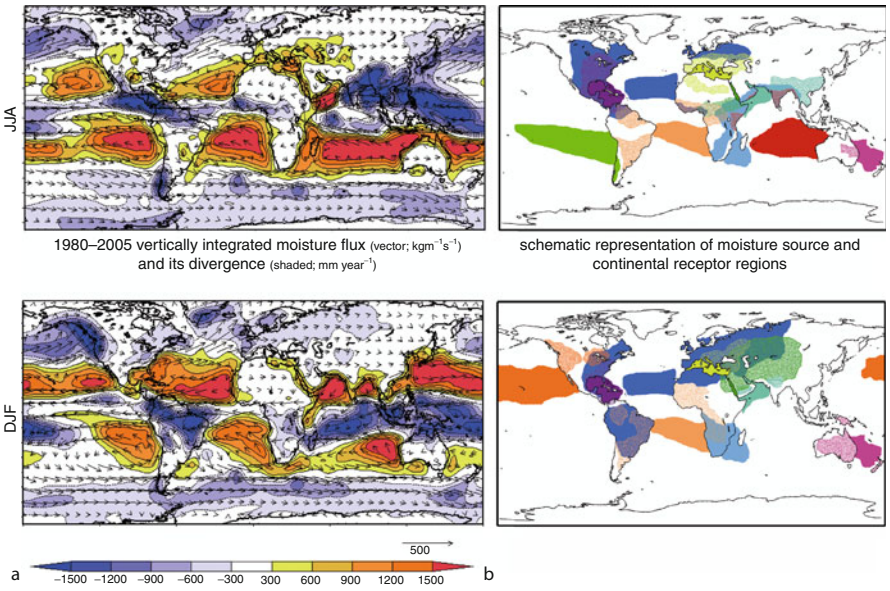

Fig. 13.5 Column **A**: 1980–2005 vertically integrated moisture flux (*vectors*; kg m^{-1} s^{-1}) and its divergence (*shaded contours*; mm $year^{-1}$) for JJA and DJF. (Data obtained from http://www.cgd.ucar.edu/cas/catalog/newbudgets/index.html#AtD). Column **B**: Schematic representation of moisture source and continental receptor regions shown in the same colors as the corresponding oceanic source regions for JJA and DJF. Overlapping regions are shown with *shaded texture* (From Gimeno et al. [75])

Figure 13.5a shows the distribution of the vertically integrated flux of moisture, and its divergence, during the boreal summer (June, July, and August; JJA) and winter (December, January, and February; DJF). The primary sources of moisture for the whole atmosphere (reddish colors) are found over the subtropical oceans, where evaporation takes place continuously, associated with the quasipermanence of the high-pressure cells. Several smaller regions also make significant contributions as sources of moisture in the Northern Hemisphere, such as the Caribbean, Mediterranean, and Red Seas. The major sinks (bluish colors) are in the tropical/subtropical convergence zones, the ocean storm tracks of the high latitudes, and the summer monsoonal rains (South America, India, the Sahel, and South Africa).

As a whole, the Southern Hemisphere exhibits a weak divergence (i.e., evaporation exceeds precipitation), and normally supplies moisture to the Northern Hemisphere [13]. The mains sources of moisture are found in the regions of the subtropical anticyclones on the western sides of South America, Africa, and Australia. Over the Indian Ocean, the divergence extends eastward from Africa to Australia in a continuous belt. Two cells of divergence dominate this belt, one located close to Madagascar, and another, stronger, cell located to the west of Australia. Another nucleus of divergence is located over eastern Africa, near the equator. Two divergent cells are prominent over the Pacific Ocean, one to the east

of Australia and the other in the central part of the eastern Pacific. The divergence over the high-pressure cells is stronger during the austral winter months (JJA), but their areal domain expands poleward with the displacement of the cells to the south during the austral summer (DJF), a season characterized by a lower hemispheric supply of moisture from the oceans to the atmosphere.

The distributions of vertically integrated moisture flux reflect the planetary behavior of the general circulation in the lower half of the troposphere, because the specific humidity acts as a weighting factor for the wind field [14]. The transport of moisture is thus characterized by westerlies in the midlatitudes and by easterlies in the tropical belt. Although the values of the meridional component of the transport of moisture are smaller than those of the zonal component, they still play an essential role in maintaining the global water balance. The meridional flux of moisture over the midlatitudes varies considerably with season, but it is predominantly poleward throughout the year. The transport is accomplished mainly by baroclinic lows associated with the polar front and by stationary eddies, such as subpolar lows and subtropical anticyclones, together with their transient pulsations. The largest variability during the year is associated with variations in the Hadley cells, whose lower branches are most effective in transporting moisture to the Inter Tropical Convergence Zone (ITCZ). In the tropics, the mean annual transports are northward to the south of the equator and southward to the north of it. The cross-equatorial flow in the Hadley cells changes direction with season, leading to a flux of water vapor into the Northern Hemisphere during JJA and a flux into the Southern Hemisphere during DJF.

Over the Southern Hemisphere, the patterns of the transport of moisture are predominantly zonal [15]. Although the central pressures are slightly greater during JJA, the high-pressure band in the subtropics is more extensive and the pressure gradient between the oceans and the continents is reduced. During DJF, the pressure gradients are strengthened because of the thermal lows that develop over the continents, resulting in a stronger meridional circulation [16]. From the maps of moisture flux, one may observe the strong northward transport of moisture in the eastern margin of the semipermanent subtropical high-pressure centers, particularly over the Pacific and Atlantic Oceans. In contrast, the major regions of southward transport are located over eastern South America and East Africa, and over almost the whole of the Pacific Ocean.

Lagrangian transport models have recently been used to provide more precise information about the relationship between the source regions of evaporation and remote precipitation. Figure 13.5b summarizes the main oceanic sources and the associated continental receptor regions of the evaporated moisture, obtained using the Lagrangian method of Stohl and James [17]. The figure shows that the productivity of the major oceanic sources of moisture for continental precipitation is not evenly distributed and that some specific oceanic sources generate more continental precipitation than others [18]. For example, the subtropical North Atlantic Ocean provides moisture for precipitation over vast geographical areas (from Mexico to large parts of Eurasia) in DJF. The North Atlantic Ocean is a relatively significant source of water vapor through net evaporation, in contrast to the North Pacific

Ocean, which produces a higher surface salinity in the Atlantic subregion than in the Pacific [19]. The absence of large mountains along the Atlantic coast in Europe favors the transport of moisture (mainly at low levels) from the Atlantic Ocean into the Eurasian continent and the Mediterranean region. In contrast, the existence of the Rocky Mountains (Andes) parallel to the west coast of North (South) America prevents moisture from the Pacific Ocean from penetrating very far into the American continent [14].

The Red Sea is the ocean basin that has the highest net evaporation [19], and provides large amounts of moisture that precipitate between the Gulf of Guinea and Indochina (JJA) and between the African Great Lakes and Asia (DJF). Although South Africa is surrounded by the Atlantic and Indian Oceans and is also located close to the vast Southern Ocean, the only air masses that cause net precipitation there are those that reach it from the Indian Ocean [19]. It is only the air masses from the Pacific Ocean that cause net precipitation over Australia, even though the landmass is surrounded by the Indian and Pacific Oceans.

Some landmasses receive moisture evaporated in the same hemisphere (e.g., Northern Europe or eastern North America), while others receive moisture from both hemispheres with large seasonal variations (e.g., northern South America). Monsoonal regimes in India, tropical Africa, and the North American Great Plains are fed by moisture provided from a large number of source regions, which highlights the complex nature of precipitation. Vast continental areas lack any appreciable direct transport of moisture from any of the major oceans, particularly those that correspond to some of the most arid inland regions (e.g., inner Asia), unless the recycling of continental moisture can compensate (albeit partly) for the absence of a direct oceanic source of moisture (e.g., in Eastern Siberia) [18].

Despite the points made in the foregoing discussion, not all the oceanic regions can be considered always to be sources of moisture. Air masses that originate in the high-latitude oceans (Hudson Bay, the Arctic, and the Southern Ocean) are extremely strong sinks for moisture when the associated air masses are transported toward lower latitudes [19]. Air masses tracked from the Atlantic, Pacific, and Indian Oceans are a significant source of moisture for the air masses of the Arctic and Southern Oceans. Even the air masses of the Mediterranean Sea, which are a strong source of water for all the Eurasian rivers that lie to the north of it, receive moisture from the river basins over Africa and India (Niger, Nile, Indus), especially during JJA.

Oceanic Heat Reservoirs (Warm Pools) and Evaporation

The term “warm pool” may be used to delineate in general terms those oceanic regions characterized by sea surface temperatures (SSTs) that exceed a fixed threshold. The vertical extent of a warm pool is relatively easy to stipulate precisely, through the use of a selected isothermal layer. However, the horizontal extent of a warm pool is much more difficult to characterize precisely.

In physical terms, a warm pool contains tropical surface water, which by definition is warm and has relatively low salinity. Because of its low density, it forms a lens of light water that floats on the denser waters below, which are subtropical in origin and therefore cooler and have higher salinity [20]. The clear correspondence of the presence of warm pools with the maxima of atmospheric total heating indicates the role of these pools in setting atmospheric global heating gradients and, by extension, the importance of warm pool for the general circulation of the atmosphere. A variety of phenomena occur both in the ocean and in the atmosphere within the tropical warm pools [21]. The warm pool is a region of net freshwater input into the ocean. Much of the moisture that is precipitated is evaporated locally from the sea surface. However, part is imported by large-scale circulation [21].

The Indian–western Pacific contains the highest SSTs in the open oceans, and has the largest annual precipitation and release of latent heat in the atmosphere [21, 22]. The Indian–western Pacific warm pool (IPWP) has been the subject of much scientific interest in recent years, due to its relationship with the development of El Niño–Southern Oscillation (ENSO) extreme events [20].

Many authors have used the 28°C isotherm as a practical compromise in their characterizations of the horizontal extent of IPWP [20]. By considering this isotherm to define the horizontal extent of the IPWP, it is possible to observe large annual variations in its boundaries. The northerly extreme of the pool is reached in September, whereas in March the pool barely reaches 10°N (Figs. 13.6 and 13.7). The annual fluctuations are less pronounced in the Southern Hemisphere, but the pool doubles in size between September and March. The area permanently covered by the pool is relatively small, from about 10°N to 10°S and from Indonesia to 170°W, and comprises only about half its average area. These large annual fluctuations in the boundaries of the pool make characterizing its size and volume rather difficult and subject to a degree of uncertainty. Its depth changes little with season. However, its horizontal extent varies considerably [20].

Air–sea interaction in the western tropical Pacific is dominated by the large-scale atmospheric convergence that is associated with the ascending branch of the Walker circulation, with the major tropical ascent occurring over the Pacific–Indian Ocean warm pool (e.g., [23]). The convergence of air and moisture from the Pacific and Indian Oceans leads to vigorous convection and heavy precipitation, together with the release of latent heat in the atmosphere, which drives the Walker circulation [24] (Figs. 13.6 and 13.7). The maximum SST of the warm pool is probably associated with the convergence of the oceanic circulation in the western tropical Pacific and the production of a relatively deep thermocline forced by the general atmospheric convergence of the Walker circulation in the area [21].

The hydrological characteristics of the region are also a matter of some interest. Along the equator from 140°E to the date line, a band of minimum evaporation coincides approximately with a region of light winds, and evaporation gradually increases to the north and south, associated with enhanced southeasterly and northeasterly trade winds [25]. The distribution of rainfall is variable in space and over time (e.g., [26–28]). Annual mean distributions of rainfall typically reveal

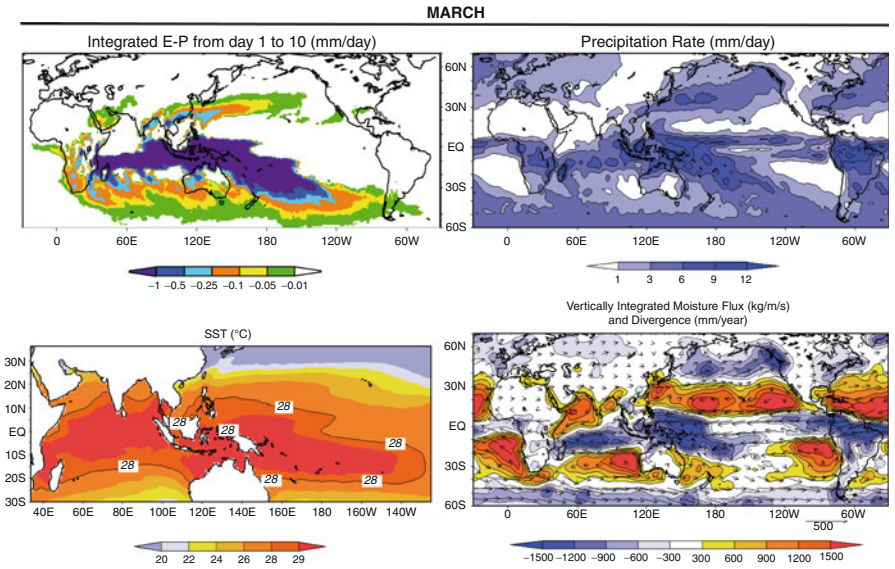

Fig. 13.6 Surface freshwater flux (E–P) integrated over a 10-day period for the month of March for the period 2000–2004 (*top left*), calculated by forward tracking from the IPWP source of moisture, indicated by the *black line* in the field of SST (*bottom left*). (*Top right*) precipitation rate and (*bottom right*) vertically integrated moisture flux (VIMF) and its divergence. Only negative values of (E–P) are shown, indicating where there is a net loss of moisture. Units of (E–P) and precipitation rate are mm day^{-1}, of SST are ºC, of *vectors* of moisture flux are kg m^{-1} s^{-1}, and of *contours* of divergence of moisture are mm year^{-1}

an east–west Inter Tropical Convergence Zone (ITCZ) across the Pacific and a band that extends southeastward from the warm pool into the Southern Hemisphere along the South Pacific convergence zone (SPCZ) (e.g., [29]) (Figs. 13.6 and 13.7). In addition, convection varies considerably over time in the western Pacific, which includes interannual, annual, seasonal, and intraseasonal oscillations (e.g., [30]).

Although less intense, the IPWP may also act as a source of moisture by providing humidity evaporated locally to remote regions via atmospheric circulation throughout its annual cycle. In March (Fig. 13.6), the IPWP (shown by the 28°C isotherm in SST) is located between 15°N and 25°S. The negative values of surface freshwater flux (E–P) that are obtained along the 10-day trajectories of the air parcels that emanate from the IPWP (selected using a Lagrangian approach) indicate that the moisture transported from this source may contribute to precipitation in remote regions, such as the Equatorial Atlantic and Southern Africa, apart from the contribution to the warm pool area itself and to the Subtropical Indian and Pacific oceans. In September (Fig. 13.7), the IPWP is displaced to the north, to cover the area between 30°N and 15°S. The net loss of moisture of the air parcels from the IPWP is high over the warm pool and Pacific ITCZ, associated with a strong convergence of tropospheric vertically integrated moisture flux (VIMF) that is observed over the region. The contribution of moisture from the IPWP is

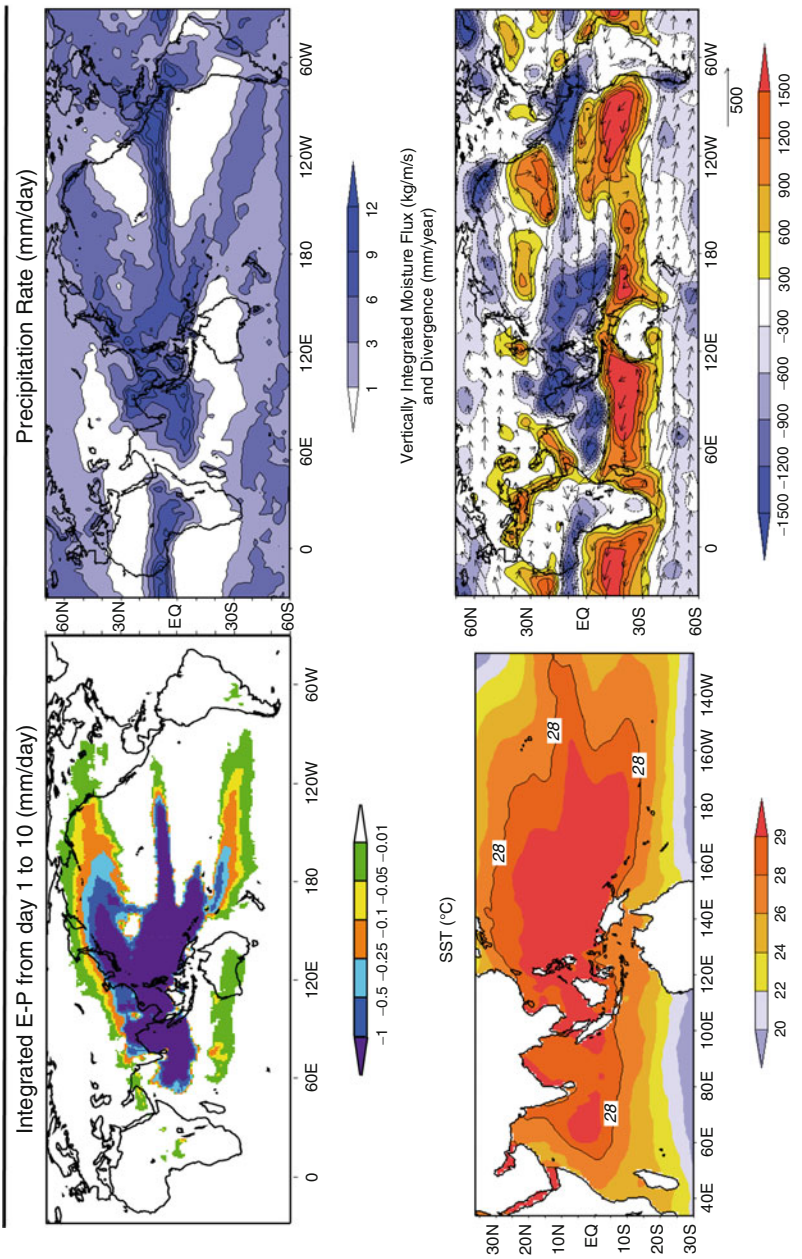

Fig. 13.7 As Fig. 13.6, for September

predominantly toward the subtropical northern Pacific Ocean during September, and even reaches East Asia and North America. However, the transport of moisture from the IPWP toward the Southern Hemisphere during September is less than it is in March.

Another region of high SSTs is also noteworthy. The tropical Western Hemisphere warm pool (WHWP) may be considered to be the second largest tropical warm pool on Earth, after the IPWP [31] (Figs. 13.3 and 13.4). In this case, the compromised threshold in their horizontal characterization extends is the 28.5°C isotherm. So, the WHWP extends over the eastern North Pacific and the west of Central America, the Intra-Americas Sea (i.e., the Gulf of Mexico and the Caribbean), as well as the western tropical North Atlantic [32]. This threshold reflects a temperature that has a significant impact on tropical convection (e.g., [33]), and on the depth of the isotherm of this temperature, which is closest to the average depth of the mixed layer in the WHWP. Differently from the IPWP, the WHWP usually disappears at the start of the boreal winter, but surface heat fluxes warm the pool throughout the spring, which leads to a maximum SST, and a maximum extent of the WHWP, in late summer/early autumn. Apart from the clear seasonal cycle, the interannual fluctuations of area and intensity are significant because the anomalies of the WHWP (in terms of SST and extent) occur at high temperatures at which small changes can have a pronounced effect on the tropical convection [34].

The characteristics of the Pacific side of the WHWP can be related directly to the variability of the ENSO, while the Atlantic side of the warm pool (Atlantic warm pool, AWP) may be considered to be a potential means of predicting summer rainfall in the United States, Mexico, the Caribbean, and Central America, including the large-scale meteorological conditions related to Atlantic hurricanes [35]. The WHWP provides a greater contribution of moisture to North America from June onward, when warmer waters may be observed over the AWP and the transport of moisture may be increased by the Great Plains low-level jet (GPLLJ) [35–38]. During the Boreal Summer, the contribution from the WHWP extends toward western Europe, probably as a result of the transport of moisture by the warm conveyor belts [38].

By using the same Lagrangian approach as mentioned earlier, it is possible to identify the role of the WHWP in providing moisture to the atmosphere throughout its annual cycle, as shown in Figs. 13.8 and 13.9. A comparison with the results presented for the IPWP (Figs. 13.6 and 13.7) may reveal the relative importance of the largest warm pools to global precipitation. In May (Fig. 13.8), a warm pool (isotherm of 28.5°C) extends over the eastern North Pacific, a phenomenon that characterizes the onset of the WHWP [32]. The negative values of (E–P) indicate that the WHWP contributes locally to moisture in the ITCZ in the Pacific, and that some moisture is transported toward North America in an anticyclonic flow centered over the Gulf of Mexico. These results are associated dynamically with the convergence of the VIMF over the Pacific ITCZ, as well as with the transport of moisture from the WHWP toward North America, possibly via the GPLLJ [38]. In September (Fig. 13.9), although the size of the warm pool in the eastern North

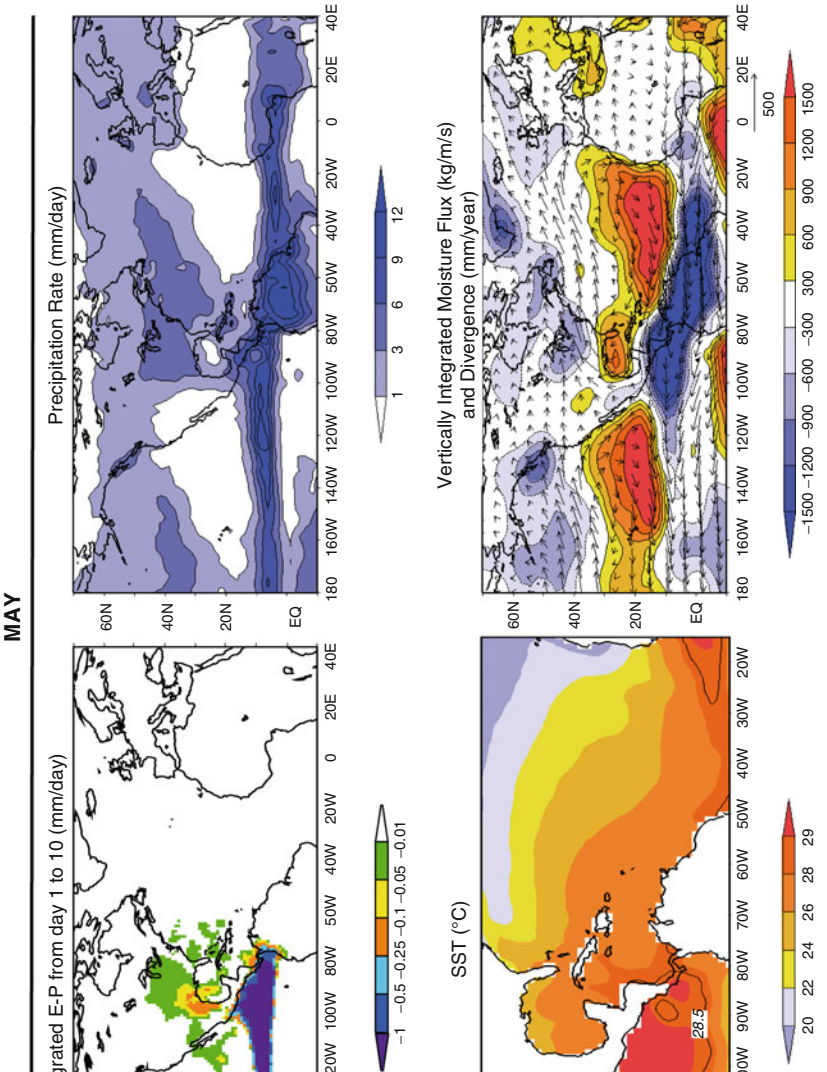

Fig. 13.8 As Fig. 13.8, but considering WHWP as source of moisture during May (From Drumond et al. [38])

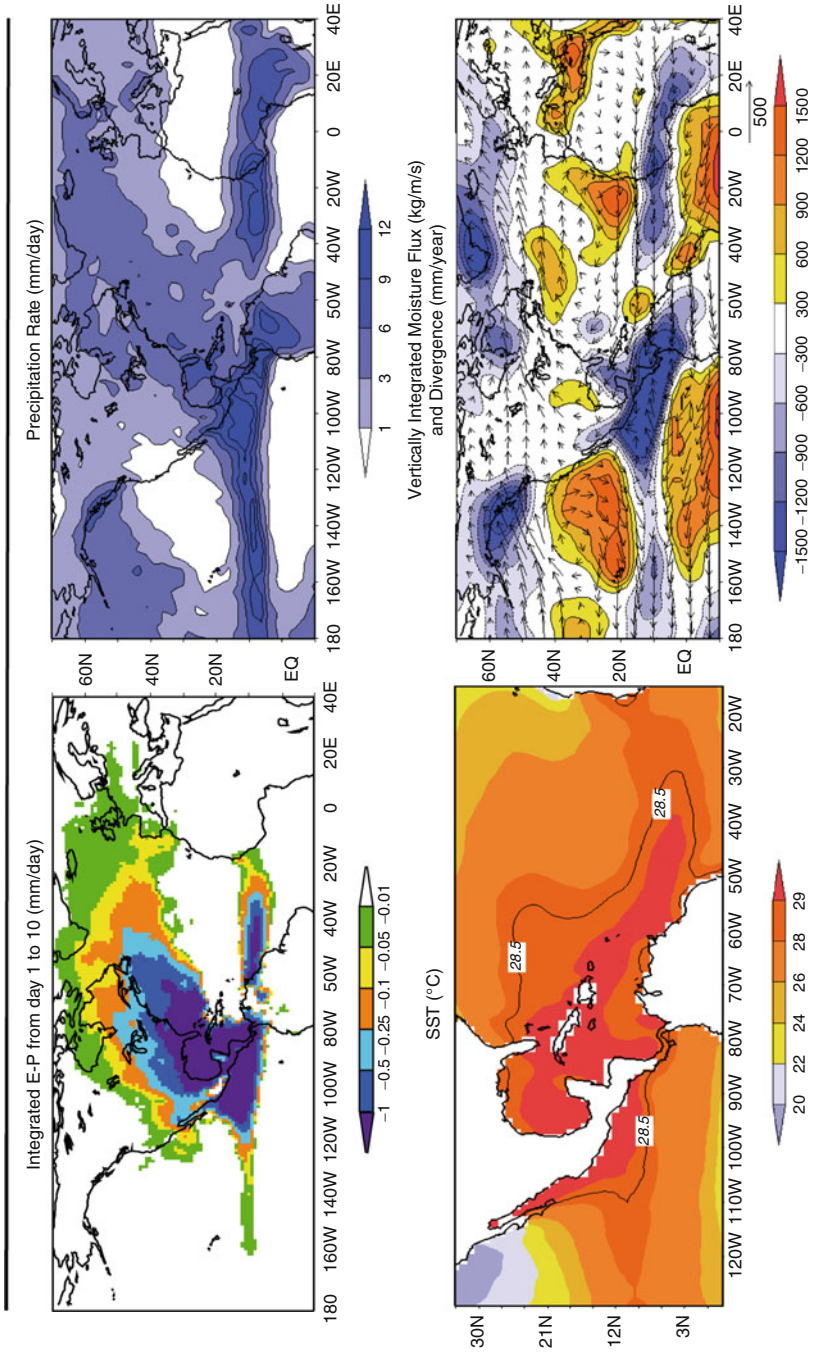

Fig. 13.9 As Fig. 13.1, but considering the WHWP as source of moisture during September (From Drumond et al. [38])

Pacific is reduced, the spatial expansion of the 28.5°C isotherm over the Intra-America Seas is at a maximum [32]. The values of (E–P) indicate a rather lower contribution of moisture to the precipitation in the Pacific ITCZ and a higher contribution to the Atlantic ITCZ, which is probably associated with the spatial expansion of the warm pool toward the equatorial Atlantic. A higher contribution of moisture to the Gulf of Mexico and to southeastern North America may also be observed in the precipitation, and is associated with the convergence of the VIMF over the area. The highest contribution of moisture to the Iberian Peninsula from the air masses that leave the WHWP occurs during September [38].

Oceanic Evaporation and Monsoonal Precipitation Regimes

Within the global distribution of precipitation, some regions are characterized by episodes of intense precipitation. Those regions, which are known to be affected by monsoonal circulations, have been studied extensively. The West African [39], the Asian [40], the Australian [41], and the American monsoonal systems [42] are now considered. To characterize these regions, Fig. 13.10 presents the seasonal patterns of precipitation and the vectors of low-level wind (925 mb) for both hemispheric summers.

The seasonal characteristics of the monsoons are well known, and the active phase of each can be distinguished easily. Despite both their intensity and seasonality, all have in common the large amount of moisture involved. The sources of

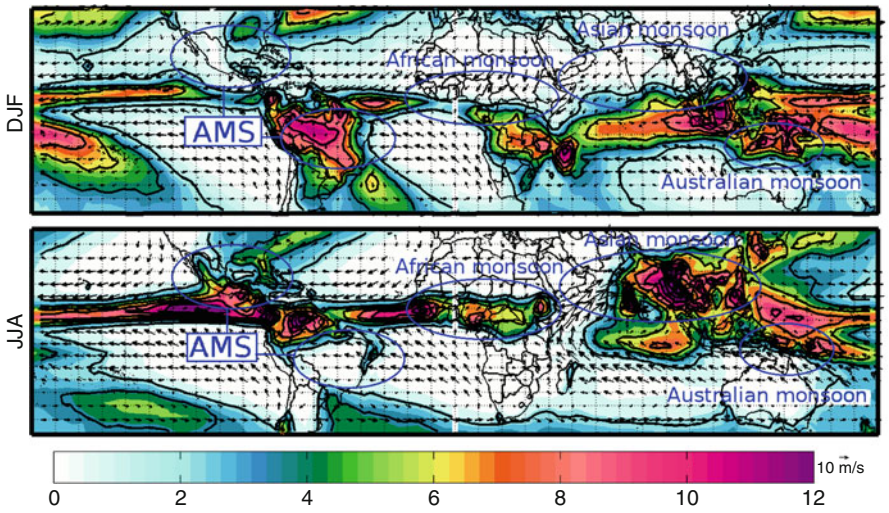

Fig. 13.10 GPCP precipitation (*shaded contours*) millimeter per day and wind speed at 925 mb (*vectors*), 1989–2008

moisture for these systems are fundamental to their understanding, and both continental and oceanic regions have been found to be important in this respect. As part of the American monsoon system (AMS), the North American monsoon (NAM) approximately accounts for at least 40% of the summer rainfall in western Mexico and the southern United States. Various authors have suggested that the dominant sources of monsoonal precipitation are the local continental evaporation and the transport of vapor from adjacent oceanic regions [43–45]. This is similar to the case for the Southern American counterpart of the AMS, namely, the SAM. Here, the intensification of precipitation during the boreal summer is related to the presence of strong low-level winds and an intense convergence of moisture related to the interaction between the Chaco Low and the trade winds from the northeast [46]. This supply of moisture from low levels corresponds to the transport of moisture due to the South American low-level jet (SALLJ) [47]. The transport of moisture is also relevant in the case of the West African monsoon, the activity of which is linked with the thermal contrast between the ocean and the surface of the land [48]. Cadet and Nnoli [49] proposed that the Gulf of Guinea and Central Africa act as sources of moisture in this case. In addition, the Mediterranean has been proposed to be a source of moisture for West Africa [50]. The African easterly jet (AEJ), which is associated with easterly fluxes of moisture, has been studied extensively in this regard [49], and is also thought to be a factor of inertial instability [51]. Furthermore, the Asian monsoon has been analyzed extensively in terms of its southwesterly and northeasterly flows. The dynamics of the Asian monsoon are of particular interest. A good description of the wind reversal circulations and of the system as a whole was provided by Wang [52]. Variations in the low-level jet (which include variations in a low-level jet over the Arabian Sea), and changes in the distribution of SSTs, are both associated with variations in precipitation, and are the basis of ocean–atmosphere coupling during the development of this monsoonal pattern. The importance of the moisture evaporated from the Arabian Sea and the South Indian Ocean has been determined and recognized, as have the contributions from the western Pacific Ocean [53]. The Australian monsoon, which is strongly connected with the Asian monsoon [54], has similar characteristics with respect to the Indian Ocean, in that this is an important source of moisture. For the purpose of summarizing this discussion, Fig. 13.11 shows the distribution of mean evaporation obtained from the OAFlux data [3], together with the vertically integrated moisture flux vectors of wind. The distribution seen during the active phase of the monsoons (see Fig. 13.10) shows the importance of evaporation from the surface of the oceans for the transport of moisture to regions influenced by monsoons.

The link between evaporation from the ocean and the transport of moisture has already been discussed. However, the importance of oceanic evaporation to monsoonal circulation is not constrained to the transport of moisture alone. In this case, evaporation from the ocean also plays a dynamic role, which has been found to be extremely important in some of the monsoons described above. This dynamic behavior may be considered in terms of the interaction between the process of convection and the water vapor itself [55]. The monsoons provide a clear example

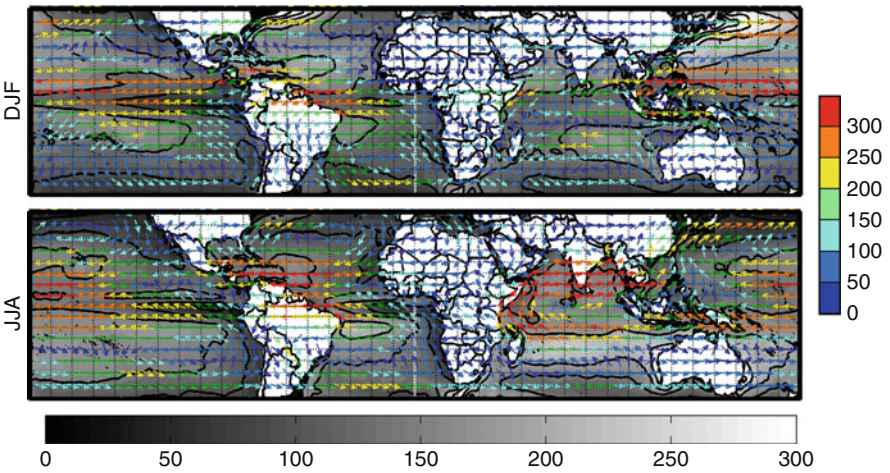

Fig. 13.11 OAFlux evaporation (*shaded contours*) in centimeter per year and ERA Interim Vertically Integrated water vapor flux (*vectors*), 1989–2008

of this interaction due to their rapid changes in wind speed, moisture content, and precipitation. As a result of this significant intraseasonal fluctuations may be observed. The relationship between SST and evaporation from the ocean has a number of different interpretations. The warming of the surface increases the rate of evaporation, leading to an increase in the amount of water vapor in the atmosphere. As the contribution to moisture transport increases, the cumulus convection is intensified [56]. This ocean–atmosphere coupling is extremely important, in the case of the West African monsoon the supply of moisture to the atmosphere is led by an intense convergence of moisture flux in the boundary layer [51] and a strong wind–evaporation–SST feedback mechanism [57]. A conceptual model of the moisture-advection feedback in the monsoons was recently developed [58]. In general terms, increases in SST speed up the rate of evaporation, and the ensuing decrease in evaporation from the surface of the ocean then contributes to an increase in SST. The relationship is quite complex, but the importance of evaporation in the development and maintenance of monsoon systems is beyond question.

Response of the Relationship Between Evaporation and Precipitation to the Forcing of the ENSO

The distribution of evaporation from the ocean has been described and it has been explained that this is related strongly to the distribution of SST, in order to show the connection between the atmosphere and the ocean, and the extreme importance of

these mechanisms for precipitation. It therefore follows that any change in SST affects the distribution and rate of evaporation, leading to changes in the distribution of precipitation. The SST is affected significantly by El Niño–Southern Oscillation (ENSO) events, which are the main mode of variability of the climate system [59]. The influence of the ENSO on the climate system that has received the most attention to date is that on precipitation. An increase in rainfall has been documented during cold ENSO phases (La Niña) while the warm phase (El Niño) is characterized by a reduction [60]. The regional variability in precipitation has been analyzed by several authors, who showed that the ENSO has a clear influence on the phenomenon (e.g., [61–64]). The variability of surface winds has also been observed to be related to the ENSO, in that the easterly flow of wind over the surface has been found to strengthen during warm ENSO events, while an equivalent weakening has been observed for the opposite phase. Evaporation also varies during ENSO events, as a result of variations in both SST and the surface wind fields [65], and the link between evaporation and the convergence of moisture flux [66] is reflected in the precipitation. Trenberth et al. [67] showed how, under the influence of the ENSO, warmer areas are associated with wetter regions, as suggested by the correspondence between the distributions of precipitation and surface temperature. These authors suggested that this finding may imply the importance of local evaporation for the distribution of precipitation during ENSO events. However, while it is clear that a relationship of this type applies over the land, the nature of the equivalent relationship over the ocean is less clear. Klein et al. [68] undertook a study in which they analyzed changes in SST and evaporation from the ocean by referring to the ENSO index. They determined the importance of evaporation from the ocean (and cloud cover) in leading the SST anomalies related to the ENSO. Furthermore, Yu and Mechoso [69] highlighted the dominance of wind-driven surface evaporation in the response of the surface heat flux to the ENSO in the tropics. A number of different authors have focused on the response of the monsoonal circulations to the ENSO and have discussed the importance of the changes to the distribution of evaporation from the oceans (e.g., [70]). The conditions produced by the ENSO have meant that the importance of evaporation from the ocean is still not fully understood, due to the complexity of the feedback mechanisms involved. These mechanisms are important not only near the surface, but also for the vertical atmospheric column. A good example of this is the "tropospheric temperature mechanism," in which it is proposed that the warming of the oceans' surface might be a response to the tropospheric warming observed in the tropics during El Niño, which causes a reduction in evaporation and therefore in precipitation [71]. The main response of the evaporation from the ocean to the ENSO is the increase of its coupling with the atmosphere through the strength of the feedback mechanisms involved [72, 73].

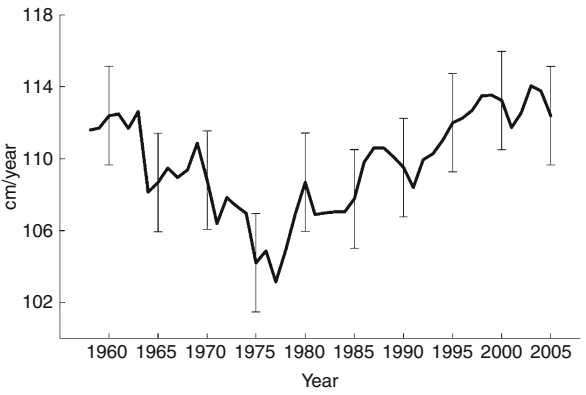

Fig. 13.12 Variations in annual mean evaporation averaged over the ice-free oceans. The error bars indicate 1 std dev from 1958 to 2005 mean (From Yu [2])

Future Research Directions

The scenarios associated with climate change suggest that the high sensitivity of saturation vapor pressure to temperature will result in an intensified hydrological cycle, with increased rates of evaporation and precipitation in a world that is warmer than it is today [5, 74]. Changing patterns of circulation will also lead to significant regional changes in the moisture budget. Furthermore, our best estimates of evaporation, such as those derived from the OAFlux data [7], have revealed strong increasing trends in evaporation from the oceans since 1978 (see Fig. 13.12), with the upward trend being most pronounced during the 1990s. The spatial distribution of these trends ([2]; not shown herein) show that while the increase in evaporation has occurred at a global scale, it has primarily been observed during the hemispheric winter accompanied by spatially coherent structures. Most important among these are the reduction in evaporation in the subtropics, the strong increase in evaporation along the paths of the global western boundary currents, and the increase over the Indo-Pacific warm pools.

In addition, climate change is likely to have effects beyond changes in evaporation. It is clear that changes in atmospheric circulation in a warming climate will result in changes in circulation between source and sink, which will redirect moisture in different ways. The general conclusion drawn by Gimeno et al. [75] was that "Those continental regions receiving moisture from only one or two source region(s) may be exposed more strongly to changes in the water cycle due to a changing climate than regions that draw on multiple moisture sources."

A further reason for understanding the source-to-sink relationships in the atmospheric water cycle in more detail lies in the role they play in extreme weather events. Convergence and transport from regions of high water vapor may trigger extreme rainfall and cause flooding [76], and the persistence of droughts could be due, in part, to the absence of transport of moisture to the continents [77, 78]. This coupling of the ocean–land–atmosphere system via the atmospheric water cycle needs to be understood in view of the potentially severe consequences for humanity that could result from changes to these relationships.

Acronyms

AEJ	African easterly jet.
AMS	American monsoon system.
AWP	Atlantic warm pool.
C-C	Clausius−Clapeyron equation.
Ce	Turbulent exchange coefficient controlled by the wind speed, the atmospheric stability, and the difference in temperature between the air and the sea.
dq	Difference between the specific humidity of saturation at the sea surface and the near-surface atmospheric specific humidity.
DJF	The months of December, January, and February.
E–P	Surface freshwater flux, defined to be the difference between the rates of evaporation (E) and precipitation (P), per unit area.
Evp	Rate of evaporation.
ENSO	El Niño–Southern Oscillation.
ERA-I	European Reanalysis Interim.
GPLLJ	Great Plains low-level jet.
GPCP	Global Precipitation Climatology Project.
JJA	The months of June, July, and August.
ITCZ	Inter Tropical Convergence Zone.
IPCC	Intergovernmental Panel on Climate Change.
IPWP	Indian–western Pacific warm pool.
NAM/NAMS	North American monsoon (system).
MERRA	Modern Era Retrospective-analysis for Research and Applications.
OAFlux	Objectively analyzed air–sea fluxes.
SALLJ	South American low-level jet.
SAM	South American monsoon.
SPCZ	South Pacific Convergence Zone.
SST	Sea surface temperature.
TCWV	Total column water vapor.
U	Near-surface wind.
VIMF	Vertically integrated moisture flux.
WAM	West African monsoon.
WHWP	Western Hemisphere warm pool.

Bibliography

Primary Literature

1. Quante M, Matthias V (2006) Water in the Earth's atmosphere. J Physique IV 139:37–61
2. Yu L (2007) Global variations in oceanic evaporation (1958–2005): the role of the changing wind speed. J Clim 20(21):5376–5390

3. Trenberth KE, Dai A, Rasmussen RM, Parsons DB (2003) The changing character of precipitation. Bull Am Meteor Soc 84:1205–1217. doi:10.1175/BAMS-84-9-1205
4. Bales RC (2003) Hydrology, overview. In: Anderson MG (ed) Encyclopedia of atmospheric sciences, 2nd edn. Elsevier, London, pp 968–973. doi:10.1016/j.physletb.2003.10.071
5. Intergovernmental Panel on Climate Change (IPCC) (2007) Summary for policymakers. In: Solomon S et al (eds) Climate change 2007: the physical science basis contribution of working group I to the fourth assessment report of the intergovernmental panel on climate change. Cambridge University Press, Cambridge, UK, pp 1–18
6. Liu WT, Katsaros K, Businger JA (1979) Bulk parameterization of air–sea exchanges of heat and water vapor including the molecular constraints at the interface. J Atmos Sci 36:1722–1735
7. Yu L, Weller RA (2007) Objectively analyzed air–sea heat fluxes for the global ice-free oceans (1981–2005). Bull Am Meteor Soc 88:527–539
8. Numaguti A (1999) Origin and recycling processes of precipitating water over the Eurasian continent: experiments using an atmospheric general circulation model. J Geophys Res 104:1957–1972
9. Trenberth KE, Fasullo JT, Mackaro J (2010) Atmospheric moisture transports from ocean to land and global energy flows in reanalyses. J Clim. doi:10.1175/2011JCLI4171.1
10. Newell RE, Zhu Y, Scott C (1992) Tropospheric rivers? A pilot study. Geophys Res Lett 19(24):2401–2404. doi:10.1029/92GL02916
11. Ralph FM, Neiman PJ, Rotunno R (2005) Dropsonde observations in low-leveljets over the northeastern Pacific Ocean from CALJET-1998 and PACJET-2001: mean vertical- profile and atmospheric- river characteristics. Monthly Weather Rev 133(4):889–910. doi:10.1175/MWR2896.1
12. Trenberth KE, Guillemot CJ (1998) Evaluation of the atmospheric moisture and hydrological cycle in the NCEP/NCAR reanalysis. Clim Dyn 14:213–231. doi:10.1007/s003820050219
13. Howarth D (1986) An analysis of the water vapor flux divergence field over the southern hemisphere. Ann Assoc Am Geograph 76(2):190–207
14. Peixoto JP, Oort AH (1992) Physics of climate. American Institute of Physics, New York, 520 pp
15. Howarth D (1983) Seasonal variations in the vertically integrated water vapor transport fields over the southern hemisphere. Monthly Weather Rev 111(6):1259–1272
16. van Loon H (1972) Pressure in the southern hemisphere. In: Newton CW (ed) Meteorology of the southern hemisphere. Meteorological monographs 35. American Meteorological Society, Boston, pp 59–86
17. Stohl A, James P (2004) A Lagrangian analysis of the atmospheric branch of the global water cycle. Part I: method description, validation, and demonstration for the August 2002 flooding in central Europe. J Hydrometeorol 5:656–678
18. Gimeno L, Drumond A, Nieto R, Trigo RM, Stohl A (2010) On the origin of continental precipitation. Geophys Res Lett 37:L13804. doi:10.1029/2010GL043712
19. Stohl A, James P (2005) A Lagrangian analysis of the atmospheric branch of the global water cycle. Part II: Earth's river catchments, ocean basins, and moisture transports between them. J Hydrometeorol 6:961–984. doi:10.1175/JHM470.1
20. Wyrtki K (1989) Some thoughts about the West Pacific warm pool. In: Western Pacific international meeting and workshop on TOGA COARE proceedings, Nouméa, New Caledonia, pp 99–109
21. Webster PJ, Lukas R (1992) TOGA COARE: the coupled ocean-atmosphere response experiment. Bull Am Meteor Soc 73:1377–1416
22. Lukas R (1990) Freshwater input to the western equatorial Pacific Ocean and air-sea interaction. In: Proceedings of the US-PRC international TOGA symposium on air-sea interaction in tropical Western Pacific. Ocean Press, Beijing, pp 305–327
23. Webster PJ (1983) The large scale structure of the tropical atmosphere. In: Hoskins BM, Pearce R (eds) General circulation of the atmosphere. Academic, London, pp 235–275

24. Cornejo-Garrido AG, Stone PH (1977) On the heat balance of the walker circulation. J Atmos Sci 34:1155–1162
25. Lin X, Johnson RH (1996) Heating, moistening and rainfall over the western pacific warm pool during TOGA COARE. J Atmos Sci 53(22):3367–3383
26. Taylor R (1973) An atlas of Pacific rainfall. Report HIG-73-9, Hawaii Institute of Geophysics, University of Hawaii at Manoa, Honolulu, Hawaii, 7 pp +13 plates
27. Legates DR, Wilmott CJ (1990) Mean seasonal and spatial variability in gauge-corrected, global precipitation. Int J Climatol 10:111–127
28. Spencer RW (1993) Global oceanic precipitation from the MSU during 1979-91 and comparisons to other climatologies. J Clim 6:1301–1326
29. Kiladis GN, von Storch H, van Loon H (1989) Origin of the South Pacific convergence zone. J Clim 2:1185–1195
30. Madden RA, Julian PR (1971) Detection of a 40-50 oscillation in the zonal wind in the tropical Pacific. J Atmos Sci 28:702–708
31. Weisberg RH (1996) On the evolution of SST over the PACS region. In: Abstracts of 76th AMS annual meeting. American Meteorology Society, Atlanta, 378 pp
32. Wang C, Enfield DB (2001) The tropical western hemisphere warm pool. Geophys Res Lett 28:1635–1638
33. Graham NE, Barnett TP (1987) Sea surface temperature, surface wind divergence, and convection over tropical oceans. Science 238:657–659
34. Wang C (2002) Atlantic climatic variability and its associated atmospheric circulation cells. J Clim 15:1516–1536
35. Wang C, Enfield DB, Lee SK, Landsea CW (2006) Influences of the Atlantic warm pool on western hemisphere summer rainfall and Atlantic hurricanes. J Clim 19:3011–3028. doi:10.1175/JCLI3770.1
36. Ruiz-Barradas A, Nigam S (2005) Warm season rainfall variability over the U. S. Great Plains in observations, NCEP and ERA-40 reanalyses, and NCAR and NASA atmospheric model simulations. J Clim 18:1808–1830. doi:10.1175/JCLI3343.1
37. Wang C, Lee SK, Enfield DB (2008) Climate response to anomalously large and small Atlantic warm pools during the summer. J Clim 21:2437–2450. doi:10.1175/2007JCLI2029.1
38. Drumond A, Nieto R, Gimeno L (2011) On the contribution of the tropical western hemisphere warm pool source of moisture to the northern hemisphere precipitation through a Lagrangian approach. J Geophys Res 116:D00Q04. doi:10.1029/2010JD015397
39. Janicot S, Harzallah A, Fontaine B, Moron V (1998) West African monsoon dynamics and eastern equatorial Atlantic and Pacific SST anomalies (1970–88). J Clim 11:1874–1882
40. Lau KM, Kim KM, Yang S (2000) Dynamical and boundary forcing characteristics of regional components of the Asian summer monsoon. J Clim 13:2461–2482. doi:10.1175/1520-0442
41. Taschetto AS, Haarsma RJ, Gupta AS, Ummenhofer CC, Hillk KJ, England MH (2010) Australian monsoon variability driven by a Gill–Matsuno-type response to central West Pacific warming. J Clim 23(18):4717–4736. doi:10.1175/2010JCLI3474.1
42. Vera C, Higgins W, Amador J, Ambrizzi T, Garreaud R, Gochis D, Gutzler D, Lettenmaier D, Marengo J, Mechoso CR, Nogues-Paegle J, Silva-Dias PL, Zhang C (2006) Toward a unified view of the American monsoon systems. J Clim 19:4977–5000
43. Higgins RW, Yao Y, Wang XL (1997) Influence of the North American monsoon system on the U.S. summer precipitation regime. J Clim 10:2600–2622. doi:10.1175/1520-0442(1997)010
44. Castro CL, McKee TB, Pielke RA (2000) The climatology and interannual variability of the North American monsoon as revealed by the NCEP/NCAR reanalysis. Preprints, 11th symposium on global change studies, Long Beach. Am Meteor Soc 2000:168–171
45. Dominguez F, Praveen K, Vivoni ER (2008) Precipitation recycling variability and ecoclimatological stability—a study using NARR data. Part II: North American monsoon region. J Clim 21:5187–5203. doi:10.1175/2008JCLI1760.1
46. Lenters JD, Cook KH (1999) Summertime precipitation variability in South America: role of the large-scale circulation. Monthly Weather Rev 127:409–431

47. Falvey M, Garreaud R (2005) Moisture variability over the SouthAmerican Altiplano during the SALLJEX observing season. J Geophys Res 110:D22105. doi:10.1029/2005JD006152
48. Thorncroft CD, Nguyen H, Zhang C, Peyrillé P (2011) Annual cycle of the West African monsoon: regional circulations and associated water vapour transport. Quart J Roy Meteor Soc 137:129–147. doi:10.1002/qj.728
49. Cadet DL, Nnoli NO (1987) Water vapour transport over Africa and the Atlantic Ocean during summer 1979. Quart J Roy Meteor 113:581–602
50. Fontaine B, Roucou P, Trzaska S (2003) Atmospheric water cycle and moisture fluxes in the West African monsoon: mean annual cycles and relationship using NCEP/NCAR reanalysis. Geophys Res Lett 30:1117. doi:10.1029/2002GL015834
51. Hagos SM, Cook KH (2007) Dynamics of the West African monsoon jump. J Clim 20:5264–5284
52. Wang B (2006) The Asian monsoon. Springer/Praxis, New York
53. Lim YK, Kim KY, Lee HS (2002) Temporal and spatial evolution of the Asian Summer monsoon in the seasonal cycle of synoptic fields. J Clim 15:3630–3644. doi:10.1175/1520-0442(2002)
54. Gu D, Li T, Ji X, Zheng B (2010) On the phase relations between the Western North Pacific, Indian, and Australian Monsoons. J Clim 23(21):5572–5589. doi:10.1175/2010JCLI2761.1
55. Sherwood SC, Roca R, Weckwerth TM, Andronova NG (2010) Tropospheric water vapor, convection, and climate. Rev Geophys 48:RG2001. doi:10.1029/2009RG000301
56. Kuo HL (1965) On the formation and intensification of tropic cyclones through latent heat release by cumulus convection. J Atmos Sci 22:40–63
57. Xie SP, Philander SG (1994) A coupled ocean-atmosphere model of relevance to the ITCZ in the eastern Pacific. Tellus 46A:340–350
58. Schewe J, Levermann A, Cheng H (2011) A critical humidity threshold for monsoon transitions. Clim Past Discuss 7:1737–1765. doi:10.5194/cpd-7-1737-2011
59. Trenberth KE, Stepaniak DP (2001) Indices of El Nino evolution. J Clim 14:1697–1701
60. Dai A, Wigley TML (2000) Global patterns of ENSO-induced precipitation. Geophys Res Lett 27:1283–1286
61. Ropelewski CF, Halpert MS (1987) Global and regional scale precipitation patterns associated with the El Niño/Southern oscillation. Monthly Weather Rev 115:1606–1626
62. Webster PJ, Yang S (1992) Monsoon and ENSO: selectively interactive systems. Quart J Roy Meteor Soc 118:877–926
63. Giannini A, Kushnir Y, Cane MA (2000) Interannual variability of caribbean rainfall, ENSO, and the Atlantic Ocean. J Clim 13:297–311
64. Lau NC, Nath MJ (2000) Impact of ENSO on the variability of the Asian-Australian monsoons as simulated in GCM experiments. J Clim 13:4287–4309
65. Ueki I (2011) Evidence of wind-evaporation-sea surface temperature (WES) feedback in the western Pacific warm pool during the mature phase of the 1997-98 El Niño. Geophys Res Lett 38:L11603. doi:10.1029/2011GL047179
66. Chikamoto Y, Tanimoto Y (2005) Role of specific humidity anomalies in Caribbean SST response to ENSO. J Meteor Soc Jpn 83:959–975
67. Trenberth KE, Caron JM, Stepaniak DP, Worley S (2002) Evolution of El Nino Southern oscillation and global atmospheric surface temperatures. J Geophys Res 107(D8):4065. doi:10.1029/2000JD000298
68. Klein SA, Soden BJ, Lau NC (1999) Remote sea surface variations during ENSO: evidence for a tropical atmospheric bridge. J Clim 12:917–932
69. Yu JY, Mechoso CR (2001) A coupled atmosphere-ocean GCM study of the ENSO cycle. J Clim 14:2329–2350
70. Chou C, Neelin JD, Su H (2001) Ocean-atmosphere-land feedbacks in an idealized monsoon. Quart J Roy Meteor Soc 127:1869–1891
71. Chiang JCH, Sobel AH (2002) Tropical tropospheric temperature variations caused by ENSO and their influence on the remote tropical climate. J Clim 15:2616–2631

72. Chiang JCH, Lintner BR (2005) Mechanisms of remote tropical surface warming during El Niño. J Clim 18:4130–4149
73. Lintner BR, Chiang JCH (2007) Adjustment of the remote tropical climate to El Niño conditions. J Clim 20:2544–2557
74. Held IM, Soden BJ (2006) Robust responses of the hydrological cycle to global warming. J Clim 19(21):5686–5699. doi:10.1175/JCLI3990.1
75. Gimeno L, Nieto R, Drumond A, Durán-Quesada AM, Stohl A, Sodemann H, Trigo RM (2011) A close look at oceanic sources of continental precipitation. Eos Trans Am Geophys Union 92(23):193–194. doi:10.1029/2011EO230001
76. Stohl A, Forster C, Sodemann H (2008) Remote sources of water vapor forming precipitation on the Norwegian west coast at 60°N: a tale of hurricanes and an atmospheric river. J Geophys Res 113:D05102. doi:10.1029/2007JD009006
77. Seneviratne SI, Lüthi D, Litschi M, Schär C (2006) Land-atmosphere coupling and climate change in Europe. Nature 443:205–209. doi:10.1038/nature05095
78. Hoerling M, Kumar A (2003) The perfect ocean for drought. Science 299(5607):691–694. doi:10.1126/science.1079053

Books and Reviews

Gleick PH (1989) Climate change, hydrology, and water resources. Rev Geophys 27(3):329–344
Huntington TG (2006) Evidence for intensification of the global water cycle: review and synthesis. J Hydrol 319:83–95
Liu WT (1993) Evaporation from the ocean. In: Gurney RJ, Foster JL, Parkinson CL (eds) Atlas of satellite observations related to global change. Cambridge University Press, Cambridge, pp 265–278
Li T, Wang B (2005) A review on the western North Pacific monsoon: synoptic-to-interannual variabilities. Terrest Atmos Oceanic Sci 16:285–314
Schott FA, Xie SP, McCreary JP (2009) Indian Ocean circulation and climate variability. Rev Geophys 47: RG1002. doi:10.1029/2007RG000245
Trenberth KE, Caron JM, Stepaniak DP (2001) The atmospheric energy budget and implications for surface fluxes and ocean heat transports. Clim Dyn 17:259–276

Chapter 14
Ocean Observatories and Information: Building a Global Ocean Observing Network

O. Schofield, S.M. Glenn, M.A. Moline, M. Oliver, A. Irwin, Y. Chao, and M. Arrott

Glossary

Ocean observatory	A collection of platforms that collect data over a range of spatial and temporal scales.

This chapter was originally published as part of the Encyclopedia of Sustainability Science and Technology edited by Robert A. Meyers. DOI:10.1007/978-1-4419-0851-3

O. Schofield (✉) • S.M. Glenn
Coastal Ocean Observation Lab, Institute of Marine and Coastal Sciences, School of Environmental and Biological Sciences, Rutgers University, New Brunswick, NJ 08901, USA
e-mail: Oscar@marine.rutgers.edu

M.A. Moline
Center for Marine and Coastal Sciences, California Polytechnic State University, San Luis Obispo, CA 93407, USA

M. Oliver
School of Marine Science and Policy, College of Earth, Ocean and Environment, University of Delaware, 700 Pilottown Rd., Lewes, DE 19958, USA

A. Irwin
Mount Allison University, Sackville, NB E4L 1A7, Canada

Y. Chao
Jet Propulsion Laboratory, 4800 Oak Grove Drive, Pasadena, CA 91109, USA

M. Arrott
Scripps Institution of Oceanography & Calit2, University of California at San Diego, La Jolla, CA 92093, USA

J. Orcutt (ed.), *Earth System Monitoring: Selected Entries from the Encyclopedia of Sustainability Science and Technology*, DOI 10.1007/978-1-4614-5684-1_14,

Definition of the Subject and Its Importance

Ocean observatories are collections of networks of sensors that are deployed to sample the ocean physics, chemistry, and biology. The goal of these networks is to overcome chronic undersampling of the oceans by providing sustained measurements in space and time. The data collected by these networks are used to address a range of basic and applied research questions, hindered by a lack of data. The ocean observatories represent collections of platforms capable of collecting data over a range of scales. The platforms include ships, satellites, radars, and a range of Lagrangian systems. Data from the individual platforms are aggregated by sophisticated cyberinfrastructure software systems, which when combined with global communications allow for two-way communication between the shoreside personnel and the networks that can be deployed anywhere in the world. This two-way communication allows the networks to be adaptively configured to improve sampling of specific processes. The maturation of these systems comes at a fortuitous time as the oceans are increasingly showing evidence of changes in the physics, chemistry, and biology over the last few decades. Understanding those changes will require the data collected by the ocean observatories.

Introduction

The Need for a Global Ocean Observing Network

The oceans cover the majority of Earth's surface, and despite centuries of human exploration, the oceans remain relatively unexplored. Oceanographers have historically collected data on the ocean and the seafloor from ships during cruises of limited duration. This expeditionary research approach has resulted in major advances that span understanding global ocean circulation, the energy associated with mesoscale circulation [1–4], plate tectonics (cf. [5]), global ocean productivity [6–8], and climate-ocean coupling [9–11]. These and many other successes have expanded our view of the role of ocean processes on Earth, and have demonstrated a need for sustained sampling spanning temporal and spatial scales that are not effectively carried out using ships. Filling these informational gaps will require the oceanographic community to develop new modes of sampling the oceans. Developing these new approaches is urgent, as data collected over the last few decades show that in many regions of the ocean the physics, chemistry, and biological properties are exhibiting significant change.

The observed changes in the oceans over the last few decades span from local scales (kilometers) to global effects operating over a wide range of spatial and temporal scales (Fig. 14.1). These changes reflect both natural cycles and increasingly reflect human activity, which now plays a significant role in structuring the

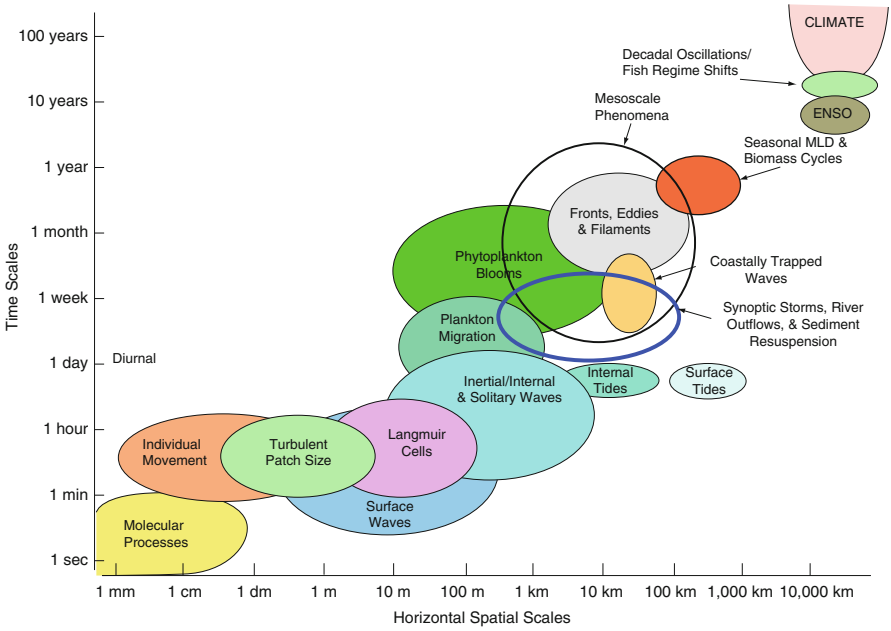

Fig. 14.1 A stommel diagram showing the range of spatial and temporal scales over which ocean processes operate. The figure was constructed by Tommy Dickey and is published with his permission

world's oceans. Local changes include alterations in circulation, increased introduction of point source concentrations of macro- and micronutrients, transport of pollutants to the sea, the introduction of invasive species, associated pressures of aquaculture efforts, and altered food web dynamics due to the overexploitation of commercially valuable species. These local features are embedded within regional and global scale changes. These large-scale changes include altered physical (temperature, salinity, sea level height), chemical (oxygen, pH, nutrients), and biological properties (fishing out of top predators).

Quantitatively understanding the relative role of natural and anthropogenic forcing of the ocean is a paramount challenge for oceanography. The urgency will only increase as in the next 20 years as anthropogenic environmental impacts associated with humans are expected to increase. This reflects the growth human populations [12] with current projections predicting the human population will reach ten billion by 2040. This will be especially prominent at the coastlines, which are predicted to show the largest population increases [13]. This will require a thorough understanding of ocean processes, which will be used to improve human health and safety, promote economic vitality, and provide the tools for sustainable environmental stewardship. These needs will require an improved fundamental understanding of the oceans.

Given the need for a quantitative understanding of the oceans, the ocean science community is fortunate to be poised to take advantage of many technical advances. These advances include a diverse set of new platforms capable of carrying sensors for sustained periods of time and the maturation of cyberinfrastructure tools that can link distributed individual observing networks to form a "system of systems." These components will provide the foundation for an international global ocean observing network. In this entry, we will outline the developments and, where appropriate, provide specific examples of how the data will be used.

Design Considerations for Building an Ocean Observing Network

Ocean observing networks are designed to address a specific need, which is used to define the required sampling resolution in space and time. Defining the appropriate scales can be a difficult problem as many large-scale (thousands of kilometers), long period (annual-to-interannual) processes are determined by small-scale, short-period variations in atmospheric forcing, and small-scale, relatively short-lived, oceanic processes [14–18]. As highlighted by Munk [19], 95% of the oceanic kinetic energy is associated with mesoscale currents having time and space scales less than about 100 days and 100 km. Other forcing factors can operate over inertial or diurnal time scales [17]; therefore, a comprehensive understanding of the oceans will require nested sampling capable of resolving the feedbacks between processes operating over different scales. This generally requires a multiplatform strategy as each system samples a specific time and space domain (Fig. 14.2). Once the sampling requirements have been defined, it is possible to choose (1) the appropriate platforms, (2) the required measurements, (3) the data latency needs for a particular observatory, and (4) the funds available for construction. The costs generally increase with the flexibility of the system (Fig. 14.3). Increased power on a platform allows for greater flexibility in carrying a wider range of sensors.

As ocean infrastructure is expensive, most large infrastructure networks must often be able to address a range of basic research and applied science needs to justify the investment. Historically, basic and applied research efforts are often treated as separate enterprises; however, major issues confronting the ocean science communities reveal numerous commonalities that reflect the chronic undersampling of the oceans. Both applied and basic science require information on the physical hydrography, circulation, biological, and chemical properties; however, it is often the real-time availability of data that defines its utility for applied science where data are used to meet real-time needs such as weather forecasting, search and rescue, and national security. When available, however, real-time information has a great deal of utility as scientists use the information to optimize adaptive sampling techniques.

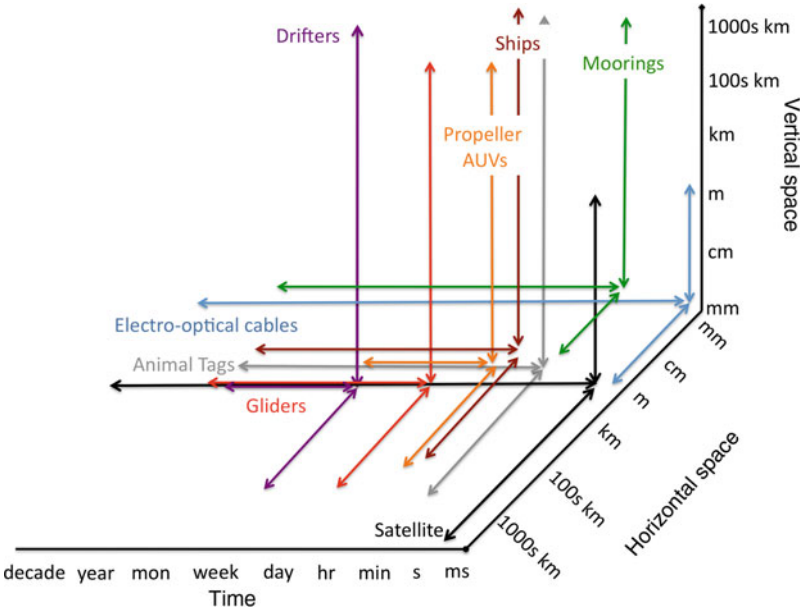

Fig. 14.2 The time and space sampling capabilities of different ocean platforms. The different colors represent different platforms

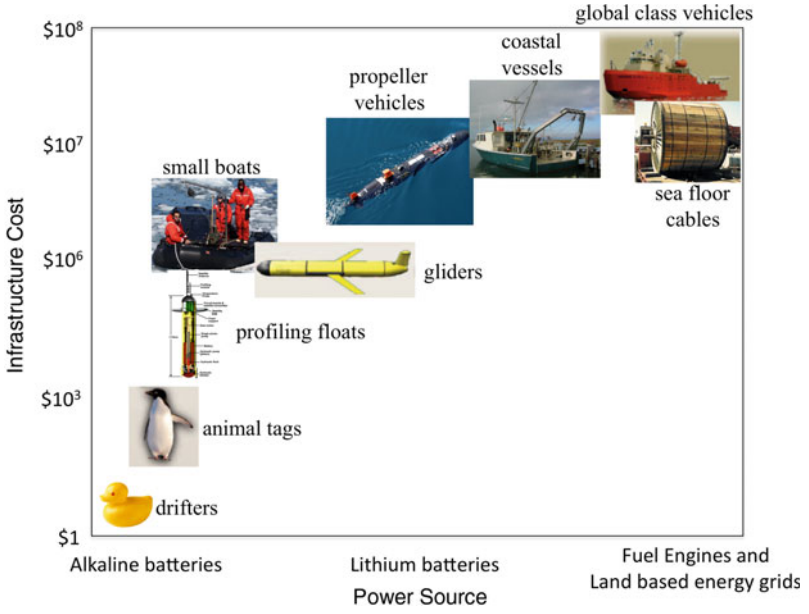

Fig. 14.3 The range of cost and power for a range of ocean sampling platforms

Platforms Available for Ocean Observing Networks

A range of platforms available for building ocean observing networks are described. Note that the list is not exhaustive, but reflects the major pieces of infrastructure widely used by the community today and form the observational backbone of the major ocean observing efforts. For this entry, we focus on physical systems that collect data about the ocean and do not discuss numerical models.

Ships. The primary tool for oceanographers for centuries has been ships and despite significant advances in new technologies (see below), ships will remain a central piece of infrastructure for the foreseeable future [18]. In the last decade, the range of ships available to the oceanographic community has grown with an expanding set of global class vessels being complemented with smaller, capable, coastal vessels. The increasing interdisciplinary needs have resulted in significant upgrades in the capabilities of the ships with improved capabilities in the dynamic positioning and station holding, multi-beam and side-scan sonar systems, and more complex sensors and instrumentation becoming routine tools when at sea.

Satellites. Satellites constitute the most important oceanographic technology innovation in modern times [19]. Satellite observations have resulted in numerous advances in our fundamental understanding of the oceans [20] by resolving both global features associated with the mesoscale circulation of physical and biological properties. It is the fundamental tool for understanding myriad ocean processes and land–air–sea interactions over decadal time scales. Satellite data are fundamental to weather and ocean state prediction. The data have revealed new phenomena over critical space and time scales that were previously inaccessible using only data from in situ observing systems. Physical parameters available from space-based sensors provide information on ocean surface temperature, wind speed and direction, sea surface height and topography, and sea ice distribution and thickness. Biogeochemical parameters are derived from ocean color radiometers (pigment concentration, phytoplankton functional groups, size distribution, particle concentration, colored dissolved organic material). A range of methods that include active scatterometry, microwave array spectrometers, microwave imagers, multi-beam altimetric lidars, altimeters, and advanced gravity missions collect these observations. The coverage provided by a satellite is dependent on its orbit. Currently most environmental satellites are polar-orbiting, covering the whole globe over a period of days. These global maps can be complemented by geostationary satellites that can map the same area of the ocean several times a day, allowing one to resolve the temporal changes such as tidal effects or river plumes. These geostationary satellites are particularly important when monitoring episodic events required for many applied efforts such as monitoring hurricanes and/or oil spills.

The significant time required and high cost of deploying satellites has focused efforts on expanding the utility of existing platforms. These approaches include the development of new algorithms. These new algorithms have focused on objectively

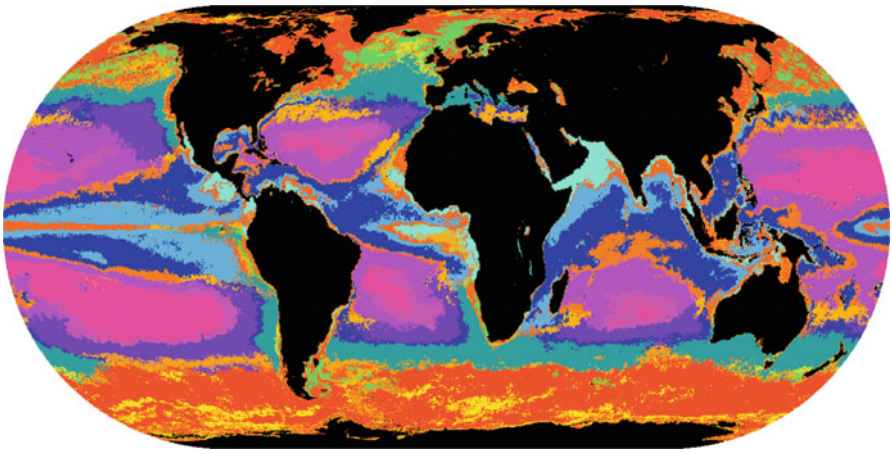

Fig. 14.4 A global map of the major ocean biomes as determined using an objective mapping algorithm [22]. The map was created by combining sea surface temperature maps with ocean color imagery, and provides a means to discriminate the major water masses by combining all available satellite remote sensing technologies. Each color represents a distinct water mass

defining water masses ([21, 22], Fig. 14.4), deriving biological rate processes [23, 24], estimating nutrient concentrations [25], and mapping ocean salinity [26–28]. Algorithms are also being developed to allow the satellites to adaptively sample the ocean. This approach has been demonstrated with the scientists re-tasking the satellite to spotlight a region [29]. As flexibility in networks increases, these approaches are likely to become more common.

High Frequency Radar. High frequency radar is a technology for measuring ocean surface current velocities over hundreds of square miles simultaneously (Fig. 14.5). The systems can provide data on approximately hourly time scales and can collect data out to about 125 miles (200 km) from shore (Fig. 14.4). The HF radar systems can resolve spatial scales of about 1–10 km, unaffected by clouds, fog, or precipitation. This technology uses low-power transmitters and small stationary antennas that are relatively simple to deploy. Each site measures the radial components of the ocean surface velocity directed toward or away from the site [30–32] and the estimated velocity components allow surface currents (upper meter of water column) to be estimated [33]. These systems are cost-effective and currently much of the coastal zone is now sampled using this technology.

HF radar provides a good example of a dual use technology. For example, HF Radar measures the movement of oceanic events like the winds in the atmosphere provide information about where and when weather systems occur (Fig. 14.5). The dynamic movements of the ocean and atmosphere are also used to determine where pollutants, man-made or natural, will travel. Modern weather now casts and forecasts generated by NOAA's National Weather Service depend on the thousands of critical wind measurements collected worldwide each hour, mostly from land

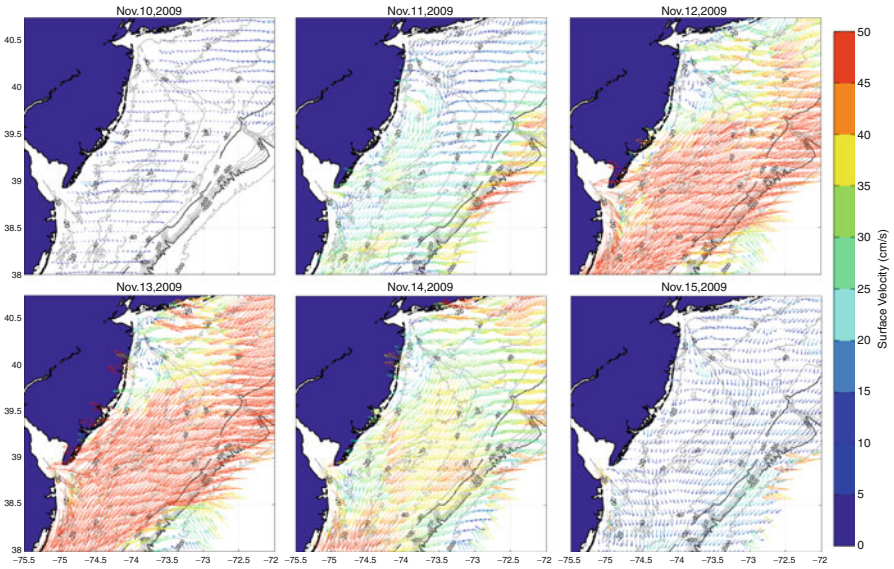

Fig. 14.5 The response of surface currents for the coastal waters offshore New Jersey (USA) due to the passage of a large coastal storm. The color of the surface current indicates the current velocity and the *arrows* indicate the direction of the current. The HF CODAR network was able to collect data throughout the storm when clouds interfered with remote sensing approaches and the violent waves would not allow for ship-based operations. Collecting data during such extreme events is of high importance to the ocean science community

and satellite-based sensors. In the coming decade, coastal managers will use HF radar data to measure the ocean current speed and direction to track plumes (rivers, pollution, oil), assist in coast guard search and rescue (SAR), assist in marine navigation, define shipping tracks and temporary anchorages offshore ports, and track the transport of harmful algal blooms. One specific example is the US Coast Guard, which currently ingests surface current data from high frequency radar sites into its SAR operations along the Mid-Atlantic coast, which has a mature HF radar network. It is estimated that if HF radar is deployed in all US coastal waters would save an additional 26–45 more lives annually and reduce the $30 M per year currently spent on rescue flights (http://ioos.gov/library/sarops_data_sources_uncert_nov2006.pdf).

Ocean Moorings. The modern ocean moorings grew out of the weather stations established in the 1940s. Since the 1960s modern buoys have enabled a wide range of studies addressing the ocean's role in climate, weather as well as providing insight into the biogeochemistry of the sea. Moorings provide the backbone to many of the global ocean networks studying ocean–atmosphere interactions and are the foundation for the global tsunami warning system network. They will continue to be a key element of ocean observing infrastructure that provides high frequency fixed location data to supplement the spatial data collected by ships, autonomous underwater vehicles, and satellite remote sensing by providing subsurface data.

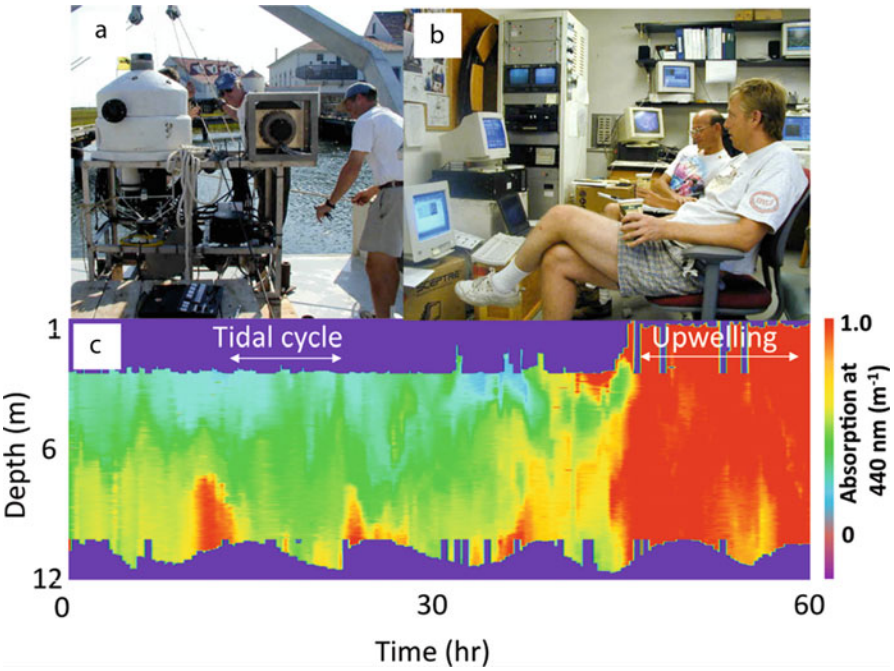

Fig. 14.6 Example of data collected by the Long term Ecosystem Observatory (LEO) which is located 5 km offshore the coast of New Jersey and is linked to shoreside laboratories via an electro-optical seafloor cable. (**a**) A profiling instrument node before being mounted to the LEO cable. (**b**) The shore side control center from where the profiler and instruments were controlled. The data was sent to shore in real time to scientists via the LEO cable. (**c**) Data collected during 60 h while continuously profiling the instrument package. The short time series represents over 600 vertical profiles. The data represents the absorption at 440 nm collected with a WetLabs absorption/attenuation meter. The high turbidity water (*red*) was associated with tidal outflows and with coastal upwelling

Seafloor Cables. Scientists often require high bandwidth and power for sustained periods of time. Seafloor electro-optic cables offer potential means for providing the sustained presence in the ocean. There have been two general strategies when deploying seafloor cables. Cables have been deployed off the east and west coasts of the United States and Canada, Hawaii, Japan, and Europe. These cables have successfully been used to study a wide range of topics which include seafloor seismicity [34, 35], tsunamis [36], seafloor dynamics [37], coastal upwelling (Fig. 14.6, [38]), ecosystem productivity [39], hydrological optics [40], ocean turbulence [41], sediment resuspension [42, 43], gas hydrates [44], marine boundary layer dynamics [45], bioluminescence [46, 47], and animal swimming behavior [48].

Drifters and Floats. Passive, autonomous, Lagrangian platforms have become an indispensable tool in creating surface and subsurface maps of ocean properties. These platforms are relatively inexpensive and thus allow thousands of these platforms to be deployed. Surface maps of ocean currents and ocean properties

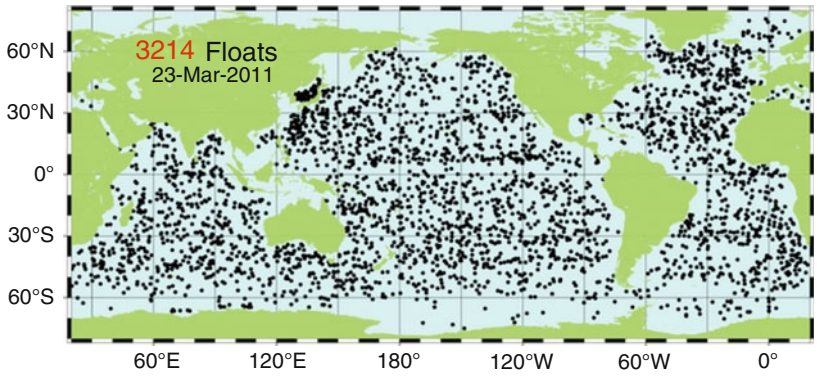

Fig. 14.7 The global distribution of ARGO profiling floats on March 23,2011. The floats are outfitted with sensors that measure temperature and salinity. A smaller number are outfitted with biogeochemical sensors [54]

(temperature) have been collected using surface drifters. Drifters have historically been a key tool for oceanography as evidenced by the important works of Benjamin Franklin [49] and Irving Langmuir [50]. Improved communications have allowed thousands of drifters to be deployed. The drifters have evolved to carry numerous sensors, which have allowed them to create global maps of surface circulation at a relatively low cost [51].

The first neutrally buoyant floats were designed to observe subsurface currents [52]. The subsurface floats were greatly enhanced in the early 1990s with communication capabilities [53] and now anchor the international ARGO program, which has over 3,000 floats deployed in the ocean (Fig. 14.7, http://www.argo.ucsd.edu/). The subsurface ARGO network has been a critical tool for oceanography [55] and to date has resulted in over 750 publications since 1998 (http://www.argo.ucsd.edu/Bibliography.html). Publications span from mapping global ocean hydrography, trended changes in ocean properties, and ocean biogeochemistry.

Gliders. Rudnick et al. [56] provided a detailed overview of glider systems for scientific uses. Gliders are a type of autonomous underwater vehicle that use small changes in buoyancy in conjunction with wings to convert vertical motion to horizontal motion, and thereby propel itself forward with very low-power consumption. These are similar in concept to profiling floats (see above) with the exception of the wings. Gliders follow a sawtooth path though the water, providing data on large temporal and spatial scales. They navigate with the help of periodic surface GPS fixes, pressure sensors, tilt sensors, and magnetic compasses. Using buoyancy-based propulsion, gliders have a significant range and duration, with missions lasting over half a year and over 3,500 km of range. There are currently three glider types [57–59] being used throughout the world's oceans (Fig. 14.8). Although the majority of gliders presently run on batteries, thermal-powered gliders, which take advantage of thermal gradients in the ocean, are being developed [59]. Gliders vary in the pressure, they are able to withstand but

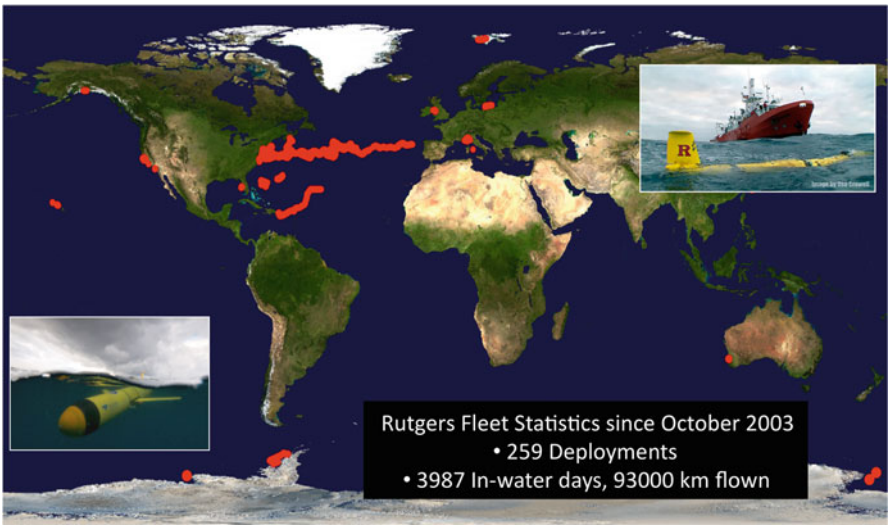

Fig. 14.8 Gliders are operated by individual laboratories and allow small groups to occupy a global presence at relatively low cost [29]. The figure shows the glider deployments conducted by Rutgers Coastal Ocean Observation Laboratory from October 2003 until February 2011. The missions represent almost 4,000 days at sea and the Rutgers glider fleet has flown 93,000 km underwater. Currently, there are over a dozen laboratories located throughout the world who maintain a similar sustained global glider presence at sea

taken together, and they effectively sample waters depths from 10 to 3,300 m. The duration of the glider mission is variable and depends on (1) the type of battery used, (2) the number of sensors the gliders carry, and (3) the water column depths in which the glider is operating. Because these vehicles are designed for duration, they have limited power for sensors. The standard measurements currently on gliders include temperature, salinity, chlorophyll fluorescence, optical backscatter, bottom depth, and occasionally acoustic Doppler velocity and backscatter. By examining displacement between surface fixes, the vertically averaged absolute velocity can also be determined. The utility of gliders have demonstrated their value in collecting high resolution spatial datasets [60–67].

Propeller-driven AUVs are powered by batteries or fuel cells and can operate in water as deep as 6,000 m. AUVs can navigate by various means; inside a net of acoustic beacons, by position relative to a surface reference ship, or when operating completely autonomously, the AUV will surface and take its own GPS fix. Like gliders, AUVs relay data and mission information to shore via satellite. Between position fixes and for precise maneuvering, inertial navigation systems are often available onboard the AUV to measure the acceleration of the vehicle and, combined with Doppler velocity technology, is used to measure rate of travel. A pressure sensor measures the vertical position. AUVs, unlike gliders, can move against most currents nominally at 3–5 knots, and, therefore, can systematically and synoptically survey a particular line,

area, and/or volume. This is particularly important for bottom surveys and operation near the coastline in areas hazardous to ships and small craft. The endurance of AUV systems depends on the size of the vehicle as well as the power consumption, but range from 6 to 40 h of operation under a single charge with ranges of 70–240 km over that period. The sensor payload is also dependent on the size of the vehicle (and battery capacity), with the standard array of sensors measuring, temperature, salinity, chlorophyll fluorescence, optical backscatter, bottom depth, and acoustic Doppler velocity and backscatter. Because of the additional power capacity of AUVs, numerous sensor suites have been integrated into AUVs and remain the primary autonomous platform for sensor development. Hundreds of different AUVs have been designed over the past 20 or so years. Blackwell et al. [68] provides an overview of the historical development of these vehicles.

Information Systems for Ocean Observatories

While the range of technologies available to oceanographers has been increasing over the last several decades, it is the availability of global communications and information technology that will allow these technologies to transform ocean sciences. Oceanographers have conducted experiments as either individuals or small groups within a single science focus at any given time; however, the broad scientific and civil demands for multidisciplinary and interdisciplinary research coupled with exponential growth in information technology are transforming oceanography. This history of working in small groups has resulted in the traditional data-centric cyberinfrastructure strategy, where typically a central data management system ingests data and serves them to users on a query basis. This approach is not sufficient to deal with the range of challenges that face ocean sciences.

Given this potential, the community is now dedicated to building the cyberinfrastructure that will be central to any global integrated ocean observing system. A modern cyberinfrastructure backbone will allow globally distributed scientists to operate as a community by aggregating data from individually deployed instruments for any experimental effort. If realized, this would allow anybody with access to the internet to utilize the global array of sensors to study any ocean process of interest.

Given the potential, ocean sciences are increasingly focused on building a system that will provide a comprehensive set of capabilities. Cyberinfrastructure systems must provide a comprehensive set of tools that include (1) end-to-end data preservation and access, (2) end-to-end, human-to-machine, and machine-to-machine control of how data are collected and analyzed, (3) direct, closed loop interaction of models with the data acquisition process, (4) virtual collaborations created on demand to drive data-model coupling and share ocean observatory resources (e.g., instruments, networks, computing, storage and workflows), (5) end-to-end preservation of the ocean observatory process and its outcomes, and (6) automation of the planning and prosecution of observational programs. Additionally the

cyberinfrastructure systems must provide the required background messaging, governance, and service frameworks that facilitate interaction in a shared environment, similar to the role of the operating system on a computer. Such a system would provide a suite of tools capable of serving both basic and applied science simultaneously.

The potential of an interactive social network for the ocean sciences is in its infancy and the community is in the process of development and is conducting pilot experiments. One such example is the NSF Ocean Observatory Initiative (OOI), which has focused significant effort on developing a sophisticated cyberinfrastructure, that will link ocean observatories, computation, modeling, storage, and network infrastructure into a coherent system-of-systems. The software is also developing a web-based social network enabled by real-time visualization and access to model outputs to allow for adaptive sampling science.

One such example was a field experiment conducted in 2009, that allowed a distributed community of scientists to assess how well the software could aggregate data from ships, autonomous underwater vehicles (AUVs), shore-based radars, and satellites and to make it available to ocean forecast models. Scientists used the model forecasts to guide future (next 24 h) glider missions which then were used to optimize data collection for model data assimilation, which demonstrated the feasibility of two-way interactivity between the sensor web and predictive models. The sensor web included the re-tasking of a satellite. The software allowed the distributed community to adaptively modify the in situ observation network throughout the experiment [29]. The net result was a science driven machine-to-machine interactive loop (Fig. 14.9). These machine networks will increasingly become standard tools for the ocean science community in the future.

As observatories consist of a series individual components that are linked to form a coherent sampling system, an often underemphasized, yet critical need is the ability to register to all components to a common time stamp. The time stamp functionality in the sensor network is necessary to compare the output of one sensor to another. This is not a trivial when sensors are dispersed geographically and the data from sensors need to be integrated with external datasets. The accuracy required is a function of the process being studied and the length of the time series to be collected. For example, seismic studies require time accuracy on the order of milliseconds, acoustic tomography of 1 μs and studies of phytoplankton growth rates require data on the time scale of hours. Additionally, avoiding drift for temporal time series will increasingly become critical as sustained time series become the norm for oceanography. Fortunately, the ability to register time accurately is increasingly improving. A dramatic example is the evolution of small low-power atomic clocks. Atomic clocks offer the frequency stability of one part in ten billion, which is equivalent to gaining or losing 1 s every 300 years. These technical developments are being powered by the evolution of Micro Electro Mechanical Systems (MEMS) chip technologies that can produce clocks with a volume of less than 0.1 cm^3 and consume power on the milli-watt scale. These advances will enable atomic clocks to be operated on

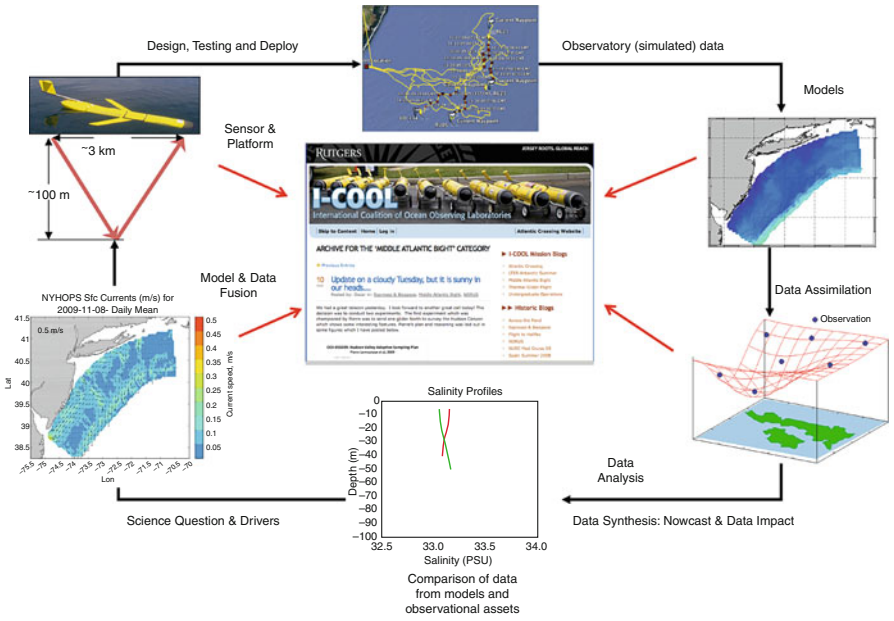

Fig. 14.9 The machine-to-machine data flow during the Ocean Observing Initiative's (OOI) Observation Simulation Experiment. A fleet of gliders were informed by model driven forecasts in order to optimize science sampling being conducted by a geographically distributed team of scientists. The observatory data was assimilated by an ensemble of numerical forecast models, which were used to optimize the glider sampling. Optimized glider data was also used to adjust the data collected by the Hyperion EO-1 satellite

batteries and could be integrated throughout the individual components of the ocean observatories.

The potential of cyberinfrastructure tools, such as described above, is dependent on the real-time availability of data; fortunately global communications have improved dramatically over the last few decades. In the early 1990s, the primary mode of communication from ship to shore was via satellite voice calls. This improved over the next decade as ship-based science was provided with limited email communication. Communications have continued to improve and now provide sufficient bandwidth to allow for video-transmission at hundreds of kilobits per second (http://hiseasnet.ucsd.edu/). These improvements are changing the type of science that ships conduct as real-time data allow scientists to adaptively sample the ocean. Additionally, the launch of low Earth orbit satellite communication systems have allowed for global communication and enabled rapidly evolving capabilities for communications to autonomous platforms. The communications have improved from one-way communications with data transmission limited to about 16,000 bits/day to global two-way communications at a rate of 2,400 bits/s.

Future Directions

The ocean science community will over the next decade construct a global ocean observing network by combining a diverse range of platforms. The multiplatform networks will allow scientists to sample over a wide range of time and space scales and the availability of real-time data transmission will allow for adaptive sampling. The development of a robust cyberinfrastructure will encourage distributed teams of scientists to conduct both applied and basic research. The research will allow the community to understand the present and future status of the oceans.

Bibliography

1. Crease J (1962) Velocity measurements in the deep water of the western North Atlantic. J Geophys Res 67:3173–3176
2. Ducet N, Le Traon PY, Reverdin G (2000) Global high-resolution mapping of ocean circulation from TOPEX/Poseidon and ERS-1 and -2. J Geophys Res 105:19477–19498
3. Schmitz WJ (1977) On the deep general circulation in the western North Atlantic. J Mar Res 35:21–28
4. Swallow JC (1971) The Aries current measurements in the western North Atlantic. Philos Trans R Soc Lond A270:451–460
5. Oreskes N (ed) (2003) Plate tectonics: an insider's history of the modern theory of the Earth. Westview Press Books, Boulder CO. 424 pp
6. Antoine D, Andre J, Morel A (1996) Oceanic pimary production 2. Estimation at global scale from satellite (coastal zone color scanner) chlorophyll. Global Biogeochem Cycles 10:57–69
7. Behrenfeld MJ, O'Malley RT, Siegel DA, McClain CR, Sarmiento JL, Feldman GC, Milligan AJ, Falkowski PG, Letelier RM, Boss ES (2006) Climate-driven trends in contemporary ocean productivity. Nature 444:752–755
8. Longhurst A, Sathyendranath S, Platt T, Caverhill C (1995) An estimate of global primary production in the ocean from satellite radiometer data. J Plankton Res 17:1245–1271
9. Graham NE (1994) Decadal-scale climate variability in the tropical and North Pacific during the 1970s and 1980s: observations and model. Climate Dynamics 10:135–162
10. Miller AJ, Schneider N (2000) Interdecadal climate regime dynamics in the North Pacific Ocean: theories, observation, and ecosystem, impacts. Prog Oceanogr 47:355–379
11. Rahmstorf S, Cazenave A, Church JA, Hansen JE, Keeling RF, Parker DE, Somerville RCJ (2007) Recent climate observations compared to projection. Science 316:709. doi:10.1126/science.1136843
12. De Souza R, Williamsn J, Meyerson FAB (2003) Critical links: population, health, and the environment. Popul Bull 58(3):3–43
13. Vitousek PM, Mooney HA, Lubchenco J, Melillo JM (1997) Human domination of Earth's ecosystems. Science 277:494–499. doi:10.1126/science.277.5325.494
14. Large WG, Holland WR, Evans JC (1991) Quasi-geostrophic ocean response to real wind forcing: the effects of temporal smoothing. Am Meteorol Soc 21(7):998–1017
15. Milliff RF, Large WG, Holland WR, McWilliams JC (1996) The general circulation responses of high-resolution North Atlantic Ocean models to synthetic scatterometer winds. J Phys Oceanogr 26:1747–1768
16. Milliff RF, Large WG, Morzel J, Danabasoglu G, Chin TM (1999) Ocean general circulation model sensitivity to forcing from scatterometer winds. J Geophys Res 104:11337–11358
17. Milliff RF, Morzel J (2001) The global distribution of the time-average wind stress curl from NSCAT. J Atmos Sci 58(2):109–131

18. National Research Council (2009) Science at sea: meeting future oceanographic goals with a Robust Academic Research Fleet. National Academy Press, Washington, DC
19. Munk W (2000) Oceanography before, and after, the advent of satellites. In: Halpern D (ed) Satellites oceanography and society. Elsevier Science, Amsterdam, pp 1–5
20. Halpern DA (2000) Satellites, oceanography and society. Elsevier Science, Amsterdam, 361 pp
21. Martin-Traykovski LV, Sosik HM (2003) Feature-based classification of optical water types in the Northwest Atlantic based on satellite ocean color data. J Geophys Res 108(C5):3150. doi:10.1029/2001JC001172
22. Oliver MJ, Kohut JT, Irwin AJ, Glenn SM, Schofield O, Moline MA, Bissett WP (2004) Bioinformatic approaches for objective detection of water masses. J Geophys Res 109:C07S04. doi:10.1029/2003JC002072
23. Beherenfeld MJ, Boss E, Siegel DA, Sutherland DM (2005) Carbon-based ocean productivity and phytoplankton physiology from space. Global Biogeochem Sci 19:GB1006. doi:10.1029/2004GB002299
24. Beherenfeld MJ, Falkowski PG (1997) A consumer's guide to phytoplankton primary productivity models. Limnol Oceanogr 42(7):1479–1491
25. Goes JI, Saino T, Oaku H, Jiang DL (1999) A method for estimation of sea surface nitrate concentrations from remotely sensed SST and chlorophyll a – a case study for the North Pacific Ocean using OCTS/ADEOS data. IEEE Trans Geosci Remote Sens 37:1633–1644
26. Swift CT, Mcintosh RE (1983) Considerations for microwave remote-sensing of ocean-surface salinity. IEEE Trans Geosci Remote Sens 21:480–491
27. Berger M, Camps A, Font J, Kerr Y, Miller J, Johannessen J, Boutin J, Drinkwater MR, Skou N, Floury N, Rast M, Rebhan H, Attema E (2002) Measuring ocean salinity with ESA's SMOS mission. ESA Bull 111:113f
28. Geiger EF, Grossi MD, Trembanis AC, Kohut JT, Oliver MJ (2011) Satellite-derived coastal ocean and estuarine salinity in the Mid-Atlantic. Cont Shelf Res (submitted)
29. Schofield O, Glenn S, Orcutt J, Arrott M, Brown W, Signell R, Moline MA, Chao Y, Chien S, Thompson D, Balasuriya A, Oliver M (2010) Automated sensor networks to advance ocean science. Trans Am Geophys Union 91(39):345–346. doi:10.1029/2010EO390001
30. Barrick DE (1972) First-order theory and analysis of mf/hf/vhf scatter from the sea. IEEE Trans Antennas Propag AP-20:2–10
31. Barrick DE, Evens MW, Weber BL (1977) Ocean surface currents mapped by radar. Science 198:138–144
32. Crombie DD (1955) Doppler spectrum of sea echo at 13.56 Mc/s. Nature 175:681–682
33. Stewart RH, Joy JW (1974) HF radio measurements of ocean surface currents. Deep Sea Res 21:1039–1049
34. Bromirski PD, Duennebier FK, Stephen RA (2005) Mid-ocean microseisms. Geochem Geophys Geosyst 6:Q04009. doi:10.1029/2004GC000768
35. Duennebier FK, Harris DW, Jolly J, Babinec J, Copson D, Stiffel K (2002) The Hawaii-2 observatory seismic system. IEEE J Oceanic Eng 27:212–217
36. Thomson DJ, Lanzerotti LJ, Maclennan CG, Medfor LV (1995) Ocean cable measurements of the tsunami signal from the 1992 Cape Mendocino earthquake. Pure Appl Geophys 144:427–440
37. Traykovski P, Hay A, Irish JD, Lynch JF (1999) Geometry, migration, and evolution of wave orbital ripples at LEO-15. J Geophys Res 104:1505–1524. doi:10.1029/1998JC900026
38. Schofield O, Bergmann T, Bissett WP, Grassle F, Haidvogel D, Kohut J, Moline M, Glenn S (2002) Linking regional coastal observatories to provide the foundation for a national ocean observation network. J Oceanic Eng 27(2):146–154
39. Grundle DS, Timothy DA, Varela DE (2009) Variations of phytoplankton productivity and biomass over an annual cycle in Saanich inlet, a British Columbia fjord. Cont Shelf Res 29:2257–2269. doi:10.1016/j.csr.2009.08.013

40. Oliver MW, Schofield O, Bergmann T, Glenn SM, Moline MA, Orrico C (2004) In-situ optically derived phytoplankton absorption properties in coastal waters and its utility for estimating primary productivity rates. J Geophys Res 109:C07S11. doi:10.1029/2002JC001627
41. Kunze E, Dower JF, Beveridge I, Dewey R, Bartlett KP (2006) Observations of biologically generated turbulence in a coastal inlet. Science 313:1168–1170. doi:10.1126/science.1129378
42. Agrawal YC (2005) The optical volume scattering function: temporal and vertical variability in the water column off the New Jersey coast. Limnol Oceanogr 50:1787–1794
43. Gargett A, Wells J, Tejada-Martinez AE, Grosch CE (2004) Langmuir supercells: a mechanism for sediment resuspension and transport in shallow seas. Science 356:1925–1928
44. Edwards RN, Schwalenberg K, Wiloughby EC, Mir R, Scholl C (2010) Marine controlled source electromagnetics and the assessment of seafloor gas hydrate. In: Riedel M, Willoughby EC, Chopra S (eds) Geophysical characterization of gas hydrates, SEG monograph. Society of Exploration Geophysicists, Tulsa
45. Sullivan PP, Edson JB, Hristov T, Williams JC (2008) Large-eddy simulations and observations of atmospheric marine boundary layers above nonequilibrium surface waves. J Atmos Sci 65:1225–1245
46. Moline MA, Oliver MJ, Mobley CD, Sundman L, Blackwell SM, Bergmann T, Bissett WP, Case J, Raymond EH, Schofield O (2007) Bioluminescence in a complex coastal environment I: temporal dynamics of night-time water-leaving radiance. J Geophys Res 112. doi:10.1029/2007JC004138
47. Oliver MJ, Moline M, Mobley C, Sundman LK, Schofield O (2007) Bioluminescence in a complex coastal environment: 2. Prediction of bioluminescent source depth from spectral water-leaving radiance. J Geophys Res. doi:10.1029/2007JC004136
48. Rousseau S, Kunze E, Dewey R, Bartlett K, Dower J (2010) On the efficiency of turbulence production by swimming marine organisms in the open ocean and coastal waters. J Phys Oceanogr 40(9):2107–2121
49. Franklin B (1785) Sundry marine observations. Trans Am Philos Soc 1(2):294–329
50. Langmuir I (1938) Surface motion of water induced by wind. Science 87:119–123
51. Niiler PP, Maximenko NA, McWilliams JC (2003) Dynamically balanced absolute sea level of the global ocean derived from near-surface velocity observations. Geophys Res Lett 30(22):2164. doi:10.1029/2003GL018628
52. Swallow JC (1955) A neutral-buoyancy float for measuring deep currents. Deep Sea Res 3:74–81
53. Davis RE, Webb DC, Regier LA, Dufour J (1992) The autonomous lagrangian circulation explorer (ALACE). J Atmos Oceanic Technol 9:264–285
54. Johnson KS, Berelson WM, Boss ES, Chase Z, Claustre H, Emerson SR, Gruber N, Kortzinger A, Perry MJ, Riser SC (2009) Observing biogeochemical cycles at global scales with profiling floats and gliders: prospects for a global array. Oceanography 22(3):216–225
55. Gould J, Roemmich D, Wijffels SH, Freeland H, Ignaszewsky M, Jianping X, Pouliquen S, Desaubies Y, Send U, Radhakrishand K, Takeuchi K, Kim K, Danchenkov M, Sutton P, King B, Owens B, Riser S (2004) Argo profiling floats bring new era of in situ ocean observations. EOS 85(19):190–191. doi:10.1126/science.1136843
56. Rudnick DL, Davis RE, Eriksen CC, Fratantoni DM, Perry MJ (2004) Underwater gliders for ocean research. Mar Technol Soc J 38:73–84
57. Eriksen CC, Osse TJ, Light RD, Wen T, Lehman TW, Sabin PL, Ballard JW, Chiodi AM (2001) Seaglider: a long-range autonomous underwater vehicle for oceanographic research. IEEE J Oceanic Eng 26:424–436
58. Sherman J, Davis RE, Owens WB, Valdes J (2001) The autonomous underwater glider "Spray". IEEE J Oceanic Eng 26:437–446
59. Webb DC, Simonetti PJ, Jones CP (2001) SLOCUM: an underwater glider propelled by environmental energy. IEEE J Oceanic Eng 26:447–452

60. Castelao R, Glenn S, Schofield O, Chant R, Wilkin J, Kohut J (2008) Seasonal evolution of hydrographic fields in the central Middle Atlantic Bight from glider observations. Geophys Res Lett 35:L03617. doi:10.1029/2007GL032335
61. Chao Y, Zhijin L, Farrara JD, Moline MA, Schofield O, Majumdar SJ (2008) Synergistic applications of autonomous underwater vehicles and regional ocean modeling system in coastal ocean forecasting. Limnol Oceanogr 53(6):2251–2263
62. Davis RE, Ohman MD, Rudnick DL, Sherman JT, Hodges B (2008) Glider surveillance of physics and biology in the southern California Current System. Limnol Oceanogr 53(5):2151–2168
63. Glenn SM, Jones C, Twardowski M, Bowers L, Kerfoot J, Webb D, Schofield O (2008) Studying resuspension processes in the Mid-Atlantic Bight using Webb slocum gliders. Limnol Oceanogr 53(6):2180–2196
64. Hjalmar H, Eriksen CC, Rhines PB (2007) Buoyant eddies entering the Labrador Sea observed with gliders and altimetry. J Phys Oceanogr 37:2838–2854
65. Hodges BA, Fratantoni DM (2009) A thin layer of phytoplankton observed in the Philippine Sea with a synthetic moored array of autonomous gliders. J Geophys Res 114:C10020. doi:10.1029/2009JC005317
66. Kahl A, Fraser W, Schofield O (2010) Autonomous gliders reveal water column features associated with Adélie penguin foraging. Integr Comp Biol. doi:10.1093/icb/icq098
67. Schofield O, Chant R, Cahill B, Castelao R, Gong D, Kahl A, Kohut J, Montes-Hugo M, Ramadurai R, Ramey P, Xu Y, Glenn SM (2008) Seasonal forcing of primary productivity on broad continental shelves. Oceanography 21(4):104–117
68. Blackwell SH, Moline MA, Schaffner A, Garrison T, Chang G (2008) Sub-kilometer length scales in coastal waters. Cont Shelf Res 28(2):215–226

Chapter 15
Oil Spill Remote Sensing

Mervin Fingas and Carl Brown

Glossary

Laser fluorosensor	A specific substance detection systems that employ a laser to excite a substance which then gives off radiation at another wavelength. This wavelength is typically unique to the substance being detected.
Microwave sensor	Devices which detect radiation in the microwave region of the electromagnetic spectrum. Some devices, such as radar, also emit waves in the microwave spectrum to analyze the reflectivity of the fields of view.
Optical sensor	Sensors which analyze the field-of-view in the electromagnetic spectrum from the infrared to the ultraviolet region. Typically the focus is the visible region.
Passive microwave sensor	A sensor which analyzes the natural microwave radiation in a field-of-view.
Radarsat	One of two radar satellites that are often used to detect and track oil spills.
Radiometer	Any device that measures electromagnetic radiation typically the abundance of radiation in a given spectral range is measured.

This chapter was originally published as part of the Encyclopedia of Sustainability Science and Technology edited by Robert A. Meyers. DOI:10.1007/978-1-4419-0851-3

M. Fingas (✉)
Spill Science, 1717 Rutherford Point, Edmonton, AB T6W 1J6, Canada
e-mail: fingasmerv@shaw.ca

C. Brown
Emergencies Science and Technology Section, Environment Canada, Ottawa, ON K1A OH3, Canada
e-mail: Carl.Brown@ec.gc.ca

J. Orcutt (ed.), *Earth System Monitoring: Selected Entries from the Encyclopedia of Sustainability Science and Technology*, DOI 10.1007/978-1-4614-5684-1_15,

Scatterometer	A device that measures the scattering of a particular spectral range of radiation.
Ship discharge	An oil spill resulting from a discharge (usually illegal) from a ship. Ships may discharge lubrication oil, oil from washing, or other waste oils.
Thickness sensor	Any oil spill sensor that specifically measures oil slick thickness.

Definition of the Subject and Its Importance

Remote-sensing for oil spills is reviewed. The technical aspects of sensors are reviewed and the benefits and limitations of each sensor are given. Oil spill response often requires that remote sensing is used to detect and map the spill of interest. A wide variety of technologies had been tried.

A common and economical sensor is an infrared camera or an IR/UV system. This sensor class has limited utility but has the lowest cost of any sensor. The inherent weaknesses include the inability to discriminate oil on beaches, among weeds or debris and under certain lighting conditions, oil is not detected. Furthermore, water-in-oil emulsions are often not detected in the infrared. The laser fluorosensor is a most-useful instrument because of its unique capability to identify oil on backgrounds that include water, soil, weeds, ice, and snow. It is the only sensor that can positively discriminate oil on most backgrounds.

Radar offers the only potential for large area searches, day/night and foul weather remote sensing. Radar is costly, requires a dedicated aircraft, and is prone to many interferences. False targets can be as high as 95%. Satellite-borne radar sensors are useful, however, their frequency of overpass and lesser spatial resolution render them useful for mapping large spills or assisting in ship and platform discharge monitoring. Much effort is currently underway to remove oil look-alikes such as low wind areas, biogenic slicks, oceanographic fronts, etc., from the imagery.

Equipment that measures relative slick thickness is still under development. Passive microwave has been studied for several years, but instruments lack sufficient spatial resolution to be practical, operational instruments. A laser-acoustic instrument, which provides the only technology to measure absolute oil thickness, has been tested.

Equipment operating in the visible spectrum, such as cameras and scanners, is useful for documentation or providing a basis for the overlay of other data. It is not useful beyond this because oil shows no spectral characteristics in the visible region. Less use is being made of visible equipment in recent years.

Sensors for measuring oil thickness and detecting oil in ice are briefly reviewed. These technologies are relatively new, although there are some promising concepts that require further research.

Introduction

Spills of oil and related petroleum products in the marine environment may have serious environmental impacts [1]. Remote sensing is playing an increasingly important role in oil spill response efforts. Public and media scrutiny is usually intense following a spill, with demands that the location and extent of the oil spill be determined. Cleanup crews require location information on at least a daily basis. Through the use of modern remote sensing instrumentation, oil can be monitored on the open ocean on a 24-h basis [2]. Another role for remote sensing has been the strong interest in detection of illegal discharges, especially in view of the large seabird mortality associated with such discharges [3].

Even though sensor design and electronics are becoming increasingly sophisticated and much less expensive, the operational use of remote sensing equipment lags behind the technology. In remote sensing, a sensor, other than the eye or conventional photography, is used to detect the target of interest at a distance. The most common forms of oil spill surveillance and mapping are still sometimes carried out with simple still or video photography. Remote sensing from an aircraft is a common form of oil spill tracking. Remote sensing from satellites using radar sensors is now becoming a common technique.

It is important to divide the uses of remote sensing into the end use or objective as the utility of the sensor or sensor system is best defined that way. Oil spill remote sensing systems used for routine surveillance certainly differ from those used to detect oil on shorelines or land. One tool does not serve all functions. For a given function, many types of systems may, in fact, be needed. Further it is necessary to consider the end use of the data. The end use of the data, be it location of the spill, enforcement or support to cleanup, may also dictate the resolution or character of the data needed.

There are several broad uses of oil spill remote sensing:

1. Enforcement of ship discharge laws
2. Surveillance and general slick detection
3. Provision of evidence for prosecution
4. Mapping of spills for various reasons
5. Direction of oil spill countermeasures
6. Determination of slick trajectories

Several general reviews of oil spill remote sensing have been prepared [4–9]. These reviews show that there is progress in oil spill remote sensing; however, that progress is not necessarily moving at the speed that one might hope. These reviews show that specialized sensors offer advantages compared to off-the-shelf sensors.

Atmospheric Properties

The atmosphere has certain windows that affect the way that one can carry out remote sensing. Figure 15.1 shows the atmospheric attenuation at different electromagnetic wavelengths. This figure shows that the commonly used wavelengths in the visible, long-wave infrared, and radar bands are relatively free of atmospheric adsorption. One must consider rain, fog, and snow which limit operations in both the visible and the infrared regions. This leaves radar as the only all-weather and day and night sensor. Radar, as noted below, has many limitations in that it does not actually detect oil but only detects the dampening of sea capillary waves at a certain range of wind speeds.

Oil Interaction with Light and Electronic Waves

Oil interacts with light and electromagnetic waves in certain specific ways, and this can yield detectability of oil.

Krol et al. measured the optical properties of fresh and weathered crude oils and a water-in-oil emulsion [10]. Weathering of oil increases the light absorption of the oil along with an increase in light scattering. An emulsion also absorbs more light and attenuates the light in the water column. Evdokimov and Losev studied the UV and visible absorption of oils for analytical purposes, noting that crude oils were opaque and thus had to be diluted. The implication for remote sensing is that UV and

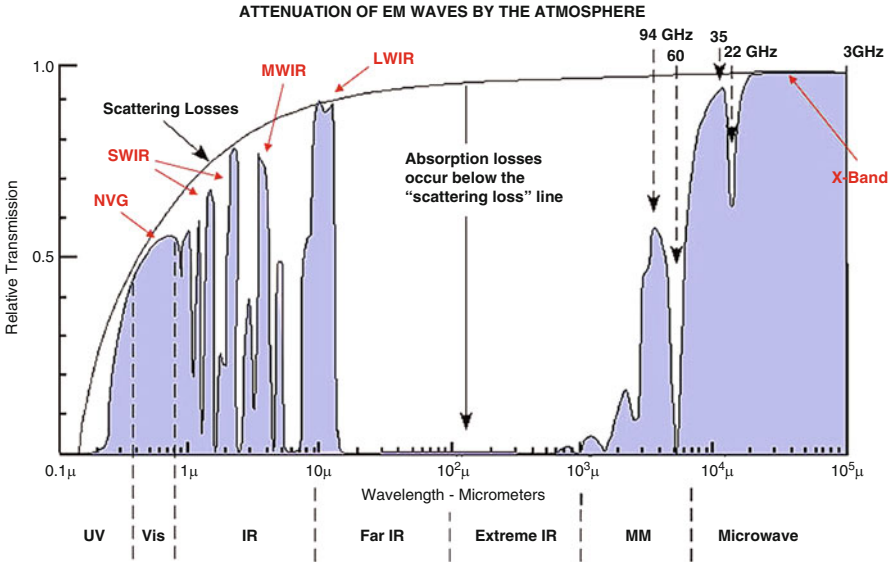

Fig. 15.1 The attenuation of the electromagnetic spectrum by the atmosphere

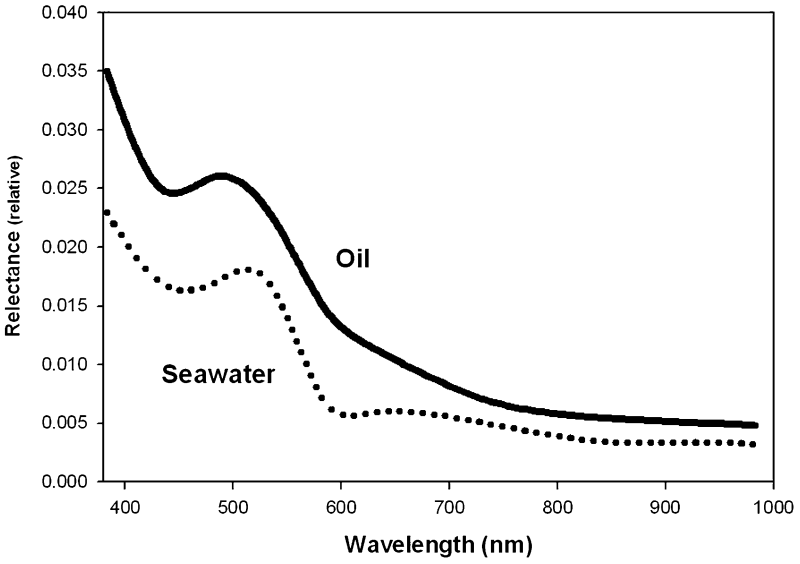

Fig. 15.2 The differential reflection of water and oil

visible signatures of oil are insufficient for characterization [11]. Otremba and co-workers studied the light reflectance of crude oils floating on water. If the oils are opaque, the reflectance is relatively free of spectral information [12–14].

Hong and Shin suggest that infrared images could be used to detect oil spills at sea at night [15]. Instead of using the IR image, they suggest that the images be used to calculate the difference in refractive indices. Seawater has a refractive index of 1.227 and oil 1.53 at IR wavelength of 10 μm. The refractive index can be calculated from the IR data (in this case MODIS), thus possibly enabling the discrimination of surface oil or water.

The reflectance of oil is greater than seawater and increases with decreasing wavelength, that is, is greater in the blue-green region. Figure 15.2 shows typical reflectance curves between oil and water. Several researchers have tried to use this reflectance difference to discriminate oils, however, the best that it can do is use it as an indicator of oil on the surface. Ma et al. noted that the spectral bands between 400 and 500 nm were particularly useful for visible detection of oil from the MODIS satellite [16].

In summary, there are few very distinct characteristics that oil has in the visible, IR, or smaller wavelengths. One depends on secondary effects for oil detection and mapping.

Visible Indications of Oil

Under many circumstances oil is not visible on the surface to the eye [8]. Other than the obvious situations of nighttime and fog, there exist many situations where oil

Fig. 15.3 A view of an oceanic front. The darker material is river water flowing into the ocean. There is no oil in this photograph

cannot be seen. A very common situation is that of thin oil such as from ship discharges or the presence of materials such as sea weed, ice, and debris that mask oil presence. Often there are conditions on the sea that may appear like oil, when indeed there is no oil. These include wind shadows from land forms, surface wind patterns on the sea, surface dampening by submerged objects or weed beds, natural oils or biogenic material and oceanic fronts. In the case of large spills, the area may be too great to be mapped visually. Several of these cases are illustrated in Figs. 15.3–15.5. All these factors dictate that remote sensing systems be used to assist in the task of mapping and identifying oil. In many cases, aerial observation and remote sensing are necessary to direct cleanup crews to slick locations. Figure 15.6 shows a case where no aerial direction was given and a skimmer crew is missing the slick by about half kilometers.

Optical Sensors

Visible

The use of human vision alone is not considered remote sensing, however, still forms the most common technique for oil-spill surveillance. In the past, major

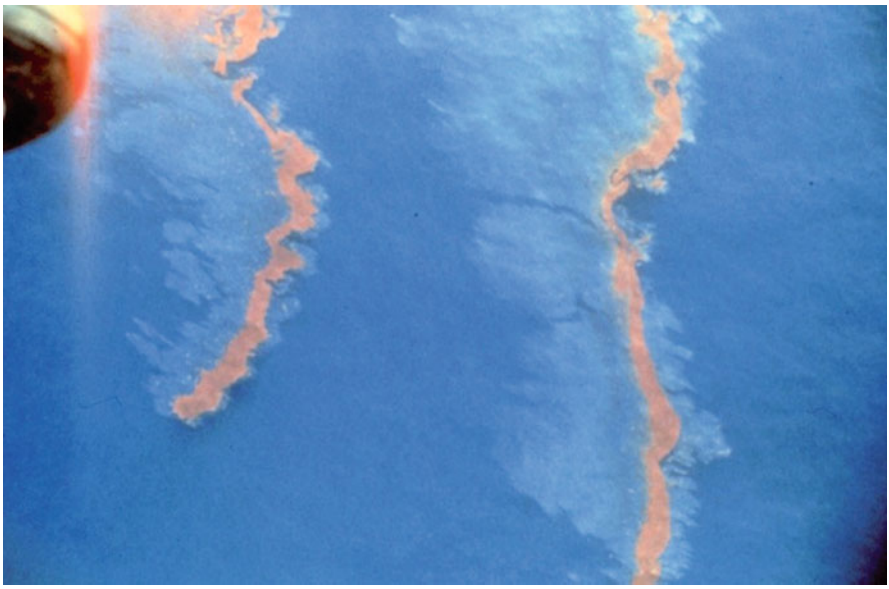

Fig. 15.4 A view of a slick that is very clear and contrasts with the background. The emulsified oil with its red color provides good contrast

Fig. 15.5 A slick that is barely visible. The rainbow sheen became visible here only after the photographer adjusted the angle with respect to the sun

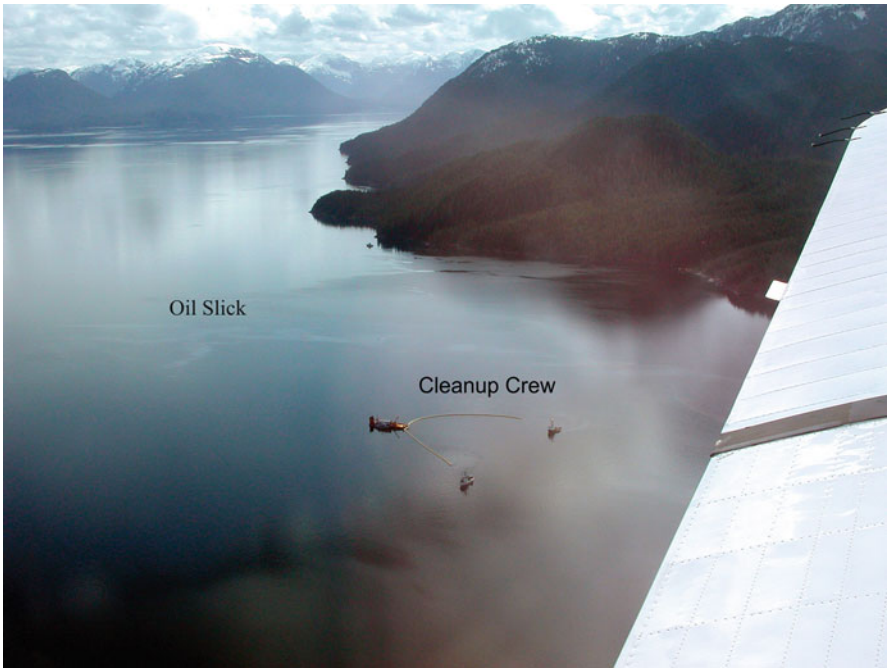

Fig. 15.6 A cleanup crew missing the slick by a wide margin as no aerial direction was given

campaigns using only human vision were mounted with varying degrees of success [4]. Optical techniques, using the same range of the visible spectrum detection, are the most common means of remote sensing. Cameras, both still and video, are common because of their low price and commercial availability. Systems are now available to directly map remote sensing data onto base maps [4].

In the visible region of the electromagnetic spectrum (approximately 400–700 nm), oil has a higher surface reflectance than water, but shows limited nonspecific absorption tendencies. Oil generally manifests throughout the entire visible spectrum. Sheen shows up silvery and reflects light over a wide spectral region down to the blue. As there is no strong information in the 500–600-nm region, this region is often filtered out to improve contrast [17]. Overall, however, oil has no specific characteristics that distinguish it from the background [18]. Taylor studied oil spectra in the laboratory and the field and observed flat spectra with no usable features distinguishing it from the background [19]. Therefore, techniques that separate specific spectral regions do not increase detection capability. Some researchers noted that while the oil spectra are flat, the presence of oil may slightly alter water spectra [20]. It has been suggested that the water peaks are raised slightly at 570–590, 780–710, and 810–710 nm. At the same time there are depressions or troughs at 650–680 nm and 740–760 nm. It has been found that high contrast in visible imagery can be achieved by setting the camera at the Brewster

angle (53° from vertical) and using a horizontally aligned polarizing filter which passes only that light reflected from the water surface [21]. This is the component that contains the information on surface oil [17]. It has been reported that this technique increases contrast by up to 100%. Filters with band-pass below 450 nm can be used to improve contrast. View angle is important and some researchers have noted that the thickness changes the optimal view angle [22].

On land, hyperspectral data (use of multiple bands, typically 10–100) has been used to delineate the extent of an oil well blowout [23]. The technique used was spectral reflectance in the various channels as well as the usual black appearance of oil.

Video cameras are often used in conjunction with filters to improve the contrast in a manner similar to that noted for still cameras. This technique has had limited success for oil spill remote sensing because of poor contrast and lack of positive discrimination [24]. With new light-enhancement technology (low lux), video cameras can be operated even in darkness. Tests of a generation III night vision camera shows that this technology is capable of providing imagery in very dark night conditions [25, 26].

Scanners were used in the past as sensors in the visible region of the spectrum. A rotating mirror or prism sweeps the field-of-view (FOV) and directs the light toward a detector. Before the advent of CCD (charge-coupled device) detectors, this sensor provided much more sensitivity and selectivity than video cameras. Another advantage of scanners was that signals were digitized and processed before display. In the current era, newer technology has evolved and similar digitization can be achieved without scanning by using a CCD imager and continually recording all elements, each of which is directed to a different field-of-view on the ground. This type of sensor, known as a push-broom scanner, has many advantages over the older scanning types. It can overcome several types of aberrations and errors, and all data are collected simultaneously for a given line perpendicular to the direction of the aircraft's flight. Several types of scanners were developed. In Canada, the MEIS (Multi-detector Electro-optical Imaging Scanner) and the CASI (Compact Airborne Spectrographic Imager) have been developed, and in the Netherlands, the Caesar system was developed [17, 27, 28]. In China, the MAMS and AISA systems have been developed [29].

Digital photography has enabled the combination of photographs and the processing of images. Locke et al. used digital photography from vertical images to form a mosaic of an area impacted by an oil spill [30]. It was then possible to form a singular image and to classify oiling areas by color within the image. Video cameras are often used in conjunction with filters to improve the contrast in a manner similar to that noted for still cameras. This technique has had limited success for oil spill remote sensing because of poor contrast and lack of positive discrimination.

The detection or measurement of oil-in-water has never been successfully accomplished using remote visible technology. There may be potential for light scattering technology. Stelmaszewski and co-workers measured the light scattering

of crude oil-in-water emulsions and noted that scattering increase with wavelength in the UV range and decreases slightly with the wavelength of visible light [31].

The use of visible techniques in oil spill remote sensing is largely restricted to documentation of the spill because there is no mechanism for positive oil detection. Furthermore, there are many interferences or false alarms. Sun glint and wind sheens can be mistaken for oil sheens. Biogenic material such as surface seaweeds or sunken kelp beds can be mistaken for oil. Oil on shorelines is difficult to identify positively because seaweeds look similar to oil and oil cannot be detected on darker shorelines. In summary, the usefulness of the visible spectrum for oil detection is limited. It is an economical way to document spills and provide baseline data on shorelines or relative positions.

Infrared

Oil, which is optically thick, absorbs solar radiation and re-emits a portion of this radiation as thermal energy, primarily in the 8–14-μm region. In infrared (IR) images, thick oil appears hot, intermediate thicknesses of oil appear cool, and thin oil or sheens are not detected. The thicknesses at which these transitions occur are poorly understood, but evidence indicates that the transition between the hot and cold layer lies between 50 and 150 μm and the minimum detectable layer is between 10 and 70 μm [32–35]. The reason for the appearance of the "cool" slick is also not fully understood. A plausible theory is that a moderately thin layer of oil on the water surface causes destructive interference of the thermal radiation waves emitted by the water, thereby reducing the amount of thermal radiation emitted by the water [8]. This is analogous to the appearance of the rainbow sheen which is explained in section "Visual Thickness Indications" below. The cool slick would correspond to the thicknesses as observed above, because the minimum destructive thickness would be about two times the wavelength which is between 8 and 10 μm. This would yield a destructive onset of about 16–20 μm to about four wavelengths or about 32–40 μm. The destructive area is usually only seen with test slicks, which might be explained by the fact that the more rapidly spreading oil is more transparent than the remaining oil and also by the fact that only a recently spilled test slick actually has such intermediate thicknesses. The onset of the hot thermal layer would in theory then be at thicknesses greater than this or at about 50 μm.

Infrared devices cannot detect emulsions (water-in-oil emulsions) under most circumstances [36]. This is probably a result of the high thermal conductivity as emulsions typically contain 70% water and thus do not show temperature differences from water.

Infrared cameras are now very common and commercial units are available from several manufacturers. In recent times, uncooled detectors are commonplace and have entirely replaced the older, cooled detectors.

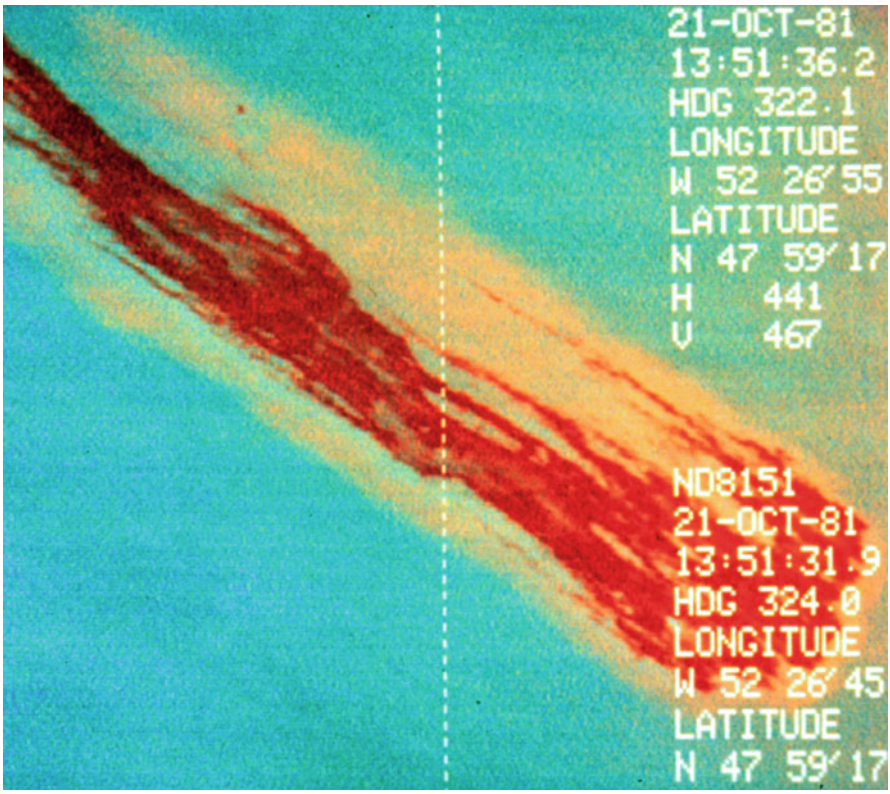

Fig. 15.7 A slick highlighted in the infrared

Most infrared sensing of oil spills takes place in the thermal infrared at wavelengths of 8–14 μm. Specific studies in the thermal infrared (8–14 μm) show that there is no spectral structure in this region [37]. Tests of a number of infrared systems show that spatial resolution is extremely important when the oil is distributed in windrows and patches, emulsions are not always visible in the IR, and cameras operating in the 3–5-μm range are only marginally useful [38, 39]. Nighttime tests of IR sensors show that there is detection of oil (oil appears cold on a warmer ocean), however, the contrast is not as good as during daytime [40].

The relative thickness information in the thermal infrared can be used to direct skimmers and other countermeasures equipment to thicker portions of the slick. Figures 15.7–15.9 illustrate the utility of infrared oil imaging compared to that of visible imaging. Oil detection in the infrared is not positive, however, as several false targets can interfere, including seaweeds, shoreline, and oceanic fronts [41]. Infrared sensors are reasonably inexpensive, and are currently a common tool used by the spill response community.

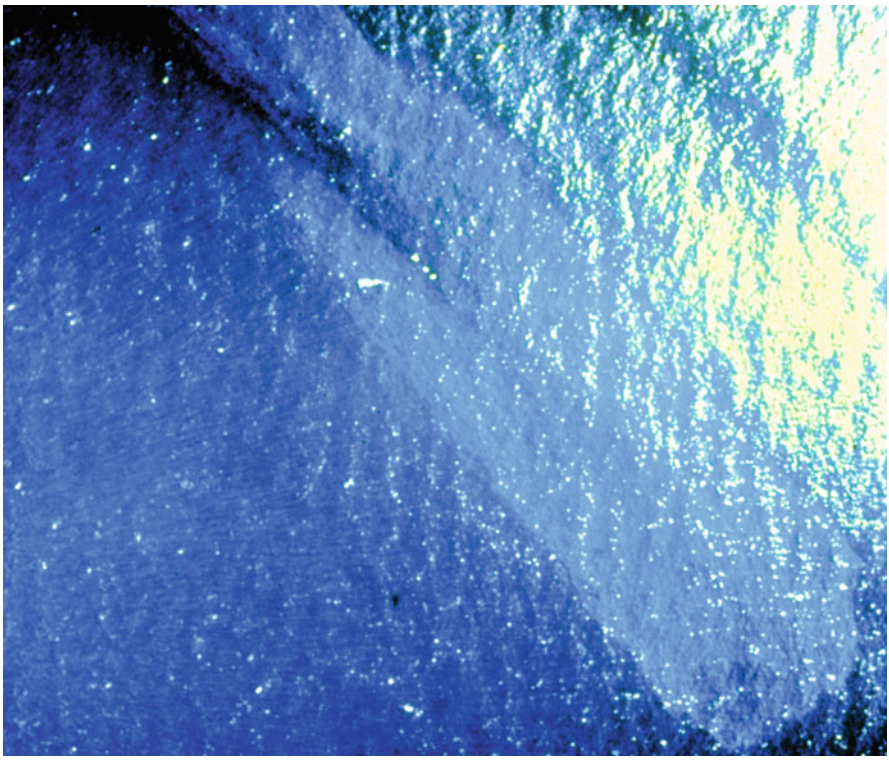

Fig. 15.8 The same slick as shown in Fig. 15.7 but in the visible. The contrast between the oil and sun glint is poor in the visible

Near-Infrared

Clark et al. and Leifer et al. proposed that color composite images assembled from both visible and near-IR wavelengths can be used to make images of thick oil, but such images also show strong reflections from clouds and the glint from the ocean surface [42, 43]. Clark et al. proposed that spectroscopic analysis of the reflectance spectra within remote-sensing imagery could resolve the absorptions due to the organic compounds in oil and can better discriminate the spectral shape of oil [42]. A method to analyze absorptions due to specific materials is called absorption-band-depth mapping Clark and others showed that simple three-point band-depth mapping will show the location of absorption features but cannot identify specific compositions of compounds causing these features when multiple compounds have absorptions near the same wavelength [42]. In the case of open ocean images, comprised of pixels containing water, oil/water mixtures, and clouds, the organic compounds in the oil and oil/water mixtures have absorption features that are

Fig. 15.9 A test slick highlighted using overlaid infrared and visible imagery. This results in a very relative "thickness map" of this particular slick. This technique is not particularly useful for most slicks as they do not show this gradient, which is only typical for small, recently spilled slicks

distinct from those from water and clouds. These spectral differences allow one to map qualitative variations in oil abundance. The researchers used the NASA Airborne Visible/Infrared Imaging Spectrometer (AVIRIS). AVIRIS provides data on the spectrum of the surface at each pixel from 0.35 to 2.5 μm (the visible spectrum is: blue: 0.4 μm, green 0.53 μm, deep red 0.7 μm) in 224 channels. AVIRIS data from oil overflights are used to produce a three-point band-depth map, indicating potential locations of thick oil, by the following methods: (1) Radiance data are converted to surface reflectance using a two-step process [42]. (2) Three-point band-depth images are computed using continuum-removed reflectance spectra using the equation, [42]

$$D = 1 - 2Rb/(Rl + Rr) \tag{15.1}$$

where Rb is the reflectance around the absorption maximum (minimum reflectance)

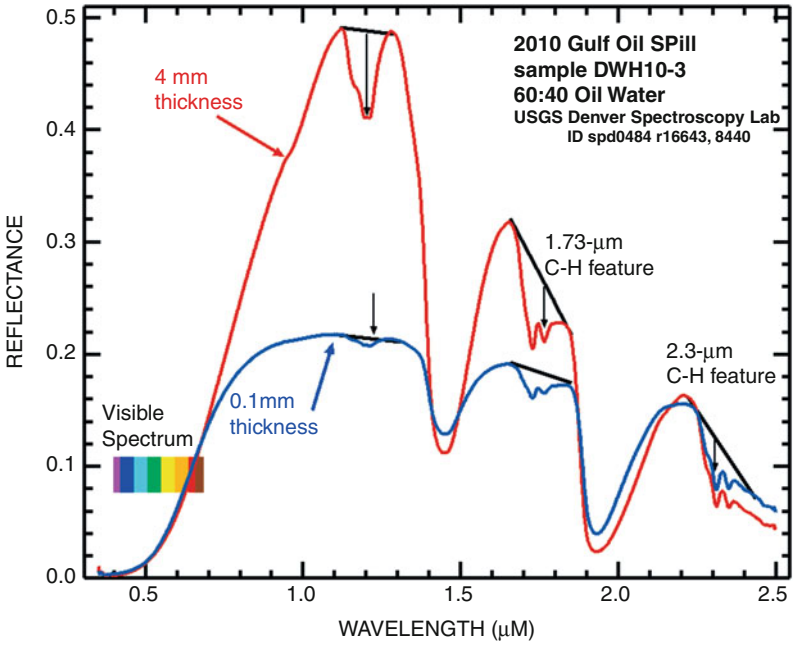

Fig. 15.10 Wavelength versus reflectance in the near infrared. This shows the wavelength proposed by Clark et al. to map slick thicknesses [43]

Rl = the reflectance of the left continuum end point
Rr = the reflectance of the right continuum end point

The proposed adsorption scheme is shown in Fig. 15.10 (from Leifer et al. [43]).

For AVIRIS, the following wavelength intervals were used in three-point band-depth computations [42]:

1.2-µm feature:
Rb = average of the channels in the interval from 1.197 to 1.216 µm
Rl = average of the channels in the interval from 1.073 to 1.102 µm
Rr = average of the channels in the interval from 1.273 to 1.293 µm

1.7-µm feature:
Rb = average of the channels in the interval from 1.712 to 1.732 µm
Rl = average of the channels in the interval from 1.622 to 1.642 µm
Rr = average of the channels in the interval from 1.782 to 1.802 µm

2.3-µm feature:
Rb = average of the channels in the interval from 2.287 to 2.327 µm
Rl = average of the channels in the interval from 2.198 to 2.238 µm
Rr = average of the channels in the interval from 2.407 to 2.447 µm

The band-depth images produced from these three calculations are combined into a color composite image as follows: the 2.3-μm feature in the red channel, the 1.73-μm feature in the green channel, and the 1.2-μm feature in the blue channel. The thicker oil then shows up in the green-blue regions of the image.

The Gulf oil spill was mapped using the AVIRUS sensor in the ER aircraft and thickness maps were plotted [42]. This method appears to work for the Gulf oil spill, however, confirmation of this technique on other spills awaits.

Ultraviolet

Ultraviolet sensors can be used to map sheens of oil since oil slicks display high reflectivity of ultraviolet (UV) radiation even at thin layers (<0.1 μm). The utility of mapping out sheen areas, which in fact contain very little oil has been questioned by many. However, overlaid ultraviolet and infrared images are often used to produce a relative thickness map of oil spills. This is illustrated in Fig. 15.9. Ultraviolet cameras, although inexpensive, are not often used in this process, however, as it is difficult to overlay camera images [44]. Data from infrared scanners and that derived from push-broom scanners can be easily superimposed to produce these IR/UV overlay maps. Ultraviolet data are also subject to many interferences or false images such as wind slicks, sun glints, and biogenic material. Since these interferences are often different than those for infrared sensing, combining IR and UV can provide a more positive indication of oil than using either technique alone.

Laser Fluorosensors

Laser fluorosensors are sensors that utilize the fact that aromatic compounds in petroleum oils absorb ultraviolet light and become electronically excited. This excitation is rapidly removed through the process of fluorescence emission, primarily in the visible region of the spectrum. Since very few other compounds show this tendency, fluorescence is a strong indication of the presence of oil. Natural fluorescing substances, such as chlorophyll, fluoresce at sufficiently different wavelengths than oil to avoid confusion. As different types of oil yield slightly different fluorescent intensities and spectral signatures, it is possible to differentiate between classes of oil under ideal conditions [45–54].

Laser fluorosensors used for oil spill detection employ a laser operating in the ultraviolet region of 308–355 nm [45, 55, 56]. With this wavelength of activation, there exists a broad range of fluorescent response for organic matter, centered at 420 nm. This is referred to as Gelbstoff or yellow matter, which can be easily annulled. Chlorophyll yields a sharp peak at 685 nm. The fluorescent response of crude oil ranges from 400 nm to 650 nm with peak centers in the 480-nm region.

The use of laser fluorosensors for chlorophyll and other applications has also been well documented [45].

Another phenomenon, known as Raman scattering, involves energy transfer between the incident light and the water molecules. When the incident ultraviolet light interacts with the water molecules, Raman scattering occurs. This involves an energy transfer between the incident light and the water molecules. The water molecules absorb some of the energy as rotational-vibrational energy and scatter light at a wavelength which is the difference between the incident radiation and the vibration-rotational energy of the molecule. The Raman signal for water occurs at 344 nm when the incident wavelength is 308 nm (XeCl laser). The water Raman signal is useful for maintaining wavelength calibration of the fluorosensor in operation, but has also been used in a limited way to estimate oil thickness, because the strong absorption by oil on the surface will suppress the water Raman signal in proportion to thickness [57, 58]. This thickness is limited and is true for only very thin slicks. The point at which the Raman signal is entirely suppressed depends on the type of oil, since each oil has a different absorption coefficient. The Raman signal suppression has led to estimates of sensors detection limits of about 0.05–0.1 μm [59].

Laser fluorosensors have shown high utility in practice and are now becoming an essential sensor in many remote sensing packages. The information in the output is unique and the technique provides a unique method of oil identification. Figure 15.11 shows an operator display of a laser fluorosensor.

Laser fluorosensors have significant potential as they may be the only means to discriminate between oiled and unoiled seaweeds and to detect oil on different types of beaches. Tests on shorelines show that this technique has been very successful [60]. Algorithms for the detection of oil on shorelines have been developed [61]. Work has been conducted on detecting oil in the water column such as occurs with the heavy, emulsified oil product, Orimulsion [62–66]. The fluorosensor is also the only reliable means of detecting oil in certain ice and snow situations. Operational use shows that the laser fluorosensor is a powerful tool for oil spill remote sensing [45]. Currently, one company makes two commercial models of the instrument.

Microwave Sensors

Radiometers

Microwave radiometers detect the presence of an oil film on water by measuring an interference pattern excited by the radiation from free space. The apparent emissivity factor of water is 0.4 compared to 0.8 for oil [67]. A passive microwave radiometer can detect this difference in emissivity and could therefore be used to detect oil. In addition, as the signal changes with thickness, in theory, the device

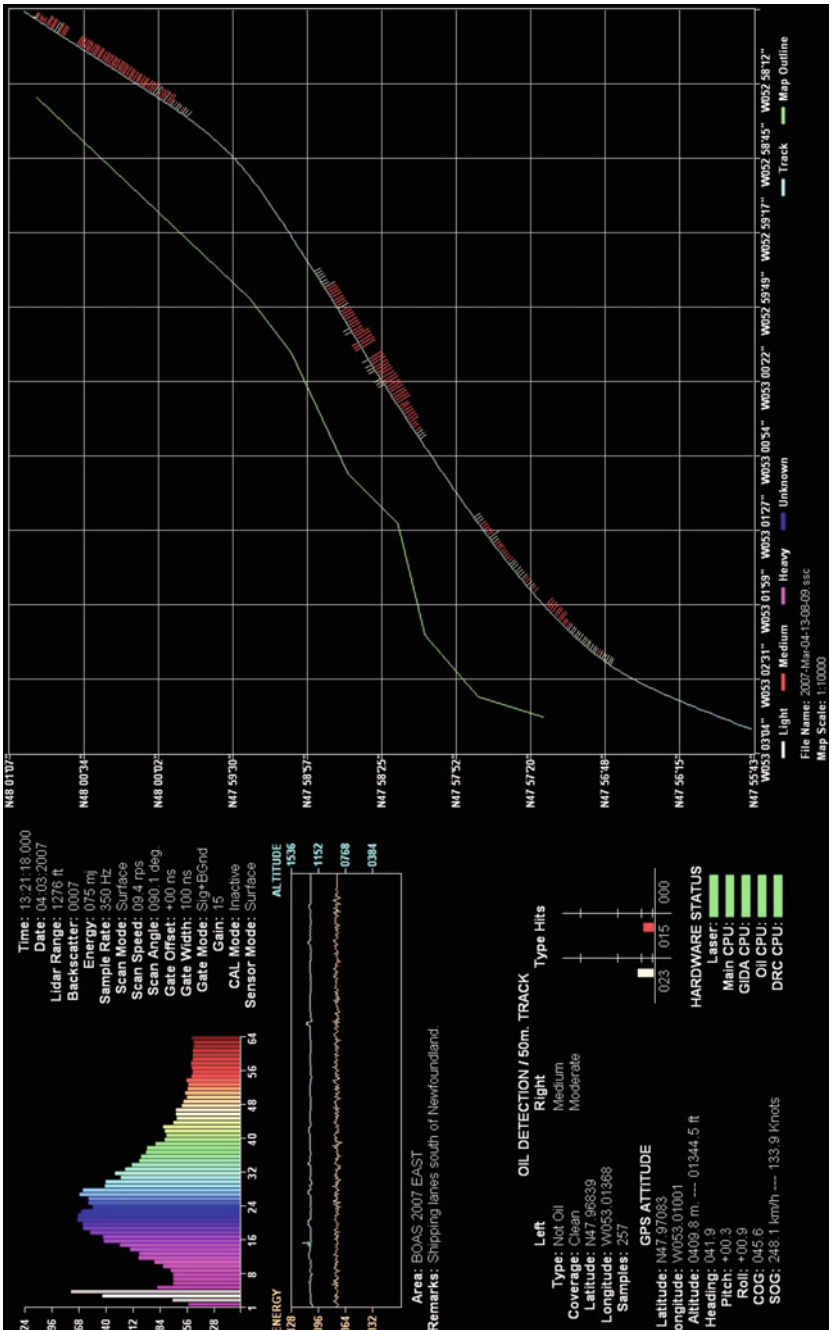

Fig. 15.11 An illustration of a fluorosensor display. On the *left* instrument and detection criteria are given. On the *right*, the flight track is annotated with oil detection "hits" shown as bars

could be used to measure thickness. This detection method has not been very successful in the field, however, as several environmental and oil-specific parameters must be known. In addition, the signal return is dependent on oil thickness but in a cyclical fashion. A given signal strength can imply any one of two or three signal film thicknesses within a given slick. One way to overcome this is to use more than one wavelength of microwave. Microwave energy emission is greatest when the effective thickness of the oil equals an odd multiple of one quarter of the wavelength of the observed energy. Biogenic materials also interfere and the signal-to-noise ratio is low. In addition, it is difficult to achieve high spatial resolution (might need resolution in meters rather than the typical tens of meters for a radiometer) [68].

The Swedish Space agency has carried out work with different systems, including a dual band, 22.4- and 31-GHz device, and a single band 37-GHz device [69]. Skou, Sorensen, and Poulson describe a 2-channel device operating at 37.5 and 10.7 GHz [70]. Mussetto and co-workers at TRW described the tests of 44-94-GHz and 94-154-GHz, 2-channel devices over oil slicks [71]. They showed that correlation with slick thickness is poor and suggests that factors other than thickness also change surface brightness. They suggest that a single-channel device might be useful as an all-weather, relative-thickness instrument. Tests of single-channel devices over oil slicks have also been described in the literature, specifically a 36-GHz and a 90-GHz device [72, 73]. A novel method of microwave radiometry has been developed in which the polarization contrasts at two orthogonal polarizations are measured in an attempt to measure oil slick thickness [74, 75]. A series of frequency-scanning radiometers have been built and appear to have overcome the difficulties with the cyclical behavior [76, 77].

In summary, passive microwave radiometers may have potential as all-weather oil sensors. Their potential as a reliable device for measuring slick thickness, however, is uncertain at this time.

Radar

Capillary waves on the ocean reflect radar energy, producing a “bright” image known as sea clutter. Since oil on the sea surface dampens capillary waves, the presence of an oil slick can be detected as a “dark” sea or one with an absence of this sea clutter [78]. Unfortunately, oil slicks are not the only phenomena that are detected in this way. There are many interferences or false targets, including freshwater slicks, wind slicks (calms), wave shadows behind land or structures, seaweed beds that calm the water just above them, glacial flour, biogenic oils, and whale and fish sperm [79–83]. As a result, radar can be ineffective in locations such as Prince William Sound, Alaska where dozens of islands, freshwater inflows, ice, and other features produce hundreds of such false targets. Figures 15.12–15.15 illustrate some of the many slick look-alikes which appear in radar displays.

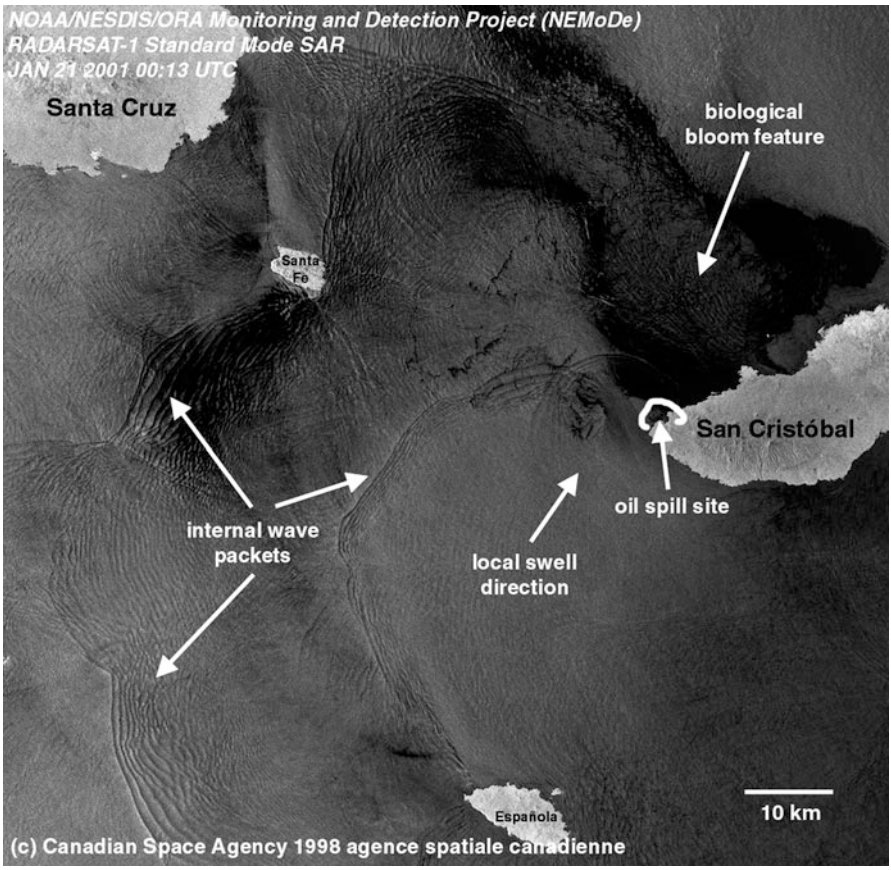

Fig. 15.12 A Radarsat I image of a spill area in the Galapagos Islands. There are so many features that dampen waves in this area that is doubtful if much oil is shown in this image

Despite these limitations, radar is an important tool for oil spill remote sensing because it is the only sensor that can be used for searches of large areas and it is one of the few sensors that can detect anomalies at night and through clouds or fog.

The two basic types of imaging radar that can be used to detect oil spills and for environmental remote sensing in general are Synthetic Aperture Radar (SAR) and Side-Looking Airborne Radar (SLAR). The latter is an older, but less expensive technology, which uses a long antenna to achieve spatial resolution. Synthetic aperture radar uses the forward motion of the aircraft to synthesize a very long antenna, thereby achieving very good spatial resolution, independent of range, with the disadvantage of requiring sophisticated electronic processing. While inherently more expensive, the SAR has greater range and resolution than the SLAR. In fact, comparative tests show that SAR is vastly superior [84–86]. Search radar systems, such as those frequently used by the military, cannot be used for oil spills as they usually remove the clutter signal, which is the primary signal of interest for oil spill

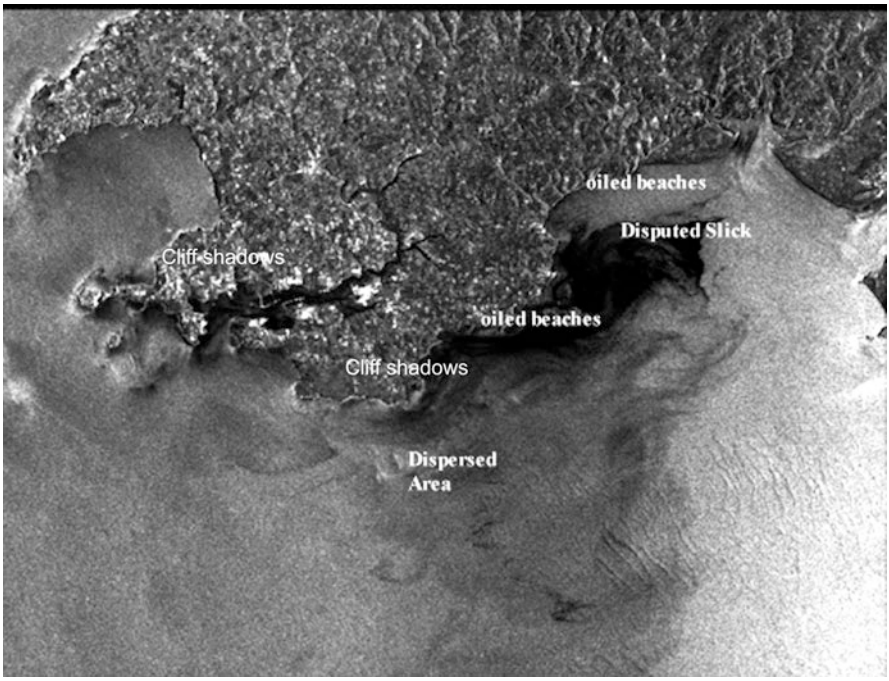

Fig. 15.13 A Radarsat I image of a spill area off the coast of Wales. The *black* areas near the shore are cliff shadows and appear also in areas where there was no oiling. The annotation shows that some of the slick were found in areas where there was not thought to be slicks

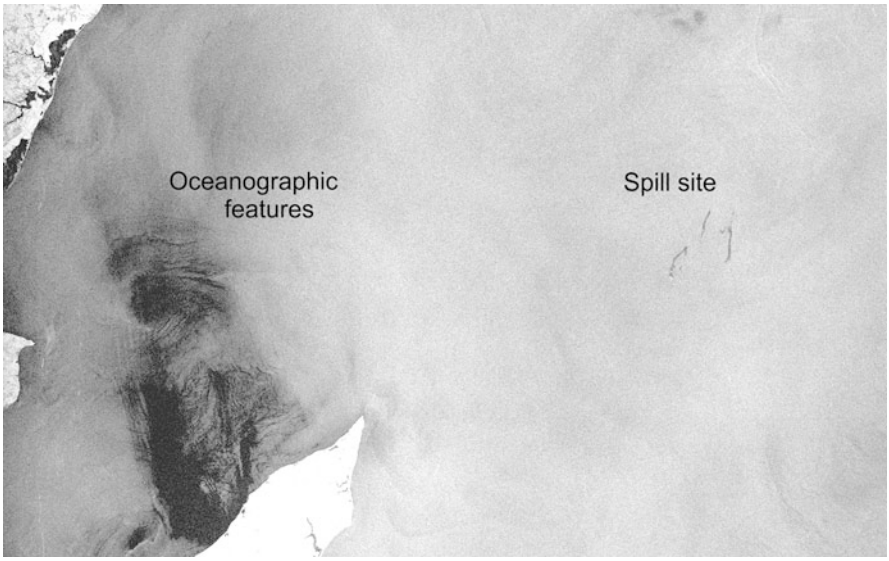

Fig. 15.14 A Radarsat I image of an area north of Prince Edward Island. Most of the image area is taken up with oceanographic features. A known spill is noted in a small area of the image

Fig. 15.15 An ERS II image off the coast of Belgium. There are many features that might appear to be oil, however, there is no oil present. The long thin object is a vessel track, there are many oceanographic features and areas near the coast that show suppressed capillary waves

detection. Furthermore, the signal processing of this type of radar is optimized to pinpoint small, hard objects, such as periscopes. This signal processing is very detrimental to oil spill detection.

SLAR has predominated airborne oil spill remote sensing, primarily because of the lower price [87, 88]. There is some recognition among the operators that SLAR is very subject to false hits, but solutions are not offered. Experimental work on oil spills has shown that X-band radar yields better data than L- or C-band radar [89, 90].

Several different polarizations exist based on vertical (V) and horizontal (H). Typically transmission and reception are in the same polarity, that is, VV or HH. But, there are actually four poles available: HH, VV, HV, and VH. Use of all four of these is designated as quadrapole. It has also been shown that vertical

antenna polarizations for both transmission and reception (VV) yield better results than other configurations [84, 91–93]. Additionally, phase differences can be used to detect oil. Migliaccio et al. calculated that the co-polarized phase difference (CPD) would yield a larger signal for oil compared to that for the sea [94].

The ability of radar to detect oil is also limited by sea state. Sea states that are too low will not produce enough sea clutter in the surrounding sea in contrast to the oil and very high seas will scatter radar sufficiently to block detection inside the troughs. Indications are that minimum wind speeds of 1.5 m/s (∼3 knots) are required to allow detectability and a maximum wind speed of 6 m/s (∼12 knots) will again remove the effect [95–97]. The most accepted limits are 1.5 m/s (∼3 knots) to 10 m/s (∼20 knots). This limits the environmental window of application of radar for detecting oil slicks. Gade et al. studied the difference between extensive systems from a spaceborne mission and a helicopter-borne system [98]. They found that at high winds, it was not possible to discriminate biogenic slicks from oil. At low wind speeds, it was found that images in the L-band showed discrimination. Under these conditions the biogenic material showed greater damping behavior in the L-band. Okamoto et al. studied the use of ERS-1 using an artificial oil (oleyl alcohol) and found that an image was detected at a wind speed of 11 m/s, but not at 13.7 m/s [99].

SAR can be polarimetric that is horizontal-horizontal (HH), vertical-vertical (VV), and cross combinations of these. Several researchers have shown that VV is best for oil spill detection and discrimination [94, 100–102]. Migliaccio et al. showed that the co-polarized phase difference – for example, the difference between the HH and VV phases, can be used to discriminate oil slicks from biogenic slicks. [100]. A larger standard deviation for the slick compared to the sea typically indicates that it is oil. Figures 15.16 and 15.17 show the differences between VV and HH polarization.

Radar has also been used to measure currents and predict oil spill movements by observing frontal movements [103]. Work has shown that frontal currents and other features can be detected by SAR [104].

Shipborne radar has similar limitations and the additional handicap of low altitude, which restricts its range to between 8 and 30 km, depending on the height of the antenna. Ship radars can be adjusted to reduce the effect of sea clutter de-enhancement. Shipborne radar successfully detected many slicks and commercial systems are now available. During the *Prestige* spill, a Netherlands vessel successfully used this technique to guide a recovery vessel into slicks [105]. The technique is, however, very limited by sea state and in all cases where it was used, the presence and location of the slick were already known or suspected. Recently researchers have carried out work on improving the imaging of slicks from shipborne radars [105]. Today, there are some commercial products to enhance the images from shipborne radar to enable some oil imaging.

Gangeskar has proposed an automatic system that could be mounted on oil drilling platforms [106]. This system would use standard X-band ship navigation units and would provide an alert if an oil spill is present. The system includes an

Fig. 15.16 A HH (horizontal-horizontal) polarized view of the sea surface

extensive post-processing system to provide both a user-friendly GUI and an automatic detection and alert system. The system has not been fully tested to date.

In summary, radar optimized for oil spills is useful in oil spill remote sensing, particularly for searches of large areas and for nighttime or foul weather work. The technique is highly prone to false targets, however, and is limited to a narrow range of wind speeds. Because of the all-weather and day-night capability, radar is now a common means of remote sensing oil spills.

Fig. 15.17 A VV polarized view of the same area of sea surface. Note that this polarization yields a slightly clearer image of sea surface details than that shown in Fig. 15.16

Radar Processing

Because radar detection of oil spills is so highly susceptible to false images, much work has taken place on means to differentiate oil slicks and false targets, often called look-alikes. These look-alikes include low wind areas, areas sheltered by land, rain cells, organic films, grease ice, wind fronts, up-welling zones, oceanic fronts, algae blooms, current shear zones, etc. [107]. The discussion in this subsection is relevant to both satellite and airborne SAR systems.

Several "automatic" systems have been designed for slick detection in the past [108, 109]. Limited testing with actual satellite output has shown that many false signals are present in most locations [110, 111]. Extensive effort on data processing appears to improve the chances of oil detection [112]. In recent years, automatic systems have given way to systems involving smart algorithms and manipulated by operators [113–115].

The most common way to eliminate wind-origin, look-alikes is to map the wind fields in the same coordinates as the radar data [112, 116]. The most common slick look-alike is low wind areas. One group of researchers used radar wind data calibrated to wind data from an ocean buoy to map oil seeps in the southern Gulf of Mexico [116].

Most researchers used some form of neural networks or fuzzy logic to assist in the discrimination of look-alikes and the intended targets [118–120]. Others used various forms of models such as range dependence models [121].

Topouzelis and co-workers developed several series of mathematical networks for differentiating slicks from look-alikes [122–126]. The basis of these networks is generally that oil slicks are imaged through a complex series of processes and conditions. Thus imaging is not a simple statistical manipulation. The same group developed a fuzzy classification to differentiate look-alikes from oil spills. The methodology involved four procedures. The first is the segmentation of the image into large image segments with different statistical values. In the second procedure, a detailed scale segmentation is carried out and statistical values of each segment compared to the threshold of the large segment it came from. Third, the dark portions are classified according to the properties of the surrounding areas. Finally, the dark areas are classified using knowledge bases. The group also examined the use of forward feed neural networks to discriminate slicks from look-alikes [122, 126]. Several topologies of forward feed neural networks were examined and none were better than others. The networks yielded classification accuracies as high as 91.3–93.6% for the given example. A recent work by Topouzelis used the inputs of shape texture, asymmetry, mean difference to neighbors, and power to the mean images in a neural network [107]. The workers used forward feed neural networks. It was found that the classification accuracy was 99.4% for the MLP network in the test case. Later, Topouzelis and coworkers used a method similar to that mentioned above to test a data set of 69 oil spills and 90 look-alikes [124]. They found that a combination of ten features out of a possible 25 features were most useful for discrimination. The ten features found to be best for discrimination are: perimeter, shape factor II, object mean value, ratio of the power to mean ratios, local area contrast ratio, mean border gradient, maximum border gradient, standard deviation border gradient, maximum border gradient, mean difference to neighbors and spectral texture. Use of these factors resulted in classification accuracies if 85.3% for oil spills and 84.4% for look-alikes.

A similar approach is to use a classification scheme that incorporates some of the same input parameters. Karantzalos and Argialas proposed a classification scheme involving processes and then a classification scheme. The first processing step involves filtering and levels [127]. The second step is segmentation of the images

to include all suspected slicks. The final step is to classify the potential slicks according to area, perimeter, shape complexity eccentricity, orientation, segment mean border gradient, inside segment standard deviation, and outside segment standard deviation.

Several researchers have used GIS databases to assist in the interpretation of SAR imagery [128–134]. The technique divides the area of interest into segments and notes data such as currents, proximity to land, wind, sea lanes, etc. These parameters are then correlated to the SAR images. For example, oil spills are much more likely under the correct wind conditions, in sea lanes and far from land. Tahvonen used data sets including wind speed and direction, sea surface temperature, heavy rain, and location of algae blooms to assist in the discrimination [128]. Muellenhoff proposed a dataset consisting of: wind information, sea surface temperature, chlorophyll-a-concentration, geostrophic currents, wave information, contextual background information, and existing oil spill databases [131]. The assigned influences were: wind speed – 30%, wind direction – 12%, Sea surface temperature – 14%, Chlorophyll-a-concentration – 10%, oil ports – 10%, and main traffic lines – 20%. Wave and current direction only accounted for 2% each.

Shu et al. used the density (concentration of the number of similar intensity points) to discriminate between oil and water [135]. A detection window is passed over all the pixels of the target image and thresholds are assigned to various spots. Then the pixels are assigned to either background or oil categories if there is a sufficient number of them (density) in the proximity. It should be noted that to be successful, this technique requires that the oil images are much larger than any oil look-alikes.

Migliaccio and group studied the processing of SAR images from an aircraft-based sensor [134, 136, 137]. It was noted that the main obstacle to analysis was speckle in the images. Speckle is caused by stray reflectances such as from rough seas. Speckle is also caused by random constructive and destructive interference. Since speckle is temporary, multi-look imaging is one way to decrease speckle by a large amount. Further processing can then be achieved by combining multi-look data with wind data, best obtained from satellite scatterometers. The technique proposed for multi-look data, is to divide the SAR imagery into sub-bands and then generating lower-resolution imagery. Then the images are averaged. This results in reduction of speckle. To process single-look data with high speckle content, filters are used. First speckle is removed and the ROA (ratio of average) filter is used. In both techniques, edge detection is used to find the actual limits of the slicks or look-alikes.

Marghany and co-workers used a fractal method to analyze SAR data [97, 138]. The images are broken into fractals and these fractals have dimensions which are different for oil spills and look-alikes. A further study under different wind speeds showed that there were differences only in the wide beam mode for low wind zones and current shear features between real oil slicks [138]. Further work showed that the fractal dimensions for the W1 (wide) mode of Radarsat I are about 1.7 for oil spills, 2.5 for low wind areas, 2.7 for look-alikes, 3.2 for sea surface roughness, and 3.7 for ships. These are similar but different for the narrow mode, S2. A similar approach was utilized by Danisi et al. [139].

Another method employed by researchers to separate oil slicks from look-alikes is to use textural analysis [140, 141]. Direct statistical methods are also employed. Tello et al. noted that an algorithm characterizing the border between oil spill candidates and the surrounding sea allows for good classification [141]. Lounis et al. used a measure of similarity between the local probability density function of clean water and of the dark area to be examined [142]. Comparing the two values is said to result in discrimination between oil and look-alikes. Pelizzari employed a similar technique using graph cuts to estimate a smoothness factor [143].

Ferraro et al. describe the development of an operational system for the Mediterranean Sea and show a procedure for the identification of oil spills as: (1) isolation and contouring of all dark signatures, (2) extraction of shape and backscattering contrast signatures, (3) test of these values against standard values, and (4) calculation of the probabilities of each patch [144, 145, 146].

Another series of techniques involves the use of two streams of information. Several researchers used both SAR and visible information from the MODIS (Moderate Resolution Imaging Spectroradiometer) satellites to discriminate between look-alikes and oil slicks [147]. The visible imagery is subject to false images, but not the same ones as SAR and thus discrimination can be achieved to a degree. Similarly, Sipelgas used visible imagery from the MODIS satellite to assist in discrimination of false images from oil slicks in the Gulf of Finland [148]. Adamo et al. used three streams for information: SAR data, MODIS, and MERIS data to discriminate look-alikes from actual spills [147].

Microwave Scatterometers

A microwave scatterometer is a device that measures the scattering of radar energy by a target. One radar scatterometer was flown over several oil slicks and used a low-power transmitter operating in the Ku band (13.3 GHz) [17]. The scatterometer detected the oil, but discrimination was poor. The "Heliscat," a device with five frequencies has been used to investigate capillary wave damping [95]. The advantage of a microwave scatterometer is that it has an aerial coverage similar to optical sensors and it can look at several incident angles. The main disadvantages include the lack of discrimination for oil and the lack of imaging capability.

Surface Wave Radars

It is possible to send radio waves along the sea using high frequency. The conductivity of the sea acts as a form of wave guide. These radars can be used to detect ships as far out as 500 km [149]. Since these are surface wave phenomena only

targets above the surface are detected, thus slicks may not be detected by this technique [150]. Modeling of the technique does not show whether there is potential for this method or not [151].

Interferometric Radar

Radars can be used to measure height, currents, and other surface elevation phenomena using interferometric techniques. Some radar systems on aircraft are fitted for this application such as the Government of Canada Convair 580. This can also be carried out in space using two satellites traveling in tandem. One research group employed the tandem satellite pairs of ERS-2 and ENVISAT to carry out such work but there are no reports on the use on oil spills [152].

Slick Thickness Determination

There has long been a need to measure oil slick thickness; this need has been expressed both within the oil spill response community and among academics in the field. There are presently no reliable methods, either in the laboratory or the field, for accurately measuring oil-on-water slick thickness. The ability to do so would significantly increase understanding of the dynamics of oil spreading and behavior. Knowledge of slick thickness would make it possible to determine the effectiveness of certain oil spill countermeasures including dispersant application and in situ burning. Indeed, the effectiveness of individual dispersants could be determined quantitatively if the oil remaining on the water surface following dispersant application could be accurately measured [153, 154, 155].

Visual Thickness Indications

A very important tool for working with oil spills has been the relationship between appearance and thickness. Careful study of the literature on this and comparing this to field experience shows that there is limited potential to scale thicknesses to visual appearance [8]. The only physical-based appearance that occurs are thicknesses of about 0.7–2.5 μm at which the rainbow colors appear as a result of multiple constructive and destructive interferences by light. Table 15.1 shows summation of the best knowledge on this phenomenon. Rainbow sheens are the only color appearance that has a physical slick thickness associated with it.

Lehr argues that the visual indications of slick thickness are so poor as to not allow for any slick thickness estimation [156]. In particular he notes that the Bonn agreement thickness code provides insufficient proof for greater thicknesses as it

Table 15.1 Relationship of thickness to appearance

	Visibility thresholds (μm)				
	Minimum/silvery	Rainbow	Darkening colors	Dull colors	Dark
Typical thickness	0.1	0.6[a]	0.9	2.7	8.5

[a]This is the only physical-based appearance phenomenon

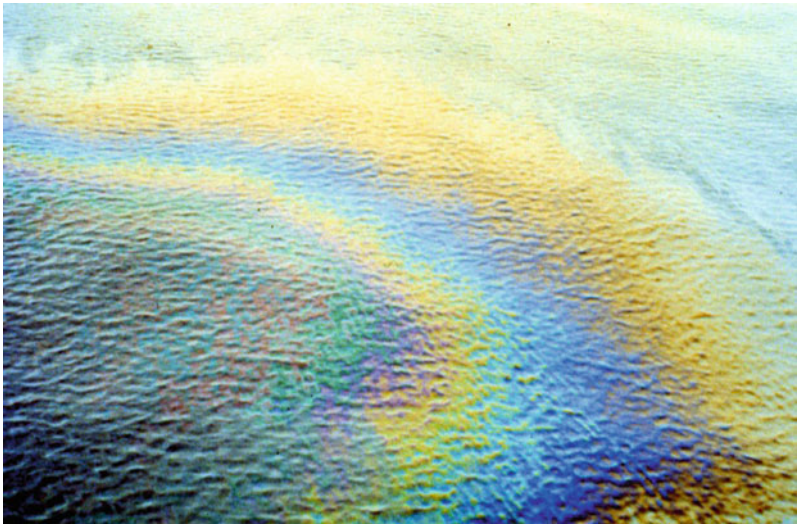

Fig. 15.18 A picture of a rainbow sheen. This is the only spill thickness that has a physical explanation

purports to. Lehr suggests that the solution to this is simply to use two thickness regimes, sheen and thicker oil and not to estimate slick volumes from this (Fig. 15.18).

Slick Thickness Relationships in Remote Sensors

A number of investigators tried to correlate slick thickness with appearance in various remote sensing instruments. Hollinger and Mennella conducted a series of eight controlled oil spills off Virginia to investigate the use of microwave radiometry to delineate oil spills [157]. They used 19.4 and 69.8 GHz radiometers on the spills. Measurements using sorbents were used to calibrate the radiometer. It was noted that the sheens typically had a thickness of 2–4 μm (considered today to be very thick). It was found that 90% of the oil was in 10% of the slick area and that the microwave threshold was about 0.1 mm (100 μm).

A series of experiments was carried out in 1979 to evaluate infrared (IR) and side-looking airborne radar (SLAR) for oil spill detection [158]. The imagery was correlated against visual and sorbent measurements, which were used to derive a thickness estimate. It was concluded that the infrared threshold was between 25 and 50 μm and for SLAR 100 nm. Further, manipulation of data showed that a mass balance could be achieved if the thickness at which the infrared showed oil to be colder at the sea occurred at 100 μm and for the heated portion of the oil at 1,000 μm.

The United Kingdom conducted Isowake Experiments in 1982 [159, 160]. On the basis of estimations and calculations it was concluded that the lowest detectable slick thickness for IR was between 10 and 50 μm, whereas hot spots in the IR image could be as much as 1,000 μm.

MacDonald used photography from the space shuttle to define up to 124 slicks in an area of the Gulf of Mexico, offshore Louisiana [161]. Similarly, a thematic image from Landsat showed at least 66 slicks in one large area. Some of the thickness relationships were based on unpublished experimental data from Duckworth.

Brown et al. conducted experiments to measure the visibility of oil slicks. The observers and an ultraviolet (UV) and visible camera were mounted in a crane basket 30 m over the slick [162]. It was found that the detection ability decreased by over 50% for most oils and for the cameras when the angle was changed from 90° to 55° from the horizontal (equivalent incidence angle of 0° to 35°). Detectability degraded to 70% and sometimes to nil as the viewing angle was decreased past 55° through 35°. Brown et al. conducted several experiments to ascertain the relationship between thickness of slicks and the density (or intensity) of the infrared image [41]. The thicknesses of oil varied between 1 and 10 mm and thicknesses were measured using an acoustic system from under water. No relationship between slick thickness and infrared brightness was found.

Specific Thickness Sensors

The suppression of the water Raman peak in laser fluorosensor data has not been fully exploited or tested. This technique may work for very thin slicks, but not necessarily for thick ones, at least not with a single excitation frequency. Attempts have been made to calibrate the thickness appearance of infrared imagery, but also without success. It is suspected that the temperatures of the slick as seen in the IR are highly dependent on oil type, sun angle, and weather conditions. It may not be possible to use IR as a calibrated tool for measuring thickness. As accurate ground-truth methods do not exist, it is very difficult to calibrate existing equipment [163, 164]. The use of sorbent techniques to measure surface thickness yields highly variable results [153]. As noted in the section on microwave radiometers, the signal strength measured by these instruments can imply one of several thicknesses.

This methodology does not appear to have potential, other than for measuring relative oil thickness.

A variety of electrical, optical, and acoustic techniques for measuring oil thickness has been investigated [163, 164]. Two promising techniques were pursued in a series of laboratory measurements. In the first technique, known as "thermal mapping," a laser is used to heat a region of oil and the resultant temperature profiles created over a small region near this heating are examined using an infrared camera [164]. The temperature profiles created are dependent on the oil thickness. A more promising technique involves laser acoustics [165–167]. The Laser Ultrasonic Remote Sensing of Oil Thickness (LURSOT) sensor consists of three lasers, one of which is coupled to an interferometer to accurately measure oil thickness [167–172]. The sensing process is initiated with a thermal pulse created in the oil layer by the absorption of a powerful CO_2 laser pulse. Rapid thermal expansion of the oil occurs near the surface where the laser beam was absorbed, which causes a step-like rise of the sample surface as well as an acoustic pulse of high frequency and large bandwidth ($\sim$15 MHz for oil). The acoustic pulse travels down through the oil until it reaches the oil–water interface where it is partially transmitted and partially reflected back towards the oil-air interface, where it slightly displaces the oil's surface. The time required for the acoustic pulse to travel through the oil and back to the surface again is a function of the thickness and the acoustic velocity of the oil. The displacement of the surface is measured by a second laser probe beam aimed at the surface. Motion of the surface induces a phase or frequency shift (Doppler shift) in the reflected probe beam. This phase or frequency modulation of the probe beam can then be demodulated with an interferometer [172]. The thickness can be determined from the time of propagation of the acoustic wave between the upper and lower surfaces of the oil slick. This is a very reliable means of studying oil thickness and has great potential. Laboratory tests have confirmed the viability of the method and a test unit has been flown to confirm its operability [163]. Figure 15.19 shows the first airborne absolute measurement of slick thickness.

Several attempts have been made to measure thickness by using visible spectral imaging. As there is no visual indications other than the rainbow sheen area around 0.8 μm, these efforts are wasted [173]. Similarly, several workers have tried to use the assumption that the oil layer is transparent, therefore the differences in reflection from the water surface and the top of the oil layer could yield a thickness measurement [174, 175]. Unfortunately, this oil is not transparent in the visible ranges, therefore such methods do not work.

Integrated Airborne Sensor Systems

Increasingly, a number of different types of airborne oil spill remote sensors are being consolidated into sensor systems. The reason for this integration is to take

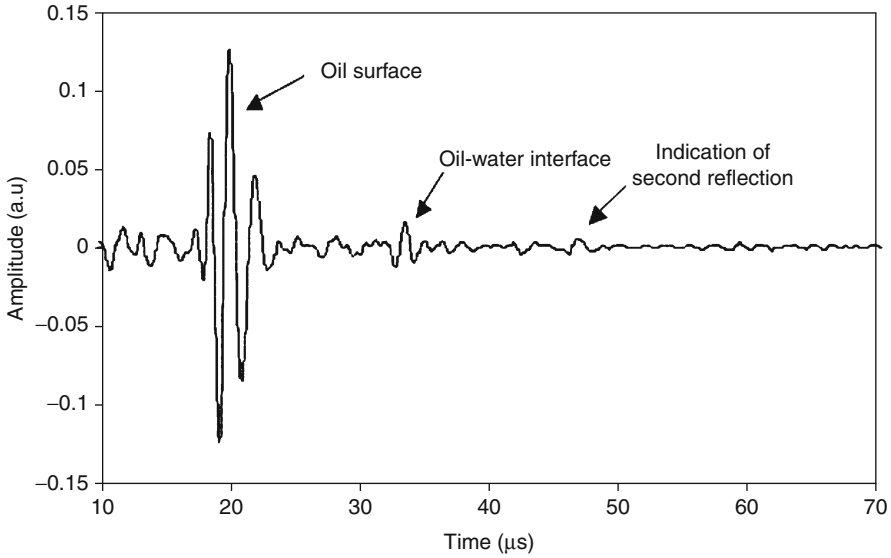

Fig. 15.19 The signal from a three-laser thickness sensor. The time corresponds to a thickness of about 6 mm. This was measured by a prototype sensor mounted in an aircraft and flying over containers with various thicknesses of oil on water

advantage of the different information provided by each of the specific sensors and combine the information to provide a more complete and comprehensive information product. Although each of the individual sensors has specific inherent weaknesses such as false detections, these false detections are often different for each sensor type, hence a consolidation of information can help resolve and remove some of the uncertainties that exist from a single data source. Furthermore, additional information such as the relative thickness of the oil slick can be deduced from the overlaying of imagery from several sensor types. Although the absolute thickness of an oil slick remains the subject of continued research and scientific opinion, the ability to locate the thicker portions of the slick is essential in terms of operational spill cleanup and response. In addition to the integration of a number of remote sensors into a sensor system, information from other sources such as marine vessel traffic surveillance systems (i.e., automatic identification system, AIS) can be integrated and can play an essential role in identifying the source of the marine pollution.

Two commercially available airborne marine oil spill remote sensing systems are the MEDUSA and the MSS 6000 [176, 177]. MEDUSA incorporates a number of sensor technologies such as laser fluorosensors, infrared/ultraviolet line scanners, forward-looking infrared sensors, microwave radiometers, side-looking airborne radar systems and camera systems, as well processing software into a flexible real-time data acquisition and processing system. The data from the various sensors are geo-referenced and fused with information from AIS and marine surveillance radars into a GIS-based display output format. The processing software is known

as the Oil Spill Scene Analysis System (OSSAS) and allows for the extraction of features such as the area of oil coverage including areas of intermediate and thicker portions of the slick. The MSS 6000 Maritime Surveillance System is comprised of a flexible suite of sensors such as side-looking airborne radar systems, infrared/ultraviolet line scanners, forward-looking infrared sensors, microwave radiometers, and camera systems, along with data processing and mission management software in order to perform the oil spill remote sensing surveillance task. The MSS 6000 also focuses on sensor integration and includes navigation and marine search radar inputs. All sensor data, imagery, slick targets, vessels etc. are annotated using navigation data from a single source to form an integrated part of a Geographic Information System (GIS). Both the MEDUSA and MSS 6000 can distribute their data in near-real time via direct downlink or satellite communications to vessels or shore-based communications centers. A large number of maritime nations are now employing integrated airborne sensor systems [178, 179].

Satellite Remote Sensing

The use of optical satellite remote sensing for oil spills has been attempted several times. The slick from the IXTOC I well blowout in Mexico was detected using GOES (Geostationary Operational Environmental Satellite) and by the AVHRR (Advanced Very High Resolution Radiometer) on the LANDSAT satellite [18]. A blowout in the Persian Gulf was subsequently detected. The large EXXON VALDEZ slick was detected on SPOT (Satellite Pour l'Observation de la Terre) satellite data [180]. Oiled ice in Gabarus Bay resulting from the KURDISTAN spill was detected using LANDSAT data [181, 182]. Several workers were able to detect the Arabian Gulf War Spill in 1991 [183–186]. The HAVEN spill near Italy was also monitored by satellite [187]. A spill in the Barents Sea was tracked using an IR band on NOAA 10 [188]. It is significant to note that, in all these cases, the position of the oil was known and data had to be processed to actually see the oil, which usually took several weeks. Newer findings show that the ability to detect oil may be a complex function of conditions, oil types and view angles [189–191].

There are several problems associated with relying on satellites operating in optical ranges, for oil spill remote sensing. The first is the timing and frequency of overpasses and the absolute need for clear skies to perform optical work [192]. The chances of the overpass and the clear skies occurring at the same time give a very low probability of seeing a spill on a satellite image. This point is well illustrated in the case of the EXXON VALDEZ spill [193]. Although the spill covered vast amounts of ocean for over a month, there was only one clear day that coincided with a satellite overpass, and that was on April 7, 1989. Another disadvantage of satellite remote sensing is the difficulty in developing algorithms to highlight the oil slicks and the long time required to do so. For the EXXON VALDEZ spill, it took over 2 months before the first group managed to "see" the oil slick in the satellite

imagery, although its location was precisely known. Recently several workers have attempted to use MODIS visible data to detect oil spills [194, 195]. These techniques generally rely on ancillary data such as suspected position or other satellite data, to be successful. However, Srivastava and Singh used only MODIS to detect known oil spills in Lake Maracaibo, Venezuela [196]. First, the use of L1B data visually did show oil, however, uncorrected features at 469, 555 and 645 nm showed significant indications of oil. Further study showed that the ratio of the difference and sum at 645 and 555 nm, normalized by 469 nm provided the best results. More recently, several workers used MODIS and other satellite data to detect the oil during the Macondo spill in the U.S. Gulf of Mexico [197].

Li et al. (highlighted the differences between optical and radar satellites [198]. This research group studied the Montara spill in the Timor Sea using the ALOS PALSAR (L-band radar), the Envisat ASAR (C-band radar) and the MODIS (AQUA – color visible) satellite data. The ALOS PALSAR did function, but as expected from L-band radar was not clear. The Envirsat ASAR data was the clearest and provide useful imagery always. The visible data from MODIS function well only during completely clear skies, but most of the time did not yield useful images. Cloud interference in the latter was cited as a reason, but the lack of specific oil coloration should have also been noted.

There is some information on slicks available from sensor angular orientation. For example, Chust and Sagarminaga used the Multi-angle Imaging SpectroRadiometer (MISR) sensors aboard a satellite to detect oil spills on Lake Maracaibo, Venezuela [199]. This sensor uses nine push-broom cameras at fixed angles from nadir to 70.5° to examine particular surfaces. A comparison of this angular sensor shows that better contrast was obtained than a simple nadir camera on another satellite. Data analysis showed that oil spills appear in greater contrast in those view angles affected by sun glitter because of the presence of oil.

IR data from satellite has been used to map the land oil pollution in Kuwait [200]. It was found that the old hydrocarbon-contaminated areas showed as much as 10°C difference from the surrounding land. Ground-truthing was used extensively in compiling the data. Casciello also made an attempt to use IR imagery from the thermal infrared region of the AVHRR satellite to locate known oil spills [201].

Radar satellites, including ERS-1 and -2, Radarsat-1 and 2, and ENVISAT, have usefulness for detecting large offshore spills and for spotting anomalies [86, 202–204]. Radarsat has been used for detecting oil seeps and smaller spills resulting from an oil barge [205, 206]. The relative location of these smaller slicks was known before the detection. A novel application of Radarsat has been the study of oil lakes in the deserts of Kuwait [207]. Radar satellites are now used routinely by a number of nations to provide imagery for larger spills and to give indications of ship discharges. ERS-1 and 2 have been used for mapping of oil spills in the Caspian Sea [208]. Fortuny describes the use of ERS-2 and ENVISAT to provide imagery during the Prestige incident off Spain [209]. Torres Palenzuela and co-workers used two ASAR (Advanced SAR) images from the Envisat satellite to study the same Prestige spill off Spain [210]. Using several techniques that were readily-available such as filtering and comparison to GIS data of the areas, several

Table 15.2 Current and future satellite-borne SAR sensors

Satellite	Launch date	Owner/operator	Band
ERS-1	1991 (end 2000)	European Space Agency	C
ERS-2	1995	European Space Agency	C
RADARSAT-1	1995	Canadian Space Agency	C
RADARSAT-2	2007	Canadian Space Agency	C
ENVISAT (ASAR)	2002	European Space Agency	C
ALOS (PALSAR)	2006 (end 2011)	Japan Aerospace Exploration Agency	L
TerraSAR-X	2007	German Aerospace Center	X
Tandem-X	TBD (was scheduled for 2009)	German Aerospace Center	X
Cosmos Skymed-1/2	2007	Italian Space Agency	X
TecSAR	2008	Israel Aerospace Industries	X
Sentinel-1	2012	European Space Agency	C
RADARSAT-Constellation (3-satellites)	2014	Canadian Space Agency	C

slicks were identified. These slicks were confirmed by recorded sightings from helicopters and ships.

Several countries have instituted satellite monitoring systems for oil pollution [211–213]. Many of these use processing methods as described above. Extensive programs are in place in the Baltic Sea, North Sea and English Channel [145]. There are now programs in the Black, Caspian and Azov Seas [213, 214]. Canada has had a program in place for several years [215]. The Mediterranean Sea has had such a program for a long time [144, 145]. A constellation of monitoring satellites is proposed for the Mediterranean Sea.

In recent years there have been a number of new satellite-borne SAR sensors launched, see Table 15.2. While one of these sensors, RADARSAT-2, operates in the traditional C-band, TerraSAR-X and Cosmos Skymed operate in the X-band, and the PALSAR sensor on ALOS operates in the L-band. As noted above, X-band is the preferred band for oil spill remote sensing in terms of Bragg scattering. All four of these new SAR satellites have polarimetric imaging modes (some are experimental vs operational modes) and much higher spatial resolution (down to 3 m) which may have application for oil spill remote sensing. RADARSAT-2, like its predecessor is an operational commercial satellite that can be tasked to respond to emergency situations like major oil spills. The time required to task RADARSAT-2 in emergency mode is now 4 h, which is a large improvement from the 12 h required to task its predecessor. As noted above VV polarization provides a superior clutter to noise ratio (CNR) over HH polarization for oil spill detection [212]. RADARSAT-2 is fully polarimetric and there is interest in investigating whether a dual polarization ScanSAR mode utilizing VV/VH polarizations will work for oil and ship detection respectively as part of the Integrated Satellite Tracking of Pollution (ISTOP) program [215]. The increased number of SAR satellites plus the plans to operate constellations of small satellites

like Cosmos (Constellation of Small Satellites for Mediterranean basin Observation) will provide increased temporal coverage with revisit times down to a few hours in some circumstances. The opportunity for increased frequency of image collection should prove useful to the oil spill response community. Figures 15.12–15.15 show the use of radar satellites and the look-alikes to oil that sometimes appear in the images.

Oil Under Ice Detection

The difficulties in detecting oil in or under ice are numerous. Ice is never a homogeneous material but rather incorporates air, sediment, salt, and water, many of which may present false oil-in-ice signals to the detection mechanisms. In addition, snow on top of the ice or even incorporated into the ice adds complications. During freeze-up and thaw in the spring, there may not be distinct layers of water and ice. There are many different types of ice and different ice crystalline orientations. This is a separate field and readers may consult the literature [216].

Underwater Detection and Tracking

Many different techniques have been tried for underwater oil detection. First, the division should be made between oil in the water column or floating on a pycnocline, and oil on the bottom. Quite different physics and conditions can apply to these different situations.

Several parties have tried to use standard sonars to detect submerged oil on the bottom. Oil on the bottom can appear as a softer surface than ordinary bottom sediment. The problem arises in that vegetation on the bottom also appears similar and thus many false positives arise. In the water column, sonar can be useful as it can locate intermediate oil on pycnoclines; however, there is no unique signature and there are often weeds and other debris on pycnoclines. Wendelboe et al. report on tests using a 200 and 400 kHz (dual-frequency) multi-beam system [217]. The contributing signal is the lower acoustic reflectivity of the oil than typical bottom geological formation or the better reflection than weed beds. Wendelboe et al. used the back scatter signals from several tests to develop algorithms for oil detection. This was tested in a tank with a 90% success rate and a 23% false detection rate [218]. Hansen reviewed various systems noting that the narrow-scan sonar systems showed promise [219].

Oil on the bottom has successfully been mapped by underwater cameras, often mounted on sleds [220–222]. The problems with this technique are the bottom visibility – often insufficient to discriminate, and the difficulty in towing the camera vehicle as slow as 1 knot, the necessary speed. Pfeifer et al. were successful in employing mosaics of photographs to determine the aerial extent of oil on the sea floor [221, 222].

A low-technology approach had been historically employed. Heavy oil, such as would sink, often adheres to oil snares or pom-poms, which are polypropylene strips mounted as a cheerleaders' pom-pom. These can be mounted on a beam and towed over the bottom and then raised periodically to see if oil has adhered [220]. Alternatively they can be mounted on an anchor with a marker buoy. These are then raised periodically to check if the subsurface oil has contacted them.

Camilli et al. have successfully applied mass spectrometry to the detection of sunken heavy oil (Fuel Oil #6) [223]. Using the small and enclosed mass spectrometer, TETHYS, the low molecular weight hydrocarbons coming from sunken oil masses are monitored. The mass spectrometer is mounted in a submersible which is driven over the sea floor. The exact position of the submersible is monitored closely using an acoustic positioning system on the surface. Signals then can be correlated closely to the position on the seafloor. Three ion peaks of m/z 43, 41, 27 are monitored to establish hydrocarbon presence. Tests show that the ion peaks provide sensitivity as low as 0.4 ppb. This is fully sufficient to monitor sunken oil. Tests were conducted in a test tank and latter over actual spills in the Gulf of Mexico. The technique was able to find concentrations of sunken oil and place the locations within 1 m. The tests in the Gulf of Mexico were conducted at depths of 200 m and confirmed by using cameras on the submersible.

Small Remote-Controlled Aircraft

Several parties have suggested remote-controlled aircraft to provide more economical solutions for response personnel [224–226]. In fact, remote-controlled aircraft have been used by a number of parties for monitoring a variety of pollutants since the 1970s [226].

Belgium employs a UAV of the B-Hunter class to routinely monitor its portion of the North Sea [225]. This is a large UAV which has visible and IR camera systems aboard. The unit has a 10-h endurance over the targets.

A variety of commercial platforms are now available which can provide carriage for small sensors such as visible and IR cameras. Further, automatic navigation technology has now made these units, especially helicopters, very much easier to fly than in previous years.

Real-Time Displays and Printers

A very important aspect of remote sensing is the production of data so that operations people can quickly and directly use it. Real-time displays are important so that remote sensor operators can adjust instruments directly in flight and provide

information quickly on the location or state of the spill. A major concern of the client is that data be rapidly available [227]. An additional concern is that the data from various sensors be available in a combined or fused form [87]. Further there is a need to correct this data for aircraft motion and to annotate the data with time and position. At this time, existing hardware and software must be adapted as commercial off-the-shelf equipment for directly outputting and printing sensor data is not yet available.

One means to overcome some of these problems is the development of entire packages for oil spill remote sensing. Robbe and Hengsterman describe the MEDUSA system which consists of an integrated system with IR, UV, SLAR, Microwave Radiometer, laser fluorosensor, and navigation systems [2].

Routine Surveillance

One of the applications of oil spill remote sensing equipment is to detect and map slicks resulting from illegal discharges of oil from ships and offshore platforms. Historically this has always been performed using visual techniques, but in the past decade has been increasingly turned over to aircraft with some instrumentation. Typical instrumentation includes a SLAR, IR/UV scanner, and cameras. This sensor package is economical compared to more ideal packages and greatly improves capability beyond just visual observation. Limitations include limited ability to "look into" ship wakes, limited night operations, and inability to positively identify oil slicks. Recent additions such as improved SLAR systems, better display systems, and nighttime cameras have added to the capability, but do not overcome these limitations.

There are many efforts to perform surveillance of illegal discharges. Most existing operative remote systems are dedicated to this function. These are estimated to be around 35, most of these around Europe [2, 179, 228]. There are intensive programs in some areas, for example, in the North Sea. Carpenter reports on the 18-year program of surveillance in the North Sea [229]. Some interesting statistics are noted. In 2004, 418 unidentified slicks were found, 65 slicks from oil rigs and 57 slicks from ships. In 2004, 3,314 h were flown in daylight and 594 in darkness. In the same year, 91 slicks were found in the darkness and 449 in daylight.

Ferraro et al. describe a routine surveillance program using satellite and aircraft data for the Mediterranean Sea [145]. Future work in the Mediterranean Sea proposes a cluster of radar satellites to constantly monitor oil pollution [230].

A word about aircraft is suitable here. A variety of aircraft are deployed as remote sensing aircraft. Typically different types are deployed for routine surveillance and for remote sensing research. The latter requires flexibility in mounting sensors and in access to the outside of the aircraft.

Future Directions

Advances in sensor technology will continue to drive the use of remote sensors as operational oil spill response tools in the future. Cameras and thermal infrared cameras that offer high sensitivity are cheap and plentiful. This improvement not only reduces the size and complexity of the sensor, but also the cost. In the next decade, advances in laser technology, in particular diode-pumped solid-state and possibly excimer lasers, will greatly reduce the size and energy consumption of laser-based remote sensors. This will promote the use of these sensors in smaller, more economical aircraft within the budget of many more regulatory agencies and maritime countries. Rapidly improving computer capabilities will allow for true real-time processing. At the present time and for the foreseeable future, there is no single "Magic Bullet" sensor that will provide all the information required to detect, classify, and quantify oil in the marine and coastal environment. An example of the improvement in recent years is that of the night vision camera. It is now possible to use this sensor to visualize oil at night.

It will require the combined advances in sensor technologies and computer capabilities noted above to gather, integrate, and merge several sources of data into a real-time format, usable by response crews in the field. If this type of information can be made available to response crews in a short enough time frame following a spill incident, then it can be used to lessen the potentially disastrous effects of a major oil spill on the marine ecosystem.

As technology in remote-controlled systems evolve, it is possible to employ such technology in oil spill remote sensing. First efforts in the deployment of remote-controlled sensing aircraft have posted success and will, no doubt, be expanded in the future [231].

Recommendations are based on the above considerations and include economy as a major factor. Table 15.3 shows the considerations related to the development state, cost, and use of the sensor. The laser fluorosensor offers the only potential for discriminating between oiled and unoiled weeds or shoreline, and for positively identifying oil pollution on ice, among ice and in a variety of other situations. This instrument, however, is large and expensive. A cheap sensor recommended for oil spill work is an infrared camera. This is the cheapest but undiscriminating device. This is the only piece of equipment that can be purchased off-the-shelf. All other sensors require special order and, often, development. Radar, although low in priority for purchase, offers the only potential for large area searches and foul weather remote sensing. Most other sensors are experimental or do not offer good potential for oil detection or mapping. Any sensor package should include a real-time printer and display, and a downlink.

In order to respond effectively to major marine oil spills, it is recommended that one employs a combination of airborne and satellite-borne sensor systems. Improvements in the resolution of satellite-based systems, particularly SAR systems combined with the increased number of such systems and the ability to steer them to image the area of the oil spill will lead to their increased use in

Table 15.3 Attributes for airborne sensor selection

Sensor	State of development	Amount of experience in use	Specific to oil	Immunity to false targets	Typical coverage (km)	Acquisition cost range k$	Aircraft physical requirements
Still Camera	High	High	Poor	Poor	0.25–2	1–5	No
Video	High	High	Poor	Poor	0.25–5	1–10	No
Night Vision Camera	Medium	Medium	Poor	Poor	0.25–2	5–20	No
IR Camera (8–14 μm)	High	Medium	Medium	Medium	0.25–2	20–50	No
UV Camera	Medium	Medium	Poor	Poor	0.25–2	4–20	No
Multispectral Scanner	Medium	Medium	Poor	Poor	0.25–2	100–200	Some
Radar	High	High	Medium	Poor	5–50	1,200–8,000	Yes-Dedicated
Microwave Radiometer	Medium	Low	Medium	Medium	1–5	400–1,000	Yes-Dedicated
Laser Fluorosensor	Medium	Low	Good	Excellent	0.01–2	300–1,000	Yes-Dedicated

a tactical role. Being capable of imaging vast areas of the open ocean will ensure that satellite-borne sensors will also continue to be used in a strategic manner. There are a number of commercially available airborne sensor systems which provide near-real-time information on oil slick location and indications of thicker areas of the pollution in an easily interpretable graphical manner. These airborne sensor systems are currently being employed by a large number of maritime nations in conjunction with satellite-based sensor systems.

There are an increasing number of satellite-borne SAR and optical sensors, some of which currently or soon will operate in constellations to provide increased coverage of the Earth's surface. These enhanced capabilities will allow for the possible use of these sensors in a tactical mode of operation. In spite of these increased capabilities, there remains an essential role for airborne oil spill remote sensing platforms. The ability to collect and deliver real-time oil slick location information will ensure the continued use of airborne systems in spite of their high operational costs.

If this type of real-time oil spill remote sensing information can be made available to response crews in a short enough timeframe following a spill incident, the information can be used to mitigate the potentially disastrous effects of a major oil spill on the marine ecosystem.

Bibliography

1. NAS (2003) Oil in the sea. National Academy of Sciences, Washington, DC
2. Robbe N, Hengstermann T (2006) Remote sensing of marine oil spills from airborne platforms using multi-sensor systems. In: Brebbia CA, Antunes do Carmo JS (eds) Water pollution VIII: modelling, monitoring and management. WIT Press, Southampton, p 347
3. Serra-Sogas N, O'Hara PD, Canessa R, Keller P, Pelot R (2008) Visualization of spatial patterns and temporal trends for aerial surveillance of illegal oil discharges in western Canadian marine waters. Mar Pollut Bull 56:815
4. Fingas M, Brown CE (2011) Oil spill remote sensing: a review. In: Fingas M (ed) Oil spill science and technology. Gulf, New York, pp 111–169 (Chap 6)
5. Fingas M, Brown CE (2005) Review of oil spill remote sensing. In: Proceedings of the 8th international conference on remote sensing for marine and coastal environments, Altarum
6. Hengstermann T, Robbe N (2008) Airborne oil spill remote sensing. Hydro Int 10:2008
7. Jha MN, Levy J, Gao Y (2008) Advances in remote sensing for oil spill disaster management: state-of-the-art sensors technology for oil spill surveillance. Sensors 8:236
8. Fingas MF, Brown CE, Gamble L (1999) The visibility and detectability of oil slicks and oil discharges on water. Arctic Mar Oilspill Progr Tech Sem 2:865
9. Brown CE, Fingas MF (2009) The latest developments in remote sensing technology for oil spill detection. In: Proceedings of the Interspill 2009, Marseille
10. Krol T, Stelmaszewski A, Freda W (2006) Variability in the optical properties of a crude oil-seawater emulsion. Oceanologia 48:203
11. Evdokimov IN, Losev AP (2007) Potential of UV-visible absorption spectroscopy for characterizing crude petroleum oils. Oil Gas Bus 1
12. Otremba Z, Piskozub J, Król T (2003) Modelling the reflectance of sea areas polluted with oil emulsion. Fresenius Environ Bull 12(9):1109–1113

13. Otremba Z, Piskozub J (2001) Modelling of the optical contrast of an oil film on a sea surface. Opt Express 9(8):411–416
14. Otremba Z, Piskozub J (2000) The modification of light flux leaving a wind-roughened, oil covered sea surface example of computations for shallow seas. Oceanol Stud 29(1):117–133
15. Hong SI, Shin I (2010) Nightime detection of oil spills on the sea surface using spaceborne infrared images. Korea Meteorological Administration
16. Ma L, Li Y, Liu Y (2009) Oil Spill monitoring based on its spectral characteristics. Environ Forensic 10:317
17. O'Neil RA, Neville R, Thompson V (1983) The arctic marine oilspill program (AMOP) remote sensing study. Environment Canada Report EPS 4-EC-83-3, Ottawa
18. Brown HM, Bittner JP, Goodman RH (1996) The limits of visibility of spilled oil sheens. In: Proceedings of the second thematic international airborne remote sensing conference and exhibition, ERIM conferences, San Francisco, vol III, p 327
19. Taylor S (1992) 0.45 to 1.1 μm spectra of Prudhoe crude oil and of beach materials in Prince William Sound, Alaska. CRREL Special Report No. 92–5. Cold Regions Research and Engineering Laboratory, Hanover
20. Huang M, Yu Y, Zhang SJ, Qi X (2008) Analysis of water spectral features of petroleum pollution and estimate models from remote sensing data. SPIE 7123:712312
21. Ahmed S, Gilerson A, Oo M, Zhou J, Chowhardy J et al (2006) The polarization properties of reflectance from coastal waters and the ocean–atmosphere system. SPIE 6360:636003
22. Carnesecchi F, Byfield V, Cipollini P, Corsini G, Diani M (2008) An optical model for the interpretation of remotely sensed multispectral images of oil. SPIE 7105:710504
23. Bianchi R, Cavalli RM, Marino CM, Pignatti S, Poscolieri M (1995) Use of airborne hyperspectral images to assess the spatial distribution of oil spilled during the Trecate blow-out (Northern Italy). SPIE 2585:352
24. Bagheri S, Stein M, Zetlin C (1995) Utility of airborne videography as an oil spill-response monitoring system. In: Cheremisinoff PN (ed) Encyclopedia of environmental control technology. Gulf, Houston, p 367
25. Brown CE, Fingas MF, Marois R (2004) Oil spill remote sensing: laser fluorosensor demonstration flights off the east coast of Canada. Arctic Mar Oilspill Progr Tech Sem 317
26. Brown CE, Fingas MF, Marois R (2005) Oil spill remote sensing flights in the coastal waters around Newfoundland. In: Proceedings of the eighth international conference on remote sensing for marine and coastal environments, Altarum
27. Palmer D, Borstad GA, Boxall SR (1994) Airborne multi spectral remote sensing of the January 1993 Shetlands oil spill. In: Proceedings of the second thematic conference on remote sensing for marine and coastal environments: needs, solutions and applications. ERIM, Ann Arbor, vol II, p 546
28. Wadsworth A, Looyen WJ, Reuter R, Petit M (1992) Aircraft experiments with visible and infrared sensors. Int J Remote Sens 13:1175
29. Wang D, Gong F, Pan D, Hao Z, Zhu Q (2010) Introduction to the airborne marine surveillance platform and its application to water quality monitoring in China. Oceanol Sin 29:33
30. Locke C, White M, Michel J, Henry C, Sellars JD, Aslaksen ML (2008) Use of vertical digital photography at the Bayou Perot, LA, spill for oil mapping and volume estimation. In: Proceedings of the IOSC 2008, Savannah, p 127
31. Stelmaszewski A, Krol T, Toczek H (2009) Light scattering in Baltic crude oil – seawater emulsion. Oceanologia 51:405
32. Hurford N (1989) Review of remote sensing technology. In: Lodge AE (ed) The remote sensing of oil slicks. Wiley, Chichester, p 7
33. Goodman RH (1989) Application of the technology in North America. In: Lodge AE (ed) The remote sensing of oil slicks. Wiley, Chichester, p 39
34. Belore RC (1982) A device for measuring oil slick thickness. Spill Tech News 7:44

35. Neville RA, Thompson V, Dagg K, O'Neil RA (1979) An analysis of multispectral line scanner imagery from two test spills. In: Proceedings of first workshop sponsored by working group I of the pilot study on the use of remote sensing for the control of marine pollution, NATO challenges of modern society, p 201
36. Bolus RL (1996) Airborne testing of a suite of remote sensors for oil spill detecting on water. In: Proceedings of the second thematic international airborne remote sensing conference and exhibition. ERIM, Ann Arbor, vol III, p 743
37. Salisbury JW, D'Aria DM, Sabins FF (1993) Thermal infrared remote sensing of crude oil slicks. Remote Sens Environ 45:225
38. Hover G (1994) Testing of infrared sensors for U.S. Coast Guard oil spill response applications. In: Proceedings of the second thematic conference on remote sensing for marine and coastal environments: needs, solutions and applications. ERIM, Ann Arbor, vol I, p 47
39. Grierson IT (1998) Use of airborne thermal imagery to detect and monitor inshore oil spill residues during darkness hours. Environ Manage 22:905
40. Shih W-C, Andrews AB (2008) Infrared contrast of crude-oil-covered water surfaces. Opt Lett 33:3019
41. Brown HM, Baschuk JJ, Goodman RH (1998) The limits of visibility of spilled oil sheens. Arctic Mar Oilspill Progr Tech Sem:805
42. Clark RN, Swayze GA, Leifer I, Livo KE, Lundeem S et al (2010) A method for qualitative mapping of thick oil using imaging spectroscopy. United States Geological Survey. http://pubs.usgs.gov/of/2010/1101/
43. Leifer IR, Clark RN, Swayse G, Roberts D, Kokaly R et al (2011) Imaging spectroscopy of the deepwater horizon spill: a 21st century oil spill response (in press)
44. Goodman RH (1988) Simple remote sensing system for the detection of oil on water. Environmental Studies Research Fund Report Number 98, Ottawa
45. Brown CE (2011) Laser fluorosensors. In: Fingas MF (ed) Oil spill science and technology. Gulf, Oxford, pp 171–184
46. Brown CE, Fingas MF, An J (2001) Laser fluorosensors: a survey of applications and developments of a versatile sensor. Arctic Mar Oilspill Progr Tech Sem 1:485
47. Brown CE, Nelson R, Fingas MF, Mullin JV (1997) Airborne laser fluorosensing: overflights during lift operations of a sunken oil barge. In: Proceedings of the fourth thematic conference on remote sensing for marine and coastal environments. ERIM, Seattle, vol I, p 23
48. Brown CE, Marois R, Fingas MF, Choquet M, Monchalin J-P, Mullin J, Goodman R (2001) Airborne oil spill sensor testing: progress and recent developments. IOSC 2001, Tampa, p 917
49. Brown CE, Fingas MF (2003) Review of the development of laser fluorosensors for oil spill application. Mar Pollut Bull 47:477
50. Hengstermann T, Reuter R (1990) Lidar fluorosensing of mineral oil spills on the sea surface. Appl Opt 29:3218
51. Balick L, DiBenedetto JA, Lutz SS (1997) Fluorescence emission spectral measurements for the detection of oil on shore. In: Proceedings of the fourth thematic conference on remote sensing for marine and coastal environments. ERIM, Ann Arbor, vol I, p 13
52. Sarma AK, Ryder AG (2006) Comparison of the fluorescence behaviour of a biocrude oil and crude petroleum oil. Energy Fuels 20:783
53. Samberg A (2007) The state-of-the-art of airborne laser systems for oil mapping. Can J Rem Sens 53:143
54. Jha MN, Gao Y (2008) Oil spill contingency planning using laser fluorosensors and web-based GIS. In: Proceedings Oceans Marine Technology Society, Quebec City
55. Diebel D (1989) Laser fluorosensing of mineral oil spirits. In: Lodge AE (ed) The remote sensing of oil slicks. Wiley, Chichester, p 127
56. Geraci AL, Landolina F, Pantani L, Cecchi G (1993) Laser and infrared techniques for water pollution control. IOSC, 525

57. Hoge FE, Swift RN (1980) Oil film thickness measurement using airborne laser-induced water Raman backscatter. Appl Opt 19:3269
58. Piskozub J, Drozdowska V, Varlamov V (1997) A lidar system for remote measurement of oil film thickness on sea surface. In: Proceedings of the fourth thematic conference on remote sensing for marine and coastal environments. ERIM, Ann Arbor, vol I, p 386
59. Goodman R, Brown CE (2005) Oil detection limits for a number of remote sensing systems. In: Proceedings of the eighth international conference on remote sensing for marine and coastal environments, Halifax, Alterum conferences
60. Dick R, Fruhwirth M, Brown C (1992) Laser fluorosensor work in Canada. In: Proceedings of the first thematic conference on remote sensing for marine and coastal environments. ERIM, p 223
61. James RTB, Dick R (1996) Design of algorithms for the real-time airborne detection of littoral oil-spills by laser-induced fluorescence. Arctic Mar Oilspill Progr Tech Sem 2:1599
62. Brown CE, Fingas MF, Gamble RL, Myslicki GE (2002) The remote detection of submerged oil. In: Proceedings of the third R&D forum on high-density oil spill response, Brest France. IMO, pp 46–54
63. Brown CE, Marois R, Myslicki G, Fingas MF (2002) Initial studies on the remote detection of submerged orimulsion with a range-gated laser fluorosensor. AMOP, Environment Canada, Ottawa, p 773
64. Brown CE, Marois R, Myslicki G, Fingas MF, MacKay R (2003) Remote detection of submerged orimulsion with a range-gated laser fluorosensor. In: Proceedings of the IOSC 2003, Vancouver, p 779
65. Brown CE, Marois R, Gamble RL, Fingas MF (2003) Further studies on the remote detection of submerged orimulsion with a range-gated laser fluorosensor. Arctic Mar Oilspill Progr Tech Sem 1:279
66. Brown CE, Fingas M, Marois R, Fieldhouse B, Gamble RL (2004) Remote sensing of water-in-oil emulsions: initial laser fluorosensor studies. Arctic Mar Oilspill Progr Tech Sem 1:295
67. Ulaby FT, Moore RK, Fung AK (1989) Microwave remote sensing: active and passive. Artech House, Norwood, 1466
68. Goodman RH (1994) Remote sensing resolution and oil slick inhomogeneities. In: Proceedings of the second thematic conference on remote sensing for marine and coastal environments: needs, solutions and applications. ERIM, Ann Arbor, p I-1-17
69. Fäst O (1986) Remote sensing of oil on water – air and space-borne systems. In: Proceedings of the DOOS seminar, Trondheim
70. Skou N, Sorensen BM, Poulson A (1994) A new airborne dual frequency microwave radiometer for mapping and quantifying mineral oil on the sea surface. In: Proceedings of the second thematic conference on remote sensing for marine and coastal environments. ERIM, Ann Arbor, p 559
71. Mussetto MS, Yujiri L, Dixon DP, Hauss BI, Eberhard CD (1994) Passive millimeter wave radiometric sensing of oil spills. In: Proceedings of the second thematic conference on remote sensing for marine and coastal environments: needs, solutions and applications. ERIM, Ann Arbor, vol I, p 35
72. Zhifu S, Wiesbeck W (1988) A study of passive microwave remote sensing. In: Proceedings of the 1988 international geoscience and remote sensing symposium, Edinburgh, p 1091
73. Süss H, Grüner K, Wilson WJ (1989) Passive millimeter wave imaging: a tool for remote sensing. Alta Freq LVIII:457
74. Pelyushenko SA (1995) Microwave radiometer system for the detection of oil slicks. Spill Sci Technol Bull 2:249
75. Pelyushenko SA (1997) The use of microwave radiometer scanning system for detecting and identification of oil spills. In: Proceedings of the fourth thematic conference on remote sensing for marine and coastal environments. ERIM, Ann Arbor, vol I, p 381
76. McMahon OB, Brown ER, Daniels GD, Murphy TJ, Hover GL (1995) Oil thickness detection using wideband radiometry. In: Proceedings of the IOSC 1995, Long Beach, CA, p 15

77. McMahon OB, Murphy TJ, Brown ER (1997) Remote measurement of oil spill thickness. In: Proceedings of the fourth thematic conference on remote sensing for marine and coastal environments. ERIM, Ann Arbor, vol I, p353
78. Nunziata F, Migliaccio M, Sobieski P (2008) A BPM two-scale contrast model. In: Proceedings of the IGARSS, Boston, vol IV, p 593
79. Frysinger GS, Asher WE, Korenowski GM, Barger WR, Klusty MA, Frew NM, Nelson RK (1992) Study of ocean slicks by nonlinear laser processes in second-harmonic generation. J Geophys Res 97:5253
80. Alpers W, Hühnerfuss H (1987) Radar signatures of oil films floating on the sea surface. In: Proceedings of the IGARSS, Ann Arbor, p 741
81. Poitevin J, Khaif C (1992) A numerical study of the backscattered radar power in presence of oil slicks on the sea surface. In: Proceedings of the first thematic conference on remote sensing for marine and coastal environments. ERIM, Ann Arbor, p 171
82. Hühnerfuss H, Alpers W, Witte F (1989) Layers of different thicknesses in mineral oil spills detected by grey level textures of real aperture radar images. Int J Remote Sens 10:1093
83. Gens R (2008) Oceanographic applications of SAR remote sensing. GISci Remote Sens 45:275
84. Bartsch N, Grüner K, Keydel W, Witte F (1987) Contribution to oil spill detection and analysis with radar and microwave radiometer: results of the Archimedes II campaign. IEEE Trans Geosci Remote GE.25:677
85. Mastin G, Mason JJ, Bradley JD, Axline RM, Hover GL (1994) A comparative evaluation of SAR and SLAR. In: Proceedings of the second thematic conference on remote sensing for marine and coastal environments: needs, solutions and applications. ERIM, Ann Arbor, vol I, p 7
86. Brown CE, Fingas MF (2003) Synthetic aperture radar sensors: viable for marine oil spill response? Arctic Mar Oilspill Progr Tech Sem 1:299
87. Zielinski O, Robbe N (2004) Past and future of airborne pollution control. In: Proceedings of the Interspill 2004, Trondheim
88. Dyring A, Fäst O (2004) MSS puts the aircraft in the oil spill tracking network. In: Proceedings of the Interspill 2004, Trondheim
89. Intera Technologies (1984) Radar surveillance in support of the 1983 COATTF oil spill trials. Environment Canada Report EE-51
90. C-CORE (Centre for Cold Ocean Resources Engineering) (1981) Microwave systems for detecting oil slicks in ice-infested waters: phase I – literature review and feasibility study. Environment Canada Report EPS 3-EC-81-3
91. Macklin JT (1992) The imaging of oil slicks by synthetic aperture radar. GEC J Res 10:19
92. Kozu TT, Umehara T, Ojima T, Suitsu T, Masuyko H, Inomata H (1987) Observation of oil slicks on the ocean by X-band SLAR. In: Proceedings of the IGARSS 1987, Ann Arbor, p 735
93. Madsen S, Skou N, Sorensen BM (1994) Comparison of VV and HH polarized SLAR for detection of oil on the sea surface. In: Proceedings of the second thematic conference on remote sensing for marine and coastal environments: needs, solutions and applications. ERIM, Ann Arbor, vol I, p 498
94. Migliaccio M, Nunziata F, Gambardella A (2009) On the co-polarized phase difference for oil spill observation. Int J Remote Sens 30:1587
95. Hühnerfuss H, Alpers W, Dannhauer H, Gade M, Lange PA, Neumann V, Wismann V (1996) Natural and man-made sea slicks in the North Sea investigated by a helicopter-borne 5-frequency radar scatterometer. Int J Remote Sens 17:1567
96. Hielm JH (1989) NIFO comparative trials. In: Lodge AE (ed) The remote sensing of oil slicks. Wiley, Chichester, p 67
97. Marghany M, Cracknell AP, Hasim M (2009) Modification of fractal algorithm for oil spill detection from RADARSAT-1 SAR data. Int J Appl Earth Observ Geoinform 11:96

98. Gade M, Alpers W, Huehnerfuss H, Wismann V (1996) Radar signatures of different oceanic surface films measured during the SIR-C-X-SAR missions. In: Proceedings of the remote sensing 1996. Balkema, Rotterdam, p 233
99. Okamoto K, Kobayashi T, Masuko H, Ochiai S, Horie H, Kumagai H, Nakamua K, Shimada M (1996) Results of experiments using synthetic aperture radar onboard the European remote sensing satellite 1–4. Artificial oil pollution detection. J Commun Res Lab 43:327
100. Migliaccio M, Gambardella A, Tranfaglia A (2007) SAR polarimetry to observe oil spills. IEEE Trans Geosci Remote 45:506
101. Gambardella A, M. Migliaccio M, De Grandi G (2007) Wavelet polarimetric SAR signature analysis of sea oil spills and look-alike features. In: Proceedings of the IGARSS 2007, Barcelona, p 983
102. Nunziata F, Gambardella A, Migliaccio M (2008) On the use of dual-polarized SAR data for oil spill observation. In: Proceedings of the IGARSS 2008, Boston, vol II, p 225
103. Forget P, Brochu P (1996) Slicks, waves and fronts observed in sea coastal area by an X-band airborne synthetic aperture radar. Remote Sens Environ 57:1
104. Marmorino GO, Thompson DR, Graber HC, Trump CL (1997) Correlation of oceanographic signatures appearing in synthetic aperature radar and interferometric synthetic aperture radar imagery with in-situ measurements. J Geophys Res 18:723
105. Nøst E, Egset CN (2006) Oil spill detection system – results from field trials. In: Proceedings oceans marine technology society
106. Gangeskar R (2004) Automatic oil-spill detection by marine X-band radars. Sea Technol 45:40–45
107. Topouzelis K, Karanthanassi V, Pavlakis VP, Rokos D (2009) Potentiality of feed-forward neural networks for classifying dark formation to oil spills and look-alikes. Geocarto Int 24:179
108. Solberg R, Theophilopoulos N (1997) ENVISYS – a solution for automatic oil spill detection in the Mediterranean. In: Proceedings of the fourth thematic conference on remote sensing for marine and coastal environments. ERIM, Ann Arbor, vol I, p 3
109. Ferraro G, Baschek B, de Montpellier G, Njoten O, Perkovic M, Vespe M (2010) On the SAR derived alert in the detection of oil spills according to the analysis of the EGEMP. Mar Pollut Bull 60:91
110. Wahl T, Eldhuset K, Skøelv Å (1993) Ship traffic monitoring and oil spill detection using ERS-1. In: Proceedings of the international symposium "operationalization of remote sensing", ITC, Enschede, p 97
111. Bern T-I, Wahl T, Anderssen T, Olsen R (1993) Oil spill detection using satellite based SAR: experience from a field experiment. Photogramm Eng Remote Sens 59:423
112. Yan X-H, Clemente-Colon P (1997) The maximum similarity share matching (MSSM) method applied to oil spill feature tracking observed in SAR imagery. In: Proceedings of the fourth thematic conference on remote sensing for marine and coastal environments. ERIM, Ann Arbor, vol I, p 43
113. Bentz CM, Politano AT, Ebecken NFF (2007) Automatic recognition of coastal and oceanic environmental events with orbital radars. In: Proceedings of the IGARSS 2007, Barcelona, p 914
114. Trivero P, Biamino W, Nirchio F (2007) High resolution COSMO-SkyMed SAR images for oil spills automatic detection. In: Proceedings of the IGARSS 2007, Barcelona, p 2
115. Tian W, Shao Y, Wang S (2008) A system for automatic identification of oil spill in ENVISAT ASAR. In: Proceedings of the IGARSS 2008, Boston, vol III, p 1394
116. Shao Y, Tian W, Wang S, Zhang F (2008) Oil spill monitoring using multi-temporal SAR and microwave scatterometer data. In: Proceedings of the IGARSS 2008, Boston, vol III, p 1378
117. Rodriguez MH, Bannerman K, Caceres RG, Pellon de Miranda F, Pedroso EC (2007) Cantarell natural seep modelling using SAR derived ocean surface wind and meteo-oceanographic buoy data. In: Proceedings of the IGARSS 2007, Barcelona, p 3257

118. Robson M, Secker J, Vachon PW (2006) Evaluation of eCognition for assisted target detection and recognition in SAR imagery. In: Proceedings of the IGARSS 2006, Denver, p 145
119. Garcia-Pineda O, MacDonald I, Zimmer B (2008) Synthetic aperture radar image processing using the supervised textural-neural network classification algorithms. In: Proceedings of the IGARSS, Boston, vol IV, p 1265
120. Morales DJ, Moctezuma M, Parmiggiani F (2008) Detection of oil slicks in SAR images using hierarchial MRF. In: Proceedings of the IGARSS, Boston, vol III, p 1390
121. Bertacca M (2006) A FEXP model short range dependence analysis for improving oil slicks and low-wind areas discrimination in SAR imagery. In: Proceedings of the IGARSS, Denver, p 959
122. Topouzelis KN (2008) Oil spill detection by SAR images: dark formation detection, feature extraction and classification algorithms. Sensors 8:6642
123. Topouzelis K, Karanthanassi V, Pavlakis P, Rokos D (2008) Dark formation detection using neural networks. Int J Remote Sens 29:4705
124. Topouzelis K, Stathakis D, Karanthanassi V (2009) Investigation of genetic contribution to feature selection for oil spill detection. Int J Remote Sens 30:179
125. Karathanassi V, Topouzelis K, Pavlakis P, Rokos D (2006) An object-oriented methodology to detect oil spills. Int J Remote Sens 27:5235
126. Topouzelis K, Karanthanassi V, Pavlakis P, Rokos D (2007) Detection and discrimination between oil spills and look-alike phenomena through neural networks. ISPRS J Photogramm Remote Sens 62:264
127. Karantzalos K, Argialas D (2008) Automatic detection and tracking of oil spills in SAR imagery with level set segmentation. Int J Remote Sens 29:6281
128. Tahvonen K, Pyhaelahti T (2006) The use of environmental data in reliability: assessment of oil spill detection by SAR imagery. In: Proceedings of the IGARSS 2006, Denver, p 3671
129. Karvonen J, Heiler I, Similae M, Tahvonen K (2006) Oil spill detection with RADARSAT-1 in the Baltic Sea. In: Proceedings of the IGARSS 2006, Denver, p 4075
130. Shi L, Ivanov AY, He M, Zhao C (2008) Oil spill mapping in the western part of the East China Sea using synthetic aperture radar imagery. Int J Remote Sens 29:6315
131. Muellenhoff O, Bulgarelli B, Ferraro G, Topouzelis K (2008) The use of ancillary metocean data for the oil spill probability assessment in SAR images. Fresenius Environ Bull 17:1382
132. Muellenhoff O, Bulgarelli B, Ferraro G, Perkovic M, Topouzelis K, Sammarini V (2008) Geospatial modelling of metocean and environmental ancillary data for the oil probability assessment in SAR images. Proc SPIE 7110:71100R
133. Assilzadeh H, Gao Y (2008) Oil spill emergency response mapping for coastal area using SAR imagery and GIS. In: Proceedings oceans marine technology society
134. Migliaccio M (2005) A physical approach for the observation of oil spills in SAR images. IEEE J Oceanic Eng 30:496
135. Shu Y, Li J, Yousef H, Gomes G (2010) Dark-spot detection from SAR intensity imagery with spatial density thresholding for oil-spill monitoring. Remote Sens Environ 114:2026
136. Migliaccio M, Ferrara G, Gambardella A, Nunziata F, Sorrentino A (2007) A physically consistent stochastic model to observe oil spills and strong scatterers on SLC SAR images. In: Proceedings of the IGARSS 2007, Barcelona, p 1322
137. Gambardella A, Giacinto G, Migliaccio M (2008) On the mathematical formulation of the SAR oil-spill observation problem. In: Proceedings of the IGARSS 2008, Boston, vol III, p 1382
138. Marghany M, Cracknell AP, Hasim M (2009) Comparison between RADARSAT-1 SAR different data modes for oil spill detection by a fractal box counting algorithm. Int J Dig Earth 2:237
139. Danisi A, Di Martino G, Iodice A, Riccio D, Ruello G et al (2007) SAR simulation of ocean scenes covered by oil slicks with arbitrary shapes. In: Proceedings of the IGARSS 2007, Barcelona, p 1314

140. Zhang F, Shao Y, Tian W, Wang S (2008) Oil spill identification based on textural information of SAR images. In: Proceedings of the IGARSS 2008, Boston, vol IV, p 1308
141. Tello M, Bonastre R, Lopez-Martinez C, Mallorqui JJ, Danisi A (2007) Characterization of local regularity in SAR imagery by means of multiscale techniques: application to oil spill detection. In: Proceedings of the IGARSS 2007, Barcelona, p 5228
142. Lounis B, Mercier G, Belhadj-Aissa A (2008) Statistical similarity measure for oil slick detection in SAR images. In: Proceedings of the IGARSS 2008, Boston, vol I, p 233
143. Pelizzari S, Bioucas-Dias J (2007) Oil spill segmentation of SAR images via graph cuts. In: Proceedings of the IGARSS 2007, Barcelona, p 1318
144. Ferraro G, Bernardini A, David M, Meyer-Roux S, Muellenhoff O et al (2007) Towards an operational use of space imagery for oil pollution monitoring in the Mediterranean basin: a demonstration in the Adriatic Sea. Mar Pollut Bull 54:403
145. Ferraro G, Meyer-Roux S, Muellenhoff O, Pavilha M, Svetak J, Tarchi D, Topouzelis K (2009) Long-term monitoring of oil spills in European seas. Int J Remote Sens 30:627
146. Ferraro G, Baschek B, De Monpellier G, Njoten O, Perkovic M (2010) On the SAR derived alert in the detection of oil spills according to the analysis of the EGEMP. Mar Pollut Bull 60:91–102
147. Adamo M, De Carolis G, De Pasquale V, Pasquariello G (2006) On the combined use of sun glint MODIS and MERIS signatures and SAR data to detect oil slicks. Proc SPIE 6360:63600G
148. Sipelgas L, Uiboupin R (2007) Elimination of oil spill like structures from radar image using MODIS data. In: Proceedings of the IGARSS 2007, Barcelona, p 429
149. Vesecky JF, Laws K, Paduan JD (2008) Monitoring of coastal vessels using surface wave HF radars: Multiple frequency, multiple site and multiple antenna considerations. In: Proceedings of the IGARSS 2008, Boston, vol I, p 405
150. Pinel N, Bourlier C (2008) Forward propagation of thick oil spills on sea surface for a coastal coherent radar. In: Proceedings of the IGARSS 2008, Boston, vol IV, p 1125
151. Demarty Y, Gobin V, Thirion L, Guinvarc'h R, Lesturgie M (2007) Exact electromagnetic modeling of the scattering of realistic sea surfaces for HFSWR applications. In: Proceedings of the IGARSS 2007, Barcelona, p 1004
152. Schultz-Stellenfleth J, Lehner S, Koenig T, Reppucci A, Brusch S (2007) Use of tandem pairs of ERS-2 and ENVIRSAT SAR data for the analysis of oceanographic and atmospheric processes. IGARSS 2007, Barcelona, p 3265
153. Goodman RH, Fingas MF (1988) The use of remote sensing for the determination of dispersant effectiveness. Arctic Mar Oilspill Progr Tech Sem 1:377
154. Jensen HV, Andersen JHS, Daling PS, Noest E (2008) Recent experience from multiple remote sensing and monitoring to improve oil spill response operations. In: Proceedings of the IOSC 2008, Savannah, p 407
155. Hollinger JP, Mennella RA (1973) Oil spills: measurements of their distributions and volumes by multifrequency microwave radiometry. Science 181:54
156. Lehr WJ (2010) Visual observations and the Bonn agreement. Arctic Mar Oilspill Progr Tech Sem 2:669
157. Horstein B (1973) The visibility of oil–water discharges. In: Proceedings of the IOSC 1973, Washington, DC, pp 91–99
158. Parker HD, Cormack D (1979) Evaluation of infrared line scan (IRLS) and side-looking airborne radar (SLAR) over controlled oil spills in the North Sea. Warren Spring Laboratory Report, Stevenage
159. Hurford N, Martinelli FN (1982) Use of an infrared line scanner and a side-looking airborne radar to detect oil discharges from ships. Warren Spring Laboratory Report, Stevenage
160. Hurford N, Martinelli FN (1984) Use of an infrared line scanner and a side-looking airborne radar to detect oil discharges from ships. In: Massin JM (ed) Remote sensing for the control of marine pollution. Plenum Press, New York, p 405

161. MacDonald IR, Guinasso NL Jr, Ackleson SG, Amos JF, Duckworth R, Sassen R, Brooks JM (1993) Natural oil slicks in the Gulf of Mexico visible from space. J Geophys Res 16:351
162. Brown HM, Bittner JP, Goodman RH (1995) Visibility limits of spilled oil sheens. Imperial Oil Internal Report, Calgary
163. Brown CE, Fingas MF, Monchalin J-P, Neron C, Padioleau C (2006) Airborne measurement of oil slick thickness. Arctic Mar Oilspill Progr Tech Sem 1:911
164. Reimer ER, Rossiter JR (1987) Measurement of oil thickness on water from aircraft; A: Active microwave spectroscopy; B: Electromagnetic thermoelastic emission. Environmental Studies Revolving Fund Report Number 078
165. Goodman R, Brown H, Bittner J (1997) The measurement of thickness of oil on water. In: Proceedings of the fourth thematic conference on remote sensing for marine and coastal environments, ERIM, Ann Arbor, vol I, p 31
166. Aussel JD, Monchalin J-P (1989) Laser-ultrasonic measurement of oil thickness on water from aircraft, feasibility study. Industrial Materials Research Institute Report, Québec
167. Krapez JC, Cielo P (1992) Optothermal evaluation of oil film thickness. J Appl Phys 72:1255
168. Choquet M, Héon R, Vaudreuil G, Monchalin J-P, Padioleau C, Goodman RH (1993) Remote thickness measurement of oil slicks on water by laser ultrasonics. IOSC, Boucherville
169. Brown CE, Fingas MF, Choquet M, Blouin A, Drolet D, Monchalin J-P, Hardwick CD (1997) The LURSOT sensor: providing absolute measurements of oil slick thickness. In: Proceedings of the fourth thematic conference on remote sensing for marine and coastal environments. ERIM, Ann Arbor, vol I, p 393
170. Brown CE, Fingas MF (2003) Development of airborne oil thickness measurements. Mar Pollut Bull 47:485
171. Brown CE, Fingas MF, Monchalin J-P, Neron C, Padioleau C (2005) Airborne oil slick thickness measurements: realization of a dream. In: Proceedings of the eighth international conference on remote sensing for marine and coastal environments, Altarum
172. Monchalin JP (1986) Optical detection of ultrasound. IEEE Trans Ultrason Ferroelectr Freq Control 33:485
173. Svejkovsky J, Muskat J, Mullin J (2008) Mapping oil spill thickness with a portable multi-spectral aerial imager. In: Proceedings of the IOSC 2008, Savannah, p 131
174. Lue L, Ge B, Yao W, Zhang Y (2011) A method for measuring the thickness of transparent oil film on water surface using laser trigonometry. Opt Lasers Eng 49:13
175. Lu Y-C, Tian Q-J, Li Z (2011) The remote sensing inversion theory of offshore oil slick thickness based on a two-beam interference model. Sci China Earth Sci 54:4154
176. Optimare (2011) http://www.optimare.de/cms/en/divisions/fek.html. Accessed June 2011
177. Swedish Space Corporation (2011) http://www.ssc.se/?id=5772. Accessed June 2011
178. Armstrong L, Fäst O, Schneider HA, Abrahamsson AH (2008) Integration of airborne AIS brings a new dimension to the detection of illegal discharge of oil spills. In: Proceedings of the IOSC 2008, Savannah, p 179
179. Brown CE, Fingas MF (2005) A review of current global oil spill surveillance, monitoring and remote sensing capabilities. Arctic Mar Oilspill Progr Tech Sem 2:789
180. Dean KG, Stringer WJ, Groves JE, Ahlinas K, Royer TC (1990) The EXXON VALDEZ oil spill: satellite analyses. In: Spaulding ML, Reed M (eds) Oil spills: management and legislative implications. ASCE, New York, p 492
181. Dawe BR, Parashar SK, Ryan TP, Worsfold RO (1981) The use of satellite imagery for tracking the KURDISTAN oil spill. Environment Canada Report EPS 4-EC-81-6, Ottawa
182. Alfoldi TT, Prout NA (1982) The use of satellite data for monitoring oil spills in Canada. Environment Canada Report EPS 3-EC-82-5, Ottawa
183. Cross A (1992) Monitoring marine oil pollution using AVHRR data: observations off the coast of Kuwait and Saudi Arabia during January 1991. Int J Remote Sens 13:781
184. Rand RS, Davis DA, Satterwhite MB, Anderson JE (1992) Methods of monitoring the Persian Gulf oil spill using digital and hardcopy multiband data. U.S. Army Corps of Engineers Report, TEC-0014

185. Al-Ghunaim I, Abuzar M, Al-Qurnas FS (1992) Delineation and monitoring of oil spill in the Arabian Gulf using landsat thematic mapper (TM) data. In: Proceedings of the Proceedings of the first thematic conference on remote sensing for marine and coastal environments. ERIM, Ann Arbor, p 1151
186. Al-Hinai KG, Khan MA, Dabbagh AE, Bader TA (1993) Analysis of landsat thematic mapper data for mapping oil slick concentrations – Arabian Gulf oil spill 1991. Arabian J Sci Eng 18:85
187. Cecamore P, Ciappa A, Perusini V (1992) Monitoring the oil spill following the wreck of the tanker HAVEN in the Gulf of Genoa through satellite remote sensing techniques. In: Proceedings of the first thematic conference on remote sensing for marine and coastal environments. ERIM, Ann Arbor, p 183
188. Voloshina IP, Sochnev OY (1992) Observations of surface contamination of the region of the Kol'shii Gulf from IR measurements. Sov J Remote Sens 9:996
189. Li Y, Yu S, Ma L, Liu M, Li Q (2008) Satellite image processing and analyzing for marine oil spills. Proc SPIE 7145:712311
190. Alawadi F, Amos C, Byfield V, Petrov P (2008) The application of hyperspectral image techniques on Modis data for the detection of oil spills in the RSA. Proc SPIE 7110:71100Q
191. Lotliker A, Mupparthy R, Kumer S, Nayak S (2008) Evaluation of hi-resolution MODIS-Aqua data for oil spill monitoring. Proc SPIE 7150:71500S
192. Clark CD (1989) Satellite remote sensing for marine pollution investigations. Mar Pollut Bull 20:92
193. Noerager JA, Goodman RH (1991) Oil tracking, containment and recovery during the EXXON VALDEZ response. In: Proceedings of the IOSC, Washington, DC, p 193
194. Li Y, Liu Y, Ma L, Li X (2007) Oil spill monitoring using MODIS data. Proc SPIE 6795:67955G
195. Li Y, Ma L, Yu S, Li C, Li Q (2008) Remote sensing of marine oil spills and its applications. SPIE :71450 C712311
196. Shrivastava H, Singh TP (2010) Assessment and development of algorithms to detection of oil spills using MODIS data. J Indian Soc Remote Sens 38:161
197. Leifer I, Lehr B, Simecek-Beatty D, Bradley E, Clark R, Dennison P, Hu Y, Matheson S, Jones C, Holt B, Roberts D, Svejkovsky J, Swayse G (2011) State of the art satellite and airborne oil spill remote sensing: application to the BP deepwater horizon oil spill. Remote Sens Environ (submitted)
198. Li X, Ge L, Hu Z, Chang H-C (2010) The 2009 Montara oil spill in the Timor sea as observed by earth observation satellites. University of New South Wales, Australia
199. Chust G, Sagarminaga Y (2007) The multi-angle view of MISR detects oil slicks under sun glitter conditions. Remote Sens Environ 107:232
200. ud Din S, Al Dousari A, Literathy P (2008) Evidence of hydrocarbon contamination from the Burgan oil field, Kuwait – interpretations from thermal remote sensing data. J Environ Manage 86:605
201. Casciello D, Lacava T, Pergola N, Tramutoli V (2007) Robust satellite techniques (RST) for oil spill detection and monitoring. In: Proceedings of the MultiTemp 2007–2007 international workshop on the analysis of multi-temporal remote sensing images, Leuven
202. Brown CE, Fingas MF (2001) New space-borne sensors for oil spill response. In: Proceedings of the IOSC 2001, Tampa, p 911
203. Brown CE, Fingas MF (2001) Upcoming satellites: potential applicability to oil spill remote sensing. Arctic Mar Oilspill Progr Tech Sem 2:495
204. Brown CE, Fingas MF, Lukowski TJ (2002) Airborne and space-borne synergies: the old dog teaches tricks to a new bird. In: Proceedings of the fifth international airborne remote sensing conference and exhibition, Veridien
205. Biegert EK, Baker RN, Berry JL, Mott S, Scantland S (1997) Gulf offshore satellite applications project detects oil slicks using RADARSAT. In: International symposium: geomatics in the era of RADARSAT, Ottawa

206. Werle D, Tittley B, Theriault E, Whitehouse B (1997) Using RADARSAT-1 SAR imagery to monitor the recovery of the Irving Whale oil barge. In: Proceedings of international symposium: geomatics in the era of RADARSAT, Ottawa
207. Kwarteng AY, Singhroy V, Saint-Jean R, Al-Ajmi D (1997) RADARSAT SAR data assessment of the oil lakes in the greater Burgan oil field, Kuwait. In: Proceedings of international symposium: geomatics in the era of RADARSAT, Ottawa
208. Ivanov AY, Ermoshkin IS (2004) Mapping of oil spills in the Caspian Sea using the ERS-1.ERS-2 SAR image quick-looks and GIS. In: Proceedings of the Interspill 2004, Trondheim
209. Fortuny J, Tarchi D, Ferraro G, Sieber A (2004) The use of satellite radar imagery in the Prestige accident. Interspill 2004, Trondheim
210. Torres Palenzuela JM, Vilas LG, Cuadrado MS (2006) Use of ASAR images to study the evolution of the Prestige oil spill off the Galician coast. Int J Remote Sens 27:1931
211. Gauthier M-F, Weir L, Ou Z, Arkett M, De Abreu R (2007) Integrated satellite tracking of pollution: a new operational program. In: Proceedings of the IGARSS 2007, Barcelona, p 967
212. Brekke C, Solberg AHS (2005) Oil spill detection by satellite remote sensing. Remote Sens Environ 95:1
213. Olga L, Marina M, Tatiana B, Andrey K, Vladimir K (2008) Multisensor approach to operational oil pollution monitoring in coastal zones. In: Proceedings of the IGARSS 2008, Boston, vol III, p 1386
214. Kostianoy A, Lavrova O, Mityagina M, Bocharova T, Litovchenko K et al (2007) Complex monitoring of oil pollution in the Baltic, Black and Caspian Seas. In: Proceedings of the Envisat symposium, Montreux, p 23
215. DeAbreu R, Gauthier M-F, Wychen W (2006) SAR-based oil pollution surveillance in Canada: operational implementation and research priorities. In: Proceedings OceanSAR 2006 – third workshop on coastal and marine applications of SAR, St. John's
216. Fingas MF, Brown CE (2002) Detection of oil in and under ice. Arctic Mar Oilspill Progr Tech Sem 2:199–214
217. Redman R, Pfeifer C, Brzozowski E, Markian R (2008) A comparison of methods for locating, tracking and quantifying submerged oil used during the T/B DBL 152 incident. In: Proceedings of the IOSC 2008, Savannah, p 255
218. Wendelboe G, Fonseca ELM, Hvidbak F, Mutschler M (2009) Detection of heavy oil on the seabed by application of a 400 kHz multibeam echo sounder. Arctic Mar Oilspill Progr Tech Sem 2:791
219. Hansen KA (2010) Research efforts for detection and recovery of submerged oil. Arctic Mar Oilspill Progr Tech Sem 2:1055
220. Michel J (2008) Spills of nonfloating oil: evaluation of response technologies. In: Proceedings of the IOSC 2008, Savannah, p 261
221. Pfeifer C, Brzozowski E, Markian R, Redman R (2008) Quantifying percent cover of submerged oil using underwater video imagery. In: Proceedings of the IOSC 2008, Savannah, p 269
222. Pfeifer C, Brzozowski E, Markian R, Redman R (2008) Long-Term monitoring of submerged oil in the Gulf of Mexico following the T/B DBL 152 incident. In: Proceedings of the IOSC 2008, Savannah, p 275
223. Camilli R, Bingham B, Reddy CM, Nelson RK, Duryea AN (2009) Method for rapid localization of seafloor petroleum contamination using concurrent mass spectrometry and acoustic positioning. Mar Pollut Bull 58:1505
224. Lehr WJ (2008) The potential use of small UAS in spill response. In: Proceedings of the IOSC 2008, Savannah, p 431
225. Donnay E (2009) Use of unmanned aerial vehicle (UAV) for the detection and surveillance of marine oil spills in the Belgian part of the North Sea. Arctic Mar Oilspill Progr Tech Sem 2:771

226. Li K, Fingas MF, Paré JRP, Boileau P, Beaudry, P Dainty E (1994) The use of remote-controlled helicopters for air sampling in an emergency response situation. Arctic Mar Oilspill Progr Tech Sem 2:139
227. Goodman RH (1994) Overview and future trends in oil spill remote sensing. Spill Sci Technol 1:11
228. Huisman J (2006) Use of surveillance technology to support response decision making and impact assessment. In: Proceedings of the Interspill 2006, London
229. Carpenter A (2007) The Bonn agreement aerial surveillance programme: trends in North Sea oil pollution: 1986–2004. Mar Pollut Bull 54:149
230. De Dominicis M, Pinardi N, Coppini G, Tonani M, Guarnieri A et al (2009) Interspill
231. Allen J, Walsh B (2008) Enhanced oil spill surveillance, detection and monitoring through the applied technology of unmanned air systems. In: Proceedings of the IOSC 2008, Savannah, p 113

Chapter 16
Remote Sensing Applications to Ocean and Human Health

Frank E. Muller-Karger

Glossary

Attenuation depth	Attenuation depth is a measure of how far electromagnetic radiation including light can penetrate into a substance. It is the depth at which the intensity of the radiation falls to 1/e (∼37%) of its original value immediately below the surface.
Diffuse attenuation coefficient	The irradiance at a wavelength λ propagates over a distance (z) as determined by the diffuse attenuation coefficient. In aquatic environments, the diffuse attenuation coefficient is an indicator of the turbidity of the water.
Hyperspectral	Hyperspectral data are collected by instruments called imaging spectrometers. These sensors are able to collect information from across the electromagnetic spectrum at a fine resolution of bands as narrow as 0.001 or smaller μm over a wide wavelength range, typically at least 0.4–2.4 μm.
Irradiance	Irradiance is a radiometry term for the power of electromagnetic radiation per unit area at a surface. Irradiance is used when the electromagnetic radiation is incident on the surface, and it has units of watts per square meter (W/m^2).

This chapter was originally published as part of the Encyclopedia of Sustainability Science and Technology edited by Robert A. Meyers. DOI:10.1007/978-1-4419-0851-3

F.E. Muller-Karger (✉)
College of Marine Science, University of South Florida, 140 7th Ave. South, St. Petersburg, FL 33701, USA
e-mail: carib@marine.usf.edu

J. Orcutt (ed.), *Earth System Monitoring: Selected Entries from the Encyclopedia of Sustainability Science and Technology*, DOI 10.1007/978-1-4614-5684-1_16,

Ocean color	Ocean color is a general term used in the study of the biological and biogeochemical properties of ocean waters through remote sensing of the reflected and transmitted visible radiation. The "color" of the ocean comes from the interaction between light, water, and substances in the water, particularly phytoplankton (microscopic, free-floating photosynthetic organisms), detritus and inorganic particulates, and colored dissolved matter.
Radiance	Radiance is a radiometric measure that describes the amount of light that passes through or is emitted from a particular surface area, contained within a given solid angle in a specified direction. It is used to characterize both emission and reflection from surfaces. The SI unit of radiance is watts per steradian per square meter ($W \cdot sr^{-1} \cdot m^{-2}$).
Thermal infrared radiation (TIR)	Thermal infrared radiation refers to electromagnetic waves with a wavelength of between 3.5 and 20 μm. These waves are used to estimate the temperature of the surface of targets. This is a radiation typically emitted by objects as opposed to visible and short-wave infrared radiation which is part of the spectrum of sunlight reflected by objects.
Turbidity	Turbidity is the relative clarity of a liquid and is an expression of the optical properties of water that causes light to be scattered and absorbed by particles and molecules rather than transmitted in a straight line through a water sample. It is a function of the concentration of suspended matter or impurities that interfere with the clarity of the water. Turbidity is a common index of water quality.
Visible, near infrared, and short-wave infrared (VIS, NIR, and SWIR)	This broad band of electromagnetic radiation is used in remote sensing of the reflectance of the Earth. Light that is visible to the human eye is visible radiation (VIS) and encompasses a wavelength range from about 380–400 nm to about 760–780 nm. Near-infrared (NIR) radiation encompasses 0.75–1.4 μm in wavelength. The short-wave infrared (SWIR) is the wavelength range 1.4–3 μm. Together, this region of the spectrum is sometimes known as VSWIR.

Definition of the Subject and Its Importance

Remote sensing is defined here as the acquisition of information about an object without physical contact by way of recording or sensing devices mounted on aircraft, satellites, or simply sited on a high hill or bluff overlooking an area of interest. Ocean and human health is the general field that assesses conditions in the marine environment including estuaries that are relevant to the well-being of living resources and to the use of these resources and seawater by humans for amenities or the sustenance of life.

Remote sensing of environmental conditions in coastal and marine waters using space-based sensors has made great progress since the deployment of the Coastal Zone Color Scanner on the Nimbus 7 satellite in 1978. Remote sensing is an important complement to observations collected from field programs, because satellites provide estimates of a number of environmental parameters over large geographic areas (hundreds of square kilometers to globally) rapidly (in minutes), frequently, and periodically (often near-daily or better), and over the long term (in some cases, now upward of two decades). These observations support research, monitoring, and public outreach, providing a cost-effective complement to traditional monitoring efforts. Yet much work remains to be done to refine the technology to address the growing challenges to the health of marine ecosystems, including humans living within them, due to marine pollution, urban sprawl, overuse of resources, and changes in climate. This entry very briefly outlines the technologies used to conduct water quality assessments, including phytoplankton standing stock, turbidity, suspended sediment load, colored dissolved organic material (CDOM), diffuse light attenuation coefficients, temperature, salinity, wind stress, wave direction, amplitude and wavelength, and current speed and direction. The student and reader are encouraged to look for further detail on how to use these observations in the scientific and technical literature. A large number of international Earth-observing satellite missions are planned for the 2010–2025 time frame to monitor the marine environment. As part of this effort, a solid scientific base for remote sensing methods of marine pollution needs to be established, and multidisciplinary, international training programs need to be developed so that operational agencies can make effective use of these technologies. It is capable human resources that we are currently lacking the most.

Introduction

Satellite remote sensing of the Earth's environment has advanced significantly every decade since the late 1950s, when the first reconnaissance satellites were launched. There continue to be leaps toward more powerful personal computing, faster and more accessible global communication networks and media, standardization of a number of file formats, large and open-access databases, widely available

photo-processing software, and online mapping and data visualization software including geographical information systems. These advances, combined with the growing computer literacy of broader segments of the world's population, permit the regular observation and application of several key terrestrial, atmospheric, and oceanic variables to understand how the environment changes at regional to global scales. Satellite-based sensors now routinely provide data that help interpret local environmental measurements in the context of large spatial scales, longer time frames, and of complex interactions between different processes. Satellite data facilitate the study of connectivity between ecosystems and human communities, of change against baseline environmental conditions over both small and larger geographic areas, and of possible natural or human-caused drivers of point and nonpoint sources of pollution and other threatening conditions.

This entry gives a brief overview of remote sensing applications in marine pollution, focusing on satellite instrumentation of singular interest, recent advances, and expectations for future directions. It is an update to the summary presented by Muller-Karger [1]. Only a few aspects of remote sensing can be presented here. For more detail on the history of the technology, the reader is referred to the references provided in that publication. While atmospheric pollutants are also relevant, here the focus is on detection of water properties or constituents in coastal regions.

Many relevant research efforts that provide a framework for analysis of the ocean's role in human health are coordinated by the International Geosphere-Biosphere Program (IGBP) and the World Climate Research Program (WCRP). The Group on Earth Observations (GEO) has a 10-year plan (2005–2015) to implement a Global Earth Observation System of Systems (GEOSS) to connect remote sensing and users, fostering a global infrastructure to assess environmental change and its impacts on ecosystems including humans. A number of countries maintain space-based programs to map Earth resources and assess changes in the environment (Argentina, Brazil, China, several European countries as well as the European community, India, Israel, Japan, Russia, South Korea, the United States, and others). The Committee on Earth Observation Satellites (CEOS), which coordinates civil spaceborne observations of the Earth provides a useful online database on relevant missions, instruments, and measurements (http://database.eohandbook.com/). This database includes tables detailing mission dates, data characteristics, and applications.

Several national and international programs are also developing interfaces to facilitate merging of satellite data with other information to assist resource managers, policymakers, educators, and scientists. For example, NASA's SERVIR initiative integrates satellite observations, ground-based data, and forecast models to monitor and forecast environmental changes and to improve response to natural disasters. In 2006, the United Nations General Assembly agreed to establish the "United Nations Platform for Space-based Information for Disaster Management and Emergency Response Space-based Information for Disaster Management and Emergency Response" (UN-SPIDER), which seeks to further broaden access to space-based information to support disaster mitigation and response. Several other

programs are being developed around the world, both by focused research efforts in academic institutions as well as by national and international government agencies. The reader is encouraged to follow the development of these global networks.

Measurable Variables

Remote sensing of the Earth's properties is based on the measurement of electromagnetic radiation reflected or emitted by a target. In terms of human health, all ocean waters are ultimately relevant as trends in global and regional ocean productivity and temperature are more than simply of academic interest. These tendencies, which can be assessed from space, may indicate large-scale changes related to climate variability [2–4]. They affect the pH of the upper ocean [5], affect lower trophic levels [6], and have impacts on higher trophic levels including fish [7, 8].

Estuarine, coastal, and continental shelf waters are directly relevant to human health. This is where much of the effort is concentrated on collecting resources from the ocean or to input our discharges. These waters support commercial and recreational boating, tourism, fisheries, and other industries and activities, and they receive materials from land either through rivers that drain inland areas, effluents from coastal cities, and from atmospheric deposition. There is a need to understand processes that change any factor in these waters that affect these uses, over both short and long time frames, as well as over short to synoptic space scales, including climate-scale changes.

While there had been some important attempts to apply remote sensing to coastal waters in the 1970s and 1980s, most of the research on coastal and estuarine waters conducted to date has been done more recently in the 1990s and the first decade of the new millennium. This research has focused on refining quantitative estimates of sediment load, turbidity or water clarity, algal concentration as a measure of eutrophication, detection of hydrocarbon slicks, and measuring temperature, bathymetry, and types of benthos. Studies by Epstein [9] highlighted the importance of remote sensing in addressing large-scale factors, including climate change, that promote the spread of disease in the coastal ocean.

Yet progress in the application of remote sensing to marine pollution, spreading of disease, or assessing the linkages between human and ocean health has been slow because few environmental parameters lend themselves to remote sensing. Often, these parameters are not easily measurable at the appropriate space and time scales. Pollution and disease vectors are time and again introduced to the marine environment at relatively small scales, and they disperse following complicated pathways. Limitations exist in observing these patterns using available satellite sensors, and the electromagnetic signal of the variables of interest is often masked or contaminated by other environmental factors. Clearly, the potential benefits of remote sensing are large, considering the high costs of monitoring using only

traditional methods, but much work is needed to refine the technology to address even basic marine pollution problems.

Progress in this field has been made through interdisciplinary studies of indicator parameters designed to detect pollution or conditions that promote pathogen growth or their vectors by proxy or through studies of dispersal processes. Such inferences are best made when measurements are based on physical principles and when users are aware of technological limitations. For example, present state-of-the-art technologies and methods still do not permit direct estimates of nutrient, heavy metal concentrations, or pH, despite some early reports suggesting that this is possible (cf. [10, 11], and numerous unpublished reports). In many cases, any correlation between remotely sensed parameters and these variables is site specific, ephemeral, and may be coincidental, necessitating statistical validation on a site-specific, image-per-image basis.

Phytoplankton standing stock, estimated in terms of chlorophyll or "pigment" concentration, is an important indicator of water quality. Among other relevant variables that may be sensed remotely are diffuse light attenuation coefficients, suspended sediment load, "turbidity," dissolved organic material (yellow substance), temperature, salinity, wind stress, wave direction, amplitude and wavelength, and current speed and direction. This entry provides a very brief overview of methods used to detect these variables.

Approaches

The most successful approach to remote sensing combines a variety of measurement platforms and data types, including automated in situ and shipboard observations for detailed ground truth and remote sensors to cover a range of spatial and temporal scales. Satellite and airborne remote sensing is typically limited to signals originating from the surface or "skin" of the ocean (microwave and infrared radiance) or, at most, a few attenuation depths from the surface of the sea (for visible light, the attenuation depth is the distance over which radiance decays by a factor of 1/e; c.f. [12]). It is therefore very important to obtain complementary measurements at greater depths to resolve one of the most important dimensions in the aquatic environments, namely the vertical. Similarly, since remote sensing only provides direct estimates of a few parameters, it is critical to establish the empirical or deterministic relationship with any proxy that may be used to asses ocean health.

Advances in telemetering of data from remote sampling sites and platforms (e.g., [13–15]) promise solutions to a range of environmental monitoring problems, including in situ measurement of chemical processes [16], contaminants [138], nutrient concentrations [17–19], precipitation [20, 21], bioluminescence [22–24], zooplankton and larger animals [25–27], light (c.f. [28–30]), and primary productivity, and other variables (see [31], and references therein). This is an area

of active development that will provide important calibration and supporting data for remote sensing work, thus facilitating ground truth efforts.

The advantage of satellites is that they augment the scope of oceanographic studies by providing frequent and repetitive coverage of large spatial scales, and that the user is rarely involved in the complicated process of collecting the raw data [32]. Many of these synoptic time series now extend for many years, and decadal datasets are now available. This permits evaluation of anomalies relative to a specific time frame and comprehensive comparative studies. However, satellite data is voluminous, and processing is computationally intensive, which leads to trade-offs between spatial and temporal resolution. Spatial resolution is also sacrificed to improve radiometric sensitivity, which is critical because many signals are weak and because target identification is usually based on narrow features in reflectance spectra.

Aircraft, including helicopters and balloons, are platforms on which prototype satellite instruments are frequently tested. Instruments flown on aircraft provide finer spatial and temporal resolution than their satellite counterparts, flexible flight patterns and altitude, and short deployment times. These features frequently make aircraft the platform of choice during catastrophic pollution events (see, e.g., [33, 34]). However, aircraft fitted for remote sensing are expensive and often are not readily available, a situation that may be at least partially remedied by drone planes and helicopters. Also, while merging observations with navigation data has become easier, sunglint, surface wave patterns, and contamination by unmeasured factors (e.g., cloud shadows, electronic aircraft system noise, calibration drift, etc.) are common.

Applications and Sensors

Since the 1970s, there have been significant advances in the development of sensors flown on international satellite missions and on aircraft to measure coastal, estuarine, and marine parameters of interest to ocean and human health. Extremely sensitive sensors are required to measure the visible sunlight reflected by materials suspended in the surface layers of the ocean or lying on the bottom in coastal waters shallower than about 20 m. Sensors finely tuned to specific infrared wavebands to which the atmosphere is relatively transparent are used routinely by many sensors to measure the temperature of lakes, coastal waters, and the world's oceans several times per day, both during daytime and nighttime. A number of microwave sensors are used to estimate wind and surface current speed and direction, temperature, ice cover, and even salinity. The satellite sensors therefore afford rapid, repeated, and synoptic assessment of a number of environmental parameters concurrently anywhere on the planet, at pixel resolutions that typically range between a few meters to hundreds of kilometers and at particular times of the day, at a relatively low or no cost to the user. Airborne sensors provide much higher spatial resolution spanning

centimeters to meters and the ability to sample a particular time of the day, but logistics are expensive, and obtaining good data quality in aquatic environments is challenging.

Remote sensing data have been tested in a number of applications over the years. Many attempts have been made to link various observable parameters to factors that affect ocean and human health. Much work remains to be done with both historical datasets as well as observations from new sensors and combining data from various sensors and automated or discrete ground observation platforms. Today, the most significant application in coastal and marine observation remains the use of various sensors to characterize a number of environmental parameters concurrently over synoptic scales rapidly and repeatedly and within the context of long time series. This allows detection of change and anomalous conditions relative to some previous condition or arbitrarily constructed "climatology." Some applications are extremely useful but still as of yet mostly underutilized by the public, resource management officials, and the public health community. Some other applications have great potential, but as of yet they have not been proven and have been oversold. A few of these applications are described in the next few paragraphs under the headings of specific technologies.

Ocean Color

Among the most useful indicators of water quality is ocean color. The color of the ocean is the result of the interaction between visible solar irradiance, water, and substances like phytoplankton, suspended sediment, colored dissolved organic matter, or with the bottom of the ocean. The color contains much information about the condition and health of water bodies [141].

Ocean color studies fall broadly under the category of aquatic bio-optics, and their objective is to gain insight on processes such as the distribution and dispersal of dissolved organic carbon, changes in oceanic primary productivity, targeting and identifying coastal phytoplankton blooms, conducting regional and global biogeochemical assessments, understanding changes in benthic communities in clear, shallow tropical coral reefs, and monitoring coastal water quality. Sensors with high, medium, and low spatial resolution have been used to develop and test applications to assess various parameters relevant to ocean and human health. Most attempts at using high spatial resolution sensors have not led to accurate assessments nor developed into widely used operational tools. At this stage, the best promise for remote sensing of biogeochemical processes in the coastal ocean remains with sensors that have high sensitivity and high dynamic range and frequent coverage. This restricts the type of sensors to those having narrow spectral bands, medium spatial and spectral resolution, repeat orbits that provide daily or near-daily observations, and well-calibrated visible radiance data, i.e., those that are commonly known as "ocean color" instruments.

An important issue that requires significant attention is the estimation of the atmospheric radiance seen by an ocean color sensor [35, 36]. Over 80–90% of the

total visible radiance received by a satellite sensor looking at the ocean is due to atmospheric scattering of solar radiation or specular reflection of light by the ocean's surface. These sources of radiance need to be estimated with high precision and accuracy exceeding 1% since an error of this order will lead errors that can exceed 10% in the water-leaving radiance. The water-leaving radiance is light backscattered by the water column, not by the surface, which is detected by a downward-looking sensor just above the surface. In addition, marine waters are dark compared to land, and coastal and estuarine waters are especially dark since materials suspended or dissolved in them typically absorb visible light strongly across the spectrum. Therefore, ocean color sensors have to be extremely well calibrated and have signal-to-noise ratios exceeding 500 to over 1,000 the typical radiance values observed over the ocean. Among the most used ocean color sensors are the following:

Satellite sensors (see CEOS; http://database.eohandbook.com/ for a complete list):

- Coastal Zone Color Scanner (CZCS; 1978–1986; NASA/USA).
- Sea-viewing Wide-Field-of-view Sensor (SeaWiFS; 1997–2010; NASA and Orbimage/GeoEye; USA).
- Moderate Resolution Imaging Spectrometer (MODIS on the NASA Terra and Aqua satellites; 1999 and 2000 launches and continuing in 2011).
- Medium Resolution Imaging Spectrometer (MERIS on the ESA ENVISAT satellite; 2002 launch and continuing in 2011).
- Ocean Color Monitor (OCM; on several ISRO Oceansat satellites; from 1999 and continuing in 2011).
- Visible/Infrared Imager/Radiometer Suite (VIIRS, planned for launch in late 2011 on the US National Polar-Orbiting Operational Environmental Satellite System Preparatory Mission/NPP and on the future Joint Polar Satellite System/JPSS with a planned launch date of 2015).
- Hyperion (on the NASA EO-1 satellite; launched in 2000 and continuing in 2011).
- Several other international missions.

Aircraft sensors:

- Airborne Visible/Infrared Imaging Spectrometer (AVIRIS).
- Compact Airborne Spectrographic Imager (CASI).
- Airborne Oceanographic Lidar (AOL).
- Several other research and commercial sensors.

Applications of Ocean Color Data

Ocean color data permit a wide range of observations relevant to ocean and human health applications. Ocean color observations are of particular interest because of their ultimate utility in estimating the spatial distribution of stocks and rate of change of various organic carbon pools in the ocean, including those associated

with living and detrital particulate materials and with colored dissolved organic matter. In addition, these data are useful for coastal applications including monitoring of suspended particulate and dissolved materials associated with river discharge and resuspension from the bottom and, in general, for assessing coastal water quality. This is accomplished primarily by retrieving chlorophyll concentration and absorption and backscattering properties of the water from spectral measurements of the surface reflectance of the ocean.

Attempts to quantify chlorophyll concentration, colored dissolved organic matter (CDOM) absorption, suspended sediment load, "turbidity," and the diffuse attenuation coefficient of light as an index of water clarity have been made using a variety of satellite sensors. Geographically, of particular interest are coastal and estuarine waters, where so many human activities are focused. River plumes often lack an infrared (IR) signature that distinguishes them from marine waters, especially as distance from the estuary increases. However, plumes are strongly colored relative to sea water. Ocean color sensors are characterized by their narrow spectral bands, very sensitive sensors, and spatial resolution of between ca. 250×250 m^2 and 1×1 km^2 pixels. The advantage of these sensors is that they cover areas $>10^6$ km^2 in only 2–3 min, with revisit times of 1–3 days.

The CZCS [37] proved the value of using ocean color satellite images for tracing plumes over long distances. CZCS bands were centered at 443, 520, 550, 670, 750, and 11,500 nm and sought to match chlorophyll absorption maxima and minima. The red channels allowed atmospheric correction. Since the CZCS was an experimental sensor, data coverage was not continuous, the instrument was less sensitive than required for coastal observations, and the calibration was hard to establish. In effect, the technology was extremely useful to visualize, for the first time, global ocean phytoplankton biomass and river plume dispersal in the open ocean; the CZCS did not allow accurate estimates of coastal water colors, coastal chlorophyll concentrations, or turbidity. The CZCS ceased operating in 1986, leaving behind a very large data set [38].

Among the most relevant ocean and human health studies were the pioneering studies of Barale et al. [39]. They used the CZCS to help calibrate numerical simulations of the circulation of the Adriatic Sea and the Po River plume to provide information on seasonal dispersal of contaminants in the region [40, 41]. Maynard et al. (1987) then used the CZCS to map the dispersal of Yukon River water and that of smaller rivers in Norton Sound (Alaska) to determine the area of impact of potential pollutants on the northern Bering Sea. Holligan et al. [42] compiled an atlas of CZCS and AVHRR images to document advection and mixing processes in the North Sea, where human impact is intense.

In an attempt to outline seasonal circulation patterns of the tropical western Atlantic, the Caribbean Sea, and the Gulf of Mexico, and to evaluate the effect of nutrient inputs via rivers into these oligotrophic seas, Muller-Karger et al. [43, 44] illustrated the seasonal dispersal of the Amazon, Orinoco, and Mississippi river plumes. CZCS imagery showed the marked seasonal variability of these plumes. These papers illustrated the connectivity between distant locations in ocean basins, with river plumes often extending hundreds to over 1,000 km from their source.

Müller-Karger et al. [45] also combined ocean color and infrared imagery (from the AVHRR) to trace eddies and other oceanic circulation features in the Gulf of Mexico. Müller-Karger et al. [45] and del Castillo et al. [46] used CZCS and SeaWiFS images to demonstrate that the Mississippi plume does not always disperse to the west of the Mississippi Delta but that it also disperses to the east and south in the Gulf of Mexico and that it can reach the Florida Keys and disperse along the eastern seaboard of the USA. The significant river influence over shelf areas can be appreciated in satellite images of many river deltas and river plumes. These studies laid some of the groundwork for analyses of potential dispersion pathways of contaminants like oil.

There effectively was a 10-year gap between the end of the CZCS mission in 1986 and the resumption of ocean color observations with the Japanese OCTS on the ADEOS-I mission. The field of ocean color research and applications moved forward significantly with the launch of the SeaWiFS sensor in 1997 shortly after the failure of the ADEOS-I satellite, and the MODIS and MERIS sensors in 1999 and 2000 as the twenty-first century began. Oceanic remote sensing moved toward complex and multidisciplinary studies of environmental change over a wide range of time and space scales. These studies merged observations from various satellites. A concerted effort was initiated to understand coastal and turbid waters [47].

The differences between sensors and missions are considerable, ranging from orbit and ground revisit time to swath width, spectral and spatial resolution, sensitivity, accuracy, and so on. Examining each is beyond the scope of this review. For the purposes of illustrating applications, NASA's Moderate Resolution Imaging Spectroradiometer (MODIS, [139]) and Orbimage's SeaWiFS [144] are focused on because of their multiyear time series, global coverage, and their high-quality observations. The SeaWiFS sensor ceased operations in 2010. MODIS sensors continue data collections, and all data from the CZCS, SeaWiFS, and MODIS satellite sensors are public. The MODIS model is of particular interest because it is the prototype for the Visible/Infrared Imager/Radiometer Suite (VIIRS), which will fly on the US National Polar-Orbiting Operational Environmental Satellite System Preparatory Mission (NPP) and the future Joint Polar Satellite System (JPSS).

The overall accuracy of retrieved geophysical parameters (water leaving radiance, CDOM absorption, chlorophyll concentration, etc.) depends on the performance of the atmospheric correction and in-water algorithms. Of primary concern are sensor calibration and characterization. Errors in water-leaving radiance estimates can easily by exacerbated or exaggerated in coastal and estuarine waters because the blue water-leaving radiance is often much smaller than that in clear ocean waters. Significant research has focused on improving the traditional multiband chlorophyll retrievals. The MODIS and MERIS sensors are also equipped with spectral bands specifically designed for measuring chlorophyll fluorescence relative to a baseline (chlorophyll fluorescence line height algorithm; [48]). The chlorophyll fluorescence efficiency varies in time and space, which is an area of research. Aggregating such data with those from other bio-optical algorithms helps address high-chlorophyll coastal waters (e.g., [49–51]). Unfortunately, the VIIRS

sensor lacks the capability to detect this solar-stimulated fluorescence, limiting its capability for coastal observations relative to MODIS and MERIS.

Water constituents are estimates based on the water-leaving radiance. Algorithms related to biological oceanographic properties are referred to as "bio-optical" algorithms. For Case I waters, where one variable (phytoplankton) dominates color, a band-ratio (blue/green) bio-optical algorithm is often effective to estimate chlorophyll-a concentration because phytoplankton absorbs more blue light than green. Robust band-ratio algorithms have been used for CZCS [52], SeaWiFS, and MODIS [53]. In turbid coastal waters where constituents do not co-vary and phytoplankton does not dominate water color, band-ratio algorithms often fail (e.g., [50]). Semi-analytical algorithms may help in these cases [54–57]. The objective is to differentiate between various constituents, namely chlorophyll, colored dissolved organic matter (CDOM), and total suspended solids (TSS). While some progress has been made over time (e.g., [50]), assumptions need to be fine-tuned regionally, as Case II waters vary in space and time. Examples of parameters that are difficult to estimate but that are required in these optical models are the spectral slope of CDOM absorption, particle backscattering, bottom reflectance, and depth.

There has been significant progress in estimating and mapping the distribution of colored dissolved organic matter in the oceans (see [58–60], and references therein) and in coastal waters. The work of the SWFDOG group [49] illustrates the importance of using time series of satellite images to detect and track anomalies in coastal water quality. They detected an event off western Florida, USA, which the media called a "black water" event and which caused significant anxiety among local coastal residents, divers, and fishermen. Daily SeaWiFS data collected between September 1997 and August 2002 showed this unique event that lasted over 4 months. The "black water" was advected into the Florida Keys National Marine Sanctuary, where it led to the death of corals and sponges. By tracking the event, it was possible to determine that the extensive dark water patch evolved from a senescent bloom that was stimulated into activity again by local river input. The dark color of the water was due to high concentrations of CDOM and decreased backscattering. A field survey showed chlorophyll concentration was 5–10 mg m^{-3} due to a nontoxic diatom (Rhizosolenia) bloom.

While chlorophyll is a parameter desired by many coastal managers, it remains very difficult to estimate with sufficient accuracy in coastal and estuarine waters. A small error in CDOM assessment significantly affects blue absorption estimates and causes large errors in chlorophyll retrievals. For example, the CDOM absorption coefficient at 443 nm in an estuarine area may be 0.3−0.4 m^{-1} or larger, while a chlorophyll concentration ~1 mg m^{-3} effects an absorption coefficient of 0.03–0.04 m^{-1} at 443 nm. Thus, a 10% error in CDOM estimates leads to 100% errors in chlorophyll estimates. Throughout the "black water" and other similar events off western Florida, it was possible to differentiate between coastal plumes that contained a phytoplankton bloom and those that were dominated by CDOM by examining both the blue and green water-leaving radiance bands of SeaWiFS and MODIS and the fluorescence line height (FLH) images from MODIS [50].

Satellite ocean color sensors have shown great advantage over traditional means to monitor the spatial extent and duration of harmful algal blooms (HAB) or red tides. The state-of-the-art primary indicator of a bloom (toxic or not) is high chlorophyll concentration. At present, there is still no reliable algorithm to discriminate between red tides and other blooms, such as one dominated by diatoms or by other nontoxic phytoplankton. For example, during Alexandrium blooms which occur in the Gulf of Maine off the northeastern United States, these organisms co-occur with significant quantities of other phytoplankton, and therefore, waters do not seem to have a particular spectral signature that would allow identification of this HAB.

Chlorophyll concentration has been used as a proxy to build a crude operational monitoring tool for Karenia blooms off Florida (e.g., [61]). However, reliable estimates of chlorophyll concentration in these coastal waters have not been achieved, and bio-optical algorithms are still the focus of intense research [62–64]. A fundamental difficulty is the presence of CDOM since a small error in CDOM estimates generates large errors in computed chlorophyll values. A positive chlorophyll concentration anomaly also does not represent proof positive of a red tide bloom. Therefore, false positives are inevitable, particularly during periods of higher river discharge or when other blooms occur. At this stage, the capability to detect an anomalous chlorophyll concentration provides an important advantage in planning proper field surveys and other responses by resource managers.

Great expectations revolve around identification of phytoplankton species by spectral analyses combined with other environmental observations [65, 140]. A recent study, for example, found that the backscattering to chlorophyll ratio is generally lower in *Karenia brevis* blooms relative to other blooms [66]. The proposed explanation is that this species experiences less grazing. How to take this scientific discovery to an algorithm and into an operational system is being investigated.

A useful and important application of remote sensing data is the assessment of suspended solids in aquatic environments. High concentration of suspended matter is an indication of erosion, resuspension of benthic sediments that may have contaminants, or of eutrophication due to a variety of causes. This condition also blocks sunlight from reaching benthic algae and sea grass, negatively affecting the health of coastal and estuarine waters. Turbidity is an index of light attenuation and water quality commonly used in estuarine and coastal areas. Several studies have demonstrated the utility of remote sensing to estimate turbidity in coastal, turbid waters. Miller and McKee [67] used MODIS 250 m data to assess total suspended matter in Lake Ponchartrain and adjacent waters in Mississippi, USA. Chen et al. [68, 69] and Moreno et al. [70] examined time series of 250 m MODIS images of Tampa Bay and showed that the synoptic satellite observations, collected every 1–3 days, are an important complement to the monthly water quality sampling program carried out in the bay. They illustrated rapid changes in spatial and temporal water clarity and turbidity conditions that were missed by the in situ surveys and were able to explain turbidity changes related to tidal, wind-driven, and discharge events. Rodríguez-Guzmán and Gilbes-Santaella [145] used 250 m

MODIS data to estimate suspended matter concentrations in Mayaguez Bay, Puerto Rico. Similar studies have been conducted in France by Doxaran et al. [71].

An interesting conceptual framework for coastal ocean and human health applications was defined by Lobitz et al. [72] and Colwell [73], who identified a need for synoptic observations of phytoplankton blooms and sea surface temperature to help assess the potential for cholera outbreak conditions in coastal and estuarine waters. Colwell [73] and Hu et al. [74] further made the case that climate change affects the distribution and frequency of diseases, many of which spread along coastal zones with biological carriers. Colwell [73] found that the spread of the phytoplankton blooms and associated cholera outbreaks throughout the tropical and subtropical Pacific Ocean coasts of South America were associated with El Niño-Southern oscillation events. Hu et al. [74] found a linkage between climate variability, as quantified by the Southern Oscillation Index (SOI), and dengue fever epidemics in Queensland, Australia. They found an increase in the numbers of dengue fever cases 3–12 months after a decrease in the average SOI (i.e., warmer conditions).

Several attempts have been made to use the Advanced Very High Resolution Radiometer (AVHRR) on the NOAA Polar Orbiters to estimate coastal and oceanic water quality parameters [75–77, 146, 147]. The AVHRR (see [78]) has a nominal pixel resolution of 1×1 km and near-infrared bands that are sensitive to reflected sunlight and which have a dynamic range that accommodates the high reflectance of land and coastal waters. Since it is an operational facility, data are available several times a day, worldwide. Stumpf et al. found that when calibrated with concurrent in situ observations, individual AVHRR images provided information on sediment load and phytoplankton concentration in estuaries. They point out that the technique can be improved by correcting for atmospheric effects.

While the moderate-resolution class of ocean color and near-infrared sensors (historically, the CZCS, SeaWiFS, MODIS and MERIS, and AVHRR) allow observation of large-scale phenomena, there is a need for high spatial resolution data to address local marine pollution problems. Landsat data from the Thematic Mapper class of sensors are available for many areas around the globe since the mid-1980s and are now free to the public and distributed by the United States Geological Survey (USGS). Attempts to map coastal and oceanic water quality parameters have been made since the 1970s, initially using Landsat sensors ([79–85]; and others). Use of Landsat and the French SPOT sensors has grown rapidly because they provide pixel resolutions of 30–80 m in spectral mode. They have been used to map suspended sediment and variations in water color in the nearshore environment [81, 84, 86–89, 143].

Since the late 1990s, higher spatial resolution imagery from several commercial satellites has become available, although at considerable cost to the user. These data are used extensively to map general land features, for urban and land-use planning, resource assessment, and disaster response efforts. Hellweger et al. [90] provide an example of the utility of high-resolution (1 m IKONOS) multispectral satellite imagery for estimating water quality patterns in the lower Charles River (Boston, USA), with limited results. Single image applications do not satisfy coastal and ocean health studies or applications. These important applications will continue to

be limited as long as the data remain costly because building any time series and/or climatology against which to assess change is prohibitively expensive.

However, compared to the ocean color sensors mentioned above, past Landsat-class sensors have broad bands; for example, the "blue" channel on Landsat TM and ETM + (0.45–0.52 μm) spans the blue chlorophyll absorption peak and blue-green shoulder, the "green" band (0.52–0.60 μm) spans part of the blue-green shoulder, the green absorption minimum, and the green-yellow shoulder. SPOT lacks blue bands. The Landsat Data Continuity Mission (LDCM), planned for launch in late 2012 or 2013, includes a new Coastal/Aerosol band spanning 0.433–0.453 μm. This will be a very important tool in coastal resource assessment.

Most attempts to evaluate concentrations of in-water constituents with Landsat or SPOT have been based on scene-specific, concurrent in situ observations to provide a statistical base. In general, good qualitative information may be obtained in the immediate nearshore environment (e.g., [91]). At best, they may provide similar information to that derived from the AVHRR in highly turbid environments using red and near-IR bands but with much better spatial resolution [92]. The high cost of these data and the long revisit times (8–17 days due to orbital characteristics and narrow swaths) precludes detailed time series analyses or even use as monitoring tools.

Two significant advantages of Landsat-class data are that historical data are available since the mid-1980s and this allows comparison of a number of parameters including shoreline location and that Landsat data are now free of cost. However, Landsat and most other high spatial resolution sensors data provide only a limited capability to conduct systematic studies of waterborne constituents such as phytoplankton or sediment concentration either in coastal zones or elsewhere because of the limited radiometric, geometric, and revisit characteristics of the sensors. They are not well suited for quantification of aquatic chlorophyll in open waters and much less in areas of high chlorophyll because of the problems listed above. An important issue is the very high-cost per square kilometer of data for data from most of the commercial high-resolution sensors. These data are of great interest to the science community, but research using these data has been hampered by their cost.

One of the most exciting developments of the last decade is the availability of data from a series of proof-of concept hyperspectral satellite sensors. Hyperspectral data provide a significant improvement over the traditional multispectral sensors that provide between four and ten bands in the visible to differentiate between various optically active constituents present in coastal and estuarine waters [93]. The most widely accessible sensor is the NASA Hyperion sensor, launched in 2000 aboard the EO-1 proof-of-technology satellite. Hyperion collects images in 220 spectral bands at 30 m resolution, compared to the ten multispectral bands flown on traditional Landsat missions. The instrument collects images spanning 7.5 km by 100 km. The Hyperion data are new to coastal water quality assessments. Brando and Dekker [94] tested the Hyperion data and found that the sensor sensitivity is sufficient to estimate colored dissolved organic matter, chlorophyll, and suspended matter in Moreton Bay, an estuary in Australia. The Hyperspectral Imager for the

Coastal Ocean (HREP-HICO; [95]), installed aboard the International Space Station since 2009, operates a visible and near-infrared (VNIR) Maritime Hyperspectral Imaging (MHSI) system. The goal is to detect, identify, and quantify coastal geophysical features and to test algorithms for water clarity, chlorophyll content, water depth, and ocean or sea floor composition for civilian and naval purposes.

Aircraft Sensors

Aircraft instruments play an important role in monitoring aquatic pollution at small scales. The AVIRIS, flown on NASA's ER-2 high-altitude aircraft (a U2), provides 224 bands of visible/infrared data at ~20 m resolution [96–98]. Its sensitivity for detecting variations in water-leaving radiance is relatively low but adequate where highly reflective constituents occur. Karaska et al. [99] used AVIRIS images of the Neuse estuary in North Carolina to estimate the concentrations of chlorophyll, suspended matter, CDOM, and turbidity and created an index of eutrophication for these waters. Bagheri and Yu [100] applied similar techniques to map water quality in the Hudson/Raritan estuary.

Another aircraft instrument is the FLI, also called the Programmable Multispectral Imager (PMI), of Moniteq Inc., Canada [101]. Dekker et al. [102] examined variations in eutrophication of the Loosdrecht Lakes in the Netherlands with the PMI and concluded that this instrument was ideally suited to examine distribution of pigments because of its high spatial resolution and sensitivity at long wavelength bands (ratios of bands between 600 and 720 nm were needed).

Among popular aircraft instruments used for water quality monitoring is the CASI of Moniteq Inc., Canada [103, 104]. Unlike others, this instrument is well calibrated, small (about the size of a personal computer), and may be used in an "imaging" mode with a few selectable bands or in a "spectral" mode in which a few pixels are collected for 288 bands between 450 and 950 nm for limited "look directions." The applicability of the CASI to marine pollution problems still needs to be better documented.

Active sensors, namely those which illuminate a target and measure electromagnetic radiation returned to the system, also show promise in water quality studies [105]. Among the most prominent is the NASA AOL. The AOL can be operated in a LIDAR mode (time gated) or as a multispectral analyzer with or without a fixed time (depth) delay [32]. This laser sensor presents many advantages, among which are specificity of response, relative simplicity of signal interpretation, low-altitude operation (including below cloud ceiling), and the potential of providing depth distribution of relevant variables by time-gating laser pulses [32]. Hoge and Swift [106] demonstrate the high correlation between fluorescent return and chlorophyll. This instrument is also useful for mapping horizontal and vertical turbidity variations [107].

Other Measurable Variables

Oil Spills, Surface Organic Slicks, Surfactants, and Yellow Substance

Traditional remote sensing techniques to address oil spills in aquatic environments include optical (passive visible and infrared, laser fluorosensors), and passive and active microwave (e.g., Synthetic Aperture Radar, SAR) using aircraft or satellites (see [108, 109, 148, 149]). Most of the satellite SAR sensors and the various airborne sensors used to detect oil at the surface of the ocean are expensive and do not provide the required high-frequency coverage. The MODIS sensors include bands that generate images at 250 and 500 m spatial resolution. These have great unexploited potential for coastal monitoring because they can be used to study small-scale features. One application is in assessments of oil spills and water quality where 1-km satellite data are often inadequate. One example was illustrated by Hu et al. [51]. The medium-resolution (250- and 500-m) MODIS Level-1 total radiance imagery from 1 December 2002 to 9 March 2003 was examined, and patterns were found within Maracaibo Lake that is suspected to be extensive spill patches; the presence of oil was confirmed by the ground surveys.

This experience was important as it helped to rapidly implement the use of MODIS and MERIS data to map surface oil features during the British Petroleum Deepwater Horizon (BP DWH) disaster in 2010. Satellite remote sensing was essential in mapping and tracking surface oil dispersal during this event (Muller-Karger, 20 May 2010, testimony before the House Subcommittee on Energy and Environment, US Congress). Exploring the promise of this technology is important to understand the potential of the VIIRS imaging bands on the NPP and JPSS satellite platforms.

Organic films on the ocean surface can be detected and mapped by laser light [110]. In 1978–1979, a series of oil spills were made off Sandy Hook, New Jersey, in waters >40 m depth. These spills were treated with helicopter-deployed dispersants containing surfactants soon after deployment and overflights with the NASA AOL were used to map the spills [111]. The results show that Raman backscatter strength can be related to oil-film thickness after removal of background and oil fluorescence contributions [111, 112]. Laser light can also be used to determine the spatial distribution of dissolved organic material in marine and estuarine environments [113, 114].

Infrared imagery such as that of the AVHRR has also proved useful to trace very large oil spills. During the Persian Gulf War of January–March 1991, oil slicks could be traced off the coast of Kuwait as sea surface temperature (SST) anomalies in the nighttime imagery. Such patterns were undetectable in the daytime AVHRR imagery (O. Brown, U. Miami, personal communication 1991).

Oil contamination of the Persian Gulf could also be traced in handheld photography collected by Space Shuttle astronauts [115]. During the Iran-Iraq war, oil slicks emanating from burning oil tankers and drilling platforms along the Iranian coast could be seen in the photography. Similarly, oil released from Kuwaiti

loading facilities and oil fields during the 1991 Gulf war could be seen spreading along the Kuwait and Saudi Arabia shorelines in sunglint photography.

Microwave sensors also have an application in monitoring oil pollution in the ocean. In particular, the SURSAT (Surveillance Satellite) program, implemented in 1977 by the Canadian government, proved the utility of microwave sensors in monitoring ocean traffic, ice coverage, weather, and ocean pollution [116]. SURSAT provided the basis for participation by Canada in the US SEASAT program. The NASA SEASAT satellite, which operated between 26 June 1978 and 10 October 1978, was a test-bed for a variety of ocean-looking instrumentation. Among the most successful instruments was a Synthetic Aperture Radar (SAR), with 25 m resolution, which seemed able to detect oil spills. However, the subtle distinctions between oil slicks and natural phenomena resembling oil slicks require further work [116, 117].

Temperature

Satellite instruments designed to measure sea surface temperature (SST) are among the most successful for both research and operational applications. Several instruments now provide routine, daily coverage of the world's coastal and marine environments, including the NOAA and MetOP AVHRR, and NASA MODIS. They provide observations that facilitate tracing of circulation features of spatial scales ranging from 10 to 1,000 km (c.f. [45]). These sensors are also used to track weather patterns and map land vegetation indices [118, 119].

An important application of satellite SST is detection of temperature extremes in coastal environments [120, 121]. Temperature variability can both enhance the resilience of coastal and marine organisms, but both cold and warm extremes can be fatal. Soto [122], for example, documented larger benthic coral reef cover in coastal areas of the Florida Keys, USA, where SST variability was larger than where SST was more stable. Satellite images are now also routinely used to assess areas around the world at risk of coral reef stress due to high-temperature anomalies [123].

Temperature contamination frequently occurs at smaller scales ($<<$100 km) as a result of industrial discharge, and the sensors with 1 km spatial resolution such as the AVHRR and MODIS are generally inadequate to resolve these scales. The Landsat TM and ETM + sensors provide a useful tool to assess surface temperature of aquatic environments at such scales, with Thermal Infrared (TIR) data at 60 m pixel resolution. For example, Thomas et al. [124] and Fisher and Mustard [125] used Landsat data to study sea surface temperature patterns off the coast of New England, USA. These studies demonstrated that it is possible to assess the dominant seasonal patterns in cross-shelf SST gradients at scales of small embayments and estuaries in coastal zones around the world. A limitation remains the repeat cycle of the Landsat-class satellites, i.e., every 16 days.

An instrument that provides higher resolution is the Precision Radiometric Thermometer Model 5 (PRT-5), deployed from aircraft or even ships. This sensor provides an operational capability to map along-track SST.

Salinity

Remote sensing of sea surface salinity from aircraft and satellites, using microwave radiometers tuned to frequencies of order of 1 GHz, has been limited primarily by the poor spatial resolutions obtained with conventional microwave antennas (i.e., >500 km from satellites). Proven aircraft capabilities are accuracies <10 practical salinity units and 0.2 units in resolution. Lagerloef et al. [126] discuss synthetic aperture antenna technology that would allow resolutions of ca. 10 km from space and higher resolutions from aircraft altitude.

Two missions are now poised to provide global satellite observations of sea surface salinity. The European Soil Moisture and Ocean Salinity Satellite (SMOS), launched in November 2009, is part of ESA's Living Planet Programme and was designed to facilitate the study of the Earth's water cycle and climate. The Aquarius/SAC-D mission, launched in June 2011, is a focused satellite mission to measure global sea surface salinity. The Aquarius/SAC-D mission was developed by NASA and the Space Agency of Argentina (Comisión Nacional de Actividades Espaciales, CONAE). These instruments are expected to have accuracies of 0.5–1.0 psu and be unaffected by cloud cover. The limited spatial resolution and accuracy, however, will be of limited use in pollution monitoring work.

Ocean Currents, Wave Height and Direction

An important capability afforded by satellites is the ability to map sea surface topography (sea level variations in space), sea level changes, and the roughness of the ocean's surface over large to global scales, repeatedly and over long periods of time. This is possible with a number of active microwave sensors (radar). Most of the radar sensors that fall under the category of "altimeters" and "scatterometers" have relatively low spatial resolution (tens of kilometers), which limits direct application to examine physical oceanographic conditions within estuaries and most coastlines. Synthetic aperture radars (SAR) on the other hand have very high spatial resolution (order of meters) and are helpful to map larger waves, including internal waves. SAR data are also very useful to map characteristics of the texture of the sea surface that may be a telltale of pollution or other conditions relevant to ocean and human health. As mentioned above, SAR data have been instrumental in mapping surface slicks, oil spills, and natural oil seeps in the ocean.

Altimeter radar sensors can today accurately measure changes in sea surface topography in the order of 1–2 cm over areas spanning from several tens of square kilometers to global. Among the most important applications of altimeters are measuring sea level and the variability in sea surface height in an ocean basin ([127, 128, 142]). The importance of understanding regional and global trends in sea level over short and longer periods cannot be overemphasized. Altimeter observations show that sea level around the turn of the millennium rose at an accelerated rate of about 3.1 mm per year. This is significantly higher than the

average rate for the twentieth century and is now considered a major threat to coastal communities by the Intergovernmental Panel on Climate Change (IPCC, [129]). Sea surface height variability also provides a means to measure regional circulation in the interior of the ocean over large scales, but these measurements have very large uncertainties near the coast and over continental shelves because of limitations in the technology and in the ability that the altimeter data has to be corrected for gravitational factors. A summary of coastal applications may be found in Emery et al. [130].

Radar altimeters are also useful to help characterize waves in the ocean [131–133]. Knowledge of ocean currents and waves is important to ocean and human health in a number of ways. For example, they affect ship routing in the ocean, they are relevant in search and rescue efforts, they are useful to fishermen or recreational boaters, and they help understand coastal erosion and flooding patterns.

Wind Speed

Wind is relevant to marine pollution because of its role in the generation of currents, waves, and the direct dispersal of contaminants. Passive remote sensing of wind is possible using visible, infrared, or microwave imagery of the ocean. Using series of visible and infrared images, wind fields may be derived by tracking identifiable clouds. However, extrapolation of such winds to the surface and lack of coverage can render these techniques unsatisfactory.

Instead, microwave emissions by the sea surface have been empirically related to surface wind speed, and several experiments were conducted with Scanning Multichannel Microwave Radiometers (SMMR) carried aboard the SEASAT and Nimbus-7 satellites to refine this relationship. The understanding of the relationship between emissivity of the ocean and wind characteristics has grown substantially since the late 1970s. Unfortunately, large uncertainties in the results occur due to sensor calibration drifts. Somewhat better accuracies are possible with the Special Sensor Microwave/Imager (SSM/I), presently operational on the Defense Meteorological Satellite Program (DMSP) satellites. Swift [134] summarizes the physical basis for passive remote sensing of wind speed, and Abbott and Chelton [135] review literature in this field.

Active painting of the sea surface with radar can provide important information on winds. Using microwave scattering techniques, it is possible to estimate near-surface wind velocity under all weather conditions [136]. In particular, the Seasat-A Satellite Scatterometer (SASS) was designed to provide an accuracy of ¬ ± 2 m/s and ¬¬ ± 20° direction over a range of 4–26 m/s wind speed. The underlying principle is that very short gravity waves, which affect the strength of Bragg scattering, are in equilibrium with near-surface wind speed. Several wind scatterometers have now been flown in space by NASA, ESA, and NASDA. The first scatterometer was the Seasat Scatterometer (SASS), launched in 1978, but again Seasat had a very short life. The ESA European Remote-Sensing Satellite ERS-1, launched in 1991, carried

a scatterometer named the Advanced Microwave Instrument (AMI) scatterometer. This was followed by the ERS-2 AMI scatterometer, launched in 1995. In 1996, NASA launched the NASA Scatterometer (NSCAT), which unfortunately also had a short lifespan. NASA then launched the first scanning scatterometer, "SeaWinds," on QuikSCAT in 1999. A second SeaWinds instrument was flown on the NASDA ADEOS-2 satellite in 1993. The only sensor of this class still operating by mid-2011 was the ASCAT sensor, launched by ESA in 2007.

Future Directions

Historical oceanographic satellite sensors have limited utility in studying or monitoring coastal zones, in part because of their coarse ground resolution and limited spectral resolution and range. Refining ground resolution, expanding the spectral resolution and range, and addressing significant absorbing aerosol contamination issues together create an enormous challenge for accurately distinguish coastal ocean components and characteristics from remote sensing imagery. The limited spectral measurements from the current suite of ocean color sensors are clearly inadequate for coastal zone remote sensing research. Coastal remote sensing presents significant technological challenges. A range of space-based observations, suborbital systems, and models need to be developed over the next 25 years to advance the understanding of coastal habitats. Foremost is the requirement to obtain frequent and synoptic observations of small-scale phenomena in both aquatic and adjacent land environments. The effective discrimination of biogeochemical constituents of the water and seafloor (e.g., colored dissolved organic matter, phytoplankton concentration and composition, suspended sediments, bottom type) and physical properties (e.g., temperature, salinity, wind, circulation, bathymetry, light attenuation) must be achieved over long-term and short-term (daily to weekly) periods, at medium spatial resolution (10–100 m), and within the topographic and bathymetric regime of coastal habitats (watershed to about 20 m depth). Model development must proceed in parallel and at equivalent scales to the new observations. Together these advanced capabilities will lead to new understandings on linkages between lower and higher trophic levels and assessing coastal and estuarine waters for safe ocean resource use and for recreation and cultural purposes. Developing a workforce capable of processing and using these advanced observing technologies and products is also critical. Significant progress can be made by establishing effective links between research and decision-support tools for coastal managers and policymakers.

The next two decades, between 2010 and 2030, will bring a new series of advanced sensors. In the USA, a series of missions is planned. The operational JPSS missions will carry a number of ocean-observing systems, with the precursor NPP satellite scheduled for launch in 2011. The NPP and JPSS will carry the Visible/Infrared Imager/Radiometer Suite (VIIRS). The VIIRS features 22

channels, based primarily on the heritage from three instruments, the NOAA AVHRR, the NASA MODIS, and the Defense Meteorological Satellite Program (DMSP) Operational Linescan System (OLS). VIIRS effectively provides some of the MODIS and SeaWiFS 1-km resolution bands and adds a number of ~300 m resolution "imaging" channels. Unfortunately, the VIIRS suite of channels, however, does not include the red bands required to estimate solar-stimulated fluorescence that are present on the MODIS and MERIS sensor. As mentioned earlier, these bands are essential to differentiate between phytoplankton blooms and CDOM patches in the coastal ocean.

The Landsat Data Continuity Mission (LDCM), planned for launch in late 2012 or 2013, continues the nearly 40-year legacy of the Landsat satellite series. The LDCM, however, includes a new band, centered at 443 nm, with a lower band edge at 433 nm and an upper band edge at 453 nm, and 30 m resolution. This band will revolutionize coastal water quality applications of the Landsat series. Nevertheless, Landsat-class sensors (NASA's Landsat, France's SPOT, Space Imaging, Inc.'s Ikonos, GEOEye's Quikbird, etc.) provide higher spatial resolution but have limited sensitivity and are unable to detect the subtle changes in reflectance linked to the geophysical properties of interest.

Designing decision-support systems that include synoptic and frequent high-resolution satellite observations to assess coastal and ocean human health is a tractable problem. This will require scientific advances in coastal aquatic environments, innovative techniques, and diverse approaches. An effective strategy must incorporate active and multispectral passive observations and both global and local measurement capabilities. Advanced sensors require expanded capabilities beyond the JPSS and NPP missions, with an aim toward high quality, high spatial, temporal, and spectral observation. Coastal observing capabilities require sensors that can dwell on dark targets or illuminate them with advanced Lidar. Observations need to be consistent and calibrated, accessible, and well-documented.

A series of relevant US missions that provide a solution is being planned following the recommendations of the National Research Council "Decadal Survey" [137]. The HyspIRI, GEO-CAPE, and ACE are a highly complementary set of missions that will provide a wide range of opportunities for multidisciplinary, international collaboration aimed at detecting and monitoring marine pollution. Each of these hyperspectral mission offers an important complementary set of capabilities. Specifically, HyspIRI will have relatively high spatial resolution (60 m), ACE will feature global coverage at medium spatial resolution, and NASA is considering the development of a Pre-ACE mission with similar characteristics, to be launched before 2020, to minimize the potential impacts of a gap in global ocean color observations. GEO-CAPE will afford high temporal coverage from a geostationary orbit. More specifically:

HyspIRI: The NASA HyspIRI (Hyperspectral Infrared Imager) is planned as a polar-orbiter mission with a mid-morning equatorial crossing time and which includes two instruments mounted on a satellite in low Earth orbit. There is an

imaging spectrometer measuring from the visible to short-wave infrared (VSWIR) and a multispectral thermal infrared (TIR) imager. The VSWIR and TIR instruments will both have a spatial resolution of 60 m at nadir. The VSWIR will have a temporal revisit of approximately 3 weeks, and the TIR will have a temporal revisit of approximately 1 week. HyspIRI is designed to address issues on both land and in aquatic environments including inland water bodies and shallow coastal environments. The science team helping design this mission seeks to use HyspIRI to examine changes in ecosystem functioning due to many factors including pests, diseases, invasive species, disturbance, climate change, and land management that can alter water quality and food services to humans.

ACE and PACE: The NASA Aerosol-Cloud-Ecology (ACE) Mission and its precursor (the pre-ACE or PACE mission) also are planned polar-orbiter missions with mid-morning equatorial crossing time. These are aerosol-cloud and ocean ecosystem research missions designed to reduce the uncertainty in climate forcing in aerosol-cloud interactions and ocean ecosystem CO_2 uptake. The marine ecosystem goals are to characterize and quantify changes in the ocean biosphere and quantify the amount of dissolved organic matter, carbon, and other biogeochemical species to define the role of the oceans in the carbon cycle (e.g., uptake and storage). The present concepts for the ACE mission includes a wide array of sensors, including Lidars, cloud radars, a multi-angle swath polarimeter for imaging aerosols and clouds, and an ocean color radiometer.

GEO-CAPE: The NASA Geostationary Coastal and Air Pollution Events (GEO-CAPE) mission was recommended to gather science that identifies human versus natural sources of aerosols and ozone precursors, tracks air pollution transport, and studies the dynamics of coastal ecosystems, river plumes, and tidal fronts. The geostationary vantage point would provide a tool with which to examine coastal events in high spatial, ($\sim$300 m), high spectral, and high temporal resolution.

The NRC [137] Decadal Survey placed the HyspIRI, GEO-CAPE, and ACE missions in a tier 2 (or phase 2) category, delayed until after a series of other missions deemed prioritary in the report are launched by the US government. Launch for these tier 2 missions is now slated for the second half of the 2010 decade or in the early 2020 decade. It is important to find ways to accelerate this timetable to implement a robust set of tools to monitor and help bridle problems in marine pollution.

It is imperative that the scientific base is strengthened to maximize the application of this technology. As part of this effort, it is important to invest in the training of scientists in the understanding of remote sensing and large multidisciplinary databases. Such scientists will contribute significantly to advances and conscious policymaking regarding marine pollution.

Bibliography

1. Muller-Karger FE (1992) Remote sensing of marine pollution: a challenge for the 1990s. Mar Pollut Bull 25(1–4):54–60
2. Boyce DG, Lewis MR, Worm B (2010) Global phytoplankton decline over the past century. Nature 466:591–596. doi:10.1038/nature09268
3. Polovina JJ, Howell EA, Abecassis M (2008) Ocean's least productive waters are expanding. Geophys Res Lett 35:L03618. doi:10.1029/2007GL031745
4. Behrenfeld MJ, O'Malley RT, Siegel DA, McClain CR, Sarmiento JL, Feldman GC, Milligan AJ, Falkowski PG, Letelier RM, Boss ES (2006) Climate-driven trends in contemporary ocean productivity. Nature 444:752–755 (7 Dec 2006). doi:10.1038/nature05317
5. Gledhill DK, Wanninkhof R, Eakin CM (2009) Observing ocean acidification from space. Oceanography 22(4):48–59
6. Orr JC et al (2005) Anthropogenic ocean acidification over the twenty-first century and its impact on calcifying organisms. Nature 437(7059):681–686
7. Chavez FP, Ryan J, Lluch-Cota SE, Miguel ÑC (2003) From anchovies to sardines and back: multidecadal change in the Pacific ocean. Science 299:217
8. Polovina JJ (2005) Climate variation, regime shifts, and implications for sustainable fisheries. Bull Mar Sci 76(2):233–244
9. Epstein PR (1999) Climate and health. Perspective. Science 285(5426):347–348. doi:10.1126/science.285.5426.347
10. Zirino A, Fiedler PC, Keir RS (1988) Surface pH, satellite imagery, and vertical models in the tropical ocean. Sci Total Environ 75:285–300
11. Dube C, Lamarche A, Alfoldi T (1989) Resultats preliminaires d'une methode d'evaluation de la dispersion des rejets des eaux usees dans le Fleuve Saint-Laurent par teledetection. In: IGARSS proceedings: quantitative remote sensing: an economic tool for the nineties, 12th Canadian symposium on remote sensing, IEEE, Vancouver, Canada, vol 5: pp2820–2824
12. Gordon HR, McCluney WR (1975) Estimation of the depth of sunlight penetration in the sea for remote sensing. Appl Opt 14:413–416
13. Boyd JD, Myrick RK, Linzell RS (1991) Isis: a portable system for near real time oceanographic analysis. In: Abstract, EOS Supplement, AGU 1992 Ocean sciences meeting, New Orleans 72(51):28
14. Frye DE, Fougere A, Kery S (1991) Prototype expendable surface mooring with inductive telemetry. In: Abstract, EOS Supplement, AGU 1992 Ocean sciences meeting, New Orleans 72(51):29
15. OSB (Ocean Studies Board) (2003) Enabling ocean research in the 21st century: implementation of a network of ocean observatories. National Research Council. The National Academies Press, Washington, DC, 221p
16. Walt D, Urban E (1991) Chemical measurement technologies for ocean science. In: Abstract, EOS Supplement, AGU 1992 Ocean sciences meeting, New Orleans 72(51):28
17. Whitledge TE, Liljestrand HM (1991) In situ nitrate analyzer: design, development and field results. In: Abstract, EOS Supplement, AGU 1992 Ocean sciences meeting, New Orleans 72(51):27
18. Johnson KS, Needoba JA, Riser SC, Showers WJ (2007) Chemical sensor networks for the aquatic environment. Am Chem Soc. doi:10.1021/cr050354e
19. Honda MC, Watanabe S (2007) Utility of an automatic water sampler to observe seasonal variability in nutrients and DIC in the northwestern North Pacific. J Oceanogr 63:349–362
20. McPhaden MJ, Milburn HB (1991) Moored precipitation measurements. In: Abstract, EOS Supplement, AGU 1992 Ocean sciences meeting, New Orleans 72(51):27
21. Serra YL, McPhaden MJ (2004) In situ observations of diurnal variability in rainfall over the tropical Pacific and Atlantic oceans. J Climate 17:3496–3509

22. Case JF, Widder EA (1991) HIDEX-type bioluminescence detectors: modifications for moored and towed use. In: Abstract, EOS Supplement, AGU 1992 Ocean sciences meeting, New Orleans 72(51):30
23. Lapota D, Geiger ML, Lavoie DM, Bernstein SH, Case JF (1991) Measurements of planktonic bioluminescence in Vestfjord, Norway using HIDEX, a new rapid profiling bathyphotometer. In: Abstract, EOS Supplement, AGU 1992 Ocean sciences meeting, New Orleans 72(51):30
24. Widder EA (2010) Bioluminescence in the ocean: origins of biological, chemical, and ecological diversity. Science 328(5979):704–708
25. Jaffe JS (1991) Three dimensional sonar sensing of underwater animals. In: Abstract, EOS Supplement, AGU 1992 Ocean sciences meeting, New Orleans 72(51):28
26. Macaulay MC (1991) Applications of hydroacoustic technology to the study of zooplankton and micronekton in open ocean and shallow water environments. In: Abstract, EOS Supplement, AGU 1992 Ocean sciences meeting, New Orleans 72(51):28
27. Remsen AW (2008) Evolution and field application of a plankton imaging system. Ph.D. dissertation, University of South Florida, 145p
28. Smith RC, Waters KJ, Baker KS (1991) Optical variability and pigment biomass in the Sargasso Sea as determined using deep-sea optical mooring data. J Geophys Res 96(C5): 8665–8686
29. Dickey T, Marra J, Granata T, Langdon C, Hamilton M, Wiggert J, Siegel D, Bratkovich A (1991) Concurrent high resolution bio-optical and physical time series observations in the Sargasso Sea during the spring of 1987. J Geophys Res 96(C5):8643–8663
30. Boss E, Behrenfeld M (2010) In situ evaluation of the initiation of the North Atlantic phytoplankton bloom. Geophys Res Lett 37(L18603):5
31. Dickey TD, Itsweire EC, Moline MA, Perry MJ (2008) Introduction to the limnology and oceanography special issue on autonomous and lagrangian platforms and sensors (ALPS). Limnol Oceanogr 53(5, part 2):2057–2061
32. Esaias WE (1980) Remote sensing of oceanic phytoplankton: present capabilities and future goals. In: Falkowski PG (ed) Primary productivity in the sea. Plenum, New York, pp 321–337
33. Freilich MH (2010) NASA Earth science activities related to the deepwater horizon oil spill. American Geophysical Union, Fall Meeting 2010, Abstract #U14A-02
34. Zielinski O, Busch JA, Cembella AD, Daly KL, Engelbrektsson J, Hannides AK, Schmidt H (2009) Detecting marine hazardous substances and organisms: sensors for pollutants, toxins, and pathogens. Ocean Sci Discuss 6:953–1005. www.ocean-sci-discuss.net/6/953/2009/
35. Chomko RM, Gordon HR (2001) Atmospheric correction of ocean color imagery: test of the spectral optimization algorithm with the sea-viewing wide field-of-view sensor. Appl Opt 40:2973–2984
36. Chomko RM, Gordon HR, Maritorena S, Siegel DA (2003) Simultaneous retrieval of oceanic and atmospheric parameters for ocean color imagery by spectral optimization: a validation. Remote Sens Environ 84:208–220
37. Hovis WA, Clark DK, Anderson F, Austin RW, Wilson WH, Baker ET, Ball D, Gordon HR, Mueller JL, El-Sayed SZ, Sturm B, Wrigley RC, Yentsch CS (1980) Nimbus-7 coastal zone color scanner: system description and initial imagery. Science 210:60–63
38. Feldman G, Kuring N, Ng C, Esaias WE, McClain C, Elrod J, Maynard N, Endres D, Evans R, Brown J, Walsh S, Carle M, Podesta G (1989) Ocean color, availability of the global data set. The oceanography report. EOS 70(23):634
39. Barale V, Rizzoli PM, Hendershott MC (1984) Remotely sensing the surface dynamics of the Adriatic Sea. Deep Sea Res 31(12):1433–1459
40. Barale V, McClain CR, Rizzoli PM (1986) Space and time variability of the surface color field in the northern Adriatic Sea. J Geophys Res 91(C11):12957–12974

41. Bergamasco A, Barale V (1988) Comparison between coastal runoffs patterns from CZCS imagery and from a general circulation model. In: Marani A (ed) Advances in environmental modelling. Elsevier, Amsterdam, pp 395–404
42. Holligan PM, Aarup T, Groom SB (1989) The North Sea satellite colour atlas. Cont Shelf Res 9(8):667–765
43. Muller-Karger FE, McClain CR, Richardson PL (1988) The dispersal of the Amazon's water. Nature 333:56–59
44. Muller-Karger FE, McClain CR, Fisher TR, Esaias WE, Varela R (1989) Pigment distribution in the Caribbean Sea: observations from space. Prog Oceanogr 23:23–69
45. Müller-Karger FE, Walsh JJ, Evans RH, Meyers MB (1991) On the seasonal phytoplankton concentration and sea surface temperature cycles of the Gulf of Mexico as determined by satellites. J Geophys Res 96(C7):12645–12665
46. Del Castillo C, Gilbes F, Coble P, Muller-Karger FE (2000) On the dispersal of riverine colored dissolved organic matter over the West Florida Shelf. Limnol Oceanogr 45(6):1425–1432
47. IOCCG (2000) Remote sensing of ocean colour in coastal, and other optically-complex waters. In: Sathyendranath S (ed) International Ocean-Colour Coordinating Group, No.3: general introduction. International Ocean-Colour Coordinating Group (IOCCG) Report, pp 5–22
48. Abbott M, Letelier R (1999) Chlorophyll fluorescence (MODIS Product No. 20). Algorithm theoretical basis document. http://modis.gsfc.nasa.gov/data/atbd/atbd_mod22.pdf. Accessed 11 October 2011
49. SWFDOG (2002) Satellite images track 'black water' event off Florida coast. EOS Trans AGU 83(281):285
50. Hu C, Hackett KE, Callahan MK, Andréfouët S, Wheaton JL, Porter JW, Muller-Karger FE (2003) The 2002 ocean color anomaly in the Florida Bight: a cause of local coral reef decline? Geophys Res Lett 30(3):1151. doi:10.1029/2002GL016479
51. Hu C, Muller-Karger FE, Taylor C, Myhre D, Murch B, Odriozola AL, Godoy G (2003) MODIS detects oil spills in Lake Maracaibo, Venezuela. Eos Trans Am Geophys Union 84(33):313–319
52. Gordon HR, Clark DK, Brown JW, Brown OB, Evans RH, Broenkow WW (1983) Phytoplankton concentrations in the Middle Atlantic Bight: comparison ship determinations and CZCS estimates. Appl Opt 22:20–35
53. O'Reilly JE et al (2000) Ocean chlorophyll-a algorithms for SeaWiFS, OC2 and OC4: Version 4. In: Hooker SB, Firestone ER (eds) SeaWiFS postlaunch calibration and validation analyses, Part 3. NASA Tech. Memo. 2000–206892, vol 11. NASA Goddard Space Flight Center, Greenbelt, pp 9–23
54. Carder KL, Chen FR, Lee ZP, Hawes S, Kamykowski D (1999) Semi-analytic MODIS algorithms for chlorophyll a and absorption with bio-optical domains based on nitrate-depletion temperatures. J Geophys Res 104(C3):5403–5421
55. Hu C, Lee ZP, Muller-Karger FE, Carder KL (2002) Application of an optimization algorithm to satellite ocean color imagery: a case study in Southwest Florida coastal waters. In: Frouin RJ, Yuan Y, Kawamura H (eds) Ocean remote sensing and applications: SPIE proceedings, Washington, USA, vol 4892, pp 70–79
56. Maritorena S, Siegel DA, Peterson AR (2002) Optimization of a semianalytical ocean color model for global-scale applications. Appl Opt 41:2705–2714
57. Lee Z, Carder KL, Arnone RA (2002) Deriving inherent optical properties from water color: a multiband quasi-analytical algorithm for optically deep waters. Appl Opt 41:5755–5772
58. Morel A, Gentili B (2009) A simple band ratio technique to quantify the colored dissolved and detrital organic material from ocean color remotely sensed data. Remote Sens Environ 113:998–1011

59. Siegel DA, Maritorena S, Nelson NB, Behrenfeld MJ (2005) Independence and interdependencies of global ocean color properties: re-assessing the bio-optical assumption. J Geophys Res 110:C07011. doi:10.1029/2004JC002527
60. Chen Z, Muller-Karger FE, Hu C (2007) Remote sensing of water clarity in Tampa Bay. Remote Sens Environ. doi:10.1016/j.rse.2007.01.002
61. Stumpf RP (2001) Applications of satellite ocean color sensors for monitoring and predicting harmful algal blooms. Hum Ecol Risk Assess 7:1363–1368
62. Hu C, Muller-Karger FE, Taylor C, Carder KL, Kelble C, Johns E, Heil CA (2005) Red tide detection and tracing using MODIS fluorescence data: a regional example in SW Florida coastal waters. Remote Sens Environ 97:311–321
63. Hu C, Cannizzaro J, Carder KL, Muller-Karger FE, Hardy R (2010) Remote detection of Trichodesmium blooms in optically complex coastal waters: examples with MODIS full-spectral data. Remote Sens Environ 114(9):2048–2058. doi:10.1016/j.rse.2010.04.011
64. Hu C, Li D, Chen C, Ge J, Muller-Karger FE, Liu J, Yu F, He M-X (2010) On the recurrent Ulva prolifera blooms in the Yellow Sea and East China Sea. J Geophys Res 115(C5). doi:10.1029/2009JC005561
65. Zhang H (2002) Detecting red tides on the West Florida shelf by classification of SeaWiFS satellite imagery. Master's thesis, Department of Computer Science and Engineering, University of South Florida
66. Cannizzaro et al (2004) Bio-optical signatures of red tides on the west Florida shelf. Cont Shelf Res 28(1):137–158
67. Miller RL, McKee BA (2004) Using MODIS Terra 250 m imagery to map concentrations of total suspended matter in coastal waters. Remote Sens Environ 93(2004):259–266
68. Chen Z, Hu C, Conmy RN, Swarzenski P, Muller-Karger F (2007) Colored dissolved organic matter in Tampa Bay, Florida. Mar Chem 104:98–109
69. Chen Z, Hu C, Muller-Karger FE (2007) Monitoring turbidity in Tampa Bay using MODIS 250 M imagery. Remote Sens Environ. doi:10.1016/j.rse.2006.12.019
70. Moreno MJ, Al-Hamdan M, Rickman D, Muller-Karger FE (2010) Using the surface reflectance MODIS terra product to estimate turbidity in Tampa Bay, Florida. Remote Sens 2(12):2713–2728. doi:10.3390/rs2122713
71. Doxaran D, Froidefond J-M, Castaing P, Babin M (2009) Dynamics of the turbidity maximum zone in a macrotidal estuary (the Gironde, France): observations from field and MODIS satellite data. Estuar Coast Shelf Sci 81:321–332
72. Lobitz B, Beck L, Huq A, Wood B, Fuchs G, Faruque ASG, Colwell R (2000) Climate and infectious disease: use of remote sensing for detection of *Vibrio cholerae* by indirect measurement. Proc Natl Acad Sci USA 97(4):1438–1443
73. Colwell RR (2005) Global climate and infectious disease: the cholera paradigm. Science 274:2025–2031
74. Hu W, Clements A, Williams G, Tong S (2010) Dengue fever and El Niño/Southern Oscillation in Queensland, Australia: a time series predictive model. Occup Environ Med 67:307–311. doi:10.1136/oem.2008.044966
75. Gagliardini DA, Karszenbaum H, Legeckis R, Klemas V (1984) Application of LANDSAT MSS, NOAA/TIROS AVHRR, and Nimbus CZCS to study the La Plata River and its interaction with the ocean. Remote Sens Environ 15:21–36
76. Stumpf RP, Tyler MA (1988) Satellite detection of bloom and pigment distributions in estuaries. Remote Sens Environ 24:385–404
77. Froidefond JM, Castaing P, Jouanneau JM, Prud'Homme R, Dinet A (1993) Method for the quantification of suspended sediments from AVHRR NOAA-11 satellite data. Int J Remote Sens 14(5):885–894
78. Maul GA (1985) Introduction to satellite oceanography. Martinus Nijhoff, Dordrecht/Boston, 606p
79. Maul GA, Gordon HR (1975) On the use of the Earth resources technology satellite (LANDSAT-1) in optical oceanography. Remote Sens Environ 4:95–128

80. Amos CL, Alfoldi TT (1979) The determination of suspended sediment concentration in a macrotidal system using Landsat data. J Sediment Petrol 49:159–174
81. Khorram S (1981) Water quality mapping from Landsat digital data. Int J Rem Sens 2(2):145–153
82. Dwivedi RM, Narain A (1987) Remote sensing of phytoplankton: An attempt from the landsat thematic mapper. Int J Remote Sens 8(10):1563–1569
83. Braga CZF, Setzer AW, Drude de Lacerda L (1993) Water quality assessment with simultaneous Landsat-5 TM data at Guanabara Bay, Rio de Janeiro, Brazil. Remote Sens Environ 45:95–106
84. Tassan S (1987) Evaluation of the potential of the tematic mapper for marine application. Int J Remote Sens 8(10):1455–1478
85. Tassan S (1993) An improved in-water algorithm for the determination of chlorophyll and suspended sediment concentration from thematic mapper data in coastal waters. Int J Remote Sens 14(6):1221–1229
86. Khorram S, Cheshire H, Geraci AL, La Rosa G (1989) IGARSS proceedings: quantitative remote sensing: an economic tool for the nineties, 12th Canadian symposium on remote sensing, IEEE, Vancouver, Canada, vol 1, pp 335–338
87. Catts GP, Khorram S, Cloern JE, Knight AW, DeGloria SD (1985) Remote sensing of tidal chlorophyll a variations in estuaries. Int J Remote Sens 6(11):1685–1706
88. Munday JC, Fedosh MS (1981) Chesapeake Bay plume dynamics from Landsat. In: Campbell JW, Thomas JP (eds) Superflux: Chesapeake Bay plume study, NASA Conference Publ 2188. NASA, Greenbelt
89. Munday JC, Alfoldi TT (1979) Landsat test of diffuse reflectance models for aquatic suspended solids measurement. Remote Sens Environ 8:169–183
90. Hellweger FL, Miller W, Oshodi KS (2007) Mapping turbidity in the Charles River, Boston using a high-resolution satellite. Environ Monit Assess 132(1–3):311–320, Epub 14 Dec 2006
91. Sorensen K, Nilsen J, Saebo HV, Holbaek-Hanssen E (1989a) Use of thematic mapper data for mapping of water quality. In: IGARSS proceedings: quantitative remote sensing: an economic tool for the nineties, 12th Canadian symposium on remote sensing, IEEE, Vancouver, Canada, vol 2, p 696
92. Sorensen K, Lindell T, Nisell J (1989b) The information content of AVHRR, MSS, TM, and SPOT data in the Skagerrak Sea. In: IGARSS proceedings: quantitative remote sensing: an economic tool for the nineties, 12th Canadian symposium on remote sensing, IEEE, Vancouver, Canada, vol 4, pp 2439–2442
93. Lee Z, Carder KL, Mobley CD, Steward RG, Patch JS (1999) Hyperspectral remote sensing for shallow waters. II. Deriving bottom depths and water properties by optimization. Appl Opt 38:3831–3843
94. Brando VE, Dekker AG (2003) Satellite hyperspectral remote sensing for estimating estuarine and coastal water quality. IEEE Trans Geosci Remote Sens 41(6):1378–1387
95. Corson MR, Korwan DR, Lucke RL, Snyder WA, Davis CO (2008) The hyperspectral imager for the coastal ocean (HICO) on the international space station. In: IEEE proceedings of the international geoscience and remote sensing symposium, Boston, USA, 978-1-4244-2808-3/08
96. Vane G, Chrisp M, Enmark H, Macenka S, Solomon J (1984a) Airborne visible/infrared imaging spectrometer: an advanced tool for earth remote sensing. In: IGARSS '84, Strasbourg, France, SP215, p 751
97. Vane G, Goetz AFH, Wellman JB (1984) Airborne imaging spectrometer: a new tool for remote sensing. IEEE Trans Geosci Remote Sens GE-22:546
98. Goetz AF (1987) High-resolution imaging spectrometer: science opportunities for the 1990s. NASA Earth observing system report: instrument panel report, vol IIc, 74p
99. Karaska MA, Huguenin RL, Beacham JL, Wang Mo-Hwa, Jensen JR, Kaufmann RS (2004) AVIRIS measurements of chlorophyll, suspended minerals, dissolved organic

carbon, and turbidity in the Neuse River, North Carolina. Photogramm Eng Remote Sensing 70(1):125–133
100. Bagheri S, Yu T (2008) Hyperspectral sensing for assessing nearshore water quality conditions of Hudson/Raritan estuary. J Environ Inf 11(2):123–130. doi:10.3808/jei.200800116
101. Gower JFR, Buxton RAH, Borstad GA (1989) The FLI airborne imaging spectrometer: experience with land and water targets. In: IGARSS proceedings: quantitative remote sensing: an economic tool for the nineties, 12th Canadian symposium on remote sensing, IEEE, Vancouver, Canada, vol 2, pp 1024–102
102. Dekker AG, Malthus TJ, Seyhan E (2002) Quantitative modelling of inland water quality for high resolution MSS-systems. Geosci Remote Sens IEEE Trans 29(1):89–95
103. Babey SK, Anger CD (1989) A compact airborne spectrographic imager (CASI). In: IGARSS proceedings: quantitative remote sensing: an economic tool for the nineties, 12th Canadian symposium on remote sensing, IEEE, Vancouver, Canada, vol 2, p 1028–1031
104. Ammenberg P, Flink P, Lindell T, Pierson D, Strombeck N (2002) Bio-optical modelling combined with remote sensing to assess water quality. Int J Remote Sens 23(8):1621–1638
105. Hengstermann T, Reuter R (1990) Lidar fluorosensing of mineral oil spills on the sea surface. Appl Opt 29(22):3218–3227
106. Hoge FE, Swift RN (1980) Application of the NASA airborne oceanographic lidar to the mapping of chlorophyll and other organic pigments. In: Campbell JW, Thomas JP (eds) Superflux: Chesapeake Bay Plume Study, Conference Publ. 2188. NASA, Greenbelt, pp 349–374
107. Hoge FE, Swift RN (1983) Airborne detection of oceanic turbidity cell structure using depth-resolved laser-induced water Raman backscatter. Appl Opt 23:3778–3786
108. Brekke C, Solberg AHS (2005) Oil spill detection by satellite remote sensing. Remote Sens Environ 95:1–13
109. Garcia-Pineda O, MacDonald I, Zimmer B, Shedd B, Roberts H (2010) Remote-sensing evaluation of geophysical anomaly sites in the outer continental slope, northern Gulf of Mexico. Deep Sea Res Part 2 Top Stud Oceanogr 57:1859–1869
110. Korenowski GM, Frysinger GS, Asher WE, Barger WR, Klusty MA (1989) Laser based optical measurement of organic surfactant concentration variations a te air/sea interface. In: IGARSS proceedings: quantitative remote sensing: an economic tool for the nineties, 12th Canadian symposium on remote sensing, IEEE, Vancouver, Canada, vol 3, pp 1506–1509
111. Hoge FE, Swift RN (1980) Oil film thickness measurement using airborne laser-induced water Raman backscatter. Appl Opt 19(19):3269–3281
112. Hoge FE, Swift RN (1983) Experimental feasibility of the airborne measurement of absolute oil fluorescence spectral conversion efficiency. Appl Opt 22(1):37–47
113. Hoge F, Swift RN (1982) Delineation of estuarine fronts in the German Bight using airborne laser-induced water Raman backscatter and fluorescence of water column constituents. Int J Remote Sens 3:475–495
114. Vodacek A (1989) Synchronous fluorescence spectroscopy of dissolved organic matter to optimize lidar detection parameters. In: IGARSS proceedings: quantitative remote sensing: an economic tool for the nineties, 12th Canadian symposium on remote sensing, IEEE, Vancouver, Canada, vol 2, pp 1046–1049
115. Duncan ME, Ackleson SG (1991) A summary of hand-held photography of the Persian Gulf area taken during space shuttle missions: 1981–1991. In: Abstract, EOS Supplement, AGU 1992 Ocean sciences meeting, New Orleans 72(51):40
116. Raney RK (1983) The Canadian SAR experience, Chapter 13. In: Allan TD (ed) Satellite microwave sensing. Wiley, Tornoto, pp 223–234
117. Wadsworth A, Robertson C, De Staerke D (1983) Use of SEASAT-SAR data in oceanography at the IFP, Chapter 14. In: Allan TD (ed) Satellite microwave sensing. Ellis Horwood Ltd , Chichester pp 235–245

118. Tucker C, Holben B, Elgin J, McMurtrey J (1989) Relationship of spectral data to grain yield variation. Photogramm Eng Remote Sensing 46(5):657–666
119. Tucker CJ, Sellers PJ (1986) Satellite remote sensing of primary production. Int J Remote Sens 7:1395–1416
120. Hu C, Muller-Karger F, Murch B, Myhre D, Taylor J, Luerssen R, Moses C, Zhang C, Gramer L, Hendee J (2009) Building an automated integrated observing system to detect sea surface temperature anomaly events in the Florida Keys. IEEE Trans Geosci Remote Sens 47(6):1607–1620
121. Barnes BB, Chuanmin Hu, Muller-Karger F (2011) An improved high-resolution SST climatology to assess cold water events off Florida. Geosci Remote Sens Lett 8:769, (Accepted Jan 2011)
122. Soto I (2006) Environmental variability in the Florida keys: impacts on coral reef health. Master's thesis, University of South Florida, College of Marine Science
123. Eakin CM, Nim CJ, Brainard RE, Aubrecht C, Elvidge C, Gledhill DK, Muller-Karger F, Mumby PJ, Skirving WJ, Strong AE, Wang M, Weeks S, Wentz F, Ziskin D (2010) Monitoring coral reefs from space. Oceanogr Soc Mag, special volume: The future of oceanography from space, Dec 2010, pp 119–133
124. Thomas A, Byrne D, Weatherbee R (2002) Coastal sea surface temperature variability from Landsat infrared data. Remote Sens Environ 81:262–272
125. Fisher JI, Mustard JF (2004) High spatial resolution sea surface climatology from Landsat thermal infrared data. Remote Sens Environ 90:293–307
126. Lagerloef GSE, Swift CT, Levine DM (1991) Remote sensing of sea surface salinity: airborne and satellite concepts. In: Abstract, EOS Supplement, AGU 1992 Ocean sciences meeting, New Orleans 72(51):29
127. Wagner CA, Cheney RE (1992) Global sea level change from satellite altimetry. J Geophys Res 97(C10):15607–15615. doi:10.1029/92JC01641
128. Merrifield MA, Merrifield ST, Mitchum GT (2010) Evidence for anomalous recent acceleration of global sea level rise. J Climate 22:5772–5781
129. Bindoff NL, Willebrand J, Artale V, Cazenave A, Gregory J, Gulev S, Hanawa K, Le Quéré C, Levitus S, Nojiri Y, Shum CK, Talley LD, Unnikrishnan A (2007) Observations: oceanic climate change and sea level. In: Solomon S, Qin D, Manning M, Chen Z, Marquis M, Averyt KB, Tignor M, Miller HL (eds) Climate change 2007: the physical science basis. Contribution of working group I to the fourth assessment report of the intergovernmental panel on climate change. Cambridge University Press, Cambridge/New York
130. Emery WJ, Strub T, Leben R, Foreman M, McWilliams JC, Han G, Ladd C, Ueno H (2010) Satellite altimetry applications off the coasts of North America. In: Vignudelli S, Kostianoy A, Cipollini P, Benveniste J (eds) Coastal altimetry. Springer Verlag, Germany, pp 417–451. doi:10.1007/978-3-642-12796-0_16
131. Hwang PA, Teague WJ, Jacobs GA, Wang DW (1998) A statistical comparison of wind speed, wave height and wave period derived from satellite altimeters and ocean buoys in the Gulf of Mexico Region. J Geophys Res 103:10451–10468
132. Hwang PA, Walsh EJ, Krabill WB, Swift RN, Manizade SS, Scott JF, Earle MD (1998) Airborne remote sensing applications to coastal wave research. J Geophys Res 103:18791–18800
133. Bidlot J-R, Holmes DJ, Wittmann PA, Lalbeharry R, Chen HS (2002) Intercomparison of the performance of operational ocean wave forecasting systems with buoy data. Weather Forecasting 17:287–310. doi:10.1175/1520-0434(2002) 017<0287:IOTPOO>2.0.CO;2
134. Swift CT (1990) Passive microwave remote sensing of ocean surface wind speed. In: Geernaert GL, Plant WJ (eds) Surface waves and fluxes, vol 2. Kluwer Academic, Dordrecht, pp 265–292
135. Abbott MR, Chelton DB (1991) Advances in passive remote sensing of the ocean. Contributions in Oceanography. U.S. National Report to International Union of Geodesy and Gophysics 1987–1990. American Geophysical Union, p 571–589

136. Guymer TH (1983) Validation and applications of SASS over JASIN, Chapter 5. In: Allan TD (ed) Satellite microwave sensing. Wiley, Toronto, pp 87–104
137. NRC (2007) Earth science and applications from space: national imperatives for the next decade and beyond. Committee on Earth science and applications from space: a community assessment and strategy for the future. National Research Council, p 456. ISBN: 978-0-309-10387-9
138. Chadwick DB, Lieberman SH, Reimers CE (1991) In-situ release rate measurements of contaminants from marine sediments. In: Abstract, EOS Supplement, AGU 1992 Ocean sciences meeting, New Orleans 72(51):29
139. Esaias W (1986) MODIS – moderate resolution imaging spectrometer. NASA Earth observing system instrument panel report, vol IIb, 59p
140. Huang WG, Lou XL (2003) AVHRR detection of red tides with neural networks. Int J Remote Sens 24:1991–1996
141. Muller-Karger FE, Hu C, Andréfouët S, Varela R (2005) The color of the coastal ocean and applications in the solution of research and management problems. In: Miller RL, Del Castillo CE, McKee BA (eds) Remote sensing of coastal aquatic environments: technologies, techniques and application. Springer, Dordrecht, pp 101–127
142. Nerem RS, Leuliette E, Cazenave A (2006) Present-day sea-level change: a review. Comptes Rendus Geoscience 338:1077–1083
143. Stumpf RP (1988) Sediment transport in chesapeake bay during floods: analysis using satellite and surface observations. J Coast Res 4(1):1–15
144. McClain, Charles R, Cleave ML, Feldman GC, Gregg WW, Hooker SB, Kuring N (1998) Science quality seaWiFS data for global biosphere research. Sea Technology. September 1998, pages 10–16
145. Rodríguez-Guzmán V, Gilbes F (2009) Estimating total suspended sediments in tropical open bay conditions using MODIS. In: Proceedings of the 8th WSEAS International Conference on Instrumentation, Measurement, Circuits and Systems, Hangzhou, China, May 20–22, 2009, pp 83–86
146. Gallegos SC, Gray TI, Crawford MM (1989) A study into the responses of the NOAA-n AVHRR reflective channels over water targets. In: Proceedings of the 1989 IEEE IGARSS Meeting, Vancouver, BC
147. Stumpf RP, Pennock JR (1991) Remote estimation of the diffuse attenuaton coefficient in a moderately turbid estuary. Rem. Sens. Environ. 38:183–191
148. Fingas MF, Brown CE (1997) Airborne oil spill remote sensors - do they have a future. In: Proceedings of the Third International Airborne Remote Sensing Conference and Exhibition, Environmental Research Institute of Michigan (ERIM), Ann Arbor, MI, pp I 715–722
149. Fingas MF, Brown CE (2000) Review of oil spill remote sensing. In: proceedings of the Sixth International Conference on Remote Sensing for Marine and Coastal Environments, Veridian ERIM International, Ann Arbor, MI, pp I211–218
150. Stumpf RP, Pennock JR (1989) Calibration of a general optical equation for remote sensing of suspended sediments in a moderately turbid estuary. J Geophys Res 94(C10):14363–14371

Chapter 17
Remote Sensing of Natural Disasters

Steve Chien and Veerachai Tanpipat

Glossary

MODIS	The MODerate resolution Imaging Spectrometer is a general purpose instrument flying on the Terra and Aqua spacecraft that can sense both visible and thermal infrared information on the earth's surface and atmosphere.
GOES	The Geostationary Operational Environmental Satellite system is a set of satellites that continuously cover fixed regions of Earth. For example, GOES-East provides continuous coverage of North and South America.
AVHRR	Advanced Very High Resolution Radiometer is a sensor carried on the National Oceanic and Atmospheric Administration (NOAA) family of polar orbiting platforms (POES). AVHRR has five wide spectral bands that sense principally the near-infrared and thermal infrared spectrum.

This chapter was originally published as part of the Encyclopedia of Sustainability Science and Technology edited by Robert A. Meyers. DOI:10.1007/978-1-4419-0851-3

S. Chien (✉)
Jet Propulsion Laboratory, California Institute of Technology, M/S 301-260, 4800 Oak Grove Drive, Pasadena, CA 91109-8099, USA
e-mail: chien@aig.jpl.nasa.gov

V. Tanpipat
Forest Fire Control Division, National Park, Wildlife and Plant Conservation Department of Thailand, 61 Pholyothin Road, Chatuchak, Bangkok 10900, Thailand
e-mail: iamtanpipat@gmail.com

J. Orcutt (ed.), *Earth System Monitoring: Selected Entries from the Encyclopedia of Sustainability Science and Technology*, DOI 10.1007/978-1-4614-5684-1_17,

ASTER	Advanced Spaceborne Thermal Emission and Reflection Radiometer is an instrument on the Terra satellite that senses visible, near-infrared, short infrared, and long-wave/thermal infrared spectrum.
Earth Observing One (EO-1)	An Earth orbiting, pointable spacecraft that has been used to demonstrate a wide range of automation and autonomic technologies including onboard mission replanning and sensorwebs.
Hyperion	The Hyperspectral instrument on EO-1 used onboard to detect flooding, volcanic activity, and cryosphere change. Hyperion is able to measure in the Very Near to Short Wave infrared spectrum.
Synthetic aperture radar (SAR)	A radar remote sensing technique in which motion of the radar is used to synthesize a large array through radar processing. SAR can be used to distinguish between various surface types such as water, land, vegetation cover type and density, and others.
Interferometric synthetic aperture radar (InSAR)	A remote sensing technique which enables detailed topography, change detection, and motion tracking with great precision. InSAR has applications to deriving digital elevation maps (DEMs) as well as tracking land motion (e.g., after earthquakes), ice sheet motion, and change detection after major disturbances such as landslides, fires, flooding, and other natural disasters.
Lahar	A mud or debris flow–caused volcanic activity combined with water, snow, or ice.

Definition: Remote Sensing of Natural Disasters

Remote sensing involves the use of instruments to study phenomena from a distance. Natural disasters derive from natural hazards such as volcanoes, flooding, fires, and weather. Practically speaking, "remote sensing of natural disasters" principally refers to the use of airborne or spaceborne sensors to study natural disasters for detecting, modeling, predicting, analyzing, and mitigating effects on human populations and activities.

Remote sensing can be further characterized by the sensitivity of the instrument. Passive sensors rely either on reflected sunlight to illuminate the target or by radiation emitted from the target. Typical passive sensors might include the visible spectrum ($\sim$1 μm wavelength) or very near and short wave infrared (up to 2.5 μm wavelength). These spectra tend to be useful for distinguishing various vegetation and surface types. Applications for monitoring of natural hazards include detection of urban areas,

plants, surface water, ice, snow, lava, lahar, and roads. Typical passive sensors for emissive targets would include sensitivity in the Thermal Infrared (TIR) spectrum (8–12 μm wavelength). Applications of TIR to natural hazards include measurement of volcanic activity, and active fire mapping.

Active sensors such as radar produce a signal to illuminate the surface of interest and rely on the surface impact on the reflected energy to distinguish different surface characteristics. For example, Synthetic Aperture Radar (SAR) emits a signal with specific polarizations (e.g., HH, VV) and measures the returned energy at various polarizations to distinguish surface characteristics. These radars are useful in that they are less affected by weather such as cloud cover and thus have unique capabilities in flooding and fire applications where clouds and smoke may obscure areas of interest.

In this entry we focus on spaceborne applications. However, all of the sensing modalities described (e.g., visible, near-infrared, very near-infrared, thermal infrared, radar, SAR, etc.) are also often provided via airborne platforms. Thus, all of the same applications of space-based remote sensing are relevant to airborne remote sensing.

Introduction

Remote sensing can provide valuable data to aid in the study and mitigation of natural disasters. Satellite instruments can provide imagery of large areas of Earth's surface and overflights can often easily provide data for hard to access locations (either due to terrain, weather, or causes of the disaster itself). Airborne instruments can also provide much of the same utility from remote sensing with the potential advantages of greater loiter or dwell time and rapid response. While in the remainder of this entry we focus on spaceborne remote sensing, generally speaking, any of the applications of remote sensing described can be deployed as airborne instruments as well.

In this entry, we provide an overview of the wide range of methods used to apply remote sensing to the study and mitigation of natural disasters. We first describe the use of remote sensing to study volcanic activity – including measurement of thermal emissions, mapping of lava flows, measurement of plumes and ash, and gas. We next describe the use of remote sensing to study flooding. MODIS is the workhorse of remote sensing of flooding; however, a range of other multispectral sensors and synthetic aperture radar (SAR) have also been used for this application. We then describe the use of remote sensing in the study of forest fires – including active fire monitoring, risk area mapping, burn scars estimation, burn severity measurement, fuel load estimation, smog and haze monitoring, and fire management. Finally we describe the use of remote sensing in change-based measurements in which before and after imagery of natural disasters can provide valuable information relating to earthquakes, tsunami, landslides, tornadoes, blowdown/tropical storms, and typhoons/hurricanes. Digital elevation maps (DEMs) are a cross-cutting application of remote sensing. These detailed topographical maps are

generally created using remote sensing data and have a wide range of applications relating to natural disasters such as prediction of lava flow movement and lahar flows for volcanoes, flooding, tsunami risk areas, landslide risk areas, fire movement modeling, and others.

Remote Sensing for the Study of Volcanic Activity

Remote sensing has many applications to volcanology. A wide range of instruments have been used to study the thermal emissions of volcanic activity. Measurement of thermal emissions can then drive models to estimate surface lava, effusion rates, and other key physical parameters of volcanic activity. GOES and AVHRR [1] have been used to detect thermal signatures of volcanic activity from space. MODVOLC uses the MODIS sensor (flying on both Terra and Aqua) to detect volcanic thermal signatures [2, 3]. These methods use the multispectral capability of the instrument to fit the thermal emissions to blackbody radiation curves to estimate the surface area emitting at a specific temperature. However, all of these methods are restricted by the low spatial resolution (and corresponding lower thermal sensitivity) of these instruments. While site-specific algorithm parameterization for background thermal signatures can increase sensitivity, higher spatial resolution instruments (typically pointable) can provide more information. In this approach, many other pointable sensors including ASTER [4] and Hyperion [5, 6] have been used to study the thermal emission of volcanic activity.

Remote sensing can also be used to study volcanic plumes. ASTER and MODIS have been used to track such activity [7, 8]. In these applications the plumes and gas emissions of volcanoes can be distinguished from the normal atmosphere due to difference in spectral response from both ash and SO_2 constituents. The AVHRR sensor has also been used in conjunction with ground measurements to study volcanic plumes [9].

Synthetic aperture radar (SAR) can also be used in an interferometric fashion to study inflation in volcanoes as both a precursor and during eruptions [10].

Tracking of lahar from volcanoes is another application of remote sensing. Visible, Near-Infrared, Synthetic Aperture Radar, and Light Detection And Ranging (LIDAR) sensors have all been used to map lahar flows (see [11] for a comparison of these methods). Note that digital elevation maps, also typically derived by remote sensing, can be used to model (predict) where lahar flows are likely.

The 2010 eruption of the Eyjafjallajökull Volcano in Iceland represents an excellent example of the use of remote sensing in volcanic study. In the weeks immediately following this eruption, data from many space-based sensors, such as MODIS, AIRS, MISR, ASTER, and ALI, were all used in the analysis of the eruption.

The MODIS instrument provides broad swath (2,000+ km wide) moderate spatial resolution (250–1,000 m/pixel) imagery of Earth in visible to thermal

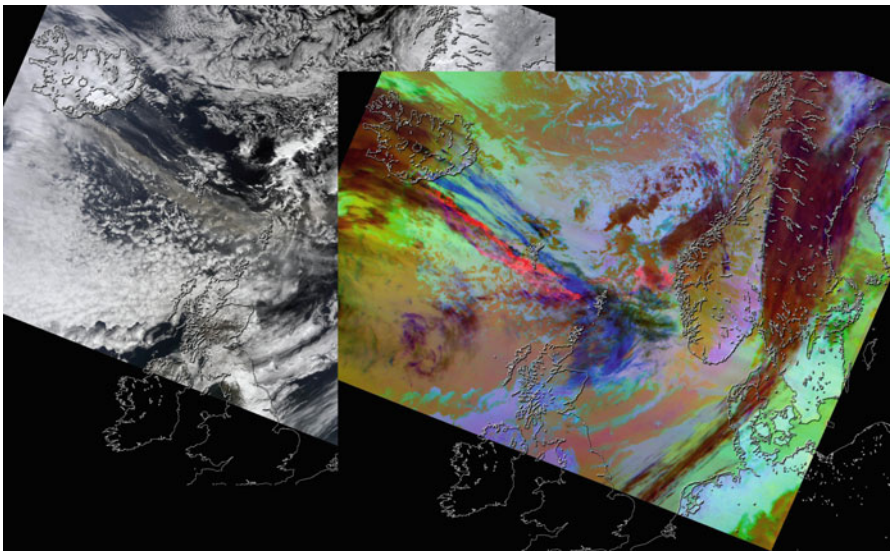

Fig. 17.1 MODIS imagery of the Eyjafjallajökull eruption (Image courtesy: NASA GSFC/JPL/Caltech)

infrared spectra. This workhorse of remote sensing has numerous applications to natural hazards including volcanology. MODIS thermal infrared channels can distinguish ash from other atmospheric conditions as shown in this April 15, 2010, imagery of the Eyjafjallajökull eruption (Fig. 17.1).

The Advanced Land Imager (ALI) on EO-1 is a targetable instrument sensitive in the visible, short wave infrared, and very near infrared spectra. Figure 17.2 shows true color (left) and false color to highlight thermal features (right) to highlight the Eyjafjallajökull volcanic activity on April 17, 2010.

The Multi-angle Imaging SpectroRadiometer (MISR) aboard NASA's Terra satellite collected data on ash height when it passed just east of the Eyjafjallajökull Volcano mid-morning on May 7. MISR uses nine different cameras with each camera viewing the event from a different angle to enable hyper-stereo reconstruction of the distance of viewed substances from the instrument. In this application of MISR, the nine angle views are used to reconstruct the distance of the plume from the MISR instrument. Because the altitude of the satellite orbit is known the height of the volcanic plume can then be calculated as shown below in Fig. 17.3.

Flooding Applications of Remote Sensing

Remote sensing is frequently used in tracking flooding worldwide. The MODIS sensor has been used to study long-term impacts from flooding, with products

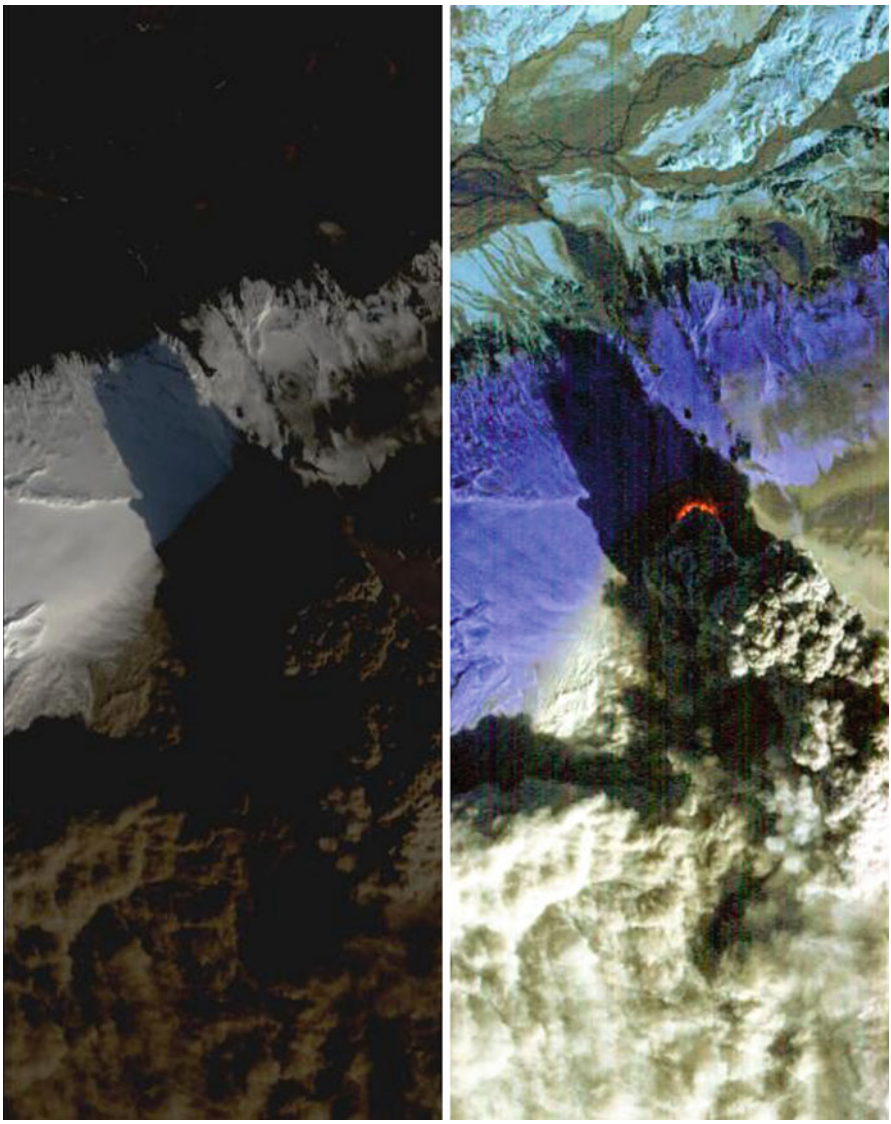

Fig. 17.2 EO-1/ALI true color (*left*) thermal enhanced (*right*) imagery acquired April 17, 2010 (Images courtesy: NASA/JPL/Caltech/EO-1 mission/GSFC/Ashley Davies)

spanning decades by the Dartmouth Flood Observatory [12, 13] and the University of Maryland [14]. These methods leverage the fact that surface water from flooded areas is very dark and thus can be distinguished spectrally from other substances. For a reliable product cloud shadow areas are removed by looking at multiple images in sequence as MODIS provides at least two daylight overflights per 24 h period.

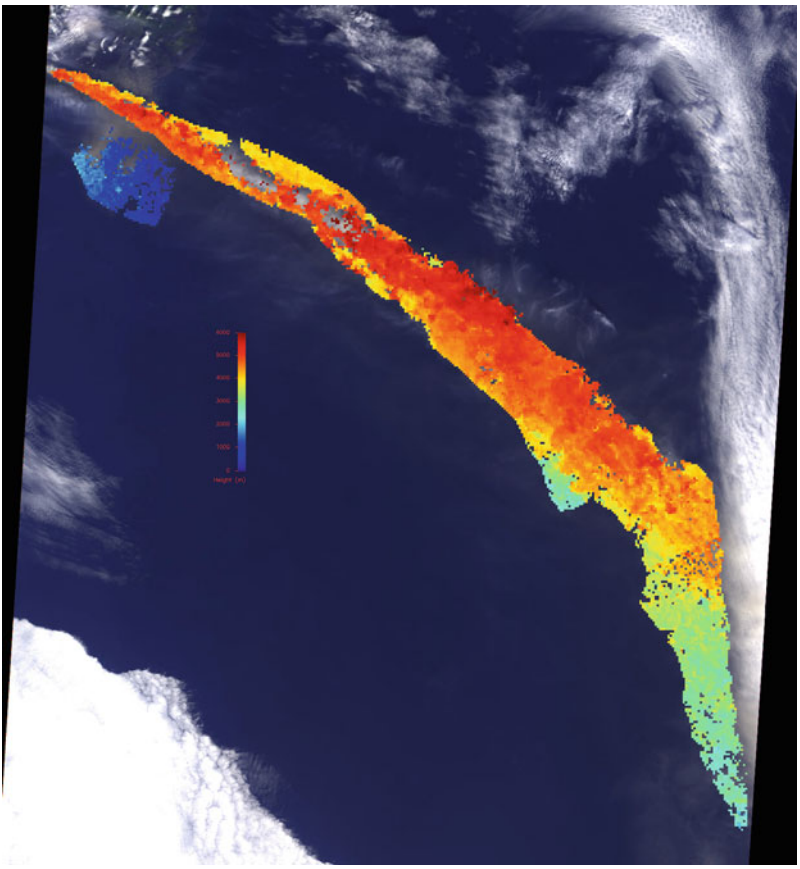

Fig. 17.3 MISR extracted plume height from the Eyjafjallajökull Volcano May 7, 2010 (NASA image courtesy: GSFC/LaRC/JPL/Caltech MISR team)

Figure 17.4 shows a MODIS-derived product developed by the University of Maryland highlighting flooding in Myanmar in 2008.

Hyperion [15] and ALI [16] have also been used to study flooding by using spectral analysis methods to automatically derive surface water extent.

Use of multispectral remote sensing to track flooding suffers from the drawback that flooding often occurs in conjunction with cloud cover. Use of radar to track flooding does not suffer from this limitation. QuikSCAT (Quick Scatterometer) has been used to study flooding worldwide [17] providing global coverage maps of flooding. Figure 17.5 shows QuikSCAT-derived mapping of flooding in China in September 2003.

On a regional scale many SARs including Radarsat-1 SAR [18] and ASAR on Envisat [19] have been used in a targeted mode to track flooding. In these applications, changes in the radar returns allow discrimination between flooded areas and other types of land surfaces such as sand, soil, and vegetation. Below

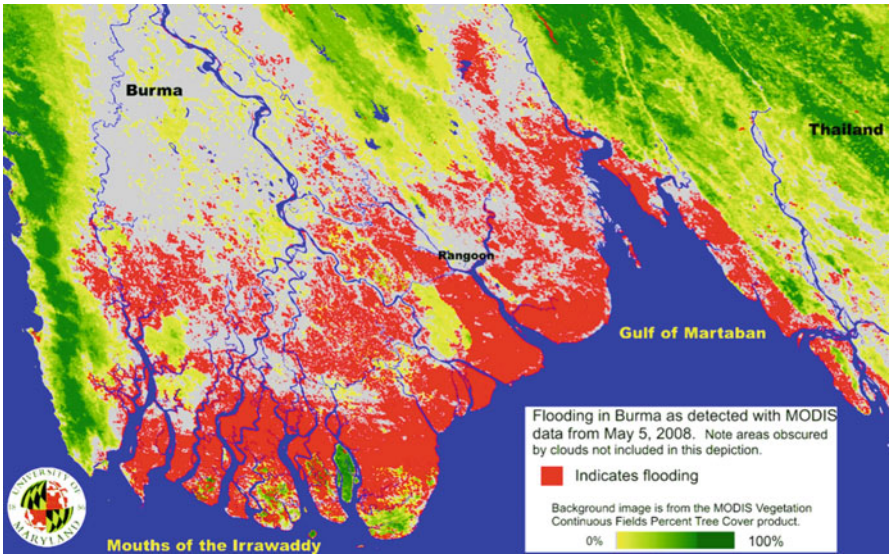

Fig. 17.4 Flooding in Myanmar May 2008 as derived from MODIS imagery (Images courtesy: University of Maryland)

Fig. 17.6a, b shows the formed SAR image and a derived surface water extent classification. The surface water can be distinguished because water has dielectric properties that differ from most land types resulting in a change in the radar returns. However, in cases where weather (e.g., wind) causes a significant change in the water surface roughness it can become more difficult to distinguish between water and land surfaces.

Fire Applications of Remote Sensing

Forest fire is one of the most significant and natural causes of terrestrial biomass change. Forest fires play a major and vital role in the deforestation of the tropical and subtropical regions, especially in the developing and underdeveloped countries. Since it is impossible to monitor forest fires of a large area at a ground level, satellite remote sensing is critical. In addition, routine monitoring via satellite remote sensing technology offers the most efficient and cost-effective means for forest fire management over larger areas [20].

An early space system used to study fires is the Advanced Very High Resolution Radiometer (AVHRR) of the National Oceanic and Atmospheric Administration (NOAA) polar orbiting platforms (POES) family. It was originally used for weather monitoring, and then employed as the main sensor in the detection of active fires, or "hotspots," on a global scale and with relatively high temporal frequency.

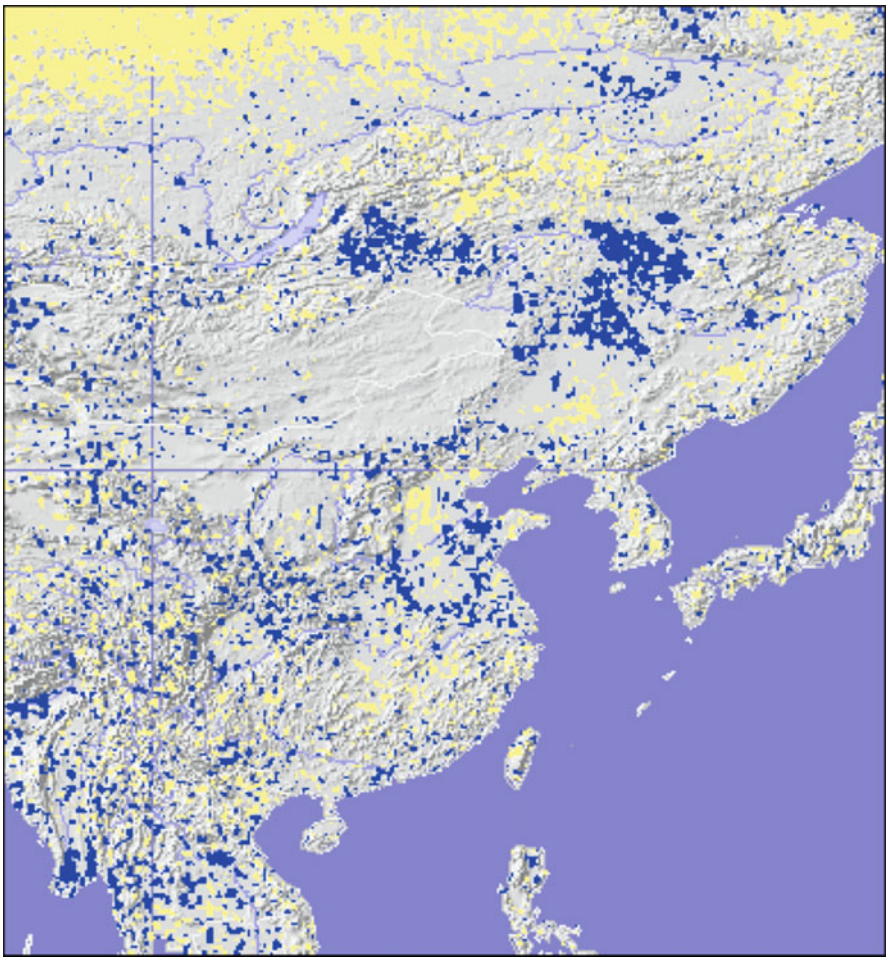

Fig. 17.5 QuikSCAT-derived flood map for September 2003. Blue indicates flooded areas (Product courtesy: R. Brakenridge/Dartmouth flood observatory & S. Nghiem/Jet propulsion laboratory)

Other sensors include those in the Geostationary Operational Environmental Satellite (GOES) such as the Visible Infrared Spin Scan Radiometer Atmospheric Sounder (VAS) [21] and the GOES Imager [22]. In addition to their main functions, the Defense Meteorological Satellite Program Operational Linescan System (DMSP-OLS) [23, 24] the Along Track Scanning Radiometer (ATSR) [25], the Tropical Rainfall Measuring Mission Visible and Infrared Scanner (TRMM-VIRS) [26] are also used in the forest fire monitoring. However, MODIS is the first sensor specifically designed and developed for the forest fires detection [27, 28].

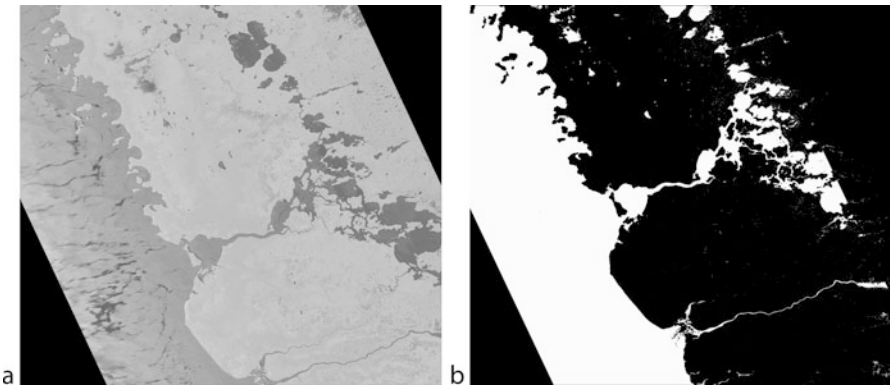

Fig. 17.6 (**a**) Synthetic aperture radar imagery from the Florida Everglades acquired by the unpiloted aerial vehicle SAR (UAVSAR) L-band SAR in 2009 (Image courtesy: UAVSAR team). (**b**) Surface water classification derived from UAVSAR L-band SAR imagery of Florida Everglades (Image courtesy: UAVSAR team and J. Doubleday/JPL/Caltech)

Figure 17.7 shows MODIS imagery of Nepal acquired in March 2009. In the image active fire detections are indicated and the large smoke plumes caused by the fire are quite evident.

An array of technologies used in the satellite remote sensing of forest fires includes spaceborne system/sensors in a variety of tasks which are active fire monitoring [29–32], risk area mapping and assessment [33–36], burn scar estimation and monitoring [37–40], burn severity measurement [41–43], fuel moisture content estimation [44, 45], smog and haze monitoring [46–48], fire behavior [49], and fire management [50]. One emphasis of current work is to increase the sensitivity of fire detection systems – MODIS capabilities can only detect moderate-sized fires. Another emphasis of current work is to allow for faster delivery of data to enable rapid response to fires before they grow in size and are harder to contain.

Other Applications of Remote Sensing to Natural Disasters

Another major application of remote sensing is the use of "before" and "after" images to assess damage from natural disasters. This type of analysis is relevant to a wide range of natural disasters including tsunamis, earthquakes, flooding, and tornadoes. For example, Fig. 17.8 shows the extent of the tsunami-induced flooding in northern Japan following the earthquake–tsunami disaster of March 2011. Figure 17.8a shows the "after" and Fig. 17.8b "before." The pair of images clearly indicates the large amount of flood damage and resultant inundation along the Kitakami river.

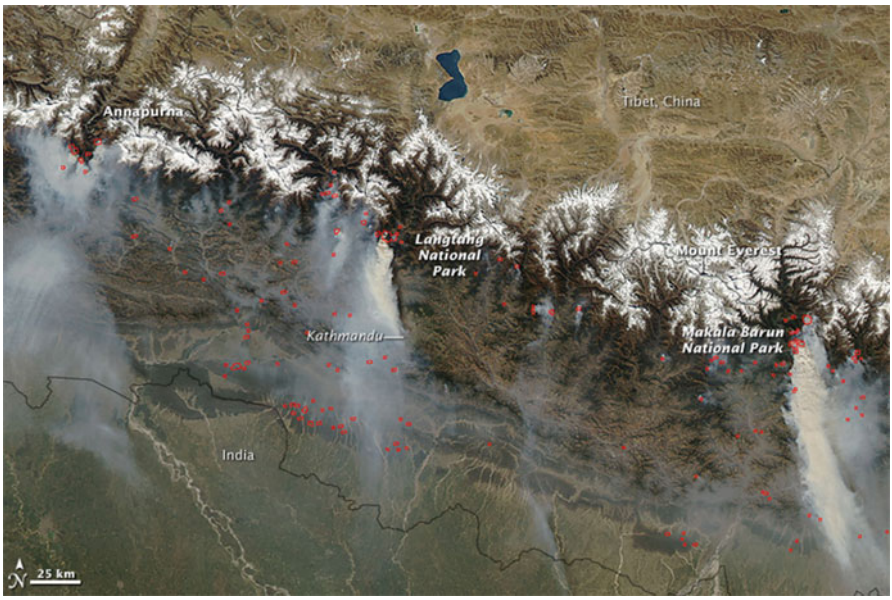

Fig. 17.7 MODIS imagery showing 2009 fires in Nepal, *red* boxes indicate active fire detections (Image courtesy: NASA and MODIS rapid response team)

Another before/after application of satellite imagery for natural disasters is tracking landslide damage. Figure 17.9 highlights the progression of a landslide in Southern Italy near the town of Maierato using Advanced Land Imager (ALI) data from the EO-1 mission.

Figure 17.10 shows the devastation caused by a tornado in La Plata, Maryland in April 2002 (imagery from May 2002). In this EO-1 Advanced Land Imager (ALI) imagery, the devastation along the tornado's path is clearly shown in the image as a linear area following the tornadoes path from left to right in the image.

Future Directions

There are many areas of current work aimed at enhancing the utility of remote sensing for assessment, response, and mitigation of natural disasters. Central areas of improvement in remote sensing are directly relevant: improving the resolution of remote sensing, reducing the time lag from acquisition of data to delivery to users, increasing the temporal frequency of coverage, and improving the ability to correct data from degradation due to atmospheric, environmental, or man-made factors.

A major area of improvement is the integration of remote sensing data with environmental models. Increasingly, sensor data are automatically processed and fed into models that perform hindcasting, nowcasting, and forecasting. These models allow for

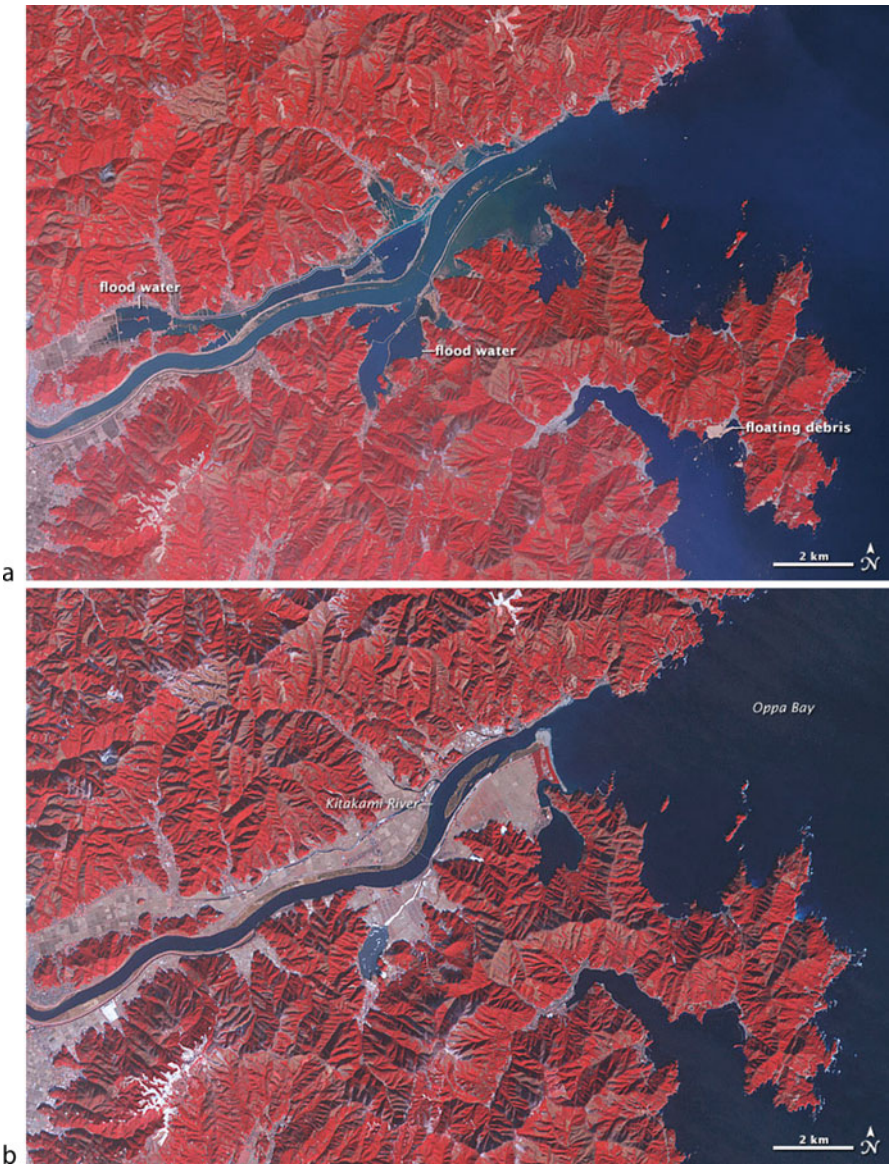

Fig. 17.8 (**a**) ASTER imagery showing the extent of Tsunami-induced flooding at the Kitakami river, March 2011 (NASA earth observatory image by Robert Simmon and Jesse Allen, using data from the GSFC/METI/ERSDAC/JAROS, and USA/Japan ASTER science team). (**b**) ASTER imagery from January 2011 showing pre-tsunami shoreline of the Kitakami river, Japan, January 2011 (NASA earth observatory image by Robert Simmon and Jesse Allen, using data from the GSFC/METI/ERSDAC/JAROS, and USA/Japan ASTER science team)

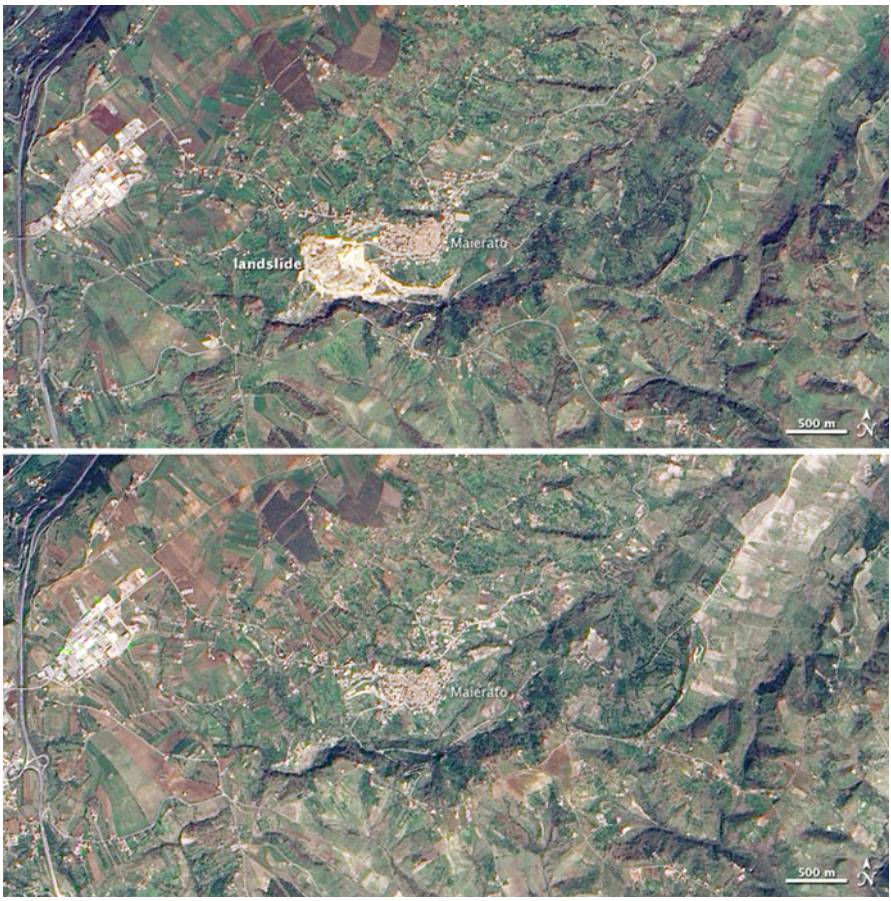

Fig. 17.9 "After" (*top*) and "before" (*bottom*) imagery of a landslide in Maierato, Italy (Image courtesy of NASA earth observatory and NASA EO-1 team)

key physical parameters to be estimated even if not directly measureable, for past or ongoing events, as well as the more typical forecasting of how events will progress. These capabilities have dramatic ramifications for natural disasters. For example, such models can be used to estimate whether volcanic activity is increasing or decreasing. Or such capabilities can combine surface water data, topographical and terrain data, and weather forecasts to estimate areas likely at risk for flooding. Active fire mapping, terrain, vegetation, and weather data can be used to estimate likely progressions for active forest fires as a third example. In all of these cases, key data (much of it being remote sensing data) combined with modeling can provide important capabilities for disaster response and mitigation.

An additional exciting new area is the use of "sensorwebs" for environmental monitoring and specifically in the use of sensing for natural disasters. In a

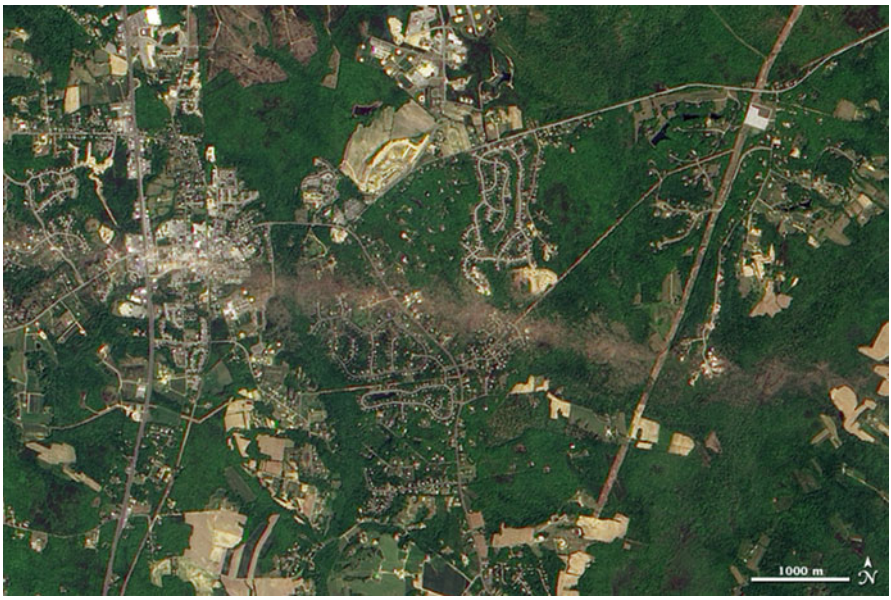

Fig. 17.10 EO-1 advanced land imager imagery of La Plata, Maryland following tornado in May 2002 (Image courtesy of NASA earth observatory and NASA EO-1 team)

sensorweb, data are processed "on the fly" and used to actively reconfigure other portions of the sensorweb to better acquire data and track an evolving phenomena [51]. For example, detections of volcanic activity by one satellite might trigger observations by other satellites [52]. Or weather reports in concert with satellite rainfall observations might trigger observations of likely flood areas [16]. These techniques, in concert with modeling, will enhance future sensing of natural disasters.

Conclusions

Remote sensing has a wide range of applications to risk assessment, tracking, response, and mitigation of natural disasters. In this entry, we have outlined only a few of the applications to several categories of natural disasters focusing volcanoes, flooding, and fires. Remote sensing also provides secondary products such as topographical maps that are widely used in modeling natural disaster phenomena. Topographical maps can be used to estimate risk (to tsunamis, flooding, landslide, etc.) as well as provide inputs to model and predict flood progression, and lava and lahar flows. All of these areas and many more are the subject of active research with new applications and techniques being developed continuously.

Acknowledgments Portions of the research described in this entry were carried out at the Jet Propulsion Laboratory, California Institute of Technology, under a contract with the National Aeronautics and Space Administration.

Bibliography

1. Harris AJ, Flynn LP, Dean K, Wooster EM, Okubo C, Mouginis-Mark P et al (2000) Real-time satellite monitoring of volcanic hot spots. Geophys Monogr 116:139–159
2. Wright R, Flynn LP, Garbeil H, Harris A, Piler E (2003) Automated volcanic eruption detection using MODIS. Remote Sens Environ 82:135–155
3. Wright R, Flynn LP, Garbeil H, Harris A, Piler E (2004) MODVOLC: near-real-time thermal monitoring of global volcanism. J Volcanol Geoth Res 135:29–49
4. Pieri D, Abrams M (2004) ASTER watches the world's volcanoes: a new paradigm for volcanological observations from orbit. J Volcanol Geoth Res 135(1–2):13–28
5. Davies AG, Chien S, Baker V, Doggett T, Dohm J, Greeley R, Ip F, Castano R, Cichy B, Rabideau G, Tran D, Sherwood R (2006) Monitoring active volcanism with the autonomous sciencecraft, experiment on EO-1. Remote Sens Environ 101:427–446
6. Davies AG, Calkins J, Scharenbroich L, Vaughan G, Wright R, Kyle P, Castano R, Chien S, Tran D (2008) Multi-instrument remote and in situ observations of the erebus volcano (Antarctica) lava lake in 2005: a comparison with the Pele lava lake on the Jovian moon Io. J Volcanol Geoth Res 177(3):705–724
7. Pieri D, Gubbels T, Hufford G, Olsson G, Realmuto V (2006) Assessing mesoscale volcanic aviation hazards using ASTER. Eos Trans AGU 87(52). Fall meet. Suppl, Abstract H33E-1554
8. Novak MA, Watson IM, Delgado-Granados H, Rose WI, Cardenas-Gonzalez L, Realmuto VJ (2008) Volcanic emissions from Popocatépetl volcano, Mexico, quantified using moderate resolution imaging spectroradiometer (MODIS) infrared data: a case study of the December 2000–January 2001 emissions. J Volcanol Geoth Res 170:76–85
9. Andronico D, Spinetti C, Cristaldi A, Buongiorno MF (2009) Observations of Mt. Etna volcanic ash plumes in 2006: an integrated approach from ground-based and polar satellite NOAA–AVHRR monitoring system. J Volcanol Geoth Res 180(2–4):135–147
10. Tralli DM, Blom RG, Zlotnicki V, Donnellan A, Evans DL (2005) Satellite remote sensing of earthquake, volcano, flood, landslide and coastal inundation hazards. ISPRS J Photogramm 59(4):185–198
11. Joyce K, Samsonov S, Manville V, Jongens R, Graettiner A, Cronin S (2009). Remote sensing data types and techniques for lahar path detection: a case study at Mt Ruapehu, New Zealand. Remote Sens Environ113(8) 1778–1786; Wright R, Flynn L, Garbeil H, Harris A, Piler E (2002). Automated volcanic eruption detection using MODIS. Remote Sens Environ 82(1) 135–155
12. Brakenridge GR, Anderson E (2005) MODIS-based flood detection, mapping, and measurement: the potential for operational hydrological applications. In: Transboundary floods, proceeding of NATO advanced research workshop, Baile Felix – Oradea, 4–8 May 2005
13. Brakenridge G R (2010). DFO MODIS flood retrieval algorithm. http://floodobservatory.colorado.edu/Tech.html. Accessed 21 Mar 2011
14. Carroll M, Townshend J, Noojipady P, DiMiceli C, Sohlberg R (2009). Surface water dynamics derived from the MODIS data record. Spring AGU
15. Ip F, Dohm J, Baker V, Doggett T, Davies A, Castano R, Chien S, Cichy B, Greeley R, Sherwood R, Tran D, Rabideau G (2006) Flood detection and monitoring with the autonomous sciencecraft experiment onboard EO-1. Remote Sens Environ 101(4):463–481
16. Chien S, Doubleday J, Mclaren D, Tran D, Khunboa C, Leelapatra W, Plergamon V, Tanpipat V, Raghavendra C, Mandl D (2011). Using multiple space assets with In-situ measurements to

track flooding in Thailand. In: 34th international symposium on remote sensing of environment, Sydney
17. Brakenridge GR, Nghiem SV, Anderson E, Chien S (2005) Space-based measurement of river runoff. Eos Trans AGU 86(19):185. doi:10.1029/2005EO190001
18. Townsend P (2001) Mapping seasonal flooding in forested wetlands using multi-temporal Radar- sat SAR. Photogramm Eng Remote Sens 67:3055–3074
19. Marti-Cardona B, Lopez-Martinez C, Dolz-Ripolles J, Blade-Castellet E (2010) ASAR polarimetric, multi-incidence angle and multitemporal characterization of Doñana wetlands for flood extent monitoring. Remote Sens Environ 114(11):2802–2815
20. Justice CO, Malingreau JP, Seltzer A (1993) Satellite remote sensing of fires: potential and limitations. In: Crutzen P, Goldammer J (eds) Fire in the environment: the ecological, atmospheric, and climatic importance of vegetation fires. Wiley, New York, pp 77–88
21. Prins EM, Menzel WP (1992) Geostationary satellite detection of biomass burning in South America. Int Remote Sens 13:2783–2799
22. Menzel WP, Prins EM (1996). Monitoring fire activity in western hemisphere with the new generation of geostationary satellites. In: 22nd conference on agricultural and forest meteorology with symposium on fire and forest meteorology, Atlanta, 28 Jan−2 Feb, 1996, pp 272–275
23. Elvidge C, Kroehl HW, Kihn EA, Baugh KE, Davis ER, Hao WM (1996) Algorithm for the retrieval of fire pixels from DMSP operational linescan system data. In: Levine JS (ed) Biomass burning and global change, vol 1. The MIT Press, Cambridge, MA, pp 73–85
24. Elvidge C, Dee WP, Elaine P, Eric AK, Jackie K, Kimberly EB (1998) Remote sensing change detection: environmental monitoring methods and applications, wildfire detection with meteorological satellite data: results from New Mexico during June of 1996 using GOES, AVHRR, and DMSP-OLS. CRC Press, Boca Raton, FL, pp 103–121
25. Arino O, Rosaz J (1999). 1997 and 1998 world ASTR fire atlas using ERS-2 ATSR-2 data. In: Neuenschwander LF, Tyan KC, Golberg GE (eds) Proceedings of the joint fire science conference, Boise, Idaho, 15–17 June 1999. University of Idaho and the International Association of Wildland Fire, Boise, pp 177–182
26. Giglio L, Kendall JD, Tucker CJ (2000) Remote Sensing of fires with TRMM VIRS. Int J Remote Sens 21:203–207
27. Giglio L, Descloitres J, Justice CO, Kaufman YJ (2003) An enhanced contextual fire detection algorithms for MODIS. Remote Sens Environ 87:273–282
28. Justice CO, Giglio L, Korontzi S, Owens J, Morisette JT, Roy D, Descloitres J, Alleaume S, Petitcolin F, Kaufman Y (2002) The MODIS fire products. Remote Sens Environ 83:244–262
29. Roy DP, Boschetti L, Justice CO, Ju J (2008) The collection 5 MODIS burned area product – Global evaluation by comparison with the MODIS active fire product. Remote Sens Environ 112(9):3690–3707. doi:10.1016/j.rse.2008.05.013, ISSN 0034-4257
30. Ressl R, Lopez G, Cruz I, Colditz RR, Schmidt M, Ressl S, Jimenez R (2009) Operational active fire mapping and burnt area identification applicable to Mexican nature protection areas using MODIS and NOAA-AVHRR direct readout data. Remote Sens Environ 113(6):1113–1126. doi:10.1016/j.rse.2008.10.016, ISSN 0034-4257
31. Amraoui M, DaCamara CC, Pereira JMC (2010) Detection and monitoring of African vegetation fires using MSG-SEVIRI imagery. Remote Sens Environ 114(5):1038–1052. doi:10.1016/j.rse.2009.12.019, ISSN 0034-4257
32. Tanpipat V, Honda K, Nuchaiya P (2009) MODIS hotspot validation over Thailand. Remote Sens 1:1043–1054. doi:10.3390/rs1041043, ISSN 2072-4292
33. Chuvieco E, Aguado I, Yebra M, Nieto H, Salas J, Martin MP, Vilar L, Martinez J, Martin S, Ibarra P, Riva JDL, Baeza J, Rodriguez F, Molina JR, Herrera MA, Zamora R (2010). Development of a framework for fire risk assessment using remote sensing and geographic information system technologies. Ecol Model 221(1 Special issue on spatial and temporal patterns of wildfires: models, theory, and reality) 46–58, doi: 10.1016/j.ecolmodel.2008.11.017, ISSN 0304–3800

34. Maeda EE, Arcoverde GFB, Pellikka PKE, Shimabukuro YE (2011) Fire risk assessment in the Brazilian Amazon using MODIS imagery and change vector analysis. Applied Geography 31(1):76–84. doi:10.1016/j.apgeog.2010.02.004, ISSN 0143-6228
35. Schneider P, Roberts DA, Kyriakidis PC (2008) A VARI-based relative greenness from MODIS data for computing the Fire Potential Index. Remote Sens Environ 112(3):1151–1167. doi:10.1016/j.rse.2007.07.010, ISSN 0034-4257
36. Huesca M, Litago J, Palacios-Orueta A, Montes F, Sebastian-Lopez A, Escribano P(2009). Assessment of forest fire seasonality using MODIS fire potential: a time series approach. Agr Forest Meteorol 149(11 Special section on water and carbon dynamics in selected ecosystems in China) 1946–1955, doi: 10.1016/j.agrformet.2009.06.022, ISSN 0168–1923
37. Giglio L, Loboda T, Roy DP, Quayle B, Justice CO (2009) An active-fire based burned area mapping algorithm for the MODIS sensor. Remote Sens Environ 113(2):408–420. doi:10.1016/j.rse.2008.10.006, ISSN 0034-4257
38. Libonati R, DaCamara CC, Pereira JMC, Peres LF (2010) Retrieving middle-infrared reflectance for burned area mapping in tropical environments using MODIS. Remote Sens Environ 114(4):831–843. doi:10.1016/j.rse.2009.11.018, ISSN 0034-4257
39. Dubinin M, Potapov P, Lushchekina A, Radeloff VC (2010) Reconstructing long time series of burned areas in arid grasslands of southern Russia by satellite remote sensing. Remote Sens Environ 114(8):1638–1648. doi:10.1016/j.rse.2010.02.010, ISSN 0034-4257
40. Zhang X, Kondragunta S (2008) Temporal and spatial variability in biomass burned areas across the USA derived from the GOES fire product. Remote Sens Environ 112(6):2886–2897. doi:10.1016/j.rse.2008.02.006, ISSN 0034-4257
41. Veraverbeke S, Lhermitte S, Verstraeten WW, Goossens R (2011) A time-integrated MODIS burn severity assessment using the multi-temporal differenced normalized burn ratio (dNBRMT). Int J Appl Earth Obs Geoinformation 13(1):52–58. doi:10.1016/j.jag.2010.06.006, ISSN 0303–2434
42. Santis AD, Asner GP, Vaughan PJ, Knapp DE (2010) Mapping burn severity and burning efficiency in California using simulation models and landsat imagery. Remote Sens Environ 114(7):1535–1545. doi:10.1016/j.rse.2010.02.008, ISSN 0034–4257
43. Fox DM, Maselli F, Carrega P (2008) Using SPOT images and field sampling to map burn severity and vegetation factors affecting post forest fire erosion risk. CATENA 75(3):326–335. doi:10.1016/j.catena.2008.08.001, ISSN 0341–8162
44. Yebra M, Chuvieco E, Riano D (2008) Estimation of live fuel moisture content from MODIS images for fire risk assessment. Agr Forest Meteorol 148(4):523–536. doi:10.1016/j.agrformet.2007.12.005, ISSN 0168–1923
45. Peterson HS, Roberts DA, Dennison PE (2008) Mapping live fuel moisture with MODIS data: A multiple regression approach. Remote Sens Environ 112(12):4272–4284. doi:10.1016/j.rse.2008.07.012, ISSN 0034–4257
46. Hyer EJ, Chew BN (2010) Aerosol transport model evaluation of an extreme smoke episode in Southeast Asia. Atmos Environ 44(11):1422–1427. doi:10.1016/j.atmosenv.2010.01.043, ISSN 1352–2310
47. Henderson SB, Burkholder B, Jackson PL, Brauer M, Ichoku C (2008) Use of MODIS products to simplify and evaluate a forest fire plume dispersion model for PM10 exposure assessment. Atmos Environ 42(36):8524–8532. doi:10.1016/j.atmosenv.2008.05.008, ISSN 1352–2310
48. Zhang X, Kondragunta S, Schmidt C, Kogan F (2008) Near real time monitoring of biomass burning particulate emissions (PM2.5) across contiguous United States using multiple satellite instruments. Atmos Environ 42(29):6959–6972. doi:10.1016/j.atmosenv.2008.04.060, ISSN 1352–2310
49. Balch JK, Nepstad DC, Curran LM, Brando PM, Portela O, Guilherme P, Reuning-Scherer JD Jr, Carvalho OD (2011) Size, species, and fire behavior predict tree and liana mortality from experimental burns in the Brazilian Amazon. Forest Ecol Manage 261(1):68–77. doi:10.1016/j.foreco.2010.09.029, ISSN 0378–1127

50. Bonazountas M, Kallidromitou D, Kassomenos P, Passas N (2006) A decision support system for managing forest fire casualities. Environ Manage. doi:10.1016/j.jenvman.2006.06.016
51. Chien S, Cichy B, Davies A, Tran D, Rabideau G, Castano R, Sherwood R, Mandl D, Frye S, Shulman S, Jones J, Grosvenor S (2005) An autonomous earth observing sensorweb. IEEE Intell Syst 20:16–24
52. Chien S, Davies A, Doubleday J, Tran D, Jones S, Kjartansson E, Vogfjord K, Gudmundsson M, Thordarson T, Mandl D (2011). Integrating multiple space and ground sensors to track volcanic activity. In: 34th international symposium on remote sensing of environment, Sydney

Chapter 18
Remote Sensing of Ocean Color

Heidi M. Dierssen and Kaylan Randolph

Glossary

Absorption, $a(\lambda)$	The fraction of a collimated beam of photons in a particular wavelength (λ), which is absorbed or scattered per unit distance within the medium (units 1/length or m^{-1}). Photons which are absorbed by ocean water alter the spectral distribution of light that can be observed remotely.
Apparent optical properties (AOP)	Optical properties which depend primarily on the medium itself but have a small dependence on the ambient light field. Typically, AOPs are derived from measurements of the ambient light field, particularly upwelling and downwelling radiance and irradiance. Principal AOPs include irradiance reflectance, remote sensing reflectance, and the diffuse attenuation coefficients.
Backscattering, $b_b(\lambda)$	Light of a particular wavelength (λ) that is scattered in a direction 90–180° away from its original path (i.e., backward hemisphere). Backscattered light is what is measured as ocean color in remote sensing, namely, downward propagating sunlight that has been redirected back toward the sea surface and out into the atmosphere. For natural waters, only a few percent of the light entering the ocean is backscattered out.

This chapter was originally published as part of the Encyclopedia of Sustainability Science and Technology edited by Robert A. Meyers. DOI:10.1007/978-1-4419-0851-3

H.M. Dierssen (✉) • K. Randolph
Department of Marine Sciences, University of Connecticut, Groton, CT 06340, USA
e-mail: heidi.dierssen@uconn.edu

J. Orcutt (ed.), *Earth System Monitoring: Selected Entries from the Encyclopedia of Sustainability Science and Technology*, DOI 10.1007/978-1-4614-5684-1_18,

Colored or chromophoric dissolved organic material (CDOM)	CDOM is yellow-brown in color and absorbs primarily ultraviolet and blue light decreasing exponentially with increasing wavelength. Produced from the decay of plant material, it consists mainly of humic and fulvic acids and is operationally defined as substances that pass though a 0.2 μm filter.
Diffraction	Light which propagates or bends along the boundary of two different mediums with different indices of refraction.
Diffuse attenuation coefficient, K(λ)	A normalized depth derivative that describes the rate of change of light, plane incident irradiance, with depth. Sunlight underwater typically decreases exponentially with depth.
Index of refraction (real), n	The speed of light in a medium, c_{med}, relative to the speed of light in a vacuum, c_v expressed as $n = c_v/c_{med}$. The real index of refraction determines the scattering of light at the boundary between two different mediums and within the medium from thermal and molecular fluctuations. The relative refractive index, n', is the ratio of the speed of light within the medium, c_m, to the speed of light within a particle, c_p. As n' deviates from 1, the scattering caused by the particle increases for a general size and shape particle (e.g., minerals and bubbles).
Inherent optical properties (IOP)	Optical properties which depend on the medium itself and are independent of the ambient light field. IOPs are defined from a parallel beam of light incident on a thin layer of the medium. Two fundamental IOPs are the absorption (a) and the volume scattering coefficient (β), which describe how light is either absorbed or directionally scattered by ocean water.
Irradiance (downward planar), $E_d(\lambda)$	The incremental amount of radiant energy per unit time (W) incident on the sensor area (m^{-2}) from all solid angles contained in the upper hemisphere, expressed per unit wavelength of light (λ, nm^{-1}). This is used to measure the amount of spectral energy from the sun reaching the sea surface.
Irradiance reflectance, R(λ)	The ratio of the upwelling irradiance, $E_u(\lambda)$, to the plane downwelling irradiance, $E_d(\lambda)$, in different wavelengths (λ).
Optical depth, ζ	A measure of how opaque a medium is to radiation. The optical depth is a function of the geometric depth and the vertical attenuation coefficient.
Optically shallow waters	An aquatic system where the spectral reflectance off the bottom contributes to radiance measured above the sea surface and is defined by the water clarity, bottom depth, and bottom composition.

Photosynthetically available radiation (PAR)	The integrated photon flux (photons per second per square meter) within the 400–700 nm wavelength range at the ocean surface. PAR is the total energy available to phytoplankton for photosynthesis and is reported in units of Q m^{-2} s^{-1}, where Q is quanta, or in μE m^{-2} s^{-1}, where E is Einsteins.
Radiance, $L(\lambda)$	The incremental amount of radiant energy per unit time (in Watts) incident on the sensor area (m^{-2}) in a solid angle view (sr^{-1}) per unit wavelength (λ) of light (nm^{-1}). A satellite measures radiance.
Reflection	At the boundary of two different mediums with different indices of refraction, a certain amount of radiation is returned at an angle equal to the angle of incidence.
Refraction	The direction of light propagation changes, or is bent, at the boundary between two mediums with different indices of refraction. The refracted light bends toward the normal boundary when the index of refraction increases from one medium to another and away from the normal boundary when the index of refraction decreases from one medium to another.
Remote sensing reflectance, $R_{rs}(\lambda)$	A specialized ratio used for remote sensing purposes formulated as the ratio of the spectral water-leaving radiance, $L_w(\lambda)$, to the plane irradiance incident on the water, $E_d(\lambda)$. It represents the spectral distribution of sunlight penetrating the sea surface that is backscattered out again and potentially measured remotely. Theoretically, it is proportional to spectral backscattering $b_b(\lambda)$ and inversely proportional to absorption $a(\lambda)$ of the surface water column.
Water-leaving radiance, $L_w(\lambda)$	The component of the radiance signal measured above the water consisting of photons that have penetrated the water column and been backscattered out through the air-sea interface. It does not include photons reflected off the sea surface, also called sun glint.

Definition of the Subject, Relevance, Motivation

The oceans cover over 70% of the earth's surface and the life inhabiting the oceans play an important role in shaping the earth's climate. Phytoplankton, the microscopic organisms in the surface ocean, are responsible for half of the photosynthesis

on the planet. These organisms at the base of the food web take up light and carbon dioxide and fix carbon into biological structures releasing oxygen. Estimating the amount of microscopic phytoplankton and their associated primary productivity over the vast expanses of the ocean is extremely challenging from ships. However, as phytoplankton take up light for photosynthesis, they change the color of the surface ocean from blue to green. Such shifts in ocean color can be measured from sensors placed high above the sea on satellites or aircraft and is called "ocean color remote sensing." In open ocean waters, the ocean color is predominantly driven by the phytoplankton concentration and ocean color remote sensing has been used to estimate the amount of chlorophyll *a*, the primary light-absorbing pigment in all phytoplankton. For the last few decades, satellite data have been used to estimate large-scale patterns of chlorophyll and to model primary productivity across the global ocean from daily to interannual timescales. Such global estimates of chlorophyll and primary productivity have been integrated into climate models and illustrate the important feedbacks between ocean life and global climate processes. In coastal and estuarine systems, ocean color is significantly influenced by other light-absorbing and light-scattering components besides phytoplankton. New approaches have been developed to evaluate the ocean color in relationship to colored dissolved organic matter, suspended sediments, and even to characterize the bathymetry and composition of the seafloor in optically shallow waters. Ocean color measurements are increasingly being used for environmental monitoring of harmful algal blooms, critical coastal habitats (e.g., seagrasses, kelps), eutrophication processes, oil spills, and a variety of hazards in the coastal zone.

Introduction

Remote sensing of ocean color allows for the estimation of phytoplankton biomass and carbon fixation over the global ocean. From these data, approximately half of the global carbon fixation is estimated to occur by ocean phytoplankton, accounting for roughly 50 Gt C year^{-1} [1, 2]. Phytoplankton are the base of the marine food web, responsible for producing organic carbon from carbon dioxide. The premise behind ocean color remote sensing is to relate the intensity and spectral distribution of visible light reflected out of the water ("ocean color") to the biological and biogeochemical processes that influence the optical properties of the water column ("bio-optical properties") [3]. The distribution, abundance, and temporal variation in various biological, physical, and chemical processes can be observed synoptically from local and regional to global spatial scales from sensors placed on satellites or aircraft. Ocean color remote sensing provides the long-term, continuous time series of phytoplankton biomass and productivity data necessary for global carbon cycle and climate research [4–6], but the uses of ocean color data are increasingly diverse from military to environmental monitoring applications [7].

Phytoplankton have a marked influence on the subsurface and emergent light field [8]. The light harvesting systems of phytoplankton, including the chlorophyll *a*

pigment which is ubiquitous among phytoplankton species, absorb light across the visible spectrum and influence the color of the near-surface ocean [9]. An increase in absorption, or reduction in reflectance, in the blue relative to the green portion of the spectrum can be empirically related to chlorophyll *a* concentration [10]. In other words, as phytoplankton are added to the water column, more blue light is absorbed and the reflected color changes from blue to green. The advent of space-based ocean color sensors in 1978 with NASA's Coastal Zone Color Scanner (CZCS) and the follow on Sea-viewing Wide Field of View Sensor (SeaWiFS) in 1997 greatly enhanced the understanding of phytoplankton distribution and concentration in the ocean [11]. Satellite ocean color imagery provides estimates of phytoplankton abundance across all ocean basins (Atlantic, Pacific, Indian, Arctic, and Southern Oceans) and quantifies the variability from seasonal to interannual timescales.

Over the last several decades, ocean color has expanded beyond chlorophyll and a whole field has emerged to study how the nature of the upwelling light field changes as a function of the quantity and composition of a variety of constituents in the near-surface ocean, including biogenic and nonbiogenic inorganic material, nonliving and living organic material (i.e., phytoplankton, bacteria and viruses), dissolved substances, and benthic habitats. Ocean color research has sought to define the fundamental relationship between the inherent optical properties of the ocean, or the absorption and scattering properties of the constituents, and water-leaving radiance. With improved technology, including radiometers with better spectral resolution, calibration, and a high signal-to-noise ratio, and in situ optical instrumentation, which provided a description of the optical properties of oceanic constituents, biogeochemical parameters are being estimated with greater accuracy and precision. Ocean color remote sensing has moved beyond estimations of chlorophyll alone and is now used to measure total suspended sediment, colored dissolved organic material, particulate inorganic carbon, and phytoplankton functional groups, as well as critical habitats and hazards influencing pelagic and coastal waters.

Optical Properties of the Water Column

Scattering and absorption of photons, the basic unit of light energy, in the surface ocean determines the intensity and spectral shape of the water-leaving light signal measured at an ocean color sensor. Photons that propagate into the ocean interact with water molecules, dissolved and particulate matter and are either absorbed or scattered. Because most of the light is propagated downward into the water column, only a small amount of the signal is scattered back out of the water column and measured remotely. The bulk optical properties of water are used to describe how the spectral and directional distribution of photons is altered within the natural water body.

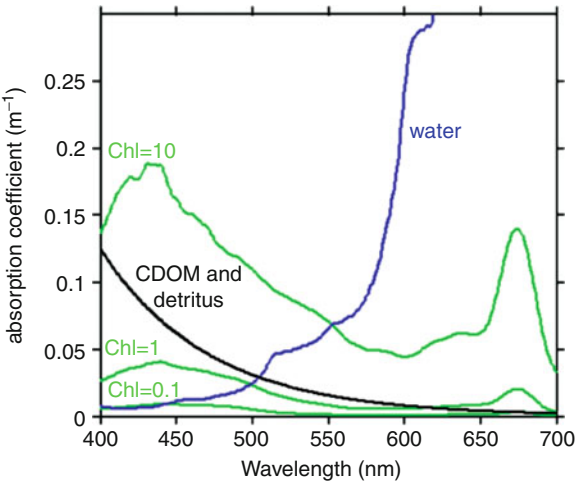

Fig. 18.1 Absorption spectrum for different constituents in seawater including water molecules, chromophoric dissolved organic matter and detritus, and phytoplankton contributions bio-optically modeled for chlorophyll at 0.1, 1 and 10 mg m^{-3} [16]

Inherent Optical Properties

The absorption and scattering properties of water molecules and the dissolved and particulate constituents within the water are called inherent optical properties (IOPs). IOPs do not depend on the ambient light conditions, but are a function of the medium alone. The two IOPs commonly used for remote sensing purposes include the *absorption* (a) and scattering (b) coefficients, which refer to the fraction of incident light, a single, narrow, collimated beam of photons, which is absorbed or scattered per unit distance within the medium (units 1/length or m^{-1}). The scattering coefficient stems from the volume scattering function (β), which is the differential scattering cross section per unit volume per solid angle, and is calculated as the integral over all directions (0–180°). The attenuation coefficient (c) accounts for the reduction in light intensity due to absorption and scattering processes combined.

Both absorption and scattering processes can change the color of the ocean as observed from a satellite. Oceanic constituents that are primarily responsible for absorption of photons include water molecules, phytoplankton pigments, particulate detritus, and *colored or chromophoric dissolved organic material* (CDOM) (Fig. 18.1). Pure water is increasingly effective at absorbing light at wavelengths greater than 550 nm and absorbs minimally in the blue and green portion of the visible spectrum. Conversely, CDOM, operationally defined as all of the colored material that passes through a 0.2 μm filter, absorbs maximally in the ultraviolet and blue portion of the spectrum, decreasing exponentially with wavelength at a rate which is related to the composition, or degradation state, of the material. CDOM is generally comprised of humic and fulvic acids and small colloidal material released through the degradation of plant tissue, whether in soils or in water [12, 13]. Commonly, CDOM is modeled with an exponential function, but a hyperbolic model may be more accurate [14]. Nonliving particulate material, called detritus or

tripton, absorbs in a manner similar to CDOM and the two components are difficult to differentiate spectrally.

Phytoplankton absorb light in a complex manner related to the composition and quantity of their photosynthetic pigments, molecules structured to absorb photons within the visible range of 400–700 nm, dubbed *photosynthetically available radiation* or PAR. There are three distinct classes of pigments, namely, chlorophylls, carotenoids, and biliproteins [101]. All phytoplankton contain chlorophyll *a* and most contain chlorophylls *b* and/or *c*. Chlorophylls *a*, *b*, and *c* have two strong absorption bands in the red and blue portions of the spectrum. Chlorophyll *a* absorption is low in the green (450–650 nm) portion of the spectrum. The presence of chlorophylls *b* and *c* extend the range of light available for photosynthesis further into both the short- and regions. Carotenoids, of which there are many types, have both light harvesting and photoprotective functions. Finally, some phytoplankton contain red or blue pigments called biliproteins, which are divided into classes based on the position of their absorption peaks. The phytoplankton absorption coefficient describes the spectral absorption for natural waters comprised of mixtures of phytoplankton and has been commonly parameterized by chlorophyll concentration and dominant cell size [15, 16].

Scattering processes, which include *refraction, reflection* and *diffraction*, occur at the boundary of a particle with a different *index of refraction*, the ratio of the speed of light in the surrounding medium to the speed of light within the particle, than the surrounding medium. Scattering is predominantly elastic, the energy of the photon is conserved, but the direction of propagation is altered. Rather than reducing light, scattering works to inhibit the straight-path vertical penetration of light. The total scattering coefficient (b) can be subdivided into light which scatters in the forward direction (b_f) (0–90°) and the backward direction (b_b) (90–180°) relative to the unattenuated beam. The backscattered light is the radiance that is scattered out of the water column and measured by a sensor as "ocean color." The magnitude of b_b is a function of the concentration, composition (i.e., index of refraction), shape, and size of particles [17].

Water molecules, salts, organic and inorganic particles, and bubbles provide strong contributions to light scattering in the ocean. Scattering by pure water is the result of density fluctuations from the random motion of water molecules and has a wavelength dependence of λ^{-4} [18]. The presence of salt increases scattering, where pure seawater, with a salinity of 35–38‰, scatters 30% more light than pure water devoid of salt. When particles are present, as in natural waters, scattering increases markedly [19]. The scattering coefficient for the clearest surface waters is an order of magnitude greater than that of pure seawater. Particles that are large relative to the wavelength of light scatter mainly in the forward direction via diffraction, where photons propagating along the particle boundary change their direction in response to the boundary in a manner proportional to the cross-sectional area of the particle. Photons entering large particles are likely absorbed. Conversely, small particles mainly reflect and refract light in a manner proportional to the volume of the particle. Small particles with an index of refraction that deviates markedly from 1, including micron (10^{-6} m)-sized calcium carbonate plates or

coccoliths generated by coccolithophorid phytoplankton ($n' = 1.25$) or bubbles ($n' = 0.75$), are highly efficient at scattering light in the backward direction [17].

The processes of absorption and scattering are considered additive, therefore the sum of the contribution of each constituent determines the magnitude of the total coefficients a_t and b_t. As such, IOPs are separated into operationally defined components which comprise a and b_b:

$$a_t = a_w + a_{ph} + a_d + a_g, \text{ and}$$
$$b_{bt} = b_{bw} + b_{bp}$$

where the subscripts correspond to water (w), algal or phytoplanktonic (ph), non-algal or detrital (d) matter, and dissolved material, originally termed "gelbstoff" (g). Dissolved material does not scatter light and the contributions of both algal and non-algal matter are generally consolidated into backscattering from particulate (p) material. Recent advances in optical instrumentation have allowed for the measurement of absorption and scattering properties in situ and contributed to advances in ocean color remote sensing [20].

Apparent Optical Properties

Measurements of how light of different wavelengths attenuates with depth in the water column have been the historical basis of optical oceanography [21] following from the use of white Secchi disks to estimate water clarity. The properties that can be derived from measurements of ambient light in the water column are generally termed "apparent" optical properties (AOP) because they operate as optical properties describing the fundamental properties of the medium with only a slight dependence on the angular distribution of the light field. Spectral radiance, L, is the fundamental radiometric quantity which describes the spatial, temporal, directional, and wavelength-dependent structure of the light field in units of radiant flux per area per wavelength per solid angle (W m^{-2} nm^{-1} sr^{-1}) [18]. Planar downwelling irradiance, E_d, is a measure of the radiant energy flux incident on the surface from all directions or solid angles contained in the upper hemisphere, with units of radiant flux per unit area per unit wavelength (W m^{-2} nm^{-1}). The same concept, applied to the lower hemisphere, describes upwelling irradiance, E_u. The ratio of the upwelling to downwelling irradiance yields *irradiance reflectance*, R, a measure of how much light of a certain wavelength entering the ocean is scattered backward by ocean molecules and particles.

For remote sensing purposes, only the radiance from a specific direction is measured by a sensor, not the entire upwelling irradiance. Hence, the color is parameterized as *remote sensing reflectance* (R_{rs}, sr^{-1}), which is the ratio of water-leaving radiance to downwelling irradiance. The term "water-leaving radiance" represents the radiance signal emerging from the water column in a nadir

direction and specifically excludes those upward-directed photons that have only reflected off the sea surface and not penetrated the water column (i.e., sun glint). The term R_{rs} represents the proportion of the downwelling light incident on the water surface that is returned through the air-water interface in the nadir direction due to differential absorption and scattering processes. The parameter R_{rs} is proportional to backscattering coefficient and inversely proportional to absorption coefficient and can be approximated as:

$$R_{rs} = \frac{f}{Q} \frac{b_b}{(a + b_b)}$$

where the ratio f/Q is related to the bidirectionality of the light field and varies from 0.09 to 0.11 for most remote sensing applications [22].

The rate of change of radiance and irradiance with depth, known as the vertical diffuse attenuation coefficient (K; m^{-1}), is another principle AOP. Irradiance and radiance decrease approximately exponentially with depth. The downward diffuse attenuation coefficient, K_d, the rate of decrease in downwelling irradiance, $E_d(0)$, with depth (z),

$$E_d(z) = E_d(0)e^{-K_d z}$$

is commonly used in biological studies and is closely linked to the absorption coefficient of the medium specifically. The optical depth, ζ, corresponding to any given physical depth is defined below:

$$\zeta = K_d z$$

Optical depths frequently used by biologists include 2.3 and 4.6, corresponding to the 10% and 1% light levels, respectively. Also, the portion of the surface water column contributing 90% of the water-leaving radiance has a depth, z, described by $z = 1/K_d$ [12]. The radiative transfer equation is the mathematical formulation that defines the relationship between the apparent and inherent optical properties of natural water bodies [18] and is the basis for the semi-analytical models used in ocean remote sensing.

Basics of Ocean Color Remote Sensing

Many challenges are inherent to remote sensing of ocean color. In comparison to land, the ocean target is dark, with an albedo of only a few percent. This means that most of the light that enters the water is propagated downward into the water column and only a few percent is scattered back out again. This is quite different from land and ice surfaces which have a much higher albedo. Most ocean color

sensors are passive in that they measure only the radiation that originates from the sun, as opposed to active sensors that produce and sense their own stream of light (e.g., Light Detection and Ranging or LIDAR). Viewed from space, moreover, the ocean is observed through a thick atmosphere which reflects sunlight back to the sensor and is significantly brighter in the visible wavelengths than the water itself. In technical terms, this is quantified as a low signal-to-noise ratio where the "signal" is the light reflected from within the ocean and the "noise" is light reflected from the atmosphere and sea surface. This section outlines the platforms, calibration, atmospheric correction, and levels of data processing critical for successful ocean color remote sensing.

Sensors and Platforms

Ocean color sensors can be mounted on space-based satellites or on suborbital platforms like aircraft or unmanned aerial vehicles. The spatial and temporal sampling and the questions that can be addressed with the data depend on the type of platform employed. Most current ocean color sensors have a wide field of view, which translates to a wide sampling swath, and are mounted on sun synchronous polar-orbiting satellites (e.g., CZCS, SeaWiFS, MODIS Aqua and Terra). These sensors have the potential to provide global coverage of the earth roughly every 3 days at the equator and more frequently at the poles. However, clouds obscure the ability of the sensor to view the ocean color and, in reality, temporal sampling for any given region is much less. Data are frequently averaged over longer time periods to produce weekly, monthly, and seasonal composite images of the global ocean (Fig. 18.2). The spatial resolution is also limited nominally to 1 km pixel widths (and down to 250 m for select channels) in these polar-orbiting sensors in part because of limitations in signal-to-noise inherent to the dark ocean surfaces (see atmosphere correction below). Global datasets are often aggregated to 4-km or 9-km pixels. However, higher spatial resolution on the scale of meters can be obtained from some space-based platforms and from ocean color sensors placed on aircraft (Fig. 18.3).

The current suite of ocean color sensors has nominally six to seven spectral bands spanning the visible wavelengths (400–700 nm). These bands are not spread uniformly across the visible spectrum, but have been selected to correspond to reflectance characteristics of open ocean waters, particularly those related to phytoplankton pigment absorption features. Three bands are generally found in the "blue" (near 410, 440, and 490 nm), one to two bands in the "green" (510 or 530, 560 nm), and one to two channels in the "red" (670, 680 nm). In addition, channels are also incorporated in the near infrared (NIR) to short-wave infrared (SWIR) for purposes of atmospheric correction (see section "Atmospheric Correction"). Most of the visible channels were selected to match absorption features of phytoplankton and other constituents. Additional channels are also needed to bridge the large 100 nm gap between 560 and 670 nm, where absorption

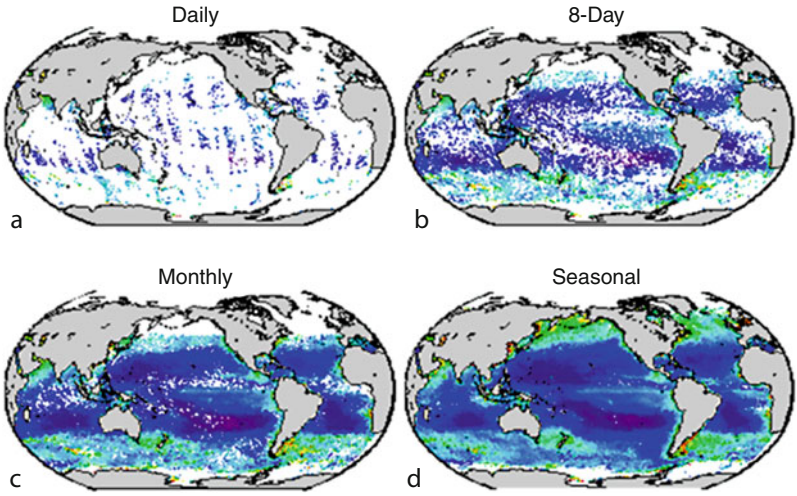

Fig. 18.2 Global maps of satellite-derived chlorophyll showing increasing levels of temporal resolution from daily to seasonal. Imagery from MODIS Aqua satellite from 2006: (**a**) 17 December; (**b**) 11–17 December; (**c**) 1–31 December; (**d**) Autumn. White spacing in imagery represents gaps in orbital coverage (daily image), as well as clouds and ice cover. Merging of imagery from different sensors can provide enhanced daily coverage [100]

features are dominated by water, to better constrain backscattering in complex coastal waters [23, 24]. New technology has allowed for the development of sensors that span the full range of visible and near infrared (NIR) spectrum or "hyperpsectral," also referred to as imaging spectrometers.

No single platform is ideal for addressing all of the temporal and spatial variability in the oceans. A constellation of ocean color imagers with complementary capabilities and specifications is ultimately required to adequately address the diverse requirements of the coastal research and applied user communities. For example, the Hyperspectral Imager for the Coastal Ocean (HICO) was recently installed on the International Space Station for the study of the coastal ocean and adjacent lands. This imaging spectrometer is intended to provide hyperspectral imagery at 100-m resolution sampling at different angles and times of the day for selected regions. Sensors are also being considered for placement on geostationary satellites, similar to the international constellation of meteorological satellites. Such sensors would look at the same regional location on earth for extended periods of time and be able to provide better temporal resolution of ocean processes and episodic hazards. Regional efforts such as the Geostationary Ocean Color Imager (GOCI) on the COMS-1 platform from South Korea are already planned for launch. In addition, higher spatial and spectral resolution polar orbiting sensors are proposed to address questions related to seasonal variability in global coastal habitats and polar ice cover.

Portable sensors flown on aircraft or unmanned aerial vehicles (UAV's) provide a critical sampling niche distinct from satellite-borne sensors that is particularly well

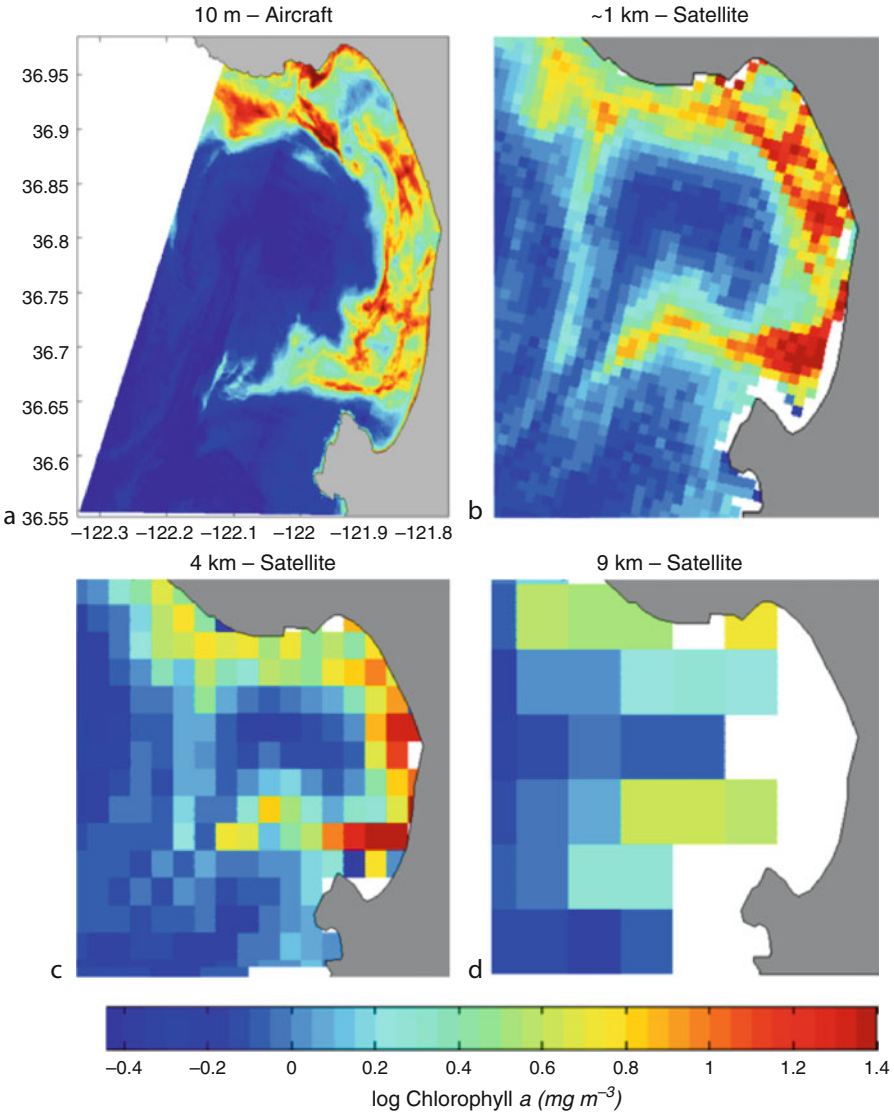

Fig. 18.3 Ocean color remote sensing imagery of Monterey Bay, California, illustrates different spatial resolutions available: (**a**) AVIRIS sensor flown on an aircraft, 10 m pixels [25]; (**b**) SeaWiFS satellite Level 2 data, 1 km pixels; (**c**) SeaWiFS satellite gridded to 4-km pixels; (**d**) SeaWiFS satellite Level 3 9-km standard product

suited for coastal applications and ice research (Fig. 18.3a) [25]. Airborne sensors can sample at finer spatial scales (meters), can operate under clouds and with nearly unlimited repeat coverage, and are effective platforms for high-resolution active sensors (e.g., LIDAR). Flight lines and scanning geometries can also be oriented to

avoid sun glint and their range can be greatly expanded by launching from ships. The technology required to build portable sensors for coastal applications is developing with wide field of views, minimum polarization dependence, high response uniformity, and optimized signal-to-noise ratio for low-light channels [26, 27]. These sensors are becoming more popular for use in the environmental management of coral reefs, seagrasses, kelps, and other coastal targets, and have the potential to monitor episodic events such as harmful algal blooms and runoff and flooding from storms.

Ocean color sensors in space have traditionally been "whisk broom" in design where a single detector collects data one pixel at a time as the telescope rotates to build up pixels along a scan line. Some satellites and most of the suborbital sensors are "pushbroom" where the entire scan line is imaged synoptically by a line of sensors arranged perpendicularly to the flight direction. In order to achieve high-quality data that can track climatological trends in ocean color, sensors are required to have very high radiometric accuracy and stability. Detectors are calibrated pre- and post-launch and degradation over time is carefully quantified with vicarious calibrations from field measurements and ideally lunar imaging. Periodic reprocessing of the satellite data is considered critical to obtaining high-quality datasets and continuity over multiple missions [5, 28].

Atmospheric Correction

One of the most challenging aspects of ocean color remote sensing is successfully removing the atmospheric signal from the water column signal. Aerosols and gas molecules are the primary contributors to the radiance measured at the top of the atmosphere. Approximately 80–85% of the radiance measured at the sensor is the result of Rayleigh scattering by molecules in the atmosphere that are small relative to the wavelength of light. Photons reaching the sensor (L_u) are a combination of those scattered by the atmosphere (L_p), reflected at the air-water interface (L_r), known as specular reflection, or have been backscattered from within the water column, dubbed water leaving radiance, or L_w (Fig. 18.4). The water-leaving radiance, used for most ocean color applications, is only a small portion of the signal retrieved at a satellite and must be differentiated from the photons scattered within the atmosphere and specularly from the sea surface in a process called "atmospheric correction."

Rayleigh scattering, which decreases with wavelength (λ) following λ^{-4}, can be estimated using a single-scattering radiative transfer equation using the atmospheric pressure and appropriate viewing geometry [29]. An additional 0–10% of the radiance signal is due to aerosols (i.e., haze, dust, and pollution), particles with sizes comparable to the wavelength of light which absorb and scatter as a complex function of their type, size, and concentration. The type and concentrations of aerosols overlying the ocean are quite variable in space and time, particularly in coastal regions subject to urban pollution and terrestrial dust [30].

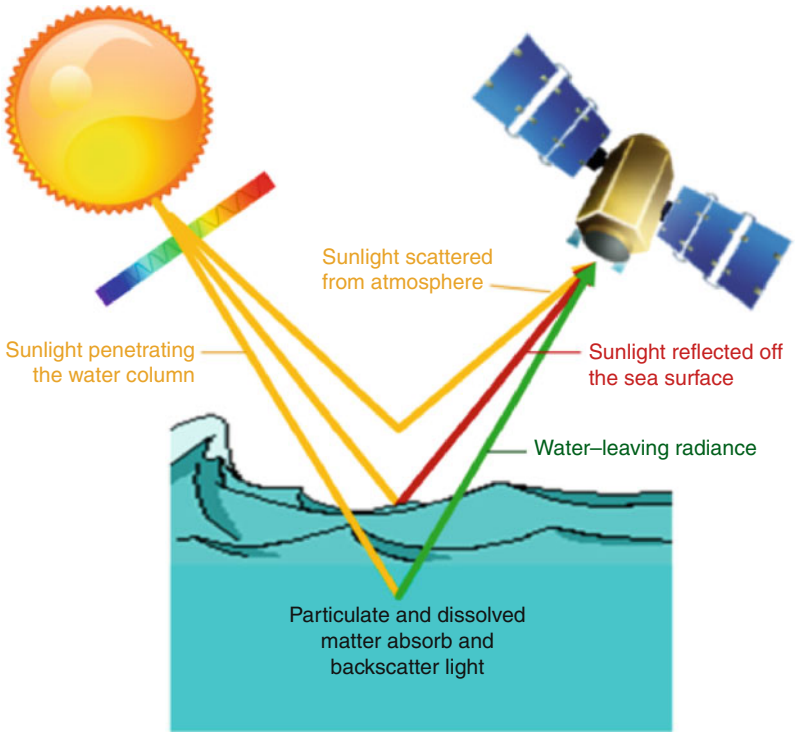

Fig. 18.4 Radiance measured by a satellite includes light scattered by the atmosphere and reflected off the sea surface (i.e., glint). In a process called "atmospheric correction," these signals are removed leaving the "water-leaving radiance" or the light that has penetrated the water column and been backscattered out to the satellite – a measure of ocean color

Atmospheric correction of aerosols remains a challenge for accurately deriving water-leaving radiance from satellites and aircraft. Approaches generally focus on channels in the NIR and even in the short wave infrared (SWIR) [29, 31, 32]. Because water absorbs so heavily in the infrared, very few photons are reflected out of water in this part of the electromagnetic spectrum and the signal is dominated by reflection from atmospheric gases and aerosols. Various types of models are used, including coupled models and multi-scattering models, to infer the contribution of aerosol reflectance in the visible portion of the spectrum from the infrared. Aerosol reflectance is not spectrally flat, but varies with wavelength, and at least two channels are necessary to determine the spectral shape of aerosol reflectance and extrapolate from the NIR to visible wavelengths [29, 33].

Dust, particularly from desert storms, can also impact the optical properties of the atmosphere and most atmospheric correction algorithms for ocean color sensors are not capable of handling absorbing mineral dust (i.e., colored dust) [34]. For example, airborne plumes of Saharan dust are observable all year on satellite images over the Tropical Atlantic and may be increasing in areas like the

Table 18.1 Levels of data processing products from ocean color satellites

Level	Processing	Spatial qualities
0	Raw data as measured directly from the spacecraft	Satellite coordinates at highest spatial resolution
1	Converted to radiance using calibrations and sensor characterization information	Satellite coordinates at highest spatial resolution
2	Atmospherically corrected to water-leaving radiance and derived products	Satellite coordinates at highest spatial resolution
3	Derived products have been mapped onto a two-dimensional grid at known spatial resolution and can be averaged over timescales (weekly, monthly)	Regular gridded data at lower spatial resolution (e.g., 4 or 9 km)
4	Products that have been merged or assimilated with data from other sensors, in situ observations, or model outputs	Regular gridded data at lower spatial resolution

Mediterranean Sea [35]. If colored dusts are not properly corrected for in the atmospheric correction schemes, then the color of the ocean is not accurately estimated resulting in errors in chlorophyll and other biogeochemical properties retrieved from the satellite data [36]. In addition to its radiative impact, it has been suggested that this mineral dust has a substantial influence on the marine productivity and may also carry pollutants to the oceans [37, 38].

Whitecaps breaking on the sea surface must also be corrected from derivations of water-leaving radiance. Whitecap reflectance is often modeled using an empirical cubic relationship to wind speed and an approximate reflectance value for an individual whitecap [39], but such models often overcorrected the imagery, and a fixed whitecap correction is applied when wind speeds exceed a threshold (e.g., 8 m s^{-1} for SeaWiFS). At high winds, some of the signal attributable to whitecaps is removed by the aerosol corrections.

Levels of Processing

Standards for ocean color data processing, developed at US National Aeronautics and Space Administration (NASA) for the SeaWiFS mission [40], are widely followed by the international community of ocean color users and involve four levels of processing (Table 18.1).

Ocean Color Algorithms

This section presents the classification of the global ocean into two optical classes: Case 1 and Case 2. The general approaches for two of the main products from ocean

color imagery, chlorophyll and primary productivity, for Case 1 waters and a description of the semi-analytical algorithms used for both Case 1 and Case 2 waters are presented.

Optical Classification of Aquatic Systems

Ocean waters have long been classified based on their color properties [41]. A classification system introduced in 1977 differentiates phytoplankton-dominated waters from those where inorganic particles are dominant, known as Case 1 and Case 2, respectively [42]. These cases have evolved from their original forms into the categories used today: Case 1 waters are those waters where optical properties are determined primarily by phytoplankton and related colored dissolved organic matter (CDOM) and detritus degradation products; Case 2 waters are waters where optical properties are significantly influenced by other constituents such as mineral particles, CDOM, or microbubbles that do not covary with the phytoplankton concentration [8, 43]. In today's world, approximately 97% of the surface ocean falls toward the optically simple, deep water, Case 1 classification. When inorganic, organic, particulate, and dissolved material all vary independently of one another, such as in coastal ecosystems with considerable riverine influence, bottom resuspension, or optically shallow regions, the system falls toward the Case 2 classification, also called "optically complex."

This binary classification scheme has been prevalent in bio-optical modeling of ocean waters and development of ocean color algorithms. However, many problems exist with use of such simplified schemes in modeling natural systems. For example, there is no sharp dividing line between the cases and each investigation tends to use as different criteria for defining Case 1 and Case 2. Commonly the two cases are defined by the relationship between chlorophyll and remote sensing reflectance or scattering. Even in the global ocean considered to be Case 1, CDOM concentrations do not covary with the instantaneous chlorophyll concentration [44], but can vary from 30% to 60% of the total non-water light absorption [45] and result from differences in water mass ventilation, water column oxidative remineralization, and photobleaching [46].

In *optically shallow waters*, in addition to the water column and its constituents (i.e., dissolved and particulate material), the bottom contributes to the water leaving radiance in a way that depends on the bottom composition and roughness. Periodic measurements of bottom types using passive remote sensing in coastal systems are valuable for describing and monitoring habitats [47]. The magnitude and spectral quality of light reflected off of the bottom material can allow separation of bottom reflectance from the water column signal, where different bottom types will have a different effect on reflectance. Shallow, clear water will yield the most information about bottom material, more readily allowing spectral discrimination of bottom

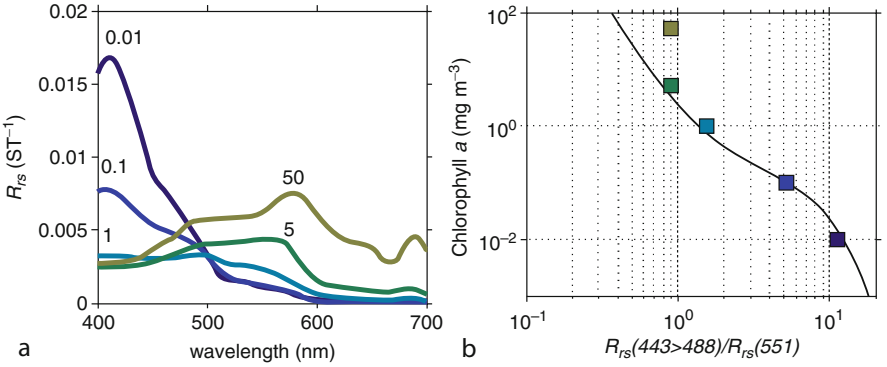

Fig. 18.5 (**a**) Remote sensing reflectance (R_{rs}) spectra modeled for different concentrations of chlorophyll *a* (Chl) from 0.01 to 50 mg m^{-3}. The color of each line represents the modeled ocean color a human might observe following [61]. (**b**) The empirical OC3M model for deriving Chl from R_{rs} for the MODIS Aqua sensor. The model uses the "blue" channel with the highest R_{rs} value (443 or 488 nm) divided by the "green" channel at 551 nm. Each *square* represents the modeled Chl for the corresponding R_{rs} spectra in panel A and demonstrates how the model becomes less accurate at high Chl

type. However, as depth and the diffuse attenuation coefficient, K_d, increase, the bottom signal becomes difficult to differentiate.

Empirical Chlorophyll Algorithms

Standard calculation of chlorophyll from ocean color imagery involves an empirical relationship developed from field observations collected throughout the global ocean [10]. Algorithms are typically not developed from the remotely sensing imagery itself, because this would incorporate any biases in calibration and atmospheric correction procedures used to derive reflectance, as well as any spatial inhomogeneity in parameters over pixel scales, and would require new algorithms for every new calibration, reprocessing, and sensor. Empirical solutions are used because an analytical solution to the problem requires an assessment of the entire radiance distribution and depth derivative and such measurements are not possible with remote sensing [48]. Only the upward flux incident upon the water-air interface at angles less than 48°, the angle at which complete internal reflection occurs, is measurable from above the sea surface [6] and generally only the flux emitted in a single viewing angle is remotely sensed.

The current empirical algorithms use the shift in ocean color from "blue" at low Chl, where R_{rs} peaks at 400 nm, to "green" at high chlorophyll, where R_{rs} peaks at 555 nm (Fig. 18.5a). Empirical ocean color algorithms have been applied to the vast majority of the global ocean considered Case 1 and use multiple ocean color bands

Table 18.2 Empirical chlorophyll algorithms for a variety of ocean color sensors

		Channels[b]		Coefficients[c]				
Name[a]	Sensor	Blue	Green	a0[c]	a1	a2	a3	a4
OC4	SeaWiFS	443 > 490 > 510	555	0.366	−3.067	1.93	0.649	−1.532
OC3S	SeaWiFS	443 > 490	555	0.2409	−2.4768	1.5296	0.1061	−1.1077
OC2S	SeaWiFS	490	555	0.2372	−2.4541	1.7114	−0.3399	−2.788
OC3M	MODIS	443 > 488	551	0.283	−2.753	1.457	0.659	−1.403
OC2M	HMODIS	469	555	0.1543	−1.9764	1.0704	−0.2327	−1.1404
OC4O	OCTS	443 > 490 > 520	565	0.4006	−3.1247	3.1041	−1.4179	−0.3654
OC3O	OCTS	443 > 490	565	0.2836	−2.1982	1.0541	0.186	−0.717
OC2O	OCTS	490	565	0.2805	−2.167	1.1789	−0.1597	−1.5591
OC3C	CZCS	443 > 520	550	0.3012	−4.4988	9.0983	−9.9821	3.235

[a]Name of ocean color (OC) algorithm incorporates the number of wavebands (2–4) used in the formulation and the initial for the sensor used (S = SeaWiFS; M = MODIS; O = OCTS; C = CZCS)
[b]The algorithms use a log-transformed ratio of "Blue" (443–520 nm) to "Green" (550–565 nm) remote sensing reflectance (R_{rs}). When more than one "Blue" channel is provided, only the channel with the highest R_{rs} is used. x = log10(R_{rs}(Blue)/R_{rs}(Green))
[c]Chlorophyll *a* is modeled as a fourth polynomial fit to the field data such that: $\text{Chl} = 10\text{^}(a0 + a1^{*}\text{x} + a2^{*}\text{x}^2 + a3^{*}\text{x}^3 + a4^{*}\text{x}^4)$

typically log-transformed and in a ratio formulation to minimize problems with atmospheric correction and differential scattering in the ocean. The coefficients for the algorithms are regularly adjusted to account for different sets of wavebands in various sensors and as new field data becomes available (Table 18.2). The OC3M algorithm developed for MODIS, for example, uses a 4th order polynomial derived from a large global dataset of field measurements of chlorophyll and R_{rs}. It uses a logarithmic ratio of blue light (either 443 and 488 nm depending on which is greater) to green light (555 nm) and follows an inverse relationship such that low Chl is retrieved or high ratios when the ocean color is blue and high Chl when more green light is reflected (Fig. 18.5b). These types of algorithms tend to work best at lower Chl (<1 mg m^{-3}), found in most of the world ocean, where the algorithm has a flatter slope [49].

For much of the open ocean where chlorophyll concentrations are low, the empirical algorithms work well and relative error is estimated to under 35% [50]. However, empirical derivations of chlorophyll in Case 1 waters can be in error by a factor of 5 or more, particularly at higher Chl [49]. Such variability is due to differences in absorption and backscattering properties of phytoplankton and related concentrations of colored dissolved organic matter (CDOM) and minerals. The empirical algorithms have built-in assumptions that follow the basic precept of biological oceanography; i.e., oligotrophic regions with low phytoplankton biomass are populated with small phytoplankton while more productive regions contain larger bloom-forming phytoplankton. With a changing world ocean, phytoplankton composition may shift in response to altered environmental forcing and CDOM and mineral concentrations may become uncoupled from phytoplankton stocks creating further uncertainty and error in the empirical approaches [49].

The empirical approach is not widely applicable in Case 2 waters, generally found near the coasts. Such waters are influenced by freshwater plumes with CDOM and minerals that significantly impact the optical properties, as well as resuspension of bottom sediments [51]. Phytoplankton assemblages can also be diverse in coastal regimes and light absorption per unit of Chl is difficult to constrain. Melting and runoff of glacial sources can increase particle concentrations in the nearshore and change phytoplankton assemblages. In order to use remote sensing in coastal waters, semi-analytical models are employed that are able to decompose the reflected color into the many absorbing and scattering constituents in the water column (see section "Semi-analytical Algorithms").

Primary Productivity Algorithms

Net primary production is a key parameter derived from ocean color data that provides a measure of how much carbon dioxide is taken up and incorporated into ocean phytoplankton during photosynthesis. Export of fixed carbon to the ocean interior, while only a fraction of the total biomass produced, provides a long-term sink for atmospheric carbon dioxide [52]. While satellite-derived Chl is not a direct measure of carbon fixation in phytoplankton, such estimates are typically derived from correlates of Chl and rates of carbon fixation [53]. Net primary productivity varies with phytoplankton species assemblages and their physiological state related to light, temperature, nutrients, and other environmental factors.

A variety of formulations have been developed for ocean color remote sensing and parameterized for the global ocean or specific regions. Models are generally restricted to parameters that can also be globally derived from remote sensing imagery, such as sea surface temperature and photosynthetically available radiation (PAR). Moving from a standing stock of phytoplankton biomass to photosynthetic rate requires a time-dependent variable. Solar radiation in the form of PAR is commonly used in formulations to convert biomass to primary productivity. The physiological response of the measured chlorophyll to light, nutrients, temperature, and other environmental variables must also be incorporated in the model. Primary productivity models can be differentiated by the degree of explicit resolution in depth and irradiance [53].

Round robin experiments have been conducted to compare the performance of models for assessing global productivity from ocean color imagery, as well as the output from ecosystem-based general circulation models [1, 54]. The third such effort found that global average primary productivity varied by a factor of two between models and the global mean productivity for the different model groups ranged from 44 to 57 Gt C year^{-1} with an average of 50.7 Gt C year^{-1}. The models diverged the most in the high-nutrient low chlorophyll waters of the Southern Ocean. Primary productivity algorithms have also been formulated from remote

sensing estimates of the inherent optical properties (such as light absorption and backscattering) directly [55, 56], without incorporating Chl and the associated uncertainties inherent in that parameter.

Semi-analytical Algorithms

The empirical algorithms used for deriving chlorophyll have been likened to a "black box" that provides no mechanistic understanding of ocean optics and are particularly challenging to apply in a changing ocean, when the water properties are different from the empirical data used to develop the formulation [57]. Analytical solutions to deriving IOPs from water-leaving radiance are not possible because the radiance can only be measured from a few angles. Semi-analytical algorithms (or "quasi-analytical") are based on a fundamental understanding of the propagation of light in the ocean and provide a more mechanistic approach to ocean color. These algorithms incorporate some empirical approximations, but do not rely on fixed predetermined relationships between the absorption and backscattering components of the water column.

In semi-analytic models, the ocean color signal is inverted to obtain estimates of the various absorbing and backscattering constituents directly. Parameterization of how water, phytoplankton, and dissolved and detrital material inherently absorb and backscatter light across the visible spectrum (i.e., their spectral shape) is used in these models. The spectral reflectance measured at the satellite is often inverted to retrieve the amounts of each individual component contributing to the absorption and backscattering of light. Such algorithms are the primary methods for obtaining CDOM distributions across the ocean surface [58]. In semi-analytical models, the biogeochemical parameters, such as Chl and total suspended matter, are derived secondarily from the IOPs. Semi-analytical formulations vary in terms of their architecture and statistical methods employed to retrieve the inherent optical properties from the remote sensing signal and the empirical parameterizations within the models [57].

Applications for Oceanography

Ocean color remote sensing is an important tool for many branches of oceanography, including biological, physical, and chemical oceanography. The section below summarizes only some of the main applications of ocean color remote sensing with the understanding that the uses of ocean color are continuously expanding. A recent monograph from the International Ocean Color Coordinating Group (IOCCG) entitled "Why Ocean Colour?: The Societal Benefits of Ocean-Colour Technology"

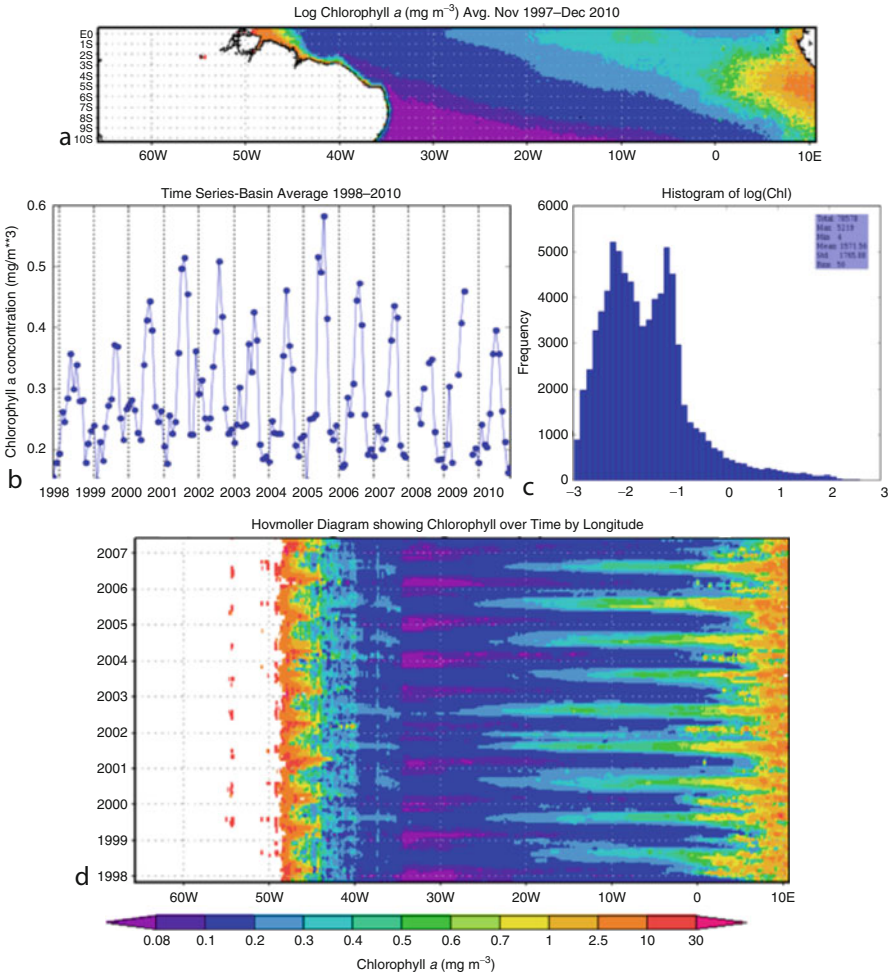

Fig. 18.6 Various times series analyses that can be conducted with standard Level 3 chlorophyll imagery including (**a**) Temporally averaged spatial distributions; (**b**) time series of interannual variability; (**c**) histograms showing the statistical distributions; (**d**) Hovmoller plots presenting both spatial (x-axis) and temporal (y-axis) variability. Such plots can be easily generated by the public with the Giovanni interface [59]

extensively documents the many uses of ocean color remote sensing from scientists to environmental managers to the general public [7]. Web-based software has also been developed, see, e.g., Giovanni [59], which allows the public to freely map and analyze ocean color imagery over time and space. Figure 18.6 provides an example of various types of figures that can be easily generated from remotely sensed chlorophyll using that software.

Biological Oceanography

Apart from estimating chlorophyll and primary productivity, ocean color remote sensing has many biological applications that range from phytoplankton physiology to assessing distributions of migrating whales. Phytoplankton physiology, particularly the efficiency of light capture and utilization, has been modeled from the natural fluorescence signature provided by ocean color remote sensing [60]. Even though the spectral resolution available in most current ocean color satellite is limited to six to eight available spectral channels [61], a variety of phytoplankton taxa and groups have also been distinguished from satellite imagery based on their unique optical properties and/or regional tuning of algorithms using knowledge of the local phytoplankton composition. Phytoplankton taxa can have unique sets of accessory pigments that differentiate them from one another and can result in unique absorbance spectra. In addition, phytoplankton can have cell walls or exterior plates comprised of different materials (e.g., silica, calcium carbonate) that can make them more or less reflective. Various approaches have been developed to map size classes (from pico- to microplankton) or major groups of phytoplankton in the global ocean [62]. Other algorithms have targeted particular phytoplankton taxa such as coccolithophores, nitrogen-fixing *Trichodesmium* [63], toxic dinoflagellates [64], and nuisance cyanobacteria [65].

Satellite-derived chlorophyll and primary productivity provide a key metric to assess marine ecosystems temporally on a global scale and have been used extensively to monitor conditions that impact other biological organisms in the sea. The relationship between satellite-derived chlorophyll data and organisms at higher trophic levels depends upon the number of linkages in the food web. For species like anchovies and sardines, which eat phytoplankton in their life cycle, the linkage can be direct [66]; whereas, many trophic levels can exist for other species and the relationship can be quite nonlinear [7]. The distribution, movement, and migration of whales, dolphins, pinnipeds, penguins, and sea turtles has been related, either directly or indirectly, to remotely sensed patterns of Chl (reviewed in [7]). Most fish have planktonic larval stages that are strongly influenced by ocean circulation and recruitment success has been found to be related to the degree of timing between spawning and the seasonal phytoplankton bloom, as observed from satellites [67]. Ocean color remote sensing has also been used to study invertebrates in the global ocean, such as shrimp in the Newfoundland-Labrador Shelf [68] and pteropods and pelagic mollusks in the Ross Sea [69]. Mean net primary productivity, determined from ocean color satellite imagery, elucidates species richness in biogeographical studies of cephalopods [70].

New techniques have also been developed to use ocean color remote sensing in optically shallow water systems to deduce changes in benthic habitats [71]. Optically shallow water occurs when the seafloor contributes to the reflectance signal observed remotely by a satellite (Fig. 18.7a) and is defined by a combination of water clarity, water depth, and bottom composition. Satellite estimates of biomass and net productivity of seagrasses, kelps, and other benthic producers

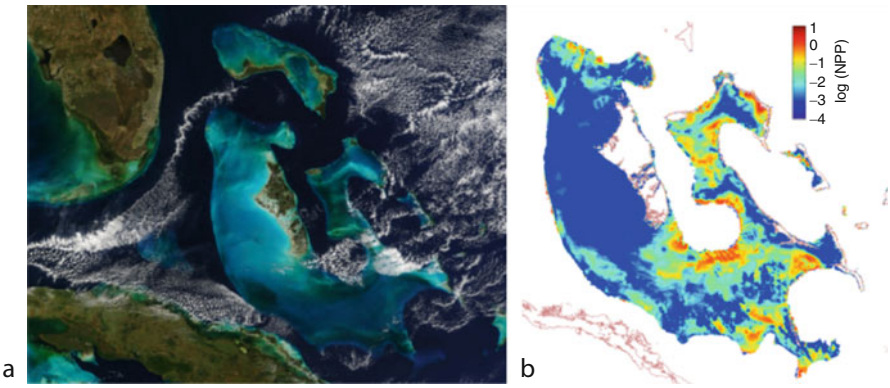

Fig. 18.7 The Great Bahama Bank is an example of optically shallow water where the seafloor color can be observed from space. (**a**) Pseudo-true color image from MODIS Aqua showing the bright Bahamas Banks with Florida, USA, to the West and Cuba to the Southwest. White wispy clouds can obscure the ocean color. (**b**) Net primary productivity (mgC m^{-2} d^{-1}) of seagrass and benthic algae estimated from ocean color imagery over the Great Bahama Bank [47]

have been conducted over regional scales [47, 72] (Fig. 18.7b). Ocean color imagery from aircraft can map fine-scale distributions of seagrasses, coral reefs, and other coastal habitats at local scales [73, 74]. Changes in ocean color signals over time can also be used to assess contributions of coastal carbon to the global carbon cycle [75, 76]. Responses of coastal regions linked to terrestrial changes can also be observed with ocean color imagery. Warming of the Eurasian landmass, for example, has led to enhanced productivity in the water column [77]. Agricultural runoff from fields in Mexico was shown to stimulate large phytoplankton blooms in the Gulf of California that alter water clarity and potentially lead to anoxic conditions [78].

Ocean Physics

Ocean color data is well suited to the detection of convergence zones and oceanic fronts, sometimes better than thermal sensors which penetrate only the skin layer, or the first 10 μm, of the water column. Interestingly, a sequence of ocean-color-derived chlorophyll images may help predict the formation of eddies days before they appear. The increased penetration of visible radiation reveals more frontal features and with greater detail than those retrieved with sea surface temperature data alone [79]. Likewise, upwelling regions, which bring cold, nutrient-rich waters up to the surface can be readily identified in ocean color images as areas with an enhanced chlorophyll concentration. The intensity of upwelling from year-to-year can be tracked through the time series of chlorophyll abundance. Chlorophyll is an effective indicator for detecting anomalous activity in the

oceanic environment. Evidence of an El Niño event beginning in November of 1997, during which phytoplankton pigment concentrations appeared anomalously low in the Equatorial Upwelling Zone, was obvious in the continuous coverage supplied by SeaWiFS. The onset of restored upwelling was likewise evident with the increased chlorophyll concentrations during the months of June and July 1998 [80].

Ocean water clarity also affects the distribution of shortwave heating in the water column. Both chlorophyll and CDOM concentrations have been linked to changes in heating of surface waters [81, 82]. Increased clarity would be expected to cool the surface and heat subsurface depths as shortwave radiation penetrates deeper into the water column. Recent studies show that water clarity, as determined from ocean color remote sensing, is an important feature in atmospheric circulation (the Hadley cells), oceanic circulation (Walker Circulation), and formation of mode water [83]. Importantly, ocean color imagery is also critical to predicting tropical cyclone activity. The presence of light-absorbing constituents (like Chl and CDOM) shapes the path of Pacific tropical cyclones and propagation to higher latitudes [84].

Chemical Oceanography

A major contributor to the ocean carbon system is colored dissolved organic material (CDOM), a mixture of compounds produced primarily by decomposition of plant matter. CDOM, when present in high enough concentrations, produces a yellow or brownish color and is highly reactive in the presence of sunlight. When CDOM undergoes photodegradation, organic compounds essential to phytoplankton and bacterial growth are released [85]. Satellite measurements collected using SeaWiFS, MODIS, and MERIS produce daily estimates of CDOM at 1 km resolution. High temporal resolution CDOM maps can be used to identify and track water masses at timescales close to the processes determining its distribution. CDOM dynamics play an important role in ocean biogeochemistry, regulating the absorption of blue and UV radiation in the surface ocean and therefore altering the depth of the euphotic zone [58] and heating surface waters [82]. Although CDOM is difficult to analyze chemically, its distribution and abundance, identifiable using ocean color remote sensing, is highly relevant to understanding carbon cycling in the ocean.

The particulate inorganic carbon (PIC) pool, calcium carbonate ($CaCO_3$), contributes substantially to the ocean carbon cycle and ocean color reflectance. Calcification reduces surface carbonate, decreasing alkalinity. Organic carbon production via photosynthesis counterbalances this effect. Coccolithophores, haptophyte algae, are responsible for the majority of the biogenic particulate inorganic carbon production. Coccolithophores generate and shed tiny white plates of calcium carbonate called coccoliths, which are highly efficient at reflecting light, ultimately producing large turquoise patches in the ocean readily visible in ocean color imagery [86].

Ocean color remote sensing algorithms have been formulated for generating quantitative estimates of particulate inorganic carbon and calcification rates on regional and global scales [87, 88]. A continued, long-term assessment of coccolithophore and particulate inorganic carbon abundance from satellite imagery will aid in understanding the impact of ocean acidification on marine organisms reliant on carbonate for the formation of shells [89].

Ocean color imagery provides the ability to expand small-scale biogeochemical studies to regional or global scales. For example, the marine inorganic carbon cycle has been shown to be not only influenced by marine plankton but also by fish that precipitate carbonates into the surface waters. Extrapolations from satellite-derived net primary productivity up several trophic levels to marine fish [90] reveal that fish may contribute 3–15% of the total oceanic carbon production [91].

Applications for Environmental Monitoring

Ocean color remote sensing plays a major role in monitoring and sustaining the health and resilience of marine ecosystems, including fisheries and endangered species [40]. Ocean color products are helping to address how environmental variability influences annual recruitment of fish stock [92] and to locate and manage fisheries [7]. Ocean color imagery coupled with other remote sensing products such as sea surface temperature is a fundamental tool in ecosystem-based management of marine resources [93].

Ocean color remote sensing can monitor a variety of acute and chronic hazards influencing the oceans including: harmful algal blooms, oil spills, coastal flooding, icebergs and marine debris [7]. A combination of ocean color, field, and meteorological datasets have been critical in identifying the onset of harmful algal blooms (HABs), which can produce toxins and create hypoxic conditions. While toxins cannot be directly observed from ocean color, the onset of potential harmful blooms can be identified using a chlorophyll anomaly method [94] in concert with other forecasting tools such as field and meteorological datasets. This information can then be passed on to coastal managers and state agencies to put strategies in place to deal with an impending bloom. A long-term time series of ocean color products can aid in elucidating forcing and transport mechanisms of these harmful blooms and help improve predictability.

New techniques are being developed for early detection, containment, and clean up of oil spills. Remote sensing can be used to detect oil spills that can change surface reflectance properties and the color of the ocean [95]. Coarse spatial and temporal resolution, limited spectral bands, cloud-cover issues and high sunlight requirements have generally restricted the usefulness of ocean color imagery for oil-spill detection from polar orbiting satellites [96]. Moreover, current processing methods may not allow data availability within hours of data capture. The spatial, temporal, and spectral resolution needed for oil spill recovery planning requires

high-resolution, hyperspectral ocean color radiometers deployed in geostationary orbit [40].

Ocean color imagery has also been used to track marine debris on the ocean surface which can entangle a variety of pelagic species, such as endangered sea turtles, seals, and whales. The nets also become ensnared on coral reefs and damage the reef structure and associated organisms that require a healthy reef ecosystem [97, 98]. Satellite ocean color data are part of the methods being developed to locate and identify potential locations of marine debris to aid their removal from these ecosystems.

Ocean color imagery is also useful in monitoring water quality in inland aquatic water bodies. Nuisance algal blooms, such as cyanobacteria, cause aesthetic degradation to lakes and reservoirs resulting in surface scum, unpleasant taste and odor in drinking water (from the production of metabolites such as methyl isoborneol and geosmin), and possible adverse effects to human health from blue-green algal toxins. Predicting the locations and timing of blue-green algal bloom using traditional sampling techniques is difficult and hyperspectral remote sensing can be an important tool in such monitoring efforts [99].

Future Directions

Within a few decades, the ability to view the global ocean color regularly through remote sensing has revolutionized the perceptions about ocean processes and feedbacks to the earth's climate. The decade of continuous ocean color imagery has provided a foundation for assessing change in the earth's systems and long-term averages or "climatologies" of products, such as chlorophyll, CDOM, and PIC, have been produced to provide a baseline of ocean biogeochemistry (Fig. 18.8). The products obtained from ocean color are now incorporated into all domains of oceanography, global climate forecasts, military applications, and environmental monitoring across the expansive global ocean and the vulnerable coastal regions where most of the human population resides [11]. While successful, the technology and processing of ocean color remote sensing is still in its infancy in terms of monitoring the ocean from immediate to climatological timescales.

The relationships between climatological forcing and biological carbon storage in the ocean are complex and not readily incorporated in models. Ocean color imagery can provide assessments of potential changes to ocean processes including primary productivity, surface heating, sediment plumes, altered food webs, harmful algal blooms, changing acidity, and alterations of benthic habitats in response to shifts in winds and upwelling, clouds and radiative forcing, and storm intensity and frequency. Recent observed changes in chlorophyll, primary production, and the size of the oligotrophic gyres from ocean color satellites are compelling evidence of significant changes in the global ocean. A recent study demonstrates that a time series of at least 40 years in length is needed to unequivocally distinguish a global

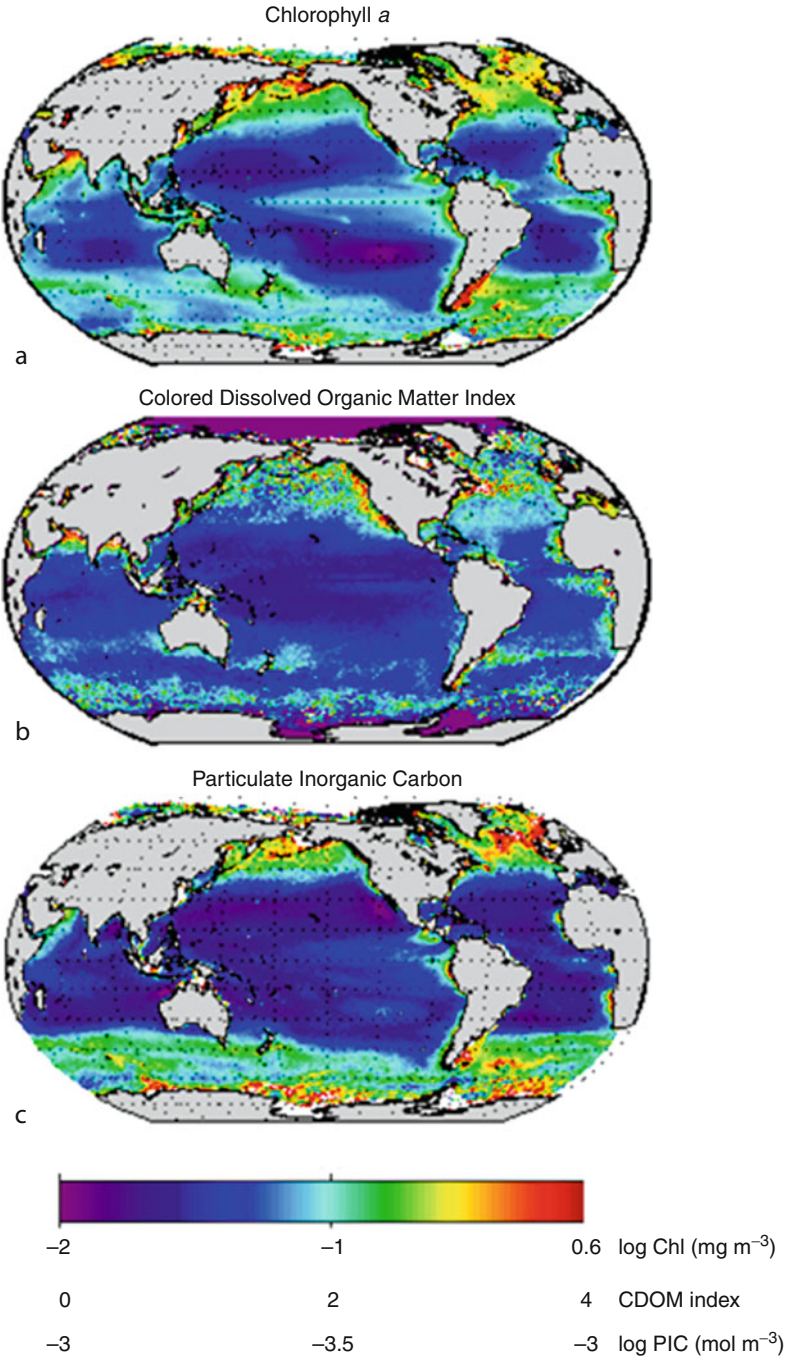

Fig. 18.8 Global climatologies or long-term averages of products derived from the Ocean Color SeaWiFS sensor from 1998–2011. (**a**) Chlorophyll *a* (mg m^{-3}); (**b**) colored dissolved organic matter (CDOM) index; (**c**) particulate inorganic carbon (PIC) (mol m^{-3})

warming trend from natural variability [6] and sustained long-term observations of ocean color are in jeopardy [40].

In addition to sustained imagery, there is a need for integrating ocean color imagery from different platforms to monitor the oceans and aquatic habitats at a variety of desired spectral, spatial, and temporal resolutions. Integration of satellite sensors with suborbital platforms will allow for better assessment of vulnerable marine and aquatic habitats, as well as responses to hazards such as harmful algal blooms, oil spills, and storms that cause coastal flooding and erosion. Active sensors, such as Light Detection and Ranging (LIDAR), will allow us to probe into the depths of the oceans. Moreover, integrating surface ocean color measurements with three-dimensional measurements and models of the ocean will be increasingly important in discerning a changing ocean [49].

Finally, the approaches or algorithms for conducting ocean color remote sensing will be augmented as more spectral channels become routinely available and as ocean properties change. Purely statistical or empirical models are only accurate when conditions are similar to past conditions. When considering a changing ocean, the cause of the color change must be carefully assessed to separate the spectral variability due to phytoplankton from other sources of variability, such as sediments, CDOM, and even atmospheric aerosols. Considerable growth is also expected in approaches and technology for remote sensing of coastal habitats and assessing acute and chronic hazards. Comprehensive and consistent field observations from ships to autonomous vehicles and floats are required to assess the accuracy of satellite-derived products, build improved algorithms, and provide better linkages between surface measurements made from space and the processes within the water column [49]. Future effort will also be directed at assimilation of ocean color imagery into global circulation and climate models. As outlined above, remote sensing of ocean color is a complex discipline requiring radiometrically accurate and calibrated sensors, advanced techniques for atmospheric correction of aerosols and dust, and approaches that can deduce the source of variability in the color signal measured by a sensor. With the many important applications of ocean color remote sensing, from climate forecasting to environmental monitoring, a consistent and coordinated international investment in education, research, and technology is required to maintain and advance this dynamic field.

Bibliography

Primary Literature

1. Carr ME et al (2006) A comparison of global estimates of marine primary production from ocean color. Deep Sea Res Part II: Top Stud Oceanogr 53:741–770
2. Field CB, Behrenfeld MJ, Randerson JT, Falkowski P (1998) Primary production of the biosphere: integrating terrestrial and oceanic components. Science 281:237–240

3. Smith RC, Baker KS (1978) Optical classification of natural waters. Limnol Oceanogr 23:260–267
4. Martinez E, Antoine D, D'Ortenzio F, Gentili B (2009) Climate-driven basin-scale decadal oscillations of oceanic phytoplankton. Science 326:1253–1256
5. Siegel DA, Franz BA (2010) Century of phytoplankton change. Nature 466:569–570
6. Henson SA et al (2010) Detection of anthropogenic climate change in satellite records of ocean chlorophyll and productivity. Biogeosciences 7:621–640
7. IOCCG (2008) Why ocean colour? the societal benefits of ocean-colour technology. In: Platt T, Hoepffner N, Stuart V, Brown C (eds) Reports of the International Ocean-Colour Coordinating Group, Dartmouth, Canada
8. Morel A (1988) Optical modeling of the upper ocean in relation to its biogenous matter content (case I waters). J Geophys Res 93:10749–10768
9. Gordon HR, Morel AY (1983) Remote assessment of ocean color for interpretation of satellite visible imagery: a review. Springer, New York
10. O'Reilly JE, Maritorena S, Mitchell BG, Siegel DA (1998) Ocean color chlorophyll algorithms for SeaWiFS. J Geophys Res 103:24937–24953
11. McClain CR (2009) A decade of satellite ocean color observations*. Annu Rev Mar Sci 1:19–42
12. Kirk JTO (1994) Light and photosynthesis in aquatic ecosystems. Cambridge University Press, Cambridge
13. Blough NV, Del Vecchio R (2002) Chromophoric DOM in the coastal environment. In: Hansell DA, Carlson CA (eds) Biogeochemistry of marine dissolved organic matter. Academic, San Diego, pp 509–546
14. Twardowski MS, Boss E, Sullivan JM, Donaghay PL (2004) Modeling the spectral shape of absorption by chromophoric dissolved organic matter. Mar Chem 89:69–88
15. Ciotti AM, Cullen JJ, Lewis MR (2002) Assessment of the relationships between dominant cell size in natural phytoplankton communities and the spectral shape of the absorption coefficient. Limnol Oceanogr 47:404–417
16. Bricaud A, Claustre H, Ras J, Oubelkheir K (2004) Natural variability of phytoplanktonic absorption in oceanic waters: influence of the size structure of algal populations. J Geophys Res 109:C11010
17. Stramski D, Boss E, Bogucki D, Voss KJ (2004) The role of seawater constituents in light backscattering in the ocean. Prog Oceanogr 61:27–56
18. Mobley CD (1994) Light and water: radiative transfer in natural waters. Academic, San Diego
19. Gordon HR et al (2009) Spectra of particulate backscattering in natural waters. Opt Express 17:16192–16208
20. Twardowski MS, Lewis M, Barnard A, Zaneveld JRV (2005) In-water instrumentation and platforms for ocean color remote sensing applications. In: Miller R, Del-Castillo C, McKeee D (eds) Remote sensing of coastal aquatic waters. Springer, Dordrecht
21. Smith RC, Baker K (1978) The bio-optical state of ocean waters and remote sensing. Limnol Oceanogr 23:247–259
22. Morel A, Gentilli B (1993) Diffuse reflectance of oceanic waters. II. Bidirectional aspects. Appl Opt 32:6864–6879
23. Lee ZP, Carder KL, Arnone RA (2002) Deriving inherent optical properties from water color: a multiband quasi-analytical algorithm for optically deep water. Appl Opt 41: 5755–5772
24. Aurin DA (2010) Developing ocean color remote sensing algorithms for retrieving optical properties and biogeochemical parameters in the optically complex waters of Long Island Sound. Ph.D. Thesis. University of Connecticut
25. Ryan JP et al (2005) Coastal ocean physics and red tides: an example from Monterey Bay, California. Oceanography 18:246–255

26. Mouroulis P, Green RO, Wilson DW (2008) Optical design of a coastal ocean imaging spectrometer. Opt Express 16:9087–9096
27. Davis CO et al (2002) Ocean PHILLS hyperspectral imager: design, characterization, and calibration. Opt Express 10(4):210–221
28. McClain CR, Cleave ML, Feldman GC, Gregg WW (1998) Science quality SeaWiFS data for global biosphere research. Sea Technol 39:10–16
29. Gordon HR (1997) Atmospheric correction of ocean color imagery in the Earth Observing System era. J Geophys Res 102:17081–17106
30. Antoine D, Morel A (1999) A multiple scattering algorithm for atmospheric correction of remotely sensed ocean color (MERIS instrument): principle and implementation for atmospheres carrying various aerosols including absorbing ones. Int J Remote Sens 20:1875–1916
31. Gao BC, Montes MJ, Ahmad Z, Davis CO (2000) Atmospheric correction algorithm for hyperspectral remote sensing of ocean color from space. Appl Opt 39:887–896
32. Wang M, Son SH, Shi W (2009) Evaluation of MODIS SWIR and NIR-SWIR atmospheric correction algorithms using SeaBASS data. Remote Sens Environ 113:635–644
33. Yan B et al (2002) Pitfalls in atmospheric correction of ocean color imagery: how should aerosol optical properties be computed? Appl Opt 41:412–423
34. Fukushima H, Toratani M (1997) Asian dust aerosol: optical effect on satellite ocean color signal and a scheme of its correction. J Geophys Res 102:17119–17130
35. Antoine D, Nobileau D (2006) Recent increase of Saharan dust transport over the Mediterranean Sea, as revealed from ocean color satellite (SeaWiFS) observations. J Geophys Res 111: D12214
36. Claustre H et al (2002) Is desert dust making oligotrophic waters greener? Geophys Res lett 29:107–1
37. Paytan A et al (2009) Toxicity of atmospheric aerosols on marine phytoplankton. Proc Natl Acad Sci 106:4601
38. Garrison VH et al (2003) African and Asian dust: from desert soils to coral reefs. Bioscience 53:469–480
39. Monahan EC, O'Muircheartaigh I (1981) Improved statement of the relationship between surface wind speed and oceanic whitecap coverage as required for the interpretation of satellite data. In: Gower JFR (ed) Oceanography from space. Plenum, New York, pp 751–755
40. National Research Council Committee on Assessing Requirements for Sustained Ocean Color Research and Operations (2011) Assessing requirements for sustained ocean color research and operations. National Academies Press, Washington DC
41. Jerlov NG (1974) Optical aspects of oceanography. Academic, London, pp 77–94
42. Morel A, Prieur L (1977) Analysis of variations in ocean color. Limnol Oceanogr 22:709–721
43. Mobley CD, Stramski D, Bissett WP, Boss E (2004) Optical modeling of ocean water: is the case 1 – case 2 classification still useful? Oceanography 17:60–67
44. Morel A, Bricaud A (1981) Theoretical results concerning light absorption in a discrete medium and application to the specific absorption of phytoplankton. Deep-Sea Res 28:1357–1393
45. Siegel DA, Maritorena S, Nelson NB, Behrenfeld MJ (2005) Independence and interdependencies among global ocean color properties: reassessing the bio-optical assumption. J Geophys Res 110:C07011
46. Swan CM, Siegel DA, Nelson NB, Carlson CA, Nasir E (2009) Biogeochemical and hydrographic controls on chromophoric dissolved organic matter distribution in the Pacific Ocean. Deep Sea Res Part I: Oceanogr Res Pap 56:2175–2192
47. Dierssen HM (2010) Benthic ecology from space: optics and net primary production in seagrass and benthic algae across the Great Bahama Bank. Mar Ecol Progress Ser 411:1–15
48. Zaneveld JRV (1989) An asymptotic closure theory for irradiance in the sea and its inversion to obtain the inherent optical properties. Limnol Oceanogr 34:1442–1452

49. Dierssen HM (2010) Perspectives on empirical approaches for ocean color remote sensing of chlorophyll in a changing climate. Proc Natl Acad Sci 107:17073
50. Moore TS, Campbell JW, Dowell MD (2009) A class-based approach to characterizing and mapping the uncertainty of the MODIS ocean chlorophyll product. Remote Sens Environ 113:2424–2430
51. Schofield O et al (2004) Watercolors in the coastal zone: what can we see? Oceanography 17:25–31
52. Falkowski P et al (2000) The global carbon cycle: a test of our knowledge of earth as a system. Science 290:291
53. Behrenfeld MJ, Falkowski PG (1997) Consumers guide to phytoplankton primary productivity models. Limnol Oceanogr 42:1479–1491
54. Campbell J et al (2002) Comparison of algorithms for estimating ocean primary production from surface chlorophyll, temperature, and irradiance. Glob Biogeochem Cycle 16:1035
55. Westberry T, Behrenfeld MJ, Siegel DA, Boss E (2008) Carbon-based primary productivity modeling with vertically resolved photoacclimation. Glob Biogeochem Cycle 22:GB2024
56. Mouw CB, Yoder JA (2005) Primary production calculations in the Mid-Atlantic Bight, including effects of phytoplankton community size structure. Limnol oceanogr 50(4):1232–1243
57. IOCCG (2006) Remote sensing of inherent optical properties: fundamentals, tests of algorithms, and applications. In: Lee ZP (ed) Reports of the International Ocean-Colour Coordinating Group, Dartmouth
58. Siegel DA, Maritorena S, Nelson NB, Hansell DA, Lorenzi-Kayser M (2002) Global distribution and dynamics of colored dissolved and detrital organic materials. J Geophys Res 107:3228
59. U.S. National Aeronautics and Space Administration, Goddard Earth Sciences, Data and Information Services Center (2011) *Giovanni*. http://disc.sci.gsfc.nasa.gov/giovanni/
60. Behrenfeld MJ et al (2009) Satellite-detected fluorescence reveals global physiology of ocean phytoplankton. Biogeosciences 6:779–794
61. Dierssen HM, Kudela RM, Ryan JP, Zimmerman RC (2006) Red and black tides: quantitative analysis of water-leaving radiance and perceived color for phytoplankton, colored dissolved organic matter, and suspended sediments. Limnol oceanogr 51:2646–2659
62. Brewin RJW et al (2011) An intercomparison of bio-optical techniques for detecting dominant phytoplankton size class from satellite remote sensing. Remote Sens Environ 115:325–339
63. Balch WM, Kilpatrick KA, Trees CC (1996) The 1991 coccolithophore bloom in the central North Atlantic. 1. Optical properties and factors affecting their distribution. Limnol Oceanogr 41:1669–1683
64. Tomlinson MC, Wynne TT, Stumpf RP (2009) An evaluation of remote sensing techniques for enhanced detection of the toxic dinoflagellate, Karenia brevis. Remote Sens Environ 113:598–609
65. Simis SGH, Peters SWM, Gons HJ (2005) Remote sensing of the cyanobacterial pigment phycocyanin in turbid inland water. Limnol Oceanogr 50:237–245
66. Chavez FP, Ryan J, Lluch-Cota SE, Niquen CM (2003) From anchovies to sardines and back: multidecadal change in the Pacific Ocean. Science 299:217–221
67. Platt T, Csar Fuentes-Yaco KTF (2003) Marine ecology: spring algal bloom and larval fish survival. Nature 423:398–399
68. Fuentes-Yaco C, Koeller PA, Sathyendranath S, Platt T (2007) Shrimp (Pandalus borealis) growth and timing of the spring phytoplankton bloom on the Newfoundland–Labrador Shelf. Fish Oceanogr 16:116–129
69. Seibel BA, Dierssen HM (2003) Cascading trophic impacts of reduced biomass in the Ross Sea, Antarctica: just the tip of the iceberg? Biol Bull 205:93–97
70. Rosa R, Dierssen HM, Gonzalez L, Seibel BA (2008) Large-scale diversity patterns of cephalopods in the Atlantic open ocean and deep sea. Ecology 89:3449–3461

71. Dekker A et al (2005) Remote sensing of seagrass ecosystems: use of spaceborne and airborne sensors. In: Larkum AWD, Orth RJ, Duarte CM (eds) Seagrasses: biology, ecology, and conservation. Springer, Dordrecht, pp 347–359
72. Cavanaugh KC, Siegel DA, Kinlan BP, Reed DC (2010) Scaling giant kelp field measurements to regional scales using satellite observations. Mar Ecol Prog Ser 403:13–27
73. Phinn S, Roelfsema C, Dekker A, Brando V, Anstee J (2008) Mapping seagrass species, cover and biomass in shallow waters: an assessment of satellite multi-spectral and airborne hyper-spectral imaging systems in Moreton Bay (Australia). Remote sens Environ 112:3413–3425
74. Lesser MP, Mobley CD (2007) Bathymetry, water optical properties, and benthic classification of coral reefs using hyperspectral remote sensing imagery. Coral Reefs 26:819–829
75. Dierssen HM, Zimmerman RC, Drake LA, Burdige DJ (2009) Potential export of unattached benthic macroalgae to the deep sea through wind-driven Langmuir circulation. Geophys Res Lett 36:L04602
76. Burdige DJ, Hu X, Zimmerman RC (2010) The widespread occurrence of coupled carbonate dissolution/reprecipitation in surface sediments on the Bahamas Bank. Am J Sci 310(6):492–521. doi:10.2475/06.2010.03
77. Goes JI, Thoppil PG, Gomes HR, Fasullo JT (2005) Warming of the Eurasian landmass is making the Arabian Sea more productive. Science 308:545–547
78. Beman JM, Arrigo KR, Matson PA (2005) Agricultural runoff fuels large phytoplankton blooms in vulnerable areas of the ocean. Nature 434:211–214
79. Dwivedi RM, Solanki HU, Nayak SR, Gulati D, Somvanshi VS (2005) Exploration of fishery resources through integration of ocean colour with sea surface temperature: Indian experience. IJMS 34:430–440
80. Chavez FP, Strutton PG, McPhaden MJ (1998) Biological-physical coupling in the Central Equatorial Pacific during the onset of the 1997–98 El Nino. Geophys Res Lett 25:3543–3546
81. Lewis MR, Platt TC (1987) Remote observation of ocean colour for prediction of upper ocean heating rates. Adv Space Res 7:127–130
82. Hill VJ (2008) Impacts of chromophoric dissolved organic material on surface ocean heating in the Chukchi Sea. J Geophys Res 113:C07024
83. Gnanadesikan A, Anderson WG (2009) Ocean water clarity and the ocean general circulation in a coupled climate model. J Phys Oceanogr 39:314–332
84. Gnanadesikan A, Emanuel K, Vecchi GA, Anderson WG, Hallberg R (2010) How ocean color can steer Pacific tropical cyclones. Geophys Res Lett 37:L18802
85. Miller WL, Moran MA (1997) Interaction of photochemical and microbial processes in the degradation of refractory dissolved organic matter from a coastal marine environment. Limnol Oceanogr 42:1317–1324
86. Ackleson SG, Balch WM, Holligan PM (1994) Response of water-leaving radiance to particulate calcite and chlorophyll a concentrations: a model for Gulf of Maine coccolithophore blooms. J Geophys Res 99:7483–7499
87. Gordon HR et al (2001) Retrieval of coccolithophore calcite concentration from SeaWiFS imagery. Geophys Res Lett 28:1587–1590
88. Balch W, Drapeau D, Bowler B, Booth E (2007) Prediction of pelagic calcification rates using satellite measurements. Deep Sea Res Part II: Top Stud Oceanogr 54:478–495
89. Balch WM, Fabry VJ (2008) Ocean acidification: documenting its impact on calcifying phytoplankton at basin scales. Mar Ecol Prog Ser 373:239–247
90. Ryther JH (1969) Photosynthesis and fish production in the sea. Science 166:72–76
91. Wilson RW et al (2009) Contribution of fish to the marine inorganic carbon cycle. Science 323:359–362
92. Platt T, Sathyendranath S, Fuentes-Yaco C (2007) Biological oceanography and fisheries management: perspective after 10 years. ICES J Marine Sci 64:863
93. Platt T, Sathyendranath S (2008) Ecological indicators for the pelagic zone of the ocean from remote sensing. Remote Sens Environ 112:3426–3436

94. Stumpf RP et al (2003) Monitoring Karenia brevis blooms in the Gulf of Mexico using satellite ocean color imagery and other data. Harmful Algae 2:147–160
95. Hu C et al (2003) MODIS detects oil spills in Lake Maracaibo, Venezuela. Eos AGU Trans 84:313–319
96. Fingas M, Brown C (2000) A review of the status of advanced technologies for the detection of oil in and with ice. Spill Sci Technol Bull 6:295–302
97. Boland RC, Donohue MJ (2003) Marine debris accumulation in the nearshore marine habitat of the endangered Hawaiian monk seal, Monachus schauinslandi 1999–2001. Mar Pollut Bull 46:1385–1394
98. Donohue MJ, Boland RC, Sramek CM, Antonelis GA (2001) Derelict fishing gear in the Northwestern Hawaiian Islands: diving surveys and debris removal in 1999 confirm threat to coral reef ecosystems. Mar Pollut Bull 42:1301–1312
99. Randolph K et al (2008) Hyperspectral remote sensing of cyanobacteria in turbid productive water using optically active pigments, chlorophyll a and phycocyanin. Remote Sens Environ 112:4009–4019
100. IOCCG (2007) Ocean-colour data merging In: Gregg W (ed) Reports of the International Ocean-Colour Coordinating Group, Dartmouth
101. Roy S, Llewellyn C, Egeland ES, Johnsen G (2011) Phytoplankton pigments: updates on characterization, chemotaxonomy and applications in oceanography. Cambridge University Press. Cambridge Environmental Chemistry Series. Cambridge, UK. pp 845. ISBN: 978110700066-7

Books and Reviews

Campbell J, Antoine D, Armstrong R, Arrigo K, Balch W, Barber R, Behrenfeld M, Bidigare R, Bishop J, Carr ME et al (2002) Comparison of algorithms for estimating ocean primary production from surface chlorophyll, temperature, and irradiance. Glob Biogeochem Cycle 16:1035

Carr ME, Friedrichs MAM, Schmeltz M, Noguchi Aita M, Antoine D, Arrigo KR, Asanuma I, Aumont O, Barber R, Behrenfeld M et al (2006) A comparison of global estimates of marine primary production from ocean color. Deep Sea ResPart II: Top Stud Oceanogr 53:741–770

GlobCOLOUR: An EO based service supporting global ocean carbon cycle research. European Space Agency. http://www.globcolour.info/

IOCCG. Reports of the International Ocean-Colour Coordinating Group No. 1–10. Dartmouth. http://www.ioccg.org/reports_ioccg.html

Jerlov NG, Nielsen ES (eds) (1974) Optical aspects of oceanography. Academic, London

Miller R, Del-Castillo C, McKee BA (eds) (2005) Remote sensing of coastal aquatic waters. Springer, Dordrecht

Morel A (1991) Optics of marine particles and marine optics. In: Demers S (ed) Particle analysis in oceanography. Springer, Berlin, pp 141–188

Morel A, Bricaud A (1986) Inherent optical properties of algal cells including picoplankton: theoretical and experimental results. Can Bull Fish Aquat Sci 214:521–559

National Aeronautics and Space Administration (NASA) Ocean optics protocols for satellite ocean color sensor validation, vol I–VI. http://oceancolor.gsfc.nasa.gov/DOCS/

National Aeronautics and Space Administration (NASA) Ocean color web. http://oceancolor.gsfc.nasa.gov/

Platt T, Nayak S (eds) (2005). Special issue on: ocean colour remote sensing. Indian J Marine Sci 34(4):341–355

Siegel D (2004) Views of ocean processes from the sea-viewing wide field- of-view sensor mission: introduction to the first special issue. Deep Sea Res Part II Top Stud Oceanogr 51(1–3):1–3. http://dx.doi.org/10.1016/j.dsr2.2003.12.001

The Oceanography Society (2004) Special issue: coastal ocean optics and dynamics. Oceanography 17(2):1–95

Thomas A, Siegel D, Marra J (2004) Views of ocean processes from the sea-viewing wide field-of-view sensor (SeaWiFS) mission: introduction to the second special issue. Deep Sea Res Part II Top Stud Oceanogr 51(10–11):911–912. http://dx.doi.org/10.1016/j.dsr2.2004.06.003

Chapter 19
Volcanoes, Observations and Impact

Clifford Thurber and Stephanie Prejean

Glossary

Caldera	Large crater formed by collapse of an overlying structure when an eruption empties a magma reservoir.
Effusive	Eruption of fluid molten material that later solidifies.
Fumarole	A volcanic vent that emits hot gas.
Infrasound	Sound waves at frequencies below the range of human hearing (<20 Hz).
Interferogram	A pattern of satellite radar wave "fringes" formed by interference, analogous to the colorful pattern from light reflected by a thin film of oil or gas, that can indicate ground deformation.
Lahar	Heavy flow of mud, water, and debris triggered by interactions of hot material with ice of water or when heavy rain falls on recently erupted unconsolidated material.
Phreatic	Explosion caused by heating and expansion of ground water.
Pyroclastic	Composed of rock fragments ejected explosively from an erupting volcano.
Tremor	Continuous vibration of the ground related to magma movement.
Volatiles	Dissolved gases contained in magma.

This chapter was originally published as part of the Encyclopedia of Sustainability Science and Technology edited by Robert A. Meyers. DOI:10.1007/978-1-4419-0851-3

C. Thurber (✉)
Department of Geoscience, University of Wisconsin-Madison, 1215 W. Dayton Street, 53706 Madison, WI, USA
e-mail: thurber@geology.wisc.edu

S. Prejean
Seismology, USGS Volcano Science Center, Alaska Volcano Observatory, 4200 University Drive, 99508 Anchorage, AK, USA
e-mail: sprejean@usgs.gov

J. Orcutt (ed.), *Earth System Monitoring: Selected Entries from the Encyclopedia of Sustainability Science and Technology*, DOI 10.1007/978-1-4614-5684-1_19,

Definition of the Subject

Volcanoes are critical geologic hazards that challenge our ability to make long-term forecasts of their eruptive behaviors. They also have direct and indirect impacts on human lives and society. As is the case with many geologic phenomena, the time scales over which volcanoes evolve greatly exceed that of a human lifetime. On the other hand, the time scale over which a volcano can move from inactivity to eruption can be rather short: months, weeks, days, and even hours. Thus, scientific study and monitoring of volcanoes is essential to mitigate risk. There are thousands of volcanoes on Earth, and it is impractical to study and implement ground-based monitoring at them all. Fortunately, there are other effective means for volcano monitoring, including increasing capabilities for satellite-based technologies.

In recent history, the destructive power of earthquakes and earthquake-induced tsunamis has been quite salient. Over the centuries and millennia, however, volcanic eruptions and eruption-induced tsunamis have had impacts that rival those of earthquakes, and in some cases have had a global reach. A prime example is the 1815 eruption of Tambora in Indonesia. That eruption is blamed for the catastrophic "Year without a Summer," when global cooling due to reflection of the Sun's energy by aerosols and ash injected into the atmosphere during the eruption led to massive crop failures and many deaths from starvation around the world [1, 2]. The Earth has also not witnessed a massive caldera-forming eruption, such as those that gave rise to Yellowstone and Long Valley calderas, since the formation of Toba caldera (also in Indonesia) about 75,000 years ago [3].

There is also a contrast between earthquakes and volcanoes in terms of predictability. Although reliable and effective earthquake prediction remains an elusive goal [4] and warning systems are operational in very few places (e.g., Japan), there are numerous examples of successful eruption forecasts and warnings. An example is the impressive success of the US Geological Survey's Volcano Disaster Assistance Program (VDAP), which reports dozens of successful eruption forecasts and warnings in the 25 years of the program's history [5]. Somewhat ironically, it is the monitoring of seismic activity that has been the key to VDAP's success.

Introduction

Although most of the world's magmatic activity occurs underneath the oceans, primarily along mid-ocean ridges, the discussion is restricted to volcanism on continents and islands. Within this subaerial class of volcanism, there are three main categories in terms of tectonic setting: subduction zones, hotspots, and continental rifts, with examples provided by Indonesia, Hawaii, and East Africa, respectively. Iceland is a special example of an above sea level section of mid-ocean ridge. The first-order classification of erupted products is based on silica content, with further distinctions based on alkali content (sodium and potassium)

[6] and the size of crystallized mineral grains. More silica-rich (felsic) lavas are predominant at subduction zones and more silica-poor (mafic) lavas are predominant at hotspots and continental rifts. In general, mafic lavas erupt more effusively whereas felsic lavas are more prone to explosiveness. For a thorough introduction to types of volcanoes and lavas and their potential for explosivity, the interested reader is referred to Lockwood and Hazlett [7].

The magnitude and violence of volcanic eruptions can be quantified in several ways. A common measure that is used in this entry is the Volcanic Explosivity Index (VEI) [8]. Volume of erupted material, ash cloud height, eruption duration, and qualitative observations describing eruption intensity are used in the calculation of VEI. Worldwide eruptions to date have been classified as VEI 0-8, with each increasing integer corresponding to an order of magnitude increase in eruption severity. The 1980 and 2004–2008 eruptions of Mount St. Helens, for example, are classified as VEI 4 (large eruption) and VEI 2 (moderate eruption), respectively. The largest eruptions of the twentieth century were of VEI 6, including the 1912 eruption of Novarupta on the Alaska Peninsula and the 1991 eruption of Mt. Pinatubo, Philippines. A second commonly used measure of eruption size is the dense-rock equivalent (DRE) of erupted material. This parameter specifies the actual amount of magma erupted and is dependent on careful field studies of erupted deposits. The Smithsonian Museum of Natural History keeps an updated database of these two eruption size parameters for recent and historical eruptions (http://www.volcano.si.edu/world/). Pyle [9] summarizes these and other measures of eruption sizes.

In this entry, the focus is mainly on geophysical observations of volcanoes and calderas as they pertain to eruption forecasting and prediction. Some key aspects of the impacts that eruptions have on humans and selected aspects related to sustainability have also been characterized.

Observations

The Role of Geologic Mapping

Our focus is primarily on geophysical volcano monitoring, but the importance of geologic mapping and associated studies cannot be overstated in providing the background information necessary to interpret these data correctly. In the case of erupting volcanoes, the past is generally the key to the present. Volcanoes often erupt similar magmas in similar volumes; thus, geological mapping to determine eruption histories provides a framework in which to interpret renewed unrest at a previously quiet volcano. In the case when a volcano's behavior diverges from its historical activity, knowledge of eruptive history allows us to understand how the magma system is evolving with time. Geologic mapping also characterizes the spatial distribution of hazards from previous eruptions including tephra fall, lahars

and pyroclastic and lava flows. These maps can have an important role in land use planning. In addition, careful petrologic, petrographic, and isotopic analyses of erupted material can provide valuable evidence regarding magma storage and transport history. These analyses complement the geophysical measurements described below to characterize the magmatic system at depth. For further details, the interested reader is referred to Decker [10], Simkin and Siebert [11], and Lockwood and Hazlett [7].

Seismology

Earthquake monitoring is certainly one of the most basic and widely used techniques for observing volcanic activity [12, 13]. In fact, seismic monitoring of volcanoes has generally been the most fruitful approach for short-term eruption prediction. The successes of the US Geological Survey's Volcano Disaster Assistance Program (VDAP) [5] in using simple measures of earthquake activity to predict eruptions is a remarkable testament to the value of real-time seismic monitoring for taking the pulse of a volcano in a state of unrest. VDAP has assisted with or directly provided more than 50 successful eruption forecasts and/or predictions for more than 30 volcanoes worldwide in the first 25 years of its history (1986–2011), using simple instrumentation and basic observations of seismicity and ground shaking [5].

Earthquakes associated with volcanoes are commonly grouped into four classes: volcano-tectonic (VT, predominant frequencies of 1–20 Hz), long-period (LP, predominant frequencies of 1–5 Hz), hybrid (VT event transitioning into an LP event), and very-long-period (VLP) [14, 15]. The former are generally believed to be normal brittle-failure earthquakes, although they commonly occur in swarms of similar-sized small events rather than a main shock-aftershock sequence style. This can be quantified by the log frequency versus magnitude (i.e., Gutenberg-Richter) relation (i.e., b-value), which is characterized by a linear trend with a slope around 1 for earthquakes on crustal faults but frequently has a higher slope, up to roughly two, for volcanic swarms.

The mechanism of LP's remains a subject of debate, centered mainly on the effect of fluids on the earthquake source versus the effects of wave propagation (path effects), and the connection between LP's and the phenomenon known as volcanic tremor is also controversial. Volcanic tremor is a more or less continuous signal lasting minutes to hours to days, with a comparable frequency content to LP's. Some researchers believe volcanic tremor is simply the superposition of repeated LP events or, in the case of harmonic tremor, VT events with the observed frequency content controlled by the earthquake repetition rate [16]. A somewhat more common hypothesis is that the tremor is due to resonant oscillations in a magma conduit or a nonlinear response to fluid flow through cracks [17, 18]. The initiation of volcanic tremor is clearly associated with the movement of magma and the potential for an eruption, and thus tremor is one of the important precursors

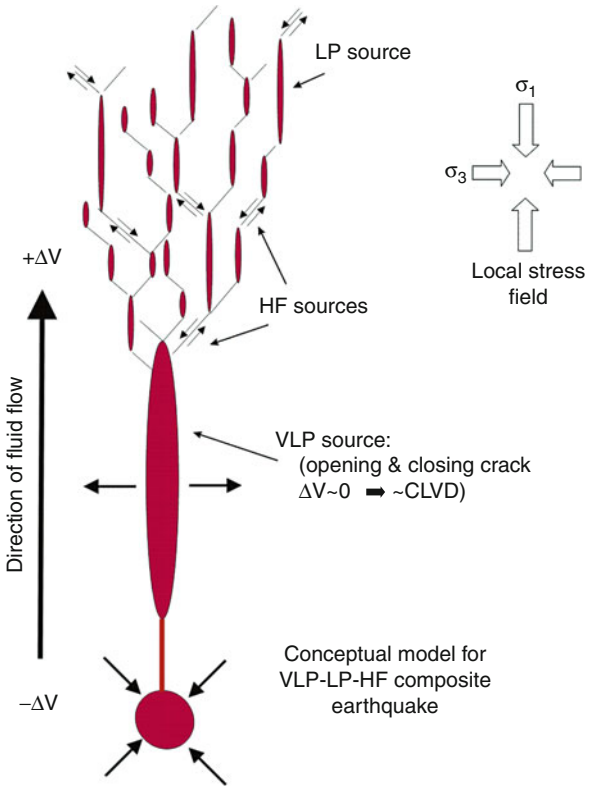

Fig. 19.1 Cartoon of the hypothetical relationship among VLP, LP, and HF (i.e., VT) earthquakes. In this model, the VLP source is upward flow of magma with volume change ΔV. Volatiles from the magma permeate the crust above the VLP event, triggering high frequency (HF) and LP earthquakes in a stress field with most and least compressive stress directions, σ_1 and σ_3 respectively, as shown (Modified from [39])

for eruption prediction [13]. In addition, deep LP's (typically 20–50 km depth) have been observed prior to a number of eruptions, presumably reflecting magma movement at depth [19–21], so additional focus has been placed on identifying these events. The nature of hybrid events is also debated, again centered on source versus path effects [22].

With the increasing use of broadband seismometers (instruments with a wide frequency range) in volcano monitoring, VLP earthquakes have been identified in many places [15, 23–38]. Similar to LP events, the source of VLP's is generally attributed to fluid-rock interaction, specifically transport of magma through the shallow crust. Waite et al. [38] for example, found that at Mount St. Helens, the VLP source is best modeled as a combination of volumetric and single-force components, the former due to compression and expansion of a shallow, magma-filled sill, and a smaller component of expansion and compression of a dike, and the latter due to mass transport in the magma conduit. A cartoon suggesting possible interrelationships among VLP, LP, and VT earthquakes based on the Hill fracture mesh concept [39] is shown in Fig. 19.1.

Some seismic path measurements have unveiled time dependencies that have been associated with eruptions, but for the most part these techniques have been applied retroactively. One of the earliest such studies was by Foulger et al. [40],

who found changes in the ratio of the velocity of P waves (primary, or compressional) to S waves (secondary, or shear) (i.e., Vp/Vs, equivalently Poisson's ratio) at Mammoth Mountain, California, that correlated spatially and temporally with increased tree kill due to CO_2 emission. They hypothesized that an increased presence of gas in fractures led to a reduction in Vp/Vs, which was imaged using seismic tomography. Such changes in Vp/Vs have also been identified at Mt. Etna, Italy [41]. Recently, temporal changes in seismic wave attenuation, in this case associated with magmatic activity, have been found at Mt. Ruapehu, New Zealand [42] as well as Mt. Etna [43].

Two other types of seismic path observations that have been reported to show temporal change associated with magmatic activity are shear wave splitting, which is caused by birefringence in the Earth, and ambient noise correlations, which yield an estimate of the wave propagation behavior (the Green's function) between two seismic stations. Miller and Savage [44] identified a change in the polarization direction of the fast shear wave at Mt. Ruapehu, which they associated with an eruption. Subsequent studies have also reported such changes elsewhere related to magmatic activity [45–49], but extreme care must be taken to separate spatial versus temporal variations. Brenguier et al. [50] compared a reference Green's function (created from 18 months of background or "ambient" noise data) to Green's functions from sequential 10-day periods of data at Piton de la Fournaise Volcano on La Reunion island and found shifts in apparent travel times corresponding to a small reduction in seismic velocity within the volcano. Their interpretation was that decreases in seismic velocity a few weeks before eruptions were related to preeruptive inflation of the volcanic edifice, presumably due to increased magma pressure.

Deformation

Uplift and subsidence associated with magmatic and eruptive activity have been recognized for centuries, with the Temple of Serapis in the town of Pozzuoli in Campi Flegrei caldera, Italy, being one of the most famous examples [51]. Geodetic surveying techniques, such as leveling and tilt measurements, began to be applied to volcanoes in the early twentieth century [52]. In the modern era, Global Positioning System (GPS) and interferometric synthetic aperture radar (InSAR), along with tilt, are the primary types of geodetic observations applied to the study and monitoring of volcanoes. The sensitivity of these different techniques is compared in Fig. 19.2. Continuous GPS (cGPS) and InSAR are quite complementary, with the former providing fine temporal resolution at particular points on the Earth's surface and the latter providing exceptional spatial resolution of position changes over a wide area for pairs of observation times. Deformation modeling is commonly done to estimate pressure changes in and the geometry of magma source zones.

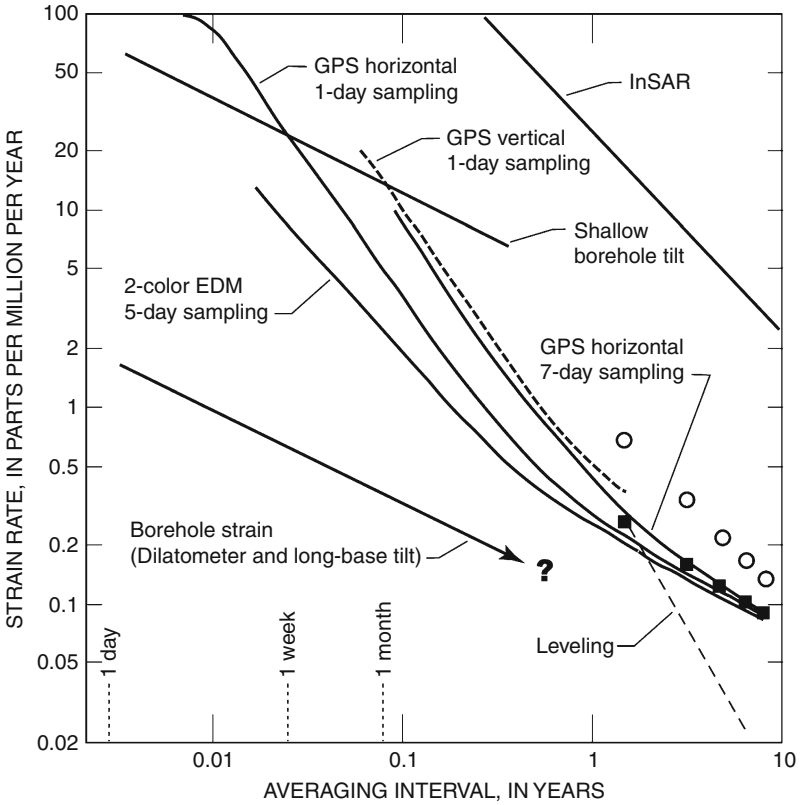

Fig. 19.2 Comparison of rate sensitivity for GPS, InSAR, borehole strainmeters at 200 m depth, and borehole tiltmeters (which measure the gradient in vertical deformation) at 2 m depth. The x-axis indicates the time period that may be spanned by the different data types. For example, daily GPS measurements may span 1 day or longer. The y-axis indicates the strain rate that can be resolved as a function of the period. Strain is the change in length (area or volume) per a unit length (area or volume), and thus is unitless and can be expressed as parts per million (ppm). As can be seen from the plot, the borehole tiltmeters and strainmeters are more sensitive than GPS at shorter periods, but at periods longer than a few days and a few months, respectively, GPS measurements provide better resolution of strain rates (Figure modified from [52])

GPS

Since the 1990s, GPS has become a central technique for volcano monitoring. Initial applications required repeated visits to benchmarks, known as campaign GPS. Continuous GPS (cGPS) has become relatively commonplace, allowing near-real-time tracking of site positions and, when multiple cGPS sites are available, a time history of volcano deformation. For example, with two cGPS sites on opposite sides of a volcano's summit or straddling a rift zone, relative changes in separation of the sites would reflect volcano inflation/deflation or rift zone extension/contraction. With enough sites, detailed modeling of deformation sources is

possible, providing constraints on the locations, depths, and pressure/volume changes of buried magma reservoirs and conduits. An example of the use of cGPS in monitoring an impending eruption at Augustine Volcano, Alaska [53] is described in some detail later.

GPS works by having a receiver on the surface of the Earth receive signals simultaneously from four or more satellites. These signals carry information about the signal origin time and the position of the satellite, so that determining the receiver position is done by trilateration, essentially analogous to locating an earthquake. The interested reader is referred to [52] for a lucid and comprehensive discussion of the details of this process.

GPS is not without its complications and limitations. GPS is a point measurement of position, so good spatial coverage requires multiple GPS sites. Data reduction requires knowledge of the GPS satellite orbits, which are known only approximately at any instant. Final orbital information is distributed by International GNSS Services (where GNSS stands for Global Navigation Satellite System) with about a 2-week delay [54]. The use of differential and kinematic GPS techniques effectively overcomes orbital (and some other) error effects, if only relative positions are desired. Atmospheric effects, due to ionosphere and troposphere delays, also impart positioning errors. Finally, elevation uncertainty is significantly greater than that for latitude and longitude.

InSAR

InSAR burst onto the geophysics scene in 1993 with the publication of the famous Landers, CA, earthquake interferogram on the cover of Nature [55]. Applications to volcanoes and calderas around the world followed soon thereafter, including Mt. Etna, Italy [56], Long Valley caldera, CA [57], Yellowstone caldera, WY [58], Piton de la Fournaise Volcano, La Reunion [59], a number of volcanoes in Alaska [60–65], the Galapagos Islands [66], Afar [67], Chile [68], and many more.

InSAR works by having a satellite (or constellation of satellites) acquire a pair of radar images of the same area on Earth from about the same point in space at different times, which are then combined, or interfered, to produce a map of the difference in phase of the two returned radar signals, represented by colored "fringes." The phase difference is related to the line-of-sight (LOS; i.e., in the direction of the satellite) displacement of the ground in the time between the two image acquisitions. Converting the phase differences into a map of LOS surface displacement is a process known as "unwrapping" [69, 70]. As in the case of GPS, source models can be derived to fit the observed displacements.

The spatial extent and resolution of InSAR coverage is extraordinary (scenes typically 10s to 100 km on a side with 1–30 m pixel size and $<$cm resolution of surface displacements). There are many more subtleties and complexities with InSAR data and their interpretation than for GPS, however. Repeated image acquisitions are limited by the configuration and orbits of the satellites. An accurate digital elevation model (DEM) is critical for removing the effects of topography

from the images. Noise in the data can lead to an incorrect assessment of LOS ground movement. Signal decorrelation, for example, due to vegetation variations, the presence of water, snow and ice, or steep topography, can yield areas with no usable signal. Atmospheric delay anomalies, due mainly to variations in tropospheric water content, can also cause artifacts in InSAR images. With the need for repeated imaging and the inherently limited temporal coverage for forming interferometric pairs, there is no guarantee that a good image can be created for a particular time interval of interest.

Tilt and Strain

Although far less ubiquitous in volcano monitoring settings than seismic and GPS instrumentation, tiltmeters and strainmeters are valuable observational tools that can provide complementary information about deformation. Both have remarkable sensitivity, with standard (bubble) tiltmeters able to measure the equivalent of 0.1 mm of uplift over a range of a kilometer (0.1 μrad, or 10^{-7} strain). Strainmeters can measure strain on the order of 10^{-11} to 10^{-12} (10 to 1 parts per billion). Tiltmeters have a number of advantages over strainmeters, including much lower cost, simpler installation, and, for biaxial sensors, the ability to provide information on the direction to the source of deformation. These advantages have been responsible for the much greater use of tiltmeters than strainmeters by volcano observatories. Due to their excellent sensitivity to vertical deformation, in contrast to GPS with its more precise determination of horizontal position, and real-time capability, tiltmeters can be of great value in volcanic crisis situations [52]. Strainmeters have also proven their value in long-term observatory settings, though, such as the successful prediction of an eruption of Hekla Volcano, Iceland, in 2000 [71].

Gravity

Gravity measurements can be used to infer vertical surface displacements with an accuracy comparable to GPS and some leveling techniques, but its real power comes from the ability to infer subsurface mass or density changes when surface deformation is constrained independently [52]. When uplift or subsidence occurs, the change in gravity can be compared to that predicted from the free-air gravity gradient. Deviations from the expected change in gravity reflect either an increase or decrease in mass in the subsurface [72], and the degree and sign of the difference constrains the density change. At Long Valley caldera, CA, for example, the combination of gravity and deformation observations allowed the inference of an intrusion of volatile-rich magma as the source of inflation in the period 1982–1999 [73].

For monitoring purposes, standard campaign-style gravity observations are of limited use, although such repeated measurements are vital for the types of research

noted above. There is significant monitoring potential with continuous networks of gravimeters [74]. An example is the continuous gravity network at Mt. Etna, Italy. Continuous gravity observations at the start of the 2002–2003 eruption, showing a reduced gravity decrease followed by recovery over a few hours, have been interpreted as indicating the initial opening of dry fractures that were subsequently filled by magma [75]. Although seismicity commenced several hours before the beginning of the gravity change, the detection of the opening of fractures would certainly be a key part of identifying the likely onset of an eruption.

Volcanic Gas

Detection of volcanic gas is an early indicator of magma ascent that can provide clues to speed of ascent, magma chemistry and explosivity, volume of intruding magma, and the state of the hydrothermal system at a volcano. As magma ascends in the Earth's crust, the decrease in confining pressure leads to exsolution of volatiles from the melt. Additional volatiles can also be released from the existing hydrothermal system as newly emplaced magma heats the surrounding rock. The resulting gases and fluids work their way toward the surface through fractures and can be observed through soil monitoring and space-, air-, and ground-based monitoring of fumaroles and gaseous plumes.

Interpreting the emission rates and compositions of volcanic gases to evaluate magmatic unrest is a challenging task. The compositions of volatiles released from magma vary with tectonic setting, melt composition, and pressure, but the most common gases include, in order of decreasing abundance, water, carbon dioxide (CO_2), sulfur dioxide (SO_2), and halogens. Arc volcanoes often host hydrothermal systems, crater lakes, or can be covered in snow and ice. For these reasons, volcanic gases emitted from arc volcanoes often have chemical reactions with water and other compounds on their way to the surface, which change their chemical form. For example, hydrolysis reactions can change SO_2 into H_2S and native sulfur [76]. This characteristic makes interpreting SO_2 emissions difficult at volcanoes with active hydrothermal systems (e.g., [77]). In contrast, because CO_2 exsolves from magma before other chemical species and because its chemical form is relatively stable as it ascends, its detection at the surface can be an early indicator that magma is ascending and accumulating beneath a volcano [78, 79]. The later appearance of increased SO_2 may then indicate continued magma ascent or drying out of the hydrothermal system. Given these complexities, it is necessary to consider the ratios of CO_2, SO_2, and H_2S to interpret the presence of these gases correctly. An additional complication in the interpretation of gas emissions is that most active volcanoes emit low levels of gas passively; therefore, background monitoring of quiescent time periods must be established before gas emissions associated with unrest can be interpreted correctly. Several strategies must be employed to measure the complete suite of emitted volcanic gases, including both continuous and

episodic ground and/or aircraft-based gas monitoring of fumaroles, satellite monitoring, and measurement of CO_2 flux through soils (see [80–82] for reviews of monitoring techniques).

Visual and Thermal Remote Sensing

Recent advances in satellite monitoring and ground-based and airborne remote sensing capabilities have revolutionized volcano monitoring and ash cloud tracking and provided a new perspective for understanding eruption dynamics. In the case of remote volcanoes that lack local seismic and GPS monitoring, satellite data often provide the only data stream documenting unrest and eruption. Data from satellites operated by the various international space agencies are primarily used for weather and climate research and forecasting, but are also used for volcano monitoring tasks including detecting and measuring anomalous thermal emissions, tracking ash clouds, and making visual observations. Rather than describe a complete list of satellite-based tools used in volcano studies, here the applicability of several satellite systems commonly used at US volcano observatories are highlighted, and readers are referred to more detailed reviews in the literature [82–84]. Some land- and aircraft-based imaging techniques are also briefly described.

When magma intrudes into a volcano, heat flow increases at the Earth's surface, resulting in hot fumaroles and fractures and melting of snow and ice. Thus, thermal remote sensing measurements can provide an early indicator of volcanic unrest in addition to defining the existence and spatial extent of lava flows, domes, and pyroclastic flows. The Moderate Resolution Imaging Spectroradiometer (MODIS) sensors on NASA research satellites and Geostationary Operational Environmental Satellite (GOES) and Advanced Very High Resolution Radiometer (AVHRR) sensors on NOAA satellites provide frequent, low resolution (~1 km pixel) data. Mid-infrared data (3.5–4 μm wavelength) from these sensors are used to study the extent and temporal development of lava and pyroclastic flows and to estimate effusion rates and thermal flux associated with an eruption.

Thermal infrared data from satellites (8–14 μm wavelength) are used to detect and track volcanic ash and gas clouds in the atmosphere, complementing ground- and satellite-based radar measurements of ash clouds. By comparing the brightness temperature difference in two different frequency bands, 11 and 12 μm, clouds containing ash can be discriminated from those containing only water using the Brightness Temperature Difference Method [85]. This method was used for tracking ash clouds from many eruptions (e.g., [86]) and has improved our understanding of the global atmospheric effects of large eruptions. The use of this technique to detect and measure volcanic ash clouds is limited by temporal coverage, atmospheric and cloud water content, tephra particle size, and thermal contrast between the cloud and the surface beneath it. Timing and intervals between images are dependent on satellite position and global location. For northern Pacific volcanoes,

for example, GOES data are available every 15 min, while AVHRR data are available 1–12 times per day depending on specific location [87]. Landsat TM and ETM+, Advanced Spaceborne Thermal Emission Reflection Radiometer (ASTER), and other high-resolution sensors provide a complementary dataset to these sensors. Although these data cannot be obtained in real time and images are less frequent, they provide high spatial resolution (15–90 m or better) for detailed visual and thermal observations. A recent compilation of capabilities to detect and measure volcanic clouds can be found in a European Space Agency report [88].

Thermal monitoring is not limited to satellite sensors. As an example of a sensor that can be hand held or mounted on an aircraft or tripod, the Forward Looking Infrared Radiometer (FLIR) camera is highlighted. FLIR surveys and installations often record simultaneous visual and infrared images or movies, providing maps of temperature distributions in ash clouds and on land surfaces. These images can be used to detect fumaroles, map pyroclastic flow deposits, and define spatial extent and structure of lava flows and domes. Frequently, gas emissions visually obscure volcanic activity, but FLIR thermal images can "see" through some gas, as demonstrated at volcanoes such as Mount St. Helens and Augustine [89, 90]. FLIR data have also been used successfully to characterize individual explosion characteristics at Stromboli Volcano [91].

Satellite remote sensing data are used for more than thermal imaging. Ultraviolet spectrometers, such as Total Ozone Mapping Spectrometers (TOMS) and the newer Ozone Monitoring Instrument (OMI) sensor operated by NOAA, can be used to map paths and concentrations of SO_2 clouds emitted from volcanoes by UV absorption of SO_2 in the atmosphere [92, 93]. Thanks to improved capabilities from the OMI sensor, scientists are better able to detect precursory SO_2 emissions in the atmosphere, to quantify eruptive SO_2 more accurately, and to track the SO_2 for longer periods of time. Thus, OMI data provide early indicators of magmatic unrest in addition to improving our understanding of eruption dynamics and hazard to aviation.

The remote sensing capabilities described here will undoubtedly evolve rapidly in the coming decade as technologies continue to advance and new satellites are launched. New remote monitoring tools will continue to emerge as well. For example, recent technical advances permit the measurement of volcanic lightning, both from ground and satellite sensors, to detect and study large ash clouds [94]. Improved resolution in digital cameras has permitted scientists to construct spectacular three-dimensional models of lava dome growth using aerophotogrammetric techniques [95].

Infrasound

Infrasound is the subaudible (<20 Hz) range of sound waves. Infrasound observations are made with either commercial or custom-built low-frequency microphones. These can be deployed individually or, more commonly, as arrays.

Array data can be stacked to diminish noise, which can be significant in these data, and can be used to determine the direction to the source. Infrasound disturbances can regularly be detected up to a few hundred kilometers from a volcano during eruptions. The use of infrasound for volcano monitoring was sufficiently rare at the beginning of the twenty-first century for the technique to be absent from some past reviews of volcano monitoring techniques (e.g., [12]), but now such observations are being made at dozens of volcanoes.

Infrasound observations are of great value for monitoring and quantifying eruptions, and are potentially useful for eruption prediction, especially in open-vent systems [96]. Unlike seismic observations, where variations in materials and structure in the Earth's crust along the seismic ray path have a strong influence on the recorded wavefield, the atmosphere alters infrasonic airwaves relatively little at high frequencies [97].This advantage makes infrasound quite useful for studying eruption dynamics and for quantitative comparisons of eruptions among different volcanoes [98]. Another advantage is that it is very difficult to distinguish between earthquakes at very shallow depths versus earthquakes directly associated with surface explosions using seismic data alone, but in many cases the absence or presence of an infrasound signal can serve to distinguish between the two possibilities and thus provide direct evidence that magmatically driven activity has reached the surface.

Infrasound data provide a new and unique perspective on the dynamics of volcanic eruption columns. Comparing ratios of seismic and acoustic energy between discrete explosions can offer compelling evidence for gas distributions in the magma column and eruption violence. Matoza et al. [99] have used infrasound data to investigate the spectra of volcanic jets and showed that they are similar to noise from aircraft jet engines. Infrasound has also been used to estimate the velocity of material ejected from volcanic vents during eruptions [100]. Observations of this sort could potentially be helpful in estimating ash output at erupting volcanoes when they cannot be observed directly.

Impacts

The literature on the impacts of volcanic eruptions is vast, so only brief and rather general information about selected topics is presented in this entry. The focus is on key primary and secondary volcanic hazards, and in particular those that have relatively immediate and direct impact. As a result, topics such as climatic effects are not covered here.

Lava Flows, Pyroclastics, and Tephra

Primary volcanic hazards that are direct eruption products can be categorized somewhat generally into lava flows, pyroclastic ejecta, and tephra. Lava is molten rock, and surface lava flows can travel many kilometers, or tens of kilometers in the case of basaltic tube-fed flows [101]. Their impact, though, will generally be spatially limited for any single eruption, although cases such as the decades-long rift eruption of Kīlauea Volcano are exceptions. Basaltic lava flows cause direct damage to the natural environment and human infrastructure, as well as igniting fires and/or touching off explosions that result in further damage. Fatalities due to basaltic lava flows are typically minimal, however, due to their modest flow rates, at least on terrain that is not particularly steep. Andesitic-dacitic stratovolcanoes, such as Mount St. Helens, grow blocky and viscous lava domes. Although generally limited in spatial extent to only the volcanic crater and its drainages, these domes can become unstable and fail, producing ash fall and hot block and ash flows down slope.

In contrast to lava flows, pyroclastic flows and surges (dense and dilute solid-gas mixtures, respectively, with a range of possible temperatures) travel at great speed, 10s of meters per second (m/s) to about 150 m/s (over 500 km/h), and large flows can travel 50 km or more from their source vents. The potential for destruction and death is summarily greater. For example, in the 1990s, deaths due to pyroclastic flows comprised the vast majority of directly caused mortality by volcanic eruptions [102].

Tephra is a general term encompassing various types of pyroclastic ejecta that are typically classified according to size, including blocks and bombs, lapilli, ash, and dust [7]. The larger fragments follow ballistic trajectories, whereas smaller particles can remain suspended in the atmosphere for some time (minutes to weeks) before falling to the surface. Tephra accumulations can amount to tens of centimeters to a few meters at distances of tens to hundreds of kilometers for very large eruptions [103]. Lockwood and Hazlett [7] point out that ballistic fragments are produced in greater abundance by smaller explosive eruptions. Annen and Wagner [102] report a similar number of deaths due to collapse of ash-covered roofs as due to pyroclastic flows and surges in the 1990s.

Lahars

Although a less familiar term to many, these mudflows or debris flows originating from volcanoes can have an enormous impact and cause many fatalities. Lahars can be generated directly and immediately by pyroclastic flows, or in a delayed manner upon collapse of volcanic deposits (for example, due to very heavy rainfall) or due to a lake breakout [104]. Flow rates are generally slower compared to pyroclastic flows, less than 10 m per second except on steep slopes.

A prime example of a lahar is from the eruption of Nevado del Ruiz, Colombia, in 1985. When the volcano erupted violently on the night of November 13, a massive lahar was initiated when pyroclastic flows caused massive melting of snow and glacial ice on the volcano. The lahar swept through and buried the town of Armero nearly 75 km away, resulting in more than 20,000 fatalities [105]. Sadly, the potential for a lahar from Nevado del Ruiz striking Armero had been well documented beforehand – mudflows from Nevado del Ruiz eruptions in 1595 and 1845 buried the same area [106]. Destructive lahars were also produced by the 1980 eruption of Mount St. Helens and the massive 1991 eruption of Mt. Pinatubo, Philippines.

Landslides, Lateral Blasts, and Tsunamis

Weaknesses in the interiors of volcanoes (fracturing and poorly consolidated material, hydrothermal alteration, etc.) leaves them prone to major landslides, which here is meant to encompass also avalanches and sector collapses. Avalanches are common on composite volcanoes, aka stratovolcanoes [7]. Some avalanches are triggered by the shaking from an earthquake. A landslide that grows and becomes more chaotic as it descends is termed a debris avalanche. At a larger scale, a sector collapse is the breaking away of a wedge-shaped flank of a volcano. When combined with an eruption, it can produce a lateral blast. Sector collapses are surprisingly common, at least on a geologic time scale. A number of Hawaii's volcanoes have experienced sector collapses, for example. The 1980 Mount St. Helens eruption began with a sector collapse producing a large debris avalanche, followed by a lateral blast and the initiation of a vertical eruption column. Lateral blasts are somewhat rare, but others have occurred at Arenal Volcano, Costa Rica [107] and Bezymianny Volcano, Russia [108]. For island volcanoes, there is the potential for landslides or especially sector collapses to produce a tsunami. The famous 1883 eruption of Krakatoa was accompanied by repeated tsunamis reportedly as high as 30–40 m around the Sunda Strait, killing tens of thousands of people [11]. Similarly, partial collapse of a volcano neighboring Unzen in 1792 generated a giant tsunami reaching heights of 60 m that caused on the order of 15,000 fatalities [7].

Volcanic Gases

As described above, volcanic gases are important indicators of magma transport, but they also represent a critical hazard. For example, although CO_2 is a significant component of the air we breathe regularly, this odorless, colorless gas is lethal at high concentrations. A tragedy involving CO_2 occurred in 1986 at Lake Nyos, Cameroon, a crater lake formed ~400 years ago. Dissolved CO_2 accumulated in the lake and was released in a discrete event, killing all living things within a 25 km radius,

including 1,700 people [109]. In the United States, CO_2 emissions at Mammoth Mountain, CA, led to the deaths of four people between 1998 and 2006. CO_2 is far from the only harmful volcanic gas, however. For example, vog, a form of air pollution resulting from emissions of SO_2 and other volcanic gases, plagues the Island of Hawaii, as the actively erupting Kīlauea Volcano is a prolific producer of several gas species [110].

Eruption Forecasting: Strategies and Challenges

Earthquakes have been recognized to herald volcanic eruptions throughout history. For example, prior to the well-known eruption of Mount Usu, Japan in 1663, earthquake ground shaking caused local residents to evacuate. Eruption forecasting became a science with the advent of real-time seismic monitoring capabilities. Although earthquake observations still form the backbone of eruption forecasting, they are now complemented by more sophisticated analyses of seismic data and data from many other disciplines. Geodesy, gas chemistry analysis, satellite remote sensing, visual observations and high-resolution photography, petrography, and geochemistry all provide critically important indicators of the state of a magmatic system. Detectable manifestations of magma ascent vary widely between volcanoes based on several factors including the magma chemistry and crystallinity, the physical state of the volcano's conduit system and surrounding crust, the tectonic setting of the volcano, and time since last eruption. Thus, no one-size-fits-all forecasting approach exists. Modern volcano observatories are dynamic organizations that integrate a variety of data streams with knowledge of volcanic history to evaluate the state of unrest and potential future activity at a volcano.

In the United States volcano observatories use a color code alert level system to describe the state of volcano unrest [111]. One of the biggest challenges in forecasting volcanic eruptions and applying this alert system is assessing the time scale over which an eruption might occur. Here, the terms "forecast" and "prediction" as defined by [112] are used. Long-term forecasts, which address hazards on time scales of decades and centuries, are based on geological mapping of volcanoes and their deposits. Correct forecasts that describe likely hazards on time scales of hours to months based on geophysical and gas monitoring are common. However, reliable short-term predictions which specify the time and size of eruptions are difficult and fraught with complexities, not only in correctly interpreting the physical processes responsible for observations but in the delicacies of communicating with the emergency managers who coordinate societal response.

Almost all volcanic eruptions have earthquakes as precursors, but seismological response to magma ascent can vary significantly in character and in magnitude between volcanic systems. Although many eruptions of VEI 3 or smaller at frequently active volcanoes have only small earthquakes (magnitude (M) less than $\sim$2.5) that may not be noticed without local seismic monitoring (e.g., [113]), large eruptions at volcanoes that erupt infrequently can have large earthquakes.

For example, the 1980 eruption of Mount St. Helens, the 1991 eruption of Pinatubo Volcano, and the 2008 eruption of Kasatochi Volcano all had associated earthquakes of M5.1 or greater [114]. The cataclysmic rhyolitic eruption of Novarupta in 1912, the largest eruption of the twentieth century, was associated with a staggering nine M6.0 and larger earthquakes [115].

Earthquakes at volcanoes often have unique characteristics that are not observed in purely tectonic systems, like the San Andreas Fault in California. The most obvious difference is that earthquakes at volcanoes tend to occur in swarms of many small earthquakes of similar size, as noted above. Unlike on tectonic faults, these earthquakes tend to increase in magnitude and frequency of occurrence with time before an eruption as magmatically driven pressure increases in the Earth's crust. The time history of seismicity is therefore critical in eruption forecasting. Earthquakes at volcanoes can also have distinctive frequency characteristics. LP and VLP earthquakes and volcanic tremor, for example, reflect fluid movement in the Earth's crust (see the "Seismology" section). Kasatochi Volcano, in the central Aleutian Islands, displayed the classic seismological eruption precursor sequence in 2008 [114]. In the 48 h prior to eruption, the rate and magnitude of earthquakes gradually increased, reflecting pressurization in the Earth's crust. In the 2 h prior to eruption and shortly after a M5.8 earthquake, strong volcanic tremor was observed, indicating that the earthquake likely increased permeability in the crust sufficiently for volatiles and magma to ascend rapidly.

Advanced analyses of seismic data, including some techniques described in the "Seismology" section, are actively being explored for eruption forecasting applications. For example, in some situations, real-time high-precision earthquake locations may be useful. In the 2000 eruption of Miyakejima, earthquakes were observed to migrate laterally as a dike was emplaced [116]. In other situations, however, such as the Long Valley caldera of California, earthquake locations can be misleading, as they reflect geothermally active areas and the fluid pathways rather than the location of magma itself.

The value of geodesy as an eruption forecasting tool was emphasized to the volcanological community during the 1980 eruption of Mount St. Helens. Prior to eruption, scientists at the Cascades Volcano Observatory documented a growing bulge on the north flank of the mountain. The eruption began as the bulge failed in an earthquake-induced landslide. The surprising and deadly horizontal blast of pyroclastic material that resulted highlighted the importance of deformation data in determining not only volume of magma intruded into volcanic edifices, but also eruption style and potential edifice collapse. Development of continuous GPS technologies in the late twentieth century made near-real-time deformation monitoring a reality. Later development of InSAR methods further improved the role of geodesy in volcano monitoring by providing spatially complete snapshots of volcano deformation. GPS is now a common component of volcano monitoring networks, although it is still significantly less common than seismic monitoring [117]. Dzurisin [118] describes monitoring strategies in which deformation data may be useful in making longer-term forecasts than are typically possible with seismic data alone.

Although seismic and geodetic monitoring are the most common data streams used in eruption forecasting, many other disciplines provide highly valuable information that can be critically important. For example, explosive eruptions of Bezymianny Volcano (Kamchatka), which generally begin with growth of a new lava dome that subsequently becomes unstable and fails, have been forecasted successfully based solely on thermal satellite data by KVERT (the Kamchatkan Volcanic Eruption Response Team). During the preeruptive stage of the 2009 eruption of Redoubt Volcano, Alaska, CO_2 levels provided one of the most conclusive early indicators that the unrest would advance to full eruption, rather than resulting in a stalled intrusion. Geochemical and physical tephra analyses often provide the first indicator that a juvenile magma is involved in an eruption, a critical indicator to understanding the size and potential explosivity of eruptions.

The challenge in interpreting geologic and geophysical indicators of eruption lies in determining the time scale and type of eruption, or even whether the magmatic activity will result in eruption at all. Earthquake swarms, for example, are common in volcanic and geothermal environments, and at least 2/3 and possibly as many as 9/10 of these do not result in eruption [119]. As magmas ascend, volatile exsolution and crystallization reduce overpressure and buoyancy in the magma body. Thus, most ascending magma bodies stall long before reaching the Earth's surface. Rejuvenation of a stalled magma body often involves an external trigger. Magma can be remobilized by many processes including accumulation of volatiles within the body, interaction of magma with water, a decrease in regional confining stress, or infusions of additional gas-rich magma from depth.

Eruption Forecasting: Case Studies

To demonstrate the variability in eruption precursors, two contrasting eruption case studies managed by the Alaska Volcano Observatory (AVO) are described: the 2006 eruption of Augustine Volcano and the 2008 eruption of Okmok Volcano. Both volcanoes were seismically and geodetically monitored, geologically mapped, and had documented historical eruptions. While the Augustine eruption exemplifies a successful eruption response, the Okmok eruption demonstrates how even thorough volcano monitoring does not guarantee that an eruption can be forecast.

The unrest preceding the 2006 eruption of Augustine Volcano, an andesitic stratovolcano located in the lower Cook Inlet of Alaska, proceeded in a "textbook" manner (see Power et al. [120] for a detailed review of the eruption). Scientists had observed this volcano erupt twice previously in 1976 and 1986, providing a template for interpreting unrest. Conveniently for the volcano observatory staff, the volcano closely followed the 1986 template. An increase in earthquake rate was first noted in late April 2005 (Fig. 19.3; [121]). Subsequently in fall 2005, airborne gas monitoring revealed that SO_2 output increased [122] and GPS monitoring showed that the volcano began to inflate [53]. These data together

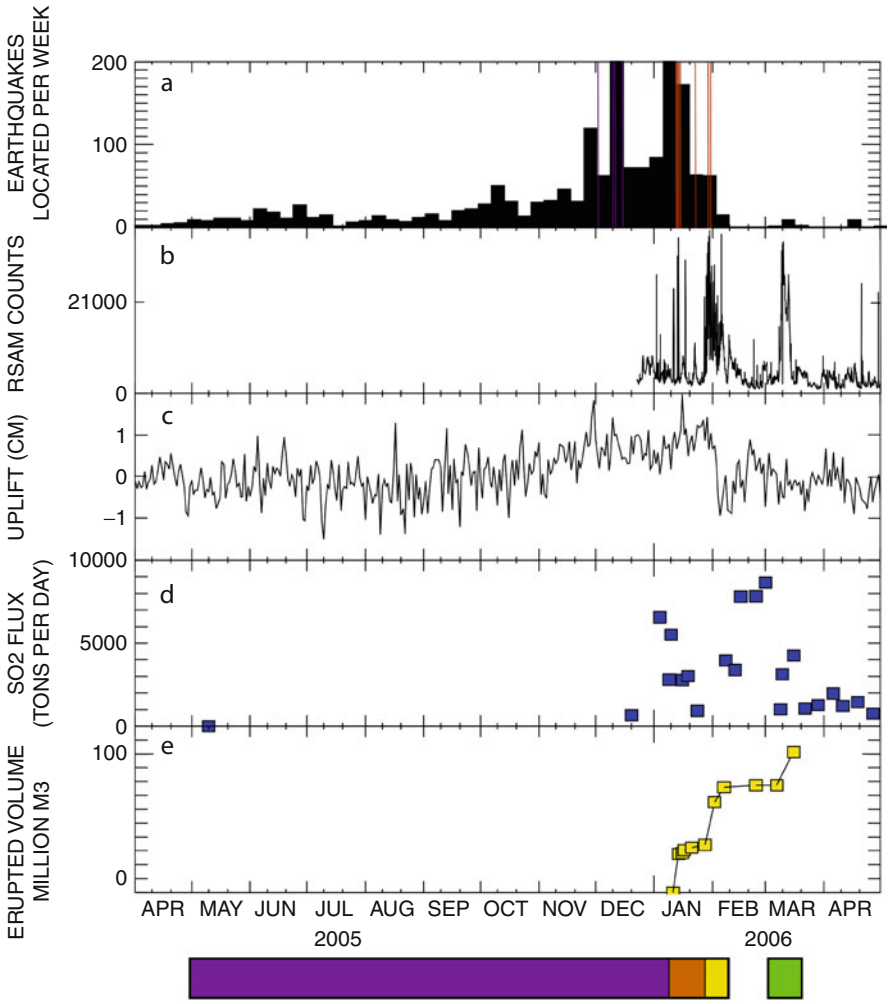

Fig. 19.3 Time history of the 2006 eruption of Augustine volcano, Alaska (From [121] and references therein). (**a**) Number of earthquakes located per week. *Purple* and *red lines* indicate phreatic and magmatic explosions, respectively; (**b**) hourly RSAM (reduced seismic amplitude measurement) from station AU13, indicating overall level of seismicity and tremor; (**c**) Uplift relative to GPS stations A59 and AV02; (**d**) SO_2 flux; and (**e**) erupted volume

strongly suggested that magma was ascending beneath and accumulating within the volcanic conduit. Thus, AVO raised the color code for level of concern from Green to Yellow in late November 2005 (see Neal et al. [123] for a detailed chronology of color codes). On December 2, 2005, the first small phreatic (steam) explosion occurred, presumably as ascending magma interacted with water in the conduit. In response to this event, the color code was raised to Orange. Explosions of this type are often interpreted as "vent clearing" events, as they open the pathway for

new magma to ascend. In the following month, anomalous activity waxed and waned, but continued to increase gradually in severity, until January 11, 2006, when the volcano had its first significant ash-rich explosion of magma, and the color code was raised to Red. This phase of the eruption continued with intermittent explosions for 2 weeks. Subsequently, the volcano effused small amounts of ash nearly continuously for two additional weeks, through early February 2006. The eruption gradually transitioned to effusive lava dome growth as magma was degassed sufficiently to permit more passive eruption of andesitic magma. A lava dome grew at the volcano's summit through mid-March 2006 and the volcano subsequently returned to a quiet state. This series of increased unrest, phreatic explosions, magmatic explosions, and effusion is relatively common in andesitic stratovolcanoes and relatively easy to forecast correctly.

Okmok Volcano, a large caldera located in the eastern Aleutian Islands, had a history of small explosions and basaltic and basaltic-andesite lava flows prior to the 2008 eruption, with the most recent of these in 1997. In the decade between eruptions, earthquakes were rare and volcanic tremor was common enough to be considered background activity for the volcano. GPS and InSAR data revealed that Okmok experienced periods of both inflation and deflation since at least 2000 and was inflating continuously for 6 months prior to eruption [124, 125]. On the morning of July 12, 2008, the volcano was quiet and deformation data revealed no unusual increase in the rate of inflation. However by 11:30 AM AKDT of that day, seismicity ramped up dramatically from quiescence to near constant small earthquakes of $M < 3$ (Fig. 19.4) over a 60 min interval. Phreato-magmatic eruptive activity followed the first earthquake in the series by less than 2 h. In response, AVO raised the color code from Green directly to Red. Unlike previous effusive lava flow eruptions at Okmok Volcano, the 2008 eruption propelled ash into the atmosphere, affecting north Pacific air traffic for several months. Geologic studies of the eruption deposits reveal that the interaction of magma with a large quantity of groundwater likely drove the eruption to be more explosive and ash-rich than previous eruptions at the volcano [126]. Johnson et al. [127] speculate that prior to the eruption, the shallow open magmatic system was able to degas easily, preventing build up of overpressure and earthquakes. Either a subtle addition of melt or sudden contact with water may have triggered the eruption. This scenario is a worst-case example in terms of forecasting. It is arguably the only eruption at a monitored United States volcano with a well-established seismic network that was not forecast since 1989.

Volcano-Earthquake Interactions

Volcanism and large earthquakes near plate margins are two different manifestations of plate tectonics; thus, over time scales of millennia the processes are closely linked. How earthquakes and volcanoes affect one another over shorter

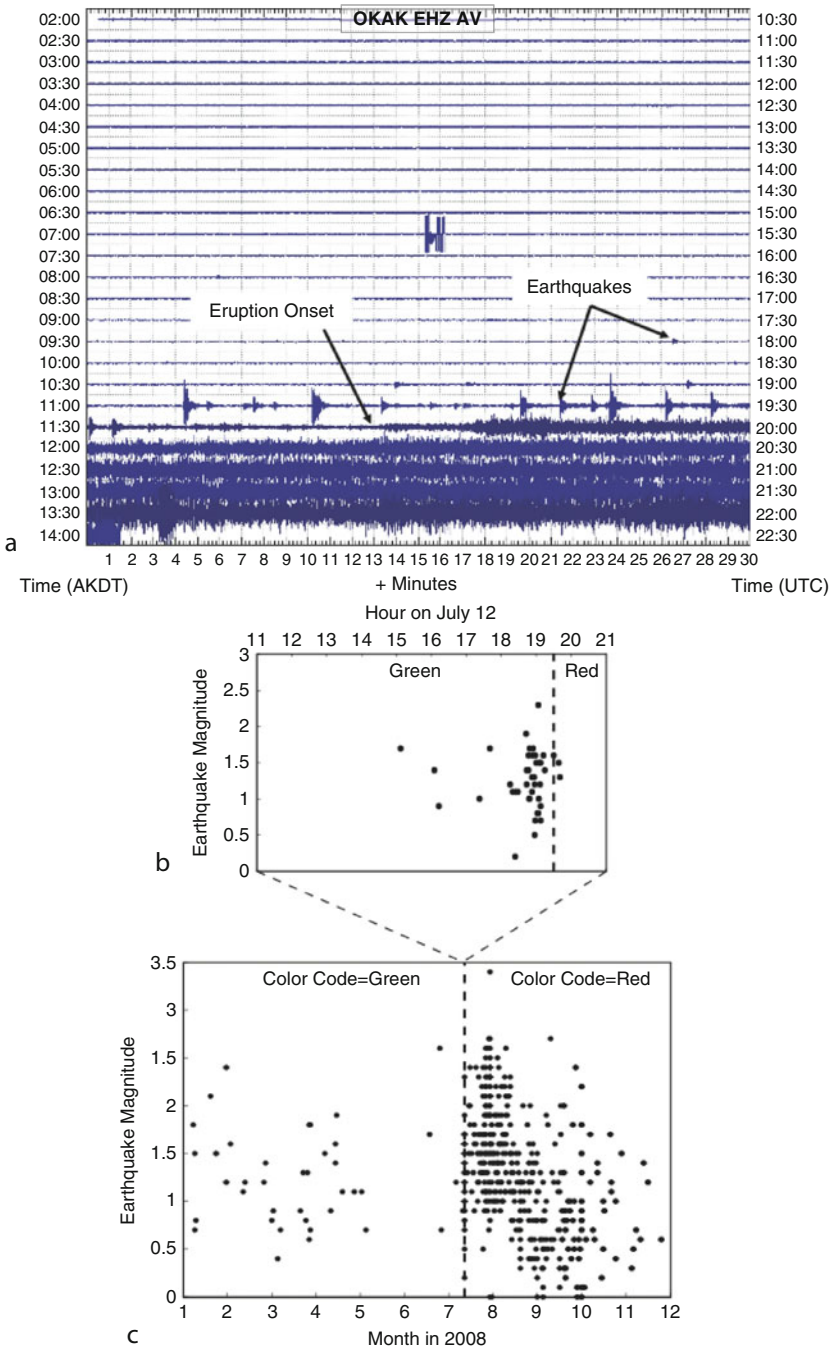

Fig. 19.4 Seismicity related to the 2008 eruption at Okmok caldera, Alaska, from [125]. (**a**) Twelve hours helicorder plot of seismic data from station OKAK, showing quiescence in the hours prior to eruption. (**b**) Located earthquakes over 10 h near the time of eruption onset. (**c**) Located earthquakes at Okmok by the Alaska Volcano Observatory in 2008. *Colors* indicate color code alert level assigned by the Alaska Volcano Observatory

timescales, such as days to months, remains an open and intriguing problem. One frequently asked question in times of crisis is, "can a large earthquake trigger eruption of a nearby volcano?" There are a few compelling examples of eruptions following large earthquakes that suggest a causal relationship between the two, such as the brief eruption of Kīlauea Volcano following the M 7.2 Kalapana Hawaii earthquake in 1975 and the eruption of Puyehue-Cordon Caulle Volcano immediately following the M 9.5 Chile earthquake in 1960. However, it is also true that large earthquakes occur commonly without related eruptions. For example, although the 1964 M9.2 Alaska earthquake occurred in a region with dozens of active volcanoes, the only report of volcanic activity in the subsequent months was a suggestion of increased steaming at Wrangell Volcano, Alaska. Establishing a causal, statistically significant relationship between a large earthquake and a subsequent volcanic eruption is difficult, as it requires an accurate understanding of the probabilities of each event occurring independently. This in turn requires a robust long-term record of eruption and earthquake occurrence, which is rarely available. Studies to date [128–130] suggest that evidence exists for earthquake-triggered eruptions, but it is not a common phenomenon. In the rare occasion where this does occur, there are several possible mechanisms that may explain eruption triggering [131]. Static stress changes in the Earth's crust related to the earthquake may change the confining pressure on a magma reservoir, destabilizing it. Alternatively, high frequency dynamic seismic waves may destabilize the magma by causing bubble nucleation or increasing convection within the reservoir. Finally, violent shaking may cause fractures, landslides, or other changes to the crustal volume surrounding a shallow magma reservoir, leading to eruption.

Large earthquakes commonly affect volcanoes in subtle ways, however. Following the 1992 M 7.3 Landers, California earthquake, volcanic and geothermal areas across the western United States showed an increase in earthquake activity [132]. Since that time, small earthquakes triggered at great distances by surprisingly small amplitude oscillatory seismic waves from large earthquakes ($\leq$0.01 MPa dynamic stress change) have been documented at many areas around the world (see Prejean and Hill [133] for review). Although dynamic triggering of small earthquakes happens in many environments, volcanoes appear to be particularly susceptible to dynamic earthquake triggering [133]. A range of physical models have been proposed to explain how small amplitude dynamic waves trigger earthquakes, including changing fluid pathways in delicate hydrothermal systems, changing the crustal stress field by disrupting magma chambers, and directly exceeding the frictional strength of faults [134]. Most models require very high pore-fluid pressures in the volume where the triggered earthquakes occur.

Volcanoes and Sustainability

The focus of this section is on three direct and immediate connections between volcanoes and sustainability. One is the societal hazard factor – as with other

geologic hazards, population growth puts more and more people at risk for possible volcanic impacts. A second, related impact is eruption effects on aviation, which received global attention in 2010 due to the eruption of Eyjafjallajökull Volcano in Iceland. The third is magmatic activity as a source of geothermal energy. Areas being tapped for commercial-scale geothermal energy are in regions of magmatic activity if not actually on the flanks of a volcano (e.g., the Puna Geothermal Venture on Kilauea). Longer-term connections between volcanoes and sustainability, including climatic effects and connections to ore deposits, are not covered here but are discussed in numerous sources (e.g., [135, 136]).

Volcanoes and Human Population

About 10% of the world's population lives on or near active volcanoes [137], and this percentage is steadily increasing with time. Lockwood and Hazlett [7] estimate that more than 100 million people live in areas near calderas that have been subjected to pyroclastic flows. There have been a number of large eruptions in the past several centuries, but nothing rivaling the very large explosive volcanic eruptions ("super volcanoes") that are present in the geologic record [138], so in historic times, humans have not experienced the full impact that volcanic eruptions can produce. However, the number of eruptions causing fatalities has steadily increased each century since the 1500s, which Simkin et al. [139] attribute to increased global population, as opposed to an increase in the frequency of eruptions.

Quantifying the hazard from volcanic eruptions is certainly a challenge, especially considering the shortness of the historic record in comparison to the frequency of occurrence of large to very large eruptions (centuries to many millennia). Interestingly, eruption size on the VEI scale [8] follows a roughly linear size-log frequency distribution, similar to the Gutenberg-Richter relation for earthquakes. Simkin and Siebert [11] found that VEI 6 eruptions occur about once or twice a century, VEI 5 about once per decade, VEI 4 once or twice a year, etc. Ewert and Harpel [140] combined the global distributions of population and volcanoes to derive a Volcano Population Index (VPI), and applied it to Central America. VPI quantifies the population within 5 (VPI5) or 10 (VPI10) km of a volcanic system, corresponding to eruptions of VEI 2–4. They found that roughly 2.5 million people were at risk as measured by VPI10, and also suggested that only Indonesia might have a larger exposed population than Central America. As in the case of earthquake and tsunami hazards, population centers in harm's way of a possible future eruption are certainly not going to relocate. Mitigation, warning strategies and systems, and education efforts are therefore essential.

Volcanoes and Aircraft

The prolonged eruption of Eyjafjallajökull in Iceland in 2010 is a prime example of the impact volcanic eruptions can have on air travel. That disruption cost airlines billions of dollars [141], and certainly caused additional losses to businesses and people impacted by the shut down in air travel. The most critical hazard is the intake of ash into jet engines, which can severely damage engine parts and potentially cause engine failure. For example, KLM Flight 867, with 245 passengers and crew on board, encountered the ash cloud from the eruption of Alaska's Redoubt Volcano on December 15, 1989, causing all four engines to shutdown. The airplane plunged nearly 15,000 ft before the pilots were able to restart the engines and ultimately land safely, albeit with tens of millions of dollars of damage to the airplane. In the 1980s through the mid 1990s, about one airplane per year experienced damage from volcanic ash on North Pacific air routes [142]. The USGS, along with Alaskan state agencies, established the Alaska Volcano Observatory in 1988 in large part to address the volcanic ash-aircraft problem in that region.

Assessing and monitoring the ash hazard to aircraft requires the application of essentially all the tools available. This includes forecasting, monitoring, and prediction efforts prior to an eruption and 24/7 geophysical monitoring and remote sensing to track eruptive activity and the spread of ash clouds during an eruption. Because volcanic ash from large eruptions can remain in the atmosphere at flight altitudes for weeks or longer, circling the globe multiple times, addressing the hazard requires international cooperation of air traffic controllers, scientists, and weather agencies. As air passenger and cargo air traffic continues to increase globally, the risk will escalate.

Volcanoes and Geothermal Energy

Volcanoes can provide part of the solution to global energy needs, as heat generated inside the Earth can be harnessed for geothermal energy. Although volcanic activity is not required for geothermal energy production in enhanced geothermal systems (EGS), such as that at Soultz-sous-Forets, France, volcanic activity brings heat nearer the Earth's surface, potentially lowering the cost of energy production. The United States is currently the largest producer of geothermal energy [143], although many other countries are developing their own resources. Successful geothermal energy plants located on active volcanoes or above magma chambers are currently in operation in the United States at Kīlauea Volcano in Hawaii, the Long Valley caldera, California, and many other sites in California, Nevada, and Idaho, although in total geothermal sources provided less than a half a percent of the electricity in the US in 2009 [144]. The potential to produce geothermal energy at additional volcanoes in Alaska and the Pacific Northwest is being explored aggressively. Most current geothermal energy operations involve tapping hot ground water. In contrast,

the Geysers, California – the largest geothermal field in the United States – is a dry steam field that taps superheated steam.

A potential risk associated with geothermal power is triggering earthquakes. Generally, earthquakes associated with geothermal production are small ($M < 2$), but occasional larger earthquakes have disrupted communities, most notably in Basel, Switzerland. A second less common but significant risk to geothermal energy production at active volcanoes in Hawaii and Alaska involves eruptions disrupting the energy supplies and potentially destroying infrastructure.

Future Directions

Technological developments to improve and expand observational capabilities are likely to have the greatest impact on the development of volcano studies in the future [145]. An example is the use of autonomous sensor networks [146, 147]. The combination of ease of deployment and networked communication makes such systems extremely appealing for volcano monitoring. Deployment of a constellation of radar satellites with wavelengths that are tuned to "see" through vegetative cover could cut InSAR repeat observation cycles to intervals of days, allowing for high spatial resolution observations of deformation on a time scale of use for eruption forecasting. One can imagine a day when radar satellites detect significant deformation of a volcano anywhere in the world (on land), an autonomous sensor network is deployed rapidly (e.g., [148]), and a team of volcanologists forecasts the activity as the episode of unrest unfolds, comparable to severe storm forecasting.

In closing, the concern that population growth and expanding commercialism (especially air travel) will inexorably lead to increasing impact of volcanic activity on humans, either directly or indirectly, is reiterated. Although volcanoes certainly cannot be controlled, monitoring technologies and strategies for forecasting and predicting their behavior can be effective. It therefore seems clear that increased efforts in volcano monitoring are required to mitigate future risks.

Bibliography

1. Oppenheimer C (2003) Climatic, environmental and human consequences of the largest known historic eruption: Tambora volcano (Indonesia) 1815. Prog Phys Geogr 27:230–259
2. Stothers RB (1984) The great Tambora eruption in 1815 and its aftermath. Science 224:1191–1198
3. Rose WI, Chesner CA (1987) Dispersal of ash in the great Toba eruption, 75 ka. Geology 15:13–917
4. Hough S (2009) Predicting the unpredictable: the tumultuous science of earthquake prediction. Princeton University Press, Princeton
5. White RA, McCausland WA, Lockhart AB (2011) Volcano monitoring: keep it simple – less can be more during volcano crises; 25 years of VDAP experience. Seism Res Lett 82:330

6. Le Bas MJ, Le Maitre RW, Streckeisen A, Zanettin B (1986) A chemical classification of volcanic rocks based on the total alkali-silica diagram. J Petrol 27:745–750
7. Lockwood JP, Hazlett W (2010) Volcanoes – global perspectives. Wiley-Blackwell, Hoboken
8. Newhall CG, Self S (1982) The volcanic explosivity index (VEI): an estimate of explosive magnitude for historical volcanism. J Geophys Res 87:1231–1238
9. Pyle DM (2000) Sizes of volcanic eruptions. In: Sigurdsson H, Houghton BF, McNutt SR, Rymer H (eds) Encyclopedia of volcanoes. Academic Press, San Diego
10. Decker RW (1986) Forecasting volcanic eruptions. Ann Rev Earth Planet Sci 14:267–291
11. Simkin T, Siebert L (1994) Volcanoes of the world. Geoscience, Tucson
12. McNutt SR (1996) Seismic monitoring of volcanoes: a review of the state-of-the-art and recent trends. In: Scarpa R, Tilling R (eds) Monitoring and mitigation of volcano hazards. Springer, Berlin
13. McNutt SR (2000) Seismic monitoring. In: Sigurdsson H, Houghton BF, McNutt SR, Rymer H (eds) Encyclopedia of volcanoes. Academic Press, San Diego
14. Lahr JC, Chouet BA, Stephens CD, Power JA, Page RA (1994) Earthquake classification, location, and error analysis in a volcanic environment: implications for the magmatic system of the 1989–1990 eruptions at Redoubt volcano, Alaska. J Volcanol Geotherm Res 62:137–151
15. Hill DP, Dawson P, Johnston MJS, Pitt AM, Biasi G, Smith K (2002) Very-long-period volcanic earthquakes beneath Mammoth Mountain, California. Geophys Res Lett 29:1370. doi:10.1029/2002GL014833
16. Hotovec AJ, Prejean SG, Vidale JE, Gomberg J (in press) Strongly gliding harmonic tremor during the 2009 eruption of Redoubt volcano. J Volcanol Geotherm Res
17. Chouet B (1985) Excitation of a buried magmatic pipe: a seismic source model for volcanic tremor. J Geophys Res 90:1881–1893
18. Julian B (1994) Volcanic tremor: nonlinear excitation by fluid flow. J Geophys Res 99:11859–11877
19. White RA (1996) Precursory deep long-period earthquakes at Mount Pinatubo: spatial-temporal link to a basaltic trigger. In: Newhall CG, Punongbayan RS (eds) Fire and mud: eruptions and lahars of Mount Pinatubo, Philippines. University of Washington Press, Seattle
20. Power JA, Stihler SD, White RA, Moran SC (2004) Observations of deep long-period (DLP) seismic events beneath Aleutian arc volcanoes; 1989–2002. J Volcanol Geotherm Res 138: 243–26
21. Mavonga T, Zana N, Durrheim RJ (2010) Studies of crustal structure, seismic precursors to volcanic eruptions and earthquake hazard in the eastern provinces of the Democratic Republic of Congo. J Afr Earth Sci 58:623–633. doi:10.1016/j.jafrearsci.2010.08.008, ISSN 1464-343X
22. Harrington RM, Brodsky EE (2007) Volcanic hybrid earthquakes that are brittle-failure events. Geophys Res Lett 34:L06308. doi:10.1029/2006GL028714
23. Kawakatsu H, Ohminato T, Ito H, Kuwahara Y (1992) Broadband seismic observation at the Sakurajima volcano, Japan. Geophys Res Lett 19:1959–1962
24. Kawakatsu H, Ohminato T, Ito H (1994) 10s-period volcanic tremors observed over a wide area in southwestern Japan. Geophys Res Lett 21:1963–1966. doi:10.1029/94GL01683
25. Neuberg J, Luckett R, Ripepe M, Braun T (1994) Highlights from a seismic broadband array on Stromboli volcano. Geophys Res Lett 21:749–752. doi:10.1029/94GL00377
26. Kaneshima S, Kawakatsu H, Matsubayashi H, Sudo Y, Tsutsui T, Ohminato T, Ito H, Uhira K, Yamasato H, Oikawa J, Takeo M, Iidaka T (1996) Mechanism of phreatic eruptions at Aso volcano inferred from near-field broadband seismic observations. Science 273:642–645
27. Ohminato T, Chouet BA, Dawson P, Kedar S (1998) Waveform inversion of very long period impulsive signals associated with magmatic injection beneath Kilauea volcano. J Geophys Res 103:23839–23862. doi:10.1029/98JB01122

28. Arciniega-Ceballos A, Chouet BA, Dawson P (1999) Very long period signals associated with vulcanian explosions at Popocate´petl volcano, Mexico. Geophys Res Lett 26:3013–3016. doi:10.1029/1999GL005390
29. Legrand D, Kaneshima S, Kawakatsu H (2000) Moment tensor analysis of near-field broadband waveforms observed at Aso volcano, Japan. J Volcanol Geotherm Res 101:155–169. doi:10.1016/S0377-0273(00)00167-0
30. Nishimura T, Kobayashi T, Ohtake M, Sato H, Nakamichi H, Tanaka S, Sato M, Ueki S, Hamaguchi H (2000) Source process of very long period seismic events associated with the 1998 activity of Iwate volcano, northeastern Japan. J Geophys Res 105:19135–19147. doi:10.1029/2000JB900155
31. Rowe CA, Aster RC, Kyle PR, Dibble RR, Schlue JW (2000) Seismic and acoustic observations at Mount Erebus volcano, Ross Island, Antarctica, 1994–1998. J Volcanol Geotherm Res 101:105–128. doi:10.1016/S0377-0273(00)00170-0
32. Kumagai H, Ohminato T, Nakano M, Ooi M, Kubo A, Inoue H, Oikawa J (2001) Very-long-period seismic signals and caldera formation at Miyake Island, Japan. Science 293:687–690. doi:10.1126/science.1062136
33. Almendros J, Chouet B, Dawson PB, Bond T (2002) Identifying elements of the plumbing system beneath Kilauea volcano, Hawaii, from the source locations of very-long-period signals. Geophys J Int 148:303–312
34. Hidayat D, Voight B, Chouet B, Dawson P, Ratdomopurbo A (2002) Source mechanism of very-long-period signals accompanying dome growth activity at Merapi volcano, Indonesia. Geophys Res Lett 29. doi:10.1029/2002GL015013
35. Aster R, Mah S, Kyle P, McIntosh W, Dunbar N, Johnson J, Ruiz M, McNamara S (2003) Very long period oscillations of Mount Erebus volcano. J Geophys Res 108:2522. doi:10.1029/2002JB002101
36. Chouet B, Dawson P, Ohminato T, Martini M, Saccorotti G, Giudicepietro F, Luca GD, Milana G, Scarpa R (2003) Source mechanisms of explosions at Stromboli volcano, Italy, determined from moment-tensor inversions of very-long-period data. J Geophys Res 108:2019. doi:10.1029/2002JB001919
37. Chouet B, Dawson P, Arciniega-Ceballos A (2005) Source mechanism of Vulcanian degassing at Popocate´petl volcano, Mexico, determined from waveform inversions of very long period signals. J Geophys Res 110:B07301. doi:10.1029/2004JB003524
38. Waite GP, Chouet BA, Dawson PB (2008) Eruption dynamics at Mount St. Helens imaged from broadband seismic waveforms: interaction of the shallow magmatic and hydrothermal systems. J Geophys Res 113:B02305. doi:10.1029/2007JB005259
39. Hill DP (1977) A model for earthquake swarms. J Geophys Res 82:1347–1352. doi:10.1029/JB082i008p01347
40. Foulger GR, Julian BR, Pitt AM, Hill DP, Malin P, Shalev E (2003) Three-dimensional crustal structure of Long Valley Caldera, California, and evidence for the migration of CO_2 under Mammoth Mountain. J Geophys Res 108:B3. doi:10.1029/2000JB000041
41. Patanè D, Barberi G, Cocina O, De Gori P, Chiarabba C (2006) Time resolved seismic tomography detects magma intrusions at Mount Etna. Science 313:821–823
42. Titzschkau T, Savage M, Hurst T (2010) Changes in attenuation related to eruptions of Mt. Ruapehu volcano, New Zealand. J Volcanol Geotherm Res 190:168–178
43. De Gori P, Chiarabba C, Giampiccolo E, Martinez-Arevalo C, Patane D (2011) Body wave attenuation heralds incoming eruptions at Mount Etna. Geology 39:503–506
44. Miller V, Savage M (2001) Changes in seismic anisotropy after volcanic eruptions: evidence from Mount Ruapehu. Science 293:2231–2233
45. Patanè D, De Gori P, Chiarabba C, Bonaccorso A (2003) Magma ascent and the pressurization of Mount Etna's volcanic system. Science 299:2061–2063
46. Volti T, Crampin S (2003) A four-year study of shear-wave splitting in Iceland: 2. Temporal changes before earthquakes and volcanic eruptions. In: Nieuwland DA (ed) New insights into

structural interpretation and modeling, Geological Society of London, Special Publication 212. Geological Society, London, pp 135–149
47. Musumeci C, Cocina O, De Gori P, Patanè D (2004) Seismological evidence of stress induced by dike injection during the 2001 Mt Etna eruption. Geophys Res Lett 31:L07617. doi:10.1029/2003GL019367
48. Bianco F, Scarfì L, Del Pezzo E, Patanè D (2006) Shear wave splitting changes associated with the 2001 volcanic eruption on Mt. Etna. Geophys J Int 167:959–967
49. Roman DC, Savage MK, Arnold R, Latchman JL, De Angelis S (2011) Analysis and forward modeling of seismic anisotropy during the ongoing eruption of the Soufrière Hills volcano, Montserrat, 1996–2007. J Geophys Res 116:B03201. doi:10.1029/2010JB007667
50. Brenguier F, Shapiro N, Campillo M, Ferrazzini V, Duputel Z, Coutant O, Nercessian A (2008) Towards forecasting volcanic eruptions using seismic noise. Nat Geosci 1:126–130
51. Poland M, Hamburger M, Newman A (2006) The changing shapes of active volcanoes: history, evolution, and future challenges for Volcano Geodesy. J Volcanol Geotherm Res 150:1–13
52. Dzurisin D (2007) Volcano deformation: geodetic monitoring techniques. Springer, Berlin
53. Cervelli PF, Fournier TJ, Freymueller JT, Power JA, Lisowski M, Pauk BA (2010) Geodetic constraints on magma movement and withdrawal during the 2006 eruption of Augustine volcano. In: Power JA, Coombs ML, Freymueller JT (eds) The 2006 eruption of Augustine volcano, Alaska, U.S. Geological Survey Professional Paper 1769. U.S. Geological Survey, Reston, pp 427–452
54. Dow JM, Neilan RE, Rizos C (2009) The International GNSS service in a changing landscape of Global Navigation Satellite Systems. J Geodesy 83:191–198. doi:10.1007/s00190-008-0300-3
55. Massonnet D, Rossi M, Carmona C, Adragna F, Peltzer G, Feigl K, Rabaute T (1993) The displacement field of the Landers earthquake mapped by radar interferometry. Nature 364:138–142
56. Massonnet D, Briole P, Arnaud A (1995) Deflation of Mount Etna monitored by spaceborne radar interferometry. Nature 375:567–570
57. Thatcher W, Massonnet D (1997) Crustal deformation at Long Valley Caldera, eastern California, 1992–1996 inferred from satellite radarinterferometry. Geophys Res Lett 24:2519–2522
58. Wicks C Jr, Thatcher W, Dzurisin D (1998) Migration of fluids Beneath Yellowstone Caldera inferred from satellite radar interferometry. Science 282:458–462
59. Sigmundsson F, Durand P, Massonnet D (1999) Opening of an eruptive fissure and seaward displacement at Piton de la Fournaise volcano measured by RADARSAT satellite radar interferometry. Geophys Res Lett 26:533–536
60. Lu Z, Fatland R, Wyss M, Li S, Eichelberer J, Dean K, Freymueller J (1997) Deformation of New Trident volcano measured by ERS-1 SAR interferometry, Katmai National Park, Alaska. Geophys Res Lett 24:695–698
61. Lu Z, Mann D, Freymueller JT, Meyer DJ (2000) Synthetic aperture radar interferometry of Okmok volcano, Alaska: radar observations. J Geophys Res Solid Earth 105:10791–10806
62. Lu Z, Wicks C, Dzurisin D, Thatcher W, Freymueller JT, McNutt SR, Mann D (2000) Aseismic inflation of Westdahl volcano Alaska, revealed by satellite radar interferometry. Geophys Res Lett 27:1567–1570
63. Lu Z, Wicks C, Power JA, Dzurisin D (2000) Ground deformation associated with the March 1996 earthquake swarm at Akutan volcano Alaska, revealed by satellite radar interferometry. J Geophys Res 105:21483–21495
64. Lu Z, Power JA, McConnell VS, Wicks C, Dzurisin D (2002) Preeruptive inflation and surface interferometric coherence characteristics revealed by satellite radar interferometry at Makushin volcano, Alaska: 1993–2000. J Geophys Res 107:B11
65. Lu Z, Masterlark T, Power J, Dzurisin D, Wicks C (2002) Subsidence at Kiska volcano, Western Aleutians, detected by satellite radar interferometry. Geophys Res Lett 29:18

66. Jonsson S, Zebker K, Cervelli P, Segall P, Garbeil H, Mouginis-Mark P, Rowland S (1999) A shallow-dipping dike fed the 1995 flank eruption at Fernandina volcano, Galapagos, observed by satellite radar interferometry. Geophys Res Lett 26:1077–1080
67. Amelung F, Oppenheimer C, Segall P, Zebker H (2000) Ground deformation near Gada 'Ale volcano, Afar, observed by radar interferometry. Geophys Res Lett 27:3093–3096
68. Pritchard ME, Simons M (2002) A satellite geodetic survey of large-scale deformation of volcanic centres in the central Andes. Nature 418:167–171
69. Goldstein RM, Zebker HA, Werner CL (1988) Satellite radar interferometry – two-dimensional phase unwrapping. Radio Sci 23:713–720
70. Gens R (2003) Two-dimensional phase unwrapping for radar interferometry: developments and new challenges. Int J Remote Sens 24:703–710
71. Sturkell E, Einarsson P, Sigmundsson F, Geirsson H, Olafsson H, Pedersen R, de Zeeuw-van Dalfsen E, Linde AT, Sacks SI, Stefansson R (2006) Volcano geodesy and magma dynamics in Iceland. J Volcanol Geotherm Res 150:14–34
72. Rymer H (1996) Microgravity monitoring. In: Scarpa R, Tilling R (eds) Monitoring and mitigation of volcano hazards. Springer, Berlin
73. Battaglia M, Hill D (2009) Analytical modeling of gravity changes and crustal deformation at volcanoes: the Long Valley Caldera (CA) case study. Tectonophysics 471:45–57
74. Williams-Jones G, Rymer H, Mauri G, Gottsmann J, Poland M, Carbone D (2008) Toward continuous 4D microgravity monitoring of volcanoes. Geophysics 73:WA19–WA28
75. Carbone D, Budettaa G, Greco F, Rymer H (2003) Combined discrete and continuous gravity observations at Mount Etna. J Volcanol Geotherm Res 123:123–135
76. Symonds RB, Gerlach TM, Reed MH (2001) Magmatic gas scrubbing: implications for volcano monitoring. J Volcanol Geotherm Res 108:303–341
77. Doukas MP, Gerlach TM (1995) Sulfur dioxide scrubbing during the 1992 eruption of Crater Peak, Mount Spurr, Alaska. In: Keith T (ed) The 1992 eruptions of Crater Peak Vent, Mount Spurr Volcano, Alaska, U.S. Geological Survey Bulletin B-2139. U.S. G.P.O.: U.S. Dept. of the Interior, US Geological Survey, Washington, DC, pp 47–57
78. Aiuppa A, Moretti R, Federico C, Giudice G, Gurrieri S, Liuzzo M, Papale P, Shinohara H, Valenza M (2007) Forecasting Etna eruptions by real-time observation of volcanic gas composition. Geology 35:1115–1118
79. Werner C, Kelly PJ, Doukas M, Lopez T, Pfeffer M, McGimsey RG, Neal CA (in press) Degassing associated with the 2009 eruption of Redoubt volcano, Alaska. J Volcanol Geotherm Res (Special Issue on the 2009 Redoubt Eruption)
80. Francis P, Horrocks L, Oppenheimer C (2000) Monitoring gases from andesite volcanoes. Philos Trans Math Phys Eng Sci 358:1567–1584
81. Edmonds M (2008) New geochemical insights into volcanic degassing. Philos Trans Math Phys Eng Sci 366:4559–4579
82. Moran SC, Freymueller JT, LaHusen RG, McGee KA, Poland MP, Power JA, Schmidt DA, Schneider DJ, Stephens G, Werner CA, White RA (2008) Instrumentation recommendations for volcano monitoring at US volcanoes under the National Volcano Early Warning System. USGS Scientific Investigations Report 2008–5114
83. Dean KG, Dehn J, Engle K, Izbekov P, Papp K (2002) Operational satellite monitoring of volcanoes at the Alaska Volcano Observatory. In: Harris AJH, Wooster M, Rothery DA (eds) Monitoring volcanic hotspots using thermal remote sensing. Adv Environ Monit Model 1:70–97
84. Mouginis-Mark PJ, Crisp JA, Fink JH (eds) (2000) Remote sensing of active volcanism, AGU Geophysical Monograph 116. American Geophysical Union, Washington, DC
85. Prata J (1989) Observations of volcanic ash clouds in the 10–12 μm window using AVHRR/2 data. Int J Remote Sens 10:751–761
86. Corradini S, Merucci L, Prata AJ, Piscini A (2010) Volcanic ash and SO_2 in the 2008 Kasatochi eruption: retrievals comparison from different IR satellite sensors. J Geophs Res 115:D00L21. doi:10.1029/2009JD013634

87. Schneider DJ, Dean KG, Dehn J, Miller TP, Kirianov VY (2000) Monitoring and analysis of volcanic activity using remote sensing data at the Alaska Volcano Observatory: case study for Kamchatka, Russia, December 1997. In: Mouginis-Mark PJ, Crisp JA, Fink JH (eds) Remote sensing of active volcanism, AGU Geophysical Monograph 116. American Geophysical Union, Washington, DC
88. Zehner E (2010) Monitoring volcanic ash from space. European Space Agency, Noordwijk, p 110
89. Schneider DJ, Vallance JW, Wessels RL, Logan M, Ramsey MS (2008) Use of thermal infrared imaging for monitoring renewed dome growth at Mount St. Helens, 2004. In: Sherrod DR, Scott WE, Stauffer PH (eds) A volcano rekindled; the renewed eruption of Mount St. Helens, 2004–2006, U.S. Geological Survey Professional Paper 1750. U.S. Dept. of the Interior, U.S. Geological Survey, Reston, p 856 and DVD-ROM [http://pubs.usgs.gov/pp/1750/]
90. Wessels RL, Coombs ML, Schneider DJ, Dehn J, Ramsey MS (2010) High-resolution satellite and airborne thermal infrared imaging of the 2006 eruption of Augustine volcano. In: Power JA, Coombs ML, Freymueller JT (eds) The 2006 eruption of Augustine volcano, Alaska, U.S. Geological Survey Professional Paper 1769. U.S. Geological Survey, Reston, pp 527–552
91. Patrick MR, Harris AJL, Ripepe M, Dehn J, Rothery DA, Calvari S (2007) Strombolian explosive styles and source conditions: insights from thermal (FLIR) video. Bull Volcanol 69:769–784
92. Krueger AJ, Schaefer SJ, Krotkov N, Bluth G, Barker S (2000) Ultraviolet remote sensing of volcanic emissions. In: Mouginis-Mark PJ, Crisp JA, Fink JH (eds) Remote sensing of active volcanism, AGU Geophysical Monograph 116. American Geophysical Union, Washington, DC
93. Carn SA, Krueger AJ, Krotkov NA, Yang K, Evans K (2009) Tracking volcanic sulfur dioxide clouds for aviation hazard mitigation. Nat Hazard 51:325–343
94. McNutt SR, Williams ER (2010) Volcanic lightening: global observations and constraints on source mechanisms. Bull Volcanol 72:1153–1167
95. Schilling SP, Thompson RA, Messerich JA, Iwatsubo EY (2008) Use of digital aerophotogrammerty to determine rates of lava dome growth, Mount St. Helens, Washington, 2004–2005. In: Sherrod DR, Scott WE, Stauffer PH (eds) A volcano rekindled; the renewed eruption of Mount St. Helens, 2004–2006, U.S. Geological Survey Professional Paper 1750. U.S. Dept. of the Interior, U.S. Geological Survey, Reston, p 856 and DVD-ROM [http://pubs.usgs.gov/pp/1750/]
96. Garces MA, Iguchi M, Ishihara K, Morrissey M, Sudo Y, Tsutsui T (1999) Infrasonic precursors to a Vulcanian eruption at Sakurajima volcano, Japan. Geophys Res Lett 26:2537–2540
97. Johnson JB (2003) Generation and propagation of infrasonic airwaves from volcanic explosions. J Volcanol Geotherm Res 121:1–14
98. Johnson JB, Aster RC, Ruiz MC, Malone SD, McChesney PJ, Lees JM, Kyle PR (2003) Interpretation and utility of infrasonic records from erupting volcanoes. J Volcanol Geotherm Res 121:15–63
99. Matoza RS, Fee D, Garces MA, Seiner JM, Ramon PA, Hedlin MAH (2009) Infrasonic jet noise from volcanic eruptions. Geophys Res Lett 36. doi:1029/2008GL036486
100. Caplan-Auerbach J, Bellesiles A, Fernandes JK (2010) Estimates of eruption velocity and plume height from infrasonic recordings of the 2006 eruption of Augustine volcano, Alaska. J Volcanol Geotherm Res 189:12–18
101. Blong R (1996) Volcanic hazards risk assessment. In: Scarpa R, Tilling R (eds) Monitoring and mitigation of volcano hazards. Springer, Berlin
102. Annen C, Wagner J-J (2003) The impact of volcanic eruptions during the 1990s. Nat Hazard Rev 4:169–175
103. Hoblitt RP, Miller CD, Scott WE (1987) Volcanic hazards with regard to siting nuclear-power plants in the Pacific Northwest. U.S. Geological Survey Open-File Report 87-297

104. Siebert L (1996) Hazards of large debris avalanches. In: Scarpa R, Tilling R (eds) Monitoring and mitigation of volcano hazards. Springer, Berlin
105. Ewert JW, Murray T, Lockhart A, Miller C (1993) Preventing volcanic catastrophe: the U. S. International Volcano Disaster Assistance Program. Earthq Volcanoes 24:270–291
106. Wright TL, Pierson TC (1992) Living with volcanoes: The U. S. Geological Survey's Volcano Hazards Program, USGS Circular 1973. United States Government Printing Office, Washington, DC
107. Alvarado GE, Soto GJ, Schmincke H-U, Blge LL, Sumita M (2006) The 1968 andesitic lateral blast eruption at Arenal volcano, Costa Rica. J Volcanol Geotherm Res 157:9–33
108. Fisher RV, Heiken G, Hulen J (1998) Volcanoes: crucibles of change. Princeton University Press, Princeton
109. Holloway M (2000) The killing lakes. Sci Am 283:92–99
110. Sutton AJ, Elias T (1993) Volcanic gases create air pollution on the Island of Hawai'i: U.S. Geological Survey. Earthq Volcanoes 24:178–196
111. Gardner CA, Guffanti MC (2006) U.S. Geological Survey's alert notification system for volcanic activity. U.S. Geological Survey Fact Sheet 2006-3139p
112. Swanson DA, Casadevall TJ, Dzurisin D, Holcomb RT, Newhall CG, Malone SD, Weaver CS (1985) Forecasts and predictions of eruptive activity at Mount St. Helens, USA: 1974–1984. Science 3:397–423
113. Power JA, Jolly A, Nye C, Harbin M (2002) A conceptual model of the Mount Spurr magmatic system from seismic and geochemical observations of the 1992 Crater Peak eruption sequence. Bull Volcanol 64:206–218
114. Ruppert NA, Prejean S, Hansen RA (2011) Seismic swarm associated with the 2008 eruption of Kasatochi volcano, Alaska: earthquake locations and source parameters. J Geophys Res 116:B00B07. doi:10.1029/2010JB007435
115. Abe K (1992) Seismicity of the caldera-making eruption of Mount Katmai, Alaska in 1912. Bull Seismol Soc Am 82:175–191
116. Japan Meteorological Agency (JMA) (2000) Recent seismic activity in the Miyakejima and Niijima-Kozushima region, Japan – the largest earthquake swarm ever recorded. Earth Planets Space 52:i–iv
117. Guffanti M, Diefenbach AK, Ewert JW, Ramsey DW, Cervelli PF, Schilling SP (2008) Volcano-monitoring instrumentation in the United States, 2008. USGS Open-File Report 2009-1165
118. Dzurisin D (2003) A comprehensive approach to monitoring volcano deformation as a window on the eruption cycle. Rev Geophys 41:1–29
119. Benoit JP, McNutt SR (1996) Global volcanic earthquake swarm database and preliminary analysis of volcanic earthquake swarm duration. Annali de Geofisca 39:221–229
120. Power JA, Coombs ML, Freymueller JT (eds) (2010) The 2006 eruption of Augustine volcano, Alaska, U.S. Geological Survey Professional Paper 1769. U.S. Geological Survey, Reston
121. Power JA, Lalla DJ (2010) Seismic observations of Augustine volcano, 1970–2007. In: Power JA, Coombs ML, Freymueller JT (eds) The 2006 eruption of Augustine volcano, Alaska, U.S. Geological Survey Professional Paper 1769. U.S. Geological Survey, Reston, pp 527–552
122. McGee KA, Doukas MP, McGimsey RG, Neal CA, Wessels RL (2010) Emission of SO_2, CO_2, and H_2S from Augustine volcano, 2002–2008. In: Power JA, Coombs ML, Freymueller JT (eds) The 2006 eruption of Augustine volcano, Alaska, U.S. Geological Survey Professional Paper 1769. U.S. Geological Survey, Reston, pp 609–630
123. Neal CA, Murray TL, Power JA, Adleman JN, Whitmore PM, Osiensky JM (2010) Hazard information management, interagency coordination, and impacts of the 2005–2006 eruption of Augustine volcano. In: Power JA, Coombs ML, Freymueller JT (eds) The 2006 eruption of Augustine volcano, Alaska, U.S. Geological Survey Professional Paper 1769. U.S. Geological Survey, Reston, pp 645–667

124. Freymueller JT, Kaufman AM (2010) Changes in the magma system during the 2008 eruption of Okmok volcano, Alaska, based on GPS measurements. J Geophys Res 115: B12415, 14 pp. doi:10.1029/2010JB007716
125. Lu Z, Dzurisin D, Biggs Wicks JC Jr, McNutt S (2010) Ground surface deformation patterns, magma supply, and magma storage at Okmok volcano, Alaska, from InSAR analysis: 1. Intereruption deformation, 1997–2008. J Geophys Res 115:B00B02. doi:10.1029/2009JB006969
126. Larsen J, Neal C, Webley P, Freymueller J, Haney M, McNutt S, Schneider D, Prejean S, Schaefer J, Wessels R (2009) Eruption of Alaska volcano breaks historic pattern. Eos Trans Am Geophys Union 90:173–174
127. Johnson JH, Prejean S, Savage MK, Townend J (2010) Anisotropy, repeating earthquakes, and seismicity associated with the 2008 eruption of Omok volcano, Alaska. J Geophs Res 115. doi:10;1029/2009JB006991
128. Linde AT, Sacks IS (1998) Triggering of volcanic eruptions. Nature 395:888–890
129. Manga M, Brodsky EE (2006) Seismic triggering of eruptions in the far field: volcanoes and geysers. Annu Rev Earth Planet Sci 34:263–291
130. Walter TR, Amelung F (2007) Volcanic eruptions following M > = 9 megathrust earthquakes: implications of the Sumatra-Andaman volcanoes. Geology 35:539–542
131. Hill DP, Pollitz F, Newhall C (2002) Earthquake-volcano interactions. Phys Today 55:41–47
132. Hill DP, Reasenberg PA, Michael AJ, Arabasz WJ, Beroza GC (1993) Seismicity remotely triggered by the magnitude 7.3 Landers, California earthquake. Science 260:1617–1623
133. Prejean SG, Hill DP (2009) Earthquakes, dynamic triggering of. In: Encyclopedia of complexity and system science, editor in-cheif Meyers RA. Complexity in earthquakes, tsunamis, and volcanoes, and forecast, Lee WHK (ed). Springer, Berlin
134. Spudich P, Steck LK, Hellweg M, Fletcher JB, Baker LM (1992) Transient stresses at Parkfield, California, produced by the M 7.4 Landers earthquake of June 28, 1992: observations from the UPSAR dense seismograph array. J Geophys Res 100:675–690. doi:10.1029/94JB02477
135. McGee KA, Doukas MP, Kessler R, Gerlach TM (1997) Impacts of volcanic gases on climate, the environment, and people. U.S. Geological Survey Open-File 97-262
136. Robb LJ (2005) Introduction to ore-forming processes. Blackwell Science, Carlton
137. Peterson DW (1996) Mitigation measures and preparedness plans for volcanic emergencies. In: Scarpa R, Tilling R (eds) Monitoring and mitigation of volcano hazards. Springer, Berlin
138. Self S (2006) The effects and consequences of very large explosive volcanic eruptions. Philos Trans R Soc A 364:2073–2097
139. Simkin T, Siebert L, Blong R (2001) Volcano fatalities: lessons from the historical record. Science 291:255
140. Ewert JW, Harpel CJ (2004) In harm's way: population and volcanic risk. Geotimes 49:14–17
141. International Air Travel Association (2010) Volcano crisis cost airlines $1.7 billion in revenue – IATA urges measures to mitigate impact, IATA press release
142. USGS (1997) Volcanic ash – danger to aircraft in the North Pacific. U.S. Geological Survey Fact Sheet 030-97
143. Geothermal Energy Association (2010) Geothermal energy: international market update, 7 pp
144. U.S. Energy Information Administration (2009) Annual Energy Review
145. Ewert JW, Guffanti M, Murray TL (2005) An assessment of volcanic threat and monitoring capabilities in the United States: framework for a National Volcano Early Warning System. USGS Open-File Report 2005-1164
146. Song W-Z, Shirazi B, Huang BR, Xu M, Peterson N, LaHusen R, Pallister J, Dzurisin D, Moran S, Lisowski M, Kedar S, Chien S, Webb F, Kiely A, Doubleday J, Davies A, Pieri D (2010) Optimized autonomous space in-situ sensor web for volcano monitoring. IEEE J Sel Topics Appl Earth Observ Remote Sens 3:541–546
147. Fleming K, Picozzi M, Milkereit C, Kuehnlenz F, Lichtblau B, Fischer J, Zulfikar C, Oezel O, Zschau J, Veit I, Jaeckel KH, Hoenig M, Nachtigall J, Woith H, Redlich JP, Ahrens K,

Eveslage I, Heglmeier S, Erdik M, Kafadar N (2009) The self-organizing seismic early warning information network (SOSEWIN). Seismol Res Lett 80:755–771

148. Huang R, Song W-Z, Xu M, Picone N, Shirazi B, LaHusen R (2011) Real-world sensor network for long-term volcano monitoring: design and findings. IEEE Trans Parallel Distrib Syst 99, doi:10.1109/TPDS.2011.170

Index

J. Orcutt (ed.), *Earth System Monitoring: Selected Entries from the Encyclopedia of Sustainability Science and Technology*, DOI 10.1007/978-1-4614-5684-1,